UC Berkeley
UC Berkeley Electronic Theses and Dissertations

Title
Microfluidic Circuitry via Additive Manufacturing

Permalink
https://escholarship.org/uc/item/4gv121n2

Author
Glick, Casey Carter

Publication Date
2017

Peer reviewed|Thesis/dissertation

eScholarship.org Powered by the California Digital Library
University of California

Microfluidic Circuitry via Additive Manufacturing

by

Casey Carter Glick

A dissertation submitted in partial satisfaction of the

requirements for the degree of

Doctor of Philosophy

in

Physics

in the

Graduate Division

of the

University of California, Berkeley

Committee in charge:

Professor Liwei Lin, Co-chair
Professor Robert Jacobsen, Co-chair
Assistant Professor Gabriel Orebi Gann
Professor Dorian Liepmann

Spring 2017

Microfluidic Circuitry via Additive Manufacturing

Copyright 2017
by
Casey Carter Glick

Abstract

Microfluidic Circuitry via Additive Manufacturing
by
Casey Carter Glick
Doctor of Philosophy in Physics
University of California, Berkeley
Professor Liwei Lin, Co-Chair
Professor Robert Jacobsen, Co-Chair

Microfluidics, the science and engineering of fluid at small scales, affords numerous benefits for applications in chemistry and biology, including rapid reaction rates, reaction uniformity and precision, and reagent minimization but the technology remains limited by the availability of appropriate control mechanisms and related microfluidic components. Microfluidic devices have traditionally been fabricated using soft-lithography, which is time-consuming, costly, and reliant on extensive facilities. Over the past decade, research has shifted towards developing alternate methods such as additive manufacturing (widely known as three-dimensional (3D) printing) to fabricate microfluidic structures. This dissertation has developed three methods for resolving the fabrication and control problems of microfluidics using a combination of standard microfluidic/MEMS techniques with newer 3D printing techniques: optofluidic lithographic microfluidic circuitry, 3D-printed transfer molding, and fully-3D-printed fluidic circuitry.

The basic theory of microfluidic control systems, including the hydraulic analogy and fluidic circuitry, the low Reynolds number approximation to the Navier-Stokes equations, and neglectable terms in microfluidic models are first investigated. Optofluidic lithography, where photocurable liquids are selectively solidified under UV exposure, is utilized as a means of fabricating moving microfluidic structures within a microchannel. Several variants of microfluidic control mechanisms are demonstrated, including current sources (for regulation of fluid flow-rates to 29.2 ± 0.8 μL/min for pressures from $5-10$ kPa), and microfluidic gain valves (for controlling a high-pressure channel with a low-pressure one to achieve a dynamic gain of 6.30 ± 0.23).

A hybrid manufacturing process, where 3D printed polymer molds are used to make multi-layer PDMS constructions by employing unique molding, bonding, alignment, and rapid assembly processes. Specifically, a novel single-layer, two-sided molding method is developed to realize two channels levels, non-planar membranes/valves, vertical interconnects (vias) between channel levels, and built-in inlet/outlet ports for fast linkages to external fluidic systems. As a demonstra-

tion, a single-layer membrane micro-valve is constructed, dramatically reducing the number of fabrication steps. Additionally, multilayer structures are fabricated through an intra-layer bonding procedure which uses custom 3D printed stamps to selectively apply uncured liquid PDMS adhesive only to bonding interfaces without clogging fluidic channels. Using built-in alignment marks to accurately position both stamps and individual layers, this technique is demonstrated by rapidly assembling a six-layer microfluidic device.

By using the multi-jet-based additive manufacturing, fully-3D-printed microfluidic circuitry components are demonstrated, including fluidic resistors, capacitors, diodes (for a diodicity of 80.6 ± 1.8), and transistors (for a dynamic pressure gain of 3.01 ± 0.78) through the combination of experimental, simulation, and analytical methods, which are integrated complex microfluidic circuits, such as half- and full-wave microfluidic rectifiers. The hydraulic analogy circuitry exhibits similar transfer functions to its electronic counterparts, but ultimately behaves more similarly to vacuum triodes than to actual transistors. When combined with fully-realized microfluidic IF-gate and CMOS-analog components, this research may allow for fabrication of analog microfluidic operational-amplifiers, which could allow for fully-analog control of microfluidic systems using high-gain amplification of small pressure signals, and the CAD-based nature of the design process makes it simple for researchers to readily combine multiple microfluidic components into larger integrated microfluidic circuit networks.

For Desi Cowan

To whom I was “Professor” by age six, and would have used this dissertation as an excuse to call me “Doctor Casey” at every opportunity;

Carolyn “Grammie” Bradley

Who taught me to love beautiful words precisely spoken, that while there are many things I *may not* do, there is nothing I *cannot*;

and Eugene “Grandpa” Glick and Ruth “Grandma” Glick

Who gave me music, creative cookery, and an unwavering example of how to be both a successful person and a *good* one.

Contents

List of Figures **vii**

List of Tables **x**

Acknowledgments **xii**

1 Introduction **1**

1.1 Microfluidic Fabrication Techniques . . . 3
1.1.1 Standard Microfluidic Soft-Lithography Fabrication . . . 3
1.1.2 Microfluidics via Additive Manufacturing . . . 5
1.1.2.1 Additive Manufacturing Approaches for Microfluidics . . . 5
1.1.2.2 Fused Deposition Modeling . . . 5
1.1.2.3 Stereolithography . . . 7
1.1.2.4 Selective Laser Sintering . . . 8
1.1.2.5 Multijet Modeling . . . 8
1.1.2.6 Laminated object manufacturing . . . 9
1.1.3 Microfluidic Systems via 3D-Printed Transfer Molding . . . 9
1.2 Microfluidic Systems with Integrated Microelectronics . . . 11
1.2.1 Fabrication of Microfluidic Systems with Integrated Electronics . . . 11
1.2.2 Applications of Microfluidic Systems with Integrated Electronics . . . 14
1.3 Microelectronics via 3D Printing . . . 15
1.3.1 Microelectronics via FDM . . . 15
1.3.2 Microelectronics via SLA . . . 16
1.3.3 Microelectronics via MJM . . . 16
1.4 Pneumatic and Pressure-controlled Microfluidics . . . 17
1.5 Notation and Naming Conventions . . . 20

2 Microfluidic Theory **21**
2.1 The Hydraulic Analogy . . . 21
2.1.1 Hydraulic Analogy Circuit Elements . . . 23
2.1.1.1 Resistance . . . 23
2.1.1.2 Capacitance . . . 24
2.1.1.3 RC Time Constant . . . 25
2.1.1.4 Inductance . . . 26
2.1.1.5 Neglecting Fluidic Inductance . . . 26
2.2 Unidirectional Flows . . . 28
2.2.1 Reducing Thin-Film Flow to Thin Film/Unidirectional Form . . . 32
2.2.2 Unidirectional Flow in Rectangular Channel . . . 36
2.3 Low *Re* Flows in a Differentially Rotating Tube . . . 41

3 Microfluidic Circuitry via Optofluidic Lithography **46**
3.1 Introduction . . . 46
3.2 Fabrication . . . 47
3.3 Analysis: Flow Behavior in Narrow Gap with Moving Plate . . . 48
3.3.1 Poiseuille-Couette Flow Solution . . . 50
3.3.2 Piston Force Balance . . . 54
3.3.3 Piston Solutions for Distinct Pressure Inputs . . . 57
3.3.3.1 Pressure Step Input . . . 57
3.3.3.2 Steady Pressure Ramp . . . 58
3.3.3.3 Sequential Step Input (General Case) . . . 59
3.3.3.4 Oscillatory Pressure Input . . . 63
3.3.4 *QP* Responses for Various Piston States . . . 65
3.3.4.1 Step Input Resistance . . . 65
3.3.5 $\mathbf{Q}/\mathbf{V}$ Trade-Offs . . . 66
3.4 Diodes . . . 67
3.4.1 Diodicity . . . 68
3.4.1.1 Sensitivity to Parasitics . . . 70
3.5 Optofluidic Current Source . . . 73
3.5.1 Results . . . 75
3.5.2 *QP* Measurement Experiments . . . 78
3.6 Gain Valves . . . 79
3.6.1 Basic Gain Mechanism . . . 79

3.6.1.1 Results . . . 82
3.6.2 Basic Gain Valve . . . 83
3.6.2.1 Default-off behavior and neutral spring position . . . 85
3.6.3 Current-Controlled Gain Valve . . . 87
3.6.3.1 Gain Valve Variations . . . 88
3.7 Summary and Future Directions . . . 92

4 3D-Printed Microfluidic Molding 93
4.1 Introduction . . . 93
4.1.1 Mold post-processing . . . 97
4.1.2 PDMS Molding Process . . . 99
4.1.2.1 Molding Containers . . . 100
4.1.2.2 Demolding Techniques . . . 101
4.1.2.3 Mold Silanization . . . 103
4.1.3 Flow rate measurement . . . 104
4.2 Results and discussion . . . 105
4.2.1 Single-sided Molding Techniques . . . 105
4.2.1.1 Glass ℓPDMS Spin Bonding . . . 107
4.2.1.2 Built-in Fluid Inlets . . . 109
4.2.2 Multi-sided and -layer Molding Techniques . . . 109
4.2.2.1 Alignment Marks . . . 110
4.2.2.2 Microfluidic Vias . . . 114
4.2.2.3 Thin Membranes . . . 115
4.2.2.4 Membrane Valve . . . 117
4.2.2.5 Double Sided Channels . . . 118
4.2.2.6 Two Sided Channel Uses . . . 120
4.2.3 Stamp Bonding and Rapid Assembly . . . 122
4.3 Technique Considerations . . . 124
4.3.1 Fabrication Technique Comparisons . . . 124
4.3.1.1 Via Fabrication . . . 124
4.3.1.2 Valve Fabrication . . . 125
4.3.2 Bonding Techniques . . . 126
4.3.2.1 Plasma Bonding . . . 126
4.3.2.2 Glass Bonding . . . 127
4.3.2.3 Delamination and inlet bursting . . . 129

4.3.3 3D-Printed Stamp . . . 130
4.3.3.1 3D-Printed Stamp Design . . . 130
4.3.3.2 Application of PDMS to Stamp. . . . 131
4.3.3.3 Cleaning Stamps. . . . 135
4.4 Summary and Future Directions . . . 136

5 3D-Printed Microfluidic Circuitry 138
5.1 Introduction . . . 138
5.2 Methods and Materials . . . 140
5.2.1 3D modeling and theoretical simulations . . . 140
5.2.2 Device Fabrication and Cleaning . . . 141
5.2.3 General Experimental setup . . . 142
5.2.4 Data Analysis and Signal Processing . . . 143
5.2.4.1 Flow Rate Alignment . . . 143
5.2.5 Flow Rate Buffering with Microfluidic Resistor . . . 143
5.3 Physical and Theoretical Considerations . . . 144
5.3.1 Radial flow of a Newtonian fluid between parallel disks . . . 144
5.3.1.1 Hydraulic Resistance . . . 145
5.3.1.2 Force Balance . . . 146
5.3.1.3 Piston Closure . . . 150
5.4 3D-Printed Resistors . . . 151
5.4.0.1 Hydrodynamic Resistance . . . 152
5.4.0.2 Quick-attachment Ports . . . 153
5.4.0.3 3D-Printed Flow Splitters . . . 153
5.4.0.4 3D-Printed Variable Microfluidic Resistors . . . 154
5.4.0.5 Simulation . . . 154
5.4.1 Experimental Setup and Results . . . 155
5.5 3D-Printed Capacitors . . . 156
5.5.1 Capacitor Simulations . . . 157
5.5.2 Experimental Capacitor Results . . . 158
5.6 3D-Printed Diode . . . 160
5.6.1 Experimental Setup . . . 161
5.6.2 Theoretical Considerations of 3D-Printed Microfluidic Diode . . . 162
5.6.2.1 Force Balance . . . 163
5.6.2.2 Force-Flow Balance . . . 165

5.6.2.3 Summary of Diode Terminology . . . 168
5.6.2.4 Asymptotic Forms . . . 169
5.6.3 Results of Experimental Diode Tests . . . 180
5.6.3.1 Diode Simulations . . . 180
5.6.4 Full-wave Rectifier Results . . . 182
5.7 3D-Printed Transistors . . . 184
5.7.1 Design Considerations . . . 185
5.7.2 Analytical form of 3D-Printed Microfluidic Transistors . . . 187
5.7.2.1 Asymptotic Forms and Limiting Variations . . . 189
5.7.2.2 On the directionality of fluidic transistors . . . 191
5.7.3 Results Summary for NOT Gate Analytical Modeling . . . 192
5.7.4 Experimental Setup . . . 199
5.7.5 Results . . . 200
5.7.6 Transistor Simulations . . . 203
5.8 Microfluidic IF-Gate: CMOS and Continuing Work . . . 204
5.8.1 Results Summary for IF-Gate Analytical Modeling . . . 206
5.9 The Question of Gain . . . 213
5.9.1 NOT-Gate Gain . . . 214
5.9.1.1 Behavior of gain under different input pressures . . . 215
5.10 Discrepancies between Theoretical and Experimental Performance . . . 220

6 Conclusions **223**

A ProJet™3000 3D Printer **226**
A.1 Printing and Material Information . . . 227
A.1.1 Surface Roughness and Mitigation . . . 228
A.1.2 Color and Texture Change . . . 230

B Syringe Pump as Current Source **232**
B.1 Analytical Model of Step-function syringe motion . . . 233
B.1.1 Addition of a parasitic resistance R_{par} . . . 236

C The Complete* Works of "Hilbert and Sullivan" **239**

Bibliography **285**

List of Figures

1.1 Summary of different microfluidic-additive manufacturing approaches 19

3.1 Optofluidic lithography fabrication process 47
3.2 Optofluidic Fabrication Process 48
3.3 Setup of moving piston thin-film problem 49
3.4 Piston position response to step pressure increases 62
3.5 Conceptual illustration of current source concept 73
3.6 Setup of optofluidic current source 74
3.7 Images of fabricated current source 75
3.8 Current source flow behavior simulations 76
3.9 Current source simulations showing later displacement forces 76
3.10 Asymmetric and Symmetric Spring Design 77
3.11 Flow data from a single microfluidic current source 78
3.12 Flow data from microfluidic current sources with differing spring amplitudes 79
3.13 Illustrations of the pressure gain device concept 80
3.14 Images of fabricated pressure gain device with an area ratio of 2:1 81
3.15 Simulation Results for Gain Valve 82
3.16 Experimental results of gain measurement 83
3.17 Schematic diagram comparing structure of optofluidic transistors 83
3.18 Conceptual image of optofluidic transverse valve in operation 84
3.19 Characteristics of Basic Longitudinal Valve 85
3.20 Contraction of a hydrogel in optofluidic lithography 86
3.21 Structure of optofluidic amplifier valve 87
3.22 Equivalent Resistances for piston edge-cases 91

4.1 3D molded microfluidic fabrication process and technical capabilities 95
4.2 Illustration of two-sided molding process, detour vias, and thin membranes. 96

4.3 Further photographs of 3D-printed transfer-molding process . . . 97
4.4 Schematic diagrams for multicomponent microfluidic device molds . . . 98
4.5 Apparatus used for PFOTS silanization . . . 99
4.6 3D-Printed molding containers and associated molding techniques . . . 100
4.7 Schematic diagrams of 3D-printed molding containers . . . 101
4.8 Removing molded PDMS components from molding containers . . . 102
4.9 Problems associated with incorrect PFOTS silanization . . . 104
4.10 Conceptual diagram showing arrangement of Fluigent™ flow control system . . . 104
4.11 Single-sided fabrication and bonding process flow . . . 106
4.12 Schematic diagrams of single-sided mold . . . 107
4.13 Comparison of results from plasma bonding and ℓPDMS spin bonding . . . 108
4.14 Alignment mark creation process flow . . . 111
4.15 Demonstration of usage of alignment marks . . . 113
4.16 Fabrication flow for vias constructed through double-sided transfer molding . . . 114
4.17 Thin membranes fabrication techniques using 3D-printed transfer molding . . . 115
4.18 Schematic diagrams of 350 μm domed membrane molds . . . 116
4.19 Illustration of membrane damage due to incorrect molding procedure . . . 117
4.20 "Quake"-style membrane valve fabrication and characterization . . . 118
4.21 "Quake"-style membrane valve mold schematics . . . 119
4.22 Photographs of process for generating fully rounded microfluidic channels . . . 120
4.23 Schematic diagrams illustrating the generation of double sided channels . . . 121
4.24 Conceptual diagram of variable-diameter microfluidic channels for optofluidic lithography . 122
4.25 Rapid assembly of multilayer PDMS devices through stamp bonding . . . 123
4.26 Microfluidic via process flow comparison . . . 124
4.27 "Quake" valve process flow comparison . . . 126
4.28 Illustration of problems that occur during glass-bonding . . . 128
4.29 Determination of delamination pressure for glass-bonded single layer microfluidic device . . 129
4.30 Stamps and individual layers used to fabricate multilayer PDMS microfluidic device . . . 130
4.31 Schematic diagrams for PDMS layers of multi-layer microfluidic device . . . 132
4.32 Photographs of stamps with differing surface profiles . . . 133
4.33 Illustration of stamping technique . . . 134
4.34 Schematic diagram illustrating the dimensions of the ℓPDMS applicator . . . 135

5.1 Summary of tested 3D-printed microfluidic transistor devices . . . 139
5.2 Projet™3000 fabrication process for $1 \leftrightarrow 8$ channel microfluidic splitter and variable resistor 141

5.3 Fluid flow past moving narrow piston . . . 147
5.4 Conceptual diagrams of 3D-printed fluidic resistor, quick-attachment ports, and splitter . . . 151
5.5 3D-printed fluidic splitters in various flow configurations . . . 153
5.6 Illustration of fluid Flow through a single 3D-Printed Variable Resistor with $d = 500$ µm . . . 154
5.7 COMSOL FEA simulations of the 500 µm variable resistor . . . 154
5.8 Experimental resistance data for variable resistors . . . 155
5.9 Experimental and simulation results from the 3D-printed microfluidic capacitor . . . 157
5.10 Experimental results of 3D-printed capacitor to point of breakage . . . 160
5.11 Experimental and simulation results from the 3D-printed microfluidic diode . . . 161
5.12 Pressure and flow-rate outputs from time sweep of 3D-printed microfluidic diode . . . 162
5.13 Resistance Layout of 3D-printed microfluidic transistor . . . 163
5.14 Conceptual diode analysis . . . 164
5.15 Effect of scaled M on device behavior . . . 175
5.16 Structure of Double Diode . . . 178
5.17 Experimental results of microfluidic full-wave rectifier . . . 183
5.18 Diodicity Results . . . 184
5.19 Conceptual NOT-Gate Gain Valve analysis . . . 185
5.20 Conceptual NOT-Gate Gain Valve analysis . . . 186
5.21 Dependence of NOT-gate response on directionality of fluid flow. . . . 192
5.22 NOT-Gate models for changes in effective area (a_{eff}). . . . 193
5.23 NOT-Gate models for changes in output pressure (p_{out}). . . . 194
5.24 NOT-Gate models for changes in valve-seat distance (h_0). . . . 195
5.25 NOT-Gate models for changes in valve-seat back-force (M). . . . 196
5.26 NOT-Gate models for changes in relative piston resistance (ρ). . . . 197
5.27 NOT-Gate models for changes in relative input resistance (ρ_{in}). . . . 198
5.28 Experimental time series data from 3D transistor performance measurement . . . 199
5.29 Experimental results for 3D-printed microfluidic transistor . . . 200
5.30 Experimental results for 3D-printed microfluidic enhanced-gain transistor . . . 201
5.31 Comparison of gate-dependent fluidic resistance for standard and gain-enhanced NOT-gates 202
5.32 Simulated results for standard NOT-gate fluidic transistor . . . 203
5.33 Conceptual IF-Gate Gain Valve analysis . . . 204
5.34 IF-Gate models for changes in effective area (a_{eff}). . . . 207
5.35 IF-Gate models for changes in output pressure (p_{out}). . . . 208
5.36 IF-Gate models for changes in valve-seat distance (h_0). . . . 209
5.37 IF-Gate models for changes in valve-seat back-force (M). . . . 210

5.38 IF-Gate models for changes in relative piston resistance (ρ). 211
5.39 IF-Gate models for changes in relative input resistance (ρ_{in}). 212
5.40 Relationship between microfluidic gain, pressure ratio, and relative flow reduction 215
5.41 Different measures of gain and scaling relationships 216
5.42 *QP* diagram for parametric P_G sweep illustrating a snap-open effect 216
5.43 Non-supercritical gain behavior with hysteresis 217
5.44 Super-critical gain behavior with hysteresis 218
5.45 Critical pressures and points at which hysteresis begins 219
5.46 SEM images showing the surface roughness of the 3D-printed fluidic diode and transistor . . 220

A.1 Conceptual view of ProJet™3000 3D Printer process 226
A.2 ProJet™3000 3D Printer output 227
A.3 Surface roughness of 3D printed mold and transferred PDMS 229
A.4 Differences in color and texture change on 3D printed transfer molds 230

B.1 Simplified leak-free circuit schematic driven by syringe pump 233
B.2 Syringe pump charging leak-free capacitor 235
B.3 Behavior of the syringe pump capacitor P_1 measurements for varying capacitances 235
B.4 QP behavior with varying C1 236
B.5 Short-term behavior of charging capacitor with parasitic resistance 238
B.6 Long-term behavior of charging capacitor with parasitic resistance 238

List of Tables

3.1 Summary of thin-film moving piston nondimensionalization constants 56
3.2 Equivalent inductances in electrical, mechanical, and hydrodynamic domains 67

5.1 Forces acting on dynamic membrane 165
5.2 Nondimensionalization factors for Standard Diode equations 168
5.3 Asymptotic behavior for standard diodes 177
5.4 Forces acting on NOT-gate transistor 188

Acknowledgments

This dissertation did not arrive in the completed[1] state you see before you without a great deal of help from those around me. At times, researching and writing this material went smoothly. These acknowledgments are for those who made my load a little lighter during the other 23 hours a day.

On the academic side, I would like to first and foremost thank Liwei Lin, my research advisor, for helping keep me on course and away from some of the many distractions that research provides, for warning me of rabbit holes I barely saw coming. My thanks as well to my dissertation committee: Bob Jacobsen, Gabriel Orebi Gann, and Dorian Liepmann. I didn't give you much time to look through this dissertation, and yet you still found time to make it better. Thank you for your forbearance and for helping me set my academic priorities.

Next, a big thanks to the members the Liwei Lin Lab and to the Micro Mechanical Methods in Biology (M3B) sub-group: To Kosuke Iwai, Nazli Pirmoradi, and especially Ryan Sochol, my M3B co-directors (and my mentors as I grew as a graduate student) you taught me to organize my research, to be careful with my data, and to value a good collaboration. To my students in M3B (in no particular order) Kevin Korner, Vishnu Jayaprakash, My Chung, Sikun Peng, Mitchell Srimongkol, Aaron Schwartz, Joseph Lin, and William Zhuang: you have done a spectacular job and I wish you luck in graduate school. And then there's Eric Sweet, who was an outstanding undergraduate student member of M3B and for some inexplicable reason decided to become an outstanding graduate student director of M3B. I thought he would have learned from my example, but his "folly" is my gain; it has been a true pleasure working with him. To Emmeline Kao, Chen Yang, Nazli Pirmoradi, and Caiwei Shen and to the our representatives of EH&S, thank you for helping me keep our lab clean, organized, and safe. Our lab has changed a lot over six years,[2] and I still haven't figure out how we fit as many people in there as we do.

To the members of the Etcheverry Hall Machine Shop, the CITRIS Invention Lab, and the Center for Integrative Biomechanics in Education and Research (CiBER), thank you for allowing me the use of your 3D printers and equipment. To Anne Takizawa and Donna Sakima in the UC Berkeley physics office: I don't know *how* you do what you do, but you always seem like the first line of defense against the harsh reality of graduate school. I know I asked you two a few more questions than was strictly necessary[3], but you always knew either the right answer or the right place to go for the right answer. To the people movers of the Berkeley Sensors and Actuators Center (BSAC), former director John Huggins, and the fantastic staff members Richard Lossing, Dalene Schwartz Corey, Kim Ly, and Brittany Skye Scott, you kept BSAC running smoothly, made me feel welcome whenever I dropped in to chat, and also let me inflict my "Hilbert and Sullivan" on unsuspecting audiences!

[1] Arguably

[2] Turns out there is a lot more space available when a 10' $\times$ 4' $\times$ 5' injection-molding machine gets put to good use (in someone else's lab)

[3] *e.g.*, those questions for which the answers are found using Google

On a more personal level, there are the many people I need to thank who made it possible to enjoy my time in graduate school. First, to my ensemble directors Marika Kuzma, Davitt Moroney, and Magen Solomon for teaching me that the little details — a breath, a well-timed consonant, a perfect vowel – are as important to music as are the notes themselves; to my theory teacher David Pereira for putting up with my questions and for providing the resolve for my own music; and a special thanks Deborah Benedict, my marvelous voice teacher, for helping me become less lock-jawed and tongue-tied, and providing a compelling musical reason to relax. A belated thanks also goes to William S. Gilbert and Sir Arthur Sullivan for introducing me to theatrical performance, and especially to Messrs *Hilbert and Sullivan* for giving me an outlet for otherwise academically inappropriate wordplay.[4] Another special thanks to the wonderful staff of *Le Bateau Ivre* in Berkeley, who kept me well-supplied with Earl Gray tea as I wrote a sizable fraction of this dissertation.[5]

To my friends and family: thank you for supporting me through my graduate career and the stress and trauma of writing this dissertation.[6] To Sedona Price and Austin Hedeman, for playing puns with me when Melanie would only roll her eyes and for sitting me down in front of some extraordinary television.[7] To Carolyn Hawkshaw for helping me write through a doctrine of MAD (Mutually Assured Dissertation). To Jen Greco, for being cheerful at all the "wrong" times[8] and for never failing to remind me that sleep and food work wonders. To Jay Daigle, for always being there for me,[9] even when he shouldn't have. I *suspect* our late-night worldbuilding exercises had some some incidental effect on thesisbuilding, although that hypothesis calls for further study.

To my brother Travis, who continues to astound me with his accomplishments: I wish you and Lucille all the best, and look forward to watching two good people become great people as well;

To my parents, who taught me to appreciate the little details and utterly failed to keep me from sweating them: you deserve more love and thanks than I can possibly fit here;

and to Melanie Veale, who has been my stability for six years: you have lightened the good times and the bad, balanced my foibles, put up with my puns (even when you didn't have to), and helped me become a better person.

[4] For a gratuitous example, see "The Complete* Works of Hilbert and Sullivan" (Page 239).
[5] And where I am as I write these words.
[6] Which was tough on me, so I can only imagine how tough it was on them!
[7] And for helping proofread this dissertation, which I think *technically* counts as more important than Futurama.
[8] *i.e.*, those times I most needed someone cheerful
[9] In a metaphoric on-the-internet sort of way

Chapter 1

Introduction

Microfluidics, the controlled manipulation of fluids at submillimeter length scales, affords numerous advantages for applications in chemistry and biology [1, 2, 3], including rapid thermal and biochemical diffusion times [4], low reagent volumes [5], laminar flow profiles [6], precision handling of microparticles (*e.g.*, microbeads and living cells) [7, 8, 9], low-cost, high-throughput platforms [10], controlled regulation of microenvironmental characteristics [11, 12]. Researchers have adapted conventional micromachining methods to construct fluidic systems at smaller scales [13, 14], transforming large-scale reactors into miniaturized "Labs-on-a-Chip" (LOC).

Initially, these protocols involved manufacturing microfluidic devices comprised of standard semiconductor materials, including silicon [15] and glass [16, 17]; however, disadvantages associated with the use of such materials for microfluidic applications engendered the predominant method for fabricating microfluidic devices: soft lithography [9, 18, 19]. Building upon the elastomeric replication methods developed at Bell Labs [20], Duffy *et al.* introduced a technique for micromolding and bonding the silicone elastomer, poly(dimethylsiloxane) (PDMS), to form enclosed channels for transporting fluids [21], known as *soft lithography* [10]. While many polymeric materials can be used, PDMS is favored due to its numerous ideal properties, including its ease in manufacturing and reasonable cost, as well as its strength, transparency, and especially biocompatibility [22, 23].

The scope of soft-lithography-based microfluidics expanded dramatically when Quake *et al.* pioneered an active pneumatic control mechanism for microfluidics [24]. The most common implementation of this method uses a two-layer microfluidic device where the upper layer (*control layer*) is applied with pressurized air which forces a series of membranes closed to block fluid flow in the lower layer (*flow layer*). A fully-connected membrane valve system functions as pressure-

controlled microfluidic resistors, where higher pressures in the control layer lead to higher resistances in the flow layer. These systems may be expanded to include a wide-range of device functionality, including transistor-like applications [25, 26, 27, 28, 29].

However, standard soft-lithography has proven relatively limited. For example, even two-layer microfluidic devices require a failure-prone bonding step, leading to a variety of approaches to compensate for the tendency for fully-cured PDMS to not adhere to other layers [30], including UV and oxygen plasma bonding [31] and adhesive-based bonding [31, 32, 33, 34, 35]. Additionally, while the standard control-system for soft-lithography usually consists of two layers for fabrication simplicity, more layers are often needed to achieve higher-level functionality [25, 36]. However, this technical flexibility comes at the cost of fabrication complexity, higher cost, and increased failure modes [37, 38]. Most importantly, standard soft-lithography techniques fabricate shapes that are monolithic in profile, which presents difficulties for valve closure [24] and limits the types of internal structures the techniques can fabricate.

Over the past decade, research has shifted towards developing alternate methods to fabricate and control microfluidic systems that overcome some of the limitations of soft-lithography. One fabrication avenue that has shown increasing promise for microfluidics is additive manufacturing (widely known as *three-dimensional* (3D) printing)[1] to fabricate microfluidic structures by performing an automated layer-by-layer deposition of material. These methods can use computer-aided design (CAD) tools to create fully-3D models of the microfluidic device which are imported to the 3D-printer [39]. Other fabrication techniques include grayscale soft-lithography, where non-binary shades of gray in the lithography process can produce rounded structures and the equivalents of multiple photolithography stages in a single exposure [40], as well as microfluidic processes in paper [41, 42, 43] and foil [44].

Additionally, increasing attention has been devoted toward producing alternative, self-regulating microfluidic technologies [25, 36, 45]. By allowing microfluidic devices to perform operations autonomously and without external controls, the number of interfaces can be drastically reduced, allowing a commensurate increase of the internal complexity without expanding the device footprint [45, 46]. However, producing dynamic microfluidic control systems in an efficient, cost-effective manner has remained a considerable challenge. For example, elastomeric LOC devices that exhibit static pressure gain require at least four layers of substrate material to achieve the desired functionality [25, 29, 47, 48]. Additionally, at low Reynolds number (*Re*) (Section 2.1.1.4) fluid behavior becomes linear and time-reversible [49, 50], static microfluidic control structures begin to have no

[1] Actually a number of related techniques

effect on fluid behavior, requiring new approaches.

Substantial research has been dedicated to overcoming these limitations. For example, systems harnessing centrifugal forces of a rotating CD-ROM have been used to generate variable and controllable "gravitational"-analog pressure flows. For example, bulk fluid experiences an outward pseudo-force from the rotating reference frame of a magnitude $m\omega^2 r$ which varies based on the fluid's location within the CD-ROM (*i.e.*, the radius r), which cannot be readily controlled from the outside, although the angular spin speed ω can be controlled [46, 51, 52]. Additionally, researchers have developed finger-powered microfluidic devices, which use human finger pressure to generate the needed pressure for a microfluidic system.[2] [53, 54, 55, 56].

A hybrid technique, *optofluidic lithography,* involves injecting photosensitive fluids into microfluidic channels fabricated through conventional single-layer soft-lithography [57]. These liquids are then selectively exposed to create freely-moving microstructures within a microfluidic channel. Microfluidic devices with integrated optofluidic components can perform flow-control operations at extremely low Reynolds numbers (*i.e.*, for $Re \lesssim 0.1$) and at low pressure where other microfluidic controllers may have limited functionality [58, 59, 60, 61]. For further details on the use of Optofluidic lithography to control microfluidic systems, see Chapter 3.

1.1 Microfluidic Fabrication Techniques

1.1.1 Standard Microfluidic Soft-Lithography Fabrication

In most cases, the soft lithography protocol for fabricating a single-layer microfluidic device consists of six fundamental steps: (i) photoresist (*e.g.*, SU-8) is spin-coated onto a Si wafer, (ii) microchannel designs are photolithographically defined (*e.g.*, using a photomask and UV light), (iii) the exposed photoresist is chemically developed, which selectively removes undesired photoresist, (iv) liquid PDMS is poured onto the Si wafer with patterned photoresist, which serves as a negative master, (v) after the PDMS is thermally cured, the molded PDMS is removed from the Si wafer, allowing individual devices to be cut and then punched with holes at designated inlet/outlet port locations, and (vi) the PDMS devices are bonded to glass slides (*e.g.*, via UV ozone or Oxygen plasma treatment) to form enclosed microchannels [62, 63]. These protocols for elastomeric polymer molding have been adapted for micromachined silicon (*e.g.*, for maximum resolution) [18],

[2] These finger-powered pressure pumps incorporate micro-scale fluidic *half-wave rectifiers* to drive forward fluid flow when finger pressure is applied and preventing fluid flow when finger pressure is released, creating pressure vacuum as the elastic structures of the finger pump restore fluid flow

milled metals (*e.g.*, for precision channels or irregular shapes) [64], as well as PDMS itself (*i.e.*, "twofold replication") for rapid production of inexpensive molds [65, 66].

Soft lithography can also be extended to construct microfluidic devices comprised of multiple discrete layers and/or levels which are bonded together — a process termed *multilayer soft lithography* [24, 67], - that has seen continued development in order to reduce soft lithography's geometrical constraints [68, 69]. Another method of increasing geometric complexity is "multilevel soft lithography" [70, 71, 72, 73], where devices are made using non-planar molds to enable features like vias [38] and particulate separation [74, 75]. Multilevel soft lithography has historically required multiple photolithography steps [72] increasing their cost further. Lithographic height gradients can be generated in a single step by using "grayscale lithography" - a process that allows more degrees of exposure than binary black/white [76]. Grayscale lithography has increasingly grown in popularity in microfluidics, having been used to fabricate micromolds with multiple heights [77], rounded features [40], and flow focusing structures [78]. Coupled with recent algorithmic improvements [79], grayscale lithography is becoming increasingly like stereolithography (a 3D-printing approach) in scope and functionality.

However, although the aforementioned methods of microdevice construction afford significant benefits in terms of microscale precision and microelectronics integration, limitations inherent to such protocols remain a pervasive impediment to progress in chemical and biological fields [80]. A critical barrier for those outside of engineering fields is that gaining access to the necessary equipment for device construction (*e.g.*, in microfabrication facilities) is often difficult, and may require considerable technical training and high usage fees [56]. Furthermore, the clean room-based procedures for Si wafer processing are typically executed manually, which can be exceedingly costly, time consuming, and labor-intensive [81]. These issues are exacerbated when fabricating multilayer device designs that require distinct layers to be manually aligned and assembled — procedures that can diminish the precision and reproducibility associated with microdevice manufacturing [39, 82]. Thus, replicating microfluidic and microelectronic advancements on-site can be challenging (especially for those outside of engineering fields). Another critical issue is the intrinsic restriction of monolithicity, which renders relatively common features of macroscale fluidic components (*e.g.*, circular channels with varying diameter, non-planar physical architectures, etc.) difficult or impossible to achieve in microscale domains. Consequently, alternative manufacturing methods capable of bypassing these limitations could provide a substantial boost to a number of diverse research fields [83, 84].

1.1.2 Microfluidics via Additive Manufacturing

Additive manufacturing — widely referred to as *three-dimensional (3D) printing* — encompasses a number of methods for building 3D structures through point-by-point and/or layer-by-layer processes. In general, computer-aided design (CAD) tools are used to generate a digital 3D model (*e.g.*, in STL file format), which is then imported into computer-aided manufacturing (CAM) software corresponding to a specific 3D printer or 3D printing process. Lastly, the resulting 3D printing code (*e.g.*, G-code) is electronically imported into the 3D printer to enable autonomous device construction. Although researchers have developed a wide range of 3D manufacturing methodologies for applications throughout broad academic and industrial fields, the submillimeter-scale 3D printing techniques with advantageous characteristics for lab-on-a-chip systems stem from five fundamental approaches: (i) fused deposition modeling (FDM), (ii) stereolithography (SLA), (iii) selective laser sintering (SLS), (iv) laminated object manufacturing (LOM), and (v) multijet modeling (MJM).

1.1.2.1 Additive Manufacturing Approaches for Microfluidics

1.1.2.2 Fused Deposition Modeling

In 1992, S. Scott Crump described and patented an extrusion-based method by which a 3D object is formed using dispensing heads (*e.g.*, nozzles) to directly deposit heated thermoplastic material onto a substrate via a point-to-point, layer-by-layer process [85]. Since the expiration of Crump's original patent in the early 2010's, many companies have begun to manufacture low-cost desktop 3D printers, leading the growing popularity of 3D printing technology. In FDM printing, a variety of low-cost commercial thermoplastic materials such as acrylonitryl butadiene styrene (ABS), polylactic acid (PLA) and polyethylene terephthalate (PET), wound in spools of long solid filaments, are typically used; however, since the extruded material generally begins to re-harden before contact with the underlying layers, interlayer bonding is low strength and thus delamination can be an issue. Thermoplastic FDM-printed components are also usually made from lower density and less durable materials and therefore have lower resolution when compared to their injection-molded counterparts.

The use of FDM techniques for 3D *bioprinting* primarily revolves around the deposition of either sacrificial materials, such as waxes or other *fugitive inks,* or cell-compatible materials, such as cell-laden gels. The Jennifer Lewis group has pioneered a number of fugitive ink-based methods.[3]

[3] Analogous to the lost-wax method of metal manufacture. Lost-wax-equivalent methods have also been used

To construct 3D vascular-inspired networks, Therriault *et al.* presented a four-step protocol: (i) a fugitive organic ink network is 3D-printed using microscale nozzles, (ii) the fugitive ink scaffold is infiltrated with a surrounding liquid resin, (iii) the surrounding resin is cured, and (iv) heat is applied to the fugitive organic ink to enable vacuum-based extraction, thereby leaving behind a 3D network of hollow, interconnected microfluidic channels [88]. Wu *et al.* adapted this method by using the group's omnidirectional printing technique [89] to extrude free-floating fugitive ink within a reservoir of photopolymerizable hydrogel [90]. Following the printing process, the surrounding hydrogel was photocured, and the liquid-phase fugitive ink was evacuated via applied pressure. The resulting system included vascular-like microfluidic channels within a hydrogel matrix [90]. Using a similar approach, Miller *et al.* printed a sacrificial 3D carbohydrate glass lattice; however, in this case, the 3D network was encapsulated with living cells and ECM [91], and Gelber *et al.* used a water-soluble sugar alcohol isomalt which was deposited into uncured liquid UV-curable resin, which used to construct fully-3D combinatorial two-fluid mixer [92]. The full construct was then placed in cell media, which dissolved the carbohydrate glass filaments, thereby allowing for the remaining fluid to be replaced (*e.g.*, by fresh medium and/or suspended cells) [91]. Kolesky *et al.* further demonstrated a novel method of direct bioprinting, wherein bioinks containing living cells and extracellular matrices were printed and then encapsulated in GelMA ink. The printed cell networks remained within the channels, creating three-dimensional vascularized heterogeneous tissue constructs that emulate microvasculature and extracellular matrixes [93].

Conventional solid thermoplastic FDM printing presents many challenges for reliable fabrication of internal microchannels; for example, the average filament size ($\approx$1mm) results in X, Y and Z axis resolutions (typically 100's of microns) insufficiently large for fabrication of common microfluidic channels and enclosed geometries such as micropillars or membranes (10's of microns), as well as interlayer delamination issues can cause random fluidic leaking throughout the device. FDM printing of thermoplastics has proven very successful for creating certain non-planar PDMS microfluidic geometries, however, by fabricating a thermoplastic replica mold that is encased by liquid PDMS prepolymer which is then cured. Specifically-shaped molds can then be extracted from the PDMS by pulling or twisting the molds out, resulting in irregularly shaped non-planar internal microchannels and structures [94, 95].

for direct manufacture of non-biological microdevices [86]. Due to the innate trade-off between nozzle size and fabrication time, as well as increased resolution for positive (as opposed to negative) features, processes involving deposition, casting, and removal of fugitive materials are popular [86, 87].

1.1.2.3 Stereolithography

The first 3D printing technique, stereolithography (SLA), was introduced by Charles W. Hull in 1986 [96]. SLA involves using a bath of liquid-phase photoreactive material and a focused light beam to photocure (*i.e.*, solidify) the material in specified locations (*e.g.*, in a layer-by-layer fashion) to ultimately fabricate a 3D object comprised of cured material [96]. In recent years, researchers have utilized SLA to construct entire microfluidic systems [39, 97, 98, 99, 100, 101]. For example, Shallan *et al.* demonstrated 3D microfluidic gradient and microdroplet generators constructed by means of digital-mirror device (DMD), projection-based SLA [100]. Au *et al.* evaluated mail-order SLA-based microfluidic devices with rectangular microchannels, revealing effective channel resolutions of approximately 300-400 μm [39, 102]. Using similar SLA methods, Bhargava *et al.* developed a number of discrete and reconfigurable elements consisting of 750×750 μm2 microchannels with varying lengths (and therefore, resistances), which were utilized for microfluidic applications including mixing and droplet generation [98]. Subsequently, Au *et al.* presented 3D-printed microfluidic systems with moving valves and pumps, which were employed to create a multi-fluid perfusion chamber for epithelial cells [97, 102]. Other groups have since also demonstrated valving capabilities for 3D-printed microfluidic devices [99].

SLA has also been used to fabricate microfluidics using the photocurable polymer low-MW poly(ethylene glycol) diacrylate (MW 250) (PEG-DA-250), notably by Urrios *et al.* in 2016 [103] who demonstrated 3D printing of complex three-dimensional resin structures upon which cells were cultured over a period of several days. The photocurability of PEG-DA, often used similar to and in conjunction with PDMS microfluidics allows for the automated, freeform, low-cost and ultra-high resolution 3D printing of the biocompatible and completely transparent polymer. An extension of SLA, in which multiphoton absorption is used for spatially-controlled photopolymerization, has enabled 3D manufacturing with resolutions down to the 100 nm range [104]. Due to this precision, researchers have applied this technique — referred to as direct laser writing (DLW) — to create geometrically-complex 3D microstructures [105, 106, 106]. The critical limitation of DLW is that the trade-off between nozzle size and 3D printing time has limited the overall build volume to the 100 to 1 mm^3 range [87]. Thus, some of the first steps toward using DLW for 3D-printed microfluidics involved direct-writing structures within pre-fabricated, single-layer PDMS microfluidic channels [107, 108]. By loading photocurable material into microfluidic channels, complex geometric structures could be photocured in situ to facilitate improved mixing dynamics [108] and multidirectional fluidic vias [107]. To date, DLW has resulted in the highest resolutions

for 3D printing [105, 106, 106]. One condition of note for SLA-based methods, however, is that many 3D designs require added, fully-integrated support structures (*e.g.*, pillar-like ribs) to facilitate successful prints [109]. Although such structures can be manually removed from macroscale objects following the 3D printing process, doing so for microscale systems can be extremely challenging or unfeasible.

1.1.2.4 Selective Laser Sintering

Since the early 2000's, selective laser sintering (SLS) has been used in manufacturing, in the automotive industry for example, to fabricate sacrificial molds for casting of complexly-shaped metallic components [110]. A focused laser beam directed into a bath of liquid wax selectively solidifies the wax, producing a solid form, that is then used for metallic investment casting. Used for composite manufacture, ceramics, plastics, wood, and especially direct metal formation

1.1.2.5 Multijet Modeling

In the early 1990's, Yamane *et al.* invented a technique for building 3D structures by inkjet printing a photosetting or thermosetting material layer-by-layer [111], which combined with the simultaneous printing of a sacrificial support material [112], became the basis for MJM approaches, referred to as *Multijet* (3D Systems, Rock Hill, SC, USA) or *PolyJet* (Stratasys, Edina, MN, USA) 3D printing. MJM technologies utilize high numbers of microscale inkjets in parallel to simultaneously deposit microdroplets of photopolymer/photoplastic materials and sacrificial support materials in a layer-by-layer process (with continual UV photocuring) to produce 3D objects. After completion of the 3D printing process, the support material — typically a water-dissolvable gel-like material or meltable wax — can be removed through post-processing [101, 113]. Although MJM technologies provide considerable advantages in terms of resolution (≈16-32 μm eature size), build volumes, print speeds, and sacrificial supports [114, 115], MJM material selection remains limited to a small number of proprietary materials. Due to this lack of material versatility, such methods are not yet well-suited for many cellular applications.

Researchers have also applied MJM technologies to construct micro/millifluidic channels with varying geometries [116]. To compare the efficacy of MJM technologies to SLA methods, Zhu *et al.* constructed a number of identical millifluidic systems for arraying and imaging zebrafish embryos [117]. Despite successful fluidic trapping performance, the majority of the MJM and SLA resins tested were found toxic and/or caused significant developmental abnormalities over

the course of multi-day experiments, with the MJM material (Visijet M3 Crystal) exhibiting the worst performance in terms of biotoxicity [117].

1.1.2.6 Laminated object manufacturing

Laminated object manufacturing (LOM) is a technique where thin layers of material are produced separately and then placed, bonded, and assembled (*e.g.*, using an adhesive) [118]. LOM techniques have more limitations than SLA or MJM; for example, the technique requires thicker layers (*i.e.*, lower resolution) than other 3D-printing techniques, have difficulty constructing overhanging or free-standing features, and require complex equipment for the pick-and-place portion of fabrication. In contrast, LOM has lower material costs than other 3D-printing techniques [119].

Although the method was more popular before 2000 than it is today, it has frequent consumer uses, including assembling layers of paper for furniture production[4] [119] and felt for toys [120]. The technique also has commercial uses, such as developing original patterns for sand casting [121]. The technique has been adapted for use with ceramic composites [122] which can achieve desired material properties through a mixing of composites with thin layers such as paper [123, 124] or aluminum foil [44]. LOM has been increasingly used in low-cost microfluidics, particularly since the Whitesides Group's development of wax and paper-based microfluidics [41], where thin layers of paper are cut, patterned with wax to control the direction of fluid flow, and then bonded [42, 43]. Similar techniques have been adapted to laminated SU8 films [125, 126], PMMA films [127], aluminum foil [44, 128], and also organic substrates [129].

1.1.3 Microfluidic Systems via 3D-Printed Transfer Molding

3D-printed transfer molding was involves shaping elastomeric polymers using a 3D-printed mold (as opposed to a mold fabricated through conventional photolithography or milling techniques) and can be used to fabricate conventional microfluidic devices such as those produced by soft lithography methods, albeit with faster prototyping and processing speeds, as well as enabling easier fabrication of complex 3D geometries, multicomponent assembly, and built-in fluidic interfaces. First pioneered by McDonald *et al.* [130] using FDM techniques in 2002, the technique has since been used with SLA [131], MJM [94, 132], as well as wax printers [133] and office-quality laserjet printers [134, 135].

[4] Mueller *et al.* note that LOM processes can create objects with material properties similar to plywood, but with much greater fabrication flexibility

While 3D-printed transfer molding does not allow the same geometric flexibility of fully 3D-printed microfluidics (although the technique has been adapted for multicomponent assembly [136, 137, 138], it possesses three notable advantages: (i) each mold can be used for multiple microfluidic devices, saving on 3D printing times and costs, (ii) many 3D printers exhibit lower resolution for features requiring support materials, and (iii) the process is compatible with conventional microfluidic fabrication materials, most notably PDMS [131, 133, 134, 136, 139]. Because PDMS transfers patterns with high fidelity, the resolution and surface finish of the mold define the resulting quality of the resulting PDMS [139], provided the mold maintains reasonable aspect ratios [94, 132].

In addition to patterning features externally, PTM has also been used to fabricate internal features, reducing some of the monolithicity constraints. Hwang *et al.* have MJM-printed molds which are surrounded by PDMS and then withdrawn after curing, relying on the flexibility of PDMS to remove the components. While similar to fugitive ink processes, fugitive ink molding has fewer geometric constraints but requires printing for every final device, while solid internal must be designed for withdrawal, but can be reused [94, 95, 132]. Chan *et al.* have used SLA to fabricate molds with overhangs in a basket weave pattern, which can be used to generate microfluidic vias in a single step, repairing demolding damage by thermally healing the PDMS [140]. Additionally, Glick *et al.* introduced a double-sided molding procedure which allows single-step fabrication of diverse structures such as thin membranes, microfluidic vias, and membrane valves [137, 138]. ar PTM is also increasingly integrated with other 3D printing processes to reduce the challenges of multi-component assembly and interfacing LOC with external systems [141]. While PTM devices may do this directly, for example through punching holes (similar to standard soft lithography processes) [135], molding open, non-adapted fluid wells [142, 143], adding connectors ports during the PDMS curing process [131, 134, 144], or by printing specialized input/output marks [137, 138]. PTM devices may also interface indirectly by attaching to 3D-printed components that do have the desired interfaces [136]. Similar to soft lithography, PTM devices are sealed with glass or other 3D-printed components to provide enclosed channels after molding (*e.g.*, through plasma bonding [130], targeted adhesive bonding [137, 138], tape [136], etc.) For further details, see Chapter 4.

1.2 Microfluidic Systems with Integrated Microelectronics

Although solely fluidic microdevices have been employed for diverse biochemical applications [25, 36, 145, 146, 147, 148, 149], the integration of microelectronics with microfluidics can greatly extend the capabilities of self-contained lab-on-a-chip systems. With well-developed micro/nano fabrication technologies (*e.g.*, lithography, thin-film deposition, etching, molding, and self-assembly) and related materials knowledge (*e.g.*, conductive, semi-conductive, piezo, photonic, thermoelectric, magnetic, and dielectric materials), microelectronic devices and information technologies continue to improve [150, 151]. An ultimate goal involves integrating a CMOS chemical sensor with microfluidic devices can enable finer sensor resolution [152], although the integration process is highly unreliable without substantial refinements because CMOS and soft-lithography techniques are generally non-compatible.

1.2.1 Fabrication of Microfluidic Systems with Integrated Electronics

The simplest lab-on-a-chip microelectronically integrated microfluidic systems are comprised of a manually inserted conducting wire [153] or other electrode material [154] into a microfluidic channel or of a planar electronics layer (*e.g.*, glass slides [155], PCB boards [156], [157], etched metal [158], etc.) bonded to a microfluidic layer (*e.g.*, microchannels in PDMS). The first technique tends to be imprecise and inconsistent, while the second presents numerous challenges in both in sealing the channels (*i.e.*, providing leak-free fluid transport and fluid manipulation) [141] and in interfacing the electronics with the sample fluids [159].

Integration techniques that involve complete encapsulation of the conductive components are often more complicated to fabricate, but can be advantageous by isolating fluid from the electrode (minimizing corrosion or contamination) and can bypass problems of PDMS adhesion to metallic components [160]. These techniques have been proven to be adequate for methods in which the electrode and fluid do not require direct contact, such as heat sources [161, 162, 163] or electrorheological fluid controls [84].

Conventional techniques for sealing microchannels must be further augmented due to the difficulty in bonding metallic components to PDMS [164] with surface treatments, such as adhesive layers [165], plasma surface modification [166]. surface functionalization [167], dielectric barrier discharge [168], modified Parylene-C layers [169], etc. Further, these techniques restrict assembly and packaging of microfluidic systems to planar geometries and layers in two-dimensions [141]. More significantly, planar systems restrict the geometry of applied electromagnetic fields [159];

for example, planar electrodes cannot generate purely in-plane electric [170] (*e.g.*, as required for optimal capacitive cell cytometry [171], capacitive droplet detection [171], or manipulation of electrorheological fields [154, 172]. Because much of the field is "wasted" in out-of-plane effects, higher system voltages are required to achieve the same in-plane effects [171], which has the unintended consequence of hydrolyzing water between electrodes. Methods have been developed to fabricate three-dimensional electrodes inside microchannels to perform enhanced microfluidic tasks in three-dimensions, such as greatly improving the efficiency of cell lysis, electroporation and dielectrophoresis [173], due to their added third-dimensional electromagnetic stimulation and sensing capabilities.

Microfluidic-electrode integration may be fabricated using MEMS fabrication techniques, such as planar metallic patterning and metal sputtering and deposition [174] or through fully additive manufacture techniques [175], but the techniques can be impractical when applied to PDMS. For example, Patel *et al.* fabricated electrodes through metal evaporation on PDMS using a sacrificial SU8 mask [176] and Rosset *et al.* have made PDMS conductive through ion implantation using milled steel shadow masks [177, 178]. While these techniques can fabricate conductive electrodes along variable channel geometries (*i.e.*, the techniques are capable of generating vertical sidewall electrodes), metal deposition suffers from poor adhesion of metals to PDMS [164]; sputtering requires a trade-off between conductivity and flexibility [178], and both techniques have difficulties with large electrode profiles [173].

Another electrode fabrication method involves deposition of photopatternable conductive polymers; however, progress in this area has been limited [179]. For example, composite-based photopolymers, where a conducting component is dispersed in a photopolymer (*e.g.*, silver in SU8 [180] or carbon nanotubes in diacrylate derivative 1 [181]) require 3-6 weight % conducting component (for conductivity $\approx$100 S/m, compared to bulk silver with conductivity $\approx 6 \cdot 10^7$ S/m [182]) which causes similar degradation of mechanical properties as PDMS-based conducting composites (*e.g.*, reduced tensile strength, elasticity, and durability) and makes the photopolymer optically opaque [183]. Conversely, Bakhtina *et al.* have developed fully transparent conductive photopolymers which suffer from poor electrical conductivity ($\approx$1 S/m) [179].

Lu *et al.* developed a technique whereby standard MEMS photolithographic patterning of SU-8 photoresist, on a substrate patterned with a planar electrode array, was used to create three-dimensional cylindrical microposts $\approx$70 μm in diameter which were then conformally coated with a 10 μm deposition of copper by electroforming. When bonded to the microfluidic later, this three-dimensional electrode micropost array exhibited enhanced leukocyte cell lysis efficiency via

electroporation as compared to conventional two-dimensional electrodes, due to the increased fluidic volume for which the strength of the three-dimensionally configured electric field is sufficient for electroporation [184]. Another low-cost process for fabricating three-dimensional electrodes requires the placement spherical bismuth electrodes in the sidewalls of microfluidic channels. Although this technique was low-cost and was capable of producing complex electromagnetic fields (*e.g.*, for diolectrophoresis and particle sorting), it still required a combination of costly photolithography, electroplating, and unreliable *manual* electrode placement, limiting the technique's overall usefulness.

Ota *et al.* has extensively demonstrated direct 3D printing of liquid-state conductive materials into channels inside a 3D-printed device, yielding 3D liquid-state wires, antennas, sensors, actuators and various circuitry components in flexible and rigid 3D-printed devices [185]. Additionally, electrodes have been fabricated through flowing and etching alloys with low melting points [159, 186, 187] and through chemical self-assembly of Silver nanowires [155], and through electroplating within microfluidic channels [144]. Relatedly, the surface properties of electrodes has been improved through fluid flow-based etching [188].

The use of electroactive PDMS composites has provided another method for the integration of electronics into microfluidic devices [84, 189, 190, 191]. The composites are fabricated by mixing PDMS with a conductive nanoparticle filler (*e.g.*, carbon black [191], silver [191], zinc[192], or carbon nanotubes [193]), this mixing may be aided by a solvent such as chloroform to aid dispersion of the nanoparticles [193]. Conductivity of the PDMS composite increases with filler concentration, particularly when the concentration exceeds the *percolation threshold* where particles are dense enough to form conducting paths through the PDMS. The percolation threshold typically varies between 0.3% for carbon nanotubes [193] and 10% for silver [189] and may reach as high as 83% for carbon black [189]. Conducting PDMS is integrated into microfluidics through a two-stage soft lithographic process. First, a negative photoresist (*e.g.*, SU8) is patterned on a wafer to form the channel mold. Next, a positive photoresist (*e.g.*, AZ 4620 [191]) is spin-coated onto the wafer and developed, forming a scaffold PDMS composite. The composite is then plastered into the cavity and the positive resist is dissolved. Standard PDMS is poured onto this mold, cured, and then pealed, incorporating the composite PDMS but leaving empty fluidic channels corresponding to the SU8 patterns. The chip is then completed by enclosing the channel through standard techniques, after which the chip is baked to enhance the conductivity of the polymers. This fabrication technique allows for the assembly of vertical sidewall electrodes directly in contact with the microfluidic channel and eliminates many of the problems associated with hand-placed elec-

trodes [172]. It can additionally be used for the placement of other active polymer composites adjacent to a microfluidic channel. For example, Grilli *et al.* incorporated ferroelectric nanoparticles into the PDMS, generating a magnetic field to drive the dielectrophoretic self-assembly of carbon nanotubes in a microfluidic channel [194].

However, integration of conducting PDMS composites into microfluidic channels has several limitations. Most notably, forming the composite cavities requires photolithography for each microfluidic device fabricated; once used, the molds are not reusable, negating many of the benefits of soft lithography. Additionally, the composites themselves are non-transparent and substantially more viscous than standard PDMS, making application more difficult, and high conductivity comes at the cost of material properties. Because composite PDMS is more brittle and less flexible than standard PDMS, the composite patterns can break during assembly, causing breaks in the conducting path and allowing fluid to percolate through the electrodes, limiting their use as a complete barrier.

1.2.2 Applications of Microfluidic Systems with Integrated Electronics

Integrated electronics may serve multiple purposes, depending on how they are integrated into the microfluidic system. For example, electrode-generated heat sources [161, 162, 163], and cell manipulation via magnetic fields [187, 195, 196] do not require direct fluid contact with the electrodes. Similarly, provided the electric field is the critical quantity, certain electrically-generated effects may be performed with isolated electrodes (*e.g.*, for fluorescence-activated cell sorting [197], electrorheological fluid [154, 198] and valve manipulation [45, 84, 199], capacitive droplet [171] [200] and droplet electrocoalescence [201, 202]).

Electrowetting-on-dielectric (EWOD), a process where individual microfluidic droplets can be manipulated by dielectrically altering their surface energy [203, 204, 205], requires only partial electrode isolation; fluid droplets remain in direct contact with a common grounding electrode but are isolated from control electrodes by a layer of dielectric material [206, 207]. EWOD devices require standard MEMS-based electrical integration techniques (including evaporation, etching, etc.) and are therefore more expensive to fabricate than soft lithography-based microfluidics [208], particularly if assembled in the alignment-free co-planar mode [209, 210]. In contrast, electrodes are directly integrated into microfluidic systems when a direct conducting path into the fluid is needed (*e.g.*, for fluid manipulation via the electrokinetic effect [211, 212], electrophoresis [213], dielectrophoresis [214, 215], hydrogel manipulation [216, 217, 218], as well as cell cytometry,

sorting, and other cellomic control [219, 220]). Lastly, all-in-one integrated systems may use multiple electrode integration methods to achieve hybrid effects [160], including electric valve control, heating, cooling, pumping, and integrated fluid sensing [84, 190, 210].

1.3 Microelectronics via 3D Printing

1.3.1 Microelectronics via FDM

To form three dimensional electrically conductive paths, thermoplastic material with added carbon particles can achieve a resistivity as low as $8 \cdot 10^{-3}$ Ωm [221, 222]. Using low-melting-temperature alloy is also a feasible method, but the melting temperature may still be too high that may re-melt adjacent thermoplastics [223]. Javey and his group recently utilized liquid metal (Galinstan) to fill the FDM fabricated channels as interconnects for flexible applications, but the resistivity is still high ($5 \cdot 10^{-5}$ Ωm) [185]. Instead, conductive ink is a much more popular choice for extrusion-based 3D printing due to lower resistivity. With the parts fabricated through extrusion-based 3D printing as the dielectric structure, electronics theoretically can be further formed through directly dispensing conductive inks in the predefined channels. However, the porosity of parts fabricated by extrusion-based 3D printing may lead to electrical shorts due to the spreading of electrically conductive inks on surface layers [224] and between stacked layers [225]. The poor spatial resolution also limits the density of the electronics. To solve the addressed issues, one way is to use micromachining technique to form fine channel features, which may need more cost of hardware and system integration [226, 227]. Another successful solution is process optimization [89, 227, 228, 229, 230], therefore promising work recently is emerging that allow us to directly 3D-print conductive ink within objects, such as the 3D printer from the Harvard spin-off Voxel8 which demonstrated their technique with a 3D-printed quadcopter [231, 232].

Conductive inks are liquid before curing, and therefore can be readily applied to a complex 3D geometrical structure. Although the measured resistivities ($5 \cdot 10^{-7}$ Ωm [232], $1.18 \cdot 10^{-7}$ Ωm [226], and $5.0 \cdot 10^{-6}$ Ωm [233]) and low ductility are still limited by low curing temperature due to the low melting point of thermoplastics, promising applications such as 3D-printed antennas and microwave devices had been presented through integrating FDM machine with conductive ink printing functions [234, 235, 236, 237, 238]. While global curing can cause systemic damage, *local* thermal curing of conductive silver traces has enabled resistivity to reach $4.3 \cdot 10^{-8}$ Ωm. Another proposed method utilizes the re-melting capability of thermoplastics surrounding embedded copper

wire and has a resistivity that approaches that of bulk-material ($1.7 \cdot 10^{-8}$ Ωm) [226, 239, 240]. Instead of fabricating the support structure and conductive path simultaneously, *post metallization* processes, such as spraying [241, 242], attaching adhesive-backed copper foil [240, 243, 244, 245], and electroplating [246], are also potential solutions for 3D electronics fabrication.

1.3.2 Microelectronics via SLA

Since 2005, Lopes *et al.* had integrated SLA and direct-writing (DW) systems to fabricated electronics [247, 248, 249, 250]. With proper controlling of the conductive inks and repeating the processes (SLA, cleaning, DW and curing), different kinds of 3D designs with embedded commercial electronic components had been presented, such as motion sensor [251], timer [252], magnetic flux sensor [226, 247], acceleration sensor [253], and gaming die [254]. Although the feasibilities have been proven, the resistivity of interconnects is still limited to the silver-based conductive inks. Choi *et al.* also utilized carbon-nanotube-based polymer to form conductive and piezoresistive components during SL/DP fabrication [255, 256]. Post metallization had also been presented through electroplating after standard SL fabrication for antenna or waveguides [246, 257, 258, 259, 260]. The Swiss Federal Institute of Technology in Lausanne and its spin-off company Swissto 12 is ready for mass production [259, 260, 261]. The photocurable material utilized in SLA currently limits the reliability of printed electronics, since the physical properties may be affected by weathering, heat aging, dimensional changes, and UV exposure behavior [226]. The production rate is even limited by the single laser and corresponding scanning motion.

1.3.3 Microelectronics via MJM

To realize 3D electronics with finer spatial resolution, MJM is an ideal choice. 3D-printed microelectronics components and circuitry have been fabricated by the combination of MJM technology and liquid metal-filling techniques [87, 262]. These components include resistors, inductors, and capacitors, as well as circuits such as LC resonant tanks. As a demonstration example, a 3D *smart cap* with embedded LC tank as the passive wireless sensor was constructed by Yang *et al.* for the application of a monitoring the quality of liquid food (*e.g.*, milk and juice). In this application, as the liquid food deteriorates, the dielectric constant of the liquid changes and the shift in the resonance frequency of the embedded 3D LC tank can be detected wirelessly by an inductively coupled reader in real-time. However, the resistivity of the process was found to be $3.6 \cdot 10^{-6}$ Ωm, due to the poor packing density of silver particles inside the channel after the solidification process.

Absent self-assembly techniques to improve metalization density, open-geometries may be used for beter metalization [263]. Nayeri also utilizing electroplating for post metallization to form antenna [264]. Instead of using conductive ink, Zhu *et al.* realized 3D-printed waveguides by MJM for the 3D geometry and followed by electroless plating and electroplating for metallization [265]. Sputtering is also demonstrated as a post metallization method [266]. Unlike FDM and SLA printing with available integrated metallization functions, there are not yet available solutions for directly printing conductive polymers with multijet/polyjet yet. Therefore, the HP MultJet fusion technology with voxel transforming agents, which could have the potential to change the resistivity of each voxel through jetting of proper transforming agents, could open a new window. Furthermore, with more materials, such as semi-conductive materials, can be printed, active components can be further realized, such as displays [267], sensing systems, actuators, transistors, and batteries.

1.4 Pneumatic and Pressure-controlled Microfluidics

Pneumatic control of microfluidics via a deflected membrane (commonly known as a *Quake Valve*) remains the dominant method of microfluidic control. With the exception of fluidic resistors, fluidic circuit components require both static (*i.e.*, fixed) and dynamic (*i.e.*, deformable or movable) physical elements. However, standard two-layer flow/control layer fabrication has proven inadequate for control of microfluidics. In response, on-chip fluidic control routines [2, 3, 268] have drawn inspiration from integrated electronic circuitry to develop integrated microfluidic circuits (IFCs) capable of autonomous functionalities [47].

For example, the standard control mechanisms for microfluidic devices can require a high number of input and output ports. Using standard binary multiplexing produces $2^{n/2}$ flow channels for n control channels.[5] For example, Thorsen *et al.* produced an array of 1024 fluid wells controlled by 20 pneumatic controls and 13 other fluidic inputs [3]. While binary combinatorics can be used to increase the number of flow channels to $\frac{(2n)!}{(n!)^2} \sim \frac{4^n}{\sqrt{\pi n}}$ [269]. However, combinatorics comes at a substantial cost in reaction speed because the control channels are no longer specialized.

Some approaches to improve the control problem have involved increased transistor-like functionality. One approach to the control problem has been to use membrane valves with multiple channel diameters such that valve triggering occurs at different threshold pressures in different channels [270]. This multiplexing method can increase the number of controlled channels from

[5] $2\log_2(m)$ control channels to manipulate fluid in m flow channels.

$2^{n/2}$ to $3^{n/2}$ for a system with three membrane areas, and to $4^{n/2} = 2^n$ for four membrane areas [271, 272]. However, the increased flexibility comes at the cost of reduced stability; whereas a binary membrane-valve system can increase the drive pressure to ensure triggering of the control channels, in a ternary or quaternary system, this increase may trigger undesired behavior. The multiple membrane-size approach has also been used to develop single-stroke pneumatic peristaltic valves, which do not require the three-or-more control inputs for standard peristaltic valves, but pump relatively little fluid as a cost [273, 274, 275].

Another approach to increased system control has been to implement fluidic gain, where lower pressures in the control layer can manipulate higher pressures in the flow layer allows for cascaded control mechanisms, improving gain, stability, and response time [25, 26, 27, 28, 29, 276]. The most common implementation is a form of *static gain,* where the difference in actuation pressure between low and high pressure sources is a constant (static) pressure [27, 277]. Static gain may be considered a small-signal gain (*dynamic gain*) of 1 where the threshold has been shifted.[6] This technique requires a third control layer which is preloaded with photoresist, pressurized to deform the membrane, and cured [29, 278]. Dynamic gain, in contrast, has been developed by employing variable area ratios, whereby a small pressure acting on a large area can push back against a high pressure acting on a smaller area [36, 60, 113]. One downside to all the above approaches is high precision required by the alignment process.

The advent of additive-manufacturing microfluidics has the potential to remove many of these limitations by dramatically increasing the geometric flexibility available to researchers. For example, Au *et al.* have demonstrated moving valves fabricated entirely through stereolithography [97, 279] in addition to single-step microfluidic bioreactors with integrated valves [39]. Chapter 4 of this thesis expands on the use of 3D-printed molds to create PDMS devices with high complexity, including a single-step membrane valve (Section 4.2.2.4). Chapter 5 expands on techniques for using multi-jet modeling for fabricating complex microfluidic transistor circuits. Combining techniques for microfluidic circuitry [36, 47] with tailored components with specific fluidic properties (*e.g.*, gain) [60], we have developed a class of microfluidic circuit elements including static resistors, as well as dynamic elements such as capacitors, diodes and transistors — circuit elements which integrate functionality of a moving piston attached to a mechanical/fluid capacitor. In addition, we develop the theory for analyzing the 3D-printed transistors and for considering which features and structural elements contribute to device performance.

A final key limitation to the standard membrane-valve approach is that membrane valves are

[6] For example, Unger *et al.* demonstrated a static gain of 14 PSI, so at actuation, $P_{\text{high}} = P_{\text{low}} + 14$ PSI

default-open (*i.e.*, NOT-gates, or PMOS-type, if using semiconductor terminology) and thus have a high leakage rate while open.[7]. The development of default-closed microfluidic logic (*i.e.*, IF-gates, or NMOS-type, if using semiconductor terminology) has thus been crucial to the implementation of low-leakage microfluidics. Common approaches have involved using a combination of vacuum pressure and *lifting gate* valves [280] or valves with sufficient static gain that the device does not open under standard operating conditions [29]. However, these devices are *not* true IF-gates because they eventually open under high enough input pressures; instead, they behave like threshold-shifted NOT-gates. To that end, Section 5.8 of this thesis expands on an alternate approach to a "true" IF-gate where 3D-printed mechanical columns link the motion of a membrane to that of a flap valve; under standard conditions, internal pressure will hold the valve shut and will only re-open the valve when an external pressure is applied to the gate.

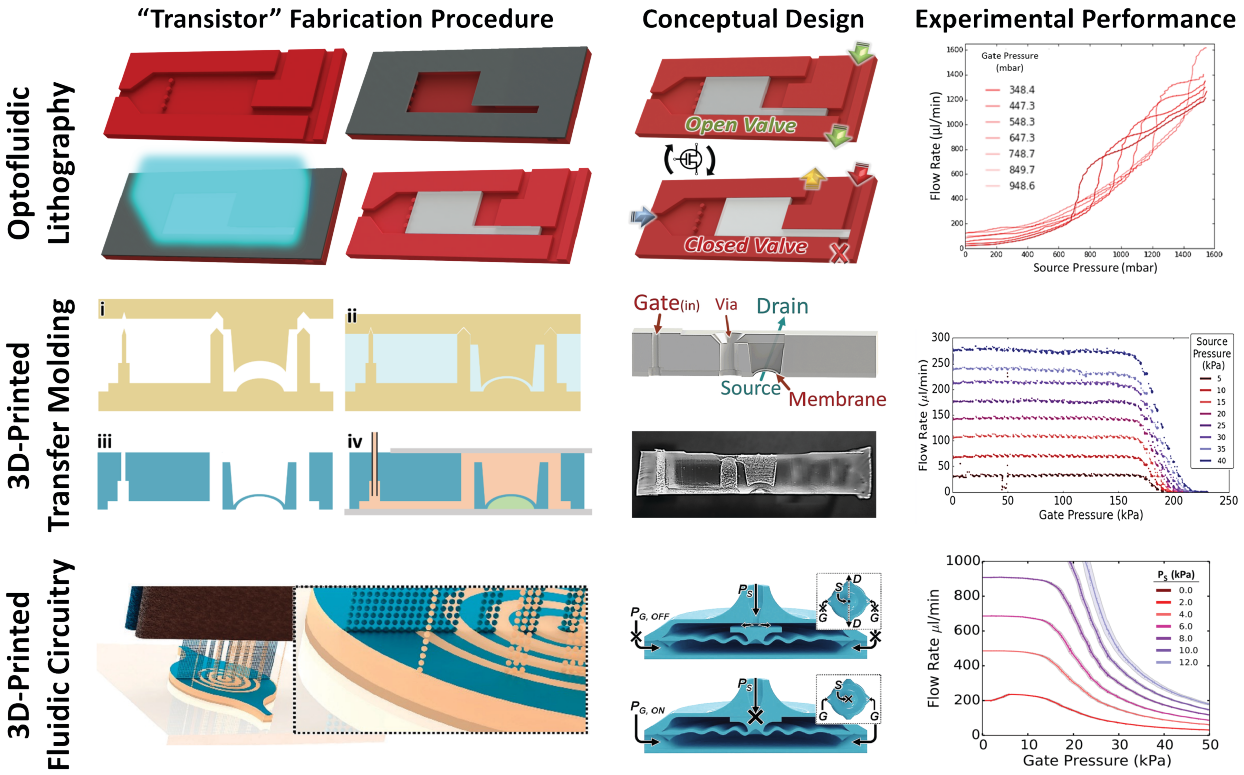


Figure 1.1 Summary of different microfluidic-additive manufacturing approaches taken in this dissertation: optofluidic lithography, the control elements are introduced into pre-existing microfluidic channels using a photo-sensitive low-viscosity polymer; 3D-printed transfer molding, where the 3D printing process is used to supplement the existing soft-lithography processes to create molds of greater complexity; and fully-3D-printed microfluidic circuitry, where microfluidic components are directly fabricated, without using any lithography or molding procedures. All three fabrication methods have been used to make "transistor" control valves, and all display similar transistor characteristics.

[7] It is generally easier to push something closed than pull it back open when using pressure forces

1.5 Notation and Naming Conventions

In this dissertation, notational conventions will be laid out at the start of each chapter. For fluid mechanics, tensorial quantities will be underlined to indicate the tensor order, *e.g.*, V for scalars, $\underline{\mathbf{V}}$ for order-1 tensors (*i.e.*, vectors), $\underline{\underline{\mathbf{A}}}$ for vectors, etc. For component notation, Euclidean *Einstein notation* will be used; because the metric tensor is unity, no attention will be paid to *covariant* or *contravariant* tensors. For example, an order-4 tensor will be represented as E_{abcd}. Summation convention will be used for tensors, where repeated indices are summed over. When possible, quantities will be non-dimensionalized for ease of analysis. Before a nondimensionalization process, dimension*al* quantities will be represented with a subscript $_*$ or a superscript * unless otherwise noted. The characteristic scale will be denoted with a subscript $_s$

For microfluidic devices that are fully bonded to glass on one side, *lower* is used to describe layers closest to the glass slide and *upper* for layers farthest from the glass slide. By convention, control components are generally placed in the upper layer and the flow components in the lower layer. Relatedly, *lower layer*, *bottom layer*, and *first layer* are used synonymously to describe the same (lower) layer which closest to the glass. Similarly, *upper layer*, *top layer*, and *Nth layer* (*i.e.*, for an N layer system) are used to describe the same (upper) layer. This upper layer may be synonymous with *input layer* because fluid inputs are frequently applied to this layer. In systems which are molded on both sides during a single molding step, *lower* and *bottom* describe the molds for the lower surfaces and *upper* and *top* describe the molds for the upper surface.

The microfluidic structures and PDMS constructs described in this dissertation will be categorized by a structural hierarchy: *systems* $\rightarrow$ *devices* $\rightarrow$ *components* $\rightarrow$ *features*. A *device* describes something fully-manufactured but not utilized. Microfluidic devices are frequently part of microfluidic *systems* which include input and output tubes, connectors, fluids, etc. A device is constructed by assembling several *components*, which must undergo a fabrication process to manufacture but are made as a single piece (*i.e.*, are not made of sub-components, unless specified). Devices and components contain one or more *features*, which are structures designed with a specific functionality. For example, the membrane valve in 4.2.2.4 is a *device* which allows the manipulation of fluid flow through the control of multiple pressure inputs. It is constructed through the assembly of three *components* (two ℓPDMS-coated glass slides and one PDMS component molded through a single-step molding process) and contains *features* such as an interior membrane, built-in inputs and outputs, and enclosed fluidic channels. The membrane valve *device* is then attached to tubing, creating a membrane-valve *system*.

Chapter 2

Microfluidic Theory: Fluidic Circuitry, and the Hydraulic Analogy

2.1 The Hydraulic Analogy: Simplifying Complex Fluid Flows

Many systems in fluid mechanics can be modeled through the Hydraulic Analogy, whereby the fluid behavior is treated like a lumped-parameter model electric circuit consisting of combinations of resistors, capacitors, inductors, and other circuit components placed in series or parallel. A lumped parameter model is a model of electronic (and electronic-analogy) circuits that makes a simplifying assumption that the individual components of the circuit (*e.g.*, resistance, capacitance, inductance, etc.) are lumped into discrete and idealized electrical components (*e.g.*, resistors, capacitors, inductors, etc.) joined by a network of perfectly conducting wires. This assumption allows complicated components to be simplified for analysis without substantial loss of accuracy and enables complex systems to be reduced to finite-space differential equations [281]. Thus, while the Navier-Stokes equations are notoriously difficult to solve [49], the systems in aggregate tend to approximately obey linear equations that have been well studied in the electrical domain. And because the differential equations are similar, the characteristic responses will be similar. In the Hydraulic Analogy, fluidic pressure P is analogous to electrical voltage and volumetric flow rate Q is analogous to electrical current. From these two definitions, we are able to put together a table of correspondences:

	Electrical		**Hydraulic**		**Dimensions**	**Units**
Potential	Voltage	V	Pressure	P	Force/Area	Pa
Quantity	Charge	Q	Volume	V	Vol	ml
Flux	Current	I	Flow Rate	Q	Vol/Time	$\mathrm{m^3\,s^{-1}}$
Flux Density	Current Density	J	Velocity	U	Current/Area	$\mathrm{m\,s^{-1}}$
Flux Opposition	Resistance	R	Resistance	R	P/Q	Ω
Quantity Storage	Capacitance	C	Capacitance	C	V/P	F
Inertia	Inductance	L	Inductance	L	$P/\frac{\mathrm{d}Q}{\mathrm{d}t}$	H

The most common method of driving fluids in microfluidic systems are pressure and flow-rate based drivers. Each generally requires some external source, however efforts have been made to reduce the reliance on complicated external mechanisms to allow for greater *point-of-care diagnostics*. Purely pressure-driven flows are often achieved by harnessing and controlling a research lab's internal pressurized air network.[1] This system, however, tends to create reliance on elaborate laboratory control apparatuses, creating a system often ironically referred to as *Chip-in-a-Lab*[2].

Often, an external pressure source is used to generate specified *pressure rails* (*i.e.*, pressure elements that are placed at a relative positive and negative pressure) which can be used to run fluidic components. Commonly, the *positive rail* is set at whatever pressure is desired from the pressure generator, and the *negative rail* is set at hydrodynamic *ground pressure* which is conventionally atmospheric pressure. Just as the 'ground' (*i.e.*, the Earth) can be approximated for most uses as a near-infinite sink of electrical charge and current, the atmosphere is considered a sink for pressure and fluidic currents.[3] On occasion, pressure-based fluidic systems may have three rails, which can frequently be implemented in one of two ways: (i) use atmospheric *ground* as the negative rail and establish an intermediate positive pressure, or (ii) use atmospheric ground as a central ground and use a vacuum pump to generate a negative rail.[4] One of the central goals of fluidic circuitry research is to create microfluidic devices that can operate entirely with constant-pressure rails. This has been achieved by the Hui group who use NOT-gates in a ring oscillator to provide a clock-mechanism to control microfluidic devices set entirely at atmospheric and vacuum pressure [276, 277, 282]

[1] Whereby building air supply is regulated using an external machine and routed to enclosed pressurized tubes, which are forced out at a specified pressure.

[2] As opposed to the desired goal of an independents *Lab-on-a-Chip*

[3] There are limits to this terminology, especially when considering non-idealities around the outlet to the outlet to the sink, but the terminology is useful nonetheless.

[4] This process is somewhat limited, because under normal conditions (*i.e.*, in a lab and not a hyperbaric chamber), it is impossible to generate more than -1 ATM of pressure (*i.e.*, total vacuum).

2.1.1 Hydraulic Analogy Circuit Elements

The behavior of fluids moving through channels can often be modeled with similar mathematics to those used in modeling electrical circuits, with models for resistance, capacitance, and inductance. This hydraulic analogy is an approximation, but it allows useful predictions of fluid behavior to be made. If we assume fluid flow through a pipe, pressure P (analogous to electrical voltage) is the driving force of the fluid, which pushes the fluid to move at a volumetric flow rate Q (analogous to electric current). The pipe constricts the fluid flow, acting like a hydraulic resistor R (analogous to electrical resistance). Temporary storage of the fluid, either through an elastic surface deforming under pressure or through compressibility of air acts like a fluidic capacitance C (analogous to electrical capacitance) and inertia in the fluid flow which resists change in flow rate acts like a fluidic inductance L (analogous to electrical inductance). Note that in microfluidic scales, inductance and related inertial effects are overwhelmed by the viscous forces and are effectively zero [50, 281, 283].

2.1.1.1 Resistance

Hydraulic resistors (hereafter resistors) follow a variation of *Ohm's Law*[5] where $\Delta P = QR$. Like capacitors, these resistors behave like their electrical counterparts following their combination in parallel and series. Poiseuille's law follows the approximate scaling relation

$$R \propto \frac{\mu L}{r^4} \tag{2.1}$$

where μ is the dynamic viscosity of the fluid, L is the length of the channel, and r is the characteristic radius of the channel (often roughly the size of the smallest dimension). For a circular channel,

$$R = \frac{8\mu L}{\pi r^4} \tag{2.2}$$

This relation is known as Poiseuille's Law and is the hydrodynamic equivalent of Ohm's law. For a rectangular channel, the resistance is approximately.

$$R \approx \frac{12\mu L}{wh^3(1-0.630h/w)} \approx \frac{12\mu L}{wh^3}, \text{ for } h \ll w \tag{2.3}$$

[5] In microfluidics, this is commonly known as *Poiseuille's Law* [283]

where h is the channel height (smallest dimension) and w is the channel width (larger dimension). More generally, an irregularly-shaped channel resistance can be approximated by [50, 283]

$$R \approx \frac{2\mu L \mathcal{P}^2}{\mathcal{A}^3} \tag{2.4}$$

where $\mathcal{A}$ is the channel cross-sectional area and $\mathcal{P}$ is the perimeter. A consequence of Poiseuille's law is that fluidic resistance is proportional to the length scale to the inverse fourth power, so halving the diameter of a channel will increase its resistance by a factor of 16; therefore, parasitic resistances are a much larger force in microfluidics than they are in electronics where resistance $R_{\text{elec}} \propto r^{-2}$ (and halving the radius leads to a factor of 4 increase in resistance).

One formulation that will be useful later is that of the *Pressure divider* (analogous to a voltage divider), where the output pressure P_{out} resulting from series resistors R_1 and R_2 and an input pressure P_{in} is

$$P_{\text{out}} = \frac{R_2}{R_1 + R_2} P_{\text{in}} \tag{2.5}$$

2.1.1.2 Capacitance

Microfluidic capacitance is a measure of fluid storage within a microfluidic system and relates pressure and volume

$$V = C\Delta P \tag{2.6}$$

or by taking the time derivative,

$$Q = C\frac{\mathrm{d}\Delta P}{\mathrm{d}t} \tag{2.7}$$

For a microfluidic channel of length L without a membrane, the microfluidic capacitance C can be analyzed as the sum of the capacitance resulting from expansion of the channel (elastic capacitance) and compression of the fluid itself.

$$C = C_{\text{mech}} + C_{\text{fluid}} = V \cdot K_{\text{mech}} + V \cdot K_{\text{fluid}} \tag{2.8}$$

$$= \mathcal{A}L(K_{\text{mech}} + K_{\text{fluid}}) \tag{2.9}$$

Here, $\mathcal{A}$ is assumed to be (relatively) constant and K represents the compressibility factor. For a perfectly rigid tube, $K_{\text{mech}} = 0$. The hydraulic compressability factor varies widely among fluids; for water, $K_{\text{fluid}} \approx 5 \times 10^{-5}$ bar^{-1} — water is highly incompressible and hydraulic capacitance

can be safely neglected — and for air, $K_{\text{fluid}} \approx 1$ bar^{-1}, so capacitance is inversely proportional to pressure [284].

2.1.1.3 RC Time Constant

The approximate time response of a microfluidic channel can be modeled using an RC time constant like the one used in electrical circuits: for a step input change in pressure:

$$p(t) = P_o(1 - e^{-t/RC}) \tag{2.10}$$

Neglecting the mechanical capacitance included in a mechanical membrane, the time constant for a microfluidic channel would be

$$\tau = RC = \frac{2\mu L\mathcal{P}^2}{\mathcal{A}^3}\mathcal{A}L(K_{\text{mech}} + K_{\text{fluid}}) \tag{2.11}$$

$$= \frac{2\mu L^2\mathcal{P}^2}{\mathcal{A}^2}(K_{\text{mech}} + K_{\text{fluid}}) \tag{2.12}$$

For a circular channel $P = 2\pi r, A = \pi r^2$, and for a square channel $P = 4h,\ A = h^2$

$$\tau_{\text{circ}} = \frac{8\mu L^2}{r^2}(K_{\text{mech}} + K_{\text{fluid}}) \tag{2.13}$$

$$\tau_{\text{squ}} = \frac{32\mu L^2}{h^2}(K_{\text{mech}} + K_{\text{fluid}}) \tag{2.14}$$

For both, we see that the key factors are the key channel width r, the channel length L, compressibility K, and viscosity μ

$$\tau \propto \frac{L^2}{r^2}\mu(K_{\text{mech}} + K_{\text{fluid}}) \tag{2.15}$$

In short, to make a microfluidic channel respond in a reasonable time, design the channel short, wide, and rigid

Aside 2.1:

The highest speed microfluidics has been reported through a glass-PDMS hybrid approach developed by the Mathies and Hui groups [27, 276, 277] where a glass substrate is etched through conventional microfluidics, and then bonded with a PDMS membrane. These high-gain valves were connected into a 22.1 Hz ring-

oscillator for an individual actuator response time of 1.74 ms [277]. The rapid response times are largely due to the extremely small size of the microfluidic channels as well as the low compliance of the glass substrate. However, the process of etching the glass substrate comes at a high manufacturing cost.

The 3D-printed transistors discussed in this thesis have a relatively low response time due to the extremely large volume of the 3D-printed transistors required by the fabrication process. For a given input flow rate $Q_{\max}$, the total time T required to fill a microfluidic devices scales like $T \sim V/Q_{\max}$.

2.1.1.4 Inductance

Inductance is a measure of the inertia of a microfluidic system. Because inertia and momentum

$$P \propto mv = \rho L^3 v \tag{2.16}$$

for a fluid, where v is the velocity, ρ is the density, and L the characteristic length, it tends to drop off more rapidly with fluidic shear rate (σ) at small length scales, because $\sigma \propto \mu L^2$, where μ is the dynamic viscosity. Therefore, the scaling relation is,

$$\frac{P}{\sigma} \quad \propto \quad \frac{\rho L^3 v}{\mu L^2} \quad = \quad \frac{\rho L v}{\mu} \quad = \quad Re \quad \ll \quad 1. \tag{2.17}$$

Therefore, microfluidic inductance tends to be of minimal importance in low Reynolds number systems (*i.e.*, microfluidics)

2.1.1.5 Neglecting Fluidic Inductance

In contrast to electronic circuits, here we have only been including hydraulic *resistance* and *capacitance*, neglecting *inductance* in the analysis. This approximation is justified in the *low Reynolds number* regime, both for mechanical "inductance" and for hydraulic "inductance" in the system.

As a mathematical concept, inductance is commonly considered to be resistance to a change in a system's *flux*. In electrical circuits, inductance L can be broken into two related concepts: *self-inductance*, whereby a change in current creates an opposing *electro-motive force* (EMF) within the system (relatedly: *Faraday's law of induction* and *Lens' Law*), and *mutual inductance*, whereby a change in current in one system creates an EMF in a nearby system [170].

Equivalent *mutual inductance* may generally be ignored in fluidic systems; because of the lack

of an external *fluidic field* generated by fluid flow,[6] there is no way to directly couple two non-connected fluid flows without either (i) active circuit components simulating mutual inductance, or (ii) the addition of actual magnetic or electric fields (*e.g.*, through the addition of ferromagnetic or ferroelectric nanoparticles [45, 154, 198]). While the interaction of electromagnetic components may generate equivalent fluidic inductance or mutual inductance [7] we will not consider these methods here. In particular, these inductive effects are the domain of *magnetohydrodynamics* (MHD), a field which is not particularly relevant at these scales and plays no part in this research.

In contrast, equivalent *self-inductance* may play a role in fluidic systems. Much as in the mechanical domain, change in flux is opposed by the inertia of the system. From a purely fluidic standpoint, the Navier-Stokes equations for an incompressible Newtonian fluid may be written

$$\rho \frac{\mathrm{D}\underline{\mathbf{U}}}{\mathrm{D}T} = -\nabla P + \underline{\mathbf{F}} + \mu \nabla^2 \underline{\mathbf{U}}, \tag{2.18}$$

where $\underline{\mathbf{u}}$ is the flow velocity and $\underline{\mathbf{F}}$ is an external *body force* on the system. When non-dimensionalized, where F_s and P_s are characteristic body forces and pressures, respectively,

$$\frac{\rho L^2}{T_s \mu} \frac{\mathrm{D}\underline{\mathbf{u}}}{\mathrm{D}t} = -\frac{P_s L^2}{\mu} \nabla p + \frac{F_s L^2}{\mu} \underline{\mathbf{f}} + \nabla^2 \underline{\mathbf{u}}. \tag{2.19}$$

If we take $T_s = L/U_s$ as the characteristic time scale of the system, the acceleration coefficient becomes $\frac{\rho U_s L}{\mu} = Re$, the *Reynolds number* of the system. Thus, in microfluidic systems with negligible Re, the inertial/inductive effects may be neglected to order $O(Re)$. Any conservative body forces (*i.e.*, $f = -\nabla\phi$) may be trivially absorbed into the analysis by letting $p \mapsto p + \phi$.

Equivalent hydraulic inductance may also be encountered when fluids are coupled with mechanical systems. Simple dimensional analysis suffices to demonstrate that mechanical inductance also plays a limited role in the behavior of microfluidic systems. Consider a mass M attached to a spring with spring constant k. The mass $M \sim L^3 \rho_m$ where L and ρ_m are the critical length scale and mass density, respectively. To a first order approximation, the object experiences a viscous drag

[6] *i.e.*, as an analog of the magnetic field generated by electrical current

[7] Through the expedient of introducing *actual* electronic inductance and mutual inductance

$f_{\mathrm{v}} \sim L \cdot \mu \cdot V$. Then the equations of motion balance to

$$F_{\mathrm{ext}} = L^3 \rho_m \dot{V} + L\mu V + kX \tag{2.20}$$

$$= \frac{L^3 \rho_m V_s}{T_s} \dot{v} + L\mu V_s v + kLx \tag{2.21}$$

$$= L^2 \rho_m V_s^2 \dot{v} + L\mu V_s v + kLx, \tag{2.22}$$

by setting $V_s = L/T_s$. Dividing then by $L\mu V_s$ gives

$$\frac{F_{\mathrm{ext}}}{\mu L V_s} = \frac{\rho_m L V_s}{\mu} \dot{v} + v + \frac{k}{\mu L V_s} x. \tag{2.23}$$

The inertial constant can then be rewritten to $\frac{\rho_m L V_s}{\mu} = \frac{\rho_m}{\rho_f} Re$, meaning that this inertial term also scales by the Reynolds number. Thus, at small length scales or large viscosity, inertia/inductance may also be neglected for coupled fluidic-mechanical systems.

2.2 Unidirectional Flows

Assuming time-variable unidirectional flows, that is $\underline{\mathbf{U}} = U_z(x,t)\underline{\mathbf{E_z}}$, we can obtain a simplified form of the incompressible Navier-Stokes equations,

$$\rho\left(\frac{\partial \underline{\mathbf{U}}}{\partial t} + \underline{\mathbf{U}} \cdot \nabla \underline{\mathbf{U}}\right) = -\nabla P + \mu \nabla^2 \underline{\mathbf{U}} \tag{2.24}$$

Starting with the $\underline{\mathbf{U}} \cdot \nabla \underline{\mathbf{U}}$ component and eliminating all zero components of $vecU$ and $\nabla vecU$

$$\underline{\mathbf{U}} \cdot \nabla \underline{\mathbf{U}} = U_z(x,t)\underline{\mathbf{E}}_z \cdot \frac{\mathrm{d}U_z}{\mathrm{d}x}\underline{\mathbf{E}}_x \tag{2.25}$$

$$= 0, \tag{2.26}$$

where $\underline{\mathbf{E}}_i$ are the Cartesian unit vectors. Furthermore, because in Cartesian coordinates, $\nabla^2 \underline{\mathbf{U}} = \left(\nabla^2 U_i\right)\underline{\mathbf{E}}_i$, we also have

$$\mu \nabla^2 \underline{\mathbf{U}} = \mu \nabla^2 U_z(x)\underline{\mathbf{E}}_z \tag{2.27}$$

$$= \mu \frac{\partial^2 U_z}{\partial x^2}\underline{\mathbf{E}}_z \tag{2.28}$$

and

$$\frac{\partial \underline{\mathbf{U}}}{\partial t} = \frac{\partial U_z}{\partial t}\underline{\mathbf{E}}_z. \tag{2.29}$$

Combining these results, we are left with the three components of the Navier-Stokes equations,

$$\hat{x}: \frac{\partial P}{\partial x} = 0 \tag{2.30}$$

$$\hat{y}: \frac{\partial P}{\partial y} = 0 \tag{2.31}$$

$$\hat{z}: \frac{\partial P}{\partial z} = -\rho\frac{\partial U_z}{\partial t} + \mu\frac{\partial^2 U_z}{\partial x^2} \tag{2.32}$$

From these equations, we can additionally determine that $P = P(z,t)$.

Next, we show that the Equation 2.32 may be considered time-independent, at least with respect to the driving pressure P; while there will be time-dependent behavior resulting from the moving piston, we can consider it to be quasi-static with respect to the driving pressure. First, we assume that pressure is being driven in a time varying fashion, and assume that the driving pressure is separable: $P(z,t) = \int_0^t p(z)e^{i\omega\tau}\,\mathrm{d}\tau$ where $p(z)$ is allowed to be complex. If we assume that $U_z(x,t) = \int_0^t u_z(x)e^{i\omega\tau}\,\mathrm{d}\tau$ has the same driving frequency (with $u_z(x)$ allowed to be complex), and holding the integral sign as implicit, we are left with

$$\frac{\partial p}{\partial z}e^{i\omega t} = -i\rho\omega u_z e^{i\omega t} + \mu\frac{\partial^2 u_z}{\partial x^2}e^{i\omega t} \tag{2.33}$$

$$\frac{\partial p}{\partial z} = -i\rho\omega u_z + \mu\frac{\partial^2 u_z}{\partial x^2} \tag{2.34}$$

$$\frac{\partial p}{\partial z} + i\rho\omega u_z = \mu\frac{\partial^2 u_z}{\partial x^2}, \tag{2.35}$$

which contains the driving force time dependencies. Next, we non-dimensionalize the equations, using a $_*$ subscript to indicate dimensional quantities, a $_s$ subscript to indicate characteristic quantities that have no obvious unit choice, and no subscript for nondimensional quantities. Choosing $x_* = Hx$, where H is the height of the narrow gap, and $z_* = Lz$, where L is the gap/piston length, as well as $p_* = P_s p$ and $u_{*z} = U_s u$, where P_s and U_s are as-yet undetermined characteristic pressures

and flow-rates, respectively,

$$\frac{\partial p_*}{\partial z_*} + i\rho\omega u_{*z} = \mu \frac{\partial^2 u_{*z}}{\partial {x_*}^2} \tag{2.36}$$

$$\frac{P_s}{L}\frac{\partial p}{\partial z} + i\rho\omega U_s u = \frac{\mu U_s}{H^2}\frac{\partial^2 u}{\partial x^2}. \tag{2.37}$$

Dividing through by $\frac{\mu U_s}{H^2}$, we obtain

$$\frac{P_s H^2}{U_s \mu L}\frac{\partial p}{\partial z} + i\frac{\rho\omega H^2}{\mu}u = \frac{\partial^2 u}{\partial x^2}. \tag{2.38}$$

In this equation, we have two dimensionless groups of units, $\frac{P_s H^2}{U_s \mu L}$ and $\frac{\rho\omega H^2}{\mu}$. For the first, we can simplify Equation 2.38 by choosing, without loss of generality,

$$U_s = \frac{P_s H^2}{\mu L}, \tag{2.39}$$

setting that grouping of units to 1. The second must be examined a little more closely. Grouping ωH together forms a sort of velocity term, allowing us to examine $i\frac{\rho(\omega H)H}{\mu}$ as a sort of complex oscillatory *Reynolds number*,

$$Re_o \equiv i\frac{\rho(\omega H)H}{\mu}. \tag{2.40}$$

From here, we can actually solve Equation 2.38,

$$\frac{\partial p}{\partial z} + Re_o u = \frac{\partial^2 u}{\partial x^2} \tag{2.41}$$

due to the independence of $u(x)$ on z, giving

$$u(x) = A\sin(\sqrt{Re_o}x) + B\cos(\sqrt{Re_o}x) - \frac{1}{Re_o}\frac{\partial p}{\partial z}, \tag{2.42}$$

where A and B are determined by applying appropriate boundary conditions. While we could work with this solution, it's messy and unnecessary because we can neglect Re_o. Going back, for Re_o to

be neglectable,

$$Re_o = i\frac{\rho(\omega H)H}{\mu} \ll 1 \tag{2.43}$$

$$\implies \omega \ll \frac{\mu}{\rho H^2} \tag{2.44}$$

In our model system, the gap thickness $H \approx 10\ \mu\text{m} = 10^{-5}$ m, the viscosity μ and density ρ are approximately those of water:[8] $\mu = \text{N cP} = \text{N} * 1 * 10^{-3}\ \text{Pa s} = \text{N} * 10^{-3}\ \text{kg m}^{-1}\text{s}^{-1}$, where N is a numerical factor to account for differing viscosity and density, and $\rho = 1\ \text{g/ml} = 10^3\ \text{kg m}^{-3}$. From this, we have the requirement

$$\omega \ll \frac{\mu}{\rho H^2} \tag{2.45}$$

$$\omega \ll \frac{\text{N} * 10^{-3}}{10^3(10^{-5})^2}\ \text{s}^{-1} \tag{2.46}$$

$$\omega \ll \text{N} * 10^4\ \text{s}^{-1} \tag{2.47}$$

$$\implies f = \frac{\omega}{2\pi} \ll \frac{\text{N}}{2\pi} * 10^4\ \text{s}^{-1} \tag{2.48}$$

$$\implies f \widetilde{\ll} 1.5 * \text{N kHz} \tag{2.49}$$

For water, where N= 1 and more-so for PEGDA, where N=20, this shows that $Re_o \ll 1$ for driving frequencies under 1 kHz. Since the Fluigent system used in this research has a maximum response speed on the order of ≈ 1 ms for pressure changes, we can safely assume that the driving-pressure transients be neglected for most purposes.

From here, we can return to Equation 2.38 and solve our unidirectional flow equation in the case that $Re_o \to 0$.

$$\frac{\partial p}{\partial z} + \cancelto{0}{Re_o u} = \frac{\partial^2 u}{\partial x^2} \tag{2.50}$$

$$\frac{\partial p}{\partial z} = \frac{\partial^2 u}{\partial x^2}, \tag{2.51}$$

which can be easily solved to produce

$$u(x) = \frac{1}{2}\frac{\partial p}{\partial z}x^2 + Ax + B, \tag{2.52}$$

[8] Many of our optofluidic lithography experiments were performed in PEGDA, where $\mu = 20$ cP and $\rho = 1.12$ g/ml

where A and B can be determined by the application of appropriate boundary conditions.

For an infinitely wide channel of height h, where the no-slip boundary conditions are applied at $x = \pm\frac{1}{2}$ and the no-shear condition applied at $x = 0$, we arrive at the solution

$$u(x) = \frac{1}{2}\frac{\partial p}{\partial z}\left(x^2 - \frac{1}{4}\right), \tag{2.53}$$

or, returning to dimensional units,

$$u_{*z} = \frac{H^2}{2\mu}\frac{\partial P}{\partial z_*}\left(\left(\frac{x_*}{H}\right)^2 - \frac{1}{4}\right) \tag{2.54}$$

Total flow rate through the channel may be found by integrating over the area,

$$Q = \int_0^W \mathrm{d}x \int_{-H/2}^{H/2} \mathrm{d}y u_{*z} \tag{2.55}$$

$$= \frac{WH^2}{2\mu}\frac{\partial P}{\partial z_*}\left(\left(\frac{x_*^2}{2H^2}\right) - \frac{x_*}{4}\right)\Bigg|_{-H/2}^{H/2} \tag{2.56}$$

$$= -\frac{WH^3}{12\mu}\frac{\partial P}{\partial z_*}. \tag{2.57}$$

Because the pressure drop is linear, $\frac{\partial P}{\partial z_*} = -\frac{\Delta P}{L}$. From here, we can find the hydraulic resistance $R = \Delta P / Q$

$$R_{\text{thin}} = \frac{12\mu}{WH^3} \tag{2.58}$$

2.2.1 Reducing Thin-Film Flow to Thin Film/Unidirectional Form

First, building upon the fact that we can safely ignore the time-dependent component of the Navier-Stokes equations, we will show that it is possible to reduce the full Navier-Stokes equations to a

unidirectional-equivalent form, which can be solved as developed above.

$$\hat{x}: \quad \frac{\partial U_{*x}}{\partial t_*} + U_{*x}\frac{\partial U_{*x}}{\partial x_*} + U_{*y}\frac{\partial U_{*x}}{\partial y_*} + U_{*z}\frac{\partial U_{*x}}{\partial z_*} = -\frac{1}{\rho}\frac{\partial P_*}{\partial x_*} + \frac{\mu}{\rho}\left(\frac{\partial^2}{\partial {x_*}^2} + \frac{\partial^2}{\partial {y_*}^2} + \frac{\partial^2}{\partial {z_*}^2}\right)U_{*x} \tag{2.59a}$$

$$\hat{y}: \quad \frac{\partial U_{*y}}{\partial t_*} + U_{*x}\frac{\partial U_{*y}}{\partial x_*} + U_{*y}\frac{\partial U_{*y}}{\partial y_*} + U_{*z}\frac{\partial U_{*y}}{\partial z_*} = -\frac{1}{\rho}\frac{\partial P_*}{\partial y_*} + \frac{\mu}{\rho}\left(\frac{\partial^2}{\partial {x_*}^2} + \frac{\partial^2}{\partial {y_*}^2} + \frac{\partial^2}{\partial {z_*}^2}\right)U_{*y} \tag{2.59b}$$

$$\hat{z}: \quad \frac{\partial U_{*z}}{\partial t_*} + U_{*x}\frac{\partial U_{*z}}{\partial x_*} + U_{*y}\frac{\partial U_{*z}}{\partial y_*} + U_{*z}\frac{\partial U_{*z}}{\partial z_*} = -\frac{1}{\rho}\frac{\partial P_*}{\partial z_*} + \frac{\mu}{\rho}\left(\frac{\partial^2}{\partial {x_*}^2} + \frac{\partial^2}{\partial {y_*}^2} + \frac{\partial^2}{\partial {z_*}^2}\right)U_{*z} \tag{2.59c}$$

Non-dimensionalizing, where U_{si} is the characteristic scaling for U_{*i} (which we will determine later), and x_*, y_*, and z_* scaling as H, W,[9] and L, respectively, and dividing through all equations by $\frac{U_{sz}}{H}$ we have

$$\hat{x}: \quad \frac{HU_{sx}}{t_s U_{sz}}\frac{\partial u_x}{\partial t} + U_{sx}\left(\frac{HU_{sx}}{HU_{sz}}u_x\frac{\partial u_x}{\partial x} + \frac{HU_{sy}}{WU_{sz}}u_y\frac{\partial u_x}{\partial y} + \frac{HU_{sz}}{LU_{sz}}u_z\frac{\partial u_x}{\partial z}\right) - \frac{HP_s}{H\rho U_{sz}}\frac{\partial P}{\partial x} + \frac{\mu U_{sx}}{H\rho U_{sz}}\left(\frac{\partial^2}{\partial x^2} + \frac{H^2}{W^2}\frac{\partial^2}{\partial y^2} + \frac{H^2}{L^2}\frac{\partial^2}{\partial z^2}\right)u_x \tag{2.60a}$$

$$\hat{y}: \quad \frac{HU_{sy}}{t_s U_{sz}}\frac{\partial u_y}{\partial t} + U_{sy}\left(\frac{HU_{sx}}{HU_{sz}}u_x\frac{\partial u_y}{\partial x} + \frac{HU_{sy}}{WU_{sz}}u_y\frac{\partial u_y}{\partial y} + \frac{HU_{sz}}{LU_{sz}}u_z\frac{\partial u_y}{\partial z}\right) - \frac{HP_s}{W\rho U_{sz}}\frac{\partial p}{\partial y} + \frac{\mu U_{sy}}{H\rho U_{sz}}\left(\frac{\partial^2}{\partial x^2} + \frac{H^2}{W^2}\frac{\partial^2}{\partial y^2} + \frac{H^2}{L^2}\frac{\partial^2}{\partial z^2}\right)u_y \tag{2.60b}$$

$$\hat{z}: \quad \frac{HU_{sz}}{t_s U_{sz}}\frac{\partial u_z}{\partial t} + U_{sz}\left(\frac{HU_{sx}}{HU_{sz}}u_x\frac{\partial u_z}{\partial x} + \frac{HU_{sy}}{WU_{sz}}u_y\frac{\partial u_z}{\partial y} + \frac{HU_{sz}}{LU_{sz}}u_z\frac{\partial u_z}{\partial z}\right) - \frac{HP_s}{L\rho U_{sz}}\frac{\partial p}{\partial z} + \frac{\mu U_{sz}}{H\rho U_{sz}}\left(\frac{\partial^2}{\partial x^2} + \frac{H^2}{W^2}\frac{\partial^2}{\partial y^2} + \frac{H^2}{L^2}\frac{\partial^2}{\partial z^2}\right)u_z. \tag{2.60c}$$

From here, we can cancel terms and use the approximations that $H/W \ll 1$ and $H/L \ll 1$ from the design of the system to reduce some terms. This cannot be done with the U_{si} terms which need the

[9] W = piston width

continuity equation.

$$\hat{x}: \quad \frac{HU_{sx}}{t_s U_{sz}}\frac{\partial u_x}{\partial t} + U_{sx}\left(\frac{U_{sx}}{U_{sz}}u_x\frac{\partial u_x}{\partial x} + \frac{HU_{sy}}{WU_{sz}}u_y\frac{\partial u_x}{\partial y} + \frac{H}{L}u_z\frac{\partial u_x}{\partial z}\right) = -\frac{P_s}{\rho U_{sz}}\frac{\partial p}{\partial x} + \frac{\mu U_{sx}}{H\rho U_{sz}}\frac{\partial^2 u_x}{\partial x^2} \tag{2.61a}$$

$$\hat{y}: \quad \frac{HU_{sy}}{t_s U_{sz}}\frac{\partial u_y}{\partial t} + U_{sy}\left(\frac{U_{sx}}{U_{sz}}u_x\frac{\partial u_y}{\partial x} + \frac{HU_{sy}}{WU_{sz}}u_y\frac{\partial u_y}{\partial y} + \frac{H}{L}u_z\frac{\partial u_y}{\partial z}\right) = -\frac{HP_s}{W\rho U_{sz}}\frac{\partial p}{\partial y} + \frac{\mu U_{sy}}{H\rho U_{sz}}\frac{\partial^2 u_y}{\partial x^2} \tag{2.61b}$$

$$\hat{z}: \quad \frac{H}{t_s}\frac{\partial u_z}{\partial t} + U_{sz}\left(\frac{U_{sx}}{U_{sz}}u_x\frac{\partial u_z}{\partial x} + \frac{HU_{sy}}{WU_{sz}}u_y\frac{\partial u_z}{\partial y} + \frac{H}{L}u_z\frac{\partial u_z}{\partial z}\right) = -\frac{HP_s}{L\rho U_{sz}}\frac{\partial p}{\partial z} + \frac{\mu}{H\rho}\frac{\partial^2 u_z}{\partial x^2} \tag{2.61c}$$

Moving to the incompressible continuity equation,

$$0 = \frac{\partial U_{*x}}{\partial x_*} + \frac{\partial U_{*y}}{\partial y_*} + \frac{\partial U_{*z}}{\partial z_*} \tag{2.62}$$

$$0 = \frac{U_{sx}}{H}\frac{\partial u_x}{\partial x} + \frac{U_{sy}}{W}\frac{\partial u_y}{\partial y} + \frac{U_{sz}}{L}\frac{\partial u_z}{\partial z}, \tag{2.63}$$

and cancelling through by $\frac{U_{sz}}{H}$, we obtain

$$0 = \frac{LU_{sx}}{HU_{sz}}\frac{\partial u_x}{\partial x} + \frac{LU_{sy}}{WU_{sz}}\frac{\partial u_y}{\partial y} + \frac{\partial u_z}{\partial z}. \tag{2.64}$$

This last system is fully non-dimensional. However, we can only balance two of the coefficients here. Because we are applying a pressure gradient primarily along the $\hat{z}$ axis, we assume that both U_{sx} and $U_{sy} \ll U_{sz}$. However, since $L > W \gg H$, we choose to balance $\frac{LU_{sx}}{HU_{sz}} \approx 1$. We can fudge the second balance by treating $\frac{NLU_{sy}}{WU_{sz}}$ where $N > 1$ is some fudge factor to make the system fully balance. This gives us our two equivalence relations

$$U_{sx} = \frac{H}{L}U_{sz} \qquad \text{and} \qquad U_{sy} = \frac{W}{NL}U_{sz} \tag{2.65}$$

We put these balances in the simplified Navier-Stokes equations, along with the pressure non-dimensionalization from Equation 2.39 $P_s = \frac{\mu L U_{sz}}{H^2}$.[10]

$$\hat{x}: \quad \frac{H^2}{t_s L}\frac{\partial u_x}{\partial t} + \frac{H}{L}U_{sz}\left(\frac{H}{L}u_x\frac{\partial u_x}{\partial x} + \frac{H}{NL}u_y\frac{\partial u_x}{\partial y} + \frac{H}{L}u_z\frac{\partial u_x}{\partial z}\right) = -\frac{\mu L}{\rho H^2}\frac{\partial p}{\partial x} + \frac{\mu}{\rho L}\frac{\partial^2 u_x}{\partial x^2} \tag{2.66a}$$

$$\hat{y}: \quad \frac{HW}{Nt_s L}\frac{\partial u_y}{\partial t} + \frac{W}{NL}U_{sz}\left(\frac{H}{L}u_x\frac{\partial u_y}{\partial x} + \frac{H}{NL}u_y\frac{\partial u_y}{\partial y} + \frac{H}{L}u_z\frac{\partial u_y}{\partial z}\right) = -\frac{\mu L}{\rho WH}\frac{\partial p}{\partial y} + \frac{\mu W}{N\rho HL}\frac{\partial^2 u_y}{\partial x^2} \tag{2.66b}$$

$$\hat{z}: \quad \frac{H}{t_s}\frac{\partial u_z}{\partial t} + U_{sz}\left(\frac{H}{L}u_x\frac{\partial u_z}{\partial x} + \frac{H}{NL}u_y\frac{\partial u_z}{\partial y} + \frac{H}{L}u_z\frac{\partial u_z}{\partial z}\right) = -\frac{\mu L}{\rho H}\frac{\partial p}{\partial z} + \frac{\mu}{H\rho}\frac{\partial^2 u_z}{\partial x^2} \tag{2.66c}$$

Now we can eliminate the convective derivative terms because they are $O\left(\frac{H}{L}\right)^2$ and therefore negligible.[11] Furthermore, we can eliminate the time derivative term from the $\hat{x}$ and $\hat{y}$ equations for being $O\left(\frac{H}{L}\right)$,

$$\hat{x}: \quad 0 = -\frac{\mu L}{\rho H^2}\frac{\partial p}{\partial x} + \frac{\mu}{\rho L}\frac{\partial^2 u_x}{\partial x^2} \tag{2.67a}$$

$$\hat{y}: \quad 0 = -\frac{\mu L}{\rho WH}\frac{\partial p}{\partial y} + \frac{\mu W}{N\rho HL}\frac{\partial^2 u_y}{\partial x^2} \tag{2.67b}$$

$$\hat{z}: \quad \frac{H}{t_s}\frac{\partial u_z}{\partial t} = -\frac{\mu L}{\rho H}\frac{\partial p}{\partial z} + \frac{\mu}{H\rho}\frac{\partial^2 u_z}{\partial x^2}, \tag{2.67c}$$

And if we note that the pressure gradient term is order $O\left(\frac{L}{H}\right)^2 \gg 1$, compared to with viscosity term, which is order $O(1)$, so we are left with the following simplification:

$$\hat{x}: \quad 0 = \frac{\partial p}{\partial x} + O\left(\frac{H}{L}\right) \tag{2.68a}$$

$$\hat{y}: \quad 0 = \frac{\partial p}{\partial y} + O\left(\frac{H}{L}\right) \tag{2.68b}$$

$$\hat{z}: \quad \frac{H}{t_s}\frac{\partial u_z}{\partial t} = -\frac{\mu L}{\rho H}\frac{\partial p}{\partial z} + \frac{\mu}{H\rho}\frac{\partial^2 u_z}{\partial x^2} + O\left(\frac{H}{L}\right), \tag{2.68c}$$

which, upon de-normalization, is exactly the equation developed in Equation 2.32. Thus, it is reasonable to use the thin-film approximation in this analysis.

[10] Since pressure is going to have a strongest drop along the $\hat{z}$ axis, we will return to our non-dimensionalization factor

[11] as we discussed before, $\frac{W}{NL} < \frac{H}{L}$ based on our balancing choices

2.2.2 Unidirectional Flow in Rectangular Channel

Unidirectional fluid flow in a rectangular channel is exactly solvable, although Equation 2.58 is the first-order approximation in the limit that the channel width $\rightarrow \infty$. However, this analysis is somewhat complicated and requires a Fourier series approximation [283, 285]. The steady 2D unidirectional fluid flow equations $\underline{\mathbf{U}} = u_{*z}(x_*, y_*)$ reduce to

$$\hat{x}: \qquad 0 = \frac{\partial P}{\partial x_*} \tag{2.69a}$$

$$\hat{y}: \qquad 0 = \frac{\partial P}{\partial y_*} \tag{2.69b}$$

$$\hat{z}: \qquad 0 = -\frac{\partial P}{\partial z_*} + \mu\left(\frac{\partial^2 u_{*z}}{\partial {x_*}^2} + \frac{\partial^2 u_{*z}}{\partial {y_*}^2}\right), \tag{2.69c}$$

From this, we see that $P = P(z_*)$ only. Because $u_{*z} \neq u_{*z}(z_*)$, we also know that $\frac{\partial P}{\partial z_*} = const$. Nondimensionalizing, and choosing $u_{*z} = U_s u$, $x_* = hx$ and $y_* = hy$, and setting $U_s = \frac{h^2}{\mu}\frac{\partial P}{\partial z_*}$, we are left with the equation

$$1 = \frac{\partial^2 u}{\partial x^2} + \frac{\partial^2 u}{\partial y^2} \tag{2.70a}$$

with the boundary conditions

$$BCs = \begin{cases} u = 0 & \text{for } x = \pm\frac{1}{2} \\ u = 0 & \text{for } y = \pm\frac{w}{2h} \\ \frac{\partial u}{\partial x} = 0 & \text{for } x = 0 \\ \frac{\partial u}{\partial y} = 0 & \text{for } y = 0, \end{cases} \tag{2.70b}$$

where the first two BC are the Dirichlet no-slip conditions at $x_* = \pm h/2$ and $y_* = \pm w/2$ and the second two are the no-shear stress conditions due to the symmetry of the expected flow profile. We will use a perturbative analysis to solve this problem, setting $u = u_0 + u_1$ where $u_0 = u_0(x)$ solve the infinite plate problem and $u_1(x,y)$ is the correction for the finite channel width. Because

$$1 = \frac{\partial^2 u_0}{\partial x^2}, \tag{2.71}$$

where $u_0(\pm\frac{1}{2}) = 0$, which solves to

$$u_0(x) = \frac{1}{2}\left(x^2 - \frac{1}{4}\right). \tag{2.72}$$

From here, we can find v_1 as the solution to a Laplace equation

$$0 = \nabla^2 u_1. \tag{2.73}$$

Applying the boundary conditions to u gives

$$u(\pm\frac{1}{2}, y) = 0 = u_0(\pm\frac{1}{2}) + u_1(\pm\frac{1}{2}, y) \tag{2.74}$$

$$\implies u_1(\pm\frac{1}{2}, y) = 0 \tag{2.75}$$

Similarly,

$$u(y, \pm\frac{w}{2h}) = u_0(x) + u_1(x, \pm\frac{w}{2h}) = 0 \tag{2.76}$$

$$= \frac{1}{2}\left(x^2 - \frac{1}{4}\right) \tag{2.77}$$

$$\implies u_1(x, \pm\frac{w}{2h}) = -\frac{1}{2}\left(x^2 - \frac{1}{4}\right). \tag{2.78}$$

This equation is easy to solve with separation of variables. Trying $u_1(x,y) = X(x)Y(y)$ as a test function results in

$$0 = \frac{X''}{X} + \frac{Y''}{Y}$$

and because the X terms depend only on x and the Y terms depend only on y, we can set $\frac{Y''}{Y} = \mu^2$. From here we get

$$Y(y) = A\sinh(\mu y) + B\cosh(\mu y) \tag{2.79}$$

where $A = 0$ due to the no-shear stress condition at $y = 0$ and

$$X(x) = C\sin(\mu x) + D\cos(\mu x) \tag{2.80}$$

where $C = 0$ due to the no-stress condition at $x = 0$. The no-slip condition at $x = \pm\frac{1}{2}$ requires $\cos(\frac{\mu}{2}) = 0$ which gives

$$\mu_n = n\pi, \quad \text{for } n \text{ odd} \tag{2.81}$$

$$\implies \mu_n = (2n+1)\pi, \quad \text{for all } n \tag{2.82}$$

so therefore

$$u_1(x,y) = \sum_{n=0}^{\infty} A_n \cosh(\mu_n y)\cos(\mu_n x). \tag{2.83}$$

The coefficients A_n are solved by applying the $y = \pm\frac{w}{2h}$ boundary condition with a Fourier cos series,

$$u_1(x, \pm\frac{w}{2h}) = -\frac{1}{2}\left(x^2 - \frac{1}{4}\right) = \sum_{n=0}^{\infty} A_n \cosh(\frac{\mu_n w}{2h})\cos(\mu_n x).$$

Because the $\cos(\mu_n)$ functions are orthogonal, we only have to account for the $m = n$ cases, and integrate x from $-\frac{1}{2}$ to $\frac{1}{2}$, leaving

$$-\int_{-1/2}^{1/2} \frac{1}{2}\left(x^2 - \frac{1}{4}\right)\cos(\mu_n x)\,\mathrm{d}x = A_n \cosh\left(\frac{\mu_n w}{2h}\right)\int_{-1/2}^{1/2} \cos^2(\mu_n x)\,\mathrm{d}x \tag{2.84}$$

$$\frac{2(-1)^n}{\mu_n^3} = A_n \cosh\left(\frac{\mu_n w}{2h}\right)\left(\frac{1}{2}\right) \tag{2.85}$$

$$\implies A_n = \frac{4(-1)^n}{\mu_n^3 \cosh\left(\frac{\mu_n w}{2h}\right)} \tag{2.86}$$

$$\implies u_1(x,y) = \sum_{n=0}^{\infty} \frac{4(-1)^n}{\mu_n^3}\frac{\cosh(\mu_n y)}{\cosh\left(\frac{\mu_n w}{2h}\right)}\cos(\mu_n x). \tag{2.87}$$

From here, we have our complete series solution for $u_{*z}(x_*, y_*)$:

$$\implies u_{*z}(x_*, y_*) = \frac{h^2}{\mu}\frac{\partial P}{\partial z_*}\left[\frac{1}{8}\left(\left(\frac{2x_*}{h}\right)^2 - 1\right) + \sum_{n=0}^{\infty} \frac{4(-1)^n}{\mu_n^3}\frac{\cosh\left(\frac{\mu_n y_*}{h}\right)}{\cosh\left(\frac{\mu_n w}{2h}\right)}\cos\left(\frac{\mu_n x_*}{h}\right)\right], \tag{2.88}$$

where $mu_n = (2n+1)\pi$. Equation 2.88 can be differentiated to find the shear stress,[12] but of more interest here is finding the hydraulic resistance, which can be obtained by integrating across the

[12] which has been left as an exercise to the Thesis Committee. Hint: $\underline{\underline{\tau}} = \nabla\underline{\mathbf{u}} + (\nabla\underline{\mathbf{u}})^T$

area of the channel,

$$Q = \int_{-w/2}^{w/2} \mathrm{d}y_* \int_{h/2}^{h/2} u_{*z}(x_*, y_*)\,\mathrm{d}x \tag{2.89}$$

$$Q = \frac{h^2}{\mu}\frac{\partial P}{\partial z_*}\left[w\int_{-h/2}^{h/2} \frac{1}{8}\left(\left(\frac{2x_*}{h}\right)^2 - 1\right)\mathrm{d}x \sum_{n=0}^{\infty} \frac{4(-1)^n}{\mu_n^3} \frac{\int_{-w/2}^{w/2}\cosh\left(\frac{\mu_n y_*}{h}\right)\mathrm{d}y}{\cosh\left(\frac{\mu_n w}{2h}\right)} \int_{-h/2}^{h/2} \cos\left(\frac{\mu_n x_*}{h}\right)\mathrm{d}x \right] \tag{2.90}$$

$$Q = \frac{h^2}{\mu}\frac{\partial P}{\partial z_*}\left[-\frac{wh}{12} + \sum_{n=0}^{\infty} \frac{4(-1)^n}{\mu_n^3}\left(\frac{2h}{\mu_n}\tanh\left(\frac{\mu_n w}{2h}\right)\right)\left(\frac{2h}{\mu_n}(-1)^n\right)\right] \tag{2.91}$$

Lastly, if we take a linear pressure gradient, $\frac{\partial P}{\partial z_*} = -\frac{\Delta P}{L}$, we are left with

$$Q = \frac{wh^3}{12\mu L}\left[1 - \frac{h}{w}\sum_{n=0}^{\infty}\frac{192}{\mu_n^5}\tanh\left(\frac{\mu_n w}{2h}\right)\right]\Delta P\,. \tag{2.92}$$

Because this coefficient provides a linear relationship between ΔP and Q, we find the resistance for a rectangular channel:

$$R_{\text{rect}} = \frac{12\mu L}{wh^3\left(1 - \frac{h}{w}\sum_{n=0}^{\infty}\frac{192}{\mu_n^5}\tanh\left(\frac{\mu_n w}{2h}\right)\right)} \tag{2.93}$$

Equation 2.93 converges extremely rapidly; because $\tanh(x) \approx 1$ for $x \tilde{>} 1$, for $h \tilde{>} w$ we can approximate $\tanh\left(\frac{\mu_n w}{2h}\right) \approx 1$. For a square channel where $h = w$,

$$R_{\text{square}} = \frac{12\mu L}{wh^3(1-0.578)} \tag{2.94}$$

$$= \frac{28.4\mu L}{h^4}. \tag{2.95}$$

For comparison, a circular channel with radius h has a resistance $R = \frac{8\mu L}{h^4}$.

In the other limit $w \gg h$,

$$R_{\text{rect}} = \frac{12\mu L}{wh^3\left(1 - 0.630\frac{h}{w}\right)}, \tag{2.96}$$

which is the standard approximation for the hydraulic resistance of a rectangular channel [283, 285]. Note that if we take this equation in the limit $h = w$, we obtain

$$R_{\text{square,rect approx}} = \frac{12\mu L}{wh^3(1-0.630)} \tag{2.97}$$

$$= \frac{32.4\mu L}{h^4}. \tag{2.98}$$

for an error of only 14.1%. Thus, Equation 2.96 is a reasonably useful approximation for the full range $w > h$. For $w < h$, we only need to switch $w \leftrightarrow h$.

Aside 2.2: Convergence of Equation 2.93

For a slightly higher precision approximation, we note that for $x > 1$,

$$\tanh(x) = \frac{1-e^{-2x}}{1+e^{-2x}} = 1 + 2\sum_{m=1}^{\infty}(-1)^m e^{-2xm} \text{ for } x \gg 1. \tag{2.99}$$

Considering the $n = 0$ and $n \neq 0$ cases,

$$\tanh\left(\frac{(2n+1)\pi w}{2h}\right) = \begin{cases} 1+2\sum_{m=1}^{\infty}(-1)^m e^{-\frac{m\pi w}{h}}, & \text{for } n = 0 \\ 1+2\sum_{m=1}^{\infty}(-1)^m e^{-\frac{(2n+1)m\pi w}{h}}, & \text{for } n \geq 1. \end{cases} \tag{2.100}$$

Because the correction terms get smaller exponentially rapidly, we consider the maximum possible error in the first correction term, where $w = h$, $n = 1$, and $m = 1$:

$$\tanh\left(\frac{(2n+1)\pi w}{2h}\right) \sim \begin{cases} 1-2e^{-\pi w/h}+O\left(e^{-2\pi w/h}\right), & \text{for } n = 0 \\ 1-2e^{-3\pi w/h}+O\left(e^{-6\pi w/h}\right), & \text{for } n = 1 \end{cases} \tag{2.101}$$

$$\sim \begin{cases} 1-0.086+0.0037+\ldots, & \text{for } n = 0 \text{ and } w = h \\ 1-0.00016+1.3\times 10^{-7}+\ldots, & \text{for } n = 1 \text{ and } w = h \end{cases} \tag{2.102}$$

Because the largest possible $n > 0$ correction term occurs for $n = 1$ and is a difference of only 0.016%, we can safely neglect it. Thus, we can comfortably make the approximation

$$\frac{192}{(2n+1)^5}\tanh\left(\frac{(2n+1)\pi w}{2h}\right) \approx \begin{cases} 192\tanh\left(\frac{\pi w}{2h}\right), & \text{for } n = 0 \\ \frac{192}{(2n+1)^5}\left(1+O\left(e^{-3\pi w/h}\right)\right), & \text{for } n \geq 1. \end{cases} \tag{2.103}$$

Using Mathematica to take the full sum, we find that this correction has a maximum error at $w = h$ of

$$\left|\sum_{n=1}^{\infty}\frac{192}{\mu_n^5}\tanh\left(\frac{\mu_n w}{2h}\right) - \sum_{n=1}^{\infty}\frac{192}{\mu_n^5}\tanh\left(\frac{\mu_n w}{2h}\right)\right| \leq 4.2 * 10^{-7}. \tag{2.104}$$

Using the sum $\sum_{n=1}^{\infty}\frac{1}{(2n+1)^{-5}} = 0.0045237$, we can list a very close approximation

to the resistance:

$$R_{\text{rect}} \approx \frac{12\mu L}{wh^3\left(1-\frac{h}{w}\frac{192}{\pi^5}\left(\tanh\left(\frac{\pi w}{2h}\right)+0.0045237+O\left(e^{-3\pi w/h}\right)\right)\right)} \tag{2.105}$$

where the $\frac{w}{h}$ correction is close to $O\left(10^{-7}\right)$.

Considering only the *most* dominant correction term,

$$\tanh(\frac{\mu_n w}{2h}) = 1-2e^{-\pi w/h}+O\left(e^{-2\pi w/h}\right),$$

where $O\left(e^{-2\pi w/h}\right) \leq 0.0037$, we can develop an approximation that is good to a factor of 10^{-3}:

$$R_{\text{rect approx2}} \approx \frac{12\mu L}{wh^3\left(1-\frac{h}{w}\frac{384}{\pi^5}\left(\left(1-e^{-\pi w/h}\right)+0.0045+O\left(e^{-2\pi w/h}\right)\right)\right)} \tag{2.106}$$

$$\approx \frac{12\mu L}{wh^3\left(1-0.630\frac{h}{w}+1.255\frac{h}{w}e^{-\pi w/h}+O\left(\frac{h}{w}e^{-2\pi w/h}\right)\right)}. \tag{2.107}$$

In the case where $w \gg h$, this reduces to the familiar $R_{\text{rect}} \approx \frac{12\mu L}{wh^3\left(1-0.630\frac{h}{w}\right)}$ and for a square, the approximation provides

$$R_{\text{rect approx2}} \xrightarrow{w\to h} \frac{28.1\mu L}{h^4}. \tag{2.108}$$

This result differs from the true answer, obtained by taking the full sum in Equation 2.93, is $\frac{28.5\mu L}{h^4}$, by only 0.6%.

2.3 Low *Re* Flows in a Differentially Rotating Tube

This derivation will determine the flow profile in a differentially rotating (but constant radius) microfluidic channel.

Assuming steady state *Stokes* flow, the Navier-Stokes equations reduce to

$$\nabla P = \mu\nabla^2\underline{\mathbf{U}}. \tag{2.109}$$

Due to the linearity and separability of the Stokes equation, we can break the fluid flow problem

into pressure driven flow $\underline{\mathbf{U}}_p$ and wall-driven flow $\underline{\mathbf{U}}_w$ which can further be separated based on axial and azimuthal wall motion. We will first consider flow driven only by radially symmetric rotating walls. Walls with radial boundaries that change periodically have been well studied by Pulsatile Flow analyses [281]. The pressure-driven flow is the previously established solution $\underline{\mathbf{U}}_p = \frac{a^2}{4\mu}\frac{\Delta P}{L}\left(1-\frac{r^2}{a^2}\right)\hat{z}$ and because the remainder of the fluid flow must necessarily be radially symmetric, eliminating non-axial pressure gradients, the pressure-driven flow also consumes the remaining pressure terms. The wall motion will be broken up into a linearly independent basis, so we will represent it with a Fourier series in a finite tube of length L:

$$\underline{\mathbf{V}}_{\text{wall}} = \hat{\phi}\,U_0 + \sum_{n=1}^{\infty} U_{a,n}\sin(2\pi nz/L) + U_{b,n}\cos(2\pi nz/L) \tag{2.110}$$

where $\frac{n\pi}{L}$ represents the wavenumber with $n = 0,1,2,\ldots$, the average wall rotation speed $U_0 = a\omega_0$ where ω_0 is the average rotation rate, and the coefficients $U_{a,n}$ and $U_{b,n}$ are velocity terms. While we consider a finite tube in this analysis, we assume that $L \gg r$ to neglect edge effects. Using no-slip, and assuming azimuthal symmetry s.t. $\frac{\partial U}{\partial \phi} = 0$ the equations of motion are

$$\hat{r}: \quad 0 = \frac{\partial}{\partial r}\left(\frac{1}{r}\frac{\partial (rU_r)}{\partial r}\right) + \frac{\partial^2 U_r}{\partial z^2} \tag{2.111}$$

$$\hat{\phi}: \quad 0 = \frac{\partial}{\partial r}\left(\frac{1}{r}\frac{\partial (rU_\phi)}{\partial r}\right) + \frac{\partial^2 U_\phi}{\partial z^2} \tag{2.112}$$

with boundary conditions

$$\underline{\mathbf{U}}_w(r=a) = \underline{\mathbf{V}}_{\text{wall}}. \tag{2.113}$$

Because the wall motion is purely azimuthal, we assume that there is no radial component to the fluid flow (*i.e.*, $\underline{\mathbf{U}}_w \cdot \hat{r} = 0$ and $U_r = 0$). Solving the $\hat{\phi}$ equation, we see if U_ϕ is separable, trying

$$U_\phi = A(r)B(z)$$

which results in the separable equation with A and B as dimensionless functions:

$$-\frac{B''}{B} = \frac{1}{A}\frac{\partial}{\partial r}\frac{1}{r}\left(\frac{\partial (rA)}{\partial r}\right) = \eta^2$$

where η is a separability constant. We easily determine that

$$B(z) = a\sin(\eta z) + b\cos(\eta z), \tag{2.114}$$

where we can form a complete set of eigenfunctions $B(z;m)$ if we choose $\eta = \eta_m = 2\pi m/L$, where $m = 0,1,2,\ldots$. Conveniently, the eigenvalues η_m will easily allow us to impose the boundary conditions from Equation 2.110.

With the refined separability constant, A equation then becomes

$$A\eta_m^2 = \frac{\partial^2 A}{\partial r^{2^2}} + \frac{1}{r}\frac{\partial A}{\partial r} - \frac{A}{r^2} \tag{2.115}$$

$$\implies 0 = \frac{\partial^2 A}{\partial r^{2^2}} + \frac{1}{r}\frac{\partial A}{\partial r} - \left(\eta_m^2 + \frac{1}{r^2}\right) \tag{2.116}$$

This is an altered Bessel equation which can be solved by the transform $r = \frac{iy}{\eta_m}$, resulting in the standard Bessel differential equation

$$0 = A'' + \frac{1}{y}A' + \left(1 - \frac{1}{y^2}\right) \tag{2.117}$$

which is solved to

$$A(r;m) = c_1 J_1(i\eta_m r) + c_2 Y_1(i\eta_m r). \tag{2.118}$$

Because the flow is assumed to be non-singular at the center of the channel, $c_2 = 0$. Additionally, because the flow is radially symmetric, we choose $A(a) = 1$ and allow the other boundary conditions to be satisfied by $B(z;n)$:

$$A(a;m) = c_1 J_1(i\eta_m a) = 1 \tag{2.119}$$

$$\implies A(r;m) = \frac{J_1(i\eta_m r)}{J_1(i\eta_m a)} \tag{2.120}$$

$$= \frac{I_1(\eta_m r)}{I_1(\eta_m a)} \tag{2.121}$$

$$= \frac{I_1(2\pi m r/L)}{I_1(2\pi m a/L)} \tag{2.122}$$

where we have used the fact that the modified Bessel function $I_\alpha(x) = i^{-\alpha}J_\alpha(ix)$. Furthermore, the $m = 0$ case is expanded by

$$A(r;0) = \lim_{m\to 0} \frac{I_1(2\pi m r/L)}{I_1(2\pi m a/L)} = \frac{r}{a}. \tag{2.123}$$

Putting everything together, we have

$$U_\phi(r,z) = \sum_{m=0}^{\infty} A(r;m)(a_n \sin(\eta_m z) + b_n \cos(\eta_m z)) \tag{2.124}$$

$$U_\phi(r,z) = \frac{b_0 r}{a} + \sum_{m=1}^{\infty} \frac{I_1(2\pi m r/L)}{I_1(2\pi m a/L)}(a_m \sin(2\pi m z/L) + b_m \cos(2\pi m z/L)) \tag{2.125}$$

Example 2.1: Uniformly Rotating Channel

A uniformly rotating channel has only the first term in the Fourier series

$$\underline{\mathbf{V}}_{\text{wall}} = \hat{\phi}\, U_0$$

requires $b_0 = U_0$

$$\implies U_\phi = \frac{U_0 r}{a} \tag{2.126}$$

$$= \omega_0 r \tag{2.127}$$

and provides the expected solid-body rotational flow profile.

Example 2.2: Arbitrary Fourier Boundary Condition

Imposing the boundary conditions from Equation 2.110 is simple due to the nature of the complete eigenbasis of functions used. At $r = a$, Equation 2.125 becomes

$$\begin{aligned} U_\phi(a,z) &= b_0 + \sum_{m=1}^{\infty} a_m \sin(2\pi m z/L) + b_m \cos(2\pi m z/L) \\ &= U_0 + \sum_{n=1}^{\infty} U_{a,n} \sin(2\pi n z/L) + U_{b,n} \cos(2\pi n z/L) = V_{\phi,\text{wall}} \end{aligned} \tag{2.128}$$

which is easily satisfied by setting $m = n$, $a_m = U_{a,n}$ and $b_m = U_{b,m}$. Thus, by applying the Fourier boundary conditions from Equation 2.110, we have

$$U_\phi(r,z) = \frac{U_0 r}{a} + \sum_{n=1}^{\infty} \frac{I_1(2\pi n r/L)}{I_1(2\pi n a/L)} \left(U_{a,n} \sin(2\pi n z/L) + U_{b,n} \cos(2\pi n z/L)\right) \tag{2.129}$$

Example 2.3: Arbitrary Function

By virtue of using the Fourier series, we can solve for the fluid motion for any arbitrary outer

cylinder rotation profile $f(z)$ where

$$a_n = \frac{2}{L}\int_0^L f(z)\sin(2\pi nz/L)\,\mathrm{d}z \tag{2.130}$$

$$b_n = \frac{2}{L}\int_0^L f(z)\cos(2\pi nz/L)\,\mathrm{d}z \tag{2.131}$$

for $n = 1,2,3,\ldots$ and

$$b_0 = \frac{1}{L}\int_0^L f(z)\,\mathrm{d}z \tag{2.132}$$

Chapter 3

Microfluidic Circuitry via Optofluidic Lithography*

3.1 Introduction

Microfluidic systems offer numerous benefits for biochemical applications, such as low cost, rapid reaction times, low reagent volumes, and the ability to mix, transport, and/or array chemical processes involving beads, cells, or other biomolecules [4, 5, 7]. The ability to dynamically control microfluidic systems in a self-regulating manner is therefore critical for the long-term development of lab-on-a-chip (LOC) technology; at present, the majority of integrated microfluidic systems require substantial external regulation during device operation [3, 24, 286]. In recent years, research has shifted toward producing alternative, self-regulating microfluidic technologies [25, 36, 45]. However, producing dynamic microfluidic control systems in an efficient, cost-effective manner has remained a considerable challenge. For example, elastomeric LOC devices that exhibit static pressure gain require at least four layers of substrate material to achieve the desired functionality [25, 29, 47, 48].

Previous works have demonstrated optofluidic lithography in Teflon-based systems to fabricate freely moving pistons and check-valves in two-to four-layer microfluidic systems. However, the efficacy of such components remains limited due to the high pressures required for operation [57, 287, 288, 289]. Maskless optofluidic lithography has been used to create railed systems which allow free movement at low pressure [290, 291, 292]. Single-layer optofluidic regulatory devices have been developed which require changes in fluid properties, such as Temperature and pH, but

* Portions of this chapter are adapted from Refs. 59, 60, 61 with permission from IEEE.

do not respond to flow parameters (*e.g.*, pressure and flow velocity) [293, 294, 295]. While many biological experiments require precise reagent flow rates unavailable through such passive controls [38, 296], building devices that function as hydraulic analogs to electronic "current sources" has proved a considerable challenge. Previously microfluidic current sources have required three PDMS layers and pressure $>$ 1 ATM for current regulation [38], or have been single-layer devices PDMS devices that only function at high Reynolds number (*i.e.*, $Re > 80$) [296].

Many lab-on-a-chip operations occur at ultra-low Reynolds numbers (*e.g.*, $Re < 0.1$), including point-of-care (POC) molecular diagnostics and on-site chemical detection. However, at low Reynolds number (Re) (Section 2.1.1.4) fluid behavior becomes linear and time-reversible [49, 50], static microfluidic control structures begin to have no effect on fluid behavior, requiring new approaches. Previously, researchers have utilized dynamic resistive elements, such as microbeads and rotational microstructures, to rectify $Re < 0.2$ flow; however, such systems require hydrodynamic forces to return the elements to their "closed state" positions, allowing undesired reverse flow during this process. Conversely, double-layer *flap-type* check valves immediately return to their closed state in the absence of forward flow; unfortunately, such valves have exhibited limited functionality for $Re \lesssim 0.3$ flow. To overcome these issues, here we introduce single-layer microfluidic "spring" diodes, which utilize free-standing polymeric microsprings that: (i) compress to promote forward flow, (ii) return to the closed position in the absence of forward flow, and (iii) remain in the closed position to obstruct reverse flow.

3.2 Fabrication

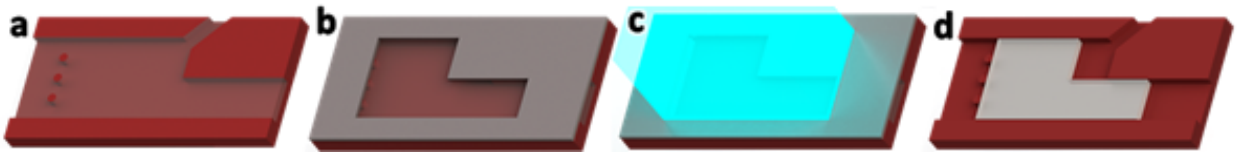


Figure 3.1 Optofluidic lithography fabrication process. **(a)** A photocurable liquid — PEGDA with 1% photoiniatator — is loaded into a PDMS microchannel. **(b)** A photomask is placed in contact with the device which is then **(c)** exposed to UV light, causing PEGDA to photopolymerize. The piston does not stick to the PDMS due to thin oxygen layers on each PDMS face of the microchannels. **(d)** The mask is removed and the remaining photocurable liquid is drained from the device.

The bulk microfluidic system was fabricated using standard soft lithography processes, as described in previous work [10, 290]. Briefly, micro-molded poly(dimethyl-siloxane) (PDMS), with microchannel heights of 110 μm, was thermally bonded to glass slides coated with an 80 μm PDMS

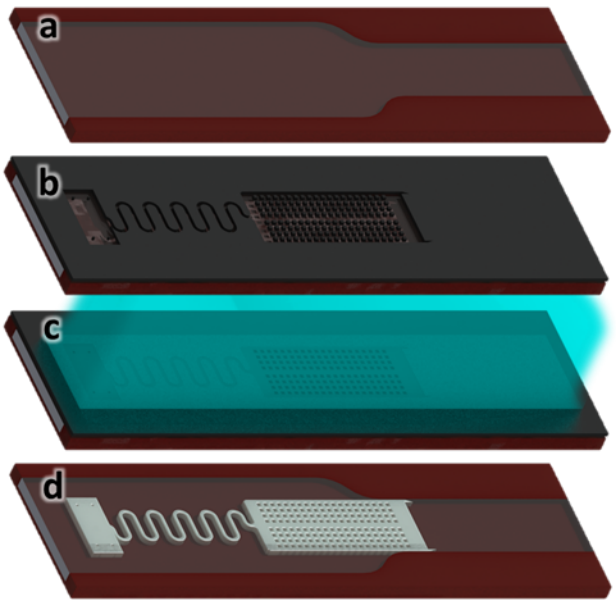


Figure 3.2 The optofluidic fabrication process. **(a)** A photocurable liquid — PEGDA with 1% photoinitator — is loaded into a PDMS microchannel. **(b)** A photomask is placed in contact with the device which is then **(c)** exposed to UV light, causing PEGDA to photopolymerize. The piston does not stick to the PDMS due to contraction of the cured PEGDA and oxygen layers in to the PDMS. **(d)** The mask is removed and the remaining photocurable liquid is drained and replaced by non-photocurable PEGDA.

layer (via PDMS-PDMS bonding techniques) to prevent the optofluidic components from sticking to the glass slides. Figure 3.1 shows conceptual illustrations of the optofluidic lithography process to create freely moving pistons within a PDMS microchannel. First, a solution of poly(ethylene glycol) diacrylate (PEGDA) with 1% photoinitiator (2,2-dimethoxy-2-phenylacetophenone) was loaded into the device (Fig. 3.1a). A photomask was placed in contact with the device and aligned (3.1b). The device was then exposed to UV, causing the PEGDA to photopolymerize. Due to a thin layer of oxygen adjacent to each PDMS face of the microchannels, the cured PEGDA did not bond to the substrate (leaving a 5-10 μm gap between the PEGDA and the PDMS) (3.1c). The remaining uncured PEGDA was drained from the device and replaced by a PEGDA solution without photoinitiator (3.1d). Figure 3.14 shows optical images of the fabricated gain device, illustrating the piston in both its “open” and “closed” positions.

3.3 Analysis: Flow Behavior in Narrow Gap with Moving Plate

In this section, we will derive the behavior of a piston attached to a spring which is driven by pressure gradients and by fluid shear drag as fluid moves through a narrow gap between the piston and an immobile section of a channel. The setup is shown in Figure 3.3.

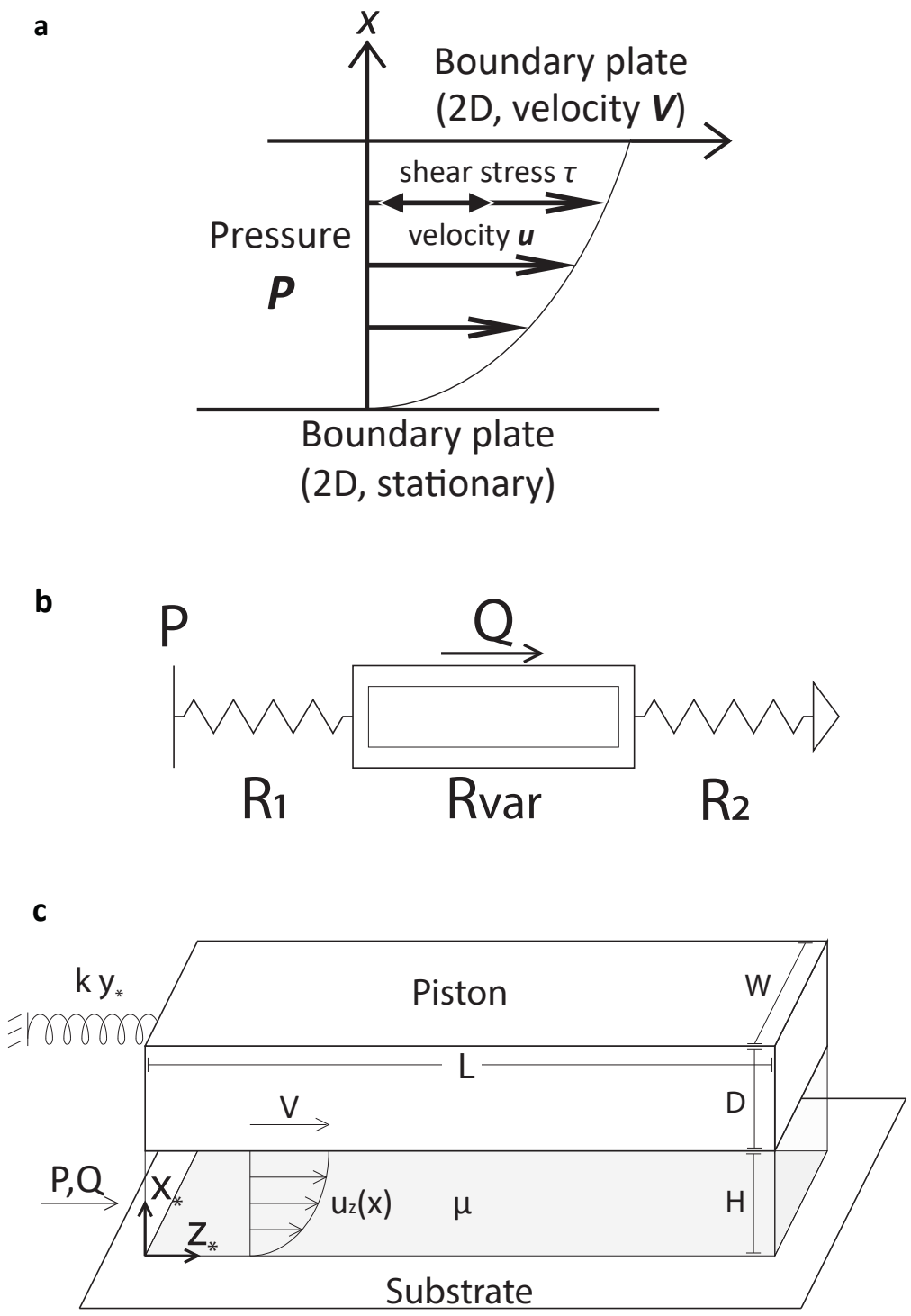


Figure 3.3 System in which fluid flows through a narrow channel with a movable piston on one side. The piston moves relative to the substrate via shear forces as well as by direct pressure forces, and is restored to equilibrium by a spring with constant y. **(a)** Stresses within a narrow gap for Couette-Poiseuille flow with upper boundary moving at velocity V and pressure input at pressure P. The no-slip boundary condition leads to a superposition of a linear Couette flow profile and a parabolic Poiseuille flow profile. **(b)** Lumped parameter circuit model illustrating the input and output resistances. **(c)** Diagram of piston with labeled dimensions.

3.3.1 Poiseuille-Couette Flow Solution

As was demonstrated in Section 2.2, the thin-film system may be treated as an unidirectional flow equation. From our figure above, we are also able to develop our boundary conditions from the no-slip condition:[1] $U_{*z}(0) = 0 \implies u(0) = 0$ and $U_{*z}(H) = V \implies u(1) = v$, where V is the piston velocity, $v = V/U_s$, and the complex oscillatory Reynolds number $Re_o \equiv i\frac{\rho(\omega H)H}{\mu}$ (Equation 2.40).

$$\begin{aligned} \frac{\partial^2 u}{\partial x^2} &= \frac{\partial p}{\partial z} + Re_o u \\ u(0) &= 0 \\ u(1) &= v, \end{aligned} \tag{3.1}$$

Which can be easily solved

$$u(x) = \frac{1}{2}\frac{\partial p}{\partial z}x^2 + Ax + B \tag{3.2}$$

$$\begin{aligned} u(0) = 0 &\implies B = 0 \\ u(1) = v &\implies A = v - \frac{1}{2}\frac{\partial p}{\partial z} \end{aligned} \tag{3.3}$$

$$\implies u(x) = \frac{1}{2}\frac{\partial p}{\partial z}(x^2 - x) + vx. \tag{3.4}$$

This equation is just a general form of *Couette flow*,[2] where flow is driven in a narrow gap with a moving plate, where the generalization accounts for a pressure boundary condition in *plane Poiseuille flow*. Note that this is only an approximation; while this model assumes an infinite plate width, our pistons are only "infinite" in the sense that $H \ll W$. The non-infinities are accounted for in the neglected $O(H/L)$ terms.

Lastly, because nothing affects fluid motion in the $\underline{\mathbf{E}}_z$ direction within the narrow gap, we can assume that $\frac{\partial p}{\partial z}$ is linear and $\frac{\partial p}{\partial z} \approx -\Delta p$.[3] This leaves us with the following equation for $u(x)$:

$$u(x) = \frac{1}{2}\Delta p\,(x - x^2) + vx \tag{3.5}$$

Note that while we ignored the time dependence of the system when considering driving pressure

[1] Note that these boundary conditions are equivalent to those used in Section 2.2 with a coordinate shift of $H/2$

[2] Named after Frenchman Maurice Marie Alfred Couette (9 January 1858, Tours – 18 August 1943, Angers) [49]

[3] $\frac{\partial p}{\partial z}$ is already normalized so the factor L in $(P_2 - P_1)/L$ has already been accounted for.

changes, we still need to account for slower-speed pressure changes. Fortunately, this dependency is contained in v, which represents the speed of the piston. In this case, we are reversing Couette flow, using the flow rate to drive the plate rather than vice-versa.

From Equation 3.5, we can find the volumetric flow rate through the gap, $Q_* = qQ_s$ as well as the shear on the upper piston, $\tau_* = \tau_s \tau$. First, because

$$Q_* = W \int_0^H U_* z(x_*)\, \mathrm{d}x_* \tag{3.6}$$

$$qQ_s = WHU_s \int_0^1 u(x)\, \mathrm{d}x, \tag{3.7}$$

where H is the gap thickness and W is the gap width. This form suggests the nondimensionalization choice of $Q_s = WHU_s$, leading to the nondimensional simplification

$$q = \int_0^1 u(x)\, \mathrm{d}x \tag{3.8}$$

$$= \int_0^1 \left(\frac{1}{2} \Delta p\, (x - x^2) + vx \right) \mathrm{d}x \tag{3.9}$$

$$= \frac{1}{2} \Delta p\, (\frac{1}{2} - \frac{1}{3}) + \frac{1}{2} v \tag{3.10}$$

$$\implies q = \frac{1}{12} \Delta p + \frac{1}{2} v. \tag{3.11}$$

This flow rate $q = q(\Delta p\,(t), v(t))$, where we assume that q can vary with time due to the implicit dependence on the moving piston, carried by v. Additionally, we can determine the relationship between q, p, (where $P_* = P_s p$ is the overall pressure applied to the system) Δp (where $\Delta P_* = P_s \Delta p$ is the pressure drop across the piston.) and v. First, we need to consider the lumped parameter model (Chapter 2) of the film-piston system. The system consists of three impedances: (i) input (R_{in}) and (ii) output (R_{out}), here assumed to be constants,[4] and (iii) piston impedance Z_{pist}. While Z_{pist} cannot be modeled as a linear resistor, it is acceptable to model it containing dependencies on other features of the system, such as v, Δp, q, etc. Completing this analysis will allow us to derive Z_{pist} more completely. The lumped parameter impedance model (Fig. 3.3b) is a linear system, allowing us to treat it as a linear system where flow rate through each of the components is uniform. Thus we have the relations $P_* = Q_*(R_{\text{in}} + Z_{\text{pist}} + R_{\text{out}})$ as well as $\Delta P_* = Q_* Z_{\text{pist}}$ from which we can determine

$$\Delta P_* = P_* - Q_*(R_{\text{in}} + R_{\text{out}}), \tag{3.12}$$

[4] *i.e.*, neglecting internal flexural capacitance of the tubing and channels due to the rigidity of the bulk channels.

or by nondimensionalizing, and defining $R = R_{\text{in}} + R_{\text{out}}$,

$$P_s \Delta p = P_s p - Q_s R q \tag{3.13}$$

$$\Delta p = p - \frac{Q_s R}{P_s} q \tag{3.14}$$

$$\Delta p = p - \rho q, \tag{3.15}$$

where $\rho \equiv \frac{Q_s R}{P_s}$ is a nondimensional unit of nonadjustable system resistance. This term may account for *parasitic resistance* within the system,[5] though it won't consider parasitic inductances or capacitances, which must be considered separately, and which are ignored in this analysis. Equation 3.15 along with the volumetric flow rate through the thin gap (Equation 3.5)

$$q = \frac{1}{12} \Delta p + \frac{1}{2} v, \tag{3.16}$$

allow us to determine relationships among the four parameters p, Δp, q, and v. In particular, we can determine two of the parameters with respect to the other two. This presents us with six options,[6] two of which are of particular use. Omitting the algebra,[7]

$$q \text{ and } p : \begin{cases} q(p,v) = \frac{p+6v}{\rho+12} \\ \Delta p\,(p,v) = \frac{12p-6\rho v}{12+\rho} \end{cases} \tag{3.17a}$$

$$\Delta p \text{ and } v : \begin{cases} \Delta p\,(q,p) = p - \rho q \\ v(q,p) = \frac{1}{6}((12+\rho)q - p) \end{cases} \tag{3.17b}$$

Equation 3.17a will be of later use when we seek to find the piston motion v solely as a function of the driving pressure p, eliminating dependence on q and dp which are not under the direct control of pneumatic control systems. For example, the Fluigent™Maesflo system allows direct control of P_* through a pressurized air input, resulting in a flow rate Q_* that is dependent on the pressure. In contrast, if we were using a syringe pump which dispenses *volume* of fluid at a controlled flow rate, we would solve the equations in terms of Q_* and V. As-is, it does not matter as the equations can be inverted relatively easily, although the process introduces error to the analysis.[8]

[5] Resistances which disrupt device performance but cannot be effectively removed

[6] $\binom{4}{2} = 6$ options

[7] Which is performed in Mathematica in any case

[8] It is in general lower-error to measure a quantity directly than indirectly

Using Equation 3.17a, if we consider a piston attached to a spring, the piston movement V is caused by a change in the piston coordinate $y_*(t_*)$, and we can determine the scaling factors for that relationship:

$$\frac{\partial y_*}{\partial t_*} = V \tag{3.18}$$

$$\frac{L}{t_s}\frac{\partial y}{\partial t} = U_s v. \tag{3.19}$$

Choosing a characteristic time $t_s = \frac{L}{U_s}$, we obtain the simpler nondimensionalized equivalence relation

$$\frac{\partial y}{\partial t} \equiv \dot{y} = v. \tag{3.20}$$

This choice of characteristic time is done without loss of generality; we are merely picking a characteristic unit system which simplifies the match considerably. [9]

Lastly, we consider the shear stress in the system. In traditional Couette flow, the shear stress of the plate on the fluid generates the fluid flow, with a plate-on-fluid stress of

$$\tau_{\text{P-F}} = \mu \left.\frac{\partial u}{\partial x}\right|_{x=H} \tag{3.21}$$

In this system, the fluid flow is applying a force to the plate, meaning

$$\tau_{\text{F-P}} = -\tau_{\text{P-M}} = -\mu \left.\frac{\partial u}{\partial x}\right|_{x=H} \tag{3.22}$$

Dropping the F-P designation and non-dimensionalizing $\tau_* = \tau_s \tau$ gives us

$$\tau_* = -\mu \left.\frac{\partial U_{*z}}{\partial x_*}\right|_{x_*=H} \tag{3.23}$$

$$\tau_s \tau = -\frac{\mu U_s}{H} \left.\frac{\partial u}{\partial x}\right|_{x=1} \tag{3.24}$$

$$\tau = -\left.\frac{\partial u}{\partial x}\right|_{x=1}, \tag{3.25}$$

if we choose $\tau_s = \frac{\mu U_s}{H} = \frac{H}{L} P_s$. Evaluating this expression using flow speed determined in Equa-

[9] If there was an external characteristic time for the system, this might present a problem as the units would conflict.

tion 3.5 gives us a numerical value for τ based on piston movement

$$\tau = -\left.\frac{\partial u(x)}{\partial x}\right|_{x=1} \tag{3.26}$$

$$= -\left.\frac{\partial}{\partial x}\left[\frac{1}{2}\Delta p\,(x-x^2)+vx\right]\right|_{x=1}, \tag{3.27}$$

$$= -\left.\frac{1}{2}\Delta p\,(1-2x)-v\right|_{x=1} \tag{3.28}$$

$$= \frac{1}{2}\Delta p - v \tag{3.29}$$

3.3.2 Piston Force Balance

We now have all the components necessary to determine the piston's equations of motion from its static force balance.[10] The piston's force balance comprises $F_{\mathrm{Sp}}+F_{\mathrm{P}}+F_{\mathrm{Sh}}$, where $F_{\mathrm{Sp}} = -ky_*$ is the displacement spring force (spring constant k), $F_{\mathrm{P}} = WD\Delta P_*$ is the static pressure forces on the piston head[11] (of area WD), and $F_{\mathrm{Sh}} = LW\frac{HP_s}{L}\left(\frac{1}{2}\Delta p - v\right)$ is the shear drag force applied over a surface area LW. Recalling that $v = \dot{y}$,

$$0 = -kLy + WDP_S\Delta p + WHP_s\left(\frac{1}{2}\Delta p - v\right) \tag{3.30}$$

$$kLy = WP_s\left(\left(D+\frac{1}{2}H\right)\Delta p - H\dot{y}\right) \tag{3.31}$$

$$y = \frac{WHP_s}{kL}\left[\left(\frac{D}{H}+\frac{1}{2}\right)\Delta p - \dot{y}\right]. \tag{3.32}$$

Assigning $P_s = \frac{kL}{WH}$, a useful simplification which neatens our notation significantly by adjusting units, but does not make any statements about the actual magnitude of P_*, and defining the piston-size ratio $d \equiv \frac{D}{H}$, we're left with the simplified equation form

$$y = \left(d+\frac{1}{2}\right)\Delta p - \dot{y}. \tag{3.33}$$

[10] Assuming no inductive/inertial/accelerative forces based on the high viscous damping.

[11] An interesting facet of the shear-stress is that τ is functionally independent of piston length L, a side-effect of the interplay between increased resistance (factor of $1/2$ in τ) and increased surface area (factor of 2 in τ).

Lastly, we account for the fact that Δp is itself dependent on other variables in the system by substituting in the non-dimensionalized form of Equation 3.17a

$$y = \left(d+\frac{1}{2}\right)\frac{12p-6\rho\dot{y}}{12+\rho} - \dot{y} \tag{3.34}$$

$$= \frac{12}{12+\rho}\left[\left(d+\frac{1}{2}\right)p - \left(1+\frac{\rho}{2}\left(d+\frac{2}{3}\right)\right)\dot{y}\right] \tag{3.35}$$

This is a simple non-dimensional ODE to solve. We have a time constant $T = \frac{12}{12+\rho}\left(1+\frac{\rho}{2}\left(d+\frac{2}{3}\right)\right)$ and a pressure coefficient $K = \frac{12}{12+\rho}\left(d+\frac{1}{2}\right)$ leading to a simplified ODE

$$T\dot{y} + y = Kp(t), \tag{3.36}$$

where $p(t)$ is the time dependent input pressure. This may be solved to produce

$$y(t) = Ce^{-t/T} + \frac{K}{T}e^{-t/T}\int_{-\infty}^{t} p(t')e^{t'/T}\,\mathrm{d}t' \tag{3.37}$$

The integration constant may be determined by noting that for $p(t) \equiv 0$, the piston will remain at $y = 0$, meaning $C = 0$. We are thus left with the solution for $y(t)$ and, by extension, $\dot{y}(t)$

$$y(t) = \frac{K}{T}e^{-t/T}\int_{-\infty}^{t} p(t')e^{t'/T}\,\mathrm{d}t' \tag{3.38a}$$

$$\dot{y}(t) = \frac{K}{T}\left(1 - \frac{1}{T}e^{-t/T}\int_{-\infty}^{t} p(t')e^{t'/T}\,\mathrm{d}t'\right). \tag{3.38b}$$

This solution clearly requires reintroduction of dimensional parameters to be a compatible with variables obtained in lab.[12] These values are summarized in Table 3.1. Of particular relevance is the ratio

$$\frac{K}{T} = \frac{\left(d+\frac{1}{2}\right)}{1+\frac{\rho}{2}\left(d+\frac{2}{3}\right)} \tag{3.39}$$

which represents (in non-dimensional form) the maximum speed the damped piston will be able to obtain immediately after a displacement from steady-state equilibrium. Note that $\frac{K}{T}$ depends only on the mechanical characteristics of the device and not on the nature of the pressure or flow inputs.

[12] In practice, the velocity will be easier to solve for $\dot{y}(t)$ once we have a known pressure input

Table 3.1 List of nondimensionalization constants for the thin-film moving piston problem.

Unit	Dimension*less*	Factor & Relations	Unit Description	Factor Description
z_*	$z = z_*/L$	L	Flow direction along channel	Piston length
y_*	$y = y_*/L$	L	Piston displacement along channel	Piston length
x_*	$x = x_*/H$	H	Height above stationary plate	Gap thickness
P_*	$p = P_*/P_s$	$P_s = \frac{kL}{WH}$	Applied pressure	Characteristic pressure
U_{*z}	$u = U_{*z}/U_s$	$U_s = \frac{P_s H^2}{\mu L}$	Flow velocity along channel	Characteristic flow velocity
V	$v = V/U_s$	U_s	Piston velocity	Characterstic flow rate
$\frac{\mathrm{d}y_*}{\mathrm{d}t_*}$	$\dot{y} = \frac{\mathrm{d}y_*}{\mathrm{d}t_*}/U_s$	$\dot{y} = v$	Piston coordinate speed	
t_*	$t = t_*/t_s$	$t_s = L/U_s = \frac{\mu L^2}{H^2} P_s{}^{-1}$	Piston time constant	Piston characteristic time
Q_*	$q = Q_*/Q_s$	$Q_s = WHU_s = \frac{WH^3}{\mu L} P_s$	Volumetric flow rate	Characteristic flow rate
τ_*	$\tau = \tau_*/\tau_s$	$\tau_s = \mu \frac{U_s}{H} = \frac{H}{L} P_s$	Fluid shear stress	Characteristic shear rate
R	$\rho = R/R_s$	$R_s = \frac{P_s}{Q_s} = \frac{\mu L}{WH^3}$	Non-variable fluidic resistance	Characteristic resistance
R_{tot}	$\rho_{\mathrm{tot}} = R_{\mathrm{tot}}/R_s$	$R_{\mathrm{tot}} = R_{\mathrm{in}} + R_{\mathrm{out}} + R_{\mathrm{piston}}$	Total fluidic resistance	
T		$T = \frac{12}{12+\rho}\left(1 + \frac{\rho}{2}\left(d + \frac{2}{3}\right)\right)$	Dimensionless piston time constant	From Equation 3.38a
K		$K = \frac{12}{12+\rho}\left(d + \frac{1}{2}\right)$	Dimensionless pressure coefficient	From Equation 3.38a

Aside 3.1: Elimination of Proxy Variable y

Because our apparatus cannot easily measure y or $\dot{y}$, we can treat it as a proxy variable and perform curve fitting from the better-known values of q and p instead. This time using Equation 3.17b, we obtain

$$y = \left(d + \frac{1}{2}\right)(p - \rho q) - \frac{1}{6}((12+\rho)q - p) \tag{3.40}$$

$$= \left[\left(d + \frac{1}{2}\right) + \frac{1}{6}\right]p - \left[\left(d + \frac{1}{2}\right)\rho + \left(2 + \frac{\rho}{6}\right)\right]q \tag{3.41}$$

$$= \left(d + \frac{2}{3}\right)p - \left[\left(d + \frac{2}{3}\right)\rho + 2\right]q \tag{3.42}$$

This equation for y is of the form $y = Ap - Bq$, which is different from the $y = Ap + Bq$ form we would expect, since it shows q working to restore the piston rather than dragging it forward (*i.e.*, the coefficient of q is negative). This effect is also explicitly visible when we take the (p, v) solution in Equation 3.17,[13]

$$y = \left(d + \frac{2}{3}\right)\Delta p - 2q. \tag{3.43}$$

The reason for this discrepancy is that the flow parameters are interdependent: higher q results in higher Δp, etc. This form will become useful when analyzing a device parametrically, such as in Section 3.5.

3.3.3 Piston Solutions for Distinct Pressure Inputs

Next, we will go through a number of common pressure inputs that may be encountered in this research. For all solutions in this section, the problem will involve a steady state pressure p_0 that is changed into another pressure $p(t)$ at time $t = t_0$. Thus, the final solution for piston displacement $y(t)$ will only be listed for time $t \geq t_0$. The solution for time $t < t_0$ can be derived from Equation 3.35 by taking the *steady-state* solution where $\dot{y} = 0$, giving

$$y(t) = \begin{cases} Kp_0, & \text{for } t < t_0 \\ y_{\text{var}}(t), & \text{for } t \geq t_0. \end{cases} \tag{3.44}$$

Clearly, it is the last part, the $y_{\text{var}}(t)$ that will present any difficulty. However, due to the linearity of Equation 3.35, we may superimpose arbitrary pressure inputs to obtain equally valid solutions.

3.3.3.1 Pressure Step Input

A common pressure input is the step input, that is

$$p(t) = \begin{cases} p_0, & \text{for } t < 0 \\ p_1, & \text{for } t \geq 0 \end{cases} \tag{3.45}$$

[13] Equation 3.17 may also be solved in the form: $p(q, \Delta p) = \Delta p + q\rho$ and $v(q, \Delta p) = -\frac{1}{6}\Delta p + 2q$

This situation is simply solve through basic integration for $t \geq t_0$

$$y(t) = \frac{K}{T}e^{-t/T}\left(p_0\int_{-\infty}^{t_0} e^{t'/T}\,\mathrm{d}t' + p_1\int_{t_0}^{t} e^{t'/T}\,\mathrm{d}t'\right) \tag{3.46}$$

$$= Kp_0e^{-t/T}\left[e^{t'/T}\right]_{-\infty}^{t_0} + Kp_1e^{-t/T}\left[e^{t'/T}\right]_{t_0}^{t} \tag{3.47}$$

$$= Kp_0e^{-(t-t_0)/T} + Kp_1(1-e^{-(t-t_0)/T}), \tag{3.48}$$

which can be simplified to

$$y(t) = Kp_1 - K(p_1-p_0)e^{-(t-t_0)/T}, \tag{3.49a}$$

$$v(t) = \frac{K}{T}(p_1-p_0)e^{-(t-t_0)/T} \tag{3.49b}$$

which shows that the piston reaches a new steady-state position with time constant T and deviates from that steady-state position by $\Delta y = -(p_1-p_0)e^{-(t-t_0)/T}$.

3.3.3.2 Steady Pressure Ramp

Next, we input a steady pressure ramp that begins at time $t = t_0$ and increases with magnitude $\frac{K}{T}$

$$p(t) = \begin{cases} p_0, & \text{for } t < t_0 \\ p_0 + p_c\frac{(t-t_0)}{T}, & \text{for } t \geq t_0, \end{cases} \tag{3.50}$$

where the ratio $\frac{p_c}{T}$ represents the constant rate of pressure change. Inputting this definition for $p(t)$ into Equation 3.38a leads to the integral

$$y(t) = \frac{K}{T}e^{-t/T}\left(p_0\int_{-\infty}^{t} e^{t'/T}\,\mathrm{d}t' + \frac{p_c}{T}\int_{t_0}^{t}(t'-t_0)e^{t'/T}\,\mathrm{d}t'\right) \tag{3.51}$$

$$= Kp_0e^{-t/T}\left[e^{t'/T}\right]_{-\infty}^{t} + Kp_ce^{-t/T}\left[e^{t'/T}\left(\frac{t'-t_0}{T}-1\right)\right]_{t_0}^{t}. \tag{3.52}$$

This equation then resolves to the piston position and velocity

$$y(t) = K\left(p_0 + p_c\left(\frac{t-t_0-T}{T}\right)\right) + Kp_ce^{-(t-t_0)/T}, \tag{3.53a}$$

$$v(t) = \frac{Kp_c}{T}(1-e^{-(t-t_0)/T}), \tag{3.53b}$$

The first position term represents the steady-state piston location, the second term represents the transient that is generated by the transition between constant pressure and ramping, and the third term represents a steady-state lag. For times $t \gg T$, the long-term steady-state behavior is

$$y_{\mathrm{SS}}(t) = Kp_0 + Kp_c\left(\frac{t - t_0 - T}{T}\right), \tag{3.54a}$$

$$v_{\mathrm{SS}}(t) = \frac{Kp_c}{T}, \tag{3.54b}$$

where the position lags behind the *ideal* steady-state location $y_{\mathrm{ideal}}(t) = Kp_0 + Kp_c\left(\frac{t-t_0}{T}\right)$ by a constant factor Kp_c; alternately the lag is by a single time constant, $\Delta t_{\mathrm{lag}} = T$. The steady-state velocity tracks the piston completely (while still lagged).

3.3.3.3 Sequential Step Input (General Case)

Many of the experiments performed with the Fluigent system have pressure which increases by step, waits, and then allows the system to equilibrate. This will function much like the step input, only within an infinite series.

$$P(t) = \begin{cases} p_0, & \text{for } t < t_0 \\ p_1, & \text{for } t_0 \le t < t_1 \\ \vdots & \vdots \\ p_i, & \text{for } t_{i-1} \le t < t_i \\ \vdots & \vdots \\ p_{N+1}, & \text{for } t_n \le t. \end{cases} \tag{3.55}$$

This leads to the integral

$$y(t) = \frac{K}{T}e^{-t/T}\left(p_0\int_{-\infty}^{t_0} e^{t'/T}\,\mathrm{d}t' + \sum_{i=1}^{N} p_i\int_{t_{i-1}}^{t_i} e^{t'/T}\,\mathrm{d}t' + p_{N+1}\int_{t_{N-1}}^{t} e^{t'/T}\,\mathrm{d}t'\right) \tag{3.56}$$

$$= Ke^{-t/T}\left(p_0 e^{t_0/T} + \sum_{i=1}^{N} p_i\left(e^{t_i/T} - e^{t_{i-1}/T}\right) + p_{N+1}e^{t/T} - P_{N+1}e^{t_N/T}\right) \tag{3.57}$$

$$= Kp_{N+1} - K\sum_{i=0}^{N}(p_{i+1} - p_i)e^{-(t-t_i)/T}. \tag{3.58}$$

For only a single step, that is $N = 0$, we are left with

$$y(t;N=1) = Kp_1 - K(p_1 - p_0)E^{-(t-t_0)/T} \tag{3.59}$$

the same single-step solution we obtained in Equation 3.49a. The general solution in Equation 3.58 can be further reduced by assuming regular time and pressure steps; that is

$$p_i = p_0 + i\Delta p \qquad \text{and} \qquad t_i = t_0 + i\Delta t, \tag{3.60}$$

this reduces to

$$y(t) = K(p_0 + (N+1)\Delta p) - K\Delta p\, e^{-(t-t_0)/T} \sum_{i=0}^{N} e^{i\Delta t/T}. \tag{3.61}$$

This expression has a closed form solution, from the series solution

$$\sum_{i=0}^{N} e^{i\Delta t/T} = \frac{e^{N\Delta t/T} - 1}{e^{\Delta t/T} - 1} \tag{3.62}$$

giving

$$y(t) = K(p_0 + (N+1)\Delta p) - K\Delta p\, e^{-(t-t_0)/T} \left(\frac{e^{(N+1)\Delta t/T} - 1}{e^{\Delta t/T} - 1} \right). \tag{3.63}$$

We take $\Delta t = fT$, where $f > 0$ is some dimensionless factor indicating the size of the time and pressure steps.[14]

$$y(t;N) = K(p_0 + (N+1)\Delta p) - K\Delta p\, e^{-(t-t_0)/T} \left(\frac{e^{f(N+1)} - 1}{e^{f} - 1} \right), \tag{3.64a}$$

$$\dot{y}(N,t) = \frac{K\Delta p}{T} e^{-(t-t_0)/T} \left(\frac{e^{f(N+1)} - 1}{e^{f} - 1} \right) \tag{3.64b}$$

Because N represents the number of steps Δt from the start of ramping, $N = \left\lfloor \frac{t-t_0}{fT} \right\rfloor$.

$$y(t) = K(p_0 + \left(\left\lfloor \frac{t-t_0}{fT} \right\rfloor + 1 \right) \Delta p) - K\Delta p\, e^{-(t-t_0)/T} \left(\frac{e^{f\left(\left\lfloor \frac{t-t_0}{fT} \right\rfloor + 1 \right)} - 1}{e^{f} - 1} \right) \tag{3.65}$$

[14] That is, the time and pressure increments every nT "seconds" (we are still in dimensionless time)

Taking $p_0 = 0$ and $t_0 = 0$, we can reduce this equation to a form which can be plotted on a graph of $y/K\Delta p$ versus $\tau \equiv t/fT$:

$$\frac{y(\tau = t/fT)}{K\Delta p} = (\lfloor \tau \rfloor + 1) - e^{-f\tau}\left(\frac{e^{f(\lfloor \tau \rfloor + 1)} - 1}{e^f - 1}\right) \tag{3.66}$$

for $f = \{0.25, 0.5, 1, 2, 5\}$ (Fig. 3.4). This plot shows a pseudo self-similar set of solutions, where different n indicate the relative amount of time each system has to reach its steady-state condition. Higher values of n indicate systems which have a long time to reach equilibrium between pressure increments and therefore reach the steady-state value relatively quickly. Low values of n take long enough to reach steady state that the develop a noticeable lag.

Alternately, we can look at the limiting case of Equation 3.65, where $f \to 0$. Noting that $\lim_{f\to 0}\left\lfloor \frac{t-t_0}{fT} \right\rfloor = \frac{t-t_0}{fT}$,[15] and taking $\Delta p = f p_c$, where p_c is some characteristic pressure,

$$\lim_{f\to 0} y(t) = \lim_{f\to 0} K\left(p_0 + \left(\frac{t-t_0}{fT} + 1\right) f p_c\right) - K f p_c e^{-(t-t_0)/T}\left(\frac{e^{f\left(\frac{t-t_0}{fT}+1\right)} - 1}{e^f - 1}\right) \tag{3.67}$$

The asymptotic value of

$$\lim_{f\to 0} f\left(\frac{e^{f\left(\frac{t-t_0}{fT}+1\right)} - 1}{e^f - 1}\right) = \lim_{f\to 0} f\left(\frac{e^{\frac{t-t_0}{T}+f} - 1}{f + O(f^2)}\right) = \left(e^{(t-t_0)/T} - 1\right)$$

allows us to determine

$$\lim_{f\to 0} y(t) = K\left(p_0 + p_c\left(\frac{t-t_0}{T}\right)\right) - K p_c e^{-(t-t_0)/T}\left(e^{(t-t_0)/T} - 1\right), \tag{3.68}$$

which ultimately simplifies to

$$y(t) = K\left(p_0 + p_c\left(\frac{t-t_0-T}{T}\right)\right) + K p_c e^{-(t-t_0)/T}, \tag{3.69}$$

which is the same as the ramped input in Equation 3.53a.

Additionally, taking the $f \to 0$ limit of 3.64b allows us to determine the continuous limit of

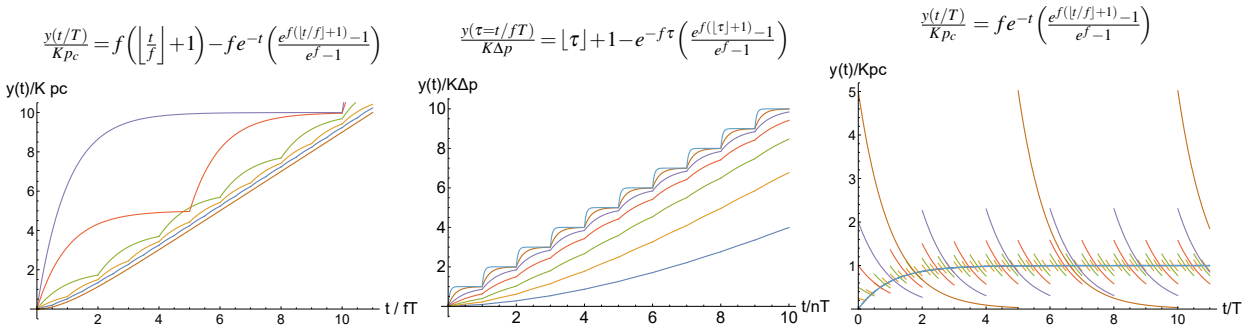
[15] In the continuous limit, the floor function becomes a continuous function

velocity through another method:

$$\lim_{f\to 0} v(t;N) = \frac{K\Delta p}{T} e^{-(t-t_0)/T}\left(e^{(t-t_0)/T} - 1\right) \tag{3.70}$$

$$= \frac{K\Delta p}{T}\left(1 - e^{-(t-t_0)/T}\right) \tag{3.71}$$

which is the same as the ramped velocity in Equation 3.53b. As expected, the limiting case of the stepped pressure input is identical to the results obtained by using the continuous ramped input from Equation 3.50.



(a) Absolute Piston Movement **(b)** Normalized Piston Movement **(c)** Piston Error

Figure 3.4 Piston response to sequentially applied pressure increases. **(a)** Absolute position, normalized by time constant T and pressure growth constant P_c, including $f \to 0$ limit. **(b)** Position normalized by f, the relative step size, showing pseudo-self-similar behavior. **(c)** Piston lag behind ideal value established by applied pressure, including $f \to 0$ limit. Note that smaller values of f approach the $\delta t = T$ lag of the limiting case.

(I) Average Piston Position and Piston Lag for Ramping Input The time average piston location during a given cycle is also of note, indicating the relative amount of time the piston remains at its equilibrium position in each cycle.

$$\overline{y(t;N)} = \frac{1}{\Delta t}\int_{t_N}^{t_{N+1}} \left[K(p_0 + (N+1)\Delta p) - K\Delta p\, e^{-(t-t_0)/T}\left(\frac{e^{\Delta t(N+1)/T} - 1}{e^{\Delta t/T} - 1}\right)\right] \mathrm{d}t \tag{3.72}$$

$$= K(p_0 + (N+1)\Delta p) - K\frac{\Delta p}{\Delta t}\left(\frac{e^{\Delta t(N+1)/T} - 1}{e^{\Delta t/T} - 1}\right)\int_{t_N}^{t_{N+1}} e^{-(t-t_0)/T}\,\mathrm{d}t \tag{3.73}$$

where

$$\int_{t_N}^{t_{N+1}} e^{-(t-t_0)/T}\,\mathrm{d}t = \int_{t_0+N\Delta t}^{t_0+(N+1)\Delta t} e^{-(t-t_0)/T}\,\mathrm{d}t = Te^{-\Delta t(N+1)/T}\left(e^{\Delta t/T}-1\right) \tag{3.74}$$

so

$$\begin{aligned}\overline{y(t;N)} &= K(p_0+(N+1)\Delta p) - K\frac{\Delta p}{\Delta t}\left(\frac{e^{\Delta t(N+1)/T}-1}{e^{\Delta t/T}-1}\right)Te^{-\Delta t(N+1)/T}\left(e^{\Delta t/T}-1\right)\\ &= K(p_0+(N+1)\Delta p) - KT\frac{\Delta p}{\Delta t}\left(1-e^{-\Delta t(N+1)/T}\right).\end{aligned} \tag{3.75}$$

Lastly, taking $\Delta t = fT$, we are left with an average position during the Nth cycle as a function of the pressure step size Δp and the relative time step size f

$$\overline{y(t;N,\Delta p)} = K(p_0+(N+1)\Delta p) - K\Delta p\left(\frac{1-e^{-f(N+1)}}{f}\right). \tag{3.76}$$

This result has different asymptotes for large N depending on the size of f. For $N \gg 1$ and $f \not\ll 1$,

$$\overline{y(t;N)} \xrightarrow{N\to\infty} K(p_0+(N+1)\Delta p) - \frac{K\Delta p}{f} \tag{3.77}$$

and for $f \ll 1$, $N \sim \frac{(t-t_0)}{fT}$ as before (where we must consider the continuous limit $\Delta p = fp_c$), we are left with the continuous case of Equation 3.50:

$$\overline{y(t;N,f)} = \begin{cases} K\left(p_0 + p_c\left(\dfrac{t-t_0}{T}\right)\right) + Kp_c\left(e^{-(t-t_0)/T}-1\right) & \text{for } f \ll 1 \\ K(p_0+(N+1)\Delta p) - \dfrac{K\Delta p}{f} & \text{for } f \not\ll 1 \text{ and } N \gg 1. \end{cases} \tag{3.78}$$

As expected, the average piston location more closely tracks the current driving pressure (*i.e.*, $K\left(p_0+p_c\left(\frac{t-t_0}{T}\right)\right)$ for $f \ll 1$ and $K(p_0+(N+1)\Delta p)$ otherwise) when f is large, when $\Delta t \gg T$.

3.3.3.4 Oscillatory Pressure Input

Last, we drive the system with an oscillating input. Because this system is linear in $p(t)$, this means we can use Fourier decomposition to determine the system response for an arbitrary oscillatory

signal.

$$p(t) = \begin{cases} p_0, & \text{for } t < t_0 \\ p_0 + p_c \sin(\omega(t-t_0)/T), & \text{for } t \geq t_0 \end{cases} \tag{3.79}$$

where ω is the driving frequency. Note that ω is fully non-dimensional and is expressed as a multiplicative factor of the characteristic frequency $1/T$. This can be placed into our model system and integrated by Mathematica, giving

$$y(t) = \frac{K}{T} p_0 e^{-t/T} \int_{-\infty}^{t} e^{t'/T}\, \mathrm{d}t' + \frac{K}{T} p_c e^{-t/T} \int_{t_0}^{t} e^{t'/T} \sin(\omega t'/T) dt' \tag{3.80}$$

which resolves to

$$y(t;\omega) = Kp_0 + \frac{Kp_c}{1+\omega^2}\left[\omega e^{-(t-t_0)/T} + \sin\left(\frac{\omega(t-t_0)}{T}\right) - \omega\cos\left(\frac{\omega(t-t_0)}{T}\right)\right], \tag{3.81a}$$

$$v(t;\omega) = \frac{Kp_c\omega}{T(1+\omega^2)}\left[-e^{-(t-t_0)/T} + \cos\left(\frac{\omega(t-t_0)}{T}\right) + \omega\sin\left(\frac{\omega(t-t_0)}{T}\right)\right]. \tag{3.81b}$$

Additionally, we want to see the device behavior for extreme values of ω. (Note that derivatives and asymptotic expansions do not commute, so $\frac{\mathrm{d}}{\mathrm{d}t}[y(t;\omega \ll 1)] \neq \dot{y}(t;\omega \ll 1)$ [297].) For $\omega \ll 1$,

$$y(t;\omega \ll 1) = Kp_0 + Kp_c \sin\left(\frac{\omega(t-t_0)}{T}\right) + O(\omega) \tag{3.82a}$$

$$v(t;\omega \ll 1) = \frac{Kp_c\omega}{T}\left[-e^{-(t-t_0)/T} + \cos\left(\frac{\omega(t-t_0)}{T}\right)\right] + O\left(\omega^2\right) \tag{3.82b}$$

this reduces to accurate positional tracking of the driving force (as expected). However, the $\omega \ll 1$ velocity feels the initial transient much more strongly than the position.

For $\omega \gg 1$,

$$y(t;\omega \gg 1) = Kp_0 + \frac{Kp_c}{\omega}\left[e^{-(t-t_0)/T} - \cos\left(\frac{\omega(t-t_0)}{T}\right)\right] + O\left(\omega^{-2}\right) \tag{3.83a}$$

$$v(t;\omega \gg 1) = \frac{Kp_c}{T}\sin\left(\frac{\omega(t-t_0)}{T}\right) + O\left(\omega^{-1}\right) \tag{3.83b}$$

the system ends up driven 270° out of phase with a smaller amplitude after the transient dies down. This analysis shows that to accurately drive the system, it is important to do so at frequencies much smaller than the natural frequency $1/T$.

3.3.4 *QP* Responses for Various Piston States

From this point, we return to the result for $q(p,v)$ from Equation 3.17a, where

$$q = \frac{p+6v}{\rho+12}. \tag{3.84}$$

In addition to determining a complete time dependence, this equation more trivially gives a value for the steady-state flow velocity q_{SS}, determined by taking $v \to 0$:

$$q_{SS} = \frac{p}{\rho+12} \tag{3.85}$$

3.3.4.1 Step Input Resistance

Moving from Equation 3.49a, we determine the spring velocity based on the current driving pressure, $p(t)$, with $p_0 = 0$.

$$v(t) = \begin{cases} 0, & \text{for } t < t_0 \\ \dfrac{K}{T} p(t) e^{-(t-t_0)/T}, & \text{for } t \geq t_0 \end{cases} \tag{3.86}$$

When combined with Equation 3.17a,

$$q(t) = \begin{cases} \dfrac{p(t)}{\rho+12}, & \text{for } t < t_0 \\ \dfrac{1+6K/Te^{-(t-t_0)/T}}{\rho+12} p(t), & \text{for } t \geq t_0, \end{cases} \tag{3.87}$$

this results in an effectively lowered fluidic resistance which decays before reaching the couette-flow steady-state value:

$$R(t) = \begin{cases} \rho+12, & \text{for } t < t_0 \\ \dfrac{(\rho+12)}{1+6K/Te^{-(t-t_0)/T}}, & \text{for } t \geq t_0 \end{cases} \tag{3.88}$$

The lowered resistance results from fluid preferentially dragging the *piston*, as opposed to achieving large flows in the narrow gap.

3.3.5 Q/V Trade-Offs

For a given pressure change Δp the fastest piston movement is associated with the single step-function; all other pressure signals studied above feature more gradual pressure changes. Therefore, the maximum piston velocity $v = \dot{y}$ is found in systems driven by a sudden change in pressure, with the maximum velocity occurring immediately after the pressure change:

$$v(t) = \frac{K\Delta p}{T} e^{-(t-t_0)/T}\Big|_{t=t_0} \tag{3.89}$$

$$\Longrightarrow v_{\max} = \frac{K\Delta p}{T}. \tag{3.90}$$

When the *nondimensional* constants are returned, we are left with

$$v_{\max} = \frac{\left(d+\frac{1}{2}\right)}{1+\frac{\rho}{2}\left(d+\frac{2}{3}\right)}\Delta p\,. \tag{3.91}$$

Comparing this result for $v_{\max}(t)$ to the steady-state fluid flow rate *qss* produces the ratio

$$\frac{q_{SS}}{v_{\max}} = \frac{1+\frac{\rho}{2}\left(d+\frac{2}{3}\right)}{(12+\rho)\left(d+\frac{1}{2}\right)}\frac{p}{\Delta p}. \tag{3.92}$$

Noting that

$$Q_{SS} \quad = \quad WHU_s\, q_{SS} \quad = \quad \frac{WH^3}{\mu L} P_s\, q_{SS},$$

$$V_{\max} \quad = \quad U_s\, v_{\max} \quad = \quad \frac{H^2}{\mu L} P_s\, v_{\max},$$

and that both p and Δp have the same dimensional factor P_s we are left with

$$\frac{Q_{SS}}{V_{\max}} = WH\frac{1+\frac{\rho}{2}\left(d+\frac{2}{3}\right)}{(12+\rho)\left(d+\frac{1}{2}\right)}\frac{P_*}{\Delta P_*}, \tag{3.93}$$

or, in the case where $\Delta P_* = P_*$,

$$\frac{Q_{SS}}{V_{\max}} = WH\frac{1+\frac{\rho}{2}\left(d+\frac{2}{3}\right)}{(12+\rho)\left(d+\frac{1}{2}\right)}. \tag{3.94}$$

While this trade-off is at least somewhat favorable — *i.e.*, $Q_{SS} \propto WH^3$ is more strongly dependent on H than $V_{\max} \propto H^2$ — the only factor that can be manipulated to reduce flow rates, W, presents

restrictions of its own. From a mathematical standpoint, if $W \not\gg H$, then the thin-film approximation from Section 2.2.1 breaks down and this analysis is no longer valid. From a more mundane physical standpoint, extremely narrow pistons are (i) hard to manufacture, and (ii) not much use when they are.

Although we will continue to use this thin-piston-based analysis for future work with optofluidic lithography, this result motivates the need to develop alternate microfluidic control mechanisms (see Section 4.2.2.6).

Table 3.2 Equivalent inductances in electrical, mechanical, and hydrodynamic domains.

Domain	Equation	Potential	Flux	Equivalent Inductance
Electrical	$v(t) = L\frac{\mathrm{d}i}{\mathrm{d}t}$	Voltage v	Current i	Inductance L
Mechanical	$F(t) = M\frac{\mathrm{d}V}{\mathrm{d}t}$	Force F	Velocity V	Mass M
Hydrodynamic	$f(t) = \rho\frac{\mathrm{D}u}{\mathrm{D}t}$	Force Density f	Flow Velocity u	Fluid Density ρ

3.4 Diodes

The simplest use for moving components in a microfluidic system is in fabricating one-way check valves. Valves without moving parts have been well-studied [298, 299, 300] and make use of the nonlinearity of the Navier-Stokes equations. For example, in Jeffrey-Hamel flow (*i.e.*, point-source fluid flow within a wedge), the angular dependence of the fluid flow follows the normalized differential equation [298]

$$f''(\theta) + 4f(\theta) + \frac{f^2(\theta)}{\nu} + K = 0 \tag{3.95a}$$

$$\mathrm{BC} = \begin{cases} f(0) = 1 \\ f(1) = 0 \\ f'(0) = 1 \end{cases} \tag{3.95b}$$

where the normalization constant F_0 is determined by the flow-rate condition.

$$Q = \int_{-1}^{1} F_0 f(\theta)\,\mathrm{d}\theta.$$

Because this equation is not linear in f, it is not symmetric upon sign-reversal of $K \mapsto -K$, meaning that with inertia present (*i.e.*, $\nu \to \infty$), source flow and sink flow will be quantitatively different. The mathematical nature of this difference is discussed further by Goldstein (1938) [301] and Schlichting (1960) [302].

In contrast, the differential equation may be solved exactly in the low Reynolds number regime, where $\nu \to \infty$.

$$f''(\theta) + 4f(\theta) + K = 0 \tag{3.96a}$$

$$\text{BC} = \begin{cases} f(0) = 1 \\ f(1) = 0 \\ f'(0) = 1 \end{cases} \tag{3.96b}$$

$$\implies f(\theta) = \frac{\cos(2) - \cos(2\theta)}{\cos(2) - 1} \tag{3.97}$$

3.4.1 Diodicity

Measurements for fluid valves use *diodicity* (*Di*) as the figure of merit, defined as the ratio of the pressure drop across the valve in the forward direction versus the drop in the reverse direction [58]:

$$Di \equiv \frac{\Delta P(Q)_{\text{rev}}}{\Delta P(Q)_{\text{fwd}}} \tag{3.98}$$

Diodicity is used because of the difficulty of accurately measuring fluidic resistance, but is an equivalent concept. At a given flow magnitude Q, the resistance-dependent flow rate $R(Q)$ can be derived from diodicity and the hydrodynamic equivalent of Ohm's Law,

$$Di = \left.\frac{\Delta P_{\text{rev}}}{\Delta P_{\text{fwd}}}\right|_{Q} \tag{3.99}$$

$$= \frac{QR_{\text{rev}}(Q)}{QR_{\text{fwd}}(Q)} \tag{3.100}$$

$$= \frac{R_{\text{rev}}(Q)}{R_{\text{fwd}}(Q)}. \tag{3.101}$$

The greatest consequence of the linearity of fluid dynamics at low Reynolds number is that non-moving-part microfluidic devices tend to converge toward a diodicity $Di = 1$; the forward and reverse flow conditions are identical. Thus, considerable effort has been dedicated to making

microfluidic diodes with moving parts [53, 293, 303, 304, 305] which can overcome the problems of time-reversal symmetry on microfluidic control [306].

Diodicity is effectively infinite in any situation where the valve fully closes and reverse flow drops to zero. However, the standard definition for diodicity suffers problems in this regime. Instead, it makes more sense to use a definition for diodicity considered at constant forward and reverse pressure drops ΔP:

$$Di(\Delta P) = \frac{R_{\text{rev}}(\Delta P)}{R_{\text{fwd}}(\Delta P)} \tag{3.102}$$

$$= \frac{R_{\text{rev}}(\Delta P)/\Delta P}{R_{\text{fwd}}(\Delta P)/\Delta P} \tag{3.103}$$

$$= \left.\frac{Q_{\text{fwd}}}{Q_{\text{rev}}}\right|_{\Delta P} \tag{3.104}$$

The Fluigent™ systems are capable of outputting a controlled pressure and measuring the resulting flow rate, meaning that this implementation of diodicity was optimal for this research. In general, however, the quantity of Diodicity does not consider the instantaneous slope of the QP curve (*i.e.*, the effective resistance), instead calculating the bulk resistance (*i.e.*, the slope between the point and $(Q,P) = (0,0)$).

In contrast, electrical diodes are not measured using diodicity, instead measuring the saturation current I_S, which is the maximum electrical leakage current that results when the diode is reverse biased [307, 308]. The electrical diode equation for a solid-state diode

$$I = I_S\left(e^{V/V_T} - 1\right)$$

converges to a constant value $I \sim -I_S$ when reverse-biased. The effective diodicity,

$$Di_{\text{eff,elec}} = I_{\text{fwd}}/I_{\text{rev}} \tag{3.105}$$

$$= \frac{e^{V/V_T} - 1}{-\left(e^{-V/V_T} - 1\right)} \tag{3.106}$$

$$= e^{V/V_T}, \tag{3.107}$$

grows exponentially in voltage drop.

3.4.1.1 Sensitivity to Parasitics

One difficulty in obtaining and measuring high diodicity comes from the fact that $R(Q) = R_{\text{diode}}(Q) + R_{\text{parasitic}}$, meaning that a high resistance $R_{\text{parasitic}}$ in the rest of the system may reduce $Di \to 1$ (*i.e.*, no differential pressures between forward and reverse flows). This lab's diodicity research attempted to correct for this by measuring diode behavior before the introduction of the microvalves.

For example, using the second definition for diodicity, if we introduce a constant resistance R_0 in line with the valve resistance R_{v},

$$Di_{\Delta P} = \left.\frac{Q_{\text{fwd}}}{Q_{\text{rev}}}\right|_{\Delta P} \tag{3.108}$$

$$= \frac{\Delta P\,(R_{\text{v,rev}} + R_0)}{\Delta P\,(R_{\text{v,fwd}} + R_0)} \tag{3.109}$$

$$= \frac{R_{\text{v,rev}} + R_0}{R_{\text{v,fwd}} + R_0}. \tag{3.110}$$

If we then clear $R_{\text{v,fwd}}$ (the open-state resistance of the valve) and choose $\rho \equiv \frac{R_0}{R_{\text{v,fwd}}}$ and Di_0 as the no-parasitic diodicity

$$Di_{\Delta P} = \frac{\frac{R_{\text{v,rev}}}{R_{\text{v,fwd}}} + \frac{R_0}{R_{\text{v,fwd}}}}{1 + \frac{R_0}{R_{\text{v,fwd}}}} \tag{3.111}$$

$$= \frac{Di_0 + \rho}{1 + \rho}. \tag{3.112}$$

From this, we see that the measured diodicity drops to half its original value when $R_0 = R_{\text{v,fwd}}$ (*i.e.*, $\rho = 1$ in the normalized condition):

$$Di_{(R_0 = R_{\text{v,fwd}})} = \frac{Di_0 + 1}{2} \tag{3.113}$$

$$= \frac{1}{2} Di_0 + \frac{1}{2} \tag{3.114}$$

$$\gtrsim \frac{1}{2} Di_0 \text{ for } Di_0 \gg 1 \tag{3.115}$$

More significantly, if $R_0 = R_{\text{v,rev}}$ (*i.e.*, $\rho = Di_0$),

$$Di_{(R_0=R_{\text{v,fwd}})} = \frac{Di_0 + Di_0}{Di_0 + 1} \tag{3.116}$$

$$\sim 2 - \frac{2}{Di} + O\left(Di^{-2}\right) \tag{3.117}$$

$$\lesssim 2 \text{ for } Di_0 \gg 1, \tag{3.118}$$

the diodicity drops to below 2. From this, it is clear that a baseline must be subtracted to usefully measure Di_0. Generally, a baseline will be measured using an identical system, but with the valve component removed.

For an electrical diode with parasitic resistance R, the equations are highly non-linear. However, for a voltage drop $\Delta V > V_T$, the diode experiences a voltage drop of $V_{\text{th}} \approx 0.6$ V. In reverse, the solid-state nature of the diode restrict the reverse current to the saturation current I_s [174, 307, 308],

$$Di_{\text{eff}} = I_{\text{fwd}}/I_{\text{rev}} \tag{3.119}$$

$$= \frac{V - V_{\text{th}}}{RI_s} \tag{3.120}$$

While this diodicity is linear, because $I_s \approx 100$ nA, for $V \gg 0.6V$,

$$Di_{\text{eff}} \sim 10\frac{V/\text{volt}}{R/\text{M}\Omega} \tag{3.121}$$

$$\sim 1000V/\text{volt} \tag{3.122}$$

for $R = 10$ kΩ. Thus, the effective electrical diodicity is far higher than the effective fluidic diodicity, even factoring in parasitic resistances.

Aside 3.2: Electrical Diode in Series.

For a diode in series with a resistor R, with a voltage drop of V across, the system,

$$I(V) = \tfrac{V_T}{R}\mathcal{W}\left(\tfrac{RI_s}{V_T}\exp\left(\tfrac{RI_S}{V_T} + \tfrac{V}{V_T}\right)\right) - I_s, \tag{3.123}$$

where $\mathcal{W}$ is the Lambert W-Function (*i.e.*, the *Product-Log*) [309]. For a standard

silicon diode, $\frac{I_s}{V_T} = \frac{4}{\text{M}\Omega}$, so for $V > V_T$ and $R < \frac{1}{4}$ MΩ, $\exp\left(\frac{V}{V_T}\right) \gg 1$ and

$$I_{\text{fwd}} \sim \frac{V_T}{R}\mathcal{W}\left(\frac{RI_s}{V_T}\exp\left(\frac{V}{V_T}\right)\right) \tag{3.124}$$

$$\sim \frac{V_T}{R}\log\left(\frac{RI_s}{V_T}\exp\left(\frac{V}{V_T}\right)\right) + O\left(\log\left(\frac{V}{V_T}\right)\right) \tag{3.125}$$

$$\sim \frac{V}{R} + O\left(\log\left(\frac{V}{V_T}\right)\right). \tag{3.126}$$

For a similar voltage magnitude in reverse bias,

$$\frac{RI_s}{V_T}\exp\left(\frac{RI_S}{V_T} + \frac{-V}{V_T}\right) \sim \exp\left(\frac{-V}{V_T}\right) \ll 1 \tag{3.127}$$

$$\implies I_{\text{rev}} \sim I_s\left(1 - \exp\left(\frac{RI_S}{V_T} - \frac{V}{V_T}\right)\right) \tag{3.128}$$

$$\sim I_s(1 + O\left(\frac{V}{V_T}\right)) \tag{3.129}$$

because $\mathcal{W}(x) \sim x + O\left(x^2\right)$ for $x \ll 1$.

Assuming a constant ΔP for the experiments, measuring forward, reverse, and baseline flows (Q_{fwd}, Q_{rev}, and Q_{b}) with errors (σ_{fwd}, σ_{rev}, and σ_{b}),

$$Di_0 = \frac{Q_{\text{fwd}} - Q_{\text{b}}}{Q_{\text{rev}} - Q_{\text{b}}} \tag{3.130}$$

with error

$$\sigma_{Di} = \frac{\sqrt{\sigma_{\text{fwd}}^2 + Di_0\sigma_{\text{rev}}^2 + (Di_0 - 1)^2\sigma_{\text{b}}^2}}{Q_{\text{r}} - Q_{\text{b}}} \tag{3.131}$$

Taking a constant error for all measurements σ and assuming $Di_0 \gg 1$,

$$\sigma_{Di} \sim Di_0\ \sigma\sqrt{2\left(1 + \frac{Q_{\text{rev}}Q_{\text{b}}}{(Q_{\text{rev}} - Q_{\text{b}})^2}\right)} \tag{3.132}$$

Previously, the Lin group has presented microfluidic diodes — which rectify fluid flow based on flow polarity — using freely-moving microstructures fabricated via optofluidic lithography. However, these diodes are passive two-terminal fluidic circuit elements and cannot actively regulate flow in parallel channels [58, 59, 305, 310]. To expand the capabilities of the optofluidic circuit elements, we introduce a single-layer microfluidic pressure gain system capable of operating at low system pressures (Fig. 3.13).

3.5 Optofluidic Current Source

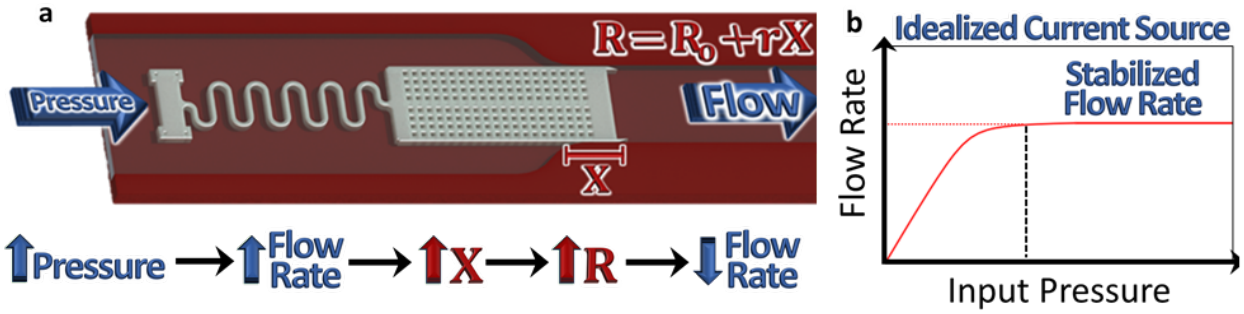


Figure 3.5 Illustrations of the current source concept. **(a)** The device consists of a spring-mounted piston which slides within a microchannel according to the fluid forces exerted on it. As pressure increases, the increased flow rate forces the piston into the high-resistivity portion of the microchannel, increasing the hydrodynamic resistance of the system. The increased resistance then lowers the flow rate in a negative feedback loop, causing the flow rate to auto-stabilize. **(b)** Behavior of an ideal current source. Once the pressure passes a critical threshold value, the flow rate remains constant regardless of the pressure applied to the device.

This work marks the first use of in-situ photopolymerization to create single-layer microfluidic devices which serve as ultra-low Reynolds Number (Re) current sources to regulate fluid flow rate independent of operating pressures. Autonomous fluidic components are an emerging aspect of micro/nanofluidic circuits and applications; however, many existing fluidic applications require specific pressure and/or flow rate conditions to perform optimally, and many require complex and expensive fabrication procedures. Here we introduce single-layer microfluidic system which utilize a spring and piston system — fabricated in situ via optofluidic lithography — to passively constrain fluid flow rate to a value independent of operating pressure. Experimental results revealed controlled flow rates of 29.2 ± 0.8 µl min (from $P = 50$-100 mbar) and a maximum small-signal resistivity of 141.1 mbar-min/ µl which represents the highest performance for a low-pressure microfluidic current source.

Figure 3.5a-c highlights the concepts behind the single-layer microfluidic current source. The device consists of a freely-moving piston mounted to a spring which moves in and out of a narrow microchannel according to action by pressure and shear hydrodynamic forces. The motion of the piston enables a negative feedback system within the current source; as pressure and flow increase, the piston's motion increase the resistance of the system, which then to stabilizes the flow rate. According to Poiseuille's Law for low Re systems, flow rate (Q) is proportional to pressure drop (ΔP) divided by hydrodynamic resistance (R). In general, R is proportional to the length of a channel and its resistivity (r), a factor which is highest where the piston is located in the narrow part of the channel.

For this system, resistance is a roughly linear function the piston's position within the narrow channel, approximated by

$$R(X) = R_0 + rX \tag{3.133}$$

where X is the length of the piston contained within the narrow channel. The microfluidic current source is designed such-that an increase in ΔP leads to a corresponding increase in resistance (R), creating a negative feedback loop which buffers the change in flow-rate Q.

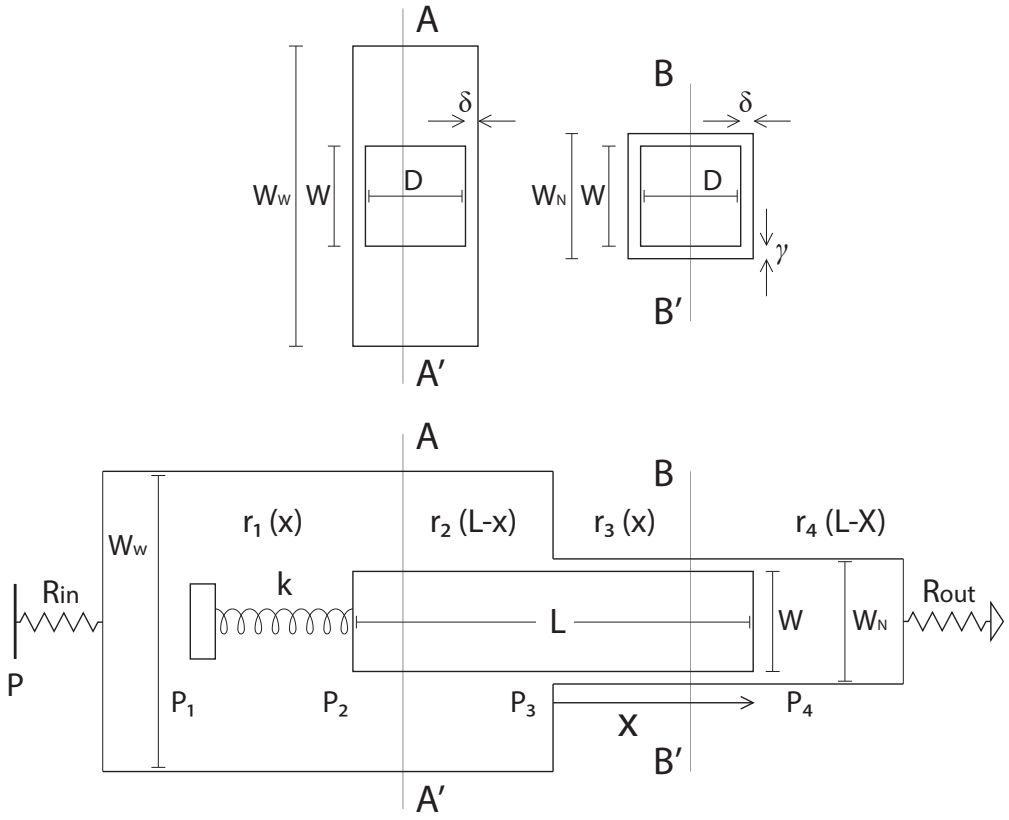


Figure 3.6 Optofluidic Current Source with critical dimensions and cross-sectional views of device behavior in location 2 (*i.e.*, for r_2) and in location 3 (*i.e.*, for the high-resistance r_3). Note that $r_3(x)$ is not a function but rather resistivity $r_3 \times x$.

The spring-dashpot-thin-film model discussed above works nicely in deriving the behavior of real microfluidic systems, such as the optofluidic *current source*. A current source is a device that is able to maintain a steady fluid flow across a range of pressure inputs:

$$Q(\Delta P) \sim \text{const.} \tag{3.134}$$

Although the linear Poiseuille model ($Q = \frac{\Delta P}{R}$) does not hold for constant R, it can be extended to a dynamic resistance $R(\Delta P)$. Thus, to allow for the leveling of fluid flow associated with a current

source, we need $R(\Delta P) \propto \Delta P$.

We can obtain *a priori* estimates on the values of the fluidic *resistivities* in the channel $r_1, r_2, r_3,$ and r_4. Using the first-order correction for resistance in a rectangular fluidic channel (Equation 2.96),

$$R_{\text{rect}} = \frac{12\mu L}{wh^3\left(1 - 0.630\,\frac{h}{w}\right)}$$

the static resistivity for each portion of the channel can be obtained and compared to the thin-film resistivity of r_3 (Fig. 3.8).

3.5.1 Results

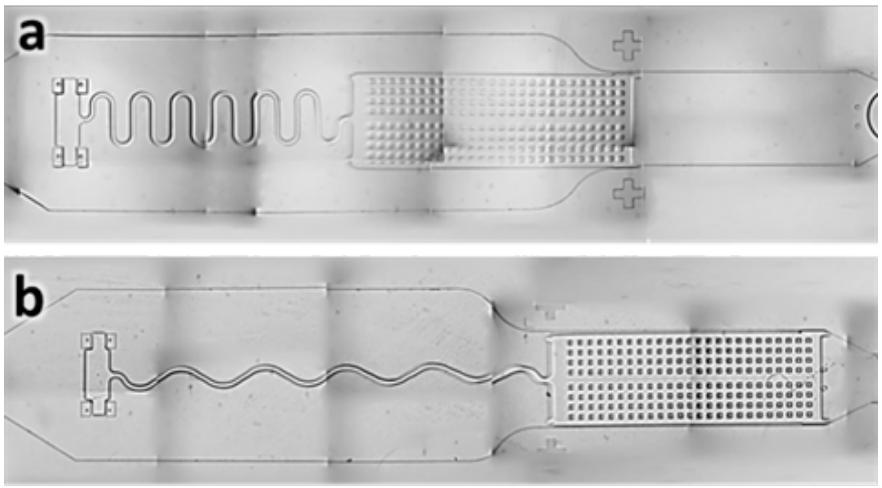


Figure 3.7 Images of fabricated current source device in **(a)** relaxed spring configuration (under no flow conditions) and **(b)** extended spring configuration (under forward fluid flow). Micrographs depict images stitched together with photo-editing software. Scale bar = 500 μm

Figure 3.7 shows optical images of the fabricated gain device, illustrating the piston in both "open" and "closed" positions. The 100×100 μm^2 holes in the top of the piston are used to prevent over-exposure of the hydrogel, a result which leads to the center of the piston being thicker than the edges and the piston refusing to move.

Figure 3.8 shows the results of three-dimensional COMSOL Multiphysics simulations of the microfluidic current source. In Figure 3.8a, fluid pressure drop across the piston occurs primarily when the piston is located within the narrow channel. This is due to the much higher resistivity in this region, as shown by the numerical results in Figure 3.8b. Note that the resistivity of the narrow channel plus piston is more than 60 $\times$ greater than the resistivities of the other sections

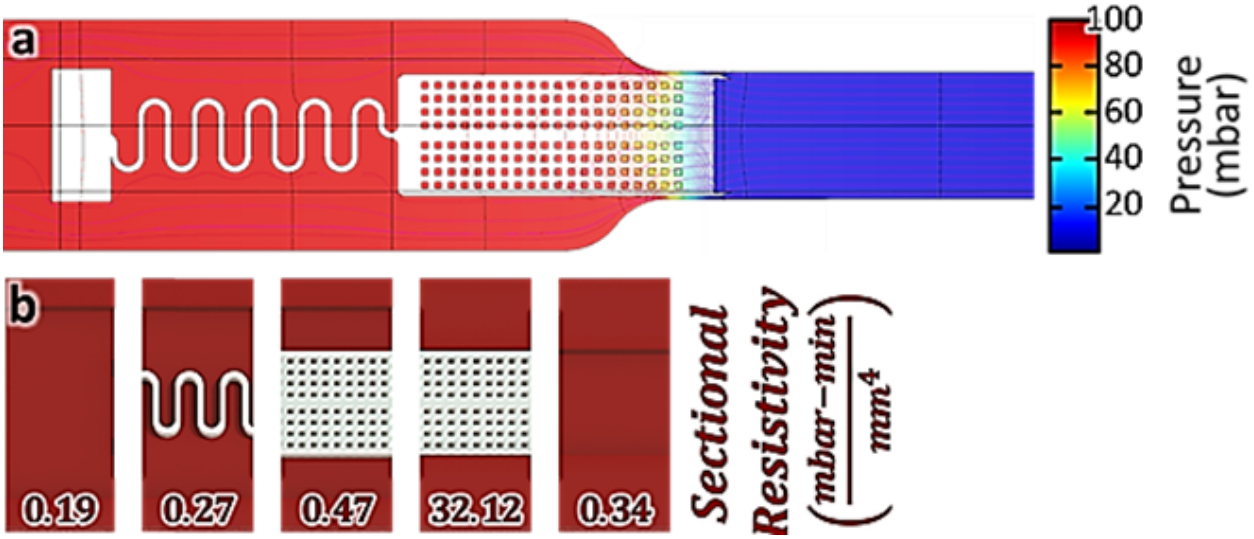


Figure 3.8 Three-dimensional COMSOL Multiphysics simulations of a microfluidic current source. **(a)** Simulation results depicting pressure field around the piston in the extended position. **(b)** Numerical results showing the resistivity of the individual sections of the current source channel. Note that the fourth resistivity (*i.e.*, the narrow channel plus piston) is $> 60\times$ higher the other parts of the current source, demonstrating that the resistance of this region dominates as the piston moves into the channel.

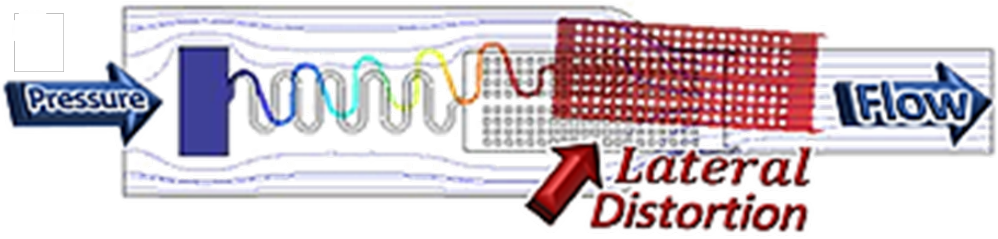


Figure 3.9 Three-dimensional COMSOL Multiphysics simulations of a microfluidic current source with lateral constraints removed. Asymmetries in the spring cause lateral distortion forces which push the piston against the wall. The resultant drag causes the device performance hysteresis seen in Figure 3.11.

of the current source, demonstrating that the resistance of this device becomes dominated by this region as the piston moves farther into the channel.

Figure 3.9 shows an important limitation for current sources using an asymmetric spring design: lateral distortion forces arise even when the spring is stretched in a purely axial direction. These lateral forces in turn push the piston against the channel walls, causing drag forces that prevent the piston from withdrawing smoothly from the channel creating the hysteresis effect seen in Figure 3.11. This effect can be mitigated by using a symmetrical spring design. However, symmetrical springs have substantially higher spring constants from equivalent asymmetrical springs, requiring a consideration of the trade-offs.

Using the small-displacement approximation from Euler beam-bending theory, $k_{\text{cantilever}} = \frac{1}{4}EH\frac{W^3}{L^3} \propto L^{-3}$, where E is the elastic modulus, H is the beam height, W is the beam width,

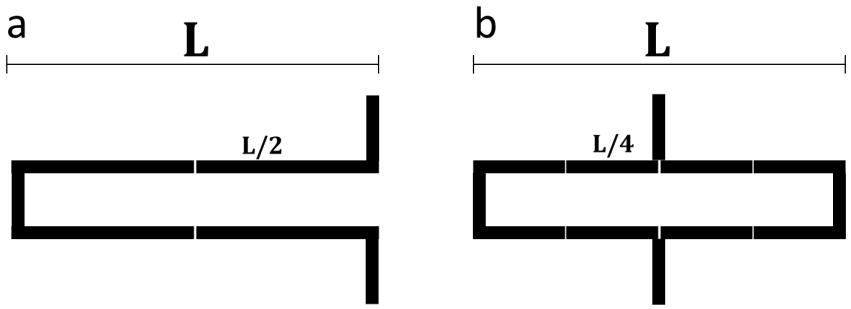


Figure 3.10 Asymmetric and Symmetric Spring Design

and L is the beam length [174]. The asymmetrical spring design shown in Figure 3.10a consists of four length $L/2$ springs in series, giving

$$k_{\text{asym}} = A * \frac{1}{4}\left(\frac{L}{2}\right)^{-3} \tag{3.135}$$

$$= 2AL^{-3}, \tag{3.136}$$

where A is the constant of proportionality. Using the same spring width L for a symmetrical spring design (Fig. 3.10b) results in two parallel instances of four length $L/4$ springs in series, giving

$$k_{\text{sym}} = A * 2\frac{1}{4}\left(\frac{L}{4}\right)^{-3} \tag{3.137}$$

$$= 32AL^{-3} \tag{3.138}$$

$$= 16k_{\text{sym}}, \tag{3.139}$$

giving us $k_{\text{sym}}/k_{\text{asym}} = 16$; per-unit, a symmetric spring design has $16\times$ the spring-constant as an asymmetric design. This may be compensated for by decreasing the beam width by half (which may introduce resolution problems) and by increasing the number of spring units.

Device hysteresis can be limited in several ways. First, the optofluidic exposure time can be reduced, which prevents overexposure of the piston sides, reducing overall friction. Second, the process can be controlled to prevent movement of the microfluidic device during exposure. Third, a symmetric spring design can be used to prevent the lateral distortions entirely — this method is sub-optimal because *ceteris paribus*, a symmetric spring has a 16x larger spring constant than that of an asymmetric spring, resulting in devices that are too stiff to move. Finally, micropillars within the channels may act to constrain the piston to axial motion within the channel.

3.5.2 *QP* Measurement Experiments

To investigate the overall performance of the current source, experiments were performed where the current source was subjected to a varying pressure sweep at its input and output terminals. Pressure differential applied and resultant flow rates were measured (Fluigent™MFCS and Flowell sensors, respectively) for the duration of the sweeps and the resultant flow rate-pressure (*QP*) curves were fitted using the aforementioned theoretical model and plotted.

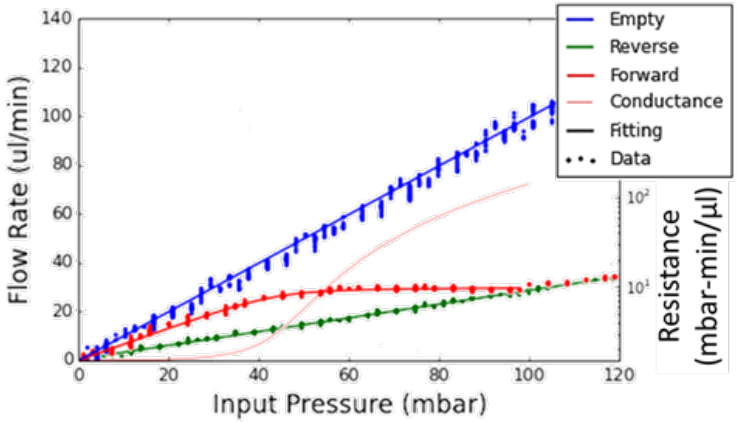


Figure 3.11 Data collected from a single microfluidic current source (spring amplitude = 600 µm). During the forward sweep (*red*), flow rate levels off at a maximum value of 30.3 µl/min due to the action of the current source. After 100 mbar, the piston reaches maximum extension and resistance (*pink*) becomes constant. When the sweep is reversed (*green*), piston drag against the channel walls leads to the hysteresis effect shown. An empty channel (*blue*) yields a linear response.

In Figure 3.11, the *QP* curve for a single current source is compared with the linear response of an equivalent empty channel. During the forward sweep (red), flow rate levels off at a maximum value of 29.2 ± 0.8 µl min (from $P = 50 - 100$ mbar due to the action of the current source. When the piston reaches maximum extension, the device begins to act as an ordinary resistor, thereby limiting the device's dynamic pressure range. This range can be extended primarily by increasing the length of the optofluidic piston. An extreme hysteresis curve (*green*) shows that during the reverse pressure sweep, the piston remained partially extended. An empty channel (*blue*) yields a linear response, as is expected from the Hagen-Poiseuille flow resistive model.

Figure 3.12 shows the *QP* curves plotted for current sources with differing spring amplitudes and spring stiffness. Note that as the spring constant increases, the current stabilization is not reached until higher pressures.

Autonomous, low-cost microfluidic circuit components offer significant potential to improve the functionality of lab-on-a-chip applications. In this work, we presented a single-layer system for implementing microfluidic current control, with fabrication via in situ optofluidic lithography. The

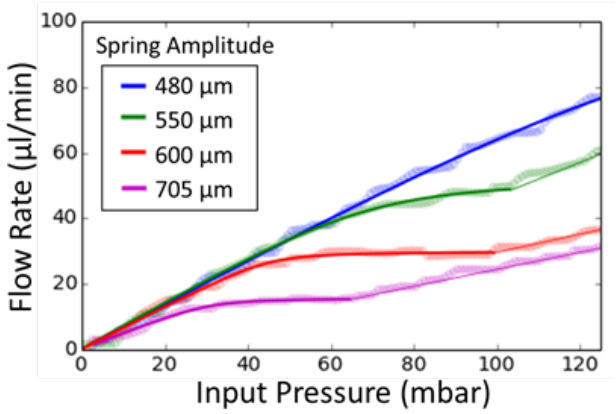


Figure 3.12 *QP*-response data of four microfluidic current source devices. Device response is determined by spring amplitude; shorter springs have stiffer spring constants and larger response times. All curves have been fitted with the same analytical model.

methodology presented has several adaptations over previous methods; for example it implements the current source using a fabrication method that requires only a single layer of PDMS substrate and two photolithographic processing steps, has enabled controlled flow rates as low as 16 µl min (*i.e.*, for $Re < 0.15$). The high pressure stability of these results suggest that the presented methodology could have numerous Lab-on-a-Chip applications in situations where precise reagent delivery is essential.

Several adaptations of this method could be used to improve regulate fluid flows in a variety of conditions. For example, decreases piston width lowers the steady-state flow rate, and increasing piston length increases the operating range. For future work, we plan to investigate hysteresis-reduction techniques to make the device behave more like an ideal fluidic current source. Due to its ease of manufacture and low flow rates available, this microfluidic current source can be adapted to offer a simple, yet versatile, component for microfluidic and lab-on-a-chip circuits and systems.

3.6 Gain Valves

3.6.1 Basic Gain Mechanism

Self-regulating and autonomous microfluidic devices are essential for the long-term development of versatile biological and chemical platforms, including point-of-care molecular diagnostics and on-site chemical assays. However, regulating microfluidic systems without substantial manufacturing complexity has proven to be a considerable challenge. Previously, researchers have utilized valve components that are directly pressure actuated. These systems can be modified to enable

pressure gain (*i.e.*, using low-pressure control channels to actuate valves in high-pressure flow channels), but have generally required at least four microfluidic layers. Thus, we introduce a single-layer microfluidic device - built from guided microstructures constructed in situ via optofluidic lithography - with differential area ratios (R) that enable a static gain much greater than unity. Non-unity gain allows moving pistons to close against a higher pressure, and could be used as a dynamic microfluidic control mechanism. COMSOL simulations suggest pressure gains approaching R. Experimental results revealed pressure gain between 6.30 ± 0.23 (for $R = 10$) and 1.94 ± 0.09 (for $R = 2$) [60].

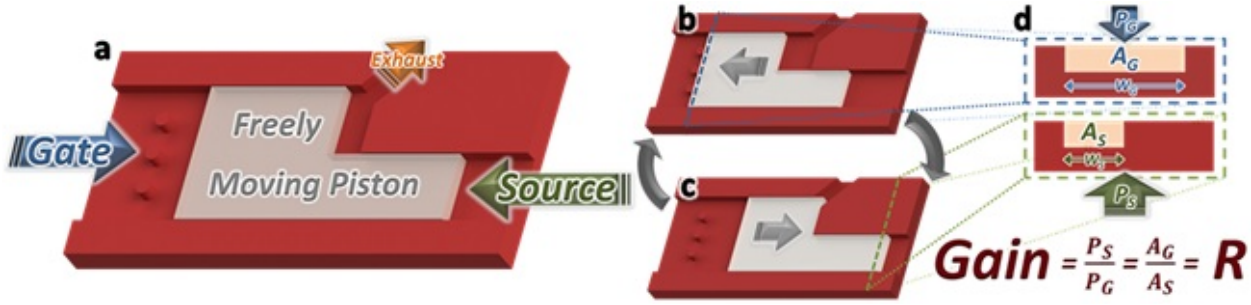


Figure 3.13 Illustrations of the pressure gain device concept. **(a)** The device consists of a piston which slides within a microchannel with three fluidic terminals: a high-pressure *source*, a low-pressure *gate*, and an atmospheric pressure *exhaust*. **(b)** In the "open" configuration, the high pressure from the source forces the piston to rest against microposts on the gate side. **(c)** When pressure at the gate reaches passes a threshold pressure, the piston slides from the gate to the source (*i.e.*, against the pressure gradient). The exhaust terminal serves as a vent for fluid trapped by the piston. **(d)** The piston includes two different cross-sectional areas — the source area (A_S) and the gate area (A_G) — which are exposed to a source pressure (P_G) and gate pressure (P_S), respectively. This differential area ratio R allows force amplification, enabling a low gate pressure to control a higher source pressure, with static gain approximately equal to R.

Figure 3.13a-c shows conceptual illustrations of the single-layer microfluidic pressure gain system, which includes a free-moving piston that slides freely within a microchannel based on two primary fluidic terminals: (i) a high-pressure source, and (ii) a low-pressure gate. In the absence of an applied gate pressure, the piston rests in the "open" position (held in place by several *blocking* microposts). When the gate pressure is increased beyond a critical threshold, the piston slides to the "closed" position. In addition, a third exhaust terminal serves to vent fluid from both the source and gate to atmospheric pressure, allowing the piston to move freely during this process. Because the piston includes two different cross-sectional areas — the source area (A_S) and the gate area (A_G) — a lower gate pressure (P_G) can overcome a higher source pressure (P_S) to close the piston [36]. This ability to achieve pressure gain is advantageous for microfluidic transistors.

Figure 3.13d illustrates the principle underlying the pressure gain mechanism. The net force

on the piston (neglecting viscous drag) is the sum of Areas * Pressures

$$F_{\text{close}} = P_G A_G - P_S A_S - P_E A_E \tag{3.140}$$

Setting the exhaust pressure $P_E = 0$, critical gate pressure (P_G^*) required to close the piston can be approximated as:

$$P_G^* = \frac{A_S}{A_G} P_S = P_S/R, \tag{3.141}$$

where $R \equiv {}^{A_G}/_{A_S}$ is the differential area ratio. Consequently, the pressure gain can be approximated as

$$\text{PressureGain} = \frac{P_s}{P_G^*} = \frac{A_G}{A_S} = \frac{W_G}{W_S}\frac{H_G}{H_S} = R. \tag{3.142}$$

By assuming devices with a uniform piston height, R reduces to the ratio of the source and gate channel widths, thereby providing basic geometric parameters through which the pressure gain can be designed to suit the application. Using channels with uniform height does result in one obvious limitation: high gain requires large width-ratios. For uniform channels, a gain factor R requires ${}^{W_G}/_{W_S} \propto R$. However, if the height of the channel is also allowed to change to the same degree, we only need ${}^{W_G}/_{W_S} \propto \sqrt{R}$. This provides a second advantage for multi-level microfluidic devices in the context of optofluidic lithography (see 4.2.2.6). Images of fully fabricated gain valves can be seen in Fig. 3.14

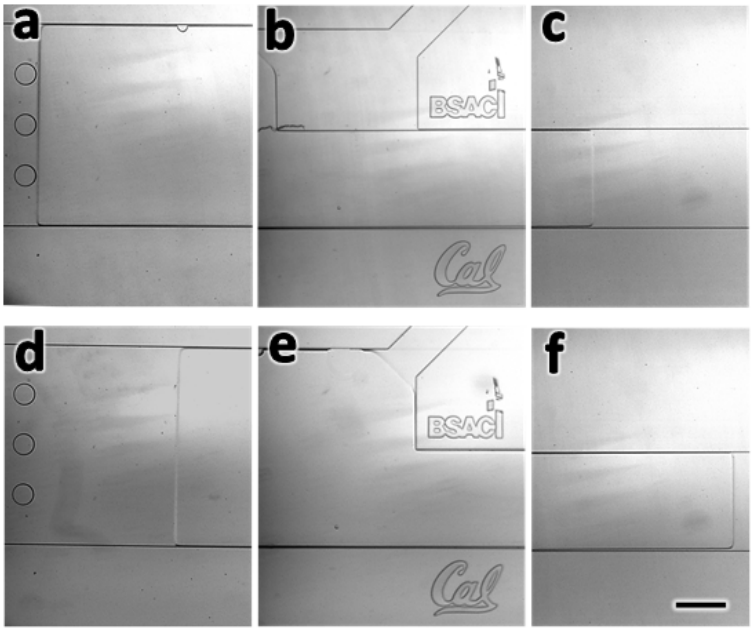
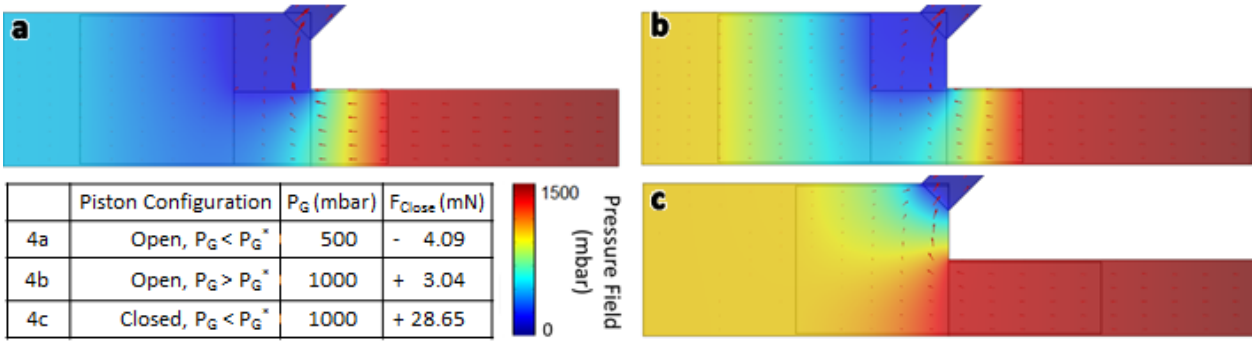


Figure 3.14 Images of fabricated pressure gain device with an area ratio of 2:1 in open position **(a-c)** and closed position **(d-e)** . Micrographs depict piston position in the gate, exhaust, and source regions. Scale bar = 500 μm

3.6.1.1 Results



	Piston Configuration	P_G (mbar)	F_{Close} (mN)
4a	Open, $P_G < P_G^*$	500	- 4.09
4b	Open, $P_G > P_G^*$	1000	+ 3.04
4c	Closed, $P_G < P_G^*$	1000	+ 28.65

Figure 3.15 COMSOL Multiphysics simulation of $R = 2$ pressure gain device; P_S set to 1500 mbar. **(a)** Gate pressure below critical; piston remains in open position. **(b)** Gate pressure above critical value. Net force on piston in rightward direction leads to **(c)** closure of the piston. Note that rightward force on the piston increases as piston moves to closed position, suggesting the devices have a tendency to remain closed at high pressures. Red arrows indicate fluid velocity vectors. All pressures given relative to 1000 mbar baseline. F_{Close} measured as sum of x-axis stresses, positive in rightward direction.

Figure 3.15 shows COMSOL Multiphysics simulations for the fluid behavior in an $R = 2$ device. Fluid flow is shown for the region above and below the piston in "open" 3.15a-b and "closed" 3.15c positions ($P_S = 1500$ mbar. The majority of fluid flows in the thin gap between the piston and PDMS substrate, moving from the source and gate regions, out through the exhaust port. The simulations indicate that the majority of the pressure drop occurs in the region occupied by the piston, allowing approximations to be made using the ideal pressure gain equation (Equation 3.142). The simulations were additionally used to calculate the total stress on the piston for $P_G = 500$ mbar (*i.e.*, $P_G < P_G^*$) which exhibited a net opening force, and $P_G = 1500$ mbar (*i.e.*, $P_G > P_G^*$) which exhibited a net closing force. The net closing force was calculated by integrating the stress over the surface of the piston.

To investigate the overall performance of the gain device for three values of R, experiments were performed varying (i) the source pressure P_S and (ii) the gate pressure P_G to determine the threshold gate pressure P_G^* necessary to move the piston from the "open" position to the "closed" position. First, the piston was placed in the "open" position by setting $P_S \ll P_G$. Then, for each P_S, P_G was slowly increased until the piston began sliding toward the "closed" position, indicating P_G^*. Figure 3.16 shows the results of these gain measurements, plotting P_S against P_G^*. The overall gain was determined by the slope of the resulting critical pressure curve, revealing pressure gains of 6.30 ± 0.23 (for $R = 10$), 3.35 ± 0.04 (for $R = 5$), and 1.94 ± 0.09 (for $R = 2$). The gain measurement results were consistent with the theoretical values determined by Equation 3.142. Although

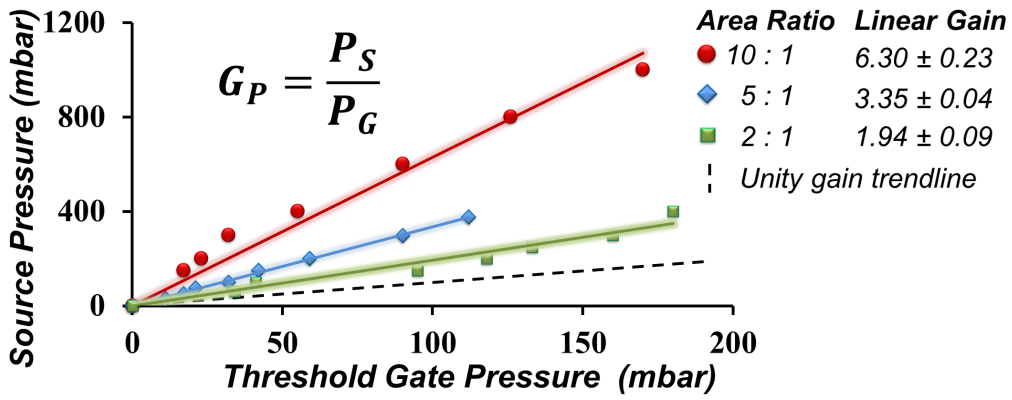


Figure 3.16 Experimental measurements of threshold pressure P_G^* needed to move piston from "open" position into "closed" position, versus source pressure P_S. Measurements were taken for pressure gain devices with three separate area ratios. Gain was extrapolated from slope of the pressure curves. Gain = 1 line is included for reference.

gain is ideally a feature of relative pressures only, it was found to be highest for low absolute pressures (relative to atmosphere), decreasing as absolute pressure increased. We hypothesize that at high pressures, PDMS begins to deform outward resulting in the piston blocking a relatively lower fraction of the microchannel, thereby decreasing the piston's hydraulic resistance and reducing the total pressure drop that takes place over the surface of the piston. Accordingly, smaller pressure differentials lead to lower forces acting on the piston.

However, these valves exhibit motion based only on flow pressure and do not respond directly to fluidic current, and thus lack some of the flexibility found in analogous electronic devices. To expand the capabilities of these optofluidic circuit elements, we introduce a hybrid current source utilizing optofluidic lithography to fabricate a single-layer microfluidic system with a moving piston element which can passively control fluid flow rates independent of operating pressures.

3.6.2 Basic Gain Valve

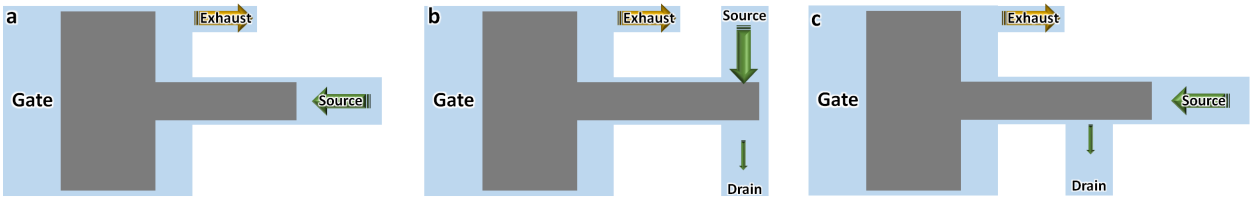


Figure 3.17 Schematic diagram comparing structure of optofluidic transistors: **(a)** basic gain mechanism, **(b)** transverse valve and **(c)** longitudinal valve

The optofluidic gain mechanism can be easily adapted to provide controllable microfluidic valving; by adding a fourth terminal, the valve can be used to block flow moving from a *source* to

a *drain*. As is standard in this optofluidic lithography method, the valve does not completely block flow due to the thin lubrication layers on the top and bottom surfaces. The basic gain mechanism (Fig. 3.17a) has three distinct variations: basic gain (but without functional features, discussed above) transverse valves, longitudinal valves. All types of these valves may also contain integrated springs to alter device performance.

(I) Transverse valve

In a *transverse valve* (Fig. 3.17b), the valve portion of the piston is perpendicular to the direction of fluid flow; as the piston is pushed forward under the action of the gate, the valve portion partially blocks the flow from source→drain. This mechanism has some limitations, however; for devices with higher gain, the piston becomes increasingly narrow in the valving region, thereby reducing the resistive effect,[16] and transverse valve resistance is not linear in piston position. Conceptual images of transverse valve operation are in Figure 3.18

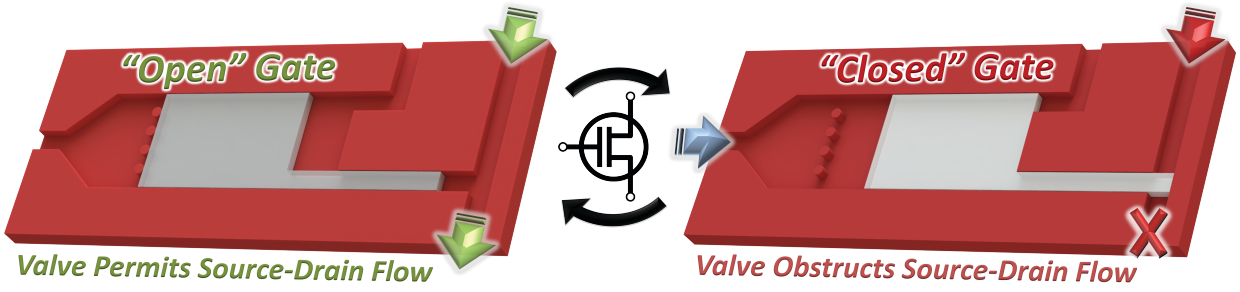


Figure 3.18 Conceptual behavior of the optofluidic transverse valve. Transverse valves have the disadvantage that high-gain valves have a relatively small area in the blocking channel, limiting their total resistance change in the open versus closed state.

(II) Longitudinal Valve

Longitudinal valves (Fig. 3.17c) direct fluid flow along the same axis as the piston movement. Longitudinal valves overcome some of the weaknesses of the transverse valve: not only is the resistance directly proportional to the length of the piston over which the fluid must travel (excluding edge effects), the device can achieve a much higher ratio of open-resistance : off-resistance. One disadvantage is that longitudinal valve must place either the source or the drain closer to the gate/exhaust region, increasing leakage effects. In general, this weakness is mitigated by placing

[16] Because $R \propto L$, where L is the channel length along the direction of fluid flow, narrower pistons have a smaller effective L.

the drain closest to the exhaust due to the lower absolute pressure of the drain region relative to the source region.

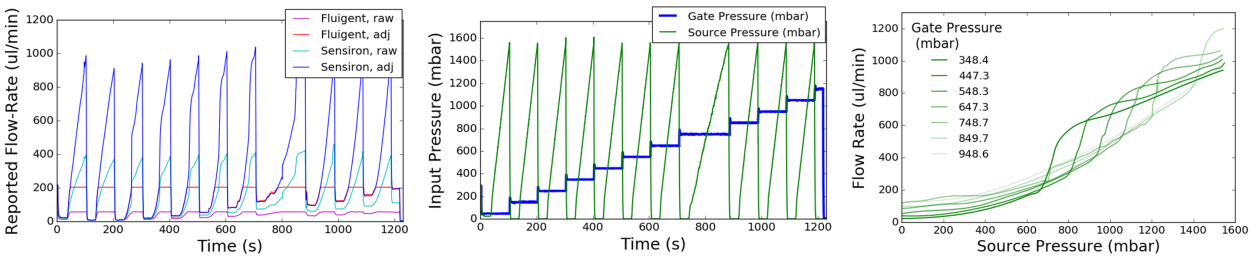


Figure 3.19 Transistor characteristics of Basic Longitudinal Valve. **(a)** Fluid flow results from Fluigent and Sensirion flow rate sensors, including recalibrated pegda fluid flow. **(b)** Time series behavior of parametric gate and source pressure sweeps. **(c)** Flow rate results for transistor with source pressure sweeps, parametrized by gate pressure. Increased gate pressure makes the valve open at increasingly higher source pressure. The overall fluid flow rate increases over the course of the parametric sweep because of the lack of seal between gate and source regions.

(III) Valves with Integrated Spring

By adding spring mechanism to the piston, the valve can be altered to return to a set position when pressure forces are in equilibrium. The spring both qualitatively and quantitatively alters the behavior of the device and can be used set a predefined *turn-off pressure*. While integrated springs lower the overall gain and response time, they can compensate for the tendency of the pistons to stick to walls.

3.6.2.1 Default-off behavior and neutral spring position

One difficulty with fabricating integrated springs using optofluidic lithography or 3D printing is that *default-off* behavior difficult to generate. Default-off devices have a higher (ideally infinite) fluidic resistance in their equilibrium state than they do when fluid is flowing, generated by valves which are tightly closed in their equilibrium state. For example, an IF Gate is a default-on transistor which has low (ideally zero) fluid flow unless pressure is applied to the gate to open the valve.

The necessarily tight seals at equilibrium are difficult to generate for two primary reasons. First, the spring's *resting* or *neutral* position is generally defined by the fabrication position of the spring; for both optofluidic and 3D printed microfluidic devices, the spring (or membrane) polymers have minimal internal stresses in whatever position they are built in. This behavior makes little difference when the spring is fabricated away from the walls of the channel, but means small displacements require very little force to actuate at neutral position. Secondly, devices are difficult to fabricate in a fully-closed position to begin with. In 3D printing, surfaces are increasingly

likely to fuse when designed closely together (especially if the surfaces are closer than the resolution of the printer).[17] In optofluidic lithography, the PEGDA hydrogels will *not* fuse with PDMS during, so overlap between the mask and channel walls is permissible (and beneficial for alignment purposes) during the exposure process; for components which must be in close contact with the channel walls, the overlap allows for good conformal channel geometry. Additionally, this hydrogel contraction allows for a thin lubrication layer to allow the devices to move freely (see Section 4.24). However, this contraction causes problems with default-off microfluidic devices, because the valves retract slightly, lowering the effective resistance of the channel at equilibrium.

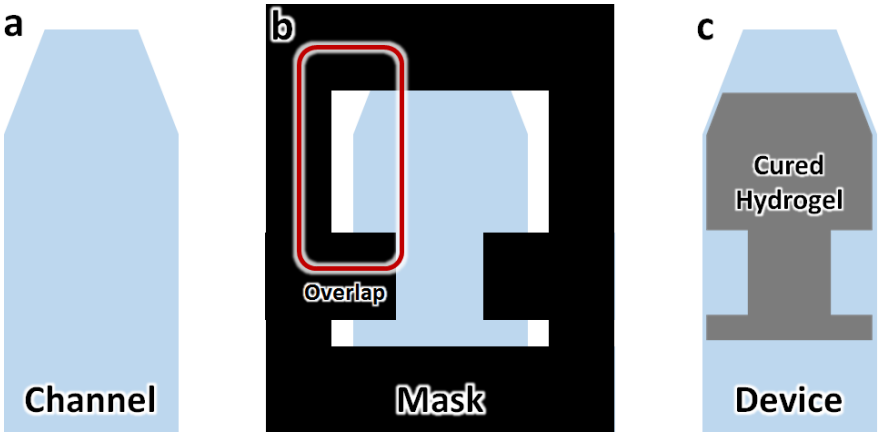


Figure 3.20 Conceptual illustration of the contraction of a hydrogel during curing, as well as of the permissibility of exposure overlap. **(a)** Channel filled with uncured PDGDA. **(b)** Position of the mask over the channel. The mask overlaps the edge of the channel, but since UV exposure has minimal effect on PDMS, the hydrogel only cures to the boundary of the channel. **(c)** Device with cured hydrogel. The hydrogel has contracted slightly, but remains similar to the shape of the channel.

Due to the contraction of hydrogel components when curing,[18] the springs tend to pull away from the walls of the channel. While the gap is relatively small (≈10 μm), it does decrease the resistance of fluid flow in the equilibrium position. For 3D printed microfluidics, valves cannot be printed to be closed by default because the printing process would fuse the components and create a single component. Through use of secondary fabrication processes (*e.g.*, thin film deposition, strain-energy depositions [174]) could alter the structure post-printing, creating sufficient surface strain energy, and create a default-closed structure, this processes is necessarily more complex than simple single-material printing.

[17] *i.e.*, a device designed in a "fully closed" position would remain fully closed, permanently.

[18] We are unsure of the reasons for this contraction, although similar effects are observed when using PDMS in soft-lithography; the fabricated device is smaller than the mold by ≈1%.

3.6.3 Current-Controlled Gain Valve

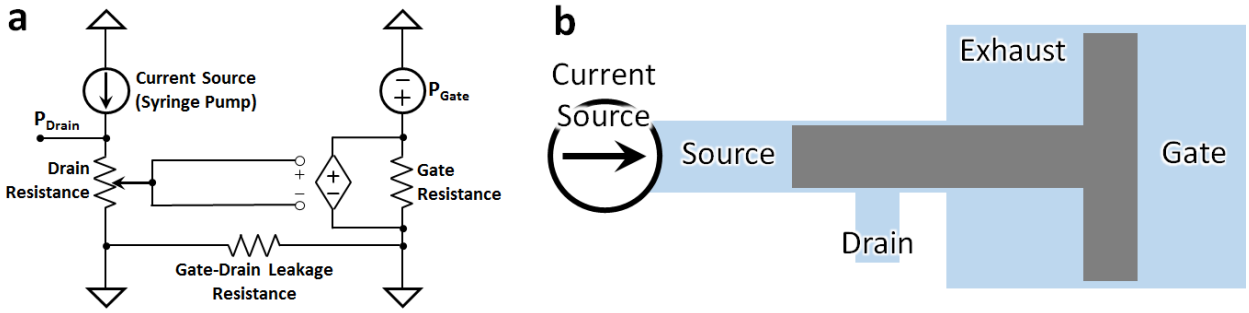


Figure 3.21 Optofluidic transverse valve connected to fluidic current source, placed in common-emitter format. **(a)** Equivalent electrical circuit. **(b)** Optofluidic valve equivalent.

Due to the linear relationship between piston position and source-drain resistance R_{SD}, longitudinal valves may be used as pressure amplifiers when connected to a constant current source Q_S – commonly provided by a device such as a syringe pump. In this setup, large changes in the source pressure ΔP_S may be actuated by smaller changes in the gate pressure ΔP_G. In the simplest approximation, we assume that (i) the exhaust ports have zero resistance, so the exhaust pressure $P_E = 0$ regardless of operating conditions; (ii) the gate-exhaust resistance R_{GE} and the drain-exhaust resistance R_{DE} are effectively infinite, preventing fluid leakage; (iii) there is no resistive load at the source; and (iv) the primary forces driving piston position are hydrostatic pressure. These assumptions can be relaxed later.

We first assume that R_{SD} is linearly dependent on the position of the piston, with $R_{SD} = R_0$ when the piston is fully retracted ($x = 0$) and R_1 when the piston is fully extended ($x = L$). We define $\Delta R \equiv R_1 - R_0 > 0$ (orienting the axes such that $+\hat{x}$ is to the left), giving

$$R_{SD}(x) = R_0 + \Delta R \frac{x}{L}. \tag{3.143}$$

Because leakage currents are blocked, the source pressure $P_S = Q_S(R_0 + \Delta R\frac{x}{L})$. The balance of pressure forces further requires

$$A_S P_S(x) = A_G P_G, \tag{3.144}$$

assuming zero exhaust pressure, leading to

$$P_S = \frac{A_G}{A_S} P_G \qquad \text{and} \qquad x = L\frac{R_0}{\Delta R}\left(\frac{A_G}{A_S}\frac{P_G}{Q_S R_0} - 1\right). \tag{3.145}$$

If we then make small oscillations around a set position x_0, where $x = x_0 + \Delta x$, $P_G = P_{G0} + \Delta P_G$,

and $P_S = P_{S0} + \Delta P_S$, we get

$$\Delta P_S = \frac{A_G}{A_S}\Delta P_G \equiv A_{\text{basic}}\Delta P_G \tag{3.146}$$

from Equation 3.144 and

$$P_S = Q_S(R_0 + \Delta R\frac{x_0 + \Delta x}{L})) = P_{S0} + \Delta P_S \tag{3.147}$$

$$\implies \Delta P_S = Q_S \Delta R\frac{\Delta x}{L}; \tag{3.148}$$

small changes in P_G create corresponding changes in P_S, amplified by the intrinsic gain of the system $\frac{A_G}{A_S}$. Lastly, we can combine these two results to get

$$\frac{\Delta x}{\Delta P_G} = L\frac{A_G}{A_S}\frac{\Delta P_G}{Q_S \Delta R} \equiv A_G/k_{\text{equiv}}. \tag{3.149}$$

Interestingly, Equation 3.149 shows that this amplifier acts like a linear spring responding to the pressure changes, where $k_{\text{equiv}} \equiv \frac{Q_S \Delta R A_S}{L}$. Thus, for this design, the inclusion of a spring is not strictly necessary, as the balance pressure forces will tend to restore it to an equilibrium position. However, adding a spring does allow the system to return to equilibrium more easily in cases where the system has received a major disruption; *i.e.*, the system is more stable to disruption.

3.6.3.1 Gain Valve Variations

(I) Inclusion of Simple Spring

This simple variation includes a spring which restores the piston to a default location x_0. The basic force balance then becomes[19]

$$A_S P_S(x) = A_G P_G - k(x - x_0) \tag{3.150}$$

These can be combined with Equation 3.143 to provide

$$P_S = \frac{1}{1 + \frac{kL}{Q_S \Delta R A_S}}\left(\frac{A_G}{A_S}P_G + \frac{k}{A_S}\left(x_0 + L\frac{R_0}{\Delta R}\right)\right) \tag{3.151}$$

[19] $+\hat{x}$ displacements to the spring produce a $-\hat{x}$ restoring force: *i.e.*, in the same direction as P_S

for a small-signal gain of

$$\Delta P_S = \frac{1}{1+k/k_{\text{equiv}}}\frac{A_G}{A_S}\Delta P_G = \frac{A_{\text{basic}}}{1+k/k_{\text{equiv}}}\Delta P_G \tag{3.152}$$

Similarly, if we take the small-signal displacement Δx, we get

$$\Delta x = \frac{L}{1+\frac{kL}{Q_S\Delta R A_S}}\frac{A_G}{A_S}\frac{\Delta P_G}{Q_S\Delta R} \tag{3.153}$$

$$= \frac{\Delta P_G A_G}{k_{\text{equiv}}\left(1+k/k_{\text{equiv}}\right)} \tag{3.154}$$

$$= \frac{\Delta P_G A_G}{k_{\text{equiv}}+k}. \tag{3.155}$$

Unsurprisingly, the addition of a physical spring increases the effective spring constant — an effect of the fluid mechanics — by a factor of $\left(1+\frac{kL}{Q_S\Delta R A_S}\right)$. Somewhat surprisingly, however, the system simplifies to an equivalent circuit where k and k_{equiv} act in parallel — the new effective spring constant $k_{\text{eff}} \mapsto k_{\text{equiv}}+k$.[20]

The increase in effective spring-constant also reduces the gain (from A_{basic}) by the same factor. Thus, this reduction in gain can be effectively considered a cost for the increased mechanical stability in the system. If the input current Q_S is increased to infinity, the small-signal gain returns to A_{basic}, even as $\Delta x \to 0$.

(II) Addition of Leakage Current Between Source and Gate

Relaxing the assumption of infinite Source/Drain - Gate resistance, we consider Drain, Drain-Exhaust, Gate-Exhaust, and Exhaust resistances of R_D, R_{DE}, R_{GE}, and R_E, respectively. We then consider $R_0 \equiv R_S + R_D$

$$\frac{\Delta P_S}{\Delta P_G} = \frac{A_G}{A_S}\cdot\frac{(R_D+R_{DE}+R_E)R_{GE}}{R_D R_E + R_E R_{DE} + (R_D+R_E)R_{GE} + R_{DE}R_{GE}} \tag{3.156}$$

$$+\frac{(R_D+R_{DE})R_E}{R_D R_E + R_E R_{DE} + (R_D+R_E)R_{GE} + R_{DE}R_{GE}} \tag{3.157}$$

[20] Note that $\frac{1}{k_{\text{equiv}}} \mapsto \frac{1}{k_{\text{equiv}}+k}$ is also equivalent to dividing by $(1+k/k_{\text{equiv}})$

The gain has then become a combination of a term dependent on the areas and a term independent of area. If we define the first coefficient as ρ_{GDE}, we can reduce that to

$$\frac{\Delta P_S}{\Delta P_G} = \left[\frac{A_G}{A_S} + \left(\frac{R_E R_D + R_E R_{DE}}{(R_D + R_E)R_{GE} + R_{DE}R_{GE}}\right)\right]\rho_{GDE} \tag{3.158a}$$

$$\frac{\Delta x}{\Delta P_G} = -\frac{(A_S R_{DE} R_E + A_G(R_D + R_{DE} + R_E)R_{GE}}{k(R_E R_{GE} + R_D(R_E + R_{GE}) + R_{DE}(R_E + R_{GE}))} \tag{3.158b}$$

With the inclusion of a spring, this becomes

$$\frac{\Delta P_S}{\Delta P_G} = \left[A_{\text{basic}} + \left(\frac{R_E R_D + R_E R_{DE}}{(R_D + R_E)R_{GE} + R_{DE}R_{GE}}\right) + \left(\frac{R_D + R_E}{(R_D + R_E)R_{GE} + R_{DE}R_{GE}}\right)\left(\frac{k}{k_{\text{equiv}}}\right)\right]\frac{\rho_{GDE}}{1 + k/k_{\text{equiv}}} \tag{3.159a}$$

$$\frac{\Delta x}{\Delta P_G} = -\frac{(A_S R_{DE} R_E + A_G(R_D + R_{DE} + R_E)R_{GE}}{\left(k + k_{\text{equiv}}\right)(R_E R_{GE} + R_D(R_E + R_{GE}) + R_{DE}(R_E + R_{GE}))} \tag{3.159b}$$

Unlike in the leak-free case, the addition of a spring does *not* exactly match the spring-less case, with the addition of a parallel spring:

$$\frac{\Delta P_S}{\Delta P_G} = \frac{\Delta P_S/\Delta P_G|_{k=0}}{1 + k/k_{\text{equiv}}} + \left(\frac{R_D R_E}{R_D R_E + R_{DE}R_E + (R_D + R_{DE} + R_E)R_{GE}}\right)\frac{k}{k + k_{\text{equiv}}} \tag{3.160a}$$

$$\frac{\Delta x}{\Delta P_G} = \frac{\Delta x/\Delta P_G|_{k=0}}{1 + k/k_{\text{equiv}}} \tag{3.160b}$$

If we gather the leakage terms into R_{out} and R_L for the drain/exhaust resistances and piston leakage resistances, respectively, and by making the approximation that the denominator term

$$(R_L^2 + 3R_L R_{\text{out}} + R_{\text{out}}^2) \approx (R_L^2 + 2R_L R_{\text{out}} + R_{\text{out}}^2) \tag{3.161}$$

$$= (R_L + R_{\text{out}})^2, \tag{3.162}$$

As a consequence,

$$\frac{\Delta P_S}{\Delta P_G} \gtrsim A_{\text{basic}}\frac{R_L + 2R_{\text{out}}}{(R_L + R_{\text{out}})^2} + \frac{R_{\text{out}}}{R_L + R_{\text{out}}} \tag{3.163a}$$

$$\frac{\Delta x}{\Delta P_G} \gtrsim -\frac{A_G}{k_{\text{equiv}}}\frac{R_L(R_L + 2R_{\text{out}})}{(R_L + R_{\text{out}})^2} - \frac{A_S}{k_{\text{equiv}}}\frac{R_L R_{\text{out}}}{(R_L + R_{\text{out}})^2} \tag{3.163b}$$

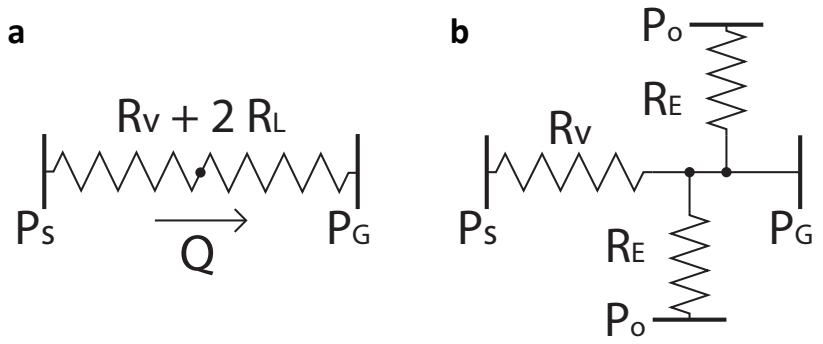


Figure 3.22 (a) Equivalent resistance diagram for $P_{\text{out}} \to \infty$. **(b)** Equivalent resistance diagram for system in which there is no piston resistance R_{DE} or R_{GE}; the drain and gate regions become a single node, and the current Q is set as a constant, $P_S = QR_V + P_G$. Because $\Delta x = 0$, $R_V = \text{const}$, so $\Delta P_S \propto \Delta P_G$. Positive flow rate is defined from left-to-right.

and in the spring-case

$$\frac{\Delta P_S}{\Delta P_G} = \frac{\Delta P_S/\Delta P_G|_{k=0}}{1+k/k_{\text{equiv}}} + \frac{R_{\text{out}}^2}{(R_L+R_{\text{out}})^2}\frac{k}{k+k_{\text{equiv}}} \tag{3.164a}$$

$$\frac{\Delta x}{\Delta P_G} = \frac{\Delta x/\Delta P_G|_{k=0}}{1+k/k_{\text{equiv}}}. \tag{3.164b}$$

These simplifications allow a few observations:

1. If either $R_{\text{out}} \to 0$ (*i.e.*, the exhaust and drain are kept as a perfect sink) or $R_L \to \infty$ (*i.e.*, no leakage past the piston), the equations return to their ideal form seen in Equations 3.155 and 3.155. The effect emerges when piston pressure is decoupled from the exhaust pressure

   (a) If $R_E \to 0$, then exhaust is at zero pressure regardless of the source/drain

   (b) If $R_{GE} \to \infty$, then the piston is completely isolated from the source.

2. If either $R_{\text{out}} \to \infty$ (*i.e.*, no drainage) or $R_L \to 0$ (*i.e.*, no non-variable piston resistance), then (a) $\Delta x = 0$ (no movement) and (b) $\Delta P_S = \Delta P_G$. This effect does not occur in isolation (*i.e.*, *both* R_E, $R_D = \infty$ or *both* R_{DE}, $R_{GE} = 0$).

   (a) If the output resistances $R_{\text{out}} = \infty$, then the system is essentially a single series resistor $R_V + R_{DE} + R_{GE}$. With all the gain removed from the system, the piston does not move ($\Delta x = 0$) until $P_S > P_G$. Thus, R is constant and because $P_S = P_G + QR_{\text{tot}}$, so $\Delta P_S \propto \Delta P_G$.

   (b) If the piston leakage resistances drop to zero, then the $P_E = P_G$ and there is no piston motion ($\Delta x = 0$) from a change in gate pressure. With zero piston motion, $\Delta P_S \propto \Delta P_G$.

3.7 Summary and Future Directions

Autonomous, low-cost microfluidic circuit components offer significant potential to improve the functionality of lab-on-a-chip applications. This chapter presents a number of approaches to using optofluidic lithography to fabricate moving components inside a microfluidic device *in situ*. The methodology presented has several adaptations over previous methods; for example it implements pressure gain using a fabrication method that requires only a single layer of PDMS substrate and two photolithographic processing steps. Using optofluidic lithography, we demonstrated several variants of microfluidic control mechanisms, including passive: diodes (which provide for one-way flow rectification) and current source (which allows fluid flow rates to remain flat within a larger pressure range); and active: microfluidic gain and microfluidic gain valves. We then presented a theory of the microfluidic gain valve and few variations, showing the effect of springs, device leakage, and device load on performance.

Several adaptations of the current method could be used to improve the overall gain performance of optofluidic piston system. For example, increasing the stiffness of the substrate material (*i.e.*, using PDMS with higher Young's moduli) would result in more uniform gain across absolute pressure ranges. Similarly, reducing the thickness of the gap between the optofluidic piston and the PDMS would increase hydraulic resistance and improve gain at all pressures. However, using the theory of thin-film and piston movement, we see a few limitations; reducing overall fluid leakage comes at the cost of speed reduction. However, if combined with multi-level soft-lithography, optofluidic lithography could be adapted to offer a simple, yet versatile, component for microfluidic and lab-on-a-chip circuits and systems.

Acknowledgments

I would like to thank Ryan D. Sochol, Ki Tae Wolf, Niloofar Shahmohhamadi, Sebastian Miller-Hack, Vishnu Jayaprakash, Kosuke Iwai, Luke P. Lee, Nazly Pirmoradi, Albert Lu, and Nicholas Scianmarello for their assistance on the Pressure Gain project, as well as Sikun Peng, My Chung, Kevin Korner, Melanie Veale, Chengming Liu, Jesse Moore, Andrew Chu, Alan Buckley, Kosuke Iwai, and Ryan D. Sochol for their assistance on the current-source project. Work on the optofluidic diode was performed jointly with Ryan D. Sochol. This research was supported in part by the DARPA N/MEMS program under the Micro/Nano Fluidics Fundamentals Focus (MF3) center.

Chapter 4

Rapid Assembly of Multilayer Microfluidic Structures via 3D-Printed Transfer Molding and Bonding*

4.1 Introduction

Traditional methods for fabricating microfluidic devices involve using photolithography to construct micro-molds with very fine features [22, 23]; however, this process can be long and costly. The increasing demand for microfluidics is particularly high for double- and multi-layered devices which allow for the implementation of more sophisticated structures and components (*e.g.*, valves, pumps, and other active control mechanisms). For example, soft lithography through micromachining processes is generally restricted to monolithic rectilinear features [3] although rounded and fully circular channels are common in large-scale fluidic systems.

One method of increasing geometric complexity is 'multilevel soft lithography' [71], where the channels are non-planar and/or rounded [311]. Although rounded channels would be beneficial for some microfluidic applications, few groups have developed appropriate fabrication techniques (see 4.2.2.5) [63, 66, 312] because multilevel soft lithography has historically required multiple photolithography steps [72]. Although 'grayscale lithography' – whereby resists are exposed to non-binary shades of gray – can potentially generate rounded microfluidic channels [73, 76, 313], the process still requires multiple exposures for larger aspect ratios [78, 79]. Furthermore, while multilayer PDMS manufacturing techniques have been demonstrated by several groups [68, 314],

* This chapter has been adapted from Ref. 138 with permission of Microsystems and Nanoengineering.

these are even more time-consuming and labor-intensive, requiring multiple lithography steps as well as precision alignment, issues which are only partially addressed by dedicated PDMS alignment apparatuses [69].

3D printing has presented a unique route for building multilevel and multilayer microfluidic devices directly, or indirectly via molding processes. For example, various groups have used 3D printers previously to make simple microfluidic devices with truly 3D geometries, including microfluidic devices without moving elements, such as resistors [315] and modular components [98], as well as those with movable components, such as capacitors, diodes and transistors [316]. Currently, 3D-printed microfluidics is limited by: (1) the available resolution of the printer [315]; (2) surface roughness [94, 117]; and (3) material types [87, 317]; however, 3D printing technologies are expected to rapidly advance and address these matters in the coming years. For further details on current 3D printer capabilities, including printer resolution and surface roughness, see reviews in [141, 318, 319, 320, 321, 322].

Although *direct* 3D printing is a rapid process for prototyping, for making multiple copies of microfluidic devices, *3D-printed transfer molding* (PTM), where polymer is poured into a 3D-printed mold, remains faster, cheaper, and more reliable. First pioneered by McDonald *et al.* using fused deposition modeling techniques [142], the technique has since been used with stereolithography [131], multijet printing [94], as well as with wax printers [133] and office-quality laserjet printers [134, 135]. While PTM does not allow the same geometric flexibility of fully 3D-printed microfluidics, it possesses three notable advantages: (i) each mold can be used for multiple microfluidic devices, saving on 3D printing times and costs, (ii) many 3D printers exhibit lower resolution for features requiring support materials, and (iii) the process is compatible with conventional microfluidic fabrication materials, most notably PDMS [131, 133, 134, 136, 139]. Because PDMS transfers patterns with high fidelity, the resolution and surface finish of the mold define the resulting quality of the resulting PDMS [18, 139], provided the mold maintains reasonable aspect ratios [94].

In addition to patterning features externally, PTM has also been used to fabricate internal features, reducing some of the monolithicity constraints. Hwang *et al.* have developed printed molds which are surrounded by PDMS and then withdrawn after curing, relying on the flexibility of PDMS to remove the components. While similar to fugitive ink processes [92, 323, 324], fugitive ink molding has fewer geometric constraints but requires printing for every final device, while solid internal must be designed for withdrawal, but can be reused [94, 95, 132]. Chan *et al.* have fabricated molds with overhangs in a basket weave pattern, which can be used to generate microfluidic

vias and valving in a single step, repairing demolding damage by thermally healing the PDMS, with the restriction that the vias be designed in parallel [140].

PTM is also increasingly integrated with other 3D printing processes to reduce the challenges of multi-component assembly and interfacing microfluidic devices with external systems [141]. While PTM devices may do this directly, for example through punching holes (*i.e.*, like standard soft lithography processes) [135], molding open wells [142, 143], adding connectors during the curing process [131, 134, 144], PTM devices may also interface indirectly by attaching to 3D-printed components that do have the desired interfaces [136]. Similar to soft lithography, PTM devices are sealed with glass or other 3D-printed components to provide enclosed channels after molding (*e.g.*, through plasma bonding [142], mechanical pressure [136], or tape [136]).

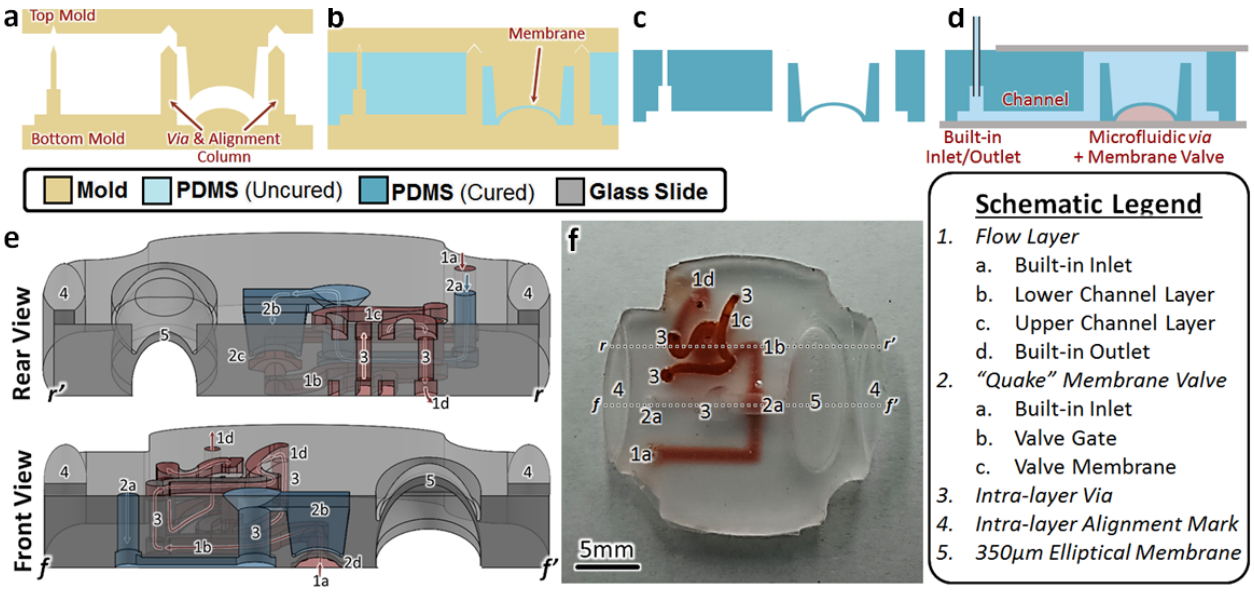


Figure 4.1 Illustration of fabrication process (*Top*) and technical capabilities (*Bottom*) of 3D-printed transfer molding for double-sided microfluidic devices. *Fabrication*: **(a)** Mold is 3D-Printed from CAD model, treated, and fitted using alignment marks, and **(b)** filled with PDMS and cured. Excess PDMS is cut away and the mold is removed. **(c)** PDMS compnent has built-in inlets/outlets, membranes, and vias, and is **(d)** bonded to glass to create a device with enclosed, arbitrary channels. *Technical capabilities*: the multi-level microfluidic device shown in cross-section in **(e)** and photographed in **(f)** is fabricated using double-sided molding techniques and exhibits design elements, such as two-layer fluid flow, multiple microfluidic vias, built-in fluid inlets/outlets, an elliptical 350 μm domed membrane, and a "Quake"-style membrane value, as well as alignment marks for use in generating multilayer devices.

This work advances 3D-printed transfer molding techniques from single-sided microfluidics [131, 134, 142] to multilayer microfluidic manufacturing, utilizing the ease of 3D printing to create multiple molds with alignment structures to shape multiple layers of PDMS structures and quickly assemble them at the end. First, we discuss details specific to the ProJet™3000 3D printer, including resolution and surface treatments. Next, we examine the single-step double-sided mold-

ing method used to create PDMS components with complex geometries — including vias, thin membranes, and rounded channels — that are difficult to achieve using standard soft lithography, as well as built-in input/output marks that do not require positioning external components during PDMS curing. Finally, we demonstrate rapid assembly of multilayer microfluidic devices including built-in alignment marks, which enable tactile – as opposed to optical – alignment of layers to within the resolution of the 3D printer (including PDMS-PDMS for multilayer assembly and mold-PDMS for interfacing with other 3D-printed objects), and bonding techniques, including a specialized variant of adhesive bonding techniques introduced by Satyanarayana *et al.* [32]. Using custom 3D-printed to selectively apply a thin layer of liquid PDMS adhesive to non-channel areas, layers were successfully bonded without the adhesive clogging narrow channels, obviating problems associated with mold surface roughness.

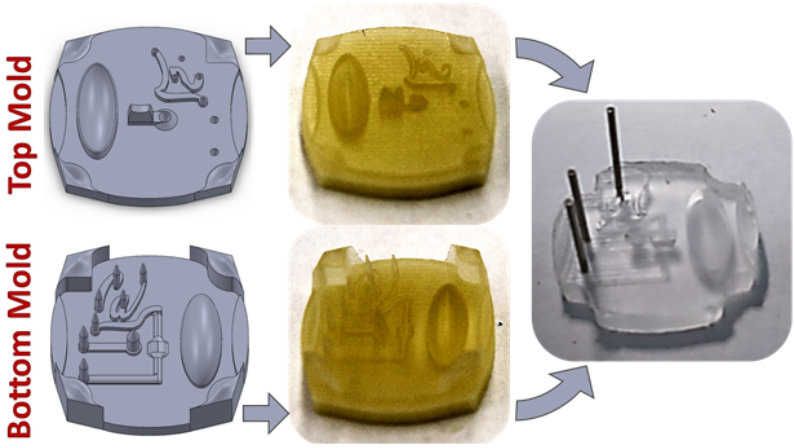


Figure 4.2 Illustration of the 3D-printed transfer molding and process for two-sided microfluidic devices with detour vias and thin membranes. The complex multi-level microfluidic device in Figure 4.1e,f is fabricated using the CAD models shown in **(a)** and resulting 3D-printed molds shown in **(b)** . The devices are then demolded **(c)** and the channels are sealed to allow enclosed fluid flow.

Figure 4.2 illustrates the process flow for fabricating multi-sided PDMS microfluidic shown in Figure Fig.fig:Demo devices using 3D-printed molds. This device has a rounded exterior profile to demonstrate that the device footprint need not be perfectly rectilinear. Note that the Cal Logo is divided up between the upper and lower molds and only shows up clearly in a direct top-down view of the final molded device. Additionally, the mold clearly shows the through-holes for the vias and the built-in inlets and outlets. Figure 4.3 shows further explanatory images of the multicomponent microfluidic device. Figure 4.3a shows a cross-sectional photograph of the membrane valve, with key features labelled. Figtext 4.3b shows the same cross-section, but in SEM image. Figtext 4.3c depicts the flow pattern through the Cal logo, clarifying which at which

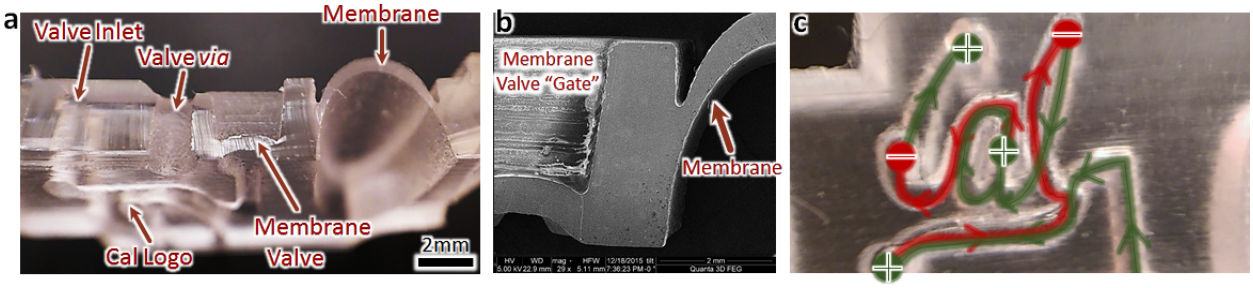


Figure 4.3 Further explanatory images of the multicomponent microfluidic device from Figure 4.1. **(a)** Photographic image of membrane cross-section (equivalent to A-A in schematic diagram, but facing opposite direction). **(b)** SEM image of membrane valve and membrane. **(c)** Annotated flow path illustrating the direction of fluid flow through the Cal logo.

part of the flow the fluid is in the upper and lower layers, and the direction in which the fluid passes through the intra-layer via marking. Note that the color does not represent fluid flow, but rather the *direction* of fluid flow. Lastly, schematic diagrams for the device molds are shown in Figure 4.4.

4.1.1 Mold post-processing

Following printing, the molds were cleaned to remove the sacrificial wax. First, the molds were baked in a VWR 1330 FM oven 75°C for 45 min to melt the sacrificial wax. The molds were then washed in a sequence of three cleaning baths for 10 min in each bath to remove leftover wax: warm Bayes mineral oil, Ajax dish detergent in water, and potable water. The baths were heated to 75°C to ensure the wax did not solidify and placed on a hotplate with a magnetic stir bar to enhance the removal of wax, oil, and soap, respectively. The molds were then dried by baking at 80°C for 60 min. EX200 devices begin to soften once past their glass transition temperature of 52.5°C and become cloudy in appearance, although this effect reverses upon cooling of the 3D-printed part. Softness continuously increases as temperatures are raised, until by 150°C, the pieces can be easily and permanently deformed with even gentle pressure from metal tweezers. Although care must therefore be taken not to place too much concentrated force on the device in a hot bath, we find below 80°C, the devices were not deformed by the tweezers when moving them in and out of their cleaning baths. More caution must be taken to preserve fine cantilevered features during cleaning, as these features can break at any temperature. Because many devices had at least one high-aspect feature (*e.g.*, input/output) break by 10 moldings due to handling error during demolding, we redesigned the input/output ports to be 50% thicker at the base and to fillet high aspect features at the base to reduce stress points; these redesigns limited feature degradation. We did not notice significant degradation of features with aspect ratios of less than 10 : 1.

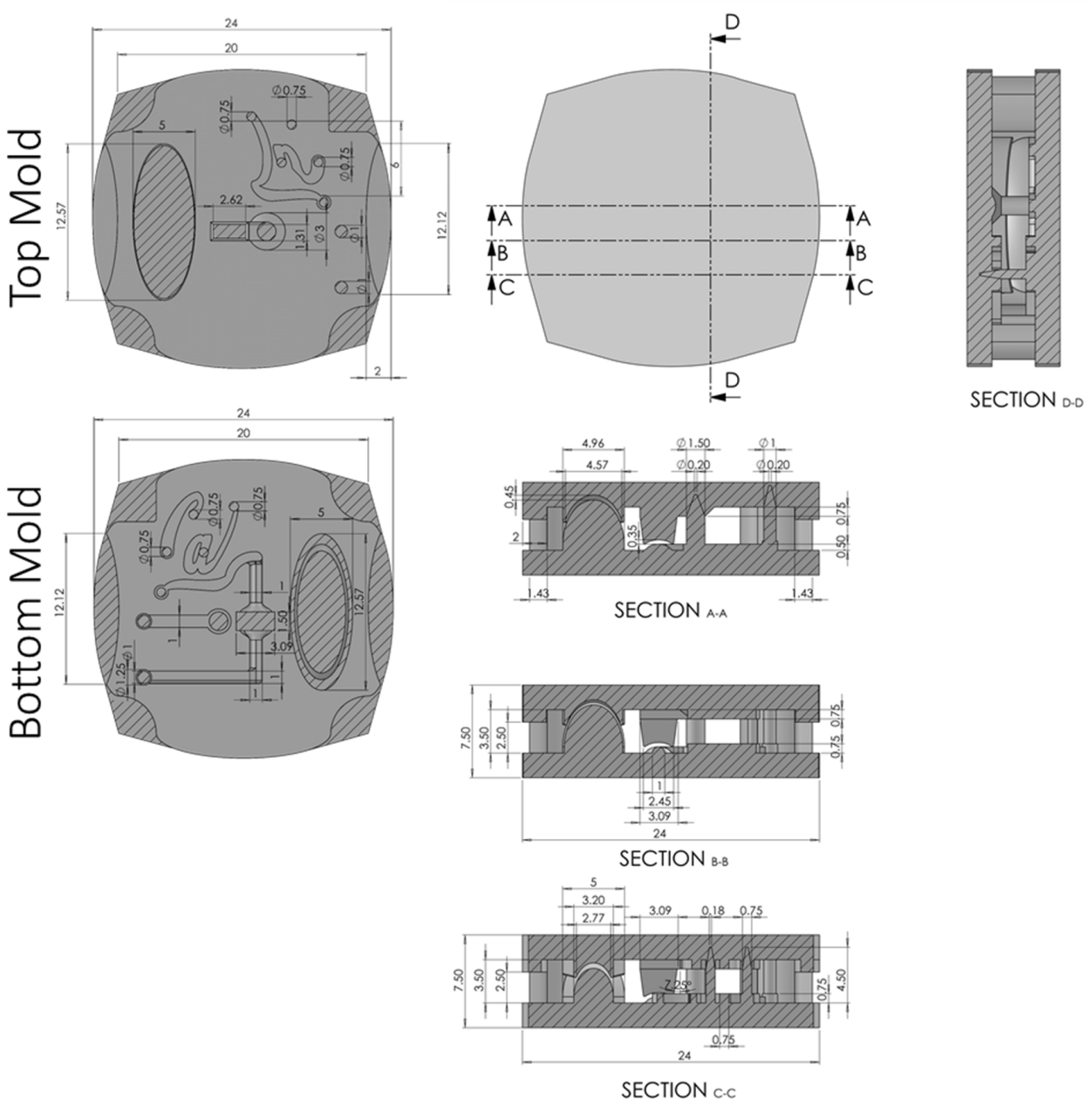


Figure 4.4 Schematic diagrams for multicomponent microfluidic device molds, including four distinct cross-sections illustrating components perpendicular to the channels.

After cleaning and drying, the 3D-printed molds were treated with an fluorinated silane anti-adhesive agent, Trichloro(1H,1H,2H,2H-perfluorooctyl)silane gas (PFOTS, Sigma Aldrich), to make the surface hydrophobic and to facilitate the rapid removal of PDMS. The molds and a 1.5 cm glass vial containing ~ 0.3 ml PFOTS agent were placed in a vacuum desiccator (Fig. 4.5), pumped under vacuum (Welch ChemStar 1400N Vacuum Pump, rated to 10^{-4} Torr) for 5 min, after which the desiccator was sealed and left to sit for 30 min. Shorter rest times resulted in PDMS

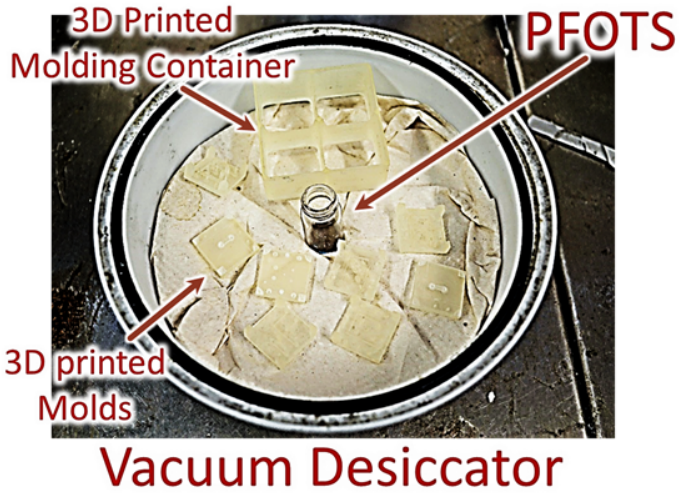


Figure 4.5 Apparatus used for PFOTS silanization. A glass vial containing PFOTS is placed in the center of a Bel-Art Nalgene vacuum desiccator, located among 3D-printed components arranged on a paper towel. The paper towel allows for PFOTS to be deposited on the bottom surface.

bonding to the mold and longer times caused a build-up of PFOTS which inhibited complete curing of the PDMS near the surface [325, 326]. Post PFOTS heat treatment (80°C for 30 min) or a single sacrificial PDMS pour were sufficient to remove excess PFOTS particulates from the surface, allowing subsequent moldings from the same mold to cure properly. Approximately every 10-20 moldings, mold hydrophobicity was refreshed by repeating the PFOTS treatment, performed when PDMS began adhering excessively to the printed mold (see 4.1.2.3 and Fig. 4.9).

4.1.2 PDMS Molding Process

The 3D-printed molds were placed onto a foil-wrapped 3D-printed molding container Fig. 4.3a, shaped to substantially reduce PDMS waste. PDMS (Sylgard 184 Elastomer Kit, Dow Corning, Midlind, MI, USA) was prepared using the standard 10:1 base : curing agent ratio. The PDMS mixture was degassed in the vacuum chamber to 10^{-4} Torr for 10 min and poured onto the 3D-printed molds. The filled molds were then returned to the vacuum chamber for 30 min to degas and increase PDMS conformity. For double sided molding processes, this degassing also serves to load uncured PDMS between the upper and lower molds. Following degassing, the molds were baked in an 80°C oven for 50 min. The PDMS microfluidic components were removed from the molds by first cutting away excess PDMS using the edge of the mold as a guide, and then by manually peeling the PDMS loose from the mold. This step was done carefully to avoid damaging the higher aspect features; without structural features such as widened bases and fillets, many devices lost at least one input/output port within 5-10 demoldings due to handling error (4.1.2.2). Provided no

features were broken during the de-molding process and PDMS did not permanently bond to the mold, the molds were reused without an additional cleaning process. Approximately every 10-20 moldings, mold hydrophobicity was refreshed by repeating the PFOTS treatment, performed when PDMS began adhering excessively to the printed mold (Fig. 4.9).

4.1.2.1 Molding Containers

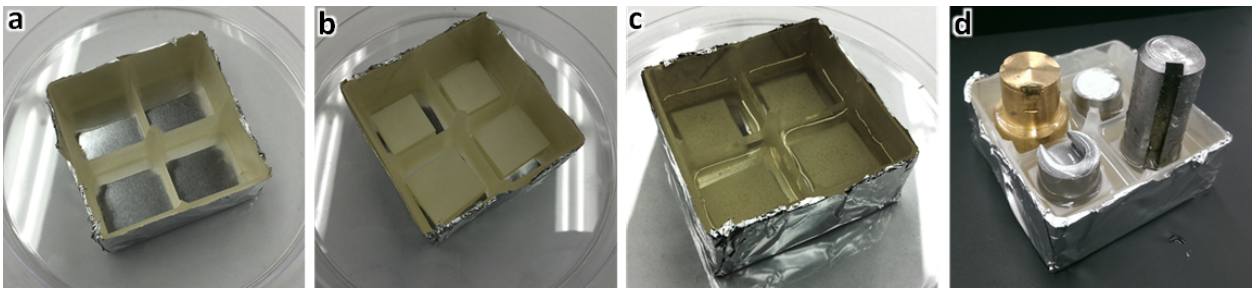


Figure 4.6 3D-Printed molding containers and associated molding techniques. An empty molding container is **(a)** wrapped with aluminum foil to prevent PDMS leakage. **(b)** Molds are placed into the container and **(c)** PDMS is poured. **(d)** For double-sided molds, metal weights between 50-100g are placed on the molds and the whole device is degassed.

PDMS soft lithography processes tend to waste PDMS, so the molds are typically placed in a foil-wrapped container. Here, we present a set of 3D-printed molding containers (fabricated, cleaned, and PFOTS treated like standard molds) which hold the 3D molds and PDMS and reduce the PDMS waste volume. First, the mold containers are wrapped with aluminum foil (Fig. 4.6a), after which the molds are placed within the container (Fig. 4.6b). Next, 20-30g degassed PDMS is poured on the molds (Fig. 4.6c) and the molds are degassed a second time. For double-sided molds, pieces of scrap metal weighing between 50 and 100 g are placed on top of the upper mold (Fig. 4.6d) to prevent bubbles from dislodging it during the degassing phase. Finally, the entire apparatus – molding container, molds, and uncured PDMS – is placed on a dish and baked. For double-sided molds, the loading/degassing process may be combined with a vacuum-assisted transfer procedure [327], which could further reduce PDMS waste.

Figure 4.7 summarizes the key geometries of the 3D-printed molding container. Each molding container has room for four mold dies, occupying a floor space of 22.5x22.5 mm^2, fitting the standard 3D-printed mold size of 20x20 mm^2; larger molds may be accommodated by larger mold containers. The design shown in Figure 4.7 requires only an additional 1.2 g PDMS per cm pour depth (0.7 cm for single-sided, 1 cm for double-sided), plus PDMS poured beyond the mold height. Each mold die is drafted outward at 5° to allow for the easy ejection of the PDMS and mold after

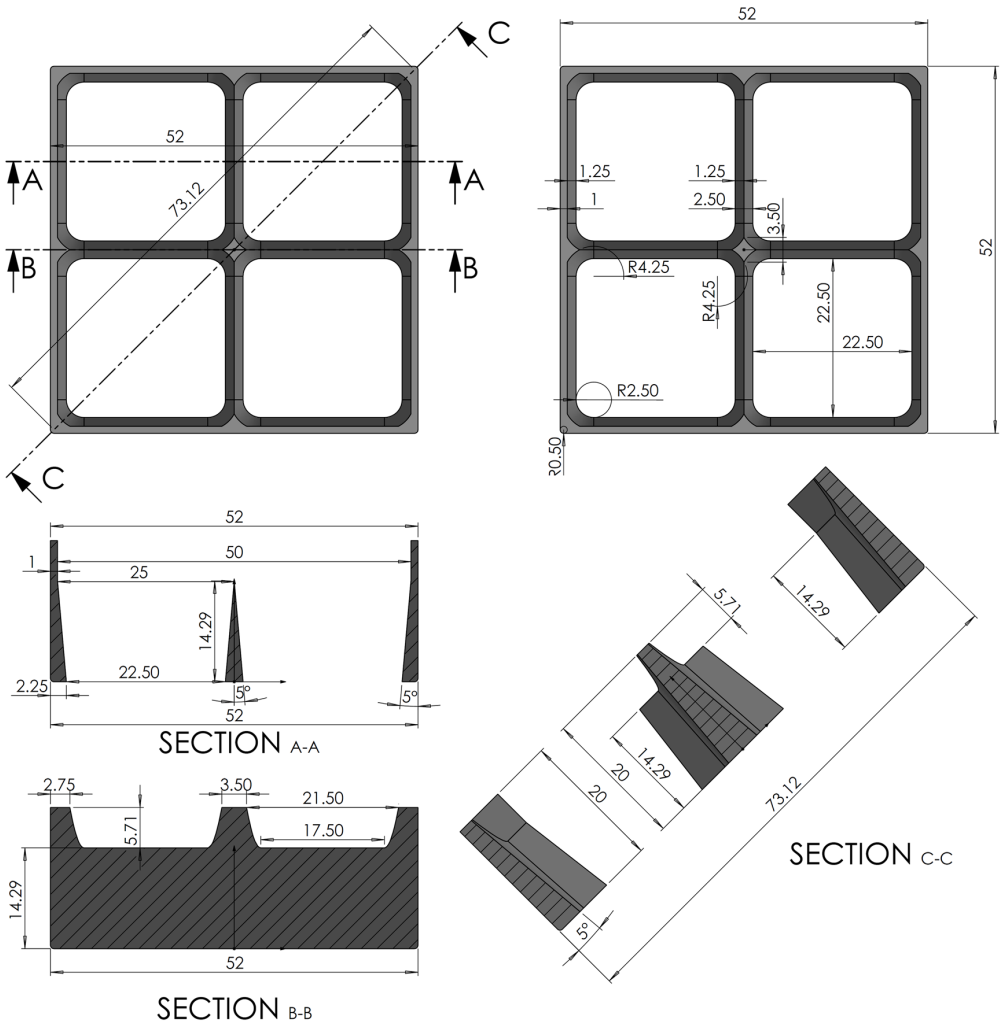


Figure 4.7 Schematic diagrams of 3D-printed molding containers with horizontal and diagonal cross-sections.

curing. Waste may be further reduced by (i) decreasing draft angle, (ii) decreasing floor space, and (iii) combining multiple devices into larger molds.

4.1.2.2 Demolding Techniques

After the devices are fully cured, the PDMS devices must be demolded, which proceeds in three main steps: (1) releasing the PDMS and mold from the molding container, (2) cutting away excess PDMS, and (3) removing the PDMS device from the mold itself.

(I) Releasing device from molding container

After the molding container cools to a temperature where working with it is no longer uncomfortable, the metal weights are pulled off (this may be easier to do at an angle) so the device can

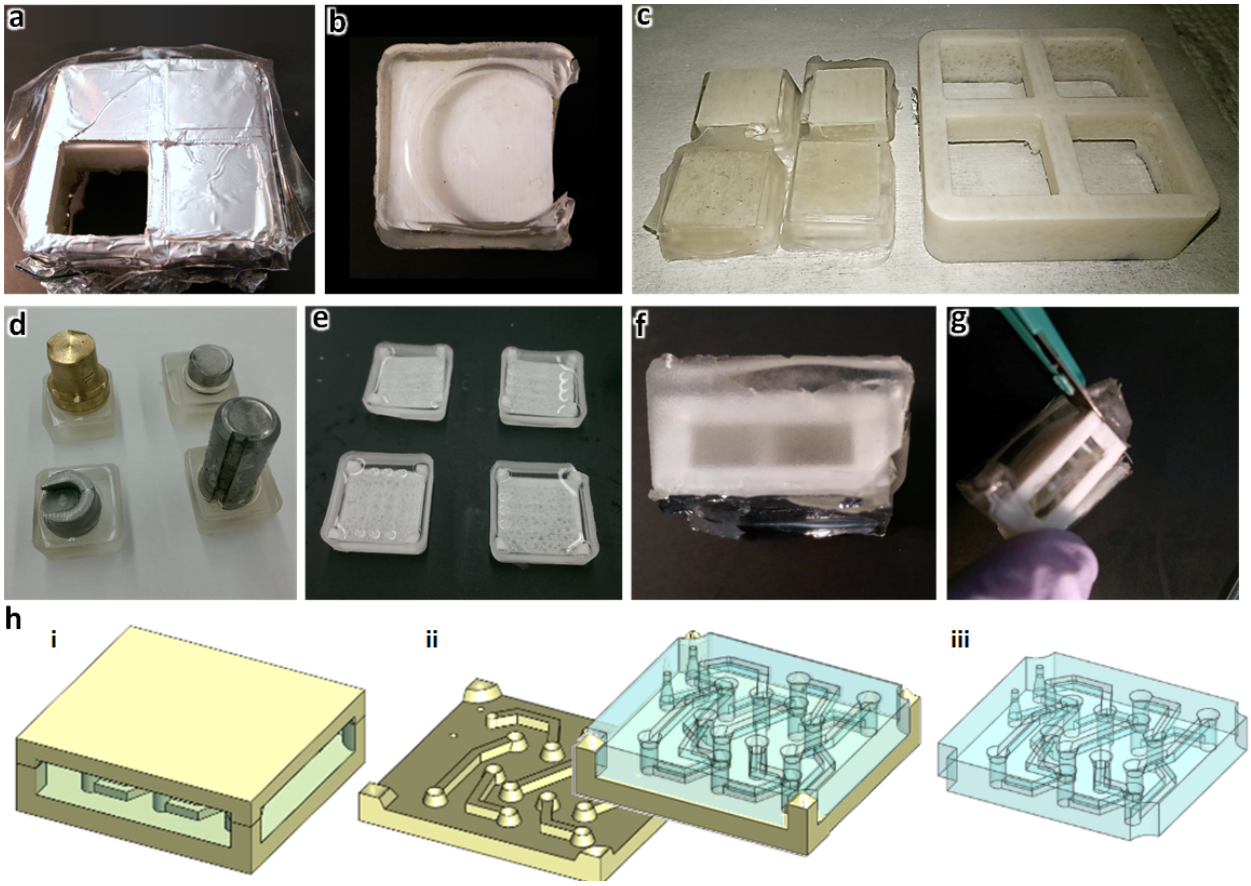


Figure 4.8 Removing molded PDMS components from molding containers and molds. **(a)** Molding containers are scored at the bottom to release individual dies which are **(b)** pushed out to remove the mold and excess PDMS. **(c)** Molding container and individual dies side-by-side **(d)** Dies with metal weights still attached, and **(e)** Single-sided mold dies. To cut the mold loose, **(f)** an individual die is placed on its side, and **(g)** PDMS is cut loose with a scalpel, using the mold as a cutting guide. *Bottom* **(h)** Schematic diagram for removal of PDMS from double-sided mold: *(i)* released mold with cured PDMS, *(ii)* top mold removed, and *(iii)* PDMS component separated from mold.

be easily inverted. This will leave a visible vacancy at the top of the mold (fig) which will be eliminated when the device is demolded. Next, a series of shallow cuts are made on the bottom of the molding container, tracing the outline of each square chamber. These cuts separate the PDMS which is surrounding the mold from PDMS which has cured underneath the molding container. The aluminum foil may be removed for this step if it comes off easily (e), but the removal is not strictly necessary (f). Next, the mold container is turned upside down and the PDMS die ejected by pressing on the bottom center. Note that using the metal weights to push helps to eject the die.

(II) Removing Excess PDMS

At this point, the independent molds are surrounded in excess PDMS, which forms a truncated pyramid (the angle of the PDMS makes it easier to eject these dies). If the device is molded on

both sides, cutting free the excess PDMS is relatively simple; (fig) the side of the molds is used as a guide for the scalpel which traces the sides. For single-sided devices, the device is placed PDMS-side down onto a cutting board and pressed downward to place the top surface of the die in full contact with the cutting board (there will be some meniscus on the PDMS from contact with the side of the molding chamber). Then, again using the edge of the mold as a guide, the scalpel cuts away the excess PDMS (fig). Lastly, for either device design, excess PDMS may be peeled from the far side of the mold surface, as it is no longer in contact with the main body of the mold.

(III) Removing PDMS from Mold

Once the excess PDMS has been cut free, the main PDMS device may be removed from the mold. Depending on the mold design, this may require more or less care. If the mold is relatively simple and compact, the PDMS may be peeled off directly without worrying about mold damage. If narrow vias or alignment marks have been used, the PDMS must be removed perpendicularly from the surface. If numerous such features are used, the PDMS must be loosened from the surface a bit at a time and then slid from the mold by rocking the device back and forth as it is moved upward. If a double sided mold is used, first, the top mold must be removed. In this project, we designed the top molds to have relatively minimal extruded features, meaning that the top mold could be leveraged off by getting a fingernail under one corner and peeling off at an angle. Note that if the mold's silanization treatment has begun to wear off, this may be difficult. After the PDMS has been demolded, it must be inspected for connected strands of PDMS that were not effectively removed during the removal of excess PDMS. These may interfere with bonding if present, and so must be cut loose. Bonding problems may be alleviated by placing a small extruded lip on the surface of the mold (resulting in an intruded lip around the edge of the PDMS) which makes it easier to remove these edge beads of PDMS.

4.1.2.3 Mold Silanization

Performing proper PFOTS silanization treatments is important for the proper functionality of the microfluidic molding process; however, the process is relatively smooth within reasonable tolerances. Insufficient silanization (less than 10-15 minutes) causes the most obvious problems (Fig. 4.9), resulting in the mold bonding permanently to parts of the PDMS. When this happens, PDMS will tear from the mold rather than peal away nicely. Additionally, because the PDMS has infused the mold, this process is not reversible, even if silanization is reapplied.

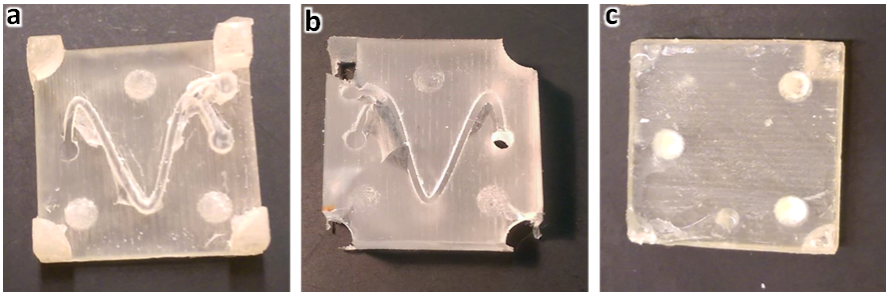


Figure 4.9 Problems associated with incorrect PFOTS silanization. (a-c) Insufficient silanization: **(a)** Bottom mold, **(b)** Resulting PDMS, and **(c)** upper mold. Note how PDMS has remained attached to the lower mold by tearing from the bulk device.

Excessive silanization (over 1 hour exposure or larger amounts of PFOTS) may also cause problems as it prevents the curing of PDMS within 1 mm of the mold surface for all but extreme bake times (*e.g.*, over one day). After demolding, the PDMS will eventually cure, but because the surface was still relatively liquid upon demolding, many fine features may be lost, including certain channel designs and membranes. Because the effect is similar to when liquid is absorbed into the 3D-printed material, we believe that the PFOTS interferes with the cross-linking of PDMS.

4.1.3 Flow rate measurement

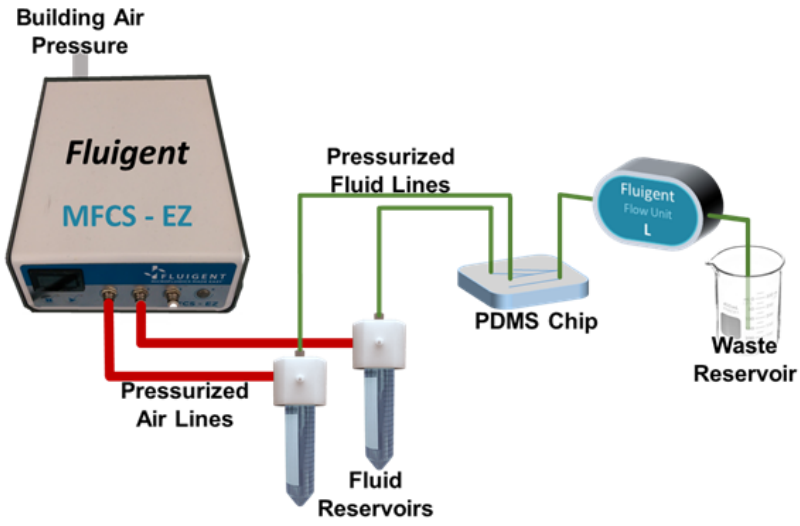


Figure 4.10 Conceptual diagram showing arrangement of MFCS-EZ pressure pump, PDMS device, and flow sensor.

Flow rate and pressure measurements were performed with a Fluigent™MFCS-EZ system. Figure 4.10 shows a conceptual view of the experimental setup used for flow analysis experiments. Building air pressure is passed to the Fluigent™MFCS-EZ system. Pressure is then sent to fluid-filled wells, which in turn force fluid to the chip at the desired pressure. On channels for which

a flow-rate measurement device was used (Fluigent™), when possible the measurement system was generally placed between the chip and the outlet, allowing the chip's internal resistance and capacitance to buffer transient flow rate spikes that result from pressure increases, here ignored because pressure pump transients are of less interest than the resulting steady-state phenomena.

4.2 Results and discussion

Figure 4.1 illustrates the process flow for fabricating multi-sided PDMS microfluidic devices using 3D-printed molds. The component mold is fabricated via the 3D printing process (Fig. 4.1a) and PDMS is applied (Fig. 4.1c), cured, and released from the mold (Fig. 4.1c) by means of the PDMS molding steps described in the Experimental section. Built-in fluid inlets (diameter 0.55 mm) are easily incorporated into the component through the mold design, which further simplifies fabrication by eliminating the need for an additional hole-punching step. The PDMS component is then glass bonded to create a complete microfluidic device with enclosed channels (Fig. 4.1d).

This 3D-printed transfer molding and bonding technique can be used to fabricate conventional microfluidic circuit devices commonly produced by the soft lithography methods (Fig. 4.11), but with faster prototyping and simpler processing, easier fabrication of complex 3D geometries, the ability to fabricate circular channel cross-sections, and built-in fluidic interfaces. Furthermore, novel techniques were developed to fabricate double-sided or multilayer microfluidic devices which maintain the basic procedure of generating a CAD model, 3D-printed mold, and PDMS replica of the mold. These techniques, including alignment marks to precisely position molds (*e.g.*, for double-sided molding) or PDMS layers (*e.g.*, for multilayer assembly) as well as PDMS-PDMS bonding using a 3D-printed stamp, enable the design, fabrication and assembly of complex microfluidic systems as shown in Figure 4.1f (4.2.2).

4.2.1 Single-sided Molding Techniques

Using 3D-printed molds, semi-circular and fully circular channel geometries are easily fabricated (Fig. 4.11); the high fidelity of PDMS transfer molding for features as small as 80 μm means that mold roughness is reliably transfered to the resulting PDMS [18]. Surface texture in ProJet™3000 multijet printing arises both from the interface between sequential rows of epoxy and from structural irregularities within a row. The interfacial texture resulted in a peak surface asperity of approximately 20 μm, measured by surface profilometry (Fig. A.3c). Structural macrorough-

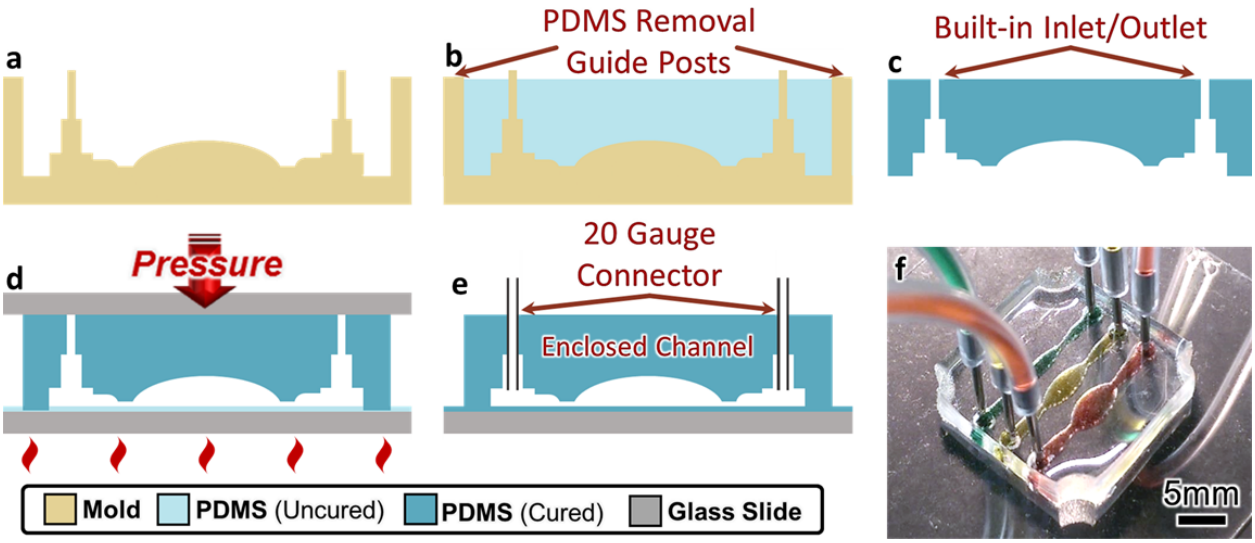


Figure 4.11 Single-sided fabrication and bonding process flow. **(a)** 3D-printed mold is printed from CAD file, including built-in inlet/outlet ports and guideposts to assist the removal of PDMS **(b)** Mold is filled with ℓPDMS, degassed, and baked and **(c)** cured PDMS is demolded. **(d)** Cured PDMS is bonded to glass using the PDMS-Glass ℓPDMS spin bonding technique to compensate for surface roughness. **(e)** Final conceptual image with enclosed channel and 20-gauge connector pins attached. **(f)** Photograph of glass-bonded device with colored fluid.

ness, measured by Walczak *et al.*, was 0.70 µm and 0.56 µm in the X and Y directions, respectively, values comparable to those achieved in micromilling [117]. Figure A.3b shows a PDMS component after release from the 3D-printed molds, with a close-up view of the surface roughness. While this value is comparable to microfluidics fabricated directly by 3D printing, transfer molded PDMS components can produce narrower channels because interior cavities have the tendency to reflow during printing. Additionally, surface roughness in 3D-printed devices is currently higher than in those fabricated by conventional soft lithography [94]. For further discussion of surface roughness and mitigation, see A.1.1.

The single-sided microfluidic device shown above was fabricated from a CAD model via the 3D printing process (Fig. 4.11a) and PDMS was applied, cured (Fig. 4.11b), and released from the mold (Fig. 4.11c) by means of the PDMS molding steps described in the Experimental section. Built-in fluid inlets (diameter 0.55 mm) can be easily incorporated to the device through the mold design, further simplifying fabrication by eliminating the need for an additional hole-punching step. Six 20-gauge stainless steel interconnectors (Instech SC20/15, outer dimeter 0.91 mm and length 15 mm) were easily inserted into the inlet ports for the connections to external fluidic pipes as shown in Fig. 4.11e. Due to the tight seal of the steel couples against the smaller built-in inlets were leak-resistant to pressures of up to 4 ATM. The PDMS device was then bonded to a glass slide to created closed microfluidic channels.

The microfluidic device consists of three microchannels with elliptical-shape reservoirs of di-

mensions 1.5x5.9 mm^2, 1.1x5.9 mm^2 and 0.7x5.9 mm^2 which were designed as shown in Fig. 4.11b. The overall dimension of the mold was 20x20x2 mm^3 with quarter-circle (R = 2.5 mm) pillars at the four corners facilitating removal of the PDMS after curing. Each channel was constructed with built-in fluid inlets and outlets molded from pillars 0.55 mm in diameter and 5 mm in height. The inlet pillars were strengthened by widening halfway down their length to 1 mm in diameter. These dimensions are summarized in the schematics shown in Figure 4.12.

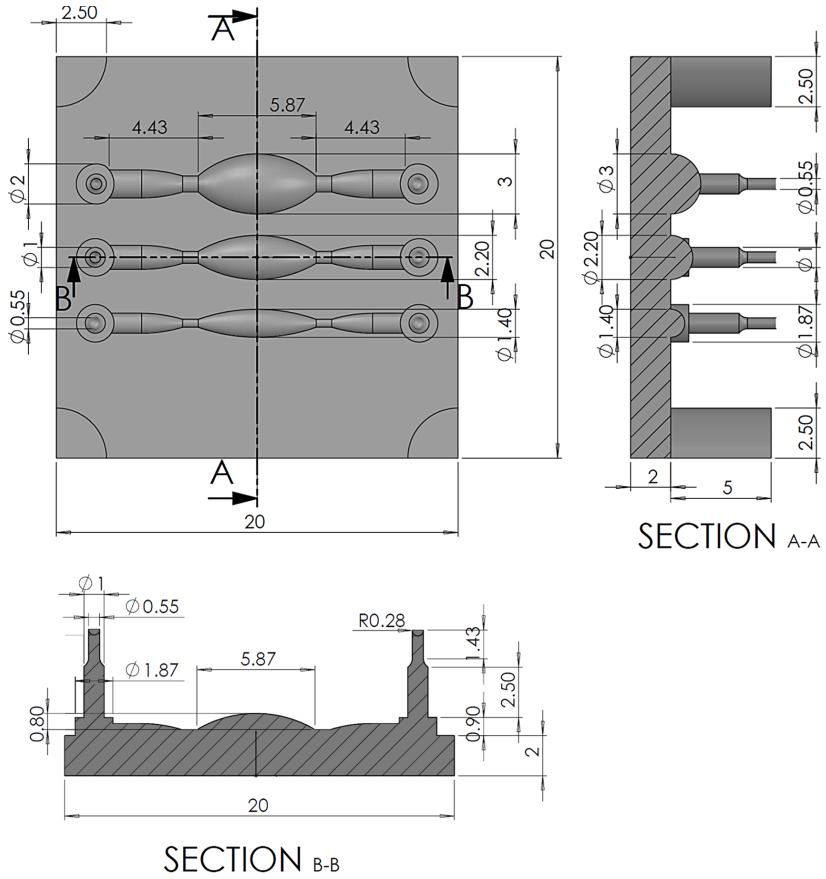


Figure 4.12 Schematic diagrams of single-sided mold, with two distinct cross-sections illustrating the channel profiles.

4.2.1.1 Glass ℓPDMS Spin Bonding

To create fully enclosed and tightly sealed microfluidic channels, a glass bonding step is required [10]. However, due to the surface roughness of the 3D-printed molds (Fig. 4.13a-d), it was difficult to achieve a tight seal when bonding PDMS to glass using standard techniques such as oxygen plasma and ozone surface treatments. For this reason, specialized bonding techniques were needed to finalize the microfluidic devices fabricated through the 3D-printed transfer molding process. While some surface roughness was reduced by performing a standard surface treatment (*e.g.*, oxy-

gen plasma) and then tightly clamping the two bonding surfaces together to mechanically compress the surface profile, this technique was unreliable and often led to broken glass during the curing stage (see 4.3.2.1).

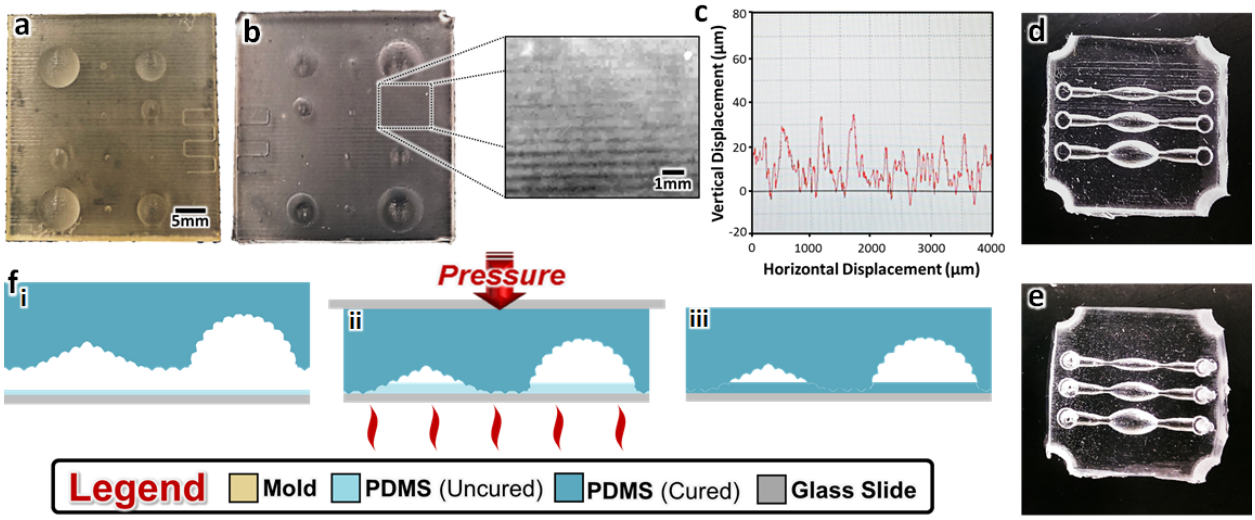


Figure 4.13 Comparison of results from plasma bonding and ℓPDMS spin bonding. **(a)** 3D-printed mold with visible roughness and **(b)** corresponding molded PDMS with magnified insert highlighting roughness. **(c)** Profilometer measurements of 3D-printed mold showing ≈20-30 µm surface asperity every 0.5 mm. **(d)** PDMS plasma-bonded to glass, showing visible roughness lines. **(e)** Process flow for glass bonding technique. *(i)* Molded device pressed into spin-coated ℓPDMS. *(ii)* Pressure is applied while device rests on a 95°C hotplate. *(iii)* Cured device. Note that ℓPDMS reflows to fill channels deeper than spin depth. **(f)** ℓPDMS spin bonded device without visible roughness lines.

A more reliable glass bonding technique uses spin-coating uncured liquid PDMS (ℓPDMS) as both bonding agent and as a filler (Fig. 4.13e,f). ℓPDMS spin-bonding overcomes drawbacks associated with surface roughness from 3D printing and achieves a tight bond between the PDMS component and the glass slide (Fig. 4.11d). First, ℓPDMS was spin-coated onto a microscope coverslip (Fischer Scientific 22x22x0.1 mm^3) at 1800RPM to achieve a thickness of 15 µm [328]. The ℓPDMS-coated slide was placed face up on TexWipe TechniCloth® resting on a hot plate at 95°C for 70 seconds to partially cure the ℓPDMS, increasing its viscosity. The molded PDMS component was then placed bonding-side down into the curing ℓPDMS and ≈ 20–30 N downward force was applied to the component via a thick non-bonding glass side (Fisher Scientific 75x25x1 mm^3) for 90 seconds. This thicker glass slide was used to apply pressure to equalize the distribution of downward load and ensure that the PDMS bonded fully to the glass slide throughout its area. Next, pressure was released and the PDMS-glass bond was left to cure on the hotplate for an additional 5 min (4.3.2.2).

For double-sided microfluidic components, this process was repeated on the reverse side, with

care taken to not fracture the fragile glass slide that had already been placed during the first bonding step. By using a smaller glass coverslip for the upper surface, the upper glass slide could be bonded in a position which maintained access input and output holes. Although the ℓPDMS spin bonding method worked for taller channels, for channels smaller than ≈ 100 µm in height, excess ℓPDMS was sometimes forced into the channels, causing permanent blockages. This problem is lessened by using a 3D-printed stamp to selectively apply ℓPDMS only to non-channel areas of the PDMS device (4.2.3). Reliability of the bonding process may be further improved through the use of a dedicated bonding platform [69], or through the use of a vacuum bonding apparatus to provide consistent, uniform pressure. For more details on spin bonding and potential improvements, see 4.3.3 [329, 330, 331, 332].

4.2.1.2 Built-in Fluid Inlets

Figure 4.11 shows a single-layer microfluidic device with built-in fluid inlets (diameter 0.55 mm), incorporated during mold design. These inlets simplify fabrication by eliminating the need for an additional hole-punching step. Six 20-gauge stainless steel interconnectors (Instech SC20/15, outer dimeter 0.91 mm and length 15 mm) were easily inserted into the inlet ports for the connections to external fluidic pipes as shown in Figure 4.11f. Due to the tight seal of the steel couples against the 40% smaller inlets ports, the inlets were leak-resistant to pressures above 4 ATM, the pressure at which the PDMS-glass bond delaminated due to untreated glass coverslips (4.3.2.3). 3D-printed guideposts in the corner of the mold assist with the removal of the PDMS without damaging narrow gauge inlets and outlets (4.1.2.2).

4.2.2 Multi-sided and -layer Molding Techniques

The increasing demand for microfluidics is particularly high for multi-layered devices [38]. Multi-layered fabrication allows for the implementation of more sophisticated and useful internal structures (*e.g.*, valves or pumps) as well as reducing geometrical constraints by enabling fluidic detours and vias. Creating multilayer microfluidic devices using conventional techniques requires at least two lithography steps and one PDMS-PDMS bonding step (*e.g.*, for "Quake" membrane valves) [24], and can require up to four lithography steps and three PDMS-PDMS bonding steps (*e.g.*, for PDMS-based fluidic transistors) [25].

Multi-layer construction is used largely to overcome the limits of 2D traditional microfluidic systems and give fluids an extra degree of freedom. These 3D devices may be constructed either

from PDMS components with features molded onto more than one side (Figs. 4.16,4.17, and 4.20), or with layers of PDMS components (Fig. 4.25). While multilayer assembly is relatively common in traditional soft-lithography (despite the aforementioned difficulties), double-sided molding is rare. Here, double-sided molding is accomplished through the use of mold alignment marks and can be used as preparation for multilayer assembly (*e.g.*, for constructing PDMS-alignment marks) or as a final device, in which case double-sided glass-bonding is performed to seal channels on both sides, leaving inlet/outlet holes uncovered on the upper surface.

4.2.2.1 Alignment Marks

With 3D-printed molding, rapid assembly of multilayer microfluidic devices is easily achievable through the use of built-in alignment marks. While two-sided molding is technically possible for traditional soft-lithography, the process is generally inconvenient due to numerous alignment difficulties. However, using a 3D printer to fabricate the molds, we can build any alignment marks directly into the design, enabling numerous fabrication techniques by allowing for the precise positioning of each layer without the need for a microscope. Figure 4.14 illustrates the four primary varieties of Alignment marks and their fabrication methods: (I) Mold-Mold alignment marks, used for fabricating double-sided PDMS components; (II) Mold-PDMS alignment marks (MPAM), used in Stamp Bonding; (III) PDMS-PDMS alignment marks (PPAM), used for fabricating double sided channels and assembling multilayer devices; and (IV) and PDMS Height Limiters, for controlling the ultimate thickness of a PDMS layer. [1]

(I) Mold-Mold Alignment Marks.

Mold-Mold Alignment Marks allow patterns to be imprinted on both sides of PDMS and with desired thickness, with alignment accuracy approximately equal to the resolution of the 3D printer (defects like device warping can lead to greater inaccuracy). These marks consist of a long columnar portion the same height as the thickness of the final PDMS, capped with a male extrusion, extending from the bottom mold, matched a female intrusion (matching the male extrusion) on the top mold. The primary MMAM are generally placed in the corners of the mold, although secondary ones can be scattered throughout the device.

Since MMAM leave vertical holes in the PDMS – the alignment marks move from the bottom to the top of the PDMS – they can be easily adapted to become built-in inputs, vias, and other

[1] For the purposes of this discussion, the bottom mold is the mold with the male halves of the alignment marks and the top mold is the mold with the female indentations.

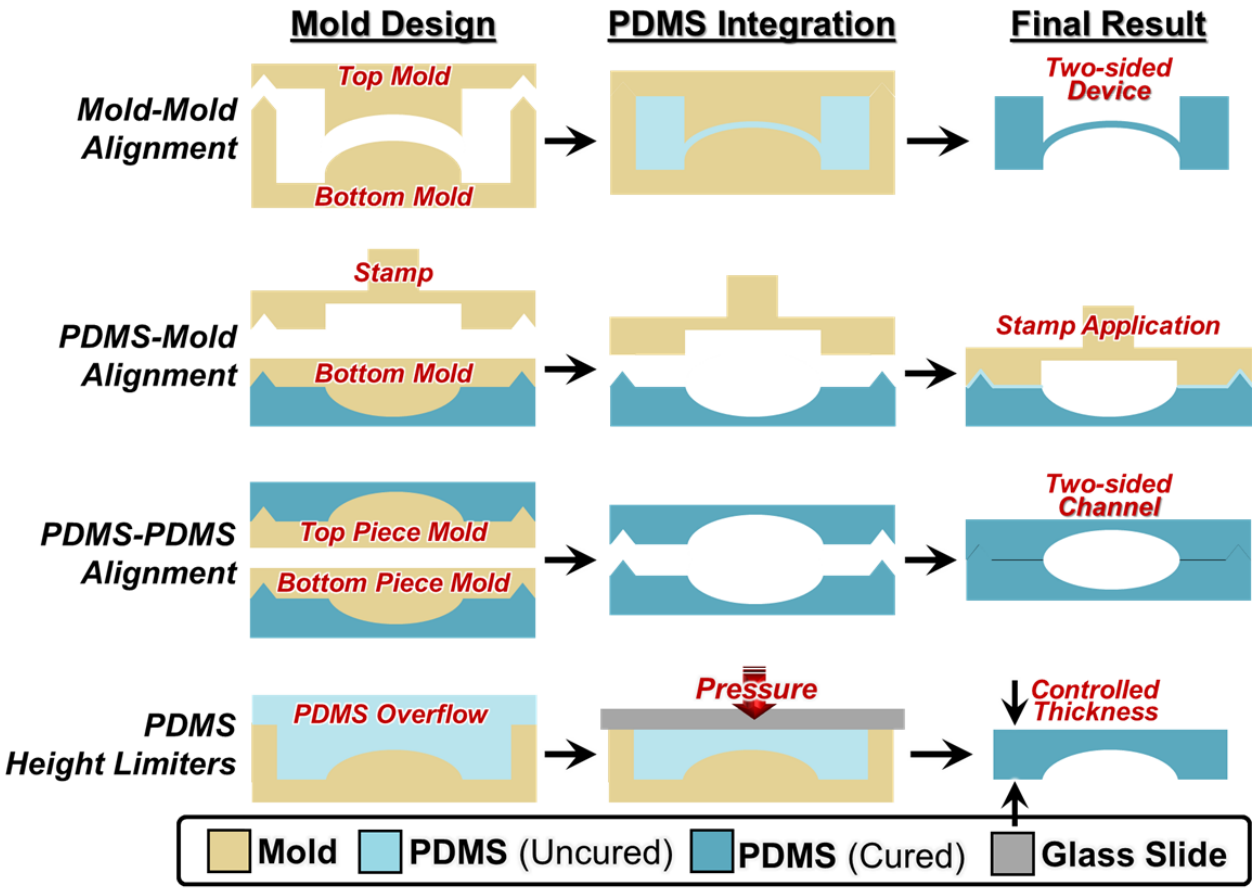


Figure 4.14 Alignment mark creation process flow. **(a)** Mold-Mold Alignment marks are directly 3D-Printed, fitted together, and filled with ℓPDMS. **(b)** Mold-PDMS Alignment marks are directly printed on the 3D stamp and indirectly printed (in negative) on the mold used to generate the PDMS. **(c)** PDMS-PDMS Alignment Marks are both indirectly printed (in negative) onto the 3D-printed mold such that the resulting PDMS fits together with the alignment marks. **(d)** PDMS Height-limiters are printed directly onto the 3D-printed mold and are flat topped columns onto which a sheet of glass or plastic is placed (under pressure) to keep PDMS to desired thickness.

through-holes in the PDMS. With MMAM narrower than the gauge of a connector syringe, a microfluidic device can be constructed with input-output ports built-in, avoiding the often tedious hole-punching process common to soft-lithography fabrication. Fluidic vias are constructed in a similar manner to smaller Mold-Mold alignment marks, and can be can be constructed that can allow fluid to flow between the top and bottom face of a single layer of PDMS. However, while fluidic vias may be useful in ensuring a proper rotational orientation of microfluidic devices, using them as MMAM is not recommended due to their narrow gauge relative fragility.

(II) PDMS-PDMS Alignment Marks.

PDMS-PDMS Alignment Marks allow multiple layers of PDMS to be easily aligned and bonded. These alignment marks are first built as negatives into the 3D-printed mold and are then transferred

to the PDMS. Unlike Mold-Mold Alignment Marks, PPAM generally consist of only the male and female alignment portions (and not the columnar support), since the two PDMS layers must be in full contact for enclosed channels. PPAM may also be constructed on one or both sides of molded PDMS. A common difficulty with PDMS-PDMS bonding, such as in "Quake" membrane valve technology, is the need to precisely align two or more layers of PDMS. Often, this must be done by hand or using a purpose-built machine to improve accuracy. By building alignment marks directly into the PDMS, a proper alignment can be facilitated (to within the tolerances of the 3D printer) without the need for visual inspection; because the marks only allow the PDMS layers to come into full contact in the correct orientation, alignment can be guided by touch. Additionally, PPAM may be constructed to allow each of the PDMS layers to be aligned in only in desired orientation to fool-proof the device manufacture, allowing for easy construction of multi-layer PDMS devices.

(III) Mold-PDMS Alignment Marks.

Mold-PDMS Alignment Marks are a hybrid of the two above methods; they allow a secondary mold (*i.e.*, not the mold that initially imprinted the PDMS) to be placed into precise alignment with the PDMS. In order to save space, MPAM are generally designed to fit in the corner cavities left by the primary Mold-Mold Alignment Marks. The PDMS-Mold alignment method is used extensively to align 3D-printed stamps with PDMS.

(IV) PDMS Height Limiters.

PDMS Height Limiters are used to keep the thickness of PDMS to a precise level while allowing a smooth PDMS upper surface. Height limiters consist of extruded columns in a single-sided mold with a planar top surface. ℓPDMS is poured onto the mold and degassed, after which a glass (or plastic) slide is placed onto the ℓPDMS and pressed down until it comes into full contact with the Height Limiters. Finally, a weight is placed on the glass slide to maintain full contact during baking. While height limitation can be accomplished using Mold-Mold alignment marks, the rough surface of the molds tends to leave the PDMS upper surface visually opaque, making a smooth and glass-molder upper surface preferable for single-layer devices. Height limiters are useful in laboratory situations where an oven is not perfectly level, causing later thickness variations, or in situations where a controlled thickness is desired but difficult to achieve. Additionally, due to the individualized nature of the height limiters, multiple PDMS heights (for multiple devices) may be achieved in a single PDMS pour.

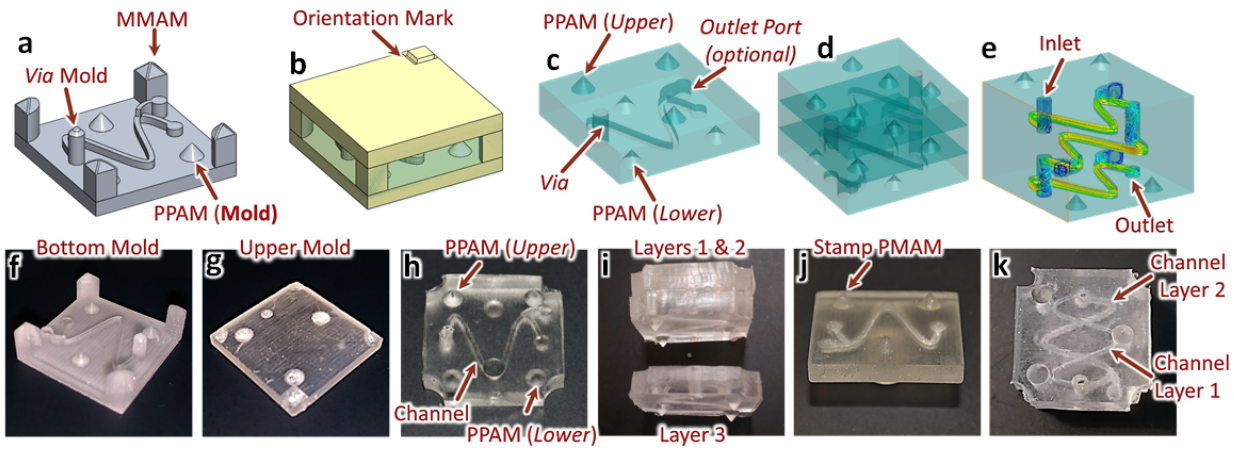


Figure 4.15 Demonstration of usage of alignment marks. The PDMS-PDMS alignment marks (PPA) force each layer to reverse 180° relative to the layer below it, allowing for more complicated 3D structures without requiring more molds. Upper: Conceptual. Lower: Photographs. **(a)** Mold contains pattern for a channel and inter-layer vias, mold-mold alignment marks to align with the upper layer, and conical alignment marks on the bottom and upper surface. The upper surface alignment marks are reversed by 180° relative to the lower surface alignment marks. **(b)** Molds are placed together, with an orientation mark helping ensure that the upper mold is placed in the correct orientation. Note that the structure of the MMAM automatically prevents misalignment, although a visual cue remains helpful. **(c)** Device is demolded after curing process **(d)** Three devices are bonded together (in alternating 180° pattern) via the stamp technique. **(e)** Flow simulation of fluid moving from upper to lower layer. **(f,g)** Device molds and **(h)** Resulting single layer of cured PDMS. **(i)** Alignment arrangement for bonding third layer and **(j)** stamp used for ℓPDMS bonding. **(k)** Multi-layered device demonstrating 180° reversal of monomer pattern.

(V) Alignment Mark Demonstration Figure 4.15 shows a demonstration for the use of alignment marks. This demo is built of stackable identical monomers, and requires two sided molding (and therefore MMAM), and each layer is imprinted with patterns for conical PPAM. The upper mold additionally contains a visual orientation mark (which does not affect the molding) that helps the user identify which corner of the top mold should be oriented toward the unique square (as opposed to quarter-circular) MMAM pillar. The PDMS-PDMS alignment marks on the upper and lower layer of the PDMS are reversed by 180°, forcing each layer to be reversed by 180° relative to the preceding layer.

Lastly, a flow simulation was run in SolidWorks showing how the fluid progresses from device inlet to outlet (Fig. 4.15e). The simulation depicts flow streamlines and shows that a small amount of vorticity is imparted to the flow as it moves between layers. Additionally, flow eddies are shown in the optional outlet ports, used to attach syringes in absence of built-in fluid inlets; the port larger to allow hole punching when the device is already bonded.

4.2.2.2 Microfluidic Vias

The ability to route fluid in three dimensions is frequently desired in microfluidics because it frees the system of a number of geometrical constraints by enabling fluidic detours [333]. However, because these microfluidic vias are time consuming and costly to fabricate (generally requiring a minimum of three lithography steps and one PDMS-PDMS alignment/bonding step) vias are not incorporated into microfluidic devices unless required for specific functionality.

With 3D-printed double-sided molding, however, fluidic vias are far simpler to fabricate (Fig. 4.16). By using double-sided molding techniques with columns that run from the bottom mold and fit into the upper mold, smaller Mold-Mold alignment marks can be constructed that can allow fluid to flow between the top and bottom face of a single layer of PDMS (Fig. 4.1a, or between layers of bonded PDMS (Fig. 4.25b), thus enabling multilayer microfluidic devices. For a comparison between via manufacture methods, see 4.3.1.1.

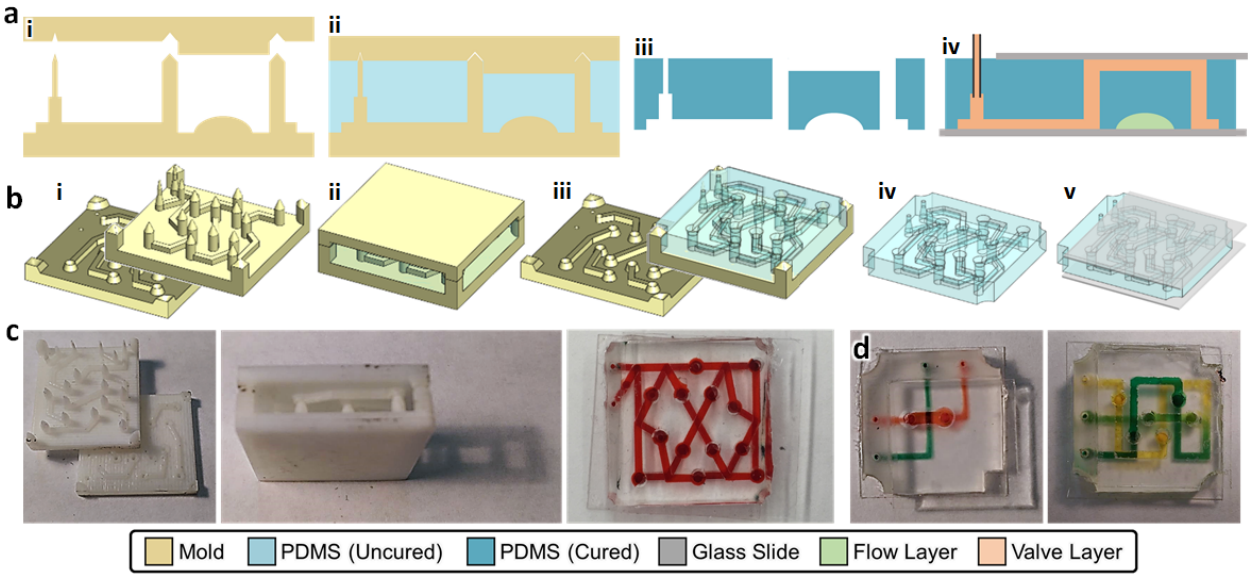


Figure 4.16 Fabrication flow for arbitrary vias constructed through double-sided transfer molding, including built-in fluidic inlet. **(a)** Conceptual fabrication flow for Celtic Knot-inspired via device: *(i)* upper and lower molds, *(ii)* molds filled with PDMS, *(iii)* demolding by removing upper layer first, *(iv)* PDMS device, and *(v)* glass bonded device. **(b)** Fabrication photographs for Celtic Knot-inspired via device *(i)* upper and lower molds, *(ii)* assembled molds, and *(iii)* Knot device with fluid flow. **(c)** Simple overpass via-based PDMS device and **(d)** vias enabling repeated crossover and mixing.

To manufacture microfluidic vias using double-sided molding, the via columns must be designed to fit into the upper mold. In order to prevent PDMS from blocking the top of the via, the designs have the column pierce the upper mold by ≈1 mm and capping it with a conical shape; more intrusion into the upper mold makes the PDMS less likely to fill this space. Similar tech-

niques work for other large-scale features that must be present on both sides of the mold.

Figures 4.16a and 4.16b illustrate conceptual illustrations for the process flow needed to generate microfluidic overpass vias - used to reroute flow around obstacles such as other channels. First, two molds are printed from CAD file and cleaned, and are then fitted together using alignment marks, filled with ℓPDMS, degassed, and baked. Excess PDMS is cut from around molds and PDMS is released and the device is bonded to glass on the top and bottom, taking care to leave input vias uncovered. This technique can be used to fabricate any number of overpass vias, including simple single-pass overpass vias (Fig. 4.16c) and multi-pass crosses with enabled mixing (Fig. 4.16d). Lastly, Figure 4.16b illustrates fabrication photographs for Celtic Knot-inspired via device including (i) upper and lower molds, (ii) assembled molds, and (iii) the finalized Knot device with interwoven fluid flow and 14 distinct vias.

4.2.2.3 Thin Membranes

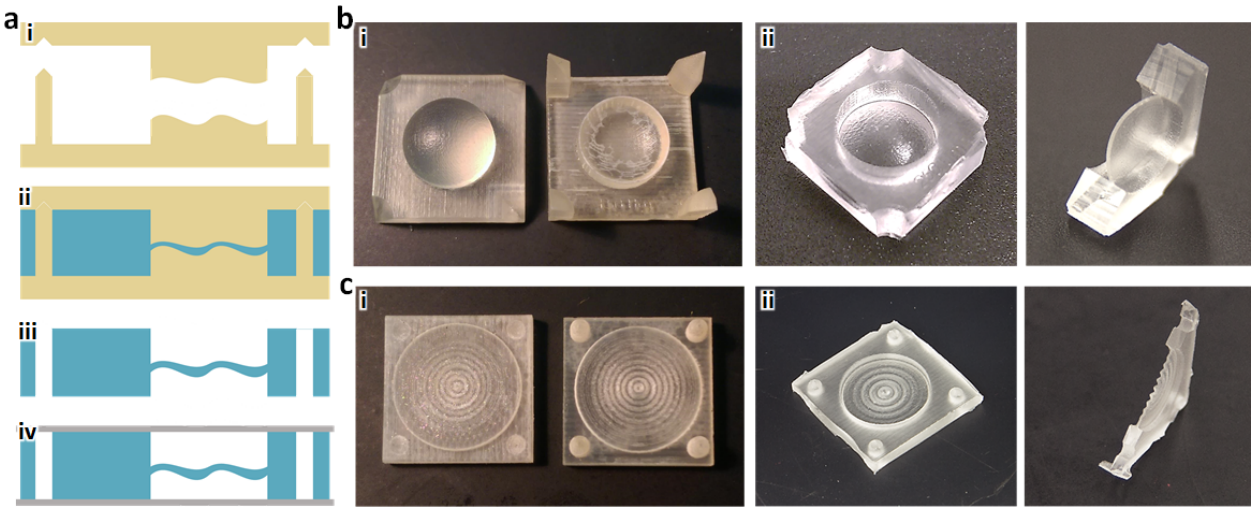


Figure 4.17 Thin membranes fabrication techniques using 3D-printed transfer molding. **(a)** Process flow for generating arbitrary thin membrane, including alignment marks which insure proper membrane nesting. **(b)** 300 µm domed membrane: *(i)* Molds, *(ii)* Isometric view, and *(iii)* side view **(c)** 300 µm sinusoidal membrane: *(i)* Molds, *(ii)* Isometric view, and *(iii)* side view. The sinusoidal pattern allows for more deformation without increasing the thickness or surface area [316].

Double-sided PDMS molding also enables the construction of integrated thin membranes. By creating nesting (but non-touching) mold features, an empty region can be created between top and bottom molds that is filled by ℓPDMS during vacuum degassing. Upon curing, this cavity forms a thin membrane. Figures 4.17b,c depict 350 µm thick membranes (domed and sinusoidal, respectively), that can potentially be used as fluidic capacitors. The sinusoidal corrugation lowers

the effective spring constant of the membrane allowing it to store more fluid. This technique generated membranes down to 200 µm thick, limited by surface interaction effects which interfered with PDMS curing [94] and caused membrane rupture upon demolding.

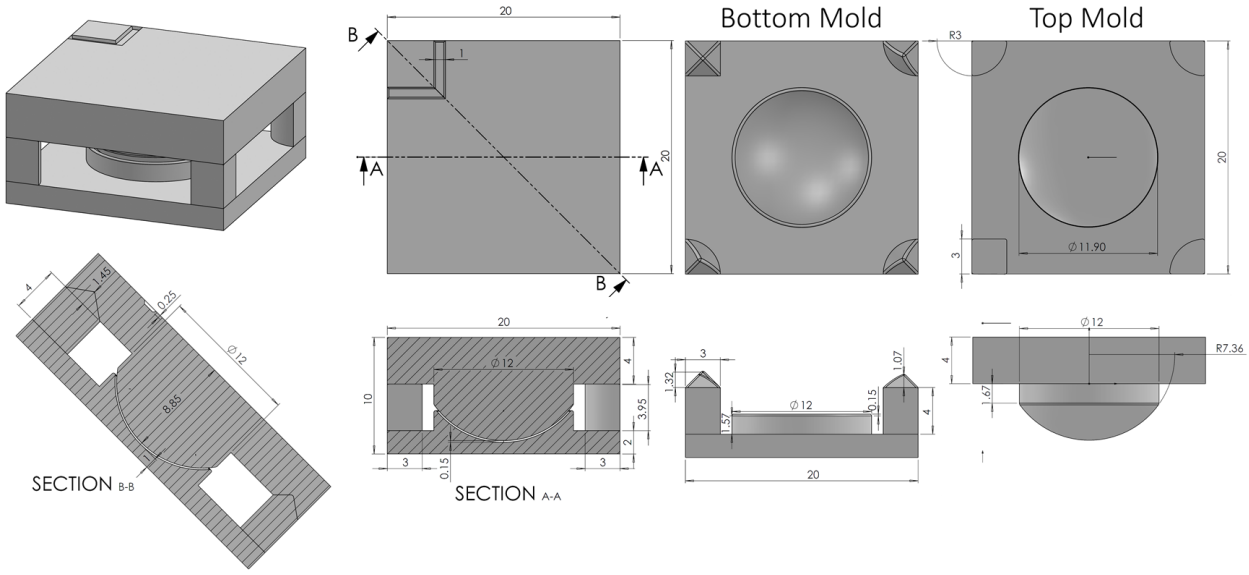


Figure 4.18 Schematic diagrams of 350 µm domed membrane molds, both nested and individually.

(I) Membrane Fabrication. Figure 4.17a illustrates the process flow used to generate arbitrary thin membranes. First, a CAD model is designed, using the final PDMS design to shape the upper and lower molds; alignment marks and via marks are designed into the mold, ensuring that the membranes nest properly. Next, the molds are filled with ℓPDMS and placed in a vacuum chamber to remove air bubbles from the PDMS, which can rupture the membrane. Note that larger membranes may require longer vacuum times or may require that the molds be vacuum pumped on their side. Finally, the molds are baked to cure the ℓPDMS and demolded. Membranes may be smooth and continuous (Fig. 4.17b) or more irregular (Fig. 4.17c). The sinusoidal pattern in 4.17c allows for increased membrane deformation and storage capacity without increasing the footprint of the membrane [316]. Schematics of the domed membrane molds are shown in Figure 4.18.

(II) Membrane Rupture This membrane formation technique can consistently generate membranes down to 200 µm thick, but below that, surface interaction effects interfere with PDMS curing. Because these membranes have not completely cured by the time baking is done, they rupture upon demolding (Fig. 4.19a,b). The exact nature of these effects is not completely known, but is possibly related to lack of oxygen [94]. Additionally, because excessive silanization or liquid

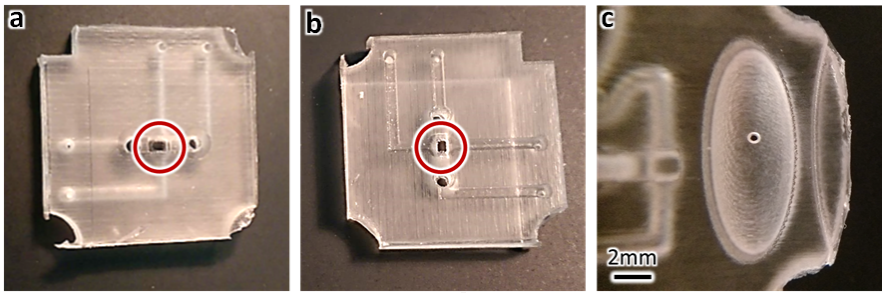


Figure 4.19 Illustration of membrane damage due to incorrect molding procedure; points of damage have been circled. "Quake" valve device with ruptured and completely non-formed membrane: **(a)** *Top view* and **(b)** *Bottom view*. **(c)** Elliptical membrane punctured by a bubble-generated 400 µm pinhole.

absorbed into the 3D-printed device interferes with the cross-linking of PDMS, they will also prevent membranes from curing properly. Additionally, if the devices have not spent a sufficient time in the vacuum chamber degassing, the presence of bubbles in the membrane will create pinholes upon curing (Fig. 4.19c)

4.2.2.4 Membrane Valve

Another common requirement by multilayer microfluidics is membrane valves, which use pneumatic or hydraulic pressure in one fluid layer to moderate fluid flow in a secondary layer [333]. Commonly, these membrane (or "Quake") valves are two-layer constructions which use a number of pneumatic inputs to control complex arrays of microfluidic reactors, although some works [36, 47] use multiple layers to implement valves with active control or built-in pressure gain.

In this work, we fabricated a Membrane Valve using a single-step double-sided microfluidic molding technique by linking a detour via with a thin membrane in an upper layer (Fig. 4.20a,b). The membrane was 350 µm thick, and the lower channel was 500 µm deep (for schematics, see Figure 4.21). While standard membrane valves need a photoresist reflow step during manufacture to allow the bottom layer to close fully, we were able to implement a rounded lower channel directly from the CAD file. To characterize the closing behavior of membrane valve, we ran a series of pressure sweeps (Fluigent MFCS™EZ) and measured (Fluigent® FlowUnit L) the resulting source-drain flow rate (Q): Gate pressure (P_G) was increased smoothly and source pressure (P_S) was increased parametrically. The valve began closing at 160 kPa and fully closed by 220 kPa, and had a mostly linear response during the transition (Fig. 4.20f). Further, P_S did not substantially affect the P_G of the initial drop in Q. Finally, to demonstrate the response time of the membrane valve within the closing pressure window, we manually cycled the gate pressure at various speeds and plotted the pressure and flow rate response curves against each other (Fig. 4.20g). Note that the

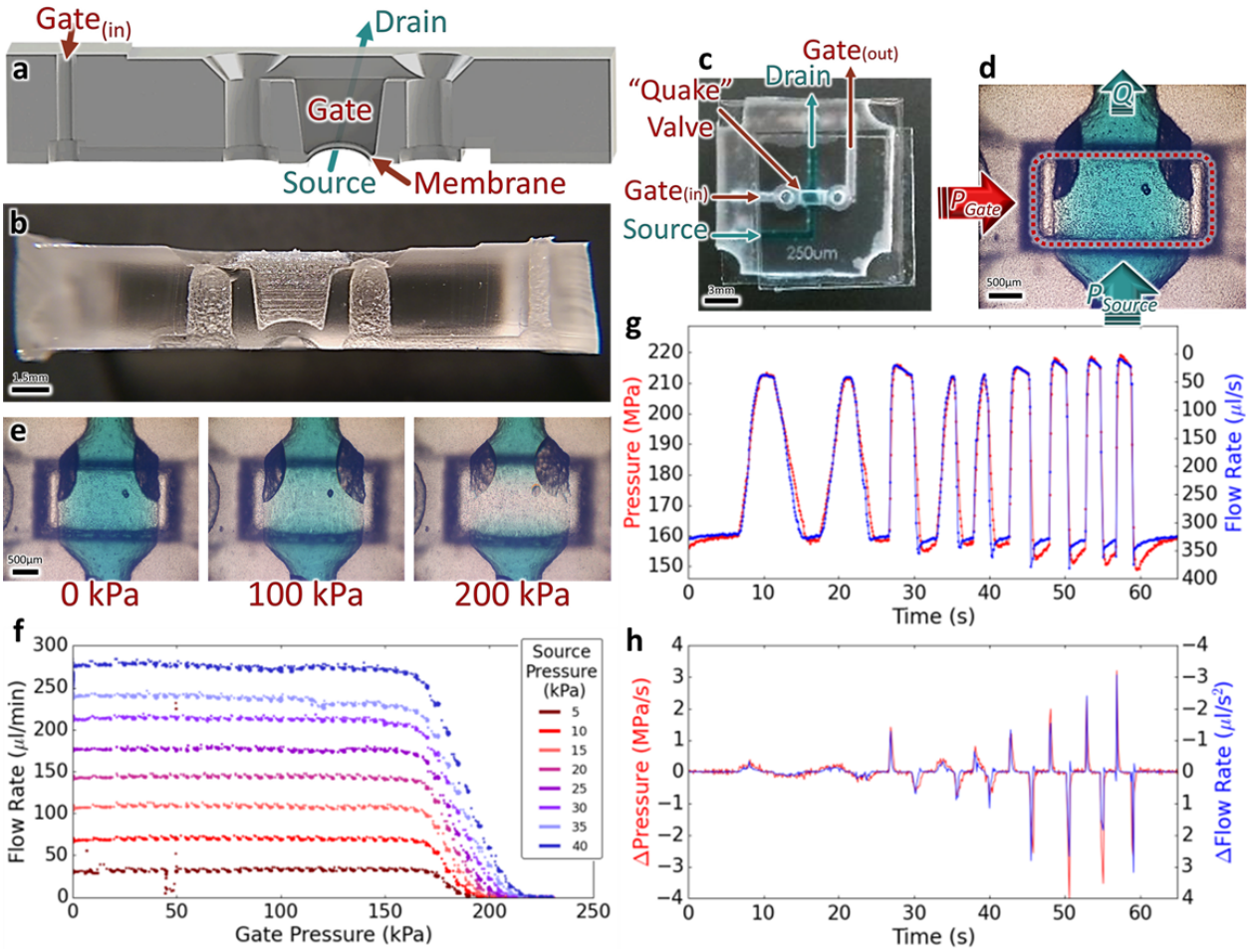


Figure 4.20 "Quake"-style membrane valves generated by single-step double-sided molding procedure. **(a)** Conceptual and **(b)** cross-sectional photograph of the membrane valve. **(c)** Top-down photograph, **(d)** microscope image illustrating the active valve region, and **(e)** microscope images of valve under various P_G. **(f)** Valve characteristic curves under parametric P_S sweep. Further P_G/Q time series analysis: **(g)** flow rate compared with varying gate pressures and **(h)** rates of change of flow rate and gate pressures.

axes have been rescaled and shifted to illustrate the high degree of qualitative agreement between pressure and flow rate. The time-differential response curves (Fig. 4.20h), illustrate the rapid response time of flow rate to changes in gate pressure. Lastly, cross-sectional schematics for the membrane valve molds are shown in Figure 4.21.

4.2.2.5 Double Sided Channels

In certain microfluidic applications (*e.g.*, optofluidic lithography), it is useful to have components completely surrounded by PDMS [291] or channels which have 360° rounding [59, 61]. Figure 4.22 shows images of a fully rounded microfluidic channel fabricated using the 3D-printed transfer molding process that avoids some of the challenges of generating fully rounded channels.

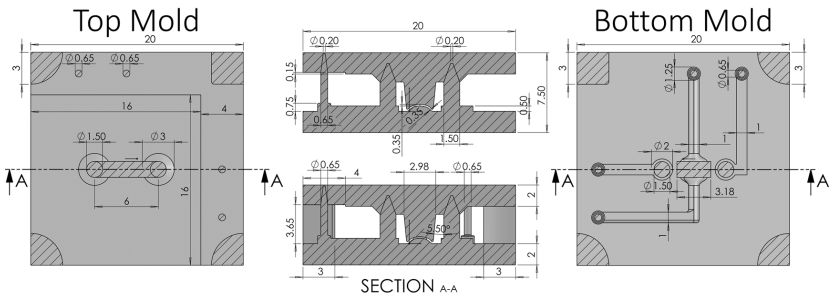


Figure 4.21 "Quake"-valve mold schematics, showing top and bottom molds, as well as nested molds. Both cross-sectional views are of the identical view and location, excepting that the bottom cross-section shows the full depth-of-field and therefore illustrates the alignment marks in the background.

Currently, there are few techniques for generating rounded channels and each can be quite sensitive. One involves vacuum-loading ℓPDMS into a formed microfluidic channel and then forcing it back out using pressurized air [63, 312]. Unfortunately, this technique is unreliable and requires constant attention to prevent blockage of channels by PDMS. Additionally, devices must be specially designed to allow for channel rounding though this technique. Finally, the rounding provided by this technique is only partial (reduction of corner sharpness) and does not lead to truly circular channels. A less sensitive technique for rounding rectangular channels uses a positive photoresist (*e.g.*, Shipley SJR 5740) to pattern the fluidic channel molds on a silicon or glass substrate. Then, the substrate is heated to 120°C for 20 min, heating the photoresist past the glass transition temperature, allowing the resist to reflow and round itself under surface tension [3, 22]. Lastly, twofold PDMS replication – where a mold is used to fabricate PDMS which is then used as a secondary mold – has been used in consort with CNC milling to fabricate rounded channels, although this technique relies on device symmetry for proper functionality [66].

Figure 4.22 shows several images of a fully rounded microfluidic channel fabricated using the simpler and more flexible 3D-printed transfer molding process, fabricated by bonding two semi-circular channel PDMS devices together. Complementary 3D-printed molds (Fig. 4.22a) are used to generate complementary PDMS with built-in PPAM (Fig. 4.22b). Next, the two halves are bonded using ℓPDMS stamp bonding using either stamp pictured in Figure 4.22c. Photographs of completed devices are shown in top-down perspective (Fig. 4.22d) and edge-on (Fig. 4.22e). Figure 4.22f shows a photograph of a cross section of a device to illustrate the circularity of the channel. SEM images (Fig. 4.22g and Fig. 4.22h) show that the two halves appear to be a single piece; smooth and mostly circular, with slight kinks where the two halves join together. Schematic diagrams for the double sided channels are shown in Figure 4.23.

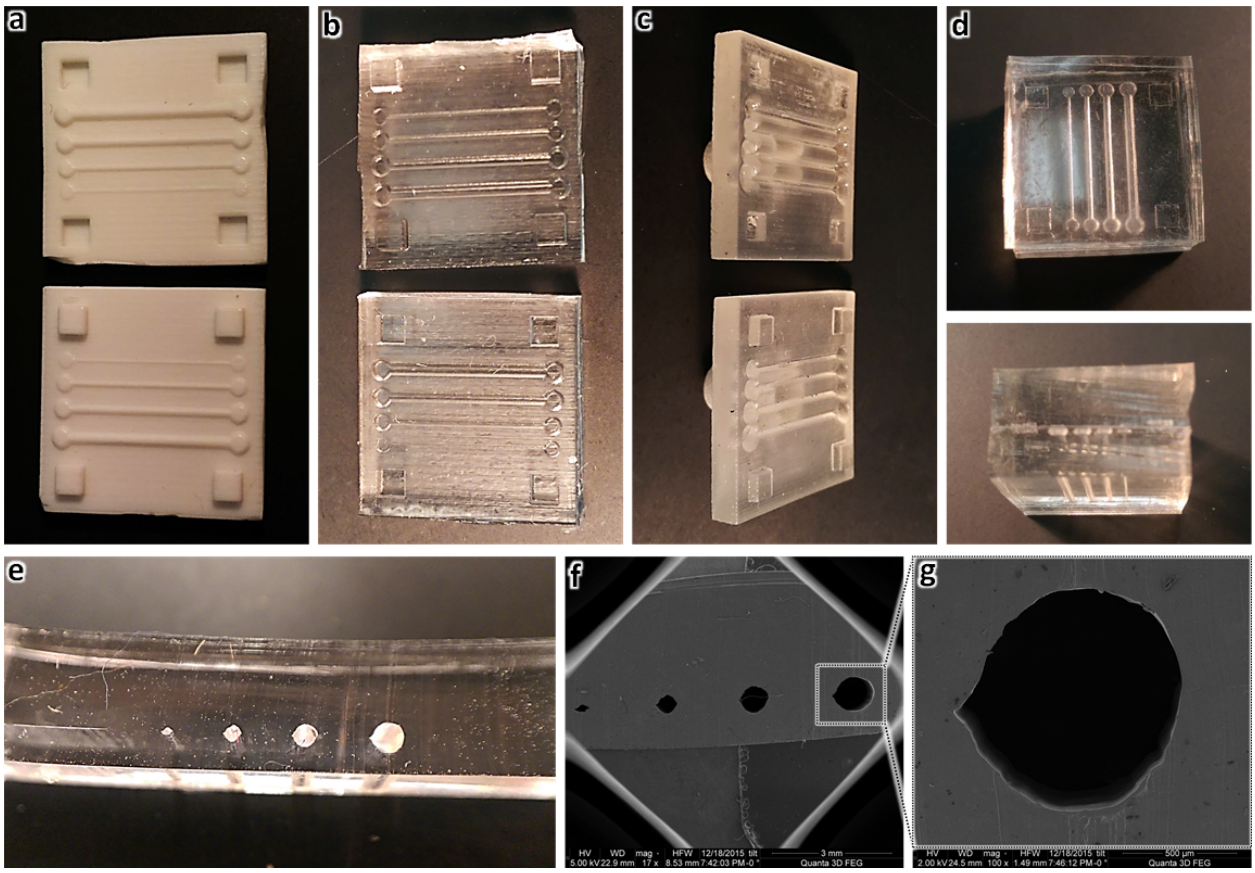


Figure 4.22 Photographs of process for generating fully rounded microfluidic channels (Radii 500, 375, 250, 125 µm). Images show *upper* and *lower* **(a)** 3D-printed molds, **(b)** resulting PDMS, and **(c)** corresponding 3D-printed stamps. **(d)** Final bonded device with rounded channels seen in top and side view. **(e)** Photographic view of channel cross-sections and **(f)** SEM image of channel cross-section with **(g)** magnification of largest channel, illustrating roundness of channels.

4.2.2.6 Uses for Two Sided and Fully Rounded Channels

(I) PDMS-enclosed fluidic channels.

Creating microfluidic channels which are enclosed on all sides may be useful for microfluidic applications in which fluids or other components cannot be in contact with glass. For example, in optofluidic lithography, photocurable hydrogels will permanently bond to a glass substrate [291]. Thus, to fabricate movable components through optofluidic lithography, PDMS-enclosed glass channels must be used.

(II) Tight seal against movable components. In optofluidic lithography, feature contraction during curing allows components to freely move. However, when used in conjunction with channels with uniform height, this lubricating fluid gap also prevents a tight seal (Fig. 4.24a,b), causing leakage within fluidic diodes or transistor-like components [60, 61]. As described in 3.3 Due to

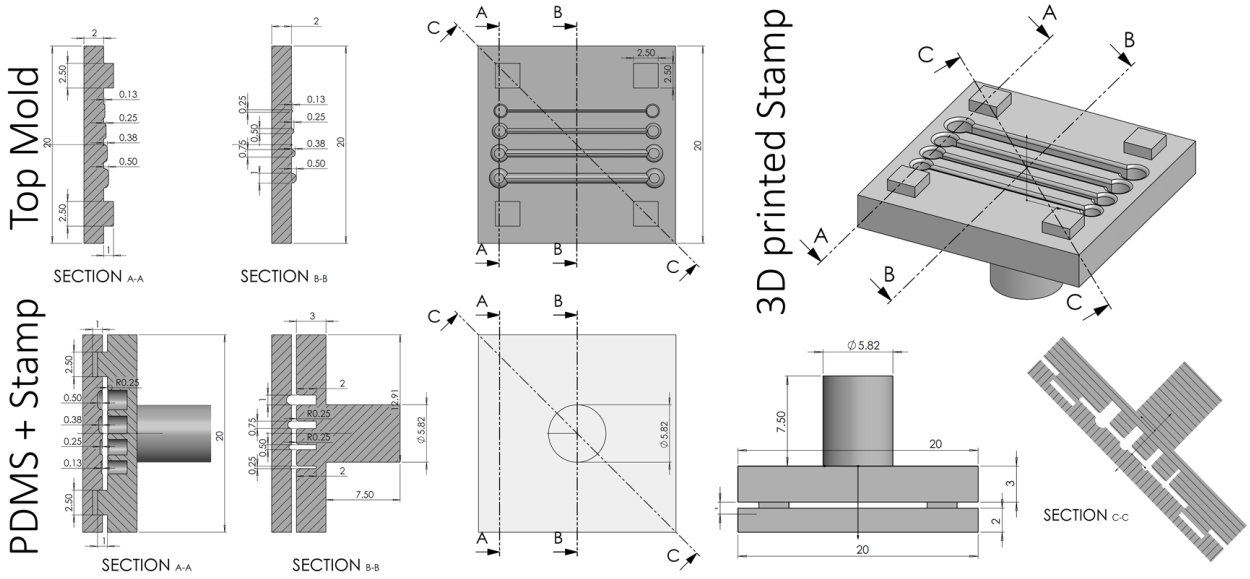


Figure 4.23 Schematic diagrams illustrating the generation of double sided channels, including the top mold (the bottom mold differs only by intruded alignment marks), the 3D-printed stamp, and stamp-PDMS alignment for the upper layer. All cross-sections are located in comparable positions from a top-down perspective.

the physics of thin film fluid flow, there is a direct trade-off between speed of optofluidic feature movement under pressure-driven flow and the rate of fluid leakage. For a given uniform thin gap d, pressure drop ΔP and viscosity μ, the leak rate

$$Q_{\text{Leak}} \propto \frac{d^3}{\mu}\Delta P. \tag{4.1}$$

However, the approximate speed of the optofluidic plug

$$V_{\text{Plug}} \propto \frac{d^2}{\mu}\Delta P. \tag{4.2}$$

While Q_{Leak} scales better with d than V_{Plug}, this scaling still reduces response time to unacceptably slow levels. However, using 3D-printed molds, we can fabricate enclosed fluidic channels with non-rectilinear profiles (Fig. 4.24c), allowing optofluidic diodes to move freely in the "open" position and shut tight in the "closed" position (Fig. 4.24d). The devices may then be constructed with plenty of movement in the wider channel. For more details, see Section 3.3.5.

(III) Rounded components for easier membrane valve-sealing.

Membrane valves do not close effectively when the membrane must fill in channel corners; with rectangular channel geometry, the center of the channel closes first, but the edges of the channels

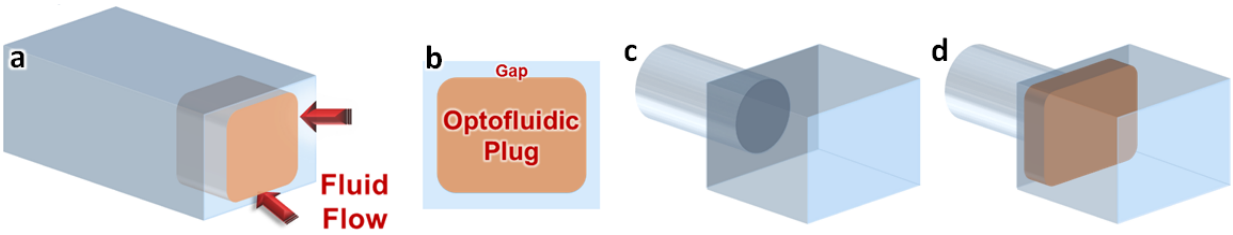


Figure 4.24 Conceptual diagram illustrating the use of variable-diameter microfluidic channels (blue) for optofluidic lithography **(a)** Due to contraction of the optofluidic lithography hydrogel plug (orange), the plug is able to move in the microfluidic channel, but **(b)** fluid can move to the side, causing leakage. **(c)** With a variable geometry channel, a plug may be constructed **(d)** that blocks the smaller portion of the channel but only partially blocks the larger channel, allowing the plug to both move and not leak.

require substantially higher pressures to close. These "islands of contact" allow fluid to pass by the valve, limiting its effectiveness. For rectangular channels, very high pressures are required to force the membrane into the corners. However, rounding the upper profile of the channel allows the channels to form a continuous contact edge, unifying the actuation-pressure gradient and enabling full valve closure at lower pressures. See Unger *et al.* for further discussion [24].

4.2.3 ℓPDMS Stamp Bonding and Multi-Layer Rapid Assembly

While double-sided PDMS molding can be completed with spin-bonding to glass, fully multilayer microfluidic devices (created by 3D-printed molding or conventional soft lithography) require a PDMS-PDMS bonding step. For 3D molded PDMS components, we have developed 3D-printed stamps to selectively apply PDMS as a more consistent bonding technique, as shown in Figure 4.25a. The stamps can easily be designed and printed from the original CAD drawings, to selectively apply uncured ℓPDMS only to non-channel areas of the PDMS component. These stamps may contain features that intrude (5c) or extrude (5d) from the plane of the stamp, which allow the stamp to be used on numerous PDMS topologies.

Using ℓPDMS Stamp Bonding, multi-layered microfluidic devices are easily assembled, allowing fluid flow within or between the various layers (Fig. 4.25b). Additionally, previously discussed techniques (*e.g.*, alignment marks, built-in inlets/outlets, and variable channels) may be used in conjunction with rapid assembly. Including the 40 min baking time, ℓPDMS stamp bonding allows a six-layer microfluidic device (Fig. 4.25e) to be assembled and bonded in under an hour. To bond two PDMS components with ℓPDMS Stamp Bonding, ℓPDMS was first applied to a TechniCloth wipe and the stamp was dipped in the PDMS. For extruded stamps, a copy of the PDMS component was used as an applicator: a template stamp used to transfer ℓPDMS to the extruded stamp. Next, the stamp was "blotted" with a clean TechniCloth to remove excess PDMS.

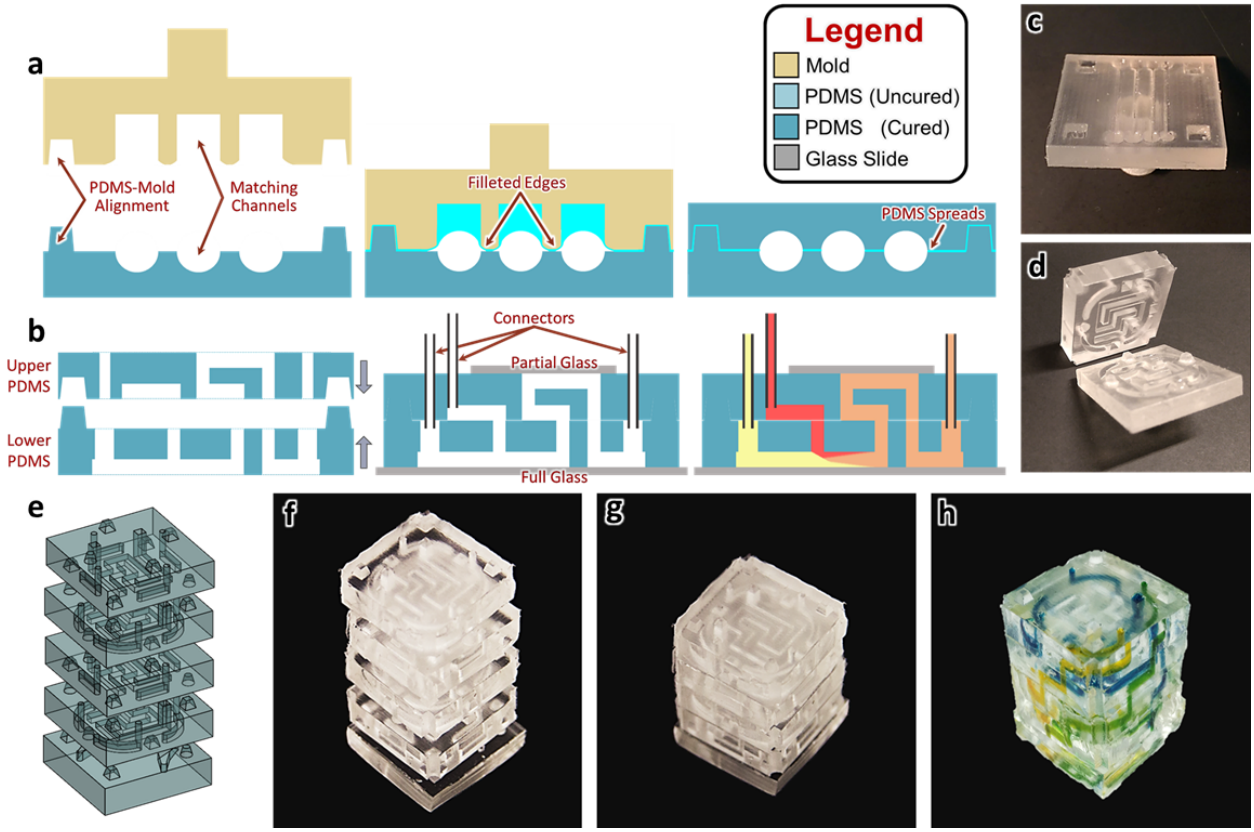


Figure 4.25 Rapid assembly of multilayer PDMS microfluidic devices achieved through 3D-printed stamp-bonding process. **(a)** Use of a 3D-printed stamp to selectively apply uncured PDMS to non-channel areas. **(b)** Conceptual illustration of alignment and assembly of multilayer microfluidic device with illustration of intra-layer fluid flow. **(c)** Intruded stamp topography. **(d)** Second layer of six-layer device with corresponding stamp, which exhibits extruded stamp topography. **(e-h)** Rapid assembly of multilayer microfluidic device: **(e)** CAD model, **(f)** stacked individual layers, **(g)** assembled and bonded, and **(h)** fluid flow spiraling between layers and mixing.

The stamp was then pressed lightly ($\approx 5-10$ N) into its complementary PDMS component to deposit a thin, uniform layer of ℓPDMS onto the 4 cm^2 PDMS component. Finally, the two PDMS components were pressed together and clamped in place to prevent shifting during curing. Clamping was performed with a $1\frac{1}{2}''$ C-clamp and was sufficiently secure when the visual roughness disappears (as ℓPDMS filled the empty spaces left by the roughness). Finally, the devices were cured at 80°C for 40 min, resulting in a complete multi-level PDMS device. For a more extensive discussion of stamp bonding techniques, see 4.3.3.

4.3 Technique Considerations

4.3.1 Standard and 3D Molding Technique Comparisons

Note that for any soft-lithography process with more than one layer, that the pattern for the upper layer must be corrected to account for shrinkage in PDMS curing. Correction requires the upper mask to be scaled up relative to the lower mask by 0.5% to 1.5% [333] Additionally, bonding multiple layers generally requires an *off-ratio bonding* wherein the control (upper) layer uses a 5:1 Base:Cure-agent ratio and the valve (lower) layer uses a 20:1 Base:Cure-agent ratio. During incubation, base and cure agent diffuse across the interface allowing for a more permanent bond. This technique is also sensitive to over-curing. This process is described in detail by Thorsen et al. (2002) [3].

4.3.1.1 Via Fabrication

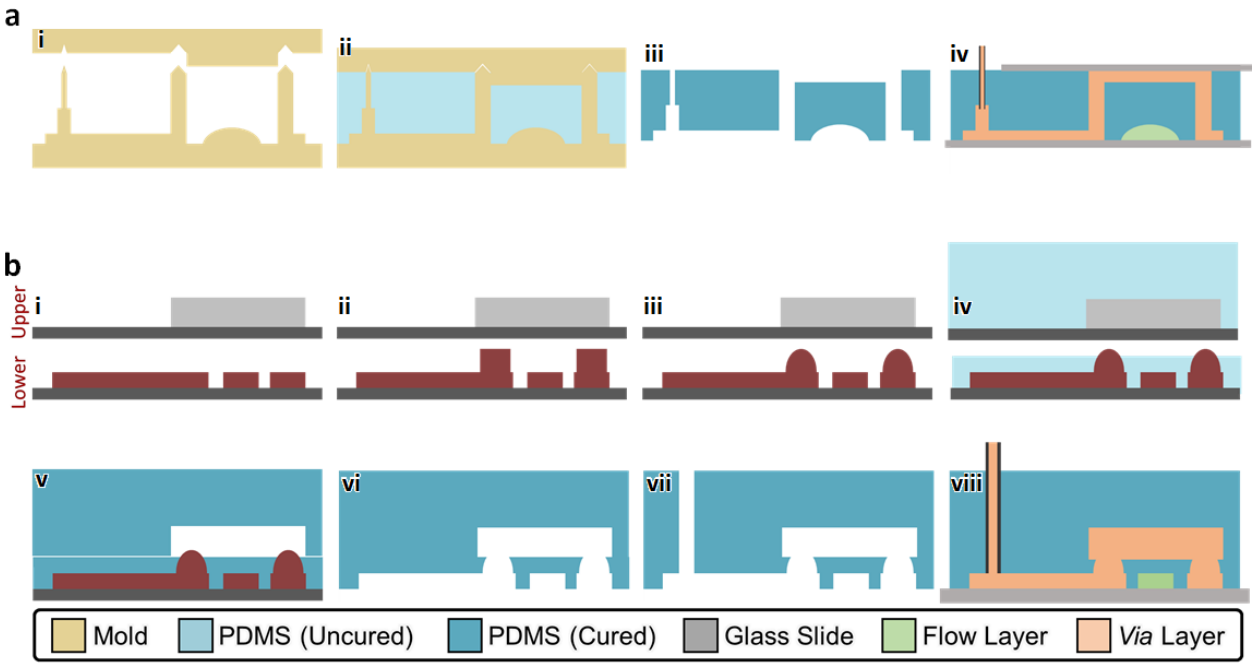


Figure 4.26 Microfluidic via process flow comparison for (a) 3D molding technique, and (b) standard soft lithography.

(I) 3D Molding process.

(i) Two molds are printed from CAD file and cleaned. (ii) Molds are fitted together using alignment marks, filled with ℓPDMS, degassed, and baked. (iii) Excess PDMS is cut from around molds and

PDMS is released. (iv) Device is bonded to glass on the top and bottom, taking care to leave input vias uncovered. This process is identical to standard double-sided molding technique.

(II) Standard soft lithography process [3, 333].

(i) Photolithography is performed to define mold for upper layer (thick) and lower layer (thin). (ii) Second photolithography process is performed for lower layer to create interconnect points. (iii) Channels for the lower layer are rounded using a heat reflow treatment. Rounding is achieved through surface tension and reduces the likelihood of PDMS covering the via interconnects. (iv) PDMS is poured onto the upper layer. PDMS is spin-coated onto lower layer, making sure to calibrate thickness such that the interconnects emerge from the PDMS. Upper and lower layers baked until cured. (v) Upper layer removed from mold, and upper and lower layers are plasma treated. Upper layer is carefully aligned (using visual alignment marks) with lower layer, placed in contact to remove bubbles, and baked at 80°C for 40-60 min to finalize curing. (vi) Bonded layers are removed from mold. (vii) Holes punched in bonded device using manual hole puncher. (viii) Bonded, punched device is plasma treated along with glass slide. Device and glass placed in contact (with care to prevent bubble formation) and then cured at 80°C for 30 min, followed by an all-night incubation to cure. Note that to enable direct fluidic control of via layer (*i.e.*, though catheter couples) rather than passive flow through the vias, an additional hole punching step must be performed between steps (iv) and (v) to allow the hole to enter only into the via layer.

4.3.1.2 Membrane Valve Fabrication

(I) 3D Molding process.

First, (i) two molds are printed from CAD file and cleaned. (ii) Molds are fitted together using alignment marks, filled with ℓPDMS, degassed, and baked. (iii) Excess PDMS is cut from around molds and PDMS is released. (iv) Device is bonded to glass on the top and bottom, taking care to leave input vias uncovered. This process is identical to standard double-sided molding technique.

(II) Standard soft lithography process for "Quake" valve generation [333].

(i) Photolithography is performed to define mold for upper valve layer (thick) and lower flow layer (thin). (ii) Channels in the lower layer are rounded using a heat reflow treatment to allow for complete closure of the Quake-valve. Rounding is achieved through surface tension reflow during heating. (iii) PDMS is poured onto the upper layer. PDMS is spin-coated onto lower layer, making

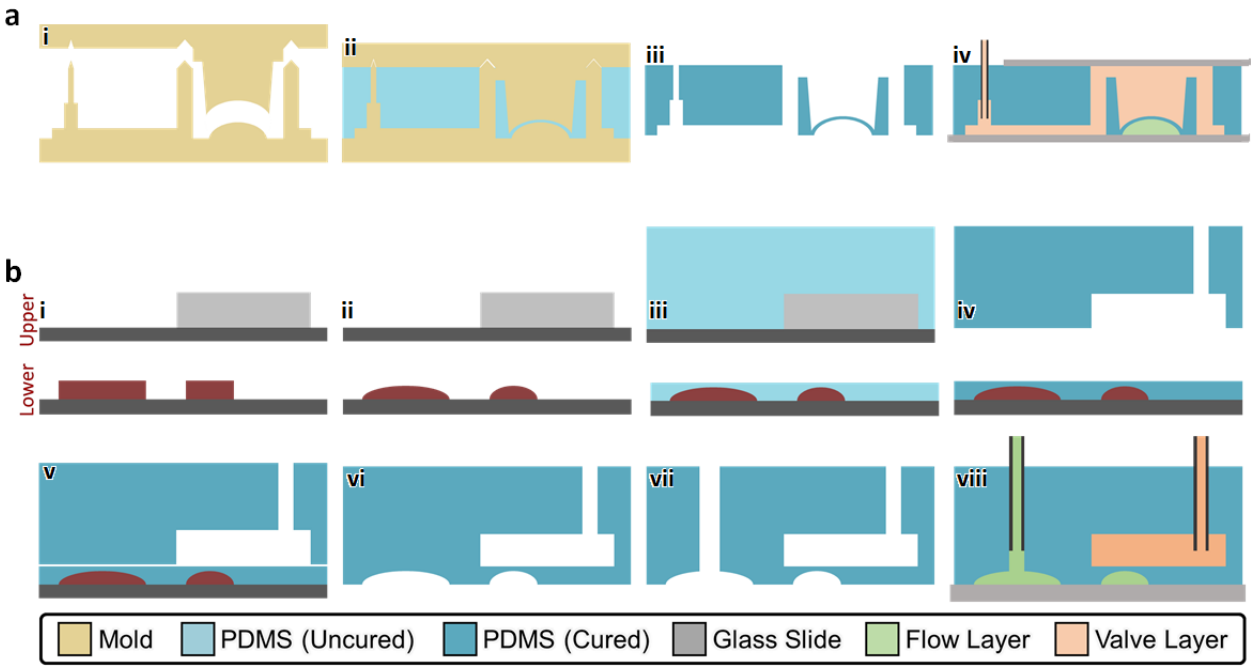


Figure 4.27 "Quake" valve process flow comparison for (a) 3D molding technique, and (b) standard soft lithography.

sure to calibrate thickness such that the interconnects emerge from the PDMS. Upper and lower layers baked until cured. (iv) Upper layer removed from mold and holes are punched using manual hole puncher to allow for direct pneumatic control in valve layer. (v) Upper and lower layers are plasma treated. Upper layer is carefully aligned (using visual alignment marks) with lower layer, placed in contact to remove bubbles, and baked at 80°C for 40 min to finalize curing. (vi) Bonded layers are removed from mold. (vii) Holes punched in bonded device using manual hole puncher. (viii) Bonded, punched device is plasma treated along with glass slide. Device and glass placed in contact (with care to prevent bubble formation), and then cured at 80°C for 30 min, followed by an all-night incubation to cure.

Note that to enable fluidic vias along with the Quake-valve architecture, an additional lithography and development step must be performed between steps (i) and (ii) to allow for the via layer interconnects. This technique also generally requires off-ratio bonding to bond firmly.

4.3.2 Strengths and Weaknesses of Bonding Techniques

4.3.2.1 Plasma Bonding

As in other bonding techniques discussed in this paper, the tightness (but not permanency) of a bonding seal can be judged visually. Non-bonding surfaces appear as areas of incomplete transparency, white patches, or patches exhibiting interference patterns. When attempting to perform

glass-bonding using a standard oxygen plasma process — plasma treat (Plasmod®) for 60 seconds, place components together, and then bake for 2 hours — a permanent bond is created with numerous vacancies which allow fluid leakage.

To attempt to create a tighter seal, after plasma treatment, our devices were placed in contact with glass, sandwiched between thicker glass slides and then clamped with a $1\frac{1}{2}''$ C-clamp and tightened until the vacancies vanished. Thicker glass slides were used to distribute the load of the clamps, and glass was used instead of metal due to the transparency; only with glass slides were we able to visually inspect the tightness of the clamp seal. By the time tightening was sufficient, roughly one-in-three devices suffered breakage of one or both glass layers. Additionally, during baking, the relative thermal expansions of glass, PDMS, and metal clamp led to the remainder of devices cracking by the time the devices were ready to extract from the oven. Finally, the high pressure needed to overcome surface roughness resulted in deformed devices, and the rotating nature of the C-clamp led to torqueing of the PDMS against the glass (a problem exacerbated in PDMS-PDMS bonding, even with alignment marks.

A possible resolution to this problem involves using a non-rotating clamping device, which would likely eliminate torqueing problems and may allow for more precise control of pressures applied. Additionally, with a calibrated bonding pressure, the glass bonding sheets could be foregone in favor of sturdier metal load distributors. However, the best solution has proven to be use of a PDMS bonding agent to fill in lacunae which exist between layers to be bonded.

4.3.2.2 Glass Bonding

There are a number of considerations for precise use of the spin bonding technique (discussed in 4.2.1.1), which are outlined below. Failure in these considerations may lead to device deformities, which are outlined in Figure 4.28.

(I) PDMS thickness.

If the PDMS coating on the glass is too thick, excess PDMS has the tendency to clog features in the PDMS device. Some of these issues can be resolved by using a spin-coated PDMS thickness on the scale of surface roughness to be removed, but smaller than the smallest features.

(II) Timing dependence.

A precise calibration of timing and temperatures is critical for this technique to proceed satisfac-

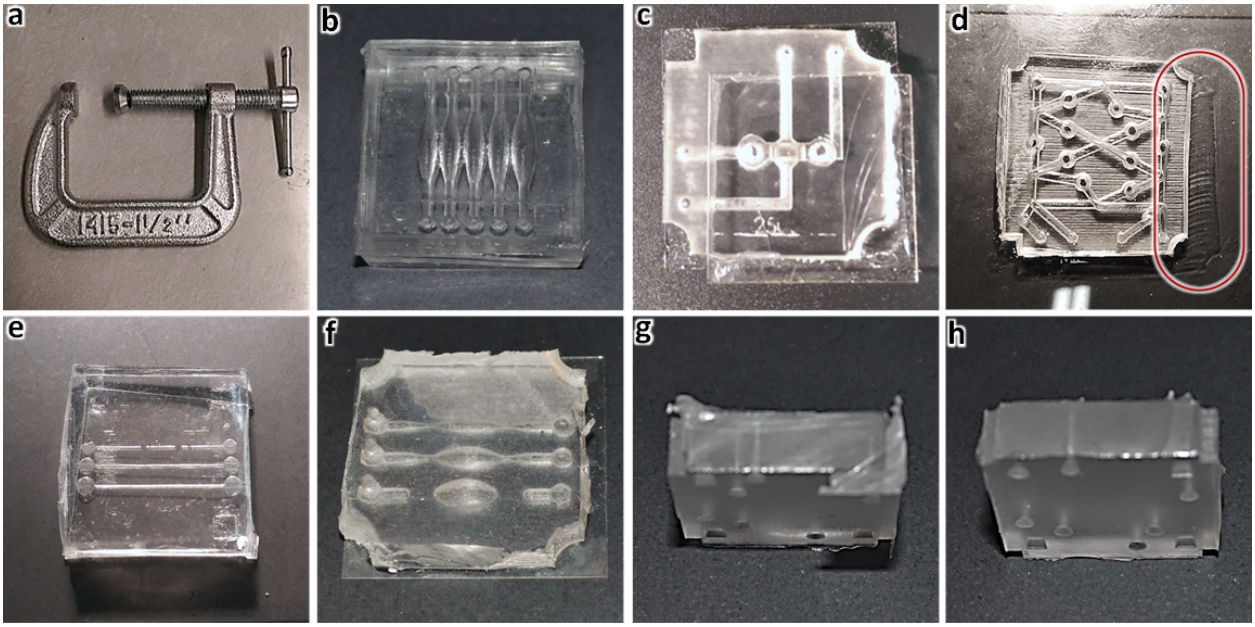


Figure 4.28 Illustration of problems that occur during glass-bonding. **(a)** $1\frac{1}{2}''$ C-clamp used to hold devices in place during bonding **(b)** Device that was excessively torqued during bonding procedure; upper and lower layers do not align properly. **(c)** Device where glass has broken due to thermal expansion during bonding. This is less of an issue in devices which use thicker glass slides. **(d)** Smeared PDMS from lateral motion during ℓPDMS spin-bonding. **(e)** Stamp-bonded device where excess ℓPDMS led to channel clogging. **(f)** Spin-bonded device where a too-thick ℓPDMS layer caused channel clogging. Additionally, due to poor trimming, other parts of the device failed to bond to the glass at all. **(g)** Filaments of PDMS that were not adequately trimmed during de-molding. This is the most common cause of insufficient bonding and may be resolved with a small lip around the edge of the 3D-printed mold or by **(h)** trimming the edge bead with a scalpel.

torily. For example, if the PDMS coating on the glass slide cures too much before bonding, or pressure is not applied evenly to the bonding surfaces, the resulting PDMS bond is too weak to be usable. In contrast, if the PDMS does not cure sufficiently, the device tends slip during application causing buildup of PDMS in the channels and creating blockages. Both these difficulties would be resolved by using an integrated clamping/bonding device compatible with a heating system, instead of using hand-pressure. The times and temperatures quoted in 4.2.1.1 have proven reliable.

(III) Planar surfaces.

Spin-coated PDMS-glass bonding is limited to PDMS pieces with no features protruding beyond the bonding plane, because protrusions prevent a strong bond between the glass slide and the PDMS piece. Additionally, since spin-coating is most effective on flat, featureless devices, this technique cannot be used to make PDMS to PDMS bonds (and therefore multi-layered microfluidic devices). While the PDMS devices may be placed in the spin-coater, the process unsurprisingly leads to PDMS flowing into channels, leading to irreparable clogs and damage to the devices.

4.3.2.3 Delamination and inlet bursting

3D transfer molded devices break in three distinct ways. First, the glass itself can fracture under pressure or mishandling. This is a more dominant issue using 0.1 mm thick glass slides, chosen due to the smaller size and favorable shape (22x22 mm^2) than in standard microscope slides. Second, the glass can delaminate from the PDMS, allowing fluid to flow between the glass and the PDMS device. Delamination may be caused by dust particles on the glass bonding surface, by chemical surface contamination, or by over-curing the PDMS device prior to bonding, which inhibits the formation of cross-links between layers. Glass delamination may be mitigated by using very clean glass slides prior to the application of ℓPDMS and not over-curing the PDMS device prior to bonding [334]. Additionally, in the latter two cases, oxygen plasma treatment may help resolve delamination issues. Lastly, high pressure can force the catheter couple out of the device inlet. Catheter ejection issues may be mitigated by using narrower built-in inlets or larger-gauged catheter couples.

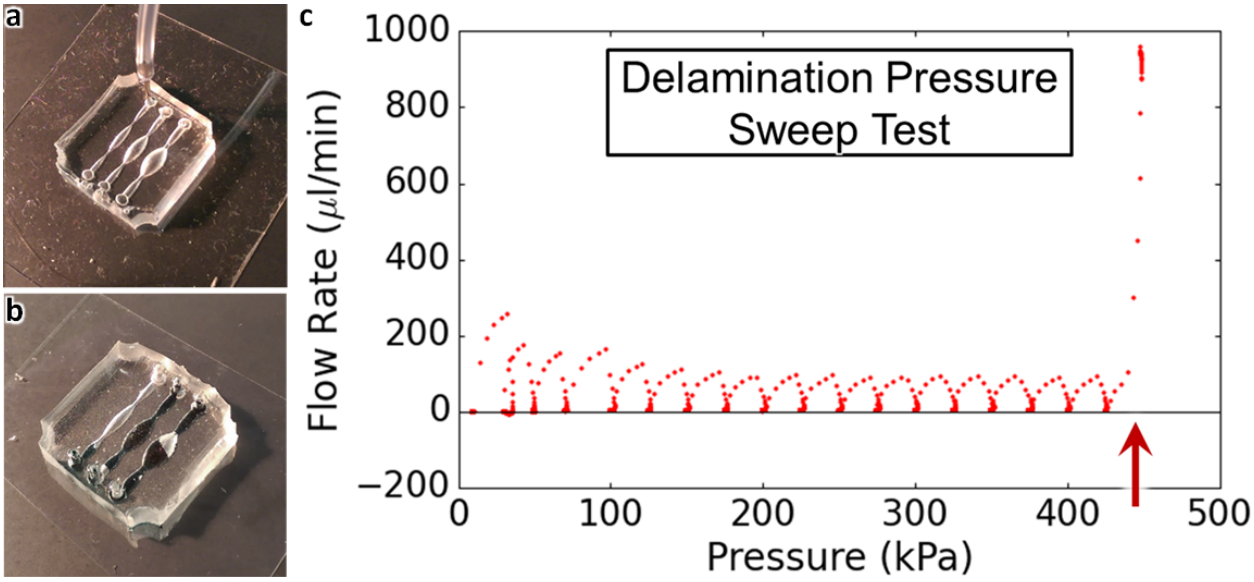


Figure 4.29 Determination of delamination pressure for glass-bonded single layer microfluidic device. (a) Setup for testing of microfluidic device. (b) Broken/delaminated device leaking colored fluid between channels (c) Graph of results of delimination test; delamination occurred at ≈ 450 kPa. The "bumps" in the graph are artifacts resulting from the hydraulic capacitance of the system.

Figure 4.29 illustrates a test to determine the delamination pressure of a bonded microfluidic device. (Fig. 4.29a) The fabrication geometry of this system was different than discussed in 4.2.1.2; in this testing geometry, only one side of each channel had built-in inlets, eliminating the need to block off the outlet channels. (Fig. 4.29b) Pressure was fed into the device and gradually

increased until the glass-PDMS bond broke and fluid began leaking rapidly. (Fig. 4.29c) The graph illustrates the resulting $Q-P$ curve, showing a rapid rise in the flow rate as the delamination occurred. The "bumps" in the graph are artifacts resulting from the hydraulic capacitance of the system; the increase in pressure from the pressure source caused compression of system air and temporary expansion of tubing, leading to an initial flow rate, which vanished as the capacitance became saturated. Delamination is permanent, and further testing of broken devices merely results in rapid increase in flow rate as the pressure is ramped up.

4.3.3 3D-Printed Stamp and Associated Techniques

This section elaborates on many of the techniques shown in 4.2.3, including an expanded discussion of stamp design, ℓPDMS application, and stamp cleaning.

4.3.3.1 3D-Printed Stamp Design

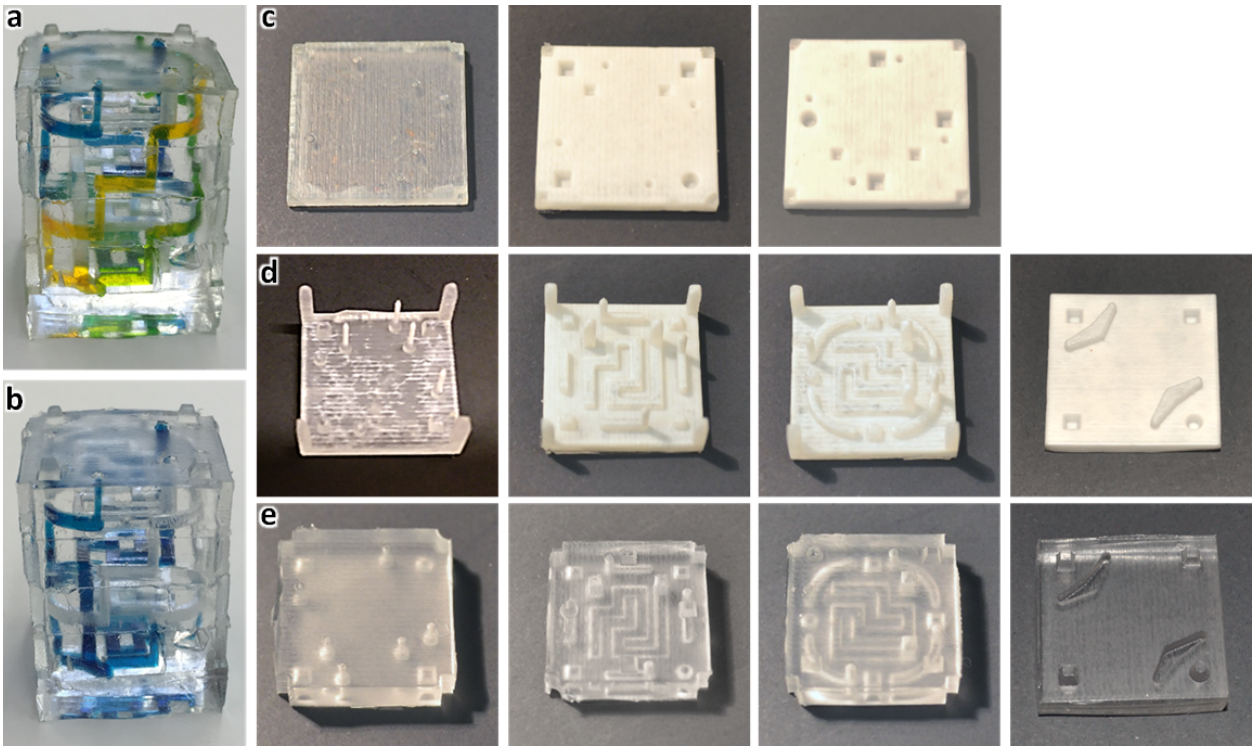


Figure 4.30 Stamps and individual layers used to fabricate multilayer PDMS microfluidic device. *Left*: Photographs of multilayer device with fluid flowing between layers with **(a)** single color, and **(b)** multiple colors with fluid mixing. *Right*: layer construction, shown from top layer with built-in inlets (left) to bottom layer (far right). **(c)** Mold upper layers with female alignment marks, **(d)** Mold lower layers with positive alignment marks and microfluidic vias, and **(e)** Resultant PDMS from each layer. Note that the bottom layer only needs a single mold.

Figure 4.30 expands upon the information in Figure 4.25, illustrating the construction of the multi-level PDMS device. (Fig. 4.30a) The device is constructed of four distinct patterns: a flow input layer, two spiraling flow layers (which are alternated and rotated, and can be repeated indefinitely), and a bottom adapter layer which allows the flow to move between the outward downward flowing spiral and the interior spiral. (Fig. 4.30b) Three distinct stamps are used to apply PDMS to the bottom of the middle layers and the upper layers, enabling PDMS to be applied to the surface without clogging the channels. Figure 4.30c shows the multi-layer CAD model, illustrating how the PDMS fits together and how flow moves between layers, and Figure 4.30d shows two final devices from a different angle than seen in Figure 5, one with only blue fluid and one with multiple fluid colors. Schematics for the four distinct PDMS components of the multi-layer microfluidic device may be found in Figure 4.31.

3D-printed stamps can fit into three distinct categories: intruded, extruded, and irregular (Fig. 4.32). Intruded stamps consist predominantly of a single flat plane with intruded channels corresponding to channels in the PDMS and use female Mold-Polymer alignment marks. Extruded stamps are similar, but include at least one male Mold-Polymer alignment mark or other feature extruded from the surface. For both intruded and extruded stamps, all ℓPDMS is applied to a single plane on the PDMS device, and both stamps topologies may use the scraper applicator method (direct and secondary application, respectively). Irregular stamps apply ℓPDMS to more than one plane or across a curved surface on the molded PDMS devices. Additionally, irregular stamps generally require direct blotting as the ℓPDMS application method, although for non-curved (but still irregular) surfaces, PDMS may be applied through a series of secondary stamping applications.

Additionally, because PDMS beading on the edges of stamp features can potentially be forced into the channels during stamping, and because PDMS applied right to the edge of the channels can be forced into the device during layer bonding, the designs have implemented *filleted* (*i.e.*, rounded) edges of the stamp's complementary channels, reducing blockage during bonding. A fillet radius of curvature of 100-250 μm is sufficient to prevent channel blockage in most cases.

4.3.3.2 Application of PDMS to Stamp.

Figure 4.33 illustrates some techniques to consider when using the 3D-printed stamps. After applying ℓPDMS to a stamp, the stamp can be used for 2-3 stampings before needing to reapply ℓPDMS. Additionally, the following stamp techniques may be used to apply PDMS to a glass slide for PDMS-Glass bonding, and tends to reduce the quantity of PDMS that fills the microchannels.

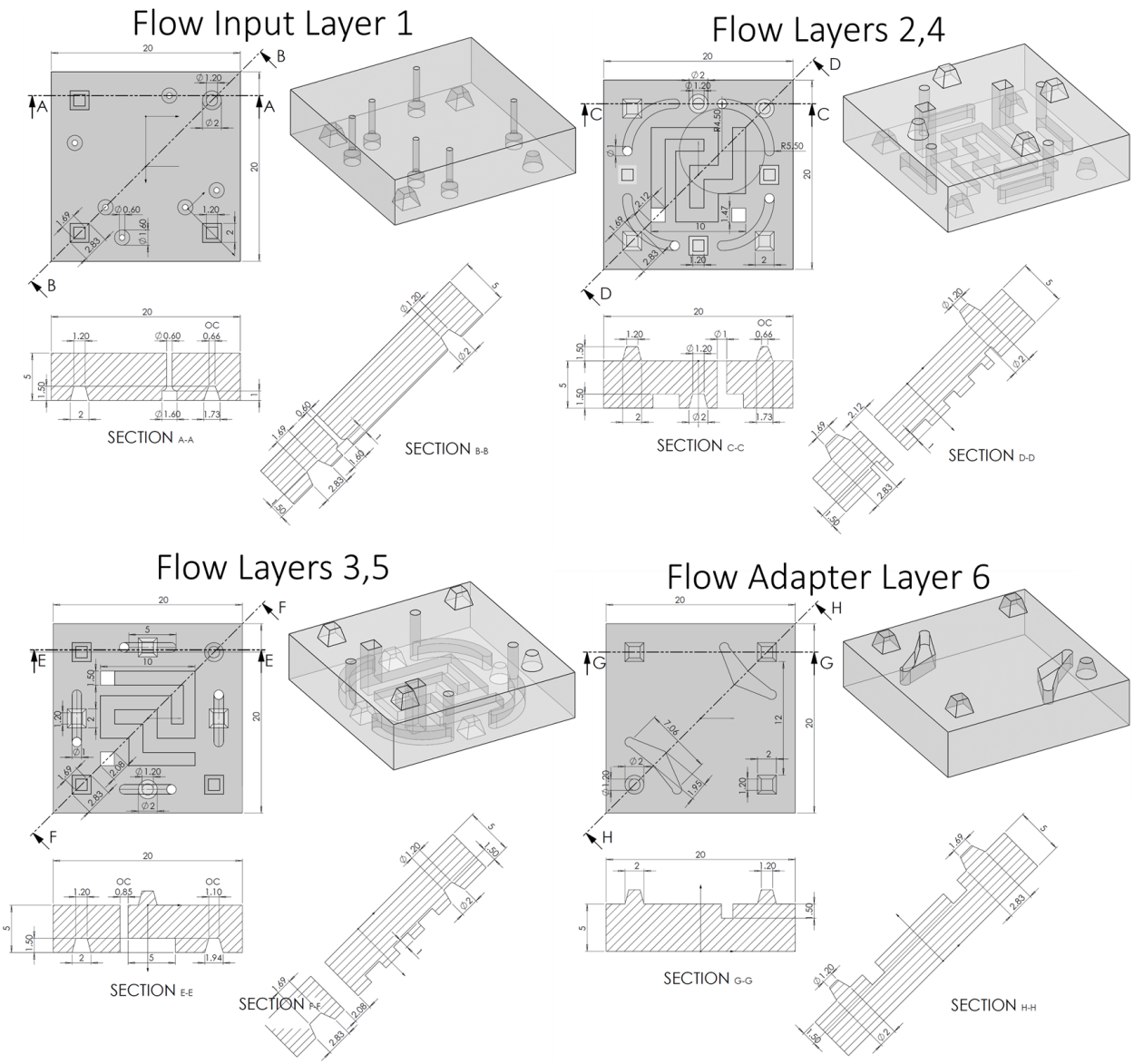


Figure 4.31 Schematic diagrams for the PDMS layers of multi-layer microfluidic device. The two-sided molds for each component should be reconstructible from the designs for the PDMS layers. Note that non-circular features in the diagonal views do not have the same dimensions as the linear direction. Additionally, *OC* indicates a feature which has dimensions analyzed while the cross-section is off-center.

However, because the stamp must be used with freshly prepared ℓPDMS, glass bonding can be challenging due to slippage of the glass against the molded PDMS, lubricated by the low viscosity ℓPDMS. We postulate that curing the molded PDMS with applied ℓPDMS for 1-2 min in an 80°C oven before bonding to the secondary layer might increase the viscosity of the ℓPDMS enough to prevent slippage, making future bonding easier, however we did not perform these experiments.

When a C-clamp is used to bind layers of PDMS together during bonding, care must be taken to not allow the layers to shear against each other (causing lateral displacement) or to torque

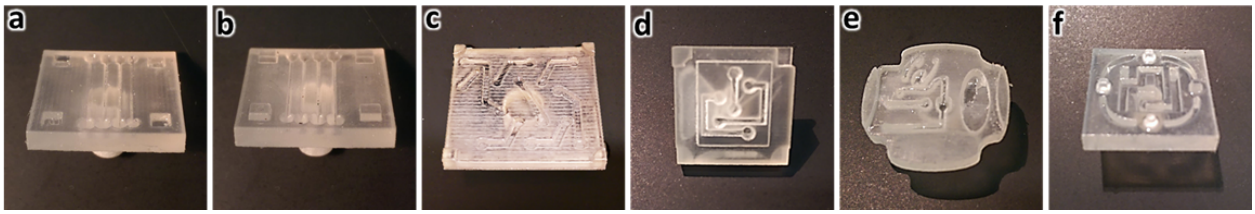


Figure 4.32 Photographs of stamps with differing surface profiles, used in multiple experiments. **(a)** Stamp for bonding rounded channel layers (Fig. 4.11i) in intruded and **(b)** intruded stamp topologies. **(c)** Extruded glass-bonding stamp for Celtic 7-knot design (Fig. 4.16). **(d)** Irregular glass-bonding stamp for crossing and overpass device (Fig. 4.11f). **(e)** Glass-bonding stamp for multicomponent device (Fig. 4.1f). **(f)** Extruded PDMS-PDMS bonding stamp for multilayer device (Fig. 4.25).

against each other (causing rotational displacement). Lateral shear emerges most readily when using PDMS that is not of uniform thickness (*e.g.*, from a tilted oven), creating a lateral stress vector resulting from the normal pressure vector. Torquing shear emerges due to the C-clamp's twisting motion during tightening and could be resolved using alternative, non-rotational clamps.

(I) Direct Blotting Method

ℓPDMS may also be applied to the 3D-printed stamps through a blotting technique. Approximately 10g of PDMS is poured onto a TechniCloth cloth and rubbed into the cloth so there is no pooled material. Then the 3D-printed stamp (or molded PDMS secondary stamp) is gently pressed into the cloth to transfer ℓPDMS to the stamp. Finally, the stamp is blotted by pressing gently and singly against a dry (non-PDMS-coated) portion of the TechniCloth to remove excess PDMS. (Note that more than one blotting tends to remove too much ℓPDMS and will make the stamping application fail.) Following blotting, the stamp is ready to apply ℓPDMS to the devices that will be bonded. When PDMS is blotted from the stamp prior to application, excess PDMS is removed from the stamps' complementary channels as well as from the surface. As a result of PDMS surface tension and PDMS fluid continuity, the PDMS tends to form a curved surface in the channel (Fig. 4.33e-g).

(II) Scraper Applicator Method.

Precise application of PDMS to intruded stamps can be enhanced slightly through use of a 3D-printed applicator (Fig. 4.33i). The applicator is designed with a relatively deep basin to store PDMS (depth=350 μm) but with lateral raised guides to prevent the stamp from sinking more than 100 μm into the basin. Then the stamp is slid along the guides to the edge of the applicator (Fig. 4.33j), where a sharp edge pulls excess ℓPDMS from the mold to collect in the bottom. In some applicator designs, we included a "scraper" which helped remove excess PDMS from below the depth of the guide rails. After application, the intruded stamp is blotted on a sheet of TexWipe

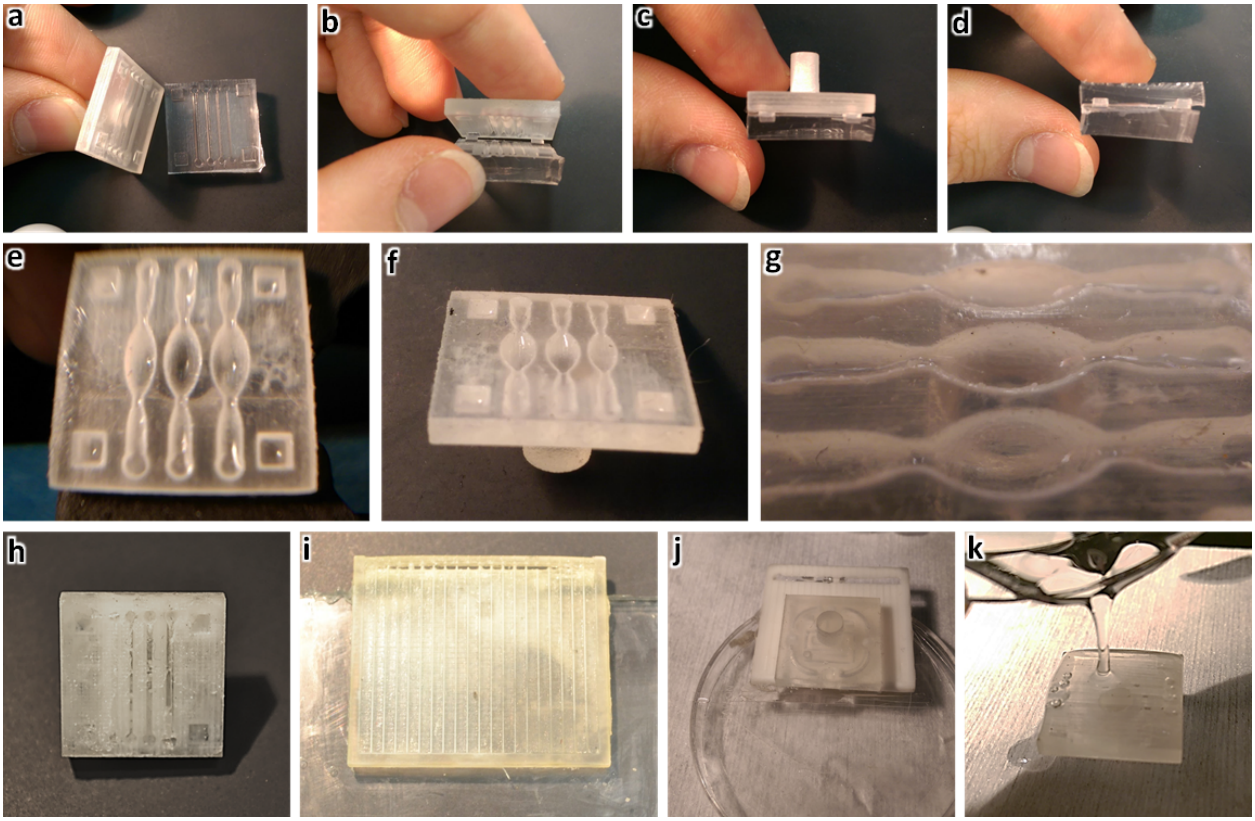


Figure 4.33 Illustration of stamping technique and other considerations. **(a-d)** Stamping procedure. **(e-g)** Stamp with internally cured PDMS forming curved structure within the channel. The stamp may still be used in this state, but may eventually need to be cleaned with excess ℓPDMS. **(h)** 3D-printed ℓPDMS applicator and **(i)** applicator with 3D-printed stamp. **(j)** Stamp in need of cleaning with crusted PDMS. **(k)** Stamp cleaning technique: excess ℓPDMS is poured onto the surface, baked, and peeled off as a single unit.

TechniCloth®. For schematics of the ℓPDMS applicator, see Figure 4.34.

The applicator may be used indirectly to apply ℓPDMS to stamps with extruded alignment marks using a *secondary stamping technique* where an identical copy of the device to be bonded is used as an ℓPDMS applicator for the stamp. First, ℓPDMS is applied to the copy, which is then blotted on TechniCloth. Then the ℓPDMS is transferred to the stamp by pressing the stamp against the PDMS applicator. Finally, the ℓPDMS is transferred from the stamp to the final piece of molded PDMS. Note that this secondary technique may be performed with a reusable 3D-printed stamp, but doing so with molded PDMS is often preferable for its lower fabrication time (new 3D-printed molds require post-processing whereas there is frequently excess molded PDMS) and lower cost (each molded PDMS has negligible cost once the mold is manufactured).

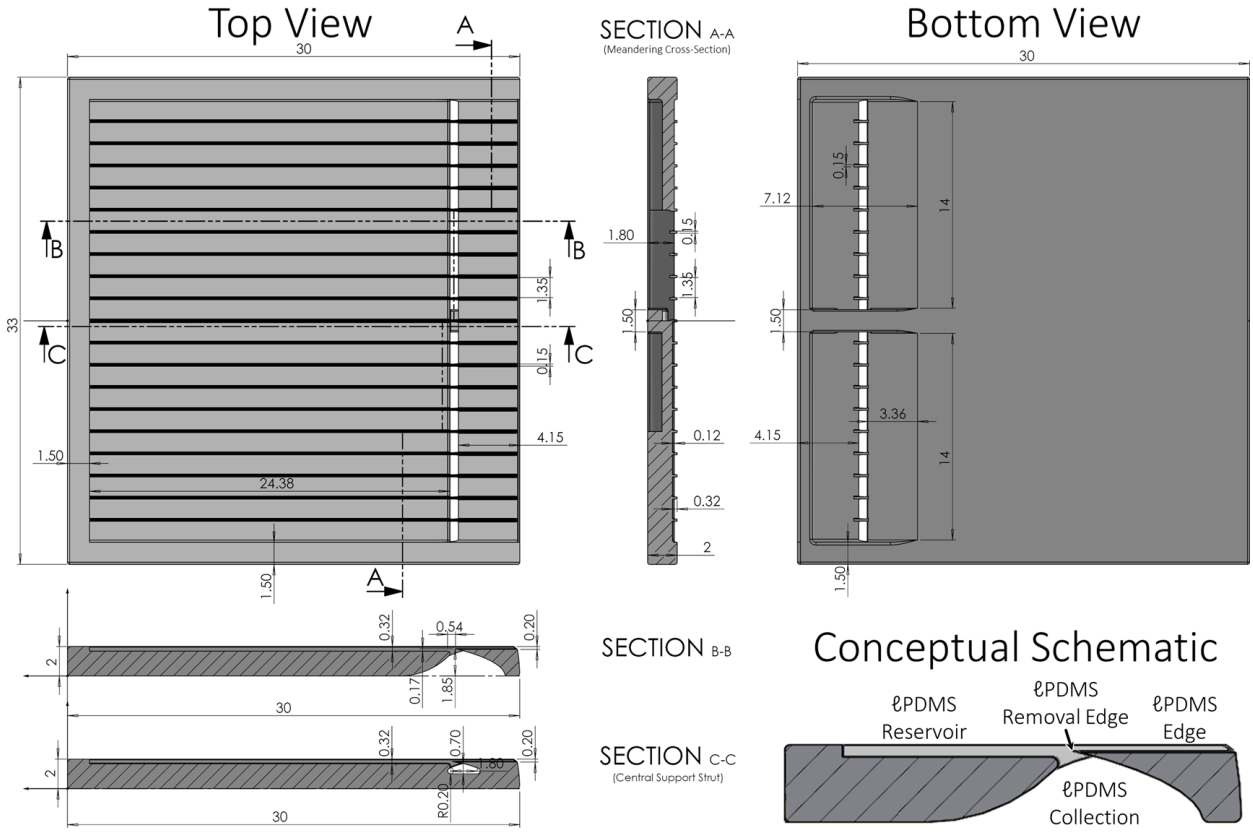


Figure 4.34 Schematic diagram illustrating the dimensions of the ℓPDMS applicator, including lengthwise cross-sections at the center and towards the edge, a variable cross-section perpendicular to the scraping direction, and a conceptual schematic cross-section.

4.3.3.3 Cleaning Stamps.

We recommend that the 3D-printed stamps be cleaned at the end of each use, otherwise crusted PDMS will block the channels and leave the stamp useless (Fig. 4.33j). However, because the optimal technique is simple as disposing of excess ℓPDMS, this process is not arduous. This method for cleaning the stamps (or for cleaning molds or the 3D-printed applicator) involves using extra ℓPDMS to clean the surface (Fig. 4.33k). ℓPDMS is poured onto the surface of the stamp such that a pool — held together with surface tension — forms. Then the stamp is placed in the oven, curing the excess ℓPDMS for 40 min until fully cured. After curing, the PDMS can be peeled off the surface as a single unit much as in the standard demolding process. This process is generally easier with thicker PDMS layers, and tends to fail for narrow, deep complementary channels in the 3D-printed stamp. The 3D-printed stamps may also be cleaned by blotting the stamp as much as possible and then rinsing with room-temperature soapy water with a high degree of agitation (note: hot soapy water will speed curing), or with a household cleaner such as GooGone®. Be

aware that GooGone has the tendency to absorb into the mold, causing permanent swelling and surface discoloration and should be rinsed off in hot soapy water as soon as feasible. Because these reasons are less effective than the cure-cleaning method above, we do not recommend them.

4.4 Summary and Future Directions

In this work, we presented a novel method for rapidly manufacturing elastomeric microfluidic devices using 3D-printed transfer molding. Although this process was limited by the resolution and surface roughness of the ProJet™3000 multijet printer, this work was able to reliably produce enclosed channels as narrow as 100 μm. In conjunction with a spin-coated ℓPDMS glass-bonding technique, designed to counteract the effects of the mold's surface roughness, this method can produce single-layer microfluidics more flexibly than those produced in standard soft-lithography fabrication processes. Additionally, the transfer molded microfluidic devices are enhanced by numerous design elements, not limited to: controllably non-rectilinear channels, built-in inlets and outlets, vias and thin membranes, and built-in alignment marks, techniques which may be applied more generally across designs of 3D printers.

However, these techniques are far more versatile than merely replicating existing soft lithography; by incorporating newly developed alignment marks and ℓPDMS stamp-bonding, this process can produce complex multi-sided and multilayer microfluidic devices with ease. Single-step double-sided manufacture (where features are patterned on both sides of the PDMS components) enables features such as microfluidic vias and membrane valves. Microfluidic vias, which allow fluids to flow in three dimensions, reduce geometrical constraints and were fabricated as narrow as 550 μm to hold 20-gauge catheter couples. 350 μm membranes were used to produce microfluidic valves with an actuation pressure of 200 kPa. Furthermore, by combining the double-sided manufacture method with novel custom 3D-printed stamps, rapid assembly of multilayer microfluidic devices was demonstrated. The 3D-printed stamps selectively apply a thin layer of ℓPDMS adhesive — used to compensate for surface roughness — to non-channel areas, preventing the PDMS from clogging the final microfluidic device. Furthermore, because adhesive bonding techniques have been used to bond disparate materials, we expect the stamp printing techniques introduced here to remain relevant past when printers have sufficient resolution to mitigate roughness issues. In total, the 3D-printed transfer molding process allows the rapid fabrication of multi-layered microfluidic devices, combining the flexibility and speed of emerging 3D printing technology with the well-known mechanical and biological properties of PDMS favored by microfluidic researchers.

Acknowledgments

I would like to thank undergraduate students Mitchell T. Srimongkol, Aaron J. Schwartz, William S. Zhuang, Joseph Lin, Dennis R. Tekell, Panitan A. Satimalee, Judy Kim, Caroline Su, Kyungna Kim, and Ariana Moini for their help performing this research. Roseanne Warren helped me prepare an early draft of manuscript from which this chapter is derived, and Xining Zhang helped me collect the SEM images.

Chapter 5

3D-Printed Microfluidic Circuitry*

5.1 Introduction

Historically, scaling fluidic systems has primarily relied on micromachining technologies that were developed for semiconductor and microelectromechanical systems (MEMS) industries [9]. However, techniques reliant on soft-lithography in PDMS have proven inadequate due to the amount of external (*i.e.*, off-chip) equipment that is required to control the microfluidic device [21, 22, 24, 335]. In response, on-chip fluidic control routines [2, 3, 268] have drawn inspiration from integrated electronic circuitry to develop integrated microfluidic circuits (IFCs) capable of autonomous functionalities [47].

A key characteristic of IFCs is that, with the exception of fluidic resistors, fluidic circuit components require both static (*i.e.*, fixed) and dynamic (*i.e.*, deformable or movable) physical elements. This condition further renders IFC construction via extrusion-based approaches impractical. Conversely, a number of SLA-based microfluidic modules — primarily resistor-like components (*e.g.*, fluidic channels, junctions, mixers, and ports) — have been demonstrated for applications including microdroplet generation and cell culture [39, 98, 99]. In particular, researchers have demonstrated IFCs comprised of two-layer fluidic capacitors [148], three-layer fluidic diodes [47, 148] and transistors [25], and five-layer fluidic transistors that enable pressure-based gain [36] for biochemical applications, using standard fabrication techniques.

However, while these standard techniques can create functional microfluidic devices, progress remains hindered by a wide range of limitations inherent to conventional IFC fabrication proto-

* Portions of this chapter are adapted from Ref. 316 and have been reproduced with permission from The Royal Society of Chemistry (RSC).

cols: (i) clean room-based wafer processing is highly cost, time, and labor-intensive, (ii) manual procedures for aligning and assembling multiple layers can be unreliable, and (iii) the intrinsic restriction of monolithicity renders relatively common features of macroscale fluidic components (*e.g.*, circular channels with varying diameter, non-monolithic architectures, etc.) challenging or impossible to recreate in microscale domains [138, 318]. Consequently, the potential for building microfluidic systems by means of additive manufacturing has gained increasing interest in recent years. In particular, multijet modeling (MJM) approaches enable resolutions on the order of tens of microns as well as numerous materials — including sacrificial support materials — to be 3D-printed simultaneously [56, 117].

Combining techniques for microfluidic circuitry [36, 47] with tailored 3D-printed components with specific fluidic properties (*e.g.*, gain) [60], we have developed a class of microfluidic circuit elements including static resistors (Fig. 5.4), as well as dynamic elements such as capacitors (Fig. 5.9), diodes (Fig. 5.11) and transistors (Figs. 5.29 and 5.30), circuit elements which all integrate functionality of a moving piston attached to a mechanical/fluid capacitor. In addition, we develop the theory for analyzing the 3D-printed transistors and for considering which features and structural elements contribute what to the performance of the microfluidic devices.

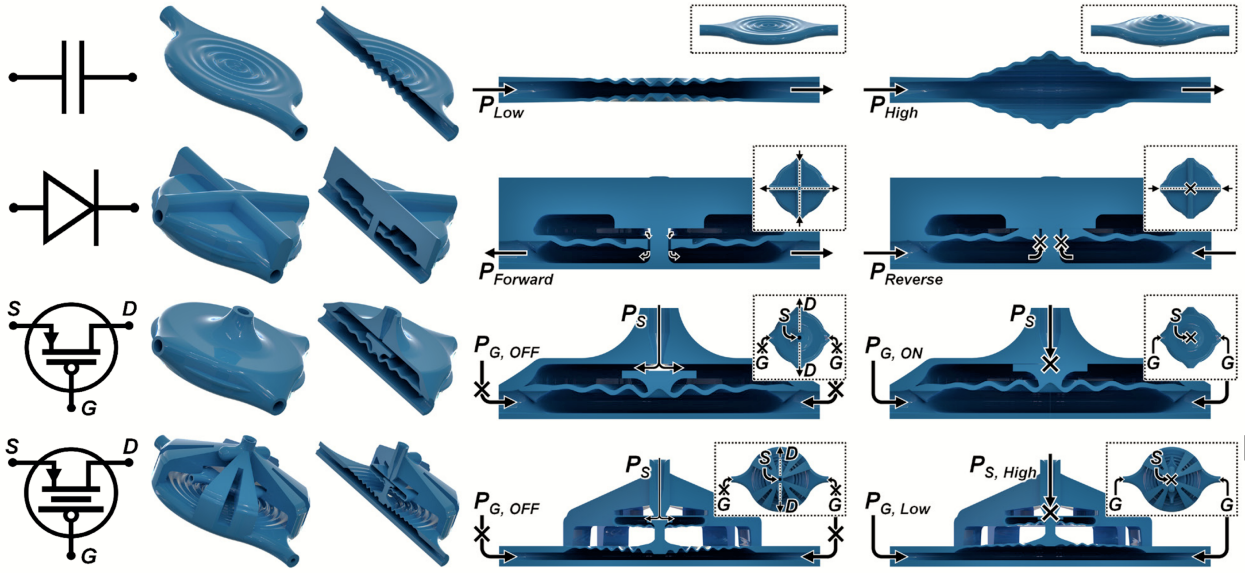


Figure 5.1 Summary of tested 3D-printed microfluidic transistor devices: **(a)** capacitor, **(b)** diode, **(c)** standard NOT-gate transistor, and **(d)** enhanced gain transistor. Adapted from Ref. 316 with permission of the RSC.

5.2 Methods and Materials

5.2.1 3D modeling and theoretical simulations

The 3D fluidic circuit components were designed using SolidWorks (SolidWorks Corp., Waltham, MA), and the conceptual illustrations were rendered using the PhotoView 360 extension in Solidworks. The 3D-printed components were designed with the primary functional component designed as one piece and the female inlet/outlet components designed as another, which were then integrated in Solidworks. The inlet/outlet components were designed to enable interface with male catheter couples (#SP20/12, Instech Laboratories, Plymouth Meeting, PA), which were then connected to external tubing or to other 3D-printed components. We assembled the 3D CAD models of the ports, components, and systems within Solidworks, and exported the assemblies to the STL format — a standard file type for 3D printers [39, 98], including the Projet™3000.

To simulate the performance of the microfluidic components, we imported the CAD models into COMSOL Multiphysics version 4.3a (COMSOL, Inc., Palo Alto, CA) to perform finite element analysis (FEA) simulations. We performed large deformation fluid-structure interaction (FSI) simulations, using a first-order adaptive element mesh to ensure adequate resolution in topologically sensitive regions of large deformations and small gaps. In addition, we designed the input pressure conditions to ensure the simulations would not proceed into configurations that would involve mesh intersection (*e.g.*, the top surface of the transistor piston contacting the source output channel). The termination conditions were determined for individual gate pressures P_G by sweeping the source pressure P_S near the approximate interface pressure and recording the lowest P_S solution that converged. The list of termination pressures conditions (P_S, P_G) were then used as starting points for later parametric sweeps.

We employed the arbitrary Lagrangian —Eulerian (ALE) method to couple the fluid flow Eulerian description with a Lagrangian description of linear-elastic solid deformation. The hydrodynamics equations assuming laminar and incompressible flow were solved using pressure inlet and outlet boundary conditions, while all other boundaries were set to have no-slip conditions. The material properties of the 3D-printed photocurable plastic material, VisiJet M3 Crystal (3D Systems, Rock Hill, SC; $\rho = 1.02 \times 10^3$ kg m^{-3}; $E = 1.46$ GPa), were used to perform all of the theoretical simulations. For the simulations of the 3D fluidic diode and fluidic transistor, we modeled water ($\rho = 10^3$ kg m^{-3}; $\eta = 10^{-3}$ Pa s) as the input fluid. For the 3D fluidic transistor simulations, solid deformation of the 3D-printed material was further determined subject to fluid boundary pressures and an applied pressure boundary load emulating the transistor gate pressure. These assumptions

allowed for a steady-state solution for each parameterized fluid and gate pressure. All simulations collected quasi-steady-state flow data about the 3D-printed circuit components, with a dynamic pressure sweep approximated by collecting results for a range of steady-state results.

5.2.2 Device Fabrication and Cleaning

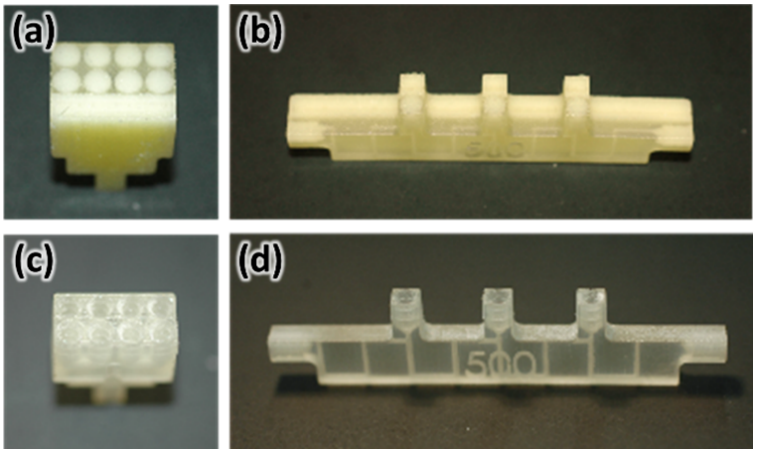


Figure 5.2 Fabrication Process of **(left)** $1 \leftrightarrow 8$ splitter and **(right)** variable resistor. CAD Design is printed on a ProJet™3000 multijet printer. **(a-b)** Printed device is covered with (and all channels filled with) sacrificial wax. **(c-d)** The devices are placed in hot mineral oil to melt remove supporting wax and then are rinsed in soap and water to remove residual oil.

Following the 3D printing process, these components were cleaned to remove the sacrificial support wax, in a process similar that described in Section 4.1.1. Unlike the 3D-printed molds, the 3D-printed fluidic circuit elements were built as fully-enclosed components and therefore a protocol was developed to remove the residual wax support material from the interior of the 3D-printed components as well as from the exterior. Initially, we placed the components in an oven heated to 80°C for ten minutes to remove the bulk of the exterior wax. Next, we immersed the devices in a bath of 100% food grade mineral oil (Bayes 160-2, Lab-Clean, Los Alamitos, CA) at 80°C for three minutes to liquefy the internal wax. Next, hot mineral oil (at 80°C) was forced through the components using a syringe to displace the internal residual wax. A second (*i.e.*, clean) mineral oil rinse was employed to ensure that wax dissolved in the first (*i.e.*, dirty) mineral oil was not redeposited in the channel. Lastly, we used pressurized air to evacuate the remaining mineral oil, and soapy water and dionized (DI) water were flushed through the components to remove residual mineral oil and soap, respectively; early results suggested that residual mineral oil—in devices not cleaned by soap—was causing interfacial stiction within the microfluidic components.

Figure 5.2 shows the cleaning process applied to the 3D-printed microfluidic flow controllers (splitters and variable resistors), which were fabricated similarly to the other ProJet™3000 devices discussed in this chapter. The wax support layer produces one technical limitation to the size of the fluidic channels; since the channels must be cleared of wax using forced pressure, the higher viscosity of the wax ($\nu_{\text{wax}} \sim 10 \times \nu_{\text{water}}$) [336] This figure is only an extrapolation from the information provided by HD Systems; the MSDS cites the S100 wax as "hydroxylated wax" with no further details. The viscosity factor $10\times$ is taken from viscosities of Paraffin wax, which has similar mechanical and chemical properties. requires a correspondingly higher pressure to remove. For example, Figure 5.8 shows a per-port resistance of 43 $\text{kPa}\,\text{s}/\text{mm}^3$, meaning a flow-rate of 1 $\mu\text{L}/\text{s}$ requires 43 kPa for water, and ~ 400 for wax. Moving to 100 µm diameter channels would require a corresponding 2 MPa=20 ATM for the same flow rate. Coupled to the fact that wax adjacent to the epoxy (a) is not completely removed (see Section 4.3.3.3) and (b) has a higher viscosity when melted, and narrower channels become extremely difficult to clear fully.

This cleaning process required that the component designs take into consideration the wax removal process. Symmetrical inlet/outlet holes were placed on each part, facilitating the removal of wax. However, on some devices (*e.g.*, the 3D fluidic diode and transistor designs), these additional ports were superfluous to device functionality and so were sealed using catheter plugs (#SP20/12, Instech) and J-B Weld (J-B Weld Company, Atlanta, Georgia, USA) after the wax was fully removed. The J-B Weld components were mixed and applied to the outlets using a toothpick, after which the components were placed in the oven at 80°C for 15 minutes to fully cure.

5.2.3 General Experimental setup

Pressure was regulated from building air pressure (≈7–8 ATM) through the MAESFLO system (Fluigent, Paris, France) and supplied to the microfluidic components through Tygon microbore tubing (#06420-03, Cole Parmer, Vernon Hills, IL), interfacing the systems via catheter couplers (Instech). Volumetric flow rate was measured using Fluigent FLOWELL microfluidic flow sensor, placed in series with the Sensirion SLI-1000 flow sensor. The flow sensors were located between the microfluidic systems and the waste collection outlet. The Fluigent components were controlled by the Microfluidic Flow Control System (MFCS), which recorded supplied pressure and resulting flow rate data simultaneously. Pressure control routines were written in the scripting language Scite which interfaced with the MAESFLO system. All experiments were conducted under room temperature environment (20–25°C).

5.2.4 Data Analysis and Signal Processing[1]

5.2.4.1 Flow Rate Alignment

Because the Fluigent FLOWELL sensor could only measure flow rates between ± 55 μL/min, a Sensirion SLI-1000 flow rate sensor (for flow rates between ± 1100 μL/min) was also included in series.[2] The FLOWELL sensor required due to its time-synced with the Fluigent pressure control inputs. An alignment program was then written to match the Fluigent pressure data with the Sensirion flow rate data using a loop which compared the Fluigent data with time-shifted Sensirion data. First, because the Fluigent-recorded and the Sensirion-recorded time steps were both irregular and different from each other (0.101 ± 0.028 s and 0.070 ± 0.012 s, respectively), the Sensirion output was linearly interpolated to the Fluigent relative time, given the current loop offset. Next, the unsaturated Fluigent flow-rate data and the interpolated Sensirion data (in the same time range) were compared and the square of the differences was recorded, after which the offset was incremented. The smallest square of differences indicated the optimal alignment offset. The data were then merged to a single csv file, after which analysis was performed.

This method has two data-dependent limitations, both of which are resolved by moving to all-Fluigent flow sensors. (1) Large outliers could disrupt the alignment procedure and required filtering or exclusion. Outliers were especially generated when bubbles moved through the flow sensors, leading to a sudden drop in the recorded pressure; however, since bubbles move through one sensor at a time, these bubble-based outliers were non-alignable. These outliers could potentially be resolved by employing a more robust comparison test. (2) This alignment procedure requires approximately $1-2$ s of non-saturated data recorded by the Fluigent sensor, otherwise the data will not be alignable. This places restrictions on experimental design, forcing pressure cycles that spend sufficient time close to $\Delta P = 0$ to prevent saturation of the flow sensor at $1100\,\mu\mathrm{L\,min}^{-1}$.

5.2.5 Flow Rate Buffering with Microfluidic Resistor

The microfluidic diodes and transistors had low internal microfluidic resistance, which was comparable to the resistance from the tubing and flow rate sensors. Additionally, the Fluigent pressure source had poor response time (1-5 s) for pressures $P \lesssim 10$ kPa, extremely poor response time (5-20 s) for $P \lesssim 2$ kPa, and was only accurate to ± 1 kPa for $P \gtrsim 10$ kPa. Accordingly, when

[1] Quantified experimental results are presented in the text as mean $\pm$ standard deviation.

[2] This problem was not present for the optofluidic experiments due to the purchase of a second Fluigent flow rate sensor which could measure flow rates between ± 1100 μL/min while being synced with the pressure sources.

the driving pressure was high enough for precision control of the system, the flow rate was high enough to saturate the flow rate sensor, as well as to run through stored fluid at an astounding rate.[3] These limitations required two adaptations to the experimental design, particularly for the transistor sweep tests. First, the absolute pressure was not allowed to drop below 2.5 kPa on any sweep, which limited lag between requested pressure and reported pressure. Second, the overall flow rate was buffered by including a 3D-printed variable microfluidic resistor in series with the pressure source. The resistor was placed between the pressure source and the device to be measured to lower capacitive spikes in the device or in the flow sensor (Section B). The resistor had channel diameter 250 μm and flow was limited to between the first and third ports. This added resistance allowed the system to report a measurable flow rates for useful pressures (Section 5.4.0.1).

5.3 Physical and Theoretical Considerations

In this analysis, we will consider the behavior of the 3D-printed *NOT-Gate* transistors through a series of models of increasing accuracy and complexity. We'll use laminar-flow fluid mechanics to analyze the fluid flow past the thin plate, spring dynamics to find the relative position of the valve-piston at various pressures and flow rates, and the hydraulic analogy to put those pieces together. The simplest explicit models (of the form $y = f(x)$) break down when parasitic resistances and flow rates increase, and the simple-spring models fail to predict the simulated behavior at large membrane deflections. In this analysis, we will consider corrections these issues

5.3.1 Radial flow of a Newtonian fluid between parallel disks

To understand the behavior of microfluidic transistors with moving parts, the important case of a radial flow between parallel disks must first be examined. In the 3D-printed microfluidic circuitry discussed here, radial flows occur with regularity whenever a valve-like component is used. These valves consist of a moving piston attached to a radial plate which, when sufficient pressure is applied, block off a central inflow/outflow channel. Although the flow profile associated with the radial valves cannot be exactly solved, at sufficiently low flow rates or narrow piston-channel gaps, the flow behavior can be closely approximated with Creeping Flow (*i.e.*, $Re = 0$) physics.

[3] Until the introduction of the buffer resistor, we would run out of stored liquid before the added gate resistance could take effect.

5.3.1.1 Hydraulic Resistance

Radial flow between two plates at low Reynolds number has been well-studied and is a common example in introductory fluid mechanics textbooks [337, 338]. For flow within a gap of thickness h_* across a pressure drop $P_1 - P_2 \equiv \Delta P_*$, the fluid velocity forms a parabolic profile in the $z-$axis (perpendicular to the plates):

$$u_r = \frac{\Delta P h_*^2}{2\mu r_* \ln(r_2/r_1)} \left(\frac{z_*}{h_*} - \left(\frac{z_*}{h_*} \right)^2 \right) \tag{5.1}$$

and pressure drop and flow rate are related by [337]:

$$Q = \left(\frac{4\pi h_*^3}{3\mu \ln(\frac{r_2}{r_1})} \right) \Delta P \tag{5.2}$$

Rearranging the terms to isolate ΔP, we get

$$\Delta P = \left(\frac{3\mu \ln(\frac{r_2}{r_1})}{4\pi h_*^3} \right) Q, \tag{5.3}$$

which corresponds to the Ohm's Law form $\Delta P = QR_v$, providing

$$R_v = \frac{3\mu \ln(\frac{r_2}{r_1})}{4\pi h_*^3} \tag{5.4}$$

For the microfluidic transistors, h_* is not constant as the piston moves, so this parallel-plate resistance will become the approximation for our variable resistance.

(I) Resistance Non-dimensionalization

From Equation 5.4, the flow rate driven by the pressure differential ΔP is

$$R = \frac{3\mu \ln(\frac{r_2}{r_1})}{4\pi h_*^3}.$$

For a system with a moving piston, R is not constant and instead depends on the gap size h_*^{-3}. The other quantities (μ, r_1, and r_2) *are* static for a given transistor and do not change during operation. Therefore, we define a quantity $r_* = \left(\frac{3\mu \ln(\frac{r_2}{r_1})}{4\pi} \right)$ such that $R(h) = r_* h^{-3}$. Since we will be frequently nondimensionalizing these equations, rewrite h as h_* (where * indicates a dimen-

sion*al* variable and lack of * indicates a dimension*less* variable). We choose h_0 as characteristic value for h_*, the equilibrium (*i.e.*, zero-pressure) spacing between piston and valve seat, allowing us to write $h_* = hh_0$. Thus we get

$$R(h_*) = r_* h_*^{-3} \text{ (Dimensional Form)} \tag{5.5}$$
$$= r_*(h_0 h)^{-3} \tag{5.6}$$
$$= (r_* h_0^{-3}) h^{-3} \tag{5.7}$$
$$= rh^{-3}, \tag{5.8}$$

where

$$r \equiv r_* h_0^{-3} \tag{5.9}$$
$$= \frac{3\mu \ln(\frac{r_2}{r_1})}{4\pi h_0^3}. \tag{5.10}$$

The formulation $R(h) = rh^{-3}$ relocates all dimensional quantities to the coefficient r allowing $h \sim O(1)$.

5.3.1.2 Force Balance

The first critical physical quantity to determine the force balance is the balance of hydrodynamic forces on the moving piston. By integrating the left side of Equation 5.3 we find the distribution of pressure throughout the gap:

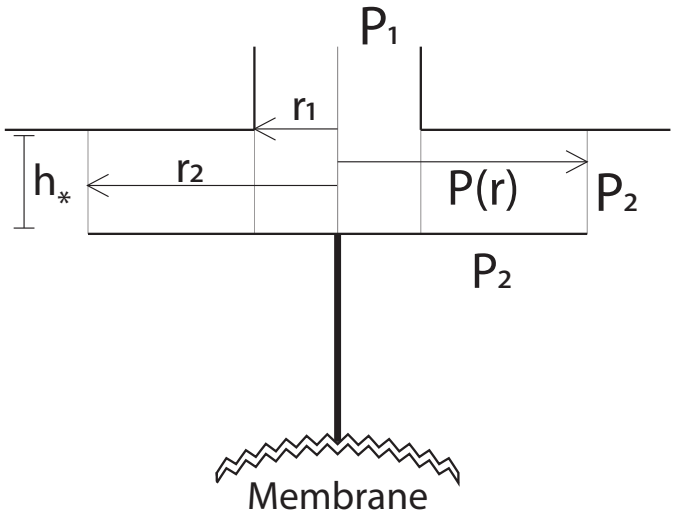
$$\frac{P - P_2}{P_1 - P_2} = \frac{\ln(r/r_2)}{\ln(r_1/r_2)} \tag{5.11}$$

If we rearrange 5.11, we can show the pressure profile as a function of radius r,

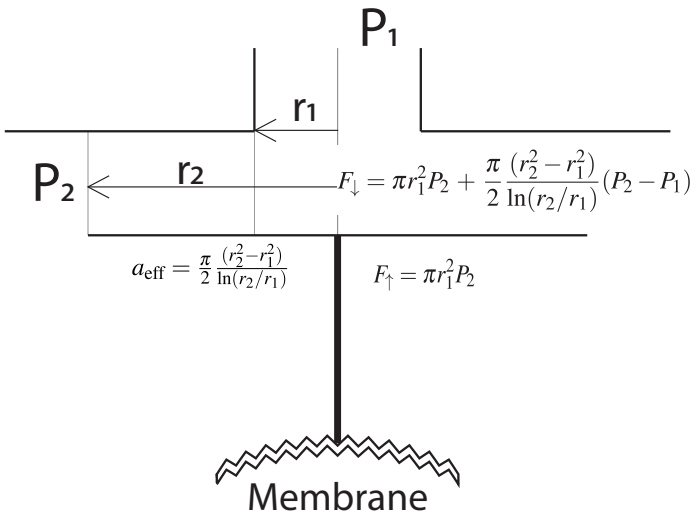
$$P(r) = \Delta P \frac{\ln(r/r_2)}{\ln(r_1/r_2)} + P_2, \tag{5.12}$$

where $\Delta P = P_1 - P_2$. Note that this equation only holds for $r_1 \leq r < r_2$. Otherwise, the pressure is set by the boundary conditions,

$$P(r) = \begin{cases} P_1 & r < r_1 \\ (\Delta P)\frac{\ln(r/r_2)}{\ln(r_1/r_2)} + P_2 & r_1 \leq r < r_2 \\ P_2 & r > r_2. \end{cases} \tag{5.13}$$



(a) Dimensions and pressures for moving piston



(b) Forces acting on piston

Figure 5.3 Setup of narrow gap system with the lower plate moving. Input and output pressures are P_1 and P_2, respectively. The mathematics of the piston behavior are identical for $P_1 > P_2$ (shown) as well as for $P_2 > P_1$ and for cases in which the valve seatmoves but the piston does not.

From Equation 5.12 and $F = \int P(r)\,\mathrm{d}A$, we can find the total outward force from between the parallel plates by integrating from $r = 0$ to $r = r_1$:

$$F = ntP(r)\,\mathrm{d}A \tag{5.14}$$

$$= \int_0^{2\pi} \mathrm{d}\theta \int_0^{r_2} P(r) r\,\mathrm{d}r \tag{5.15}$$

$$= 2\pi \int_0^{r_1} P_1 r\,\mathrm{d}r + 2\pi \int_{r_1}^{r_2} \Delta P \frac{\ln(r/r_2)}{\ln(r_1/r_2)} r\,\mathrm{d}r \tag{5.16}$$

(using rotational symmetry), which provides

$$= \pi r_1^2 P_1 + \frac{2\pi\Delta P}{\ln(r_1/r_2)} \int_{r_1}^{r_2} \ln(\frac{r}{r_2}) r \, \mathrm{d}r. \tag{5.17}$$

Next, using the fact that

$$\int_a^b \ln(u) u \, \mathrm{d}u = \left[\frac{u^2}{2} \ln(u) - \frac{u^2}{4} \right]_a^b, \tag{5.18}$$

Next, we analyze

$$\int_{r_1}^{r_2} \ln(\frac{r}{r_2}) r \, \mathrm{d}r = r_2^2 \int_{r_1/r_2}^{1} \ln(u) u \, \mathrm{d}u, (\text{where } u = r/r_2) \tag{5.19}$$

$$= r_2^2 \left[\frac{u^2}{2} \ln(u) - \frac{u^2}{4} \right]_{(r_1/r_2}^{1} \tag{5.20}$$

$$= r_2^2 \left[\frac{u^2}{2} \left(\ln(u) - \frac{1}{2} \right) \right]_{(r_1/r_2}^{1} \tag{5.21}$$

$$= r_2^2 \left[\frac{1}{2} \left(\ln(1) - \frac{1}{2} \right) - \frac{1}{2} \left(\frac{r_1}{r_2} \right)^2 \left(\ln\left(\frac{r_1}{r_2} \right) - \frac{1}{2} \right) \right] \tag{5.22}$$

$$= -\frac{r_2}{4} + \frac{r_1^2}{4} - \frac{r_1^2}{2} \ln\left(\frac{r_1}{r_2} \right) \tag{5.23}$$

$$= \frac{1}{4}(r_1^2 - r_2^2) - \frac{r_1^2}{2} \ln\left(\frac{r_1}{r_2} \right). \tag{5.24}$$

Combining this with Equation 5.17, we get an expression for the total outward force on the plates,

$$F_\downarrow = \pi r_1^2 P_1 + \frac{2\pi\Delta P}{\ln(r_1/r_2)} \left[\frac{1}{4}(r_1^2 - r_2^2) - \frac{r_1^2}{2} \ln\left(\frac{r_1}{r_2} \right) \right] \quad = \pi r_1^2 P_1 + \frac{\pi}{2} \frac{(r_1^2 - r_2^2)}{\ln(r_1/r_2)} \Delta P - \pi r_1^2 \Delta P. \tag{5.25}$$

By combining terms and rearranging r_1 and r_2 terms, we obtain

$$F_\downarrow = \pi r_1^2 P_2 + \frac{\pi}{2} \frac{(r_2^2 - r_1^2)}{\ln(r_2/r_1)} \Delta P. \tag{5.26}$$

Lastly, if we have a setup with a moving lower plate acting as a piston as in Figure 5.3, where the bottom side of the piston is acted on by the uniform pressure P_2 producing a total upward force

$F_\uparrow = \pi r_2^2 P_2$, the total downward force on the piston

$$F_{\text{tot}} = F_\downarrow - F_\uparrow \tag{5.27}$$

$$= \pi r_1^2 P_2 + \frac{\pi}{2}\frac{(r_2^2 - r_1^2)}{\ln(r_2/r_1)}\Delta P - \pi r_2^2 P_2 \tag{5.28}$$

$$= \frac{\pi}{2}\frac{(r_2^2 - r_1^2)}{\ln(r_2/r_1)}\Delta P \tag{5.29}$$

$$= a_{\text{eff}}\Delta P \tag{5.30}$$

where the effective piston area

$$a_{\text{eff}} \equiv \frac{\pi}{2}\frac{(r_2^2 - r_1^2)}{\ln(r_2/r_1)}. \tag{5.31}$$

Critically, $F_{\text{tot}} = a_{\text{eff}}\Delta P$ holds both when the piston plate is wider than the stationary plate and when the directions of flow are reversed, provided F is defined in the same direction as the pressure gradient ΔP (Fig. 5.3). Equation 5.30 will be essential later when we consider the balance of forces inside the 3D-printed microfluidic circuitry.

Aside 5.1: Relative magnitude of a_{eff}

To compare the relative sizes of πr_1^2, a_{eff}, and πr_2^2, we rewrite r_2 in terms of r_1, choosing $r_2 = f r_1$, where $f \geq 1$, and then divide by the common factor of πr_1^2:

$$\pi r_1^2 \quad \stackrel{?}{=} \quad \frac{\pi}{2}\frac{(r_2^2 - r_1^2)}{\ln(r_2/r_1)} \quad \stackrel{?}{=} \quad \pi r_2^2 \tag{5.32}$$

$$\pi r_1^2 \quad \stackrel{?}{=} \quad \frac{\pi r_1^2}{2}\frac{(f^2 - 1)}{\ln(f)} \quad \stackrel{?}{=} \quad \pi r_1^2 f^2 \tag{5.33}$$

$$1 \quad \stackrel{?}{=} \quad \frac{1}{2}\frac{(f^2 - 1)}{\ln(f)} \quad \stackrel{?}{=} \quad f^2. \tag{5.34}$$

Noting that $\lim_{f\to 1}\frac{1}{2}\frac{(f^2-1)}{\ln(f)} = 1$, the ordering is trivial for $f \geq 1$:

$$1 \quad \leq \quad \frac{1}{2}\frac{(f^2 - 1)}{\ln(f)} \quad \leq \quad f^2, \tag{5.35}$$

This demonstrates the final ordering of the relative piston areas:

$$\pi r_1^2 \quad \leq \quad a_{\text{eff}} \quad \leq \quad \pi r_2^2 \tag{5.36}$$

with equality holding strictly for the case of $f = 1$ (*i.e.*, $r_1 = r_2$).

5.3.1.3 Piston Closure

Due to microscale roughness, the microfluidic pistons do not close perfectly tightly as soon as the piston plate makes contact with the **valve seat**. Additionally, there is a restoring force pushing the piston away from the valve seat that is not totally binary (*i.e.*, 0 for $h > 0$ and equal to applied force for $h = 0$). Since both phenomena are related, we can model them both by introducing a piston restoring force $F_{\text{rest}} = F_{\text{rest}}(h)$ that grows as the gap between the Piston and the valve seat approaches 0 and is directed in opposition to the closing force.

The simplest repulsive force that meets these requirements is a simple power law,

$$F_{\text{rest}}(h_*) = m_* h_*^{-\beta}, \tag{5.37}$$

where $m_* \geq 0$ is a positive coefficient illustrating the relative magnitude of the restoring effect, and $\beta > 0$ is the power law behavior of the repulsive force. Renormalizing, we get

$$F_{\text{rest}}(h) = m h^{-\beta}, \tag{5.38}$$

where $m = m_* h_0^{-\beta}$. Like r in $R(h) = rh^{-3}$ above, the coefficient m in $F_{\text{rest}}(h) = mh^{-\beta}$ has dimensions of [Force].

As we will see later, the asymptotic form of the valve-closing flow rate $Q(F)$ (*i.e.*, flow rate $Q(P)$ parametrized by closing force F) depends on the value of β. As the force driving the piston against the upper $F_{\uparrow} \to \infty$,

$$Q(P; F \to \infty) \sim \begin{cases} 0 & \beta < 3 \\ \text{const} & \beta = 3 \\ \infty & \beta > 3. \end{cases} \tag{5.39}$$

Phenomenologically, we observe Case II; that the valve never fully closes. Thus we will generally consider $\beta = 3$ for the purposes of subsequent analyses. The asymptotic implications of this will be investigated in Section 5.6.2.4.

Proper buffering of fluid flows is critical in microfluidic experiments when using sensitive apparatus. However, pressure-based flow controls with poor pressure resolution (*i.e.*,large pressure steps) may cause the pressure and flow rate through the system to reach unacceptably high levels. The standard option for on-demand microfluidic devices has long been device fabrication using soft lithography [10, 24]. However, the necessarily planar structures of those devices present numerous limitations [290], as does the relative fragility of the PDMS-glass bonding process.

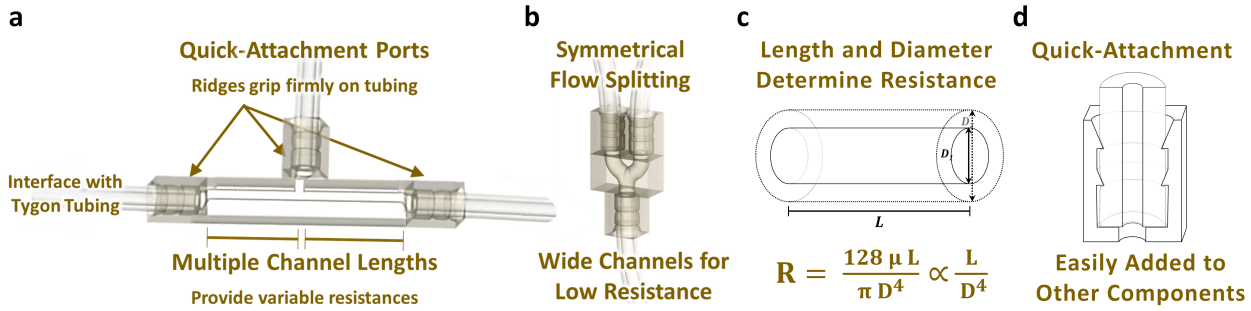


Figure 5.4 Conceptual diagrams depicting the major features of the 3D-printed microfluidic components (resistor, quick-attachment, and splitter). **(a)** Variable resistors allow researchers to regulate fluid flow. The availability of multiple fluid path lengths in the resistors allows a single device to be tuned to provide an appropriate resistance. **(b)** Flow splitters allow for flows to be split or recombined as desired without costly flow control equipment. **(c)** Diameter and path length of the fluidic channel determine overall fluidic resistance. **(d)** Ridges in the quick attachment ports grip tubing. These ports are easily added to other microfluidic components.

As an alternative to soft lithography (with its inherent design limitations) and to purchasing new active machinery (which can be prohibitively expensive), we introduce 3D-printed passive flow controllers which can be designed and printed on-demand to desired specifications. First we demonstrate the manufacture technique used to produce microfluidic devices from the ProJet™3000 3D multijet printer. Next, we present 3D-printed splitters which can split (or recombine) two or more fluid flows from a single input (to a single output) without significant input impedance, as well as the quick-attachment ports which directly connect the splitters to external tubing. Finally, we demonstrate a method of producing 3D-printed variable fluidic resistors to buffer fluid flows from other microfluidic equipment. Because 3D-printed parts need not be limited to standard component sizes, this method provides significant flexibility to laboratory workers hoping to control or redirect microfluidic flows in laboratory settings.

5.4 3D-Printed Microfluidic Resistors and Flow Controllers

In microfluidics research, it is often desirable to use as few dynamic flow controllers as possible; because dynamic flow controls are frequently expensive and require computerized interfaces, purely passive methods that affect the direction, amount, and branching of the fluid flow may be preferred. A rigid microfluidic channel behaves like a fluidic resistor under the hydrodynamic analogy (see 5.4.0.1). As in electronic systems, while using purely resistive electronics has its limits, branching of flows can still be well controlled if proper impedance matching is used. For example, if a user wants equal fluid flow through multiple channels actuated by the same pressure, the hydrodynamic resistance in each channel must be equal. By 3D printing fluidic resistors in

a variety of resistances (including variable resistors), we maintain a store of resistors with which to perform impedance matching, and by 3D printing flow splitters, we can use a single pressure source to actuate multiple channels (Fig. 5.4).

5.4.0.1 Hydrodynamic Resistance

Hydrodynamic resistance is a measure of a system's opposition to fluid flow and is analogous to electronic resistance, which measures opposition to electronic flow. In a microfluidic system exhibiting laminar flow profiles, fluid flows are generally free of inertial effects (*e.g.*,turbulence) which would otherwise create inductance effects. Additionally, a rigid body without flexible components (*e.g.*,our 3D-printed variable resistors) is free of substantial capacitance effects. Thus, the 3D-printed variable resistors behave like a hydrodynamic conductor with a linear relationship between flow rate (Q) and pressure (P).

Unidirectional laminar flow through a circular channel—at low enough Reynolds numbers that turbulent effects are negligible—is governed by the Hagan-Poiseuille Equation [49],

$$\Delta P = \frac{128 \mu L Q}{\pi d^4} \tag{5.40}$$

where μ is the kinematic viscosity, L is the length of the channel, and d is the diameter of the channel. From this, we see that the resistance R is linearly proportional to channel length L and inversely proportional to channel diameter d to the fourth power, implying that resistance is highly sensitive to channel diameter.

Hence, we have designed these individual variable resistors to utilize multiple different channel path lengths L to provide up to four different resistances in a single device (*e.g.*,L, $2L$, $3L$, and $4L$) by controlling which input/output ports are utilized (Fig. 5.6). By varying diameter d between variable resistors, we are able to create a set of resistors with a wide range of resistances. Intermediate resistances can be obtained within an individual variable resistor by using three or more individual ports in parallel, or among two or more resistors connected in series or parallel. Because our 3D-printed material is rigid (and therefore free of capacitive effects) and the channels are sufficiently small (ensuring laminar inductance-less flows), we can determine the hydrodynamic resistance by sweeping P and determining the slope of the measured QP curve, which is analogous to an electronic IV curve.

5.4.0.2 Quick-attachment Ports

Another common difficulty in using 3D-printed microfluidic components has been attaching the components to external tubing without leakage. Sochol *et al.* rinted components which connected to 20-Gauge tubing interconnects, which in turn connected to the external tubing [316]. However, this interconnect-based method is prone to leakage, and the need for several connectors per device can lead to a dramatic increase in cost. In this work, we improve over this existing method by printing features which can directly attach to 20-gauge tubing, eliminating the intermediate components. Although the surface of the 3D-printed object is rough at a scale of 20 µm the deformability of the tubing and the ridges of the interconnect allow for a tight seal.

5.4.0.3 3D-Printed Flow Splitters

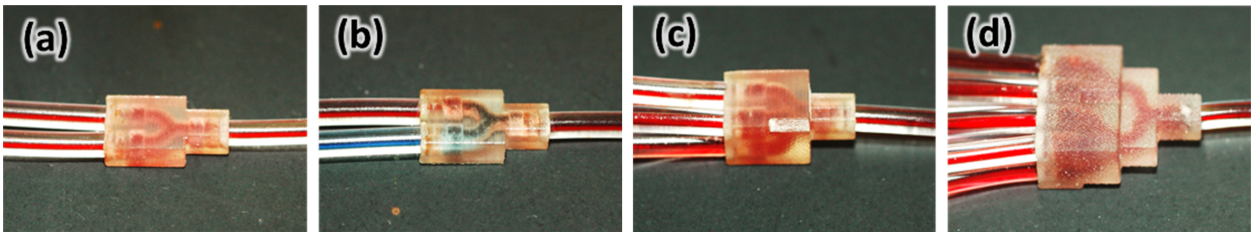


Figure 5.5 3D-printed fluidic splitters in various flow configurations. **(a)** $1 \leftrightarrow 2$ device in recombination combination. Note the fluid mixing in the outflow tube (bottom) **(b)** $1 \leftrightarrow 2$ device in splitting configuration. **(c)** $1 \leftrightarrow 4$ device in splitting configuration. **(d)** $1 \leftrightarrow 8$ device in splitting configuration.

By printing several quick-attachment ports on one device, we are able to 3D-print fluidic splitters which can take one fluid flow and split it into any desired number of outputs, or conversely, combine any number of inputs into a single output. These splitters allow researchers dramatically increased flexibility in microfluidic research by enabling on-demand production of any desired attachment and flow splitting configuration, some of which may not be available commercially. In Figure 5.5, we demonstrate three splitter ($1 \leftrightarrow 2$, $1 \leftrightarrow 4$, $1 \leftrightarrow 8$) designs in flow-splitting/recombination configurations, showing the versatility of the attachment ports when integrated into a splitting geometry. Due to the symmetries within the three splitters, the fluidic resistances of each output channel are equal, meaning the splitters themselves do not appreciably redirect fluid flow within the device.

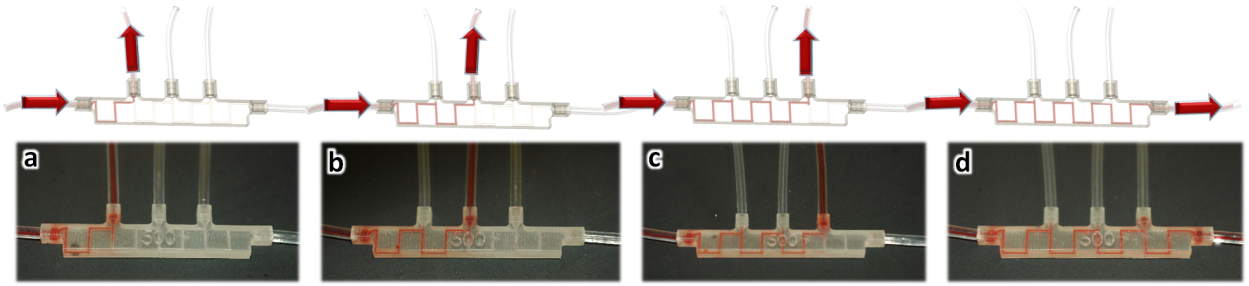


Figure 5.6 Fluid Flow through a single 3D-Printed Variable Resistor with $d = 500$ µm, conceptual *(Top)* and photographs *(Bottom)* . Because resistance is proportional to path length L, more ports (*i.e.*,longer paths) have higher resistances. Resistances are shown from lowest to highest: **(a)** one port, **(b)** two ports, **(c)** three ports, and **(d)** four ports. Other resistances can be obtained by utilizing three or more individual ports in parallel or two or more resistors in series/parallel.

5.4.0.4 3D-Printed Variable Microfluidic Resistors

Lab-ready microfluidic devices can be readily constructed using quick-attachment ports in consort with a 3D-printed channel. In particular, by varying the length and diameter of the channel, we are able to create microfluidic resistors which can buffer fluid flows in a laboratory setting. Additionally, by constructing microfluidic resistors with multiple inlets and outlets, we can to generate *variable resistors* which are capable of exhibiting several different resistances in a single device.

5.4.0.5 Simulation

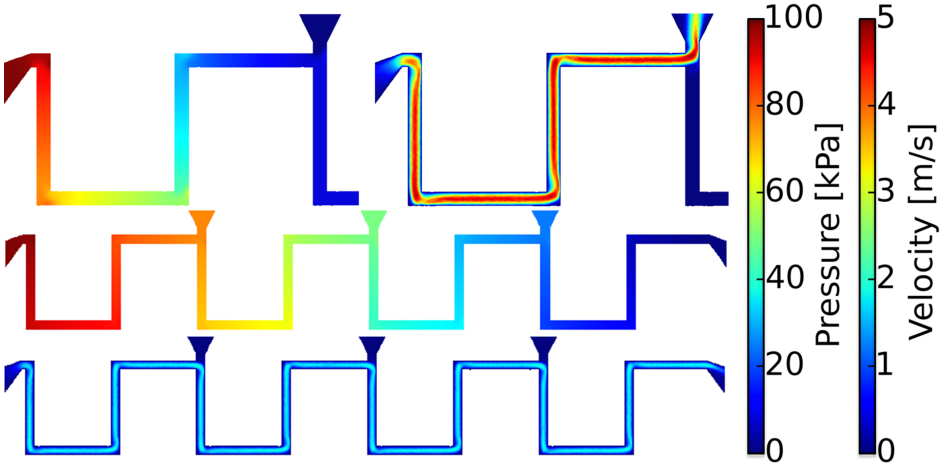
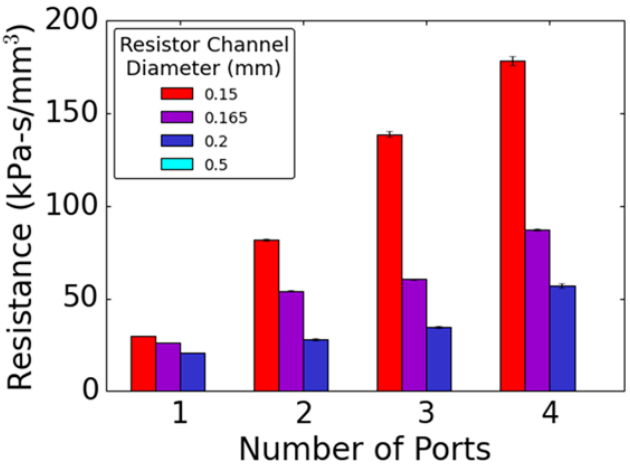


Figure 5.7 2D bisecting slices showing inertial Poiseuille flow structure in the COMSOL FEA simulations for the 500 µm resistor. Pressure **(a)** and Fluid Velocity **(b)** are shown for the lowest resistance configuration (*i.e.*, one port); Pressure **(c)** and Fluid Velocity **(d)** of the highest resistance configuration (*i.e.*, four ports).

Fully 3D Finite Element Analysis computation was used to supplement experimental data of both 200 µm nd 500 µm esistors. Non-compliant steady laminar flow simulations were performed on the

imported resistor pipe geometries constructed in an external 3D CAD software. The final steady-state flow was determined using a sparse matrix direct solver. The set of hydrodynamics equations assuming laminar and incompressible flow were solved using pressure inlet and outlet boundary conditions. Each outlet defined as *closed* was instead prescribed a zero-viscous stress boundary to approximate an air-fluid interface at the boundary.

5.4.1 Experimental Setup and Results



Channel Diameter (mm)	Per-port Resistance (kPa-s/mm³)
0.15	43.056 ± 4.62
0.165	24.031 ± 2.93
0.2	14.862 ± 2.94
0.5	0.056 ± 0.02

Variable Resistor Per-Port Resistances

Figure 5.8 Experimental resistance data for variable resistors **(a)** with four different channel diameters and four different channel lengths. Resistance data was determined by performing three Q-P sweeps and then determining the slope (i.e., the fluid resistance) through linear regression. These individual resistances are then averaged. The relative increase in resistance per port is roughly linear; deviations depend on factors such as degree of wax removal and printer accuracy. **(b)** Tabulated values and standard deviations for average resistance per port for several variable resistors.

To measure the hydrodynamic resistance of the 3D-printed variable resistors on a port-by-port basis, we first plugged three of the five resistor ports and then connected the remaining two ports to a pressure generator (Fluigent MFCS) and through the Fluigent and Sensirion flow-rate sensors to record the *QP* response. After each *P* sweep was completed, one of the plugged ports was swapped with one of the active ports until the experiment had been performed for all four resistor lengths (*i.e.*,between the first port and the remaining four). The results are summarized in Figure 5.8. As expected, the resistance is approximately linear in number of ports. Figure 5.8b shows the average per-port hydrodynamic resistance, which varies from 43.056 ± 4.62 kPa $-$ s mm^{-3} for 150 µm channels to 0.056 ± 0.02 kPa $-$ s mm^{-3} for 500 µm channels. Because these 3D-printed flow controllers can be produced on-demand, this method presents a versatile alternative to purchasing costly additional equipment for microfluidics research.

These results demonstrate for the first time the use of 3D Multijet Printing to fabricate variable microfluidic resistors as flow controllers to buffer microfluidic fluid flows. Together with a 3D-printed quick-attachment port, these resistors can be produced on demand and to desired specifications for a wide range of applications. Although variable resistors offer more flexibility *per-unit*, single-resistor units have also been produced and can be used to provide a fluidic analogy of a "resistor drawer". Subsequent work described in this chapter utilizes 2-port 250 μm variable resistors to buffer fluid flows in measurements for the 3D-printed diodes and transistors.

5.5 3D-Printed Microfluidic Capacitor

Properly emulating electronic diodes and transistors in the hydrodynamic analogy necessitated spring-based components to allow 3D-printed components to move and return to a default position. However, early work showed that adapting bent beam- and coil-based springs was not practical for the Projet™3000 due to the difficulty in cleaning these components adequately. Therefore, we turned to a membrane-based capacitor system as the moving part in our 3D-printed microfluidic devices. These planar membranes proved much easier to clean than coiled springs, and were capable of relatively large break-free displacement, making them ideal for inclusion in other components; capacitor-like structures (Fig. 5.9a-c) facilitated the fabrication of components such as transistors by using this moving membrane to open and shut valves, emulating MOSFET-like functionality where the gate was fully isolated from the source-drain flow.[4]

Because planar (*i.e.*, flat) membranes had relatively low displacements, we investigated whether corrugating the structure would reduce the effective spring constant of the membrane, allowing the corrugated capacitors to move farther—of use in valving-based applications—and to store more fluid—of use in microfluidic storage mechanisms. Our corrugated structure used a damped sinusoidal radial design which reduced the second derivative when the capacitor merged with the surrounding walls; this damping would reduced stress-concentration and led to fewer broken capacitors. When used as capacitors (Fig. 5.9b,c), the membrane-based structures deformed outward in response to a pressure differential, storing volumes of fluid within the component. When pressure was reduced, the stored energy in the membrane forced the fluid back out. Therefore, the component stored fluid under pressure, analogously to electrical capacitance:

$$dV = C\,dP$$

[4] Due to the lack of quantum effects in microfluidics, a bipolar junction transistor-like structure was impossible

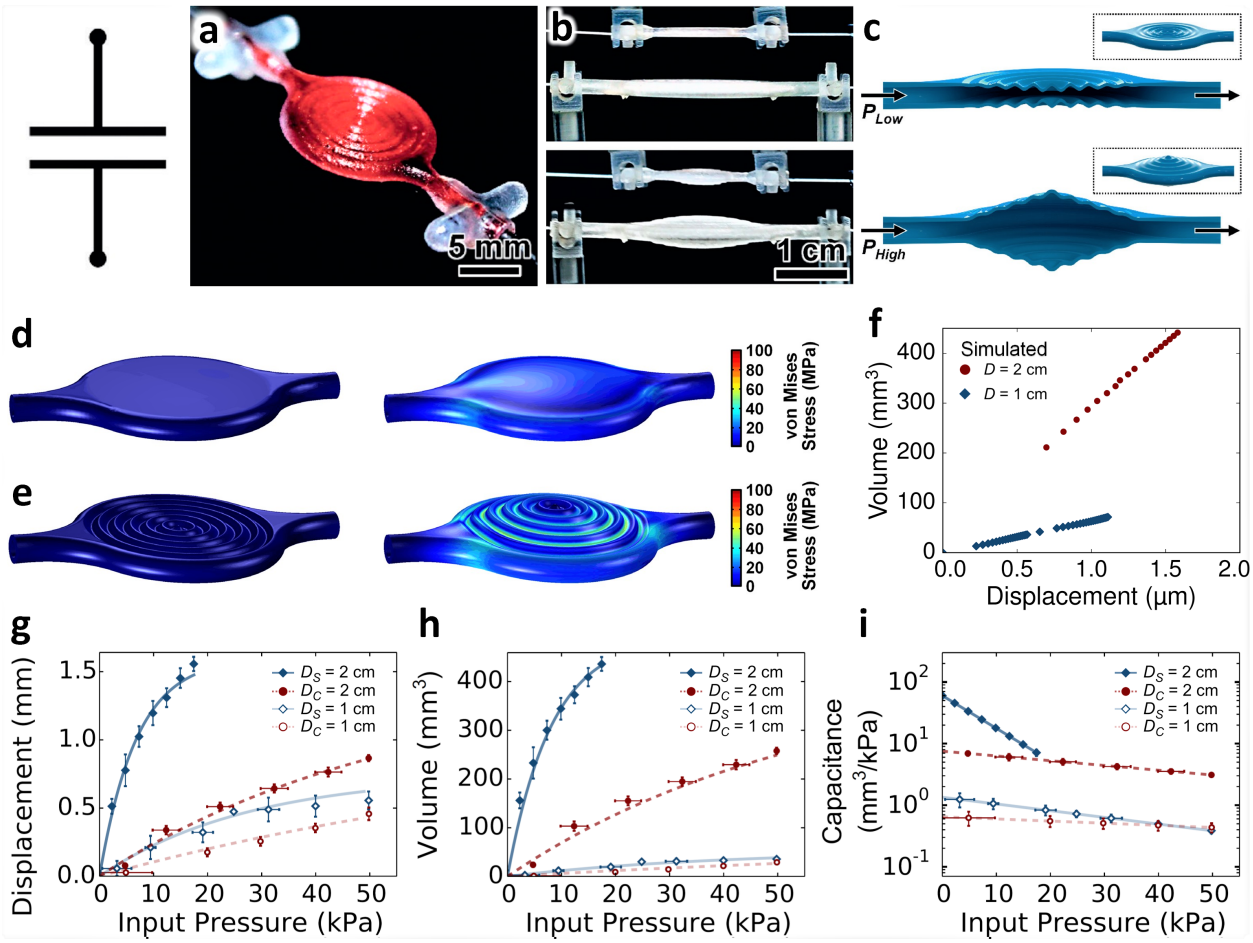


Figure 5.9 Experimental and simulation results from the 3D-printed microfluidic capacitor. **(a)** Photograph of 3D-printed capacitor with red food dye. Photographic **(b)** and conceptual **(c)** side-view of capacitor *(top)* in resting position and *(bottom)* inflated under pressure. **(d,e)** COMSOL Multiphysics simulations of microfluidic capacitors ((**d**) planar and **(e)** sinusoidal) under in *(left)* resting position and *(right)* inflated under pressure. **(f)** Simulated results of capacitor volume change versus displacement, used in extrapolating experimental capacitance and volume change from measured displacement. **(g)** Experimental displacement measurements, **(h)** derived volume versus pressure, and **(i)** derived capacitance measurements for four 3D-printed microfluidic capacitors (planar and sinusoidal, 1 cm and 2 cm). Error bars in the x and y directions denote pressure standard deviation and displacement standard error of measurement, respectively. Subfigures **(a-d,g)** adapted from Ref. 316 with permission of the RSC.

where dV is change in volume, dP is change in pressure, and C is the microfluidic capacitance.

5.5.1 Capacitor Simulations

To examine the mechanical stresses in the microfluidic capacitors, we performed COMSOL Multiphysics simulations for 3D-printed fluidic capacitors (both 1 and 2 cm in diameter) with diaphragms designed with: (i) a damped sinusoidal cross-section, (ii) a planar cross-section, simulating the capacitors with an elastic modulus $E = 50$ MPa, or $1/20$ the value reported by HD Systems [339]. The simulation results revealed four primary design results (Fig. 5.9d-f). Firstly,

the 2 cm capacitors experienced a larger displacement and were able to hold a higher volume of fluid than the 1 cm capacitors. They also had an accordingly higher capacitance. As expected, displacement changes were7 approximately doubled and volumetric changes were approximately cubed. Secondly, the sinusoidal membraned capacitors were able to hold a higher volume of fluid than the planar membraned capacitors at the same pressure, given the effective reduction in spring-constant of the damped membrane. Thirdly, although the sinusoidal capacitors experienced a higher displacement and were able to hold more fluid at a given pressure, the displacement-volume relationship was similar for damped and undamped capacitors. Thus, for extrapolation of the experimental capacitors, we used the undamped membrane simulation results to determine volumetric changes. Lastly, the simulation results revealed that the planar capacitors had somewhat lower magnitudes of maximum von Mises stresses in response to applied pressure, with the stresses focused at peaks and troughs of the damped sinusoidal wave.

5.5.2 Experimental Capacitor Results

To measure the performance of the physical 3D-printed fluidic capacitors (in planar and damped-sinusoidal membrane structure), we connected the input port to a Fluigent pressure source and sealed the outlet port using a catheter plug (Instech) and J-B Weld. Using the MFCS software, we incrementally increased the pressure supplied to the capacitor. Due to fluctuations in the MAES-FLO system, we recorded the supplied pressure for 30 seconds after pressure had stabilized, providing the reported pressure average and standard deviation. At each pressure, the diameter of the fluidic capacitors was measured using calipers to determined the pressure-based deformation. Displacement standard error of measurement was 1 μm — the resolution of the calipers.

The experimental capacitance was measured through a two-step extrapolation procedure by merging experimental displacement results with simulation results because we could not accurately measure the volume changes directly. First, the simulated displacement and volume change of each capacitor were plotted against each other, parametrized by the input pressure; although different membrane designs (same diameter) and elastic moduli had different volume or displacements for a given pressure, for each diameter, these changes were not significant when the displacement-volume curve was plotted. Next, we combined the *measured* displacement with the *simulated* displacement-volume curves to extrapolate the experimental volume change. We fitted the pressure-volume curve using an exponential fit, and used the fit to determine the capacitance, which was the slope of the pressure-volume curve at a given volume. Empirically, an exponential curve was the

best fitting function, and had some basis in theory, derived from the behavior of a membrane that does not want to stretch past a displacement x_0, with a spring constant $k \propto 1/\left(1-\frac{x}{x_0}\right)$ (see 5.2).[5]

Aside 5.2: Basic Asymptotic Spring

If we consider a spring that starts as a linear spring at $x = x_0 \equiv 0$ but becomes increasingly stiff until it reaches a maximum length X, we can apply a basic spring inconstant[6] of $k(x) = k_0/\left(1-\frac{x}{X}\right)$, which approaches infinity as $x \to X$ The non-linear spring equation becomes

$$dF = k(x)\,\mathrm{d}x \tag{5.41}$$

$$dF = k_0\,\mathrm{d}x/\left(1-\frac{x}{X}\right) \tag{5.42}$$

$$\implies F(x) = -k_0 X \log\left(1-\frac{x}{X}\right), \tag{5.43}$$

where F is the upward force on the membrane.[7] From here, we make the (simplistic) assumption that the $F = PA$ where A is the area of the membrane. We also use the results of the simulations, that $V \propto x$ and choose an effective area (a_{eff}) as the coefficient. This gives $V = a_{\text{eff}}\,x$ and $V_0 \equiv a_{\text{eff}}\,X$, giving

$$\frac{PA}{k_0 X} = -\log\left(1-\frac{V}{V_0}\right) \tag{5.44}$$

$$\implies V(P) = V_0\left(1-e^{-\frac{PA}{k_0 X}}\right). \tag{5.45}$$

From this analysis, we see that a decaying exponential fit is reasonable, of the form $V(P) = V_0\left(1-e^{-P/P_0}\right)$, where V_0 and P_0 are the fitting coefficients. We also see that the hydrodynamic capacitance $C(P)$ under this model (derived from $C(P) = \frac{\mathrm{d}V}{\mathrm{d}P}$) would take the form

$$C(P) = \frac{V_0}{P_0}e^{-\frac{P}{P_0}}, \tag{5.46}$$

explaining the linearity of the capacitance plot (Figure 5.9i) when capacitance was shown on a log axis (*i.e.*, $\log C \propto -P$).

[5] An exponential fit was the simplest monotonically increasing fitting function with a negative second derivative; whereas spline fitting merely amplified the noise in the capacitance measurement data.

[6] (Pun intended)

[7] This spring relation behaves like a linear spring for small displacements in x: $F(x)\ -k_0 x + O(()x^2)$

As expected, increasing the diaphragm diameter drastically improved the diaphragm displacement, volume change, and capacitive performance. Additionally, the sinusoidal membranes were capable of storing much more fluid at each pressure, and accordingly demonstrated a higher capacitance (Fig. 5.9g-i). However, the sinusoidal membrane-based capacitors broke at substantial lower input pressures than the planar membrane-based capacitors (Fig. 5.10): 100 kPa versus 150 kPa for the 1 cm capacitors and 20 kPa versus 120 kPa for the 2 cm capacitors.[8]

Thus, for cases in which both diaphragm movement and fluidic storage capacity are critical requirements, these results suggest that the damped sinusoidal cross-sectional design is best suited among the designs tested. However, the sinusoidal design is both more fragile and harder to clean, and therefore the planar structure should be considered in cases where membrane integrity is of highest concern.

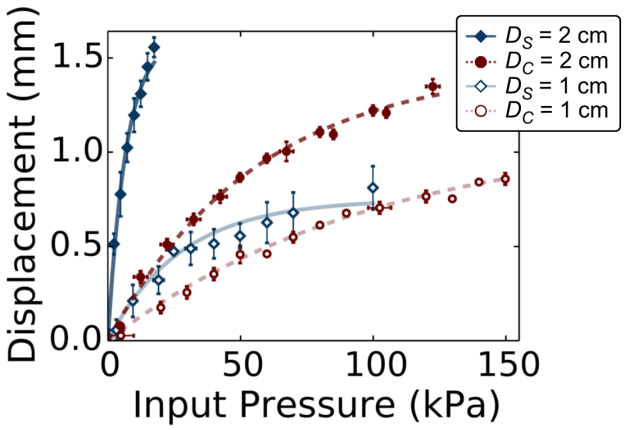


Figure 5.10 Experimental results of 3D-printed capacitor, with displacement plotted until the capacitor broke.

5.6 3D-Printed Microfluidic Diode

We next adapted the membrane-based capacitor into a microfluidic diode (*i.e.*, a passive fluid flow rectifier). We designed a circular aperture in the center of the membrane with which allowed fluid flow from the upper to the lower chamber (Fig. 5.11b). We formed a rigid annulus around the aperture and placed a plate close to the membrane in the upper chamber but farther away in the lower chamber. Thus, the membrane could freely deflect downward when a positive pressure gradient was applied (top-to-bottom) but would press against the plate when a negative pressure gradient was applied (bottom-to-top). The contact between the annulus and the top plate would

[8] We suspect the lower breakage pressure for larger diameter capacitors to be related to the higher frequency for 3D printer-induced defects in the capacitor structure.

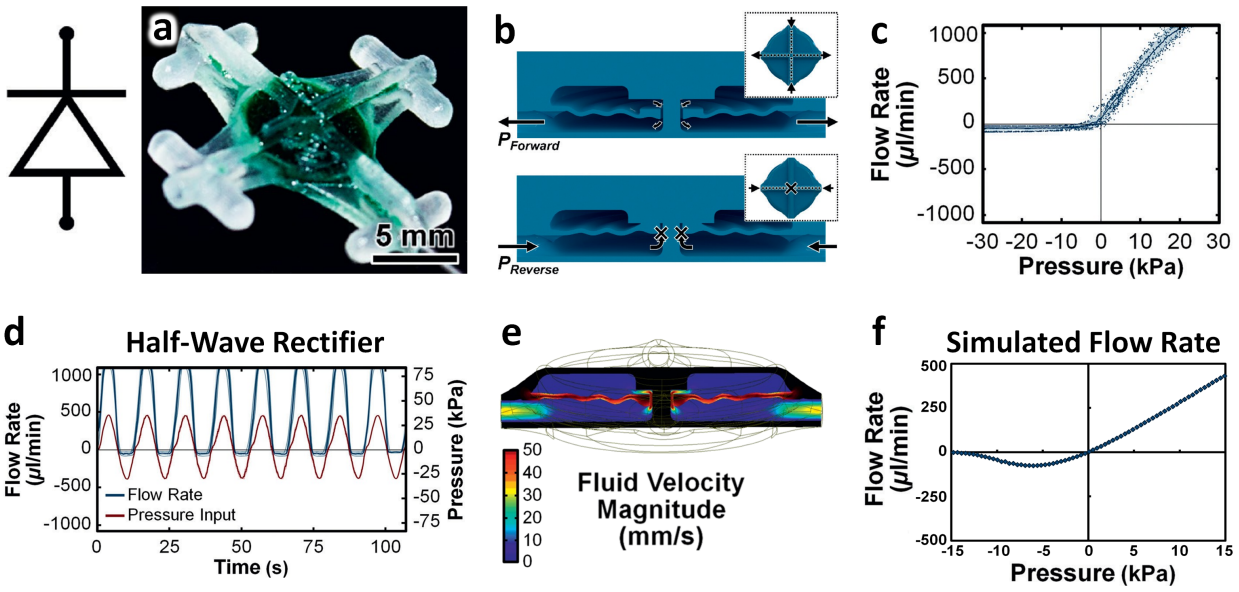


Figure 5.11 Experimental and simulation results from the 3D-printed microfluidic diode. **(a)** Photograph of diode filled with green food dye. The diode has four inlets/outlets for cleaning purposes; opposite inlets/outlets are linked to the same chamber and one is blocked during testing. **(b)** Conceptual image of the diode and membrane deflection under *(top)* forward and *(bottom)* reverse flow. **(c)** Experimental *QP* diagram showing the flow rates resulting from three different diodes under a series of forward and reverse pressure sweeps. **(d)** Time-series plot of the diode (in half-wave rectifier configuration) showing the applied pressure differential and resulting flow rates, as well as the difference between forward and backward pressure gradients. **(e,f)** COMSOL Multiphysics simulation of the 3D-printed diode: **(e)** flow velocity within the diode is maximal in the small regions near the outlets and when flowing around the membrane, and **(f)** flow rate (determined by integration of flow velocity across the outlets) for a range of pressures. Note the qualitative agreement with **(c)** . Error bands denote standard deviation; negative pressures/flow rates denote positive pressure/flow in the reverse direction. Adapted from Ref. 316 with permission of the RSC.

then obstruct fluid flow. The narrow column between the top and bottom plates, running through the center of the aperture, was included for mechanical rigidity, preventing the top plate from bowing outward under a high internal pressure supply.

5.6.1 Experimental Setup

To experimentally test the diode behavior, the diode inlet and outlet were connected to the *forward* and *backward* pressure sources, respectively, and the remaining two cleaning ports were sealed with catheter plugs and J-B Weld. To monitor the direction and magnitude of fluid flow, we connected the Fluigent and Sensirion flow rate sensors in series with the flow path, with the Sensirion sensor placed adjacent to the bottom channel port of the fluidic diode. The two pressure sources were changed in opposition (*i.e.*, 180° out of phase). Using two independent pressure sources enabled a larger pressure differential to form using smaller pressure increments on each pressure source. Additionally, using two opposing pressure sources at the inlet and outlet allowed us to

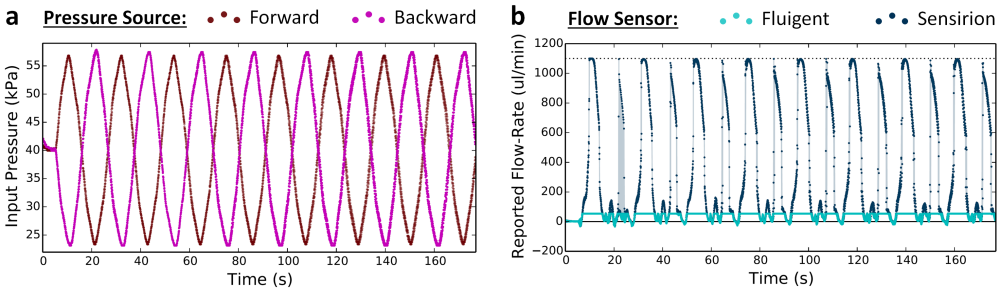


Figure 5.12 Pressure and flow-rate outputs from time sweep of 3D-printed microfluidic diode. **(a)** The diode inlet and outlet were connected to the *forward* and *backward* pressure sources, respectively, which were swept in opposition in an approximation of a sine wave, allowing a larger pressure differential to form using smaller pressure increments on each pressure source. **(b)** Aligned flow rate outputs from the Fluigent and Sensirion flow rate sensors, connected in series.

experience negative flow polarity through the diode. In the forward pressure differential case (*i.e.*, forward flow), the pressure corresponding to the inlet channel was greater, resulting in (forward) flow from the inlet to the outlet. In contrast, in the reverse pressure differential case (*i.e.*, reverse flow), the pressure corresponding to the output channel was greater, resulting in (backward) flow from the outlet to the inlet (albeit partially blocked by the diode's internal components).

To test the half-wave rectifier functionality for the 3D-printed fluidic diode, we wrote a pressure control script in Scite designed to apply repeated sinusoidal pressure sweeps with a total pressure range of 60 kPa (from -30 kPa to $+30$ kPa (Fig. 5.12a).[9] The resulting flow-rate output was recorded by the two flow rate sensors, after which the data was aligned so pressure and flow rate could be compared between disparate sensors (Fig. 5.12b).

5.6.2 Theoretical Considerations of 3D-Printed Microfluidic Diode

A standard fluidic diode is a system which allows one-way fluid flow, opening in the 'forward' direction and closing in the reverse direction. The standard 3D-Printed diodes consist of a large central cavity separated by a septum made from flexible membrane, which is constructed with a sinusoidal pattern to increase its dynamic range of motion. At the center of the membrane is a flat annulus that serves an equivalent purpose to the valve seat (except dynamic rather than static). In the upper cavity, there is a rigid block of material that serves as the piston (except static rather than dynamic) which is not present in the lower cavity. This asymmetry allows the membrane to deform downward when pressure is applied from the upper to the lower cavity, enabling free fluid flow in the *forward* direction. Conversely, the 'piston' block abuts the valve seat when pressure is applied

[9] Vacuum (*i.e.*, negative) pressure were not used during these experiments, instead relying on polarity of the applied pressure differential to drive fluid flow in the reverse direction.

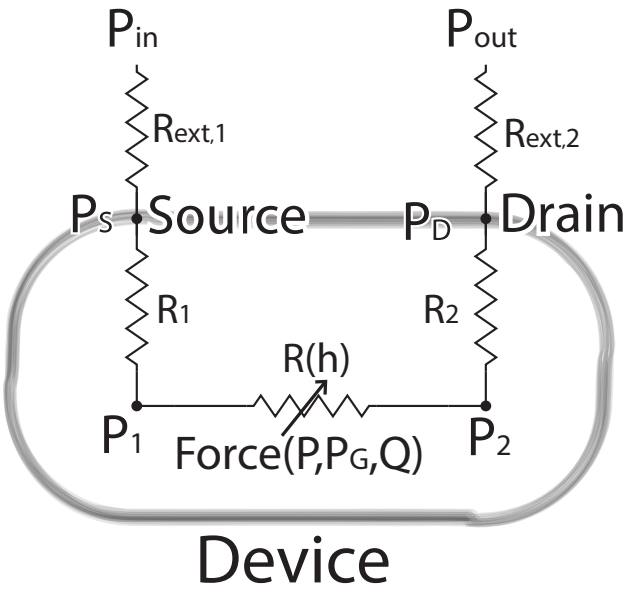


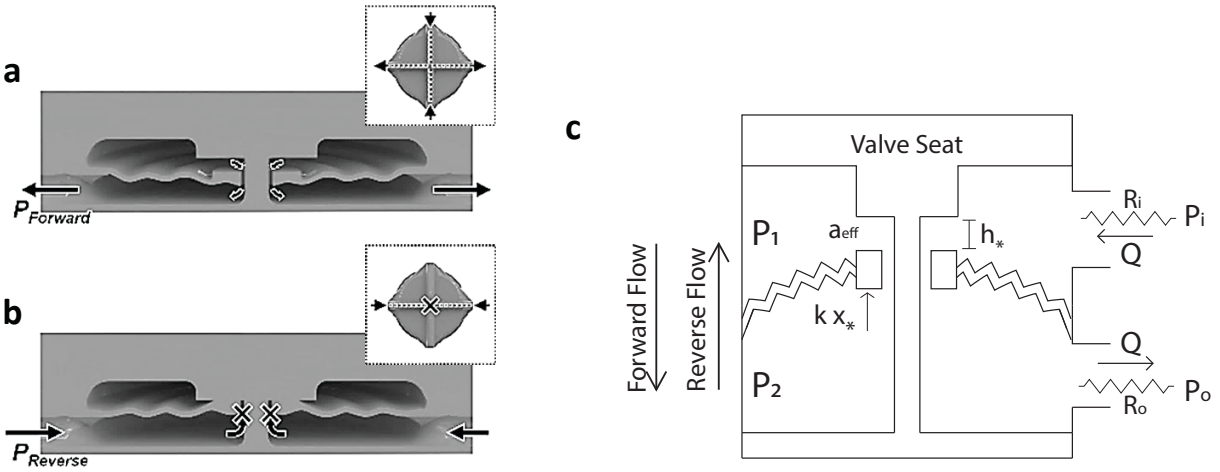
Figure 5.13 Conceptual layout of the internal resistances of the 3D-printed microfluidic diode and resistor. All 3D-printed devices experience R_{ext}, external input and output resistances that can be controlled by the parasitics of the apparatus the devices is attached to. Beyond that, there is an input and output node (source and drain) with a variable internal resistance ($R(h)$, where h is the size of a variable gap), which is affected by the internal pressures and flow rates. For the 3D-printed transistor, there is an additional node for a Gate (P_G) that can further alter the internal variable resistance.

from the lower cavity to the upper cavity, obstructing fluid flow in the *reverse* direction.

5.6.2.1 Force Balance

To determine the behavior of the diode, we consider forces in the upward direction (*i.e.*, the direction in which the diode closes). There are four dominant sources for the dynamic forces inside the diode: (a) hydrostatic membrane pressure (pressure on the non-closing portions of the membrane), (b) piston actuation pressure (pressure, (c) closing restorative pressures (preventing the valve seat and the piston from closing fully), and (d) membrane spring forces (which pulls the spring counter to the direction of motion). Pressures P_{in} and P_{out} are applied at the inlet and outlet, respectively (with $\Delta P \equiv P_{\text{in}} - P_{\text{out}}$). Pressures directly above and below the membrane are P_1 and P_2 (with $\delta P \equiv P_1 - P_2$), respectively are generally not identical to P_{in} and P_{out}, due to the presence of input and output hydrodynamic resistances R_1 and R_2, respectively. As a result, $\delta P \neq \Delta P$.

First we split the full septum area A_{tot} into A and a where A is the area of the non-closing membrane, and a is area of the closing portion of the valve seat. Note that the piston actuation pressure effectively acts over the area a_{eff} (Equation 5.30) while the direct membrane deformation acts over A. We treat the elastic restoring behavior of the membrane as if it is a simple linear Hookean



Standard diode flow behavior Conceptual force-body diagram

Figure 5.14 Setup of diode physical analysis with the key dimensional quantities labeled. Note that the constructed diode has a support pillar down the center for structural purposes. The pillar does not substantially alter the radial flow pattern through the outflow.

spring obeying $F_{\text{spring}} = -kx_*$ where k is the spring constant and x_* is the dimension*al* deviation from zero-pressure equilibrium (x_* is defined in the upward direction). To further simplify, we can nondimensionalize the spring forces by considering that

$$x_* = h_0 - h_* \tag{5.47}$$

$$x_* = h_0(1 - h_*/h_0) \tag{5.48}$$

$$x_* = h_0(1 - h) \tag{5.49}$$

$$x = (1 - h) \tag{5.50}$$

where $x \equiv x_*/h_0$ and represents the dimension*less* deviation from zero-pressure equilibrium. Thus $F_{\text{spring}} = -kh_0(1-h)$

To make this analysis as simple as possible, we consider primarily linear forces on the membrane. For example, we treat a deforming simple membrane as if it obeys the force balance $\Delta PA = kx_*$ (*i.e.*, as a balance between direct pressure forces and spring forces), which only holds for small x_*. At a certain level of 'ballooning', the membrane will be resistant to further expansion as the membrane reaches the limit of its elasticity; the effective spring constant tends to increase with x_* (see Analysis 5.2). Additionally, we assume that because the width of the piston is small ($\sim 200\mu m$), the drag forces through the hole are negligible. For a summary of these forces, see Table 5.1.

Force Mechanism	Location of Action	Label	Upward Force ($F_\uparrow$)
Hydrostatic Membrane Pressure	Flexible Membrane	F_{mem}	$+\delta PA$
Membrane Spring Forces	Flexible Membrane	F_{spr}	$-kh_0x$
Piston Actuation Pressure	Valve Seat	F_{pist}	$+\delta P a_{\text{eff}}$
Closing Restorative Force	Valve Seat	F_{rest}	$-mh^{-\beta}$

Table 5.1 Forces acting on the dynamic membrane within the diode. The hydrostatic membrane pressure and membrane spring forces are only linear in P and x, respectively, for small deviations around $x = 0$. Note that x and h are dimensionless. δP is also defined in the upward direction.

Combining the forces acting on the diode, we obtain a force balance

$$F_\uparrow = 0 = \delta PA + \delta P a_{\text{eff}} - kh_0x - mh^{-\beta} \tag{5.51}$$

$$= \delta P(A + a_{\text{eff}}) - kh_0(1-h) - mh^{-\beta}, \tag{5.52}$$

where $h > 0$, which when rearranged gives us

$$\delta P(A + a_{\text{eff}}) = kh_0(1-h) + mh^{-\beta}, \tag{5.53}$$

5.6.2.2 Force-Flow Balance

To finalize the physics of the diode, we must develop one additional equation which relates applied pressure ΔP, flow rate Q, and piston location h. Firstly, we find the overall flow behavior, from the Ohm's Law formulation of microfluidics, where $\Delta P = QR_{\text{tot}}$. R_{tot} is merely the sum of the total resistances,

$$R_{\text{tot}} = R_{\text{in}} + R(h) + R_H + R_{\text{out}}, \tag{5.54}$$

where $R(h) = rh^{-3}$ is the resistance of the moving piston and R_H is the (presumably small) resistance through the central hole of the moving piston. Defining

$$R \equiv R_{\text{in}} + R_H + R_{\text{out}}, \tag{5.55}$$

we can simplify and nondimensionalize the flow equation. Using the dimensionless quantities $\Delta p = \Delta P / \Delta P_s$ and $q = Q/Q_s$ (where ΔP_s and Q_s are the characteristic pressure and flow rate,

respectively), we obtain,

$$\Delta P = Q(R + rh^{-3}) \tag{5.56}$$

$$\Delta P_s \Delta p = qQ_s R(1 + \frac{r}{R}h^{-3}) \tag{5.57}$$

$$\Delta p = q\frac{Q_s R}{\Delta P_s}(1 + \frac{r}{R}h^{-3}) \tag{5.58}$$

Finally, because we can freely choose Q_s, we define $Q_s \equiv \Delta P_s/R$ without loss of generality (*i.e.*, using a characterestic version of Ohm's Law), giving us

$$\Delta p = q(1 + \rho h^{-3}), \tag{5.59}$$

where $\rho \equiv r/R$ is a nondimensional unit describing the relative resistance of the radial resistance in the zero-pressure state.

Next, we use a partial version of Ohm's Law to describe the flow behavior on either side of the membrane, pulling out a factor of R resulting in

$$\delta P = Q(R(h) + R_H) \tag{5.60}$$

$$= qQ_s R(\frac{r}{R}h^{-3} + \frac{R_H}{R}) \tag{5.61}$$

$$= qP_s\frac{r}{R}(h^{-3} + \frac{R_H/R}{r/R}) \tag{5.62}$$

$$= qP_s(\rho h^{-3} + \rho_H) \tag{5.63}$$

$$\delta p = q(\rho h^{-3} + \rho_H) \tag{5.64}$$

where $\rho_H \equiv R_H/R$ and $\delta P = \delta p P_s$. Alternately, we can use Ohm's Law to find the relationship between $\Delta P and \delta P$:

$$\Delta P = Q(R_{\text{in}} + R_{\text{out}} + R_H - R_H) + Q(R(h) + R_H) \tag{5.65}$$

$$= Q(R - R_H) + \delta P \tag{5.66}$$

$$\implies \delta p = \Delta p - q(1 - \rho_H) \tag{5.67}$$

Putting Equation 5.63 and Equation 5.53 together, we obtain,

$$\delta P\,(A + a_{\text{eff}}) = kh_0(1-h) + mh^{-\beta} \tag{5.68}$$

$$qP_s(\rho h^{-3} + \rho_H)(A + a_{\text{eff}}) = kh_0(1-h) + mh^{-\beta}. \tag{5.69}$$

$$qP_sA(\rho h^{-3} + \rho_H)(1 + \frac{a_{\text{eff}}}{A}) = kh_0(1-h) + mh^{-\beta}. \tag{5.70}$$

Dividing both sides by kh_0,

$$\frac{P_sA}{kh_0}\; q\; \rho(h^{-3} + \hat{\rho}_H)(1+\alpha) = (1-h) + \frac{m}{kh_0}h^{-\beta}, \tag{5.71}$$

where $\alpha \equiv a_{\text{eff}}/A$ represents an effective area ratio. Finally, we choose $P_s = \frac{kh_0}{A}$ as our characteristic pressure and define a nondimensional repulsion constant $M = \frac{m}{kh_0}$, resulting in

$$q\;(1+\alpha)(\rho h^{-3} + \rho_H) = (1-h) + Mh^{-\beta}. \tag{5.72}$$

Rearranging terms, we find an expression for $q(h)$,

$$q(h) = \frac{(1-h) + Mh^{-\beta}}{(1+\alpha)(\rho h^{-3} + \rho_H)} \tag{5.73}$$

$$= \frac{(1-h) + Mh^{-\beta}}{(1+\alpha)(\rho + \rho_H h^3)h^{-3}} \tag{5.74}$$

$$= \frac{(1-h) + Mh^{-\beta}}{(1+\alpha)(\rho + \rho_H h^3)}h^3 \tag{5.75}$$

Combining this with the Ohm's Law formulation, (Equation 5.59)

$$\Delta p\,(h) = q\;\left(\rho h^{-3} + 1\right) \tag{5.76}$$

$$= q\;\frac{\left(\rho + h^3\right)}{h^3}, \tag{5.77}$$

we obtain the fully nondimensionalized parametric diode equations $(\Delta p\,(h), q(h))$:

$$\Delta p\,(h) = \left((1-h) + Mh^{-\beta}\right)\frac{(\rho + h^3)}{(1+\alpha)(\rho + \rho_H h^3)} \tag{5.78}$$

$$q(h) = \left((1-h) + Mh^{-\beta}\right)\frac{h^3}{(1+\alpha)(\rho + \rho_H h^3)}. \tag{5.79}$$

Dimensional	Dimensionless	Other Relations	Description
x_*	$x = x_*/h_0$		Piston Displacement from Equilibrium
h_*	$h = h_*/h_0$	$h = 1 - x$	Equilibrium Gap between Piston and valve seat
P	$p = P/P_s$	$P_s = kh_0/A$	Absolute Pressure
ΔP	$\Delta p = \Delta P/P_s$		Applied Pressure Difference
Q	$q = Q/Q_s$	$Q_s = P_s/R$	Flow Rate
R		$R \equiv R_{\text{in}} + R_H + R_{\text{out}}$	Total static resistance
a_{eff}	$\alpha = a_{\text{eff}}/A$	$a_{\text{eff}} = \frac{\pi}{2}\frac{(r_2^2 - r_1^2)}{\ln(r_2/r_1)}$	Relative area of piston effect
m_*	$M = m_* h_0^{-\beta}/kh_0$		Closing Restorative Force Parameter
R		$R = R_{\text{in}} + R_H + R_{\text{out}}$	Total Static Resistance
R_H	$\rho_H = R_H/R$		Piston Hole Resistance (Static)
r	$\rho = r/R$	$r = \begin{cases} r_* h_0^{-3} \\ \frac{3\mu \ln(r_2/r_1)}{4\pi h_0^3} \end{cases}$	Piston Equilibrium Resistance
F_{spr}	$f_{\text{spr}} = F_{\text{spr}}/(kh_0)$		Membrane Spring Force
F_{mem}	$f_{\text{mem}} = F_{\text{mem}}/(kh_0)$		Membrane Pressure Force
F_{pist}	$f_{\text{pist}} = F_{\text{pist}}/(kh_0)$		Piston Closure Force
F_{rest}	$f_{\text{rest}} = F_{\text{rest}}/(kh_0)$		Closing Restorative Force

Table 5.2 Summary of the nondimensionalization factors used in the single-sided diode equations.

5.6.2.3 Summary of Diode Terminology

These equations are parametrized by five dimensionless numbers which are set by the physics of the system:

1. β, the closing repulsion power
2. M, the closing repulsion constant
3. ρ, the ratio between zero-pressure piston resistance and total static resistance
4. ρ_H the ratio between the (static) hole resistance and total static resistance
5. α, a constant representing the effective area ratio of the membrane

If this set of parametric equations is plotted for $h > 0$, we can see the full behavior of the diode for a range of pressures and under various conditions of the five dimensionless parameters.

5.6.2.4 Asymptotic Forms

While the Diode Equations are too complex to obtain analytically useful closed-form solutions, it is useful to examine device behavior in an asymptotic fashion. We will consider three major asymptotic forms: (i) the open *forward flow* behavior ($h \gg 1$), (ii) the low pressure/flow rate behavior (h 1), and the closed *reverse flow* behavior ($h \ll 1$).

Note: $\sim$ indicates asymptotic behavior, not approximation

(I) Open (Forward) Flow ($h \gg 1$)

Taking the diode equations in the limit that $h \gg 1$, we can approximate the device behavior in the open condition. First, let $h = \varepsilon H$, where $\varepsilon \gg 1$ and $H \sim O(1)$, we can take the limits of Δp and q as $\varepsilon - > \infty$.

$$q(h) = \left((1 - H\varepsilon) + MH^{-\beta}\varepsilon^{-\beta}\right)\frac{H^3\varepsilon^3}{(1+\alpha)(\rho + \rho_H H^3\varepsilon^3)} \tag{5.80}$$

$$\sim (1 - H\varepsilon)\frac{H^3}{(1+\alpha)(\rho_H H^3)}, \text{ as } \varepsilon \to \infty \tag{5.81}$$

$$\Rightarrow q(h) \sim \frac{1-h}{\rho_H(1+\alpha)}, \text{ as } h \to \infty \tag{5.82}$$

and

$$\Delta p\,(h) = \left((1 - H\varepsilon) + MH^{-\beta}\varepsilon^{-\beta}\right)\frac{(\rho + H^3\varepsilon^3)}{(1+\alpha)(\rho + \rho_H H^3\varepsilon^3)} \tag{5.83}$$

$$\sim (1 - H\varepsilon)\frac{H^3}{(1+\alpha)(\rho_H H^3)}, \text{ as } \varepsilon \to \infty \tag{5.84}$$

$$\sim \frac{1 - H\varepsilon}{(1+\alpha)(\rho_H)} \tag{5.85}$$

$$\Rightarrow \Delta p\,(h) \sim \frac{1-h}{\rho_H(1+\alpha)} \tag{5.86}$$

As expected for an 'open' flow pattern, $\Delta p\,(h) \sim q(h)$, indicating a linear resistive relationship between pressure and flow rate. If we return to the dimension*al* form,

$$\Delta p\,(h) \sim q(h) \tag{5.87}$$

$$\frac{\Delta P\,(h)}{P_s} \sim \frac{Q(h)}{Q_s}. \tag{5.88}$$

And since $P_s = Q_s R$, we can simplify the dimensional form

$$\frac{\Delta P\,(h)}{P_s} \sim \frac{Q(h)}{P_s/R} \tag{5.89}$$

$$\Rightarrow \Delta P\,(h) \sim Q(h)R, \tag{5.90}$$

showing us our expected Ohm's Law formulation, where R contains all static resistnaces in the system.

Lastly, if we solve for h, we see that h depends linearly on pressure, as per the linear Hookean spring model:

$$h \sim 1 - \Delta p\,\rho_H(1+\alpha). \tag{5.91}$$

Although we used a linear spring model, any spring model would leave the diode equations mostly unchanged. Recall that the common spring term $(1-h)$ in both the $\Delta p\,(h)$ and $q(h)$ equations comes from the nondimensionalized spring force

$$\frac{F_{\text{spring}}}{kh_0} = 1 - h. \tag{5.92}$$

Thus, the forward flow (asymptotic) linear relationship between Δp and q would be maintained, even if the specific dependence on h would not.

(II) Low Pressure/Flow Rate ($h \sim 1$)

To determine the device behavior at low pressure and flow rate, we first note that under these conditions, the total piston displacement is likely to be small relative to the initial gap (*i.e.*, $x << h$). Thus, we will linearize the diode equations in h by expanding around $h = 1$. First note that the near-field plate repulsive forces ($Mh^{-\beta}$) will be very small for the piston far from the valve seat. Because $h^{-\beta} \sim O(1)$ for $h \sim 1$, we expect that this 'smallness' will be contained in the coefficient M, and for this linearization will take $M \to 0$. Skipping this step vastly complicates the asymptotic form

for little apparent benefit. Lastly, we simplify the analysis by setting $x = (1-h)$ and expanding about $x = 0$. Thus our new diode equations are

$$\Delta p\,(x) \sim x\frac{(\rho + (1-x)^3)}{(1+\alpha)(\rho + \rho_H(1-x)^3)} + O(M) \tag{5.93a}$$

$$q(x) \sim x\frac{(1-x)^3}{(1+\alpha)(\rho + \rho_H(1-x)^3)} + O(M) \tag{5.93b}$$

Because both equations include a factor $O(x)$, to obtain a linear expansion, we take only the $O(1)$ term of

$$(1-x)^3 \sim 1 + O(x),$$

leaving us with equations that are $O(x)$

$$\Delta p\,(x) \sim x\frac{1+\rho}{(1+\alpha)(\rho + \rho_h)} + O\big(M; x^2\big) \tag{5.94a}$$

$$q(x) \sim x\frac{1}{(1+\alpha)(\rho + \rho_h)} + O\big(M; x^2\big) \tag{5.94b}$$

From here, we can quickly solve for $q(\Delta p\,)$. Knowing that

$$\frac{x}{(1+\alpha)(\rho + \rho_h)} = \frac{\Delta p}{1+\rho}, \tag{5.95}$$

we find that

$$q(\Delta p\,) = \frac{\Delta p}{1+\rho}. \tag{5.96}$$

Compared to the forward flow case, the nondimensional resistance ($\frac{\mathrm{d}q}{\mathrm{d}\Delta p}$) has increased by a factor of $(1+\rho)$ showing the effects of the piston in increasing device resistance. However, the device is still mostly 'open'.

(III) Closed (Reverse) Flow ($h \ll 1$)

In high pressure reverse flow, the piston is forced extremely close to the valve seat, prompting a series expansion around $h \sim 0$. To facilitate the analysis, we perform a change of variables, setting

$$h \equiv H/\varepsilon, \tag{5.97}$$

where $H \sim O(1)$, and $\varepsilon \to \infty$ carries the asymptotic behavior.

$$\Delta p\,(h) = \Big((1-H/\varepsilon) + MH^{-\beta}\varepsilon^{\beta}\Big)\frac{(\rho + (H/\varepsilon)^3)}{(1+\alpha)(\rho+\rho_H(H/\varepsilon)^3)} \tag{5.98a}$$

$$q(h) = \Big((1-H/\varepsilon) + MH^{-\beta}\varepsilon^{\beta}\Big)\frac{(H/\varepsilon)^3}{(1+\alpha)(\rho+\rho_H(H/\varepsilon)^3)} \tag{5.98b}$$

Noting that to $O\big(\varepsilon^{-6}\big)$,

$$\frac{1}{\rho+\rho_H(H/\varepsilon)^3} = \frac{1}{\rho\Big(1+\frac{\rho_H}{\rho}(H/\varepsilon)^3\Big)} \tag{5.99}$$

$$\sim \frac{1}{\rho}\left(1-\frac{\rho_H}{\rho}(H/\varepsilon)^3\right) + O\Big(\varepsilon^{-6}\Big), \tag{5.100}$$

$$\Delta p\,(h) \sim \frac{(1-H/\varepsilon)+M(H/\varepsilon)^{-\beta}}{\rho(1+\alpha)}\big(\rho+(H/\varepsilon)^3\big)\left(1-\frac{\rho_H}{\rho}(H/\varepsilon)^3 + O\Big(\varepsilon^{-6}\Big)\right) \tag{5.101a}$$

$$q(h) \sim \frac{(1-H/\varepsilon)+M(H/\varepsilon)^{-\beta}}{\rho(1+\alpha)}(H/\varepsilon)^3\left(1-\frac{\rho_H}{\rho}(H/\varepsilon)^3 + O\Big(\varepsilon^{-6}\Big)\right) \tag{5.101b}$$

$$\Delta p\,(h) \sim \frac{(1-H/\varepsilon)+M(H/\varepsilon)^{-\beta}}{\rho(1+\alpha)}\Big(\rho+(1-\rho_H)(H/\varepsilon)^3 + O\Big(\varepsilon^{-6}\Big)\Big) \tag{5.102a}$$

$$q(h) \sim \frac{(1-H/\varepsilon)+M(H/\varepsilon)^{-\beta}}{\rho(1+\alpha)}\Big((H/\varepsilon)^3 + O\Big(\varepsilon^{-6}\Big)\Big) \tag{5.102b}$$

$$\Delta p\,(h) \sim \frac{(1-H/\varepsilon)+M(H/\varepsilon)^{-\beta}}{\rho(1+\alpha)}\Big(\rho+(1-\rho_H)(H/\varepsilon)^3 + O\Big(\varepsilon^{-6}\Big)\Big) \tag{5.103a}$$

$$q(h) \sim \frac{(1-H/\varepsilon)+M(H/\varepsilon)^{-\beta}}{\rho(1+\alpha)}\Big((H/\varepsilon)^3 + O\Big(\varepsilon^{-6}\Big)\Big) \tag{5.103b}$$

$$\Delta p\,(h) \sim \frac{\rho\Big((1-H/\varepsilon)+M(H/\varepsilon)^{-\beta}\Big) + (1-\rho_H)\Big((H/\varepsilon)^3 + (H/\varepsilon)^{3-\beta}\Big)}{\rho(1+\alpha)} + O\Big(\varepsilon^{-6+\beta}\Big) \tag{5.104a}$$

$$q(h) \sim \frac{(H/\varepsilon)^3 + M(H/\varepsilon)^{3-\beta}}{\rho(1+\alpha)} + O\Big(\varepsilon^{-6+\beta}\Big). \tag{5.104b}$$

Taking only the largest order terms as $\varepsilon \to \infty$, we get

$$\Delta p\,(h) \sim \frac{M(H/\varepsilon)^{-\beta}}{1+\alpha} + O\Big(\varepsilon^{-3+\beta}\Big) \tag{5.105a}$$

$$q(h) \sim \frac{M(H/\varepsilon)^{3-\beta}}{\rho(1+\alpha)} + O\big(\varepsilon^{-3}\big). \tag{5.105b}$$

or

$$\Delta p\,(h) \sim \frac{Mh^{-\beta}}{1+\alpha} \tag{5.106a}$$

$$q(h) \sim \frac{Mh^{3-\beta}}{\rho(1+\alpha)}. \tag{5.106b}$$

Solving for h, we get

$$h \sim \left(q\frac{\rho(1+\alpha)}{M}\right)^{1/(3-\beta)} \tag{5.107}$$

$$\Rightarrow \Delta p\,(q) \sim \frac{M}{1+\alpha}\left(q\,\frac{\rho(1+\alpha)}{M}\right)^{-\beta/(3-\beta)} \tag{5.108}$$

$$\sim \left(\frac{M}{1+\alpha}\right)^{1-\beta/(\beta-3)} (\rho\; q)^{\beta/(\beta-3)} \tag{5.109}$$

$$\sim \left(\frac{M}{1+\alpha}\right)^{-3/(\beta-3)} (\rho\; q)^{\beta/(\beta-3)} \tag{5.110}$$

$$\Rightarrow q(\Delta p) \sim \frac{1}{\rho}\left(\frac{M}{1+\alpha}\right)^{3/\beta} (\Delta p)^{(\beta-3)/\beta}, \text{ as } \Delta p \to \infty \tag{5.111}$$

From here, we can clearly see how the asymptotic behavior as $h \to \infty$ (or, equivalently, as $\Delta p \to \infty$) depends on the value of the Closing Power β. To leading power,

$$\lim_{\Delta p \to \infty} q(\Delta p) \sim \begin{cases} 0 & \beta < 3 \\ \frac{M}{1+\alpha} & \beta = 3 \\ \infty & \beta > 3, \end{cases} \tag{5.112}$$

although $q(\Delta p)$ grows sub-linearly for all values of $\beta > 3$. In particular, we see the value of the constant flow rate for the critical value of $\beta = 3$ that we were unable to determine from Equation 5.39. Given the form of the repulsive force condition, $f_{\text{rest}} = -Mh^{-\beta}$, we can immediately discount values of $\beta \leq 1$ because the force does not decay to zero sufficiently rapidly.

One other possibility from the diode results in Section 5.6.3 is that under high reverse flow rates, the piston stops moving and the diode behaves resistively (*i.e.*, $q \propto \Delta p$). In that case, $(\beta - 3)/\beta = 1 \implies \beta \to \infty$. One problem with this approach is that the value of the force grows rapidly at $h = 0$. While we can adjust the formalism by requiring the piston asymptotically approaches a point (δh) slightly offset from the valve seat, where the non-dimensional repulsive force would be written $M(h - \delta h)^{-\beta}$, a more effective means is to include a second (nondimensional) renormalization factor h_s in the force equation:

$$f_{\text{rest}} = \frac{F_{\text{rest}}}{kh_0} = Mh^{-\beta} \tag{5.113}$$

$$= Mh_s^{-\beta}\left(\frac{h}{h_s}\right)^{-\beta} \tag{5.114}$$

$$= M'\left(\frac{h}{h_s}\right)^{-\beta}, \tag{5.115}$$

where the distance $h_s h_0$ is effectively the farthest distance the piston can travel before stopping and $M' \equiv Mh_s^{-\beta}$. We also now expect $M' \sim O(1)$. With this change, the asymptotic equation Equation 5.111 becomes

$$q(\Delta p) \sim \frac{1}{\rho}\left(\frac{M'h_s^{\beta}}{1+\alpha}\right)^{3/\beta}(\Delta p)^{(\beta-3)/\beta}, \text{ as } \Delta p \to \infty \tag{5.116}$$

$$\sim \frac{h_s^3}{\rho}\left(\frac{M'}{1+\alpha}\right)^{3/\beta}(\Delta p)^{(\beta-3)/\beta}, \text{ as } \Delta p \to \infty. \tag{5.117}$$

Finally, as we take $\beta \to \infty$, we get a flow equation that looks like a radial flow through a constant thin gap with thickness $h_s h_0$:

$$q(\Delta p) \sim \frac{h_s^3}{\rho}\Delta p, \text{ as } \Delta p, \beta \to \infty \tag{5.118}$$

$$\implies Q(\Delta P) \sim \left(\frac{4\pi(h_s h_0)^3}{3\mu \ln\left(\frac{r_2}{r_1}\right)}\right)\Delta P \tag{5.119}$$

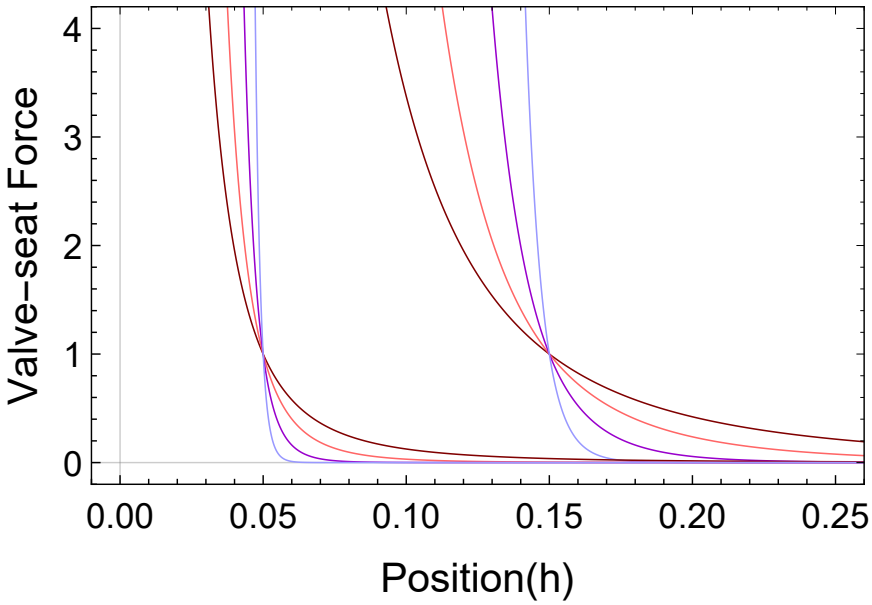


Figure 5.15 Effect of scaled M on device behavior. Note that while the ultimate asymptote for both sets of curves is the same (*i.e.*, $x = 0$), by shifting M, we can control when the curve family reaches $F = 1$, the applying the same reverse force as the spring at that distance.

(IV) Smooth Piston ($m = 0$)

The last case to consider is one in which the piston and the valve seat are perfectly smooth, blocking fluid flow completely when they come in contact. This form may be taken by assuming no repulsive force between the piston and the valve seat (*i.e.*, $m = 0$). To find these equations, we take the $m = 0$ form of Equation 5.53 and nondimensionalize,

$$\delta P\,(A + a_{\text{eff}}) = kh_0(1-h) \tag{5.120}$$

$$\frac{P_s(A + a_{\text{eff}})}{kh_0}\delta p = 1 - h \tag{5.121}$$

$$h = 1 - (1+\alpha)\delta P\,, \tag{5.122}$$

where we use the same nondimensionalization $P_s = \frac{kh_0}{A}$ that was used above, before solving for $h(\delta p)$. Combining this result with Equation 5.59, we obtain the implicit equation

$$\Delta p = q\Big(1 + \rho(1 - (1+\alpha)\delta P)^{-3}\Big) \tag{5.123}$$

$$= q\Big(1 + \rho(1 - (1+\alpha)(\Delta p - q(1-\rho_H)))^{-3}\Big) \tag{5.124}$$

which shows a the flow-dependent (nondimensionalized) resistance

$$r(\Delta p, q) = 1 + \frac{\rho}{(1-(1+\alpha)(\Delta p - q(1-\rho_H)))^3}. \tag{5.125}$$

This resistance equation admits a solution for complete valve closure ($q = 0$), when $r(\Delta p, q = 0) \to \infty$:

$$r(\Delta p, q = 0) = 1 + \frac{\rho}{(1-(1+\alpha)\Delta p)^3} \to \infty \tag{5.126}$$

$$\implies \Delta p_{\text{close}} = \frac{1}{1+\alpha} \tag{5.127}$$

$$\implies \Delta P_{\text{close}} = \frac{k h_0}{A + a_{\text{eff}}}. \tag{5.128}$$

This closing solution ΔP_{close} explains why the diode simulations in Section 5.6.3.1 closed completely under reverse flow; the analytical model simulated a perfectly smooth surface (*i.e.*, $m = 0$). Lastly, from Equation 5.78 the $m = 0$ diode equations ($(\Delta p(h), q(h))$) take the trivial form

$$\Delta p(h) = \frac{(1-h)(\rho + h^3)}{(1+\alpha)(\rho + \rho_H h^3)} \tag{5.129}$$

$$q(h) = \frac{(1-h)h^3}{(1+\alpha)(\rho + \rho_H h^3)}, \tag{5.130}$$

which exhibits an approximate maximum at $h = \frac{3}{4}\left(1 - \frac{1}{4}\frac{\rho_h}{2.4\rho - \rho_h}\right)$, for $\rho_h \ll \rho$. To a first order approximation (the limit of low hole resistance, $\rho_h = 0$), the maximum occurs at $\left(\Delta p\left(\frac{3}{4}\right), q\left(\frac{3}{4}\right)\right) = \left(\frac{27}{256}\frac{2.4\rho+1}{(1+\alpha)\rho}, \frac{27}{256}\frac{1}{(1+\alpha)\rho}\right)$.

(V) Asymptotics Summary The four asymptotic regions are summarized in Table 5.3.

Analysis 1: Double-Sided ("Anti-Zener") Diode

The diode equations can easily be modified to take into account the possibility for a diode that disallows flow in either direction. First, we choose the distance between the piston and the upper and lower plates to be h_{*1} and h_{*2}, respectively (at zero equilibrium, h_{o1} and h_{o2}), and note that the total distance between the upper and lower plates, $h_{o1} + h_{o2} \equiv H$ is constant regardless of how the

Pressure Regime	h	Δp	**Flow Rate:** *Nondimensional* *Dimensional*	**Resistance:** *Nondimensional* *Dimensional*
High Forward	$h \gg 1$	$\Delta p \gg +1$	$q \sim \Delta p$ $Q \sim \Delta P / R$	$r_{\text{eff}} = 1$ $R_{\text{eff}} = R$
Low Absolute	$h \sim 1$	$\lvert\Delta p\rvert \ll 1$	$q \sim \dfrac{\Delta p}{1+\rho}$ $Q \sim \dfrac{\Delta P / R}{1 + r/R}$	$r_{\text{eff}} = 1 + \rho$ $R_{\text{eff}} = R + r$
High Reverse	$h \ll 1$	$\Delta p \ll -1$	$q \sim \frac{1}{\rho}\left(\frac{M}{1+\alpha}\right)^{3/\beta} (\Delta p)^{(\beta-3)/\beta}$ $Q \sim \frac{1}{r_*}\left(\frac{m_*}{A+a_{\text{eff}}}\right)^{3/\beta} \Delta P^{(\beta-3)/\beta}$	$r_{\text{eff}} \sim \begin{cases} \rho \frac{\beta}{\beta-3}\left(\frac{1+\alpha}{M}\Delta p\right)^{3/\beta} & \beta \neq 3 \\ 0 + O\left(\frac{1}{\Delta p}\right) & \beta = 3 \end{cases}$ $R_{\text{eff}} \sim \begin{cases} r_* \frac{\beta}{\beta-3}\left(\frac{A+a_{\text{eff}}}{m_*}\Delta P\right)^{3/\beta} & \beta \neq 3 \\ 0 + O\left(\frac{1}{\Delta P}\right) & \beta = 3 \end{cases}$
$M = 0$ Reverse	$h \ll 1$	$\Delta p \lesssim \frac{1}{1+\alpha}$	$q \sim \frac{\Delta p}{\rho}(1 - \Delta p(1+\alpha))^3$ $Q \sim \frac{\Delta P}{r}\left(1 - \Delta P\left(\frac{A+a_{\text{eff}}}{kh_0}\right)\right)^3$	$r_{\text{eff}} \sim \frac{-\rho}{2}(1 - \Delta p(1+\alpha))^{-2}$ $R_{\text{eff}} \sim \frac{-r}{2}\left(1 - \Delta P(\frac{A+a_{\text{eff}}}{kh_0})\right)^{-2}$

Table 5.3 Summary of asymptotic behavior for standard diodes in Dimensional and Dimensionless cases. Note that in the high pressure limit, Reverse Flow does not depend on the initial value of h_0, and instead comes from a balance between the Closing Restoring Force and the Piston Force. In the $M = 0$ case, h may be eliminated, resulting in a closed-form piston solution, as well as a non-infinite closing pressure. As defined above:

$$r_* \equiv \left(\frac{3\mu \ln(\frac{r_2}{r_1})}{4\pi}\right) \qquad \text{and} \qquad r \equiv \left(\frac{3\mu \ln(\frac{r_2}{r_1})}{4\pi h_0^3}\right)$$

piston (and therefore h_{*1} and h_{*2} move:

$$H = h_{*1} + h_{*2} \tag{5.131}$$

$$h_{*2} = H - h_{*1} \tag{5.132}$$

$$= h_{o1}\left(\frac{H}{h_{o1}} - h_1\right) \tag{5.133}$$

$$= h_{o1}\left(\frac{1}{\eta_1} - h_1\right), \tag{5.134}$$

where $\eta_1 \equiv h_{o1}/H$ and h_1 and h_2 are dimension*less* quantities.

Next, we can determine the nondimensionalized flow equations. We insert these terms into a

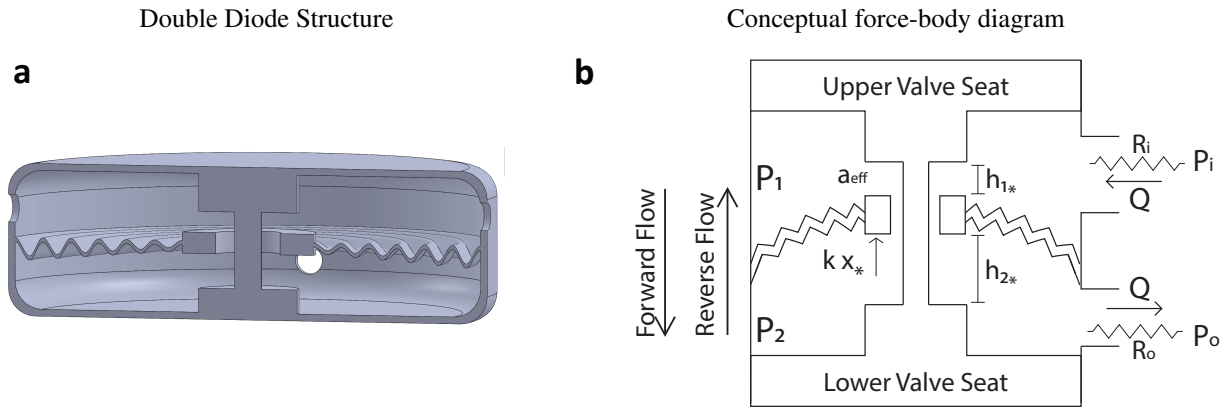


Figure 5.16 Structure of the Double Diode. **(a)** Rendered diagram of Double Diode. **(b)** Setup of Double Diode with the key dimensional quantities labeled.

modified form of the resistance, taken to account for two-sided fluid blockage and find

$$R_{\text{tot}} = R_{\text{in}} + R(h_{*1}) + R_H + R(h_{*2}) + R_{\text{out}} \tag{5.135}$$

$$= R + r_* h_{o1}^{-3} h_1^{-3} + r_* h_{o1}^{-3} \left(\frac{1}{\eta_1} - h_1 \right)^{-3} \tag{5.136}$$

$$= R + r h_1^{-3} + r \left(\frac{1}{\eta_1} - h_1 \right)^{-3} \tag{5.137}$$

$$= R \left[1 + \rho \left(h_1^{-3} + \left(\frac{1}{\eta_1} - h_1 \right)^{-3} \right) \right] \tag{5.138}$$

where $r \equiv r_* h_{o1}^{-3}$ as before. Combining this with the usual Ohm's law formulation gives us,

$$\Delta P = Q \left[1 + \rho \left(h_1^{-3} + \left(\frac{1}{\eta_1} - h_1 \right)^{-3} \right) \right] \tag{5.139}$$

$$\Rightarrow \Delta p = q \left[1 + \rho \left(h_1^{-3} + \left(\frac{1}{\eta_1} - h_1 \right)^{-3} \right) \right], \tag{5.140}$$

using the same nondimensionalization factors as before.

The Closing Restorative Force is modified only slightly to account for the upward restoring force at the bottom piston. Assuming that the plate geometries are equivalent (and therefore $m_1 = m_2 \equiv m$):

$$F_{\text{rest}} = -m_* h_{*1}^{-\beta} + m_* h_{*2}^{-\beta} \tag{5.141}$$

and can be simplified to the form

$$= -mh_1^{-\beta} + m\left(\frac{1}{\eta_1} - h_1\right)^{-\beta}. \tag{5.142}$$

Lastly, piston actuation force (F_{pist}), the hydrostatic membrane force (F_{memb}), and the spring force (F_{sp}) are entirely unchanged from their form in the standard diode derivation (provided the radial geometry of the lower channel is similar to that in the upper channel

$$F_{\text{pist}} = \delta P a_{\text{eff}} \tag{5.143}$$

$$F_{\text{memb}} = \delta P A \tag{5.144}$$

$$F_{\text{spring}} = -kx = -kh_{o1}(1-h_1). \tag{5.145}$$

As before, we determine δP in terms of the key quantities (*e.g.*, ΔP and Q):

$$\delta P = Q[R(h_{*1} + R_H + R(h_{*2})] \tag{5.146}$$

$$= Q\left[rh_1^{-3} + r\left(\frac{1}{\eta_1} - h_1\right)^{-3} + R_H\right] \tag{5.147}$$

$$= qP_s\left[\rho\left(h_1^{-3} + \left(\frac{1}{\eta_1} - h_1\right)^{-3}\right) + \rho_H\right]. \tag{5.148}$$

Finally, putting together the entire force balance for the modified diode, we obtain,

$$F_{\uparrow} = 0 = F_{\text{pist}} + F_{\text{memb}} + F_{\text{spring}} + F_{\text{rest}} \tag{5.149}$$

$$= \delta P\,(A + a_{\text{eff}}) - kh_{o1}(1-h_1) - mh_1^{-\beta} + m\left(\frac{1}{\eta_1} - h_1\right)^{-\beta}. \tag{5.150}$$

Rearranging and applying the previous nondimensionalization procedure:

$$\delta P\,(A + a_{\text{eff}}) = kh_{o1}(1-h_1) + mh_1^{-\beta} - m\left(\frac{1}{\eta_1} - h_1\right)^{-\beta} \tag{5.151a}$$

$$q\left[\rho\left(h_1^{-3} + \left(\frac{1}{\eta_1} - h_1\right)^{-3}\right) + \rho_H\right](1+\alpha) = (1-h_1) + M\left[h_1^{-\beta} - \left(\frac{1}{\eta_1} - h_1\right)^{-\beta}\right], \tag{5.151b}$$

where $P_s = kh_{o1}/A$ and $M \equiv M/kh_{o1}$ as before. Thus, we obtain the nondimensionalized double-

sided diode equations:

$$q = \frac{1}{1+\alpha}\frac{(1-h_1)+M\left[h_1^{-\beta}-\left(\frac{1}{\eta_1}-h_1\right)^{-\beta}\right]}{\rho\left(h_1^{-3}+\left(\frac{1}{\eta_1}-h_1\right)^{-3}\right)+\rho_H} \tag{5.152a}$$

$$\Delta p = q\left[1+\rho\left(h_1^{-3}+\left(\frac{1}{\eta_1}-h_1\right)^{-3}\right)\right] \tag{5.152b}$$

As a sanity check, consider the case where $h_{*2} \gg h_{*1}$ (*i.e.*, $H \gg h_{o1}$). In this case, $\eta_1 = h_{o1}/H \to 0$ and therefore both $\left(\frac{1}{\eta_1}-h_1\right)^{-\beta} \to 0$ and $\left(\frac{1}{\eta_1}-h_1\right)^{-3} \to 0$. Thus,

$$\lim_{\eta_1\to 0} q \equiv q|_{h_2\gg h_1} = \frac{1}{1+\alpha}\frac{(1-h_1)+M\left(h_1^{-\beta}-0\right)}{\rho\left(h_1^{-3}+0\right)+\rho_H} \tag{5.153}$$

$$= \left((1-h_1)+Mh_1^{-\beta}\right)\frac{1}{(1+\alpha)(\rho h_1^{-3}+\rho_H)} \tag{5.154}$$

$$= \left((1-h_1)+Mh_1^{-\beta}\right)\frac{h_1^3}{(1+\alpha)(\rho+\rho_H h_1^3)}, \tag{5.155}$$

and

$$\lim_{\eta_1\to 0} \Delta p \equiv \Delta p|_{h_2\gg h_1} = q|_{h_2\gg h_1}\left[1+\rho\left(h_1^{-3}+0\right)\right] \tag{5.156}$$

$$= q|_{h_2\gg h_1}\frac{\rho+h_1^3}{h_1^3} \tag{5.157}$$

$$= \left((1-h_1)+Mh_1^{-\beta}\right)\frac{\rho+h_1^3}{(1+\alpha)(\rho+\rho_H h_1^3)}. \tag{5.158}$$

In the One-sided limit (*i.e.*, $h_{*2} \gg h_{*1}$), the double diode equations $(\Delta p(h_1), q(h_1))$ behave identically to the single sided diode.

5.6.3 Results of Experimental Diode Tests

5.6.3.1 Diode Simulations

To better understand the structural and fluidic behavior of the 3D-printed fluidic diode, we simulated the behavior using COMSOL Multiphysics (Fig. 5.11e,f). The simulated von Mises stress distribution on the diode's diaphragm was consistent with simulated results for the 3D fluidic capacitor (Fig. 5.9d-f) within the range of modeled input pressures. Fluid flow simulations indicated

a clear dependence on flow polarity, with forward (top-to-bottom) flow exhibiting a nearly linear (*i.e.*, resistive) *QP* curve, but reverse flow (bottom-to-top) behaving non-linearly. Near $P = 0$, fluid flow behaved mostly linearly (and similarly to the forward flow case). However, as $|P_{\text{Reverse}}|$ increased, the diaphragm element was forced increasingly close to the upper plate, increasing the internal resistance. As the plate moved, reverse flow grew increasingly slowly, reaching a maximum reverse flow rate of 77.28 $\mu\text{L}\,\text{min}^{-1}$for $P_{\text{Reverse}} = -6.02$ kPa, before closing completely at $P_{\text{Reverse}} = -15.7$ kPa.

Because the simulated diodes were able to close sharply and fully, the diodes were only simulated to a maximum reverse pressure, above which the fluid flow shut off and the simulation experienced intersecting geometries. For an analysis of asymptotic closing behavior, see Section (III).

In contrast, the experimental results did not show that cutoff pressure, instead demonstrating a relatively constant reverse flow rate regardless of the reverse driving pressure, lending support to the use of h^{-3} as the wall-plate repulsion term discussed in Section 5.6.2.1. To measure the performance of the diode, we used the resistance-based calculation of diodicity:

$$Di = \frac{R_{\text{reverse}}}{R_{\text{Forward}}}, \tag{5.159}$$

where R_i represents the hydrodynamic resistance in the forward (top-to-bottom) and reverse (bottom-to-top) directions. We determined the resistances through linear regression, excluding fluid flow in the range $P < |5|$ kPa to exclude fluid behavior in the transitional region near $P = 0$. We determined that for $P > |5|$, $R_{\text{reverse}} = 1.55 \pm 0.03$ kPa min μL^{-1}, $R_{\text{forward}} = 0.0193 \pm 6.3 \times 10^{-5}$ kPa min μL^{-1}, which yielded the approximate *Di* of 80.6 ± 1.8 (Fig. 5.11c).

In addition, we demonstrated the effectiveness of the diode by using in a half-wave rectifier (Fig. 5.11d). We applied an oscillating input pressure and observed a significant forward bias in diode behavior based on flow polarity. The 3D-printed fluidic diodes did not demonstrate substantial changes to performance after approximately 75 periods of repeated forward and reverse pressure cycling of over 25 kPa.[10] At very high forward flow rates ($P > 80$ kPa), the diodes again experience flow rectification, presumably as the diode membrane impacts the bottom of the chamber. This cut-off pressure is much higher due to the larger required displacement. This effect could be eliminated by a redesign of the diode interior (*e.g.*, by preventing full blocking contact with the bottom plate) or enhanced by making the diode interior symmetrical (or semi-symmetrical), creating a "anti-zener" diode which only allows fluid flow in a narrow pressure range. Anti-zener

[10] Note, the flow data is cut at 1100 $\mu\text{L}\,\text{min}^{-1}$ due to the performance range of the Sensirion SLI-1000 flow sensor.

diodes could be useful as internal regulators, preventing sensitive internal components of a larger microfluidic device from experiencing damaging pressure gradients.

Analysis 2: Estimation of Smoothing Wave with Capacitor

Commonly in electrical circuits, full-wave rectifiers are accompanied by capacitors to buffer the oscillating current, turning the output into a smooth and ideally nearly constant output. For the diodes tested here, with a period of 15 s per cycle, the time constant $\tau = RC$ would need to be approximately 15 s. With the external resistance $R \sim \frac{30}{1200} \frac{\text{kPa-min}}{\mu\text{L}}$ results in a needed buffer capacitance $C \sim 10\ \mu\text{L}^3/\text{kPa}^{-1}$, which is within range of the 2 cm sinusoidal capacitors. However, when compared to the internal resistance ($\sim 1/10$ of the total resistance), the needed capacitance grows to $> 100\ \mu\text{L}^3/\text{kPa}^{-1}$, which is larger than the integrated capacitances. This value could be reached by placing several 3D-printed capacitors in parallel, or by surrounding the microfluidic diode with these capacitors.

5.6.4 Full-wave Rectifier Results

To demonstrate the capability of MJM-based fluidic circuit components to be combined into larger fluidic networks, we designed a full-wave bridge rectifier circuit by combiningfour fluidic diodes into a Wheatstone bridge configuration (Fig. 5.17). A full-wave fluidic rectifier is able to maintain consistently unidirectional fluid flow regardless of the input pressure polarity, making this device a useful for fluidic systems which would be disrupted by flow variations [340]. In contrast to configurations in which fluidic channels are fully-embedded within rectilinear blocks (*e.g.*, conventional soft lithography-based devices), this approach minimized material requirements by building suspended fluidic interconnects between individual diodes. We built two full-wave rectifier configurations using this principal: a planar system arranged much like the traditional Wheatstone bridge diagram (Fig. 5.17a, *middle*) and one laid out in a stacked configuration, designed to minimize the device footprint (Fig. 5.17a, *bottom*).

We experimentally tested the full-wave recertification using the same methodology applied to test the 3D-printed half-wave rectifier (Fig. 5.17b). We connected two ports to independently-controlled pressure sources from the Fluigent system, sealed the remaining eight cleaning ports using J-B Weld, and subjected the rectifier to two pressure inputs oscillating independently 180° out of phase of each other (red). For each rectifier, we performed three independent experiments, aligned the results based on pressure input, and averaged the results. The flow rate output (blue) showed that both configurations had a high potential for flow-rate rectification; however, the

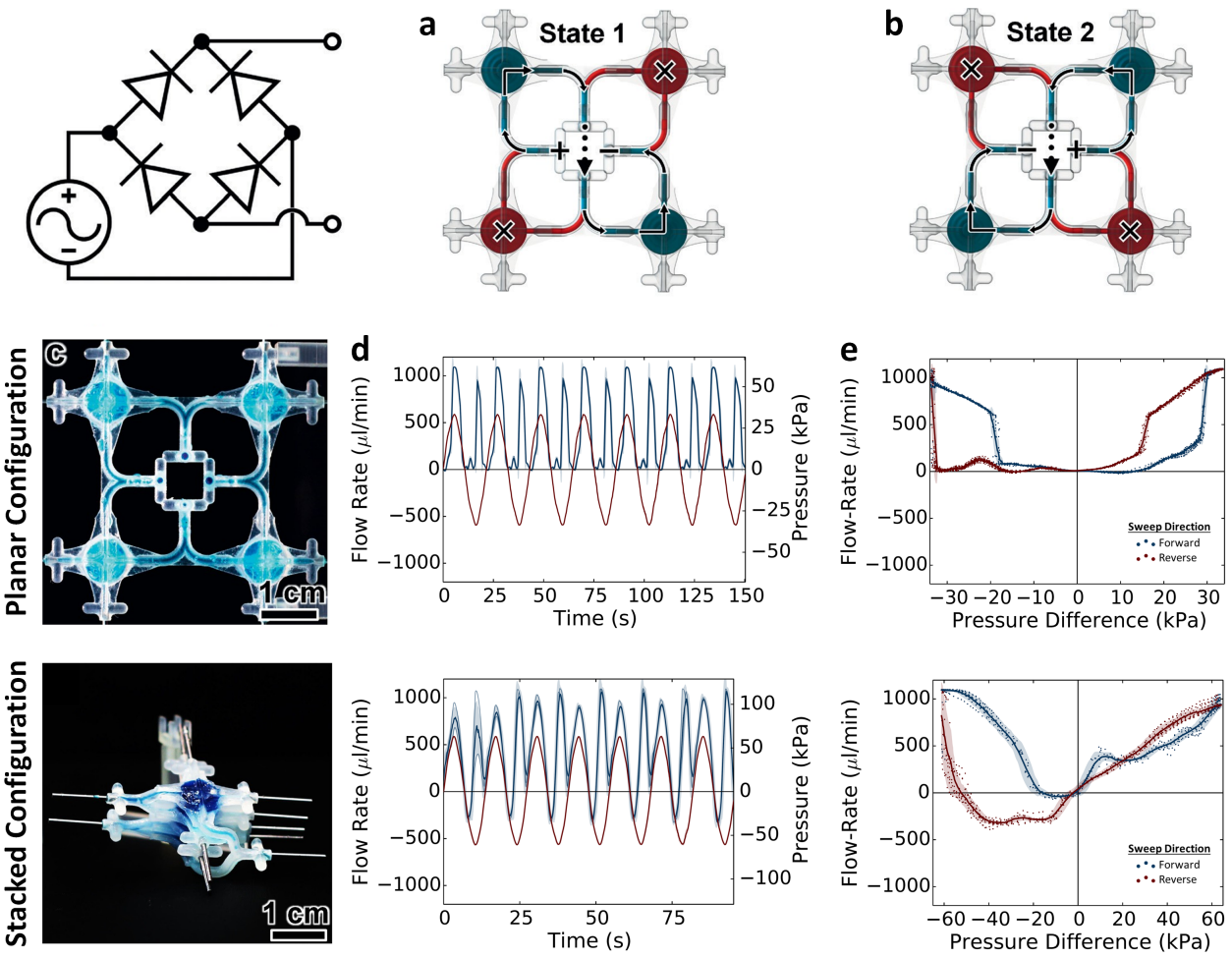


Figure 5.17 Microfluidic full-wave rectifier, obtained by connecting four 3D-printed diodes into a Wheatstone Bridge configuration. **(a,b)** Conceptual diagram illustrating the flow patterns through the diode under forward (*(State 1)*) and reverse (*(State 2)*) flow, demonstrating the principal behind which output fluid flow is independent of input pressure differential. Diodes are in a planar rectifier configuration, and red and teal colored fluids denote obstructed and unobstructed flow, respectively. **(c-e)** Experimental results of full-wave rectifier in planar *(top)* and stacked *(bottom)* configuration. **(c)** Photograph of rectifier containing blue food dye. **(d)** Time series response of flow rate to pressure differential, illustrating full-wave rectification. **(e)** *QP* diagram illustrating hysteretic behavior of flow rectification. Note that the *QP* response is more symmetric in the planar case than in the stacked case, suggesting that one-or-more of the stacked valves was not functioning properly. Data the results of three independent tests, with the dark line denoting the running average and the error bands denoting standard deviation; negative pressures/flow rates denote positive pressure/flow in the reverse direction. Subfigures **(a-c)** reproduced from Ref. 316 with permission of the RSC.

stacked configuration was less efficient, exhibiting a small, short-term leakage current during the first segment of the reverse pressure cycle. Additionally, the devices maintained their internal integrity and performance after approximately 45 repeated cycles of oscillating input pressure (*e.g.*, flow patterns that indicate internal leakage)

Lastly, we plotted the time series data on a *QP* diagram, visually separating the results based

on whether the pressure was increasing (blue) or decreasing (red) (Fig. 5.17c).[11] The *QP* diagram clearly shows the diode-based hysteresis as valves snap closed but take longer to re-open. For the planar configuration, the diagram indicates that the rectifier was designed and cleaned symmetrically. However, for the stacked configuration, the diagram indicates that at least one valve had difficulty closing, and therefore caused the back-flow visible on the time-series diagram. Moreover, the failure of the stacked rectifier to rectify on the first back-flow cycle on two of the three experiments additionally indicates near-failure in that particular valve. We further hypothesize that the small "humps" visible in the time series diagram and on the *QP* diagram are indicative of diodes taking time to close under back flow.

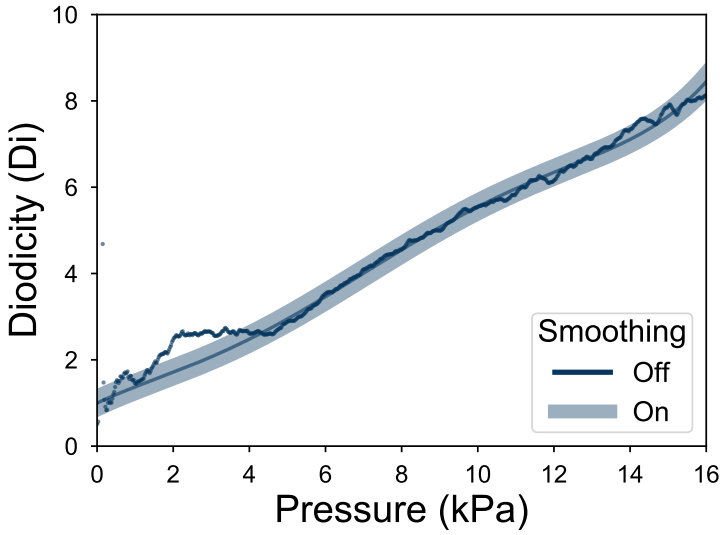
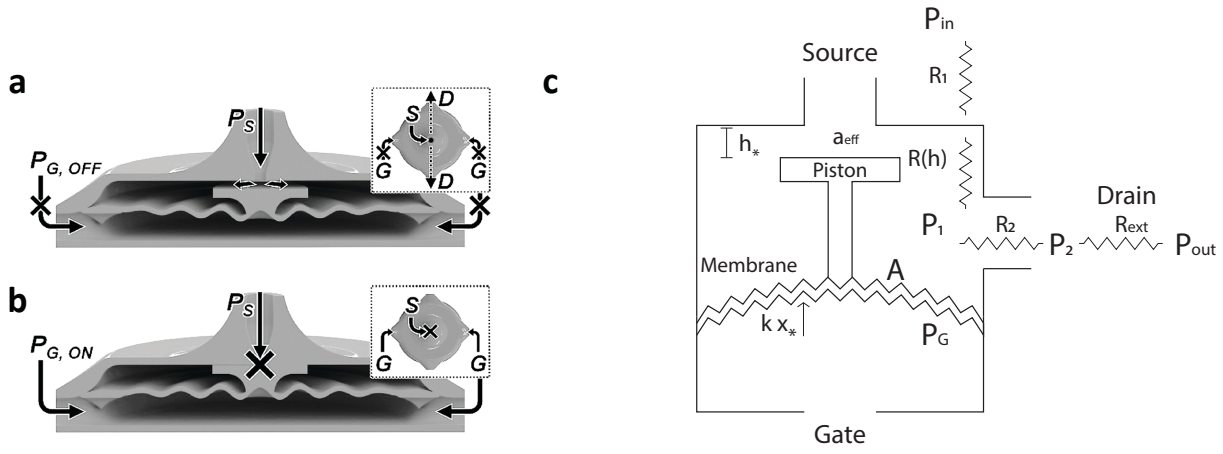


Figure 5.18 Direct measurement of diodicity, extracted from half-wave rectifier experimental results. These calculations of diodicity do not factor in external resistances used in measuring performance and so are relatively low.

5.7 3D-Printed Microfluidic Transistors

One of the most critical features to microfluidic circuitry is the integration of valve mechanisms [3, 24, 47, 341]. Although passive components, such as diodes or simple oscillators [25] are useful for directing fluidic flow, actively controlled valves (*i.e.*, transistor-like components) are critical for integrated fluidic circuitry.

[11] We removed the first two cycles of the stacked rectifier plot due to diode failure-to-open in this graph.



Standard NOT-gate flow behavior

Conceptual force-body diagram

Figure 5.19 Setup of 3D-printed gain-valve transistor analysis with the key dimensional quantities labeled. Pressures P_1 and P_G act on membrane area A and control the position of the piston. Pressures P_1 and P_2 act on the piston, which has an effective area a_{eff} (Equation 5.31).

5.7.1 Design Considerations

To achieve transistor-like functionality, we drew upon the concept behind MOSFETs[12] in the triode (also known as the *linear* or *ohmic*) mode, where potential applied to a "gate" modulates the width of a narrow conducting channel that regulates electrical current between a "source" and a "drain." Analogously (Fig. 5.19a, 5.29b), the 3D-printed transistor designs consists of a narrow channel that allows fluid flow from a Source input (top) to a larger Drain region (center), which then flows to outlets. The drain region is separated from the gate region by a flexible diaphragm capacitor, which allows a change in gate pressure (P_G) to move the diaphragm but does not permit direct current fluid flow between the regions. We attached a piston feature into the center of the diaphragm, which could be forced upward and pressed against the plate of the source-drain channel, increasing the hydrodynamic resistance.

Similar to a p-channel MOSFET (PMOS), which conducts in the absence of a voltage applied to the gate, this fluidic transistor experiences unobstructed flow from the source to the drain (Q_{SD}) in the absence of a sufficient gate pressure (P_G). Therefore, we considered the design to be a "NOT-Gate" transistor design. Because the fluidic resistance R_{SD} depends on the distance from the piston to the "source plate," the magnitude of Q_{SD} can be actively regulated by modulating P_G with respect to the source pressure (P_S) (Fig. 5.29b, *bottom*). Note that although we use the term "transistor," because the modulated quantity was resistance, the devices behaved more like a

[12] Metal Oxide Semiconductor Field Effect Transistors

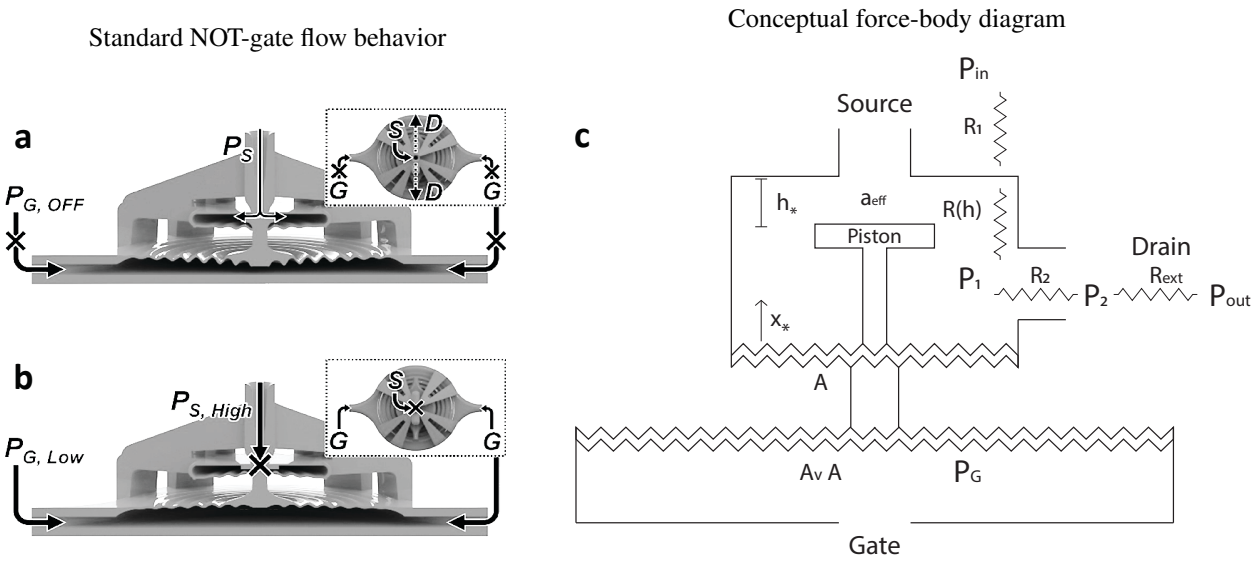


Figure 5.20 Setup of 3D-printed gain-valve transistor analysis with the key dimensional quantities labeled. Pressures P_1 and P_G act on membrane area A and control the position of the piston. For the Gain Valve, the secondary membrane has size $A_v \times A$ and permits a force amplification and allows a lower P_G to control the valve against a higher P_{in}.

vacuum tube[13] or triode-region MOSFETS.

One significant feature of electronic transistors is gain, whereby a transistor can effect a large output signal with a small input. In the hydrodynamic analogy, gain (A_P) is a property that allows a small P_G to control a larger P_S [36, 60]:

$$A_P = \frac{P_S}{P_G} \tag{5.160}$$

For the NOT-Gate transistors, $A_P \sim 1$ because the vertical deflection of the membrane was determined largely by the relative magnitudes of P_G and $P_D \sim P_S$. As a rough heuristic, R_{SD} increased when $P_G > P_D$; however, because the design was asymmetric, when $P_D > P_G$ and the diaphragm deforms downward, resistance is not substantially decreased.

To create a microfluidic transistor with enhanced gain, we used a system of area ratios to magnify the effectiveness of the gate pressure. We designed a 3D-printed fluidic transistor in which the drain region diaphragm is connected to a larger, but separate gate region diaphragm through an piston linkage (Figs. 5.30b, 5.20). The piston passes through air, meaning that the back pressure on each membrane is "ground" (*i.e.*, atmospheric) pressure, so the back pressure is functionally independent of device functionality. The piston couples the vertical displacement of the gate diaphragm to that of the drain diaphragm. Because force on the capacitor-based diaphragms is roughly applied

[13] Without the vacuum

pressure (P_i) times the membrane area (A_i), the net upward force on the coupled membrane system

$$F_{\text{up}} \sim P_G A_G - P_D A_D \tag{5.161}$$

means that a net upward force (*i.e.*, $F_{\text{up}} > 0$) can be generated for situations in which $\frac{P_G}{P_D} > \frac{A_D}{A_G} > 1$. Thus, a lower P_G can overcome a higher P_S and restrict Q_{SD} with a gain of approximately $\frac{A_D}{A_G}$.

5.7.2 Analytical form of 3D-Printed Microfluidic Transistors

In this system, we consider three resistors placed in series. There are two "parasitic" resistors modeling the input and output resistances: R_1 and R_2, as well as the variable resistor $R_v = R(h_*)$ which models the resistance caused by the opening and closing of the piston. The input pressure is P_s (from the MOSFET-analogy *source pressure*), the pressure immediately before and after R_v are P_1 and P_2, respectively, the pressure drop across the variable resistor is $\delta P = P_1 - P_2$ and the overall flow through the system is Q (Fig. 5.13). Note that P_2 is effectively the internal drain pressure.

From Ohm's Law, the fluid flow across the entire device behaves like

$$P_{\text{in}} - P_{\text{out}} = Q(R_1 + R_v + R_2) = Q(R + R_v) \equiv \Delta P \tag{5.162}$$

$$P_1 = P_{\text{in}} - QR_1 \tag{5.163}$$

$$P_2 = P_{\text{out}} + QR_2 \tag{5.164}$$

$$P_1 - P_2 = \Delta P - QR \equiv \delta P \tag{5.165}$$

where R is static resistance in the system, R_1 is the input (source) resistance, R_2 is the output (drain) resistance, and R_v is the variable piston resistance, which follows the same behavior as the diode: $R_v = r_* h_*^{-3} = rh^{-3}$, where $r = \left(\frac{3\mu \ln\left(\frac{r_2}{r_1}\right)}{4\pi h_0^3} \right)$. Nondimensionalizing by taking $P_i = P_s\, p_i$ (where P_i is some specified pressure), $Q = Q_s\, q$ and choosing $P_s = Q_S R$, and redefining non-dimensional constant ratios $\rho_1 \equiv \frac{R_1}{R}$, $\rho_2 \equiv \frac{R_2}{R}$, and $\rho \equiv \frac{r}{R}$,

$$\Delta p = p_{\text{in}} - p_{\text{out}} = q(1 + \rho h^{-3}) \tag{5.166}$$

$$p_1 = p_{\text{in}} - q\rho_1 \tag{5.167}$$

$$p_2 = p_{\text{out}} + q\rho_2 \tag{5.168}$$

$$\delta p = \Delta p - q. \tag{5.169}$$

These non-dimensionalized Ohm's Law equations can then be solved and compared to the force-ballance equations.

Force Mechanism	Location of Action	Label	Upward Force ($F_\uparrow$)
Hydrostatic Membrane Pressure	Flexible Membrane	F_{mem}	$(A_v P_G - P_2)A$
Membrane Spring Forces	Flexible Membrane	F_{spr}	$-kx_* = -k(h_0 - h_*)$
Piston Actuation Pressure	Valve Seat	F_{pist}	$-(P_1 - P_2)a_{\text{eff}}$
Closing Restorative Force	Valve Seat	F_{rest}	$-Mh_*^{-\beta}$

Table 5.4 Forces acting on the membrane within the standard NOT-gate transistor. The hydrostatic membrane pressure and membrane spring forces are assumed linear in P and x_*, respectively, for small deviations around $x = 0$. Transistors with built-in area-ratio gain exhibit $A_v > 1$, while standard transistors can be considered to exhibit $A_v = 1$.

There are several forces acting on the system, all considered in the upward direction, summarized in Table 5.4. These forces include the effective piston force ($-(P_1 - P_2)a_{\text{eff}}$), the gate and drain pressure forces balance on the membrane ($(A_V P_G - P_2)A$), the restoring spring force $-k(h_0 - h_*)$ (which pulls the spring downward when $h_* < h_0$), and the piston repulsive force $Mh_*^{-\beta}$. At equilibrium, $F_\uparrow = 0$:

$$F_\uparrow = 0 = (A_V P_G - P_2)A - (P_1 - P_2)a_{\text{eff}} - k(h_0 - h_*) - Mh_*^{-\beta} \tag{5.170}$$

The force balance then can be rearranged and simplified (with membrane area A, effective piston area a_{eff}, and transistor gain A_v, derived from the drain/gate area ratio)

$$(A_v P_G - P_2)A - (P_1 - P_2)a_{\text{eff}} = k(h_0 - h_*) + Mh_*^{-\beta} \tag{5.171}$$

$$(A_v P_G - (P_{\text{out}} + QR_2))A - (P_{\text{in}} - P_{\text{out}} - QR)a_{\text{eff}} = kh_0(1-h) + Mh_0^{-\beta}h^{-\beta} \tag{5.172}$$

$$Q_s RA(A_v p_g - p_{\text{out}} - q\rho_2) - Q_s Ra_{\text{eff}}(p_{\text{in}} - p_{\text{out}} - q) = kh_0\left(1 - h + \frac{Mh_0^{-\beta}}{kh_0}h^{-\beta}\right) \tag{5.173}$$

$$\frac{Q_s RA}{kh_0}\left[(A_v p_g - p_{\text{out}} - q\rho_2) - \frac{a_{\text{eff}}}{A}(p_{\text{in}} - p_{\text{out}} - q)\right] = 1 - h + mh^{-\beta} \tag{5.174}$$

$$(A_v p_g - p_{\text{out}} - q\rho_2) - \alpha(p_{\text{in}} - p_{\text{out}} - q) = 1 - h + mh^{-\beta} \tag{5.175}$$

$$A_v p_g - \alpha\Delta p - p_{\text{out}} - (\alpha - \rho_2)q = 1 - h + mh^{-\beta} \tag{5.176}$$

where $m \equiv \frac{Mh_0^{-\beta}}{kh_0}$, $\alpha \equiv \frac{a_{\text{eff}}}{A}$, and Q_s is chosen such that $\frac{Q_s Ra_{\text{eff}}}{kh_0} = 1$.

Combining Equations 5.166 and 5.176 provides us with the non-dimensionalized transistor

equations:

$$\Delta p = q(1+\rho h^{-3}) \tag{5.177a}$$

$$A_v p_g - \alpha\Delta p - p_{\text{out}} - (\alpha-\rho_2)q = 1-h+mh^{-\beta}. \tag{5.177b}$$

These equations, which can be plotted parametrically in h, immediately illustrate two interesting properties. First, the outlet pressure p_{out} has a parasitic effect on the transistor, preventing it from being solely a function of applied pressure differential Δp; because the drain pressure p_2 interacts with the gate pressure p_g, higher p_{out} can lower the overall efficiency of the transistor.

5.7.2.1 Asymptotic Forms and Limiting Variations

(I) Smooth Piston: $m = 0$

$$\Delta p = q(1+\rho h^{-3}) \tag{5.178a}$$

$$A_v p_g - \alpha\Delta p - p_{\text{out}} - (\alpha-\rho_2)q = 1-h \tag{5.178b}$$

In the case of a smooth piston, $m = 0$ the device is able to fully close because there is no repulsive force that blows up as $h \to 0$. We find that $q = 0$ for $\Delta p = 0$[14]. Additionally, a *closed* valve requires $h = 0$, as well as

$$A_v p_g \geq \alpha\Delta p + p_{\text{out}} + 1 \tag{5.179}$$

$$A(A_v P_G - P_{\text{out}}) \geq a_{\text{eff}}(P_{\text{in}} - P_{\text{out}}) + kh_0; \tag{5.180}$$

i.e., the upward membrane pressure is able to overcome the downward effective piston force and the membrane restoring force.

While this model breaks down when $h = 0$ due to the cutoff of radial fluid flow past the membrane, we can implicitly correct the model at $h = 0$. By adjusting $a_{\text{eff}}(P_{\text{in}} - P_{\text{out}}) \to \pi r_1^2 P_{\text{in}} - \pi r_2^2 P_{\text{out}}$, we correct the dynamic piston forces to become purely static. One consequence of this

[14] As expected for a case with zero source-to-drain flow

change is that although the valve *closes* for

$$A(A_v P_G - P_{\text{out}}) \geq a_{\text{eff}}(P_{\text{in}} - P_{\text{out}}) + kh_0, \tag{5.181}$$

the valve will not *reopen* unless

$$A(A_v P_G - P_{\text{out}}) < \pi r_1^2 P_{\text{in}} - \pi r_2^2 P_{\text{out}} + kh_0 \tag{5.182}$$

$$< a_{\text{eff}}(P_{\text{in}} - P_{\text{out}}) + kh_0 \tag{5.183}$$

due to $\pi r_1^2 < a_{\text{eff}} < \pi r_2^2$ for $r_1 < r_2$ (Equation 5.36). There exists hysteresis at the point of valve closure, as there is overlap between the (higher) upward pressure required to close the valve and the (lower) upward pressure required to open it again.

(II) Diode-connected Transistor: $p_{\text{in}} = p_g$ In this configuration, we connect the gate and the source of the transistor to obtain a diode-like configuration. Setting $p_{\text{in}} \to p_g$,

$$p_g - p_{\text{out}} = q(1 + \rho h^{-3}) \tag{5.184a}$$

$$(A_v - \alpha)p_g - (\alpha - \rho_2)q - (1 - \alpha)p_{\text{out}} = 1 - h + mh^{-\beta}. \tag{5.184b}$$

If we ground p_{out} by setting it equal to zero,[15] we can solve for $q(h)$ and $p_g(h)$:

$$q(h) = \frac{\left(1 - h + mh^{-\beta}\right)h^3}{(A_v - \alpha)\rho + \alpha(A_v - 2\alpha + \rho_2)h^3} \tag{5.185a}$$

$$p(h) = \frac{\left(1 - h + mh^{-\beta}\right)\left(\rho + h^3\right)}{(A_v - \alpha)\rho + \alpha(A_v - 2\alpha + \rho_2)h^3} \tag{5.185b}$$

a form fundamentally similar[16] to the Diode Equations (5.79), albeit with more parameters to work with. Interestingly, the directionality of the diode can be selected by proper choice of A_v; if we choose both $A_v > \alpha = a_{\text{eff}}/A$ and $A_v > 2\alpha - \rho_2$, we can produce the standard form of the diode equations shown in Equation 5.79; the high gain on the gate closes the valve when flow moves from source-to-drain regardless of the input source pressure, while permitting flow when the pressure polarity is drain-to-source. In contrast, if we select both $A_v < \alpha = a_{\text{eff}}/A$ and $A_v < 2\alpha - \rho_2$ (a case in which the gate pressure has very little effect on the performance of the transistor), the device

[15] Or raise the values of p_g and p_{in} by p_{out}

[16] As expected, given the section name

closes under reverse flow. For $A_v = 0$, the second condition requires

$$2\alpha > \rho_2 \tag{5.186}$$

$$\implies 2a_{\text{eff}} > A\frac{R_2}{R}, \tag{5.187}$$

implying that the effective area of the piston is large enough to drive the behavior of the device instead of the membrane; if the membrane is large enough, the downward force from the drain region will tend to keep the valve open.

For $A_v = a_{\text{eff}}$, the device will not close, because

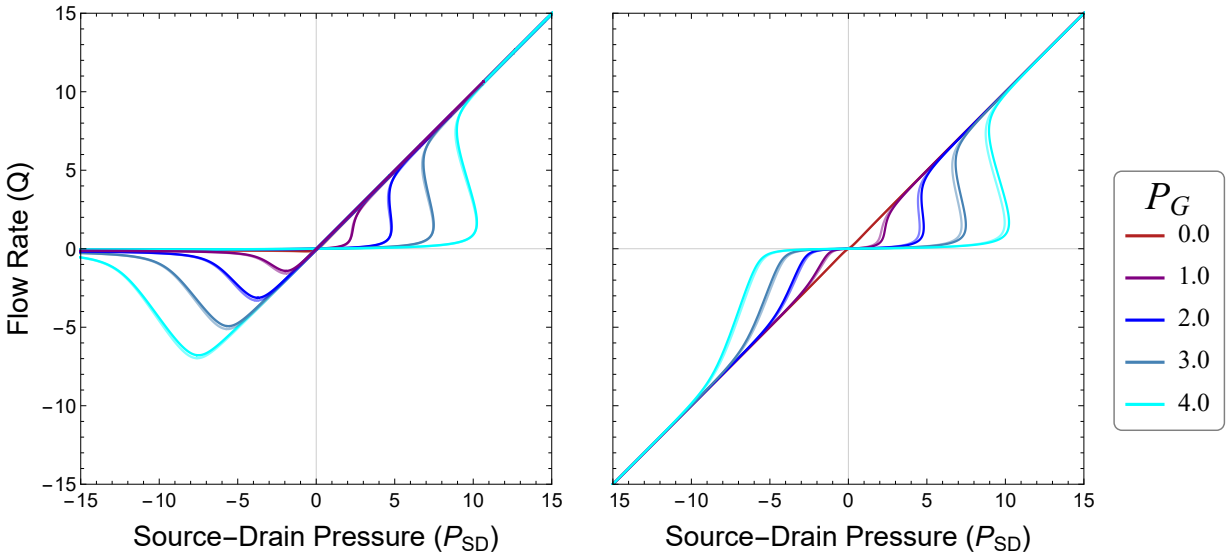
$$q(h) = \frac{(1 - h + mh^{-\beta})}{\alpha(A_v - 2\alpha + \rho_2)} \tag{5.188}$$

$$\implies q(h) = 0 \text{ for } h \approx 1, \tag{5.189}$$

and $h = 1$ only for $p_g \approx 0$ (to $O(m)$).

5.7.2.2 On the directionality of fluidic transistors

The transistor equations can be plotted for a wide-range of input and output pressures, although some solutions are more physically meaningful than others. The two primary solutions of interest are the "forward" pressure solution and the "positive" pressure solution. In the "forward" solution, the pressure is fixed at the outlet and swept from negative to positive at the inlet, meaning that fluid flow is defined purely in the forward (*i.e.*, inlet to outlet) direction and reverse flow is obtained through negative (*i.e.*, vacuum) inlet conditions. In the "positive" solution, reverse flow is obtained by setting the outlet pressure to a higher positive pressure than the inlet. While the forward condition is easier to manage in terms of running simulations, it is less physically meaningful than the positive solution due to the difficulty in obtaining vacuum in the lab (and the absolute impossibility of obtaining vacuum greater than 1 atmosphere). Comparisons between the forward and positive solutions for the 3D-printed NOT-gate are plotted in Figure 5.21. Note that the positive solution is semi-symmetrical reflecting the fact that high drain pressure will tend to force the gate membrane downward, yet will tend to force the piston upward.



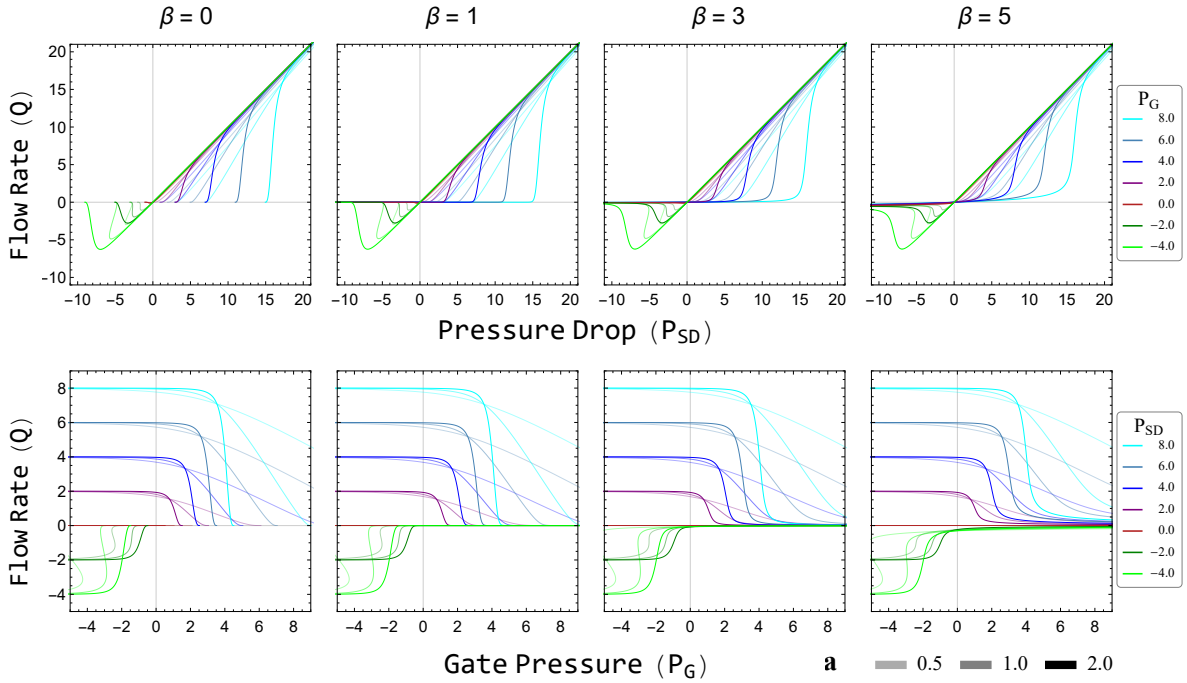
(a) "Forward" pressures only **(b)** Positive pressures only

Figure 5.21 Dependence of NOT-gate response on directionality of fluid flow.

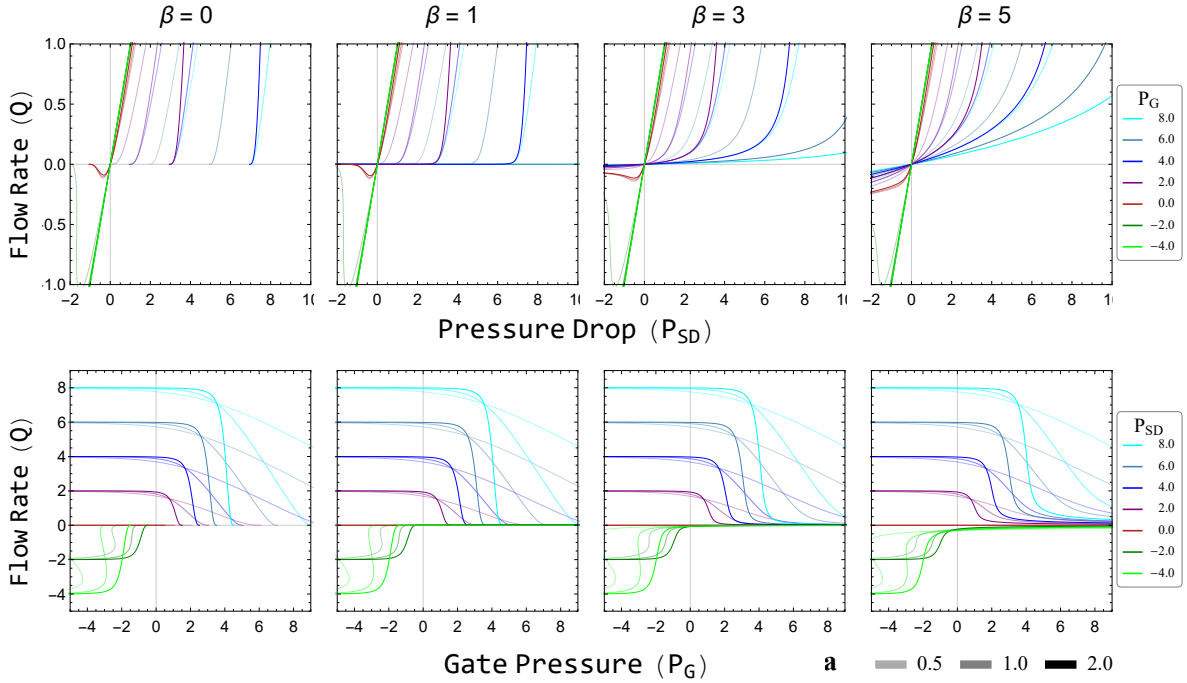
5.7.3 Results Summary for NOT Gate Analytical Modeling

The following figures show the results from analytical models of the NOT-Gate parametric equations. The NOT-Gates are "driven" with positive source pressure and zero drain pressure, except for the final set of plots which show the (non-linear) variance in behavior for alteration in drain pressure. Each plot consists of a linear sweep in source/gate pressure and discrete changes in gate/source pressure, and show behavior in the near-field (low pressure) and the far-field (high pressure) ranges. One thing to note are the conditions under which hysteresis begins to emerge, particularly for large area ratios α and for high input source pressures.

Figure 5.22 NOT-Gate analytical models showing behavior for changes in **effective area** ($\mathbf{a}_{\text{eff}}$).
(Top) source-drain pressure (P_{SD}) sweep with parameterized gate pressure (P_G) changes and *(Bottom)* gate pressure (P_G) sweep with parameterized source-drain pressure (P_{SD}) changes.

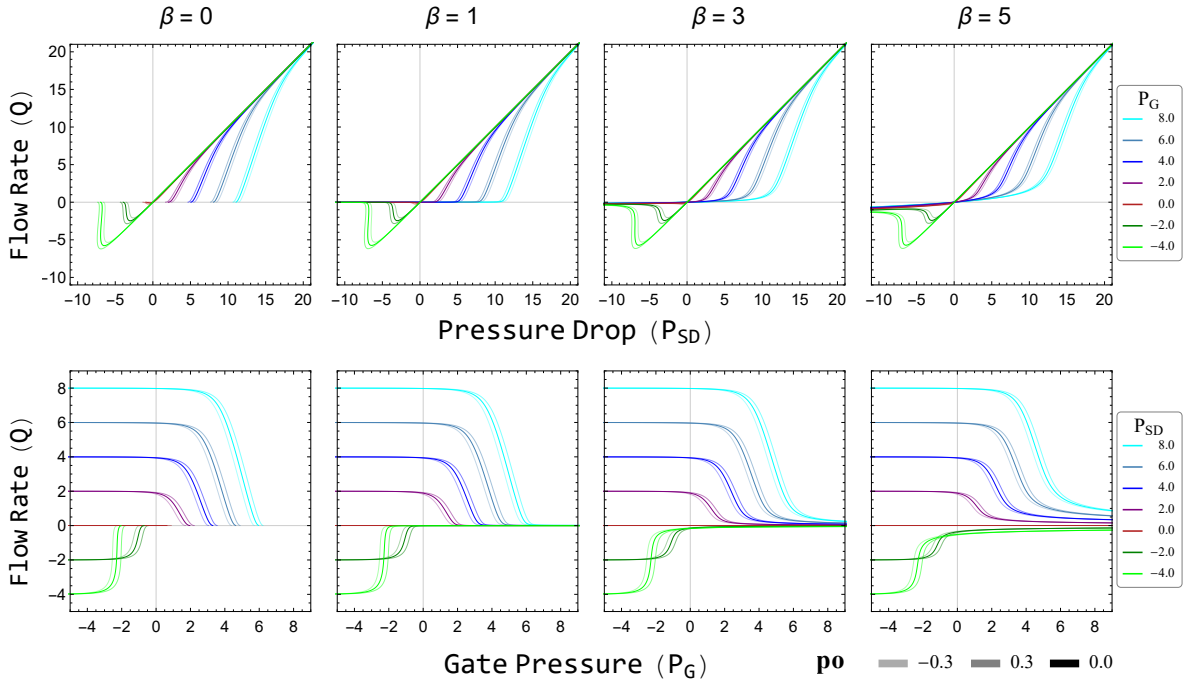


(a) NOT-Gate standard flow-rate view

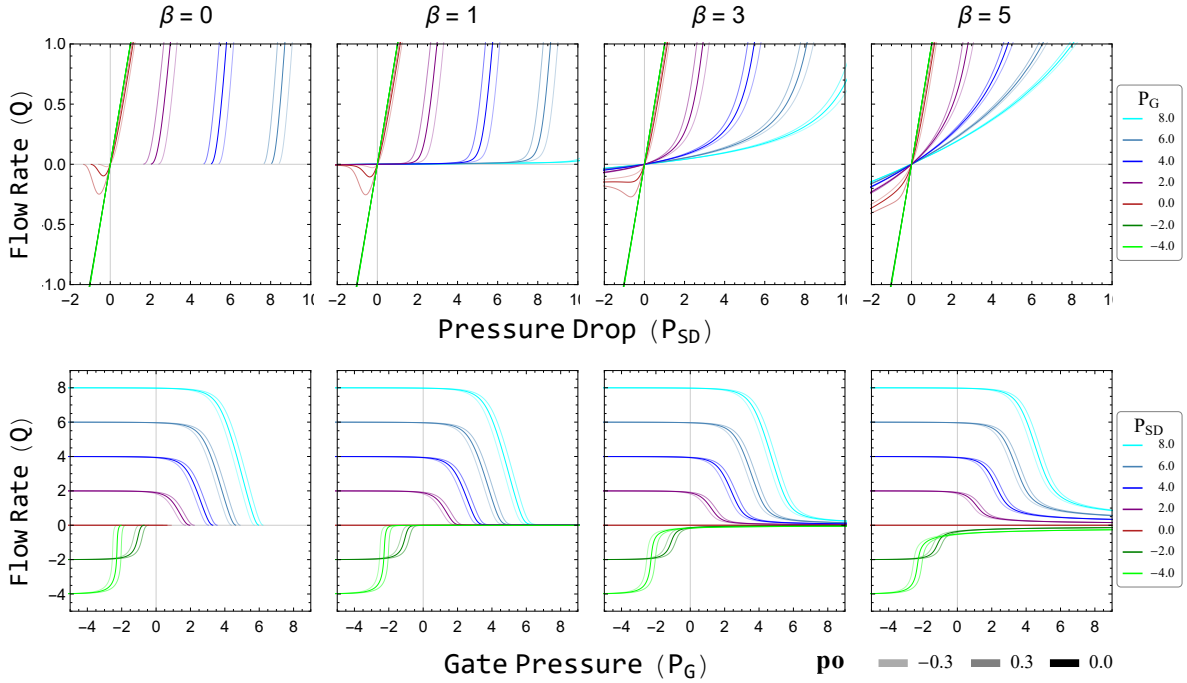


(b) NOT-Gate low-flow-rate view

Figure 5.23 NOT-Gate analytical models showing behavior for changes in **output pressure** ($\mathbf{p}_{\text{out}}$).
(Top) source-drain pressure (P_{SD}) sweep with parameterized gate pressure (P_G) changes and *(Bottom)* gate pressure (P_G) sweep with parameterized source-drain pressure (P_{SD}) changes.

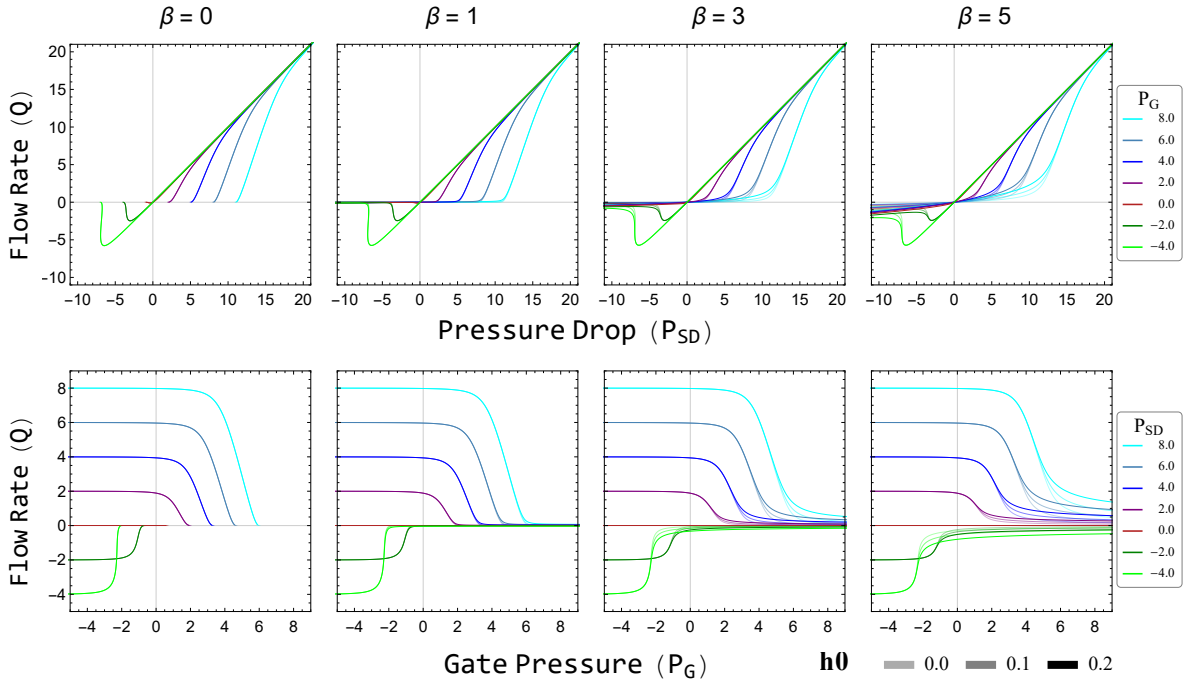


(a) NOT-Gate standard flow-rate view

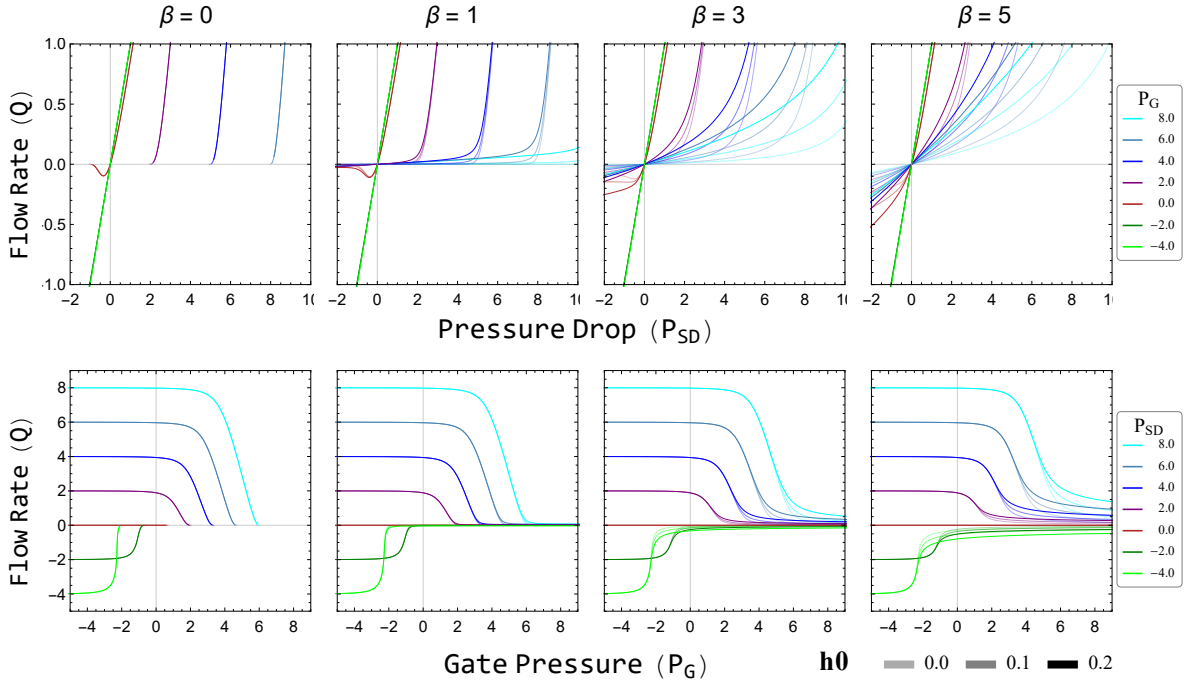


(b) NOT-Gate low-flow-rate view

Figure 5.24 NOT-Gate analytical models showing behavior for changes in **valve-seat distance** ($\mathbf{h_0}$). *(Top)* source-drain pressure (P_{SD}) sweep with parameterized gate pressure (P_G) changes and *(Bottom)* gate pressure (P_G) sweep with parameterized source-drain pressure (P_{SD}) changes.

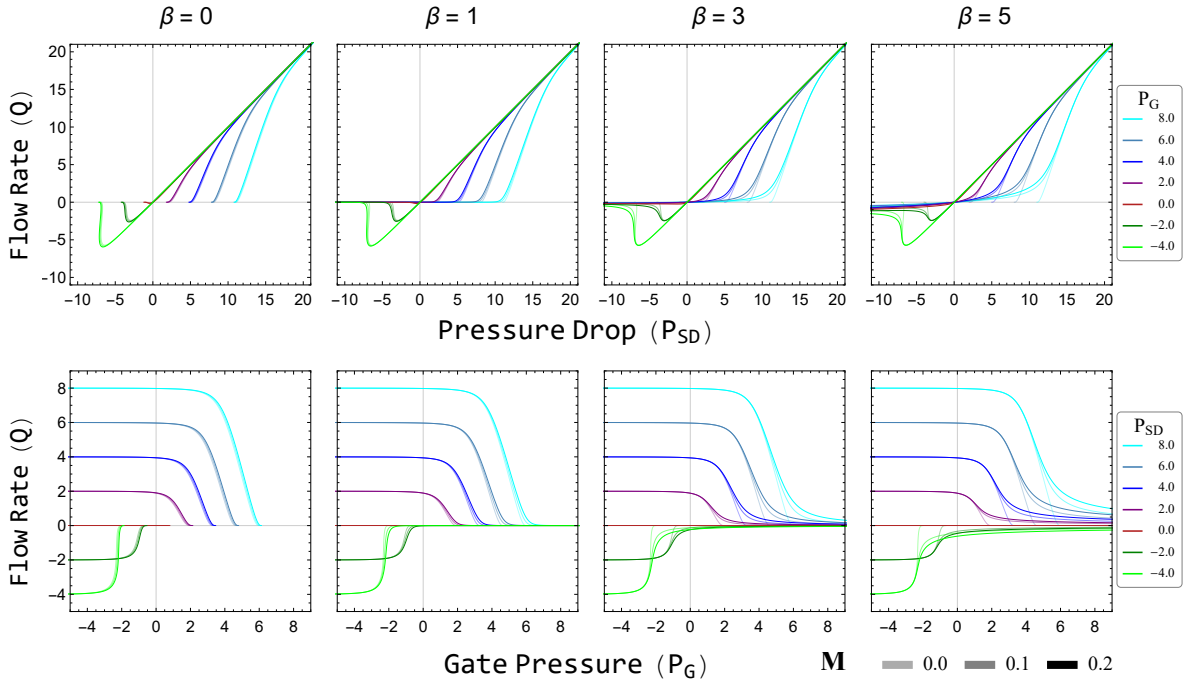


(a) NOT-Gate standard flow-rate view

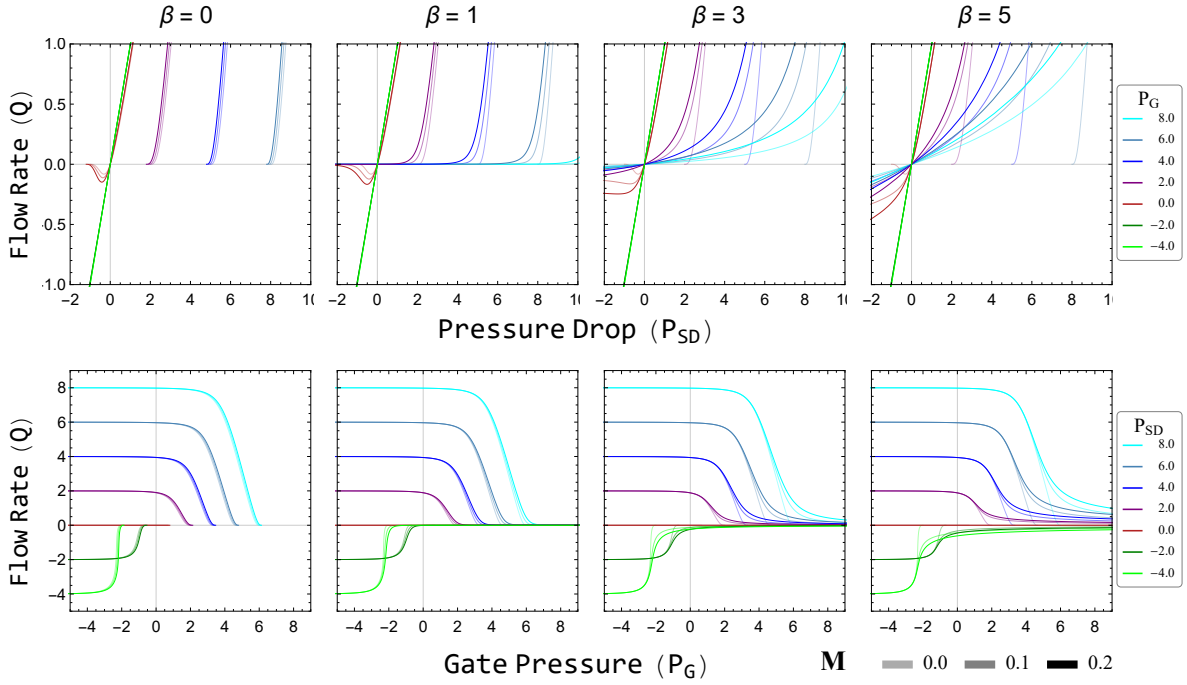


(b) NOT-Gate low-flow-rate view

Figure 5.25 NOT-Gate analytical models showing behavior for changes in **valve-seat back-force** (**M**). *(Top)* source-drain pressure (P_{SD}) sweep with parameterized gate pressure (P_G) changes and *(Bottom)* gate pressure (P_G) sweep with parameterized source-drain pressure (P_{SD}) changes.

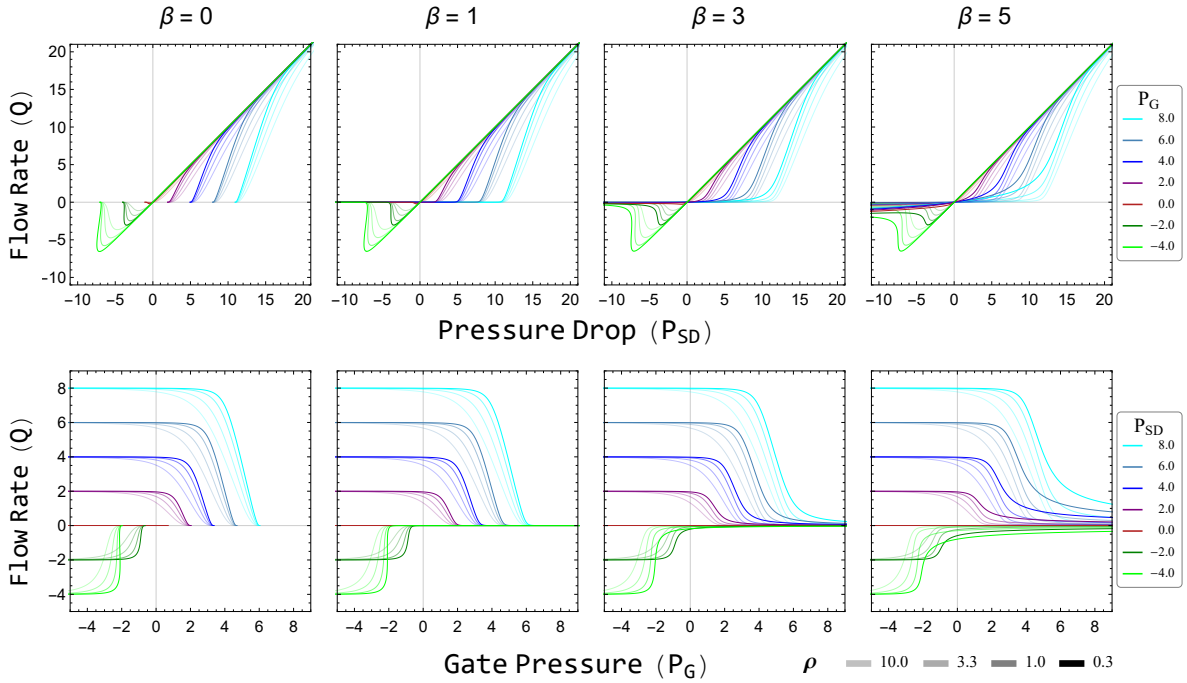


(a) NOT-Gate standard flow-rate view

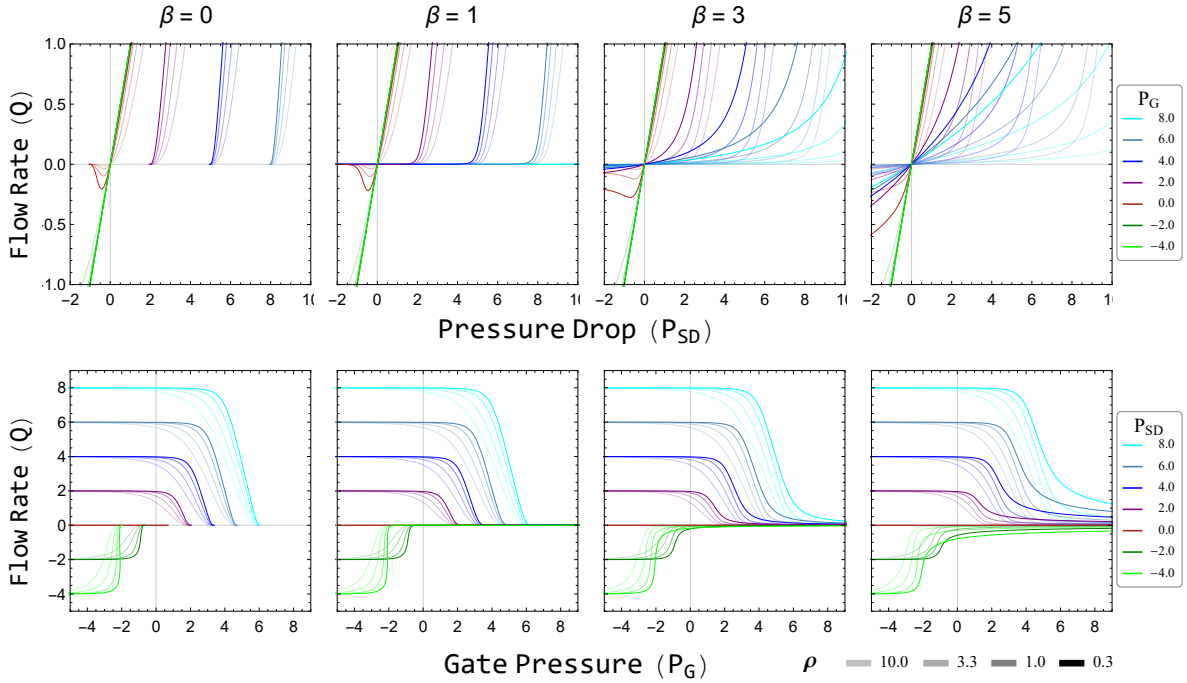


(b) NOT-Gate low-flow-rate view

Figure 5.26 NOT-Gate analytical models showing behavior for changes in **relative piston resistance** (ρ). *(Top)* source-drain pressure (P_{SD}) sweep with parameterized gate pressure (P_G) changes and *(Bottom)* gate pressure (P_G) sweep with parameterized source-drain pressure (P_{SD}) changes.

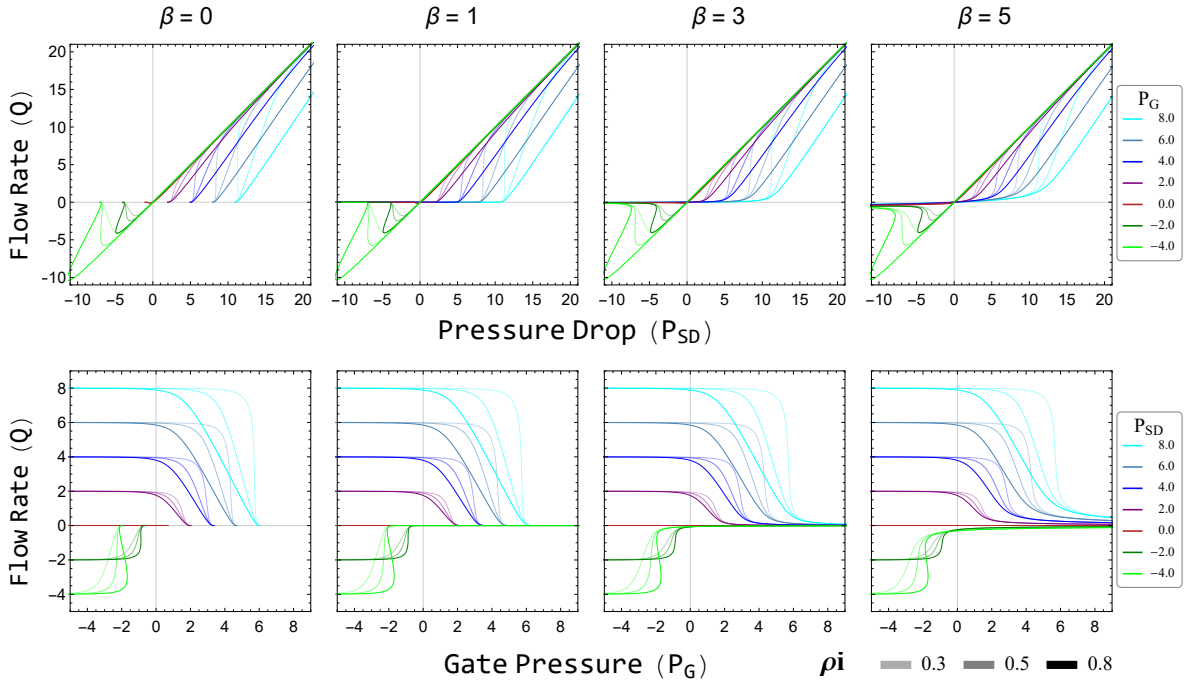


(a) NOT-Gate standard flow-rate view

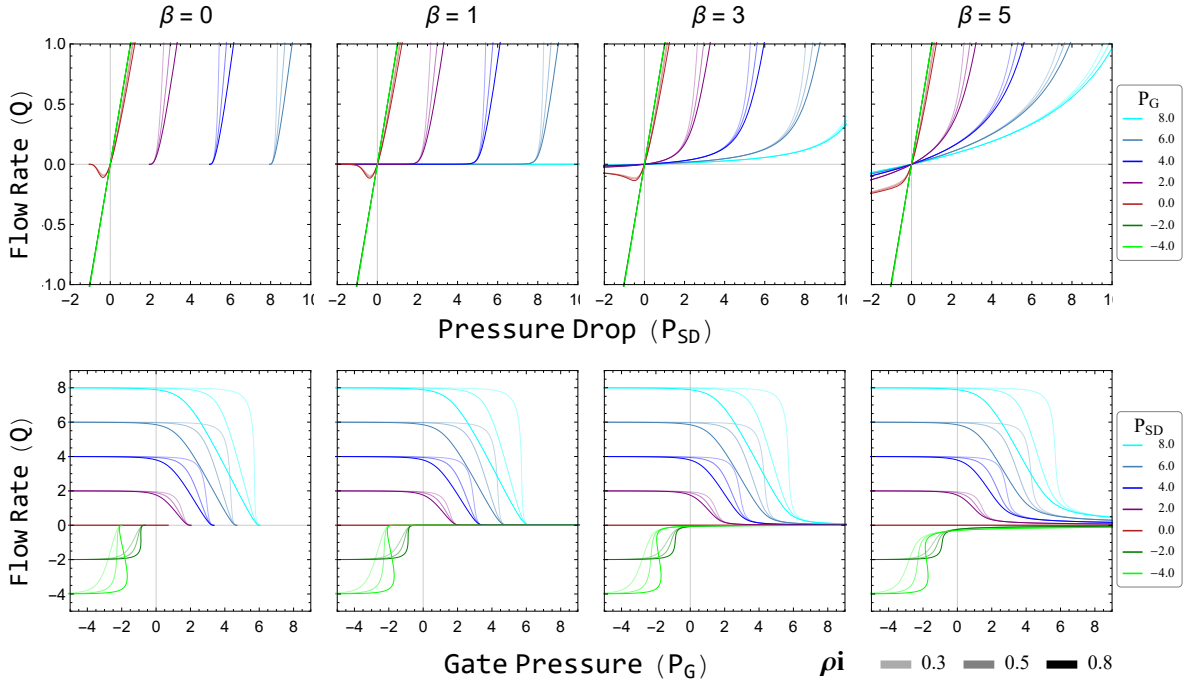


(b) NOT-Gate low-flow-rate view

Figure 5.27 NOT-Gate analytical models showing behavior for changes in **relative input resistance** (ρ_{in}). *(Top)* source-drain pressure (P_{SD}) sweep with parameterized gate pressure (P_G) changes and *(Bottom)* gate pressure (P_G) sweep with parameterized source-drain pressure (P_{SD}) changes.



(a) NOT-Gate standard flow-rate view



(b) NOT-Gate low-flow-rate view

5.7.4 Experimental Setup

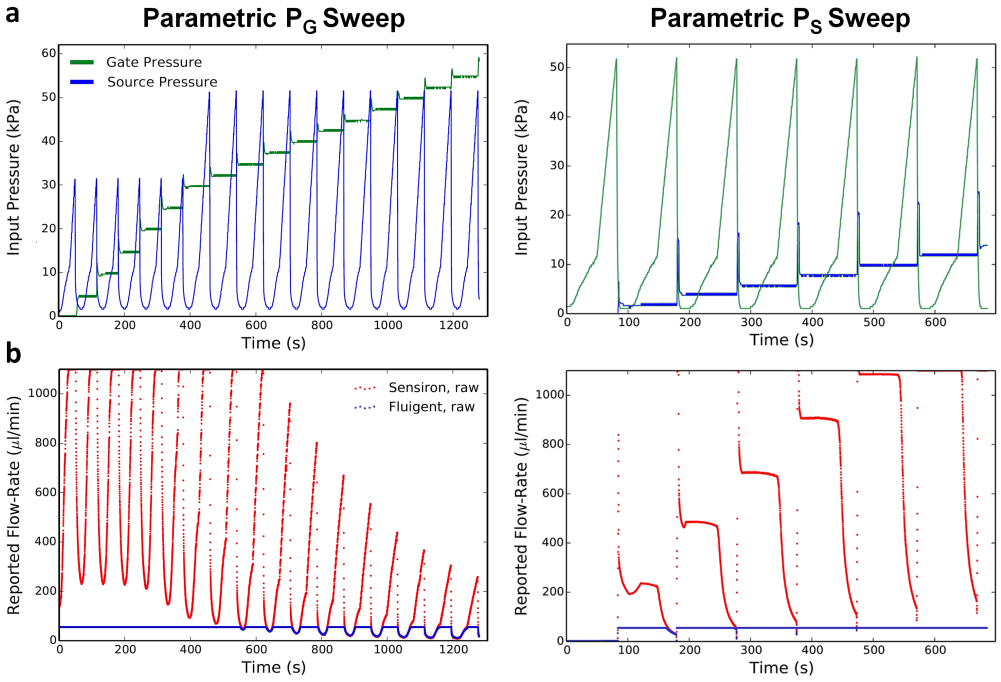


Figure 5.28 Time series data from 3D transistor performance measurement. **(a)** pressure sweep parameters and **(b)** aligned flow rate outputs from the Fluigent and Sensirion flow rate sensors, connected in series. *(left)* Results from a parametric gate pressure (P_G) sweep, performed over a rapid source pressure (P_S) sweep. *(right)* Results from a parametric P_S sweep, performed over a rapid P_G sweep. Note that the achieved pressures differ throughout the run for time-saving or fluid-saving purposes.

To determine the transistor characteristics curves of both 3D-printed fluidic transistor designs (*i.e.*, with and without gain-enhancement), we attached the source input port (P_S) to one channel of the Fluigent system (via a buffer resistor) and the drain output port to a waste container at ground pressure (viahe serially connected Fluigent and Sensirion flow rate sensors to measure Q_{SD}). We then attached the gate input directly to a second Fluigent pressure channel (P_G), driving gate movement through air pressure and sealed the remaining two inlet/outlet ports (*i.e.*, one drain port and one gate port, used for cleaning). We then ran a double pressure sweep (written in the Fluigent Scite software) to record the transistor output under multiple pressure conditions.

We ran two distinct double pressure sweeps were used to determine specific transistor characteristics (Fig. 5.28). A parametric P_G sweep (*i.e.*, a pressure sweep parametrized by P_G) consisted of repeated smooth sweeps of P_S from low to high pressure, with the value of P_G incremented after each P_S cycle. This sweep was used to determine the opening characteristics of the transistor and to measure the hydrodynamic resistance at each P_G. In contrast, a parametric P_S sweep (*i.e.*, a pressure sweep parametrized by P_S) consisted of repeated smooth sweeps of P_G from low to high

pressure, with the value of P_S incremented after each P_G cycle. This sweep showed the behavior of the transistor as it was closed under higher and higher gate pressures, indicating the transition regions and tail effects of the transistor performance.

5.7.5 Results

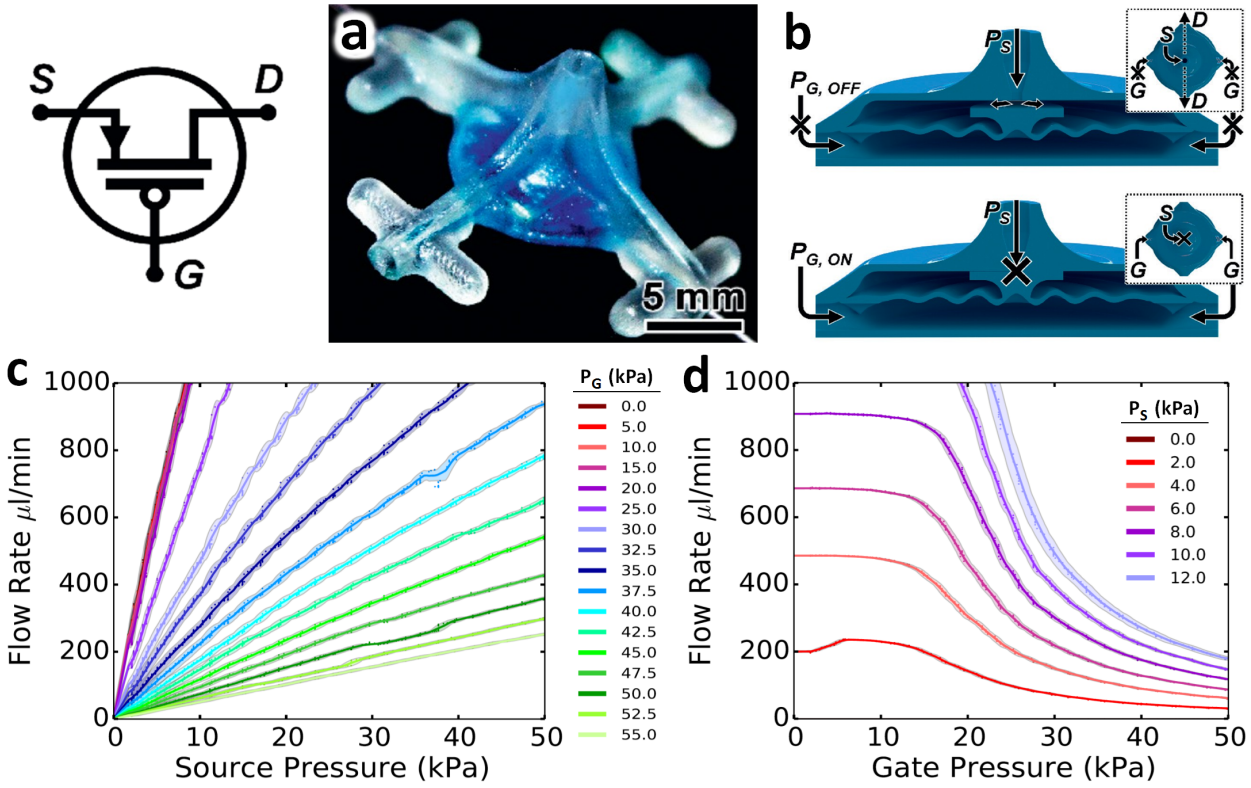


Figure 5.29 Experimental results for 3D-printed microfluidic transistor. **(a)** Photograph of transistor with blue food dye. **(b)** Conceptual cross-sectional view of transistor illustrating the path of fluid flow through the transistor and membrane deflection under driving source and gate pressures, P_S and P_G, respectively. **(c)** Experimental QP diagram illustrating source-drain flow rate through the transistor under a parametric P_G sweep; linear source-drain resistance decreases as P_G is increased. **(d)** Experimental QP diagram illustrating flow rate through the transistor under a parametric P_S sweep, showing self-similar valve-closing behavior under a variety of constant P_S. Error bands denote standard deviation of the running average. Subfigures **(a-c)** adapted from Ref. 316 with permission of the RSC.

From the parametric P_G sweep of the standard NOT-gate and the enhanced gain transistor, we determined that the transistors did not demonstrate a noticeable change in Q_{SD} prior to threshold activation pressures ($P_{G,Th}$) of 15 kPa and 5 kPa, respectively; *i.e.*, Q_{SD} was independent of gate pressure for $P_G < P_{G,Th}$. This result is further validated by simulation results which showed no substantial change in Q_{SD} for $P_G < 0$ (Fig. 5.32). For $P_G > P_{G,Th}$), increasing P_G decreased Q_{SD}, with the enhanced-gain design supporting reduced flow rates at comparatively lower P_G inputs.

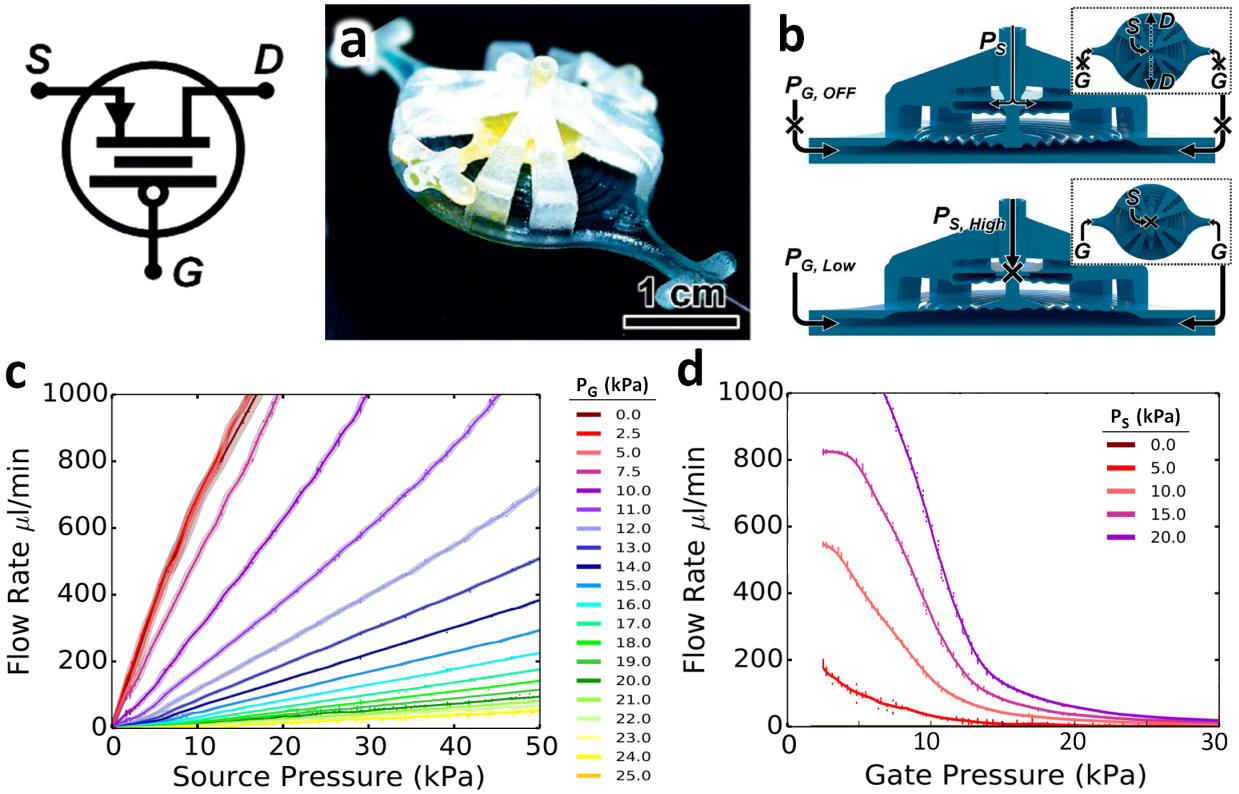


Figure 5.30 Experimental results for 3D-printed microfluidic enhanced-gain transistor. **(a)** Photograph of transistor with blue and yellow food dye in the gate and drain regions, respectively. A piston couples the lower gate region to the upper source region, enabling area-ratio-based pressure gain. **(b)** Conceptual cross-sectional view of transistor illustrating the path of fluid flow through the transistor and membrane deflection under driving source and gate pressures, P_S and P_G, respectively. **(c)** Experimental *QP* diagram illustrating source-drain flow rate through the enhanced-gain transistor under a parametric P_G sweep; linear source-drain resistance decreases as P_G is increased. **(d)** Experimental *QP* diagram illustrating flow rate through the enhanced-gain transistor under a parametric P_S sweep, showing self-similar valve-closing behavior under a variety of constant P_S. Note that valve closing occurs under much lower gate pressures than for the standard transistor. Error bands denote standard deviation of the running average. Subfigures **(a-c)** adapted from Ref. 316 with permission of the RSC.

Quantified results revealed A_P of 0.87 ± 0.23 and 3.01 ± 0.78 for the fluidic transistor without and with gain enhancement, respectively. The linear response of Q_{SD} to changes in P_S (for a given P_G parameterization) shows that the devices do indeed exhibit behavior analogous to vacuum triodes or p-channel MOSFETs biased in the triode region; due to the lack of field-based phenomenon, the flow rate never achieved saturation (*i.e.*, flow rate independent of applied pressure) such as occurs in MOSFETs, vacuum tetrodes, or pentodes [342, 343].[17]

The parametric P_S sweep was somewhat harder to quantify due to experimental error introduced by the relatively slow Fluigent MAESFLO response time at lower pressures; because P_G lagged in the sweeps for $P_G < 2.5$ kPa, we were not able to experimentally measure device performance

[17] In particular, MOSFETs achieve saturation due to the quantum tunnelling-based effect known as *pinch-off* [307, 308]

in that region. While the standard NOT-gate transistor had reasonably constant flow rate for $P_G < P_{G,Th}$ (Fig. 5.29d) for the enhanced gain transistors (Fig. 5.29d), valve closing began at a much lower P_G, therefore leading to a loss of some important results. The fluctuation near $P_G = 0$ on the $P_S = 2.0$ kPa parameterization was a result of the MAESFLO system responding slowly after being kept at low pressures for extended times.

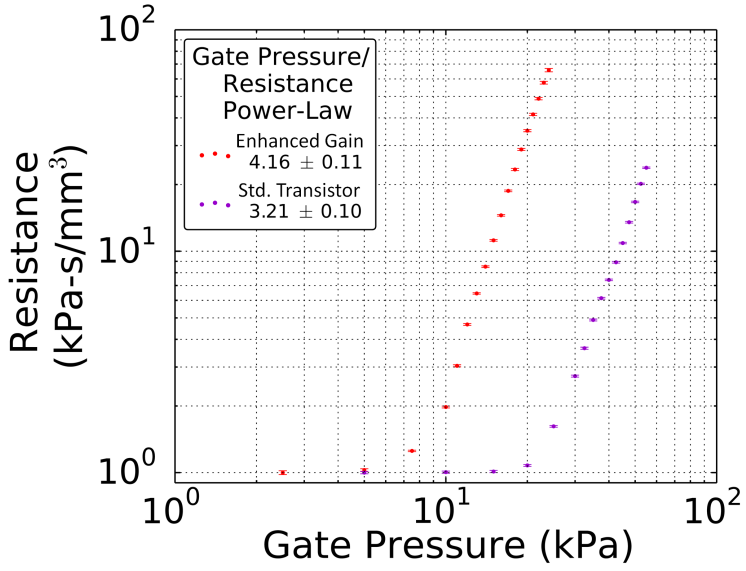


Figure 5.31 Comparison of gate pressure-dependent Source-Drain resistance for standard and enhanced gain transistors. After the threshold gate pressure ($P_{G,th}$), both devices experienced a power-law resistance (ρ_{trans}), indicating a constant sensitivity of R_SD to changes in gate pressure, for $P_G > P_{G,Th}$. Note, results have been normalized by $R(P_G = 0)$

Lastly, we quantified the source-drain resistance (R_{SD}) for each cycle of the parametric P_G sweep, determining R_{SD} as a function of P_G. We plotted the resistances on a log-log plot, normalizing the device resistance by its resistance at $P = 0$ (Fig. 5.31). For $P_G > P_{G,Th}$, the resistance displayed a power-log relationship for both standard and enhanced-gain transistors, of the form

$$R_{SD}(P_G > P_{G,Th}) \sim \rho(P_G - P_{G,Th})^{\alpha}, \tag{5.190}$$

where β is the normalization coefficient. α was determined to be 3.21 ± 0.10 and 4.16 ± 0.11 for the standard and enhanced-gain transistor, respectively. Additionally, if we consider the sensitivity

S of the resistance to changes in pressure for $P_G > P_{G,Th}$,

$$S(R_{SD};P_G) \equiv \frac{\partial R_{SD}}{\partial P_G} \times \frac{\left(P_G - P_{G,Th}\right)}{R_{SD}} \tag{5.191}$$

$$= \alpha \left(\beta \left(P_G - P_{G,Th}\right)^{\alpha-1}\right) \times \frac{\left(P_G - P_{G,Th}\right)}{R_{SD}} \tag{5.192}$$

$$= \alpha \frac{R_{SD}}{\left(P_G - P_{G,Th}\right)} \times \frac{\left(P_G - P_{G,Th}\right)}{R_{SD}} \tag{5.193}$$

$$= \alpha \tag{5.194}$$

we find out that the log coefficient $\alpha = S(R_{SD};P_G)$.

5.7.6 Transistor Simulations

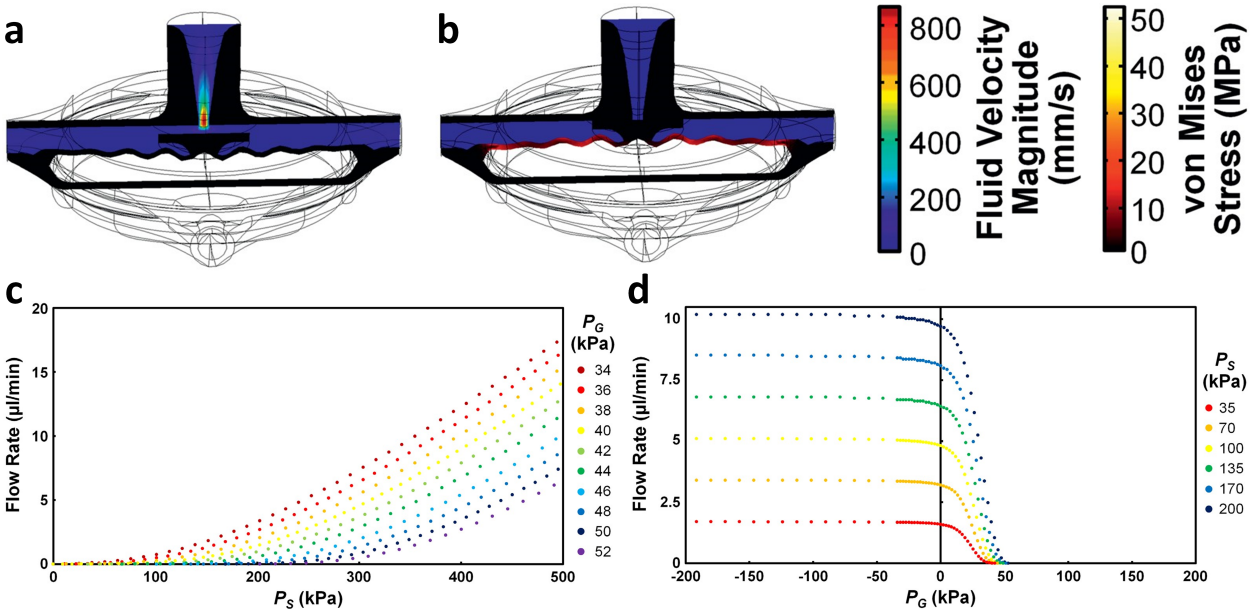


Figure 5.32 Simulation results for standard NOT-gate 3D fluidic transistor. **(a,b)** Cross-sectional views of transistor illustrating fluid velocity field and von Mises stress distributions for $P_S = 30$ kPa and **(a)** $P_G = 0$ kPa and **(b)** $P_G = 200$ kPa. **(c,d)** Simulated pressure sweeps for *ideal* 3D-printed transistor: **(c)** long P_G sweep and **(d)** long P_S sweep. Unlike the physical transistor, the simulation could measure performance at negative gate pressures. Additionally, the simulated transistors experienced complete closure when the piston and the wall contacted, creating a much sharper cut-off pressure. Adapted from Ref. 316 with permission of the RSC.

To obtain a greater understanding of the fluidic and structural behavior of the 3D-printed fluidic transistor (without gain enhancement), we analyzed the performance using COMSOL multiphysics simulations (Fig. 5.32). The von Mises stress distribution on the transistor diaphragm was consistent with simulated results for both the 3D fluidic capacitor (Fig. 5.9d-f) and the 3D fluidic

diode (Fig. 5.11e,f) within the range of input pressures modeled. We performed both parametric P_G (Fig. 5.32c) and parametric P_S (Fig. 5.32d) sweeps, additionally examining the device behavior under the application of vacuum (*i.e.*, negative, relative to atmospheric "ground") pressure to the gate (*i.e.*, $P_G < 0$), showing an increase of Q_{SD} (at $P_G = -200$ kPa) of only 4.97% relative to the flow rate at $P_G = 0$; further withdrawal of the piston from the default position did not appreciably decrease the device resistance, an expected result under the model $Q_{SD} \sim R_0 + rh^{-3}$. Additionally, the simulations revealed that fluid flow rate was highest ($V \approx 800$ m/s at the narrowest portion of the source inlet (300 μm in diameter). Thus, the peak simulated Reynolds number was $Re \sim 240$ for a pressure gradient of $P_S = 30$ kPa across the transistor.

Note that the measured transistors were exposed to a much lower pressure gradient through the addition of both resistive outlets (which would act as device parasitics, reducing optimal performance) and through the addition of the upstream buffer resistor. Because the buffer resistance was $> 10\times$ larger than the intrinsic device resistance, none of the practical transistors were likely to have experienced pressure gradients as high as the simulated transistors.

5.8 Microfluidic IF-Gate: CMOS and Continuing Work

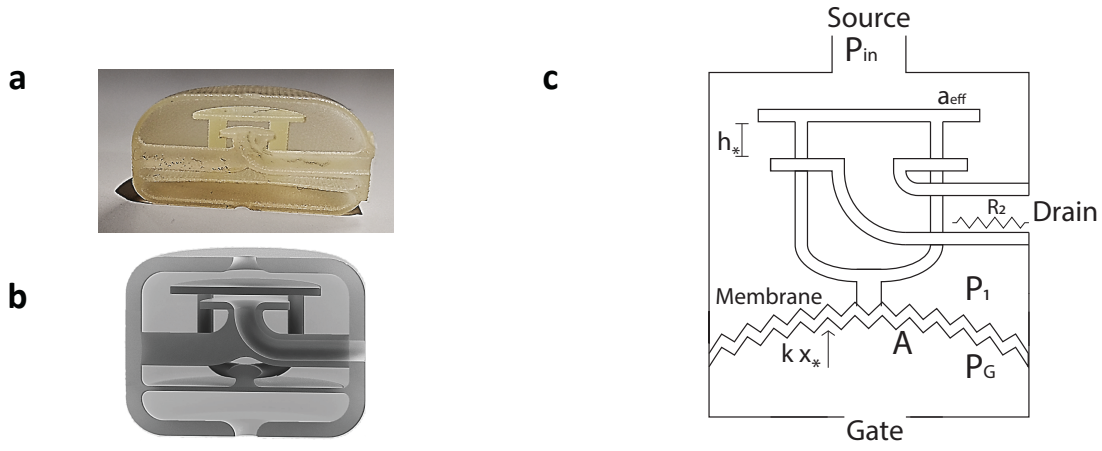


Figure 5.33 Setup of 3D-printed IF-gate transistor analysis with the key dimensional quantities labeled. **(a)** Photograph of fabricated IF-Gate 3D-printed transistor. **(b)** SolidWorks CAD drawing. **(c)** free-body diagram. Pressures P_1 and P_G act on membrane area A and control the position of the piston; in contrast to the NOT-gate, when pressure P1 increases and the membrane is deflected downward, the mechanical linkages force the plate (with effective area a_{eff} (Equation 5.31)) downward on the valve seat, closing the device, and increasing gate pressure restores fluid flow.

Developing a default-closed valve is essential for generating low-fluid microfluidic control mechanisms. Because these valves are off when gate pressure is off and turn on after the gate is pres-

surized, these microfluidic devices behave like IF logic: if Gate then Flow. There are a number of approaches to microfluidic IF Gates, although several are not true IF logic. For example, work by Unger *et al.* have developed microfluidic devices with static gain by sandwiching the valve between two control layers and preloading the upper layer with pressurized and cured photoresist. This preloading forces the flow layer shut under $P_{SD} = 0$ conditions. Subsequently, the valves can be reopened by applying a negative pressure to the gate region. This architecture can be used to provide a "static gain" between the gate pressure P_G and the flow pressure P_{SD}, where the valve only opens for $P_{SD} - P_G > A$. Critically for the development of default-off logic, A can be positive, meaning fluid flow will be inhibited for all $P_{SD} \leq A$ unless $P_G < 0$. However, these devices are *not* true IF-gates and are instead NOT-gates with the opening pressures shifted by a static amount; similar effects could be generated by the 3D-printed NOT-gates discussed here where the membrane is pre-stressed upward. In contrast, true IF-gates remain closed below for positive P_{SD}[18] because the fluid pressure itself maintains the device closure. The difficulty arises because pressure within a microfluidic channel (P_{SD}) tends to force the device open while pressure outside the channel is much more easily used to force the channel closed again; doing the opposite requires some method of force reversal (*i.e.*, using pressure at the gate to either pull a channel apart or push at the opposite side of a channel).

Her we present an alternate approach to a "true" IF-gate where 3D-printed mechanical columns link the motion of a membrane to that of a flap valve; under standard conditions, internal pressure will hold the valve shut and will only re-open the valve when an external pressure is applied to the gate. Although these IF-gate designs have not yet been tested, they could enable a viable route to developing Complementary microfluidic logic (analogous to semiconductor CMOS technology). By combining default-on with default-off microfluidic switches, we could develop fluidic control networks that only drew on fluid when switching states between on and off, drastically reducing the fluid requirement.

The geometry of the standard microfluidic IF-gate is summarized in Figure 5.33. Because the analysis has been performed twice — for the 3D-printed diodes and NOT-gates — the derivation for the parametric IF-gate equations will be omitted here, and the results will be summarized for a

[18] Provided P_{SD} is below the breaking pressure of the device

device with no external load:

$$\Delta P = Q(R + r_* h_*^{-3}) \tag{5.195a}$$

$$(\Delta P - QR)a_{\text{eff}} + (\Delta P + P_D - QR_S - A_v P_G) = k(h_0 - h_*) + m_* h_*^{-\beta}, \tag{5.195b}$$

where R_S is the input (source) resistance and P_D. In non-dimensionalized form, the equations become

$$\Delta p = q(1 + \rho h^{-3}) \tag{5.196a}$$

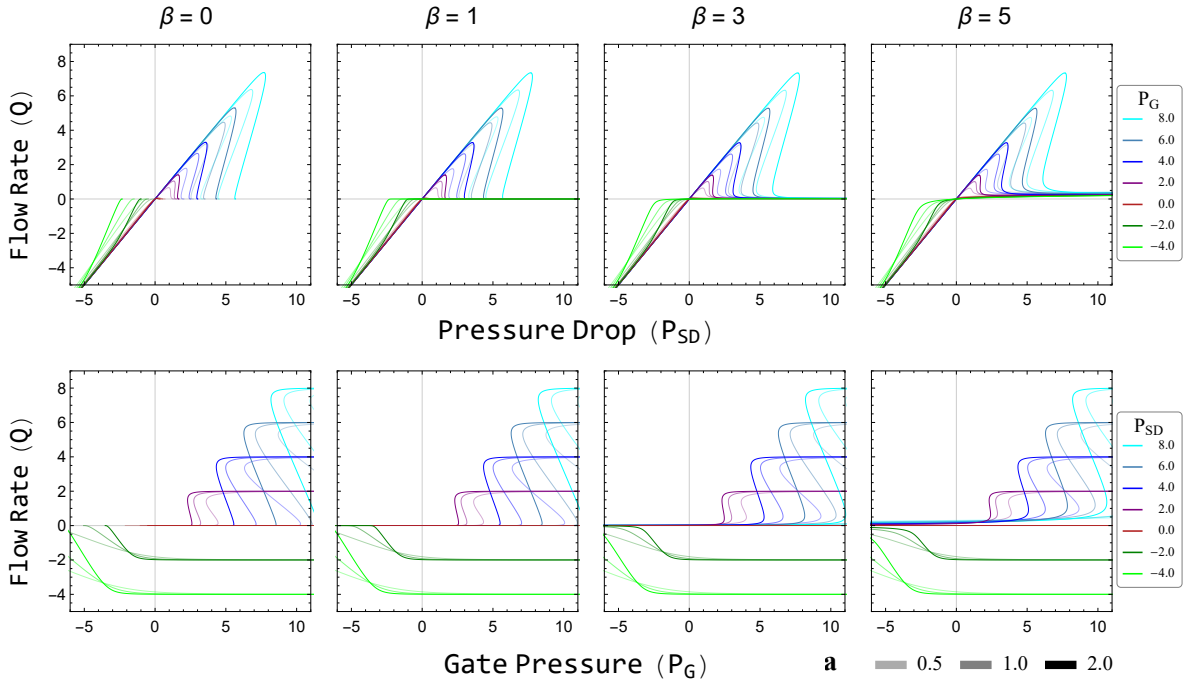
$$(\Delta p - q)\alpha + (\Delta p + p_d - q\rho_i - A_v p_g) = (1 - h) + Mh^{-\beta}. \tag{5.196b}$$

The key difference between the IF-gate equations and Equation 5.177b is the sign of the spring term relative to the rest of the equations, reflecting that the primary direction of motion is downwards and the gate tends to restore the position of the membrane.

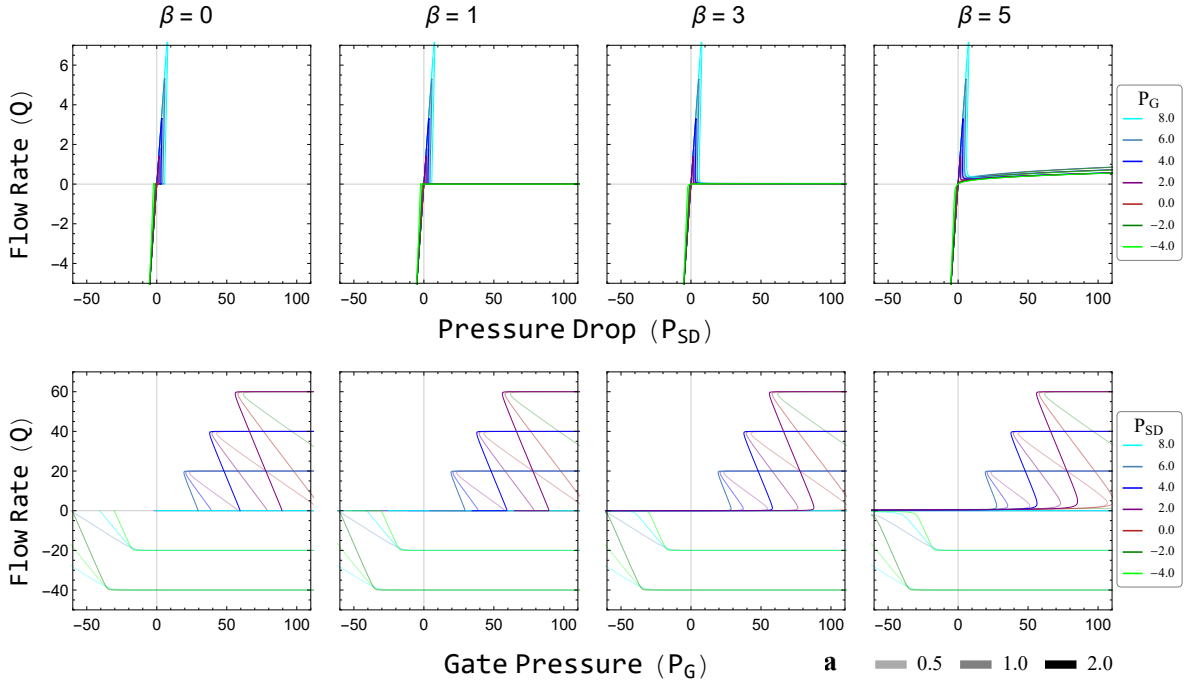
5.8.1 Results Summary for IF-Gate Analytical Modeling

The following figures show the results from analytical models of the IF-Gate parametric equations. The IF-Gates are "driven" with positive source pressure and zero drain pressure, except for the final set of plots which show the (non-linear) variance in behavior for alteration in drain pressure. Each plot consists of a linear sweep in source/gate pressure and discrete changes in gate/source pressure, and show behavior in the near-field and the far-field ranges. One thing to note are the conditions under which hysteresis begins to emerge, particularly for large area ratios α and for high input source pressures.

Figure 5.34 IF-Gate analytical models showing behavior for changes in **effective area** ($\mathbf{a}_{\text{eff}}$).
(Top) source-drain pressure (P_{SD}) sweep with parameterized gate pressure (P_G) changes and *(Bottom)* gate pressure (P_G) sweep with parameterized source-drain pressure (P_{SD}) changes.

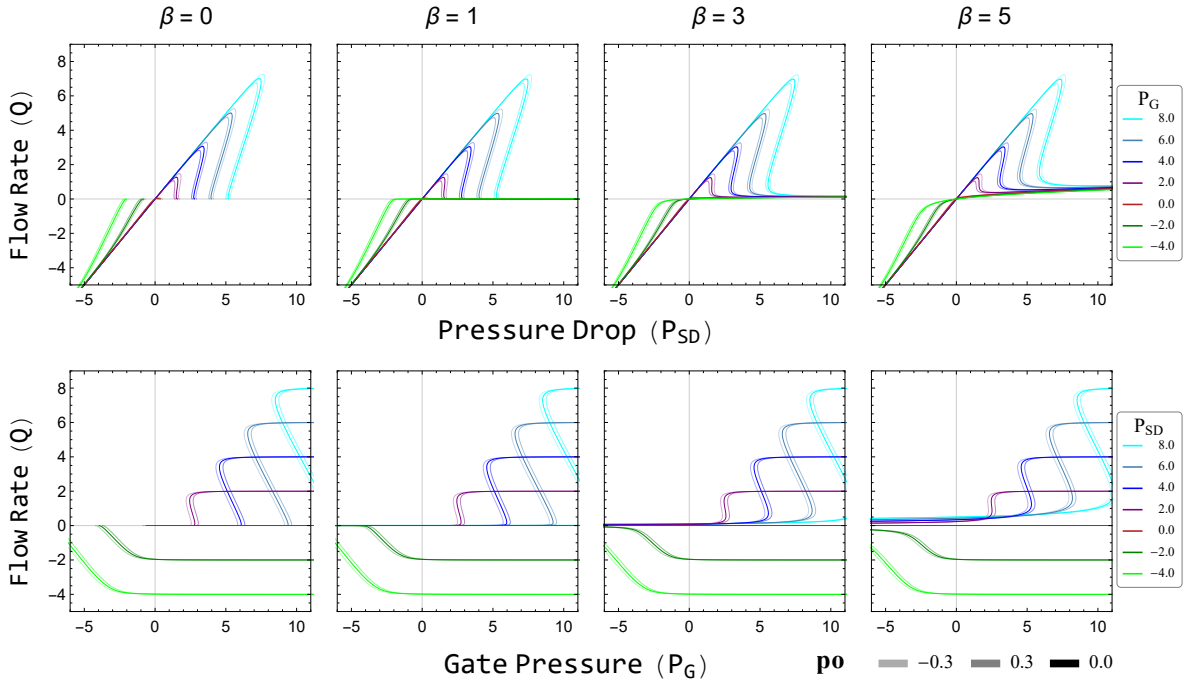


(a) IF-Gate near-field (low-pressure) view

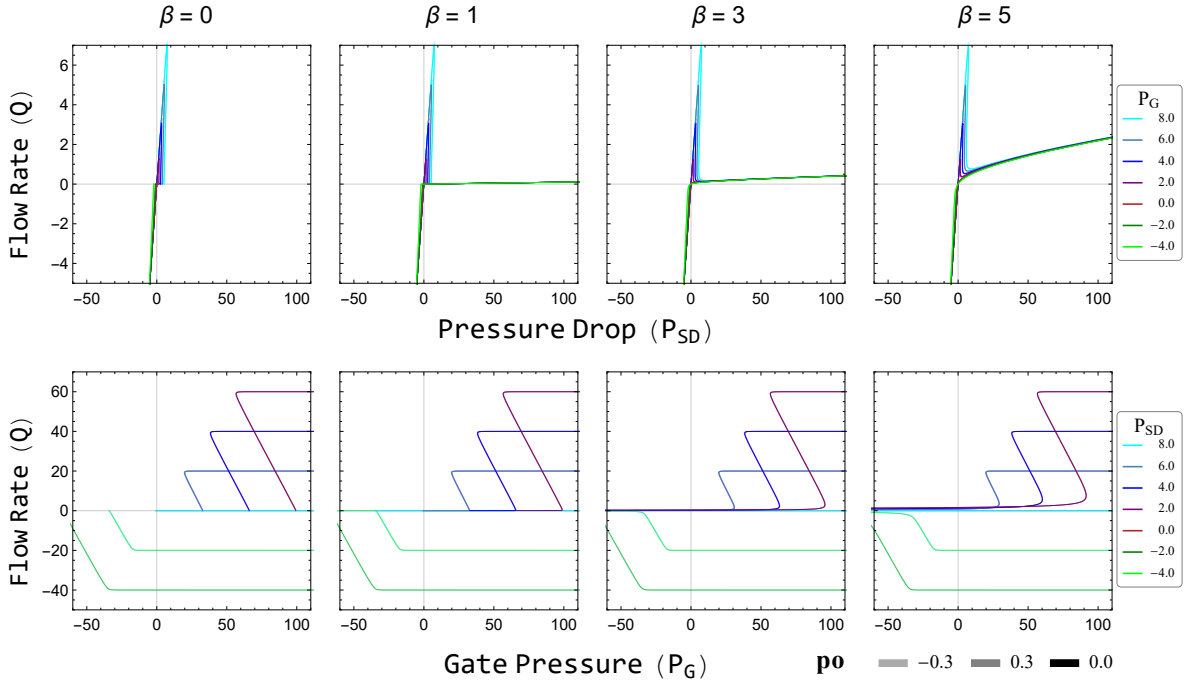


(b) IF-Gate far-field (high pressure) view

Figure 5.35 IF-Gate analytical models showing behavior for changes in **output pressure** ($\mathbf{p}_{\text{out}}$).
(Top) source-drain pressure (P_{SD}) sweep with parameterized gate pressure (P_G) changes and *(Bottom)* gate pressure (P_G) sweep with parameterized source-drain pressure (P_{SD}) changes.

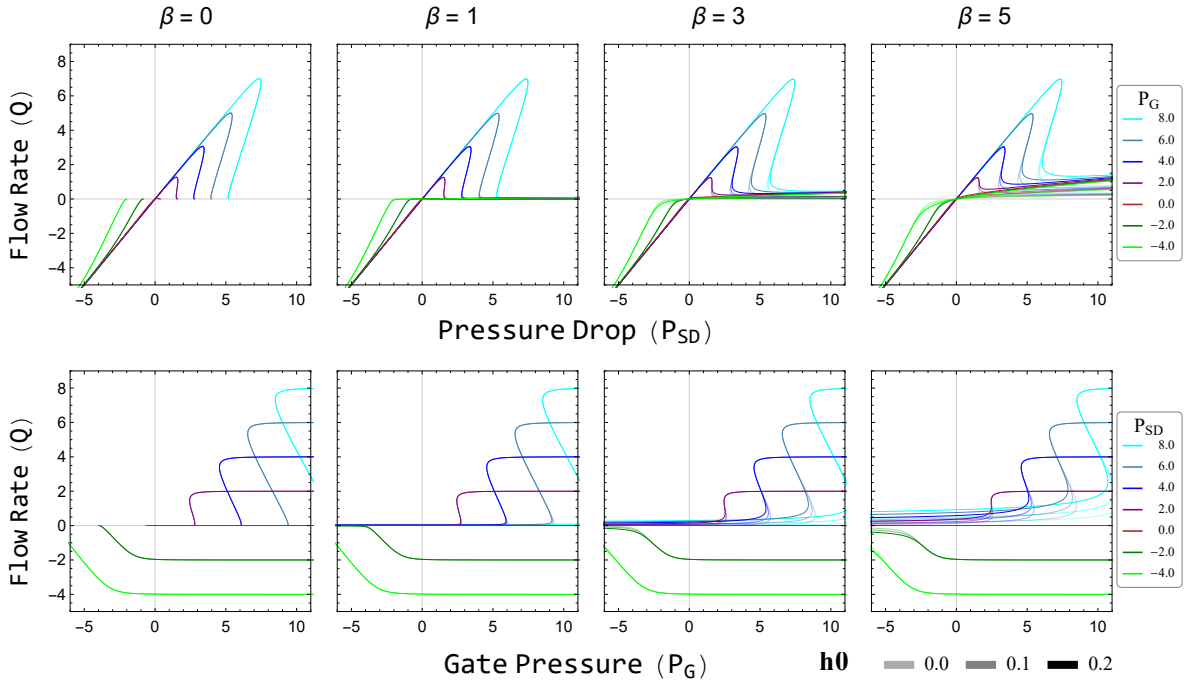


(a) IF-Gate near-field (low-pressure) view

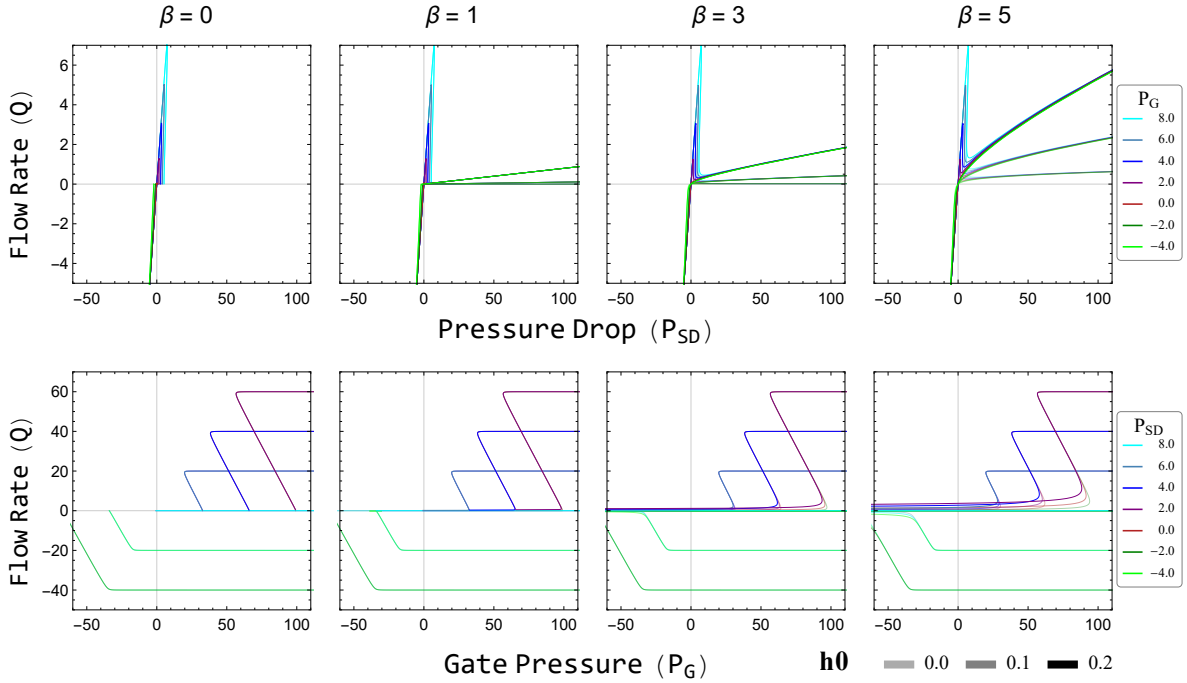


(b) IF-Gate far-field (high pressure) view

Figure 5.36 IF-Gate analytical models showing behavior for changes in **valve-seat distance** ($\mathbf{h_0}$).
(Top) source-drain pressure (P_{SD}) sweep with parameterized gate pressure (P_G) changes and *(Bottom)* gate pressure (P_G) sweep with parameterized source-drain pressure (P_{SD}) changes.

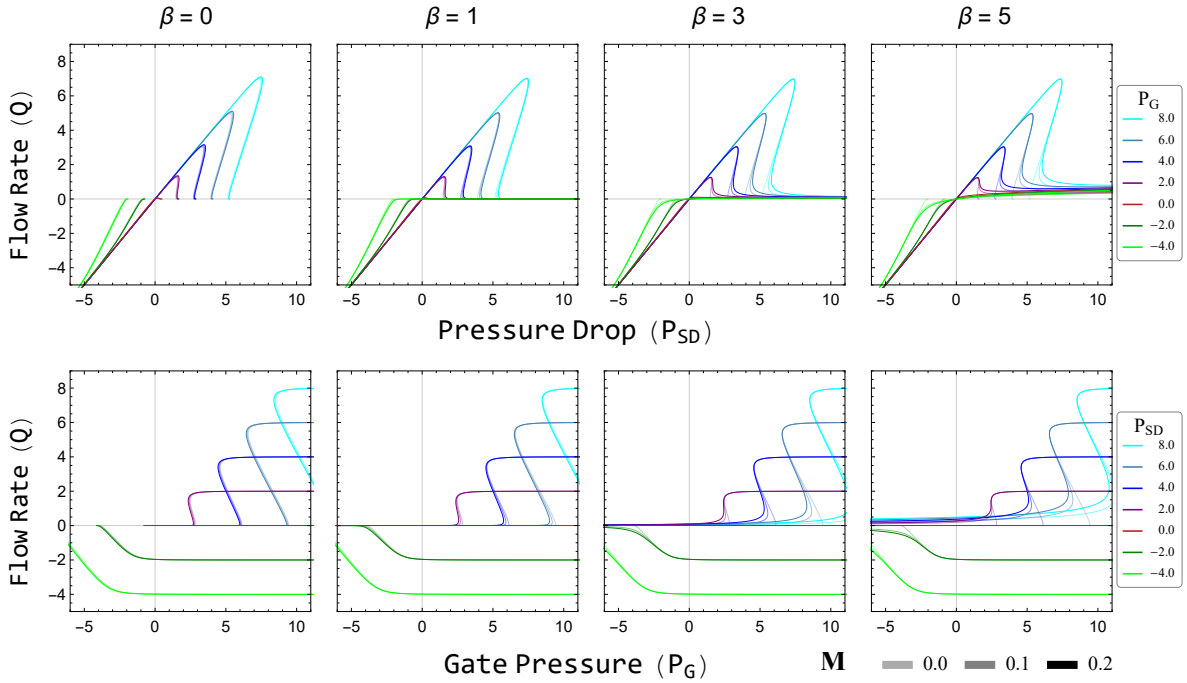


(a) IF-Gate near-field (low-pressure) view

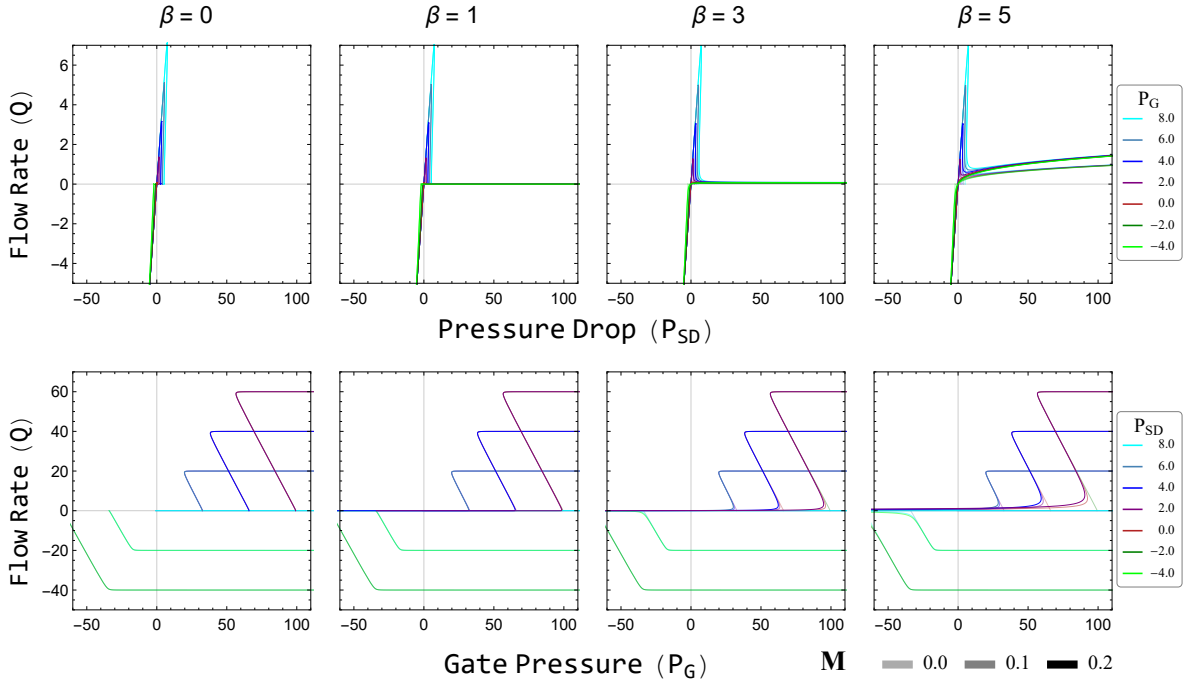


(b) IF-Gate far-field (high pressure) view

Figure 5.37 IF-Gate analytical models showing behavior for changes in **valve-seat back-force** (**M**). *(Top)* source-drain pressure (P_{SD}) sweep with parameterized gate pressure (P_G) changes and *(Bottom)* gate pressure (P_G) sweep with parameterized source-drain pressure (P_{SD}) changes.

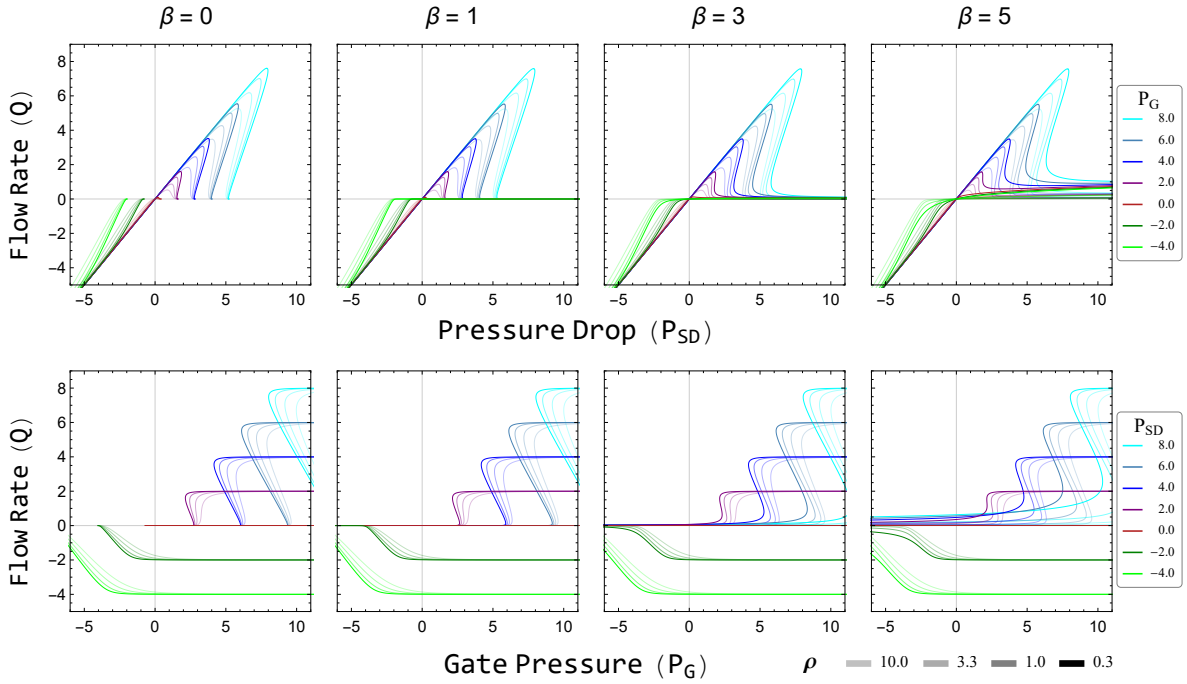


(a) IF-Gate near-field (low-pressure) view

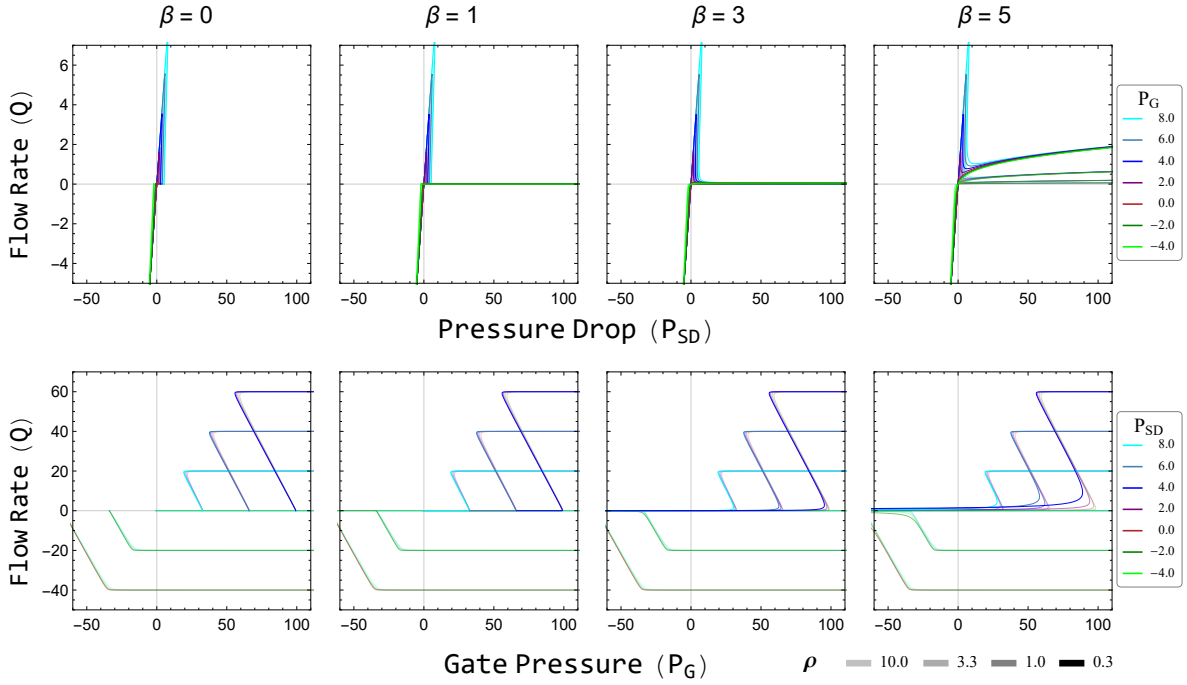


(b) IF-Gate far-field (high pressure) view

Figure 5.38 IF-Gate analytical models showing behavior for changes in **relative piston resistance** (ρ). *(Top)* source-drain pressure (P_{SD}) sweep with parameterized gate pressure (P_G) changes and *(Bottom)* gate pressure (P_G) sweep with parameterized source-drain pressure (P_{SD}) changes.

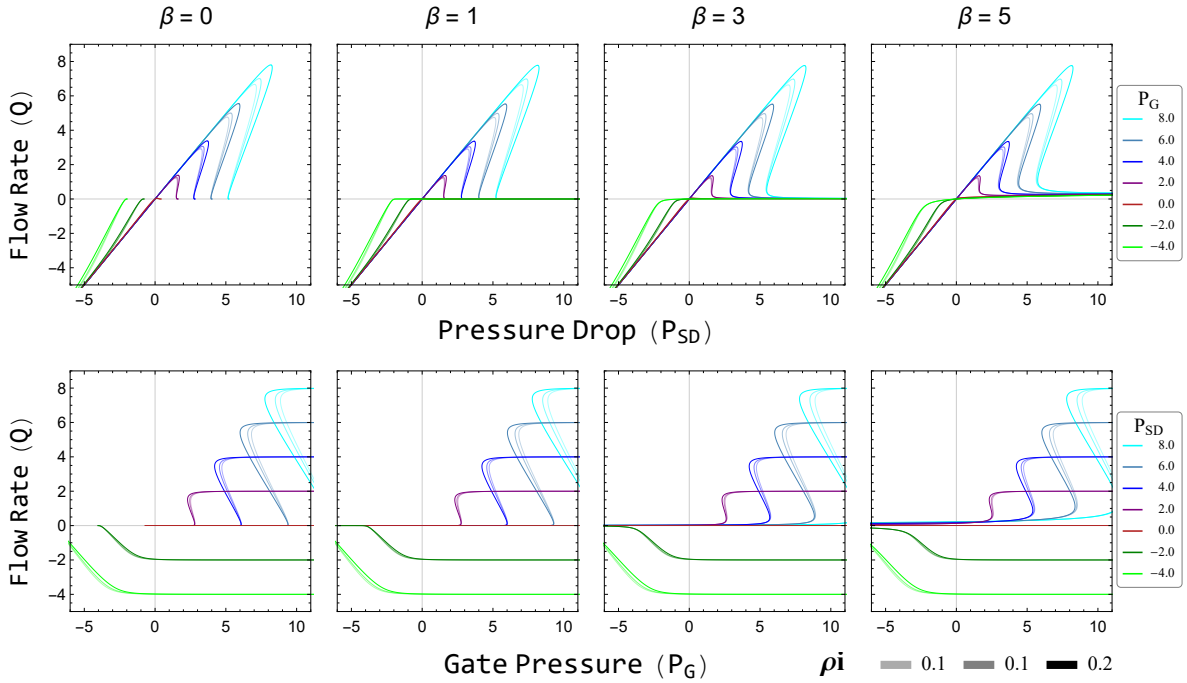


(a) IF-Gate near-field (low-pressure) view

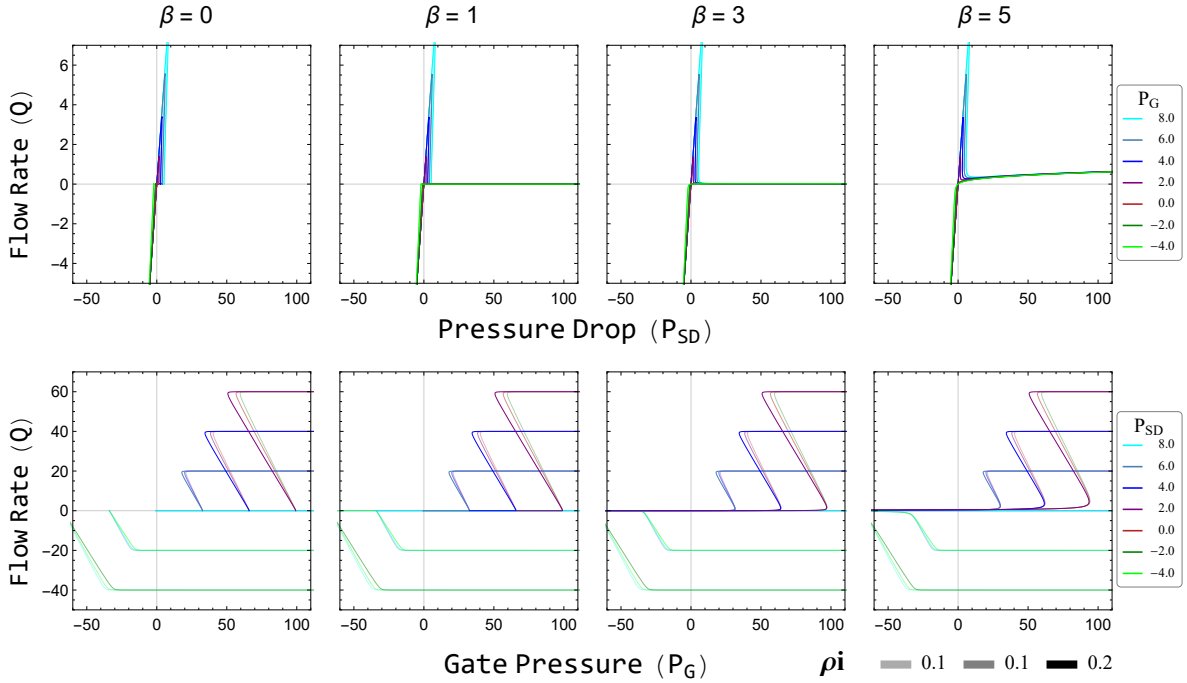


(b) IF-Gate far-field (high pressure) view

Figure 5.39 IF-Gate analytical models showing behavior for changes in **relative input resistance** (ρ_{in}). *(Top)* source-drain pressure (P_{SD}) sweep with parameterized gate pressure (P_G) changes and *(Bottom)* gate pressure (P_G) sweep with parameterized source-drain pressure (P_{SD}) changes.



(a) IF-Gate near-field (low-pressure) view



(b) IF-Gate far-field (high pressure) view

5.9 The Question of Gain

The nature of *gain* in microfluidic transistors is not easy to address. The basic definition "ratio of control pressure to device pressure needed to close a valve" is often inadequate. Among other questions that need to be addressed, we have

- What is meant by "closed" for valves that do not open or shut instantly, and may have a range of closing pressures?
- Under what operating conditions to we define gain?
- Is gain a single value or a range of values?
- If gain is the slope of a transfer characteristic curve, which slope?
- How is gain defined if there is hysteresis?
- What definition for gain G removes the most dependencies on external inputs?

For the optofluidic gain measurements, gain was considered at the pressure for which the pistons began moving (in both the opening and closing directions). For the 3D-printed transistor analysis, gain was not truly considered at all, and was instead depicted using a *transresistance* analysis — the relationship between source-drain resistance and gate pressure.

Here, we will consider another definition: the ratio of $P_S : P_G$ needed to change Q from $Q_{\max} \rightarrow fQ_{\max}$, where $0 < f < 1$ is some fraction.[19] A gain $G > 1$ implies that $P_G < P_S$ at the critical threshold. For this analysis, $P_S > P_D$. To simplify the analysis, we make our analysis in the region far enough from the valve seat that the valve closing resistance is negligible, *i.e.*, $M \rightarrow 0$. Gain G is different from area-ratio gain A_v for force amplification on the gate, although a higher A_v will in general lead to a higher G.

The general equation for fluid flow through a microfluidic transistor is $P_{\text{source}} = P_{\text{drain}} = Q(R_{\text{fixed}} + R_{\text{variable}})$, where Q and R are functions of both the pressure differential and of the absolute pressures P_S, P_D, and the control pressure P_G. Due to the number of measurable variables ()P_S, P_D, P_G, Q) and the internal variables (R_V, h, R_{fixed}), there are numerous ways to treat the analysis of gain. Due to the non-linearities in the system, many of these methods will not be absolute measures of gain, but instead will be condition-dependent.

[19] For example, for a 3 dB change, $f = \sqrt{2} \approx 0.707$ and for a doubling of resistance, $f = \frac{1}{2}$.

Gate pressure for flow reduction f

In this analysis, P_S and P_D are fixed and P_G is swept from vacuum to the highest pressure needed. The flow rate Q is normalized by $Q_{\max}$, where $f \equiv Q/Q_{\max}$. Gain is then considered for a given f; in other words, what is the pressure ratio needed to achieve a given flow ratio f. Gain G_f is then defined

$$G_f \equiv \left.\frac{P_S}{P_G}\right|_f = 1/\left.\frac{P_G}{P_S}\right|_f \tag{5.197}$$

and will be plotted with f on the x-axis and $1/\frac{P_G}{P_S}$ on the y-axis. Multiple curves can be plotted for various P_S and P_D values.

Small-signal flow rate change

$$G \equiv \left.\frac{P_S}{Q_{\max}}\frac{\mathrm{d}Q}{\mathrm{d}P_G}\right|_{P_G} \tag{5.198}$$

The relative change in flow rate that occurs for a small change in P_G for fixed P_S and P_D

Small-signal pressure change at inlet/oulet

The value of P_D is allowed to float.

Small-signal pressure change with current source

Q is fixed at outlet/inlet (for NOT/IF-Gate, respectively) and the pressure swing at outlet/inlet is compared to gate-pressure change.

5.9.1 NOT-Gate Gain

The figures in this section make use of the expanded transistor equations below were then solved to obtain the parametric diode equations. Different values for gain G were compared to piston position, input pressure, and flow-ratio f (Fig. 5.40).

$$\text{Pressure Drop:} \quad \Delta p = p_{\text{in}} - p_{\text{out}} \tag{5.199}$$

$$\text{External Pressure Drop:} \quad p_{\text{out}} = q\rho_{\text{ext}} \tag{5.200}$$

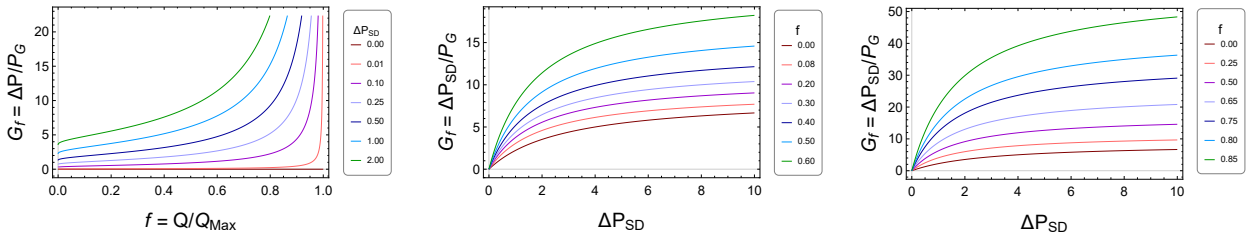
$$\text{Internal Resistance:} \quad p_{\text{in}} - p_{\text{out}} = q(1+\rho h^{-3}) \tag{5.201}$$

$$\text{Total Resistance:} \quad p_{\text{in}} = q(1+\rho_{\text{ext}}+\rho h^{-3}) \tag{5.202}$$

$$\text{Force Balance:} \quad (h-1) - mh^{-\beta} = p_g + (\Delta p - q) + \alpha(p_{\text{out}} + q\rho 2) - \alpha \text{Av} \tag{5.203}$$

where p_i and p_o were fixed.

Because $q \to q_{\max}$ for $h \to \infty$, there is no limiting value for $p_{g,\max} \propto h$. We can treat consider the "maximum" p_g to be the gate pressure necessary to achieve $q = 90\% q_{\max}$ or similar value. This analysis is compatible with our choice of f as the ratio of $q/q_{\max}$.



(a) Varying f for fixed ΔP_{SD} **(b)** Varying ΔP_{SD} for *low* f values **(c)** Varying ΔP_{SD} for *high* f values

Figure 5.40 Relationship between microfluidic gain, pressure ratio, and relative flow reduction. As $f \to 1$, the gain approaches infinity; however this is an artifact of the definitions used because $f = 1$ implies no change in the flow of the transistor, which can be achieved with zero gate pressure.

5.9.1.1 Behavior of gain under different input pressures

Beyond a critical $\alpha = \frac{2}{1+\rho 2}$, the numerical simulations indicate that the NOT-gate begins to experience hysteresis:

$$\frac{dPo}{dPg} = \frac{\alpha A_v}{\alpha(\rho 2+1)-2} \tag{5.204}$$

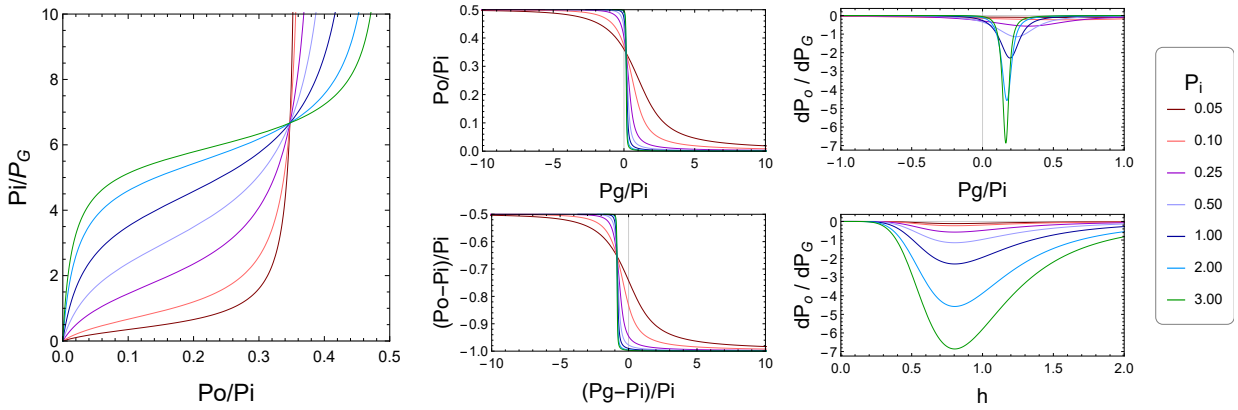
$$= \frac{A_v}{(\rho 2+1)-\frac{2}{\alpha}} \tag{5.205}$$

$$= \frac{A_v}{\left(\frac{R_2}{R_{\text{ext}}}+1\right)-\frac{2a_{\text{eff}}}{A}} \tag{5.206}$$

This analysis shows that there exist combinations of P_i and P_G that are effective discontinuities in the device opening rate. This snap-open effect can be seen in some experiments where the 3D-printed NOT-gates transition rapidly from relatively closed to mostly open suddenly (Fig. 5.42).

Because these effects happen far from the wall, it is entirely appropriate to simplify the equations by setting $m = 0$, since $m \neq 0$ is only an approximation that we take to allow for a continuous function. However, far from the wall, m should not affect the behavior of the analysis. Here, the total slope is defined by the relation

$$\mathrm{S} = \frac{\mathrm{d}p_{\text{out}}}{\mathrm{d}p_g} = \frac{\mathrm{d}p_{\text{out}}}{\mathrm{d}h} \Big/ \frac{\mathrm{d}p_g}{\mathrm{d}h} \tag{5.207}$$



(a) Gain vs input pressure ratio **(b)** Gain vs. input gate pressure **(c)** Slope of pressure gain

Figure 5.41 Different measures of gain and scaling relationships. At the critical point, $\rho_2 = 0.5$, $\rho = 1$, $A_v = 5$, $m = 0.05$, $\rho_{ext} = 1$, $\alpha_{\text{discont}} = \frac{1+\rho_{\text{ext}}}{\rho_2+\rho_{\text{ext}}} = \frac{4}{3}$.

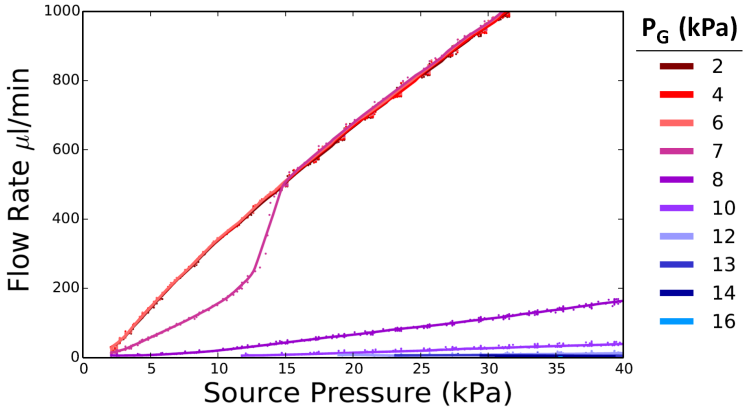


Figure 5.42 *QP* diagram for enhanced-gain transistor under a parametric P_G sweep, illustrating a snap-open effect as discussed in Section 5.9.1.1

and has a specific value

$$\frac{3\alpha A_v h^2 p_{\text{in}} \rho \rho_{\text{ext}}}{\rho^2 + h^6(\rho_{\text{ext}}+1)^2 + 2h^3\rho(\rho_{\text{ext}}+1) - 3h^2 p_{\text{in}}\rho(\alpha(\rho_2+\rho_{\text{ext}}) - (\rho_{\text{ext}}+1))}. \tag{5.208}$$

The slope can only become singular when the coefficient of p_{in} in the denominator

$$3\rho(\alpha(\rho_2+1) - (\rho_{\text{ext}}+1)) \geq 0, \tag{5.209}$$

which can only happen when $\alpha(\rho_2+1) - (\rho_{\text{ext}}+1) > 0$. We can achieve some simplifications in the analysis then by treating that whole coefficient of h^2 as a single effective pressure p_{eff}:

$$p_{\text{eff}} \equiv 3\rho(\alpha(\rho_2+1) - (\rho_{\text{ext}}+1))p_{\text{in}} \geq 0 \tag{5.210}$$

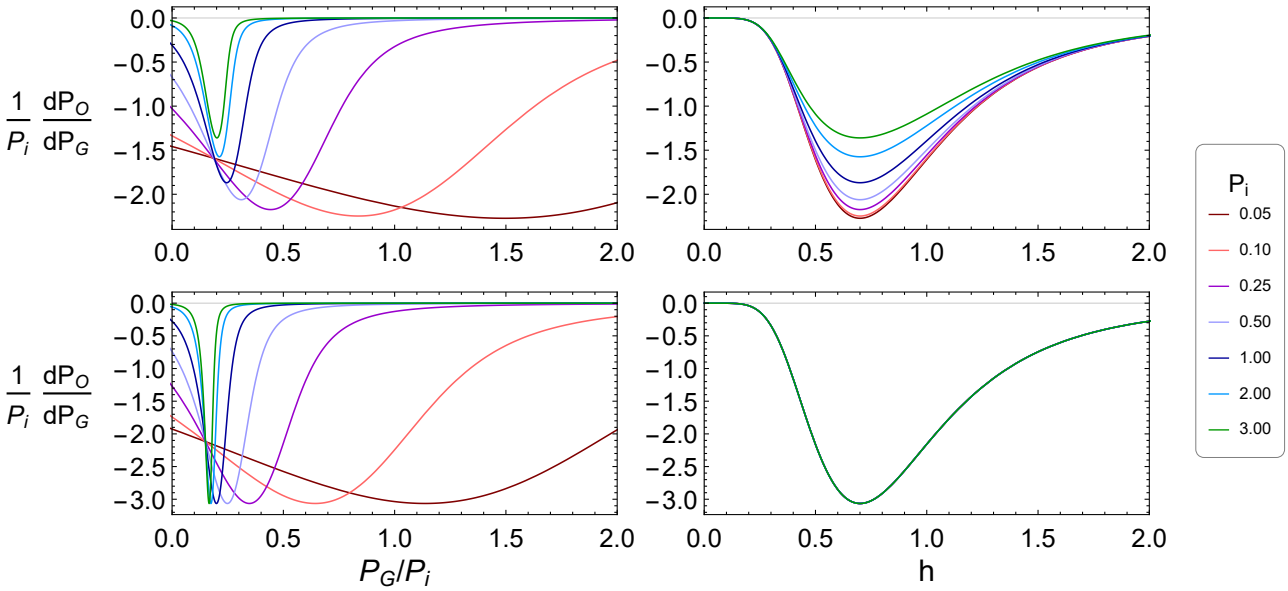


Figure 5.43 Non-supercritical gain scaling relationships

and inserting this definition for effective pressure into the denominator of the slope (Equation 5.207) by replacing p_{in} with p_{eff}, we get a "simplified" slope

$$\mathrm{S} = \frac{-\left(\dfrac{\alpha A_v h^2 \rho_{\text{ext}}}{\alpha(\rho_2+1)-(\rho_{\text{ext}}+1)}\right) p_{\text{eff}}}{\rho^2 + 2h^3\rho(\rho_{\text{ext}}+1) + h^6(\rho_{\text{ext}}+1)^2 - h^2\left(\dfrac{\alpha(\rho_2+\rho_{\text{ext}})-(\rho_{\text{ext}}+1)}{\alpha(\rho_2+1)-(\rho_{\text{ext}}+1)}\right) p_{\text{eff}}} \tag{5.211}$$

Here is the first evidence that setting $R_{\text{ext}} = R_{\text{tot}}$ (or $\rho_{ext} = \rho_{\text{tot}} \equiv 1$) confers analytical benefits, since the coefficient

$$h^2\left(\frac{\alpha(\rho_2+\rho_{\text{ext}})-(\rho_{\text{ext}}+1)}{\alpha(\rho_2+1)-(\rho_{\text{ext}}+1)}\right) p_{\text{eff}} \tag{5.212}$$

$$\xrightarrow{\rho_{\text{ext}}\to 1} h^2 p_{\text{eff}} \tag{5.213}$$

and therefore

$$\mathrm{S} \xrightarrow{\rho_{\text{ext}}\to 1} -\frac{\left(\dfrac{\alpha A_v h^2 \rho_{\text{ext}}}{\alpha(\rho_2+1)-2}\right) p_{\text{eff}}}{\rho^2 + 4h^3\rho + 4h^6 - h^2 p_{\text{eff}}} \tag{5.214}$$

which goes to ∞ when the denominator equals zero. While we cannot solve directly for h (at least not without a substantially unwieldy implicit inverse function), we can treat the problem

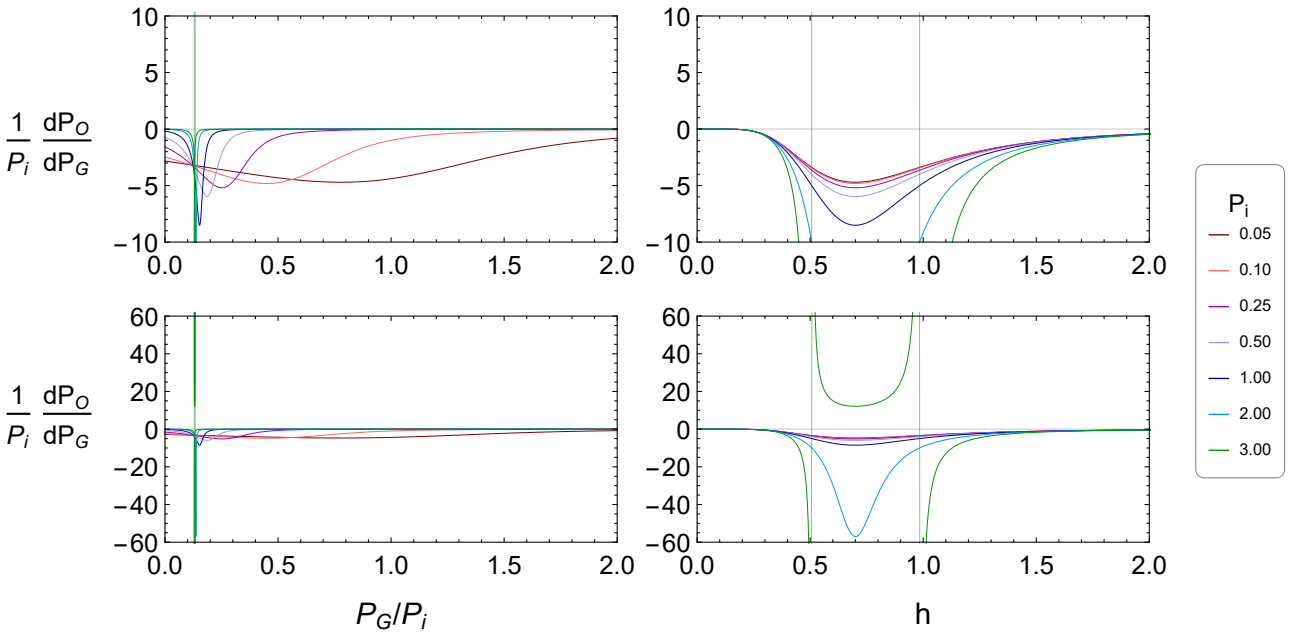


Figure 5.44 Super-critical gain

parametrically and solve for $p_{\text{eff}}(h)$:

$$p_{\text{eff,crit}} = \frac{\left(h^3(\rho_{\text{ext}}+1)+\rho\right)^2(\alpha(\rho_2+1)-(\rho_{\text{ext}}+1))}{h^2(\alpha(\rho_2+\rho_{\text{ext}})-(\rho_{\text{ext}}+1))}. \tag{5.215}$$

When $\rho_{\text{ext}} \to 1$, the effective critical pressure simplifies dramatically to

$$p_{\text{eff,crit}} \xrightarrow{\rho_{\text{ext}}\to 1} \frac{\left(2h^3+\rho\right)^2}{h^2}, \tag{5.216}$$

which eliminates all dependencies other than the ratio $\rho = r_{\text{piston}}/R_{\text{tot}}$.

The minimum input pressure needed to create an infinite slope (and therefore a point of hysteresis in the system) can be found indirectly by minimizing $p_{\text{eff,crit}}$ with respect to h and then solving for ρ, giving $\rho_{\text{min}} = 2h^3(1+\rho_{\text{ext}})$, leading to

$$p_{\text{crit,min}} = \frac{9h^4(\rho_{\text{ext}}+1)^2(\alpha(\rho_2+1)-(\rho_{\text{ext}}+1))}{\alpha(\rho_2+\rho_{\text{ext}})-(\rho_{\text{ext}}+1)} \tag{5.217}$$

$$\xrightarrow{\rho_{\text{ext}}\to 1} 36h^4. \tag{5.218}$$

The critical input pressure can be plotted against h to show the conditions under which the device snaps shut for a given piston position (Fig. 5.45)

Alternately, we can find the piston position at which the device experiences hysteresis for the

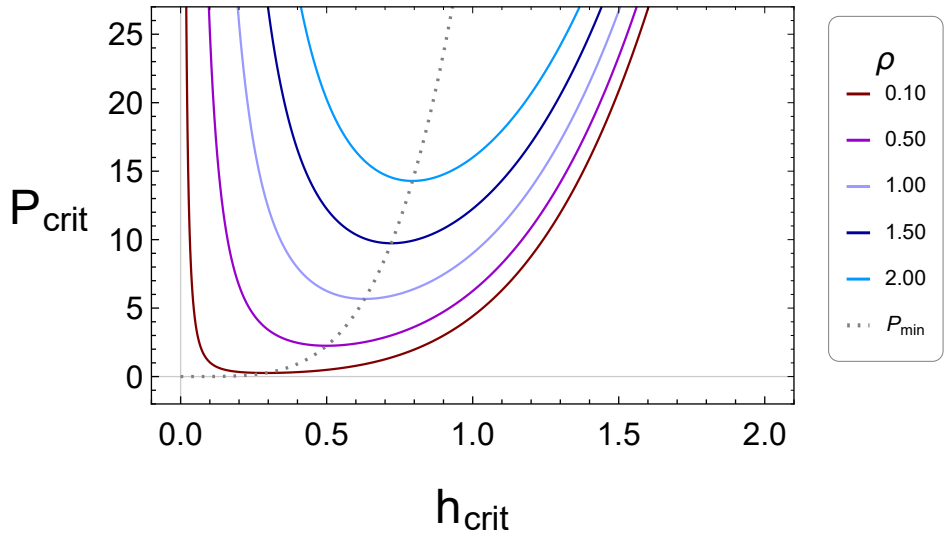


Figure 5.45 Critical pressures and points at which hysteresis begins

minimum input pressure,

$$h_{\text{min}} = \left(\frac{\rho}{2+2\rho_{\text{ext}}}\right)^{1/3}. \tag{5.219}$$

From here, we see that the piston can experience a hysteresis at $h = 1$, the zero-stress position, for

$$\rho = 2(1+\rho_{\text{ext}}) \tag{5.220}$$

$$r = 2(R+R_{\text{ext}}). \tag{5.221}$$

Putting the results Equation 5.219 into Equation 5.215 provides the slightly less elegant solution

$$p_{\text{crit,min}} = 9\left(\frac{\rho^2(\rho_{\text{ext}}+1)}{4}\right)^{2/3}\left(\frac{\alpha(\rho_2+1)-(\rho_{\text{ext}}+1)}{\alpha(\rho_2+\rho_{\text{ext}})-(\rho_{\text{ext}}+1)}\right) \tag{5.222}$$

which fully eliminates h. However, this solution can be substantially simplified by taking $\rho_{\text{ext}} \to 1$:

$$p_{\text{crit,min}} \xrightarrow{\rho_{\text{ext}}\to 1} 36\left(\frac{\rho}{2}\right)^{4/3}. \tag{5.223}$$

Combining these definitions for the effective pressure with the definition in Equation 5.210, we can solve for the input pressure. Since this analysis has assumed that $\alpha(\rho_2+\rho_{\text{ext}})-(1+\rho_{\text{ext}}) \geq 0$, we

can now determine that for input pressures

$$p_{\text{in}} \leq \frac{3\left(\frac{\rho}{16}(1+\rho_{\text{ext}})^2\right)^{1/3}}{\alpha(\rho_2+\rho_{\text{ext}})-(1+\rho_{\text{ext}})} \tag{5.224}$$

$$\xrightarrow{\rho_{\text{ext}}\to 1} p_{\text{in}} \leq \frac{3(\rho/4)^{1/3}}{\alpha(\rho_2+1)-2}, \tag{5.225}$$

there will be no hysteresis during device operation.

5.10 Discrepancies between Theoretical and Experimental Performance of 3D-Printed Circuitry

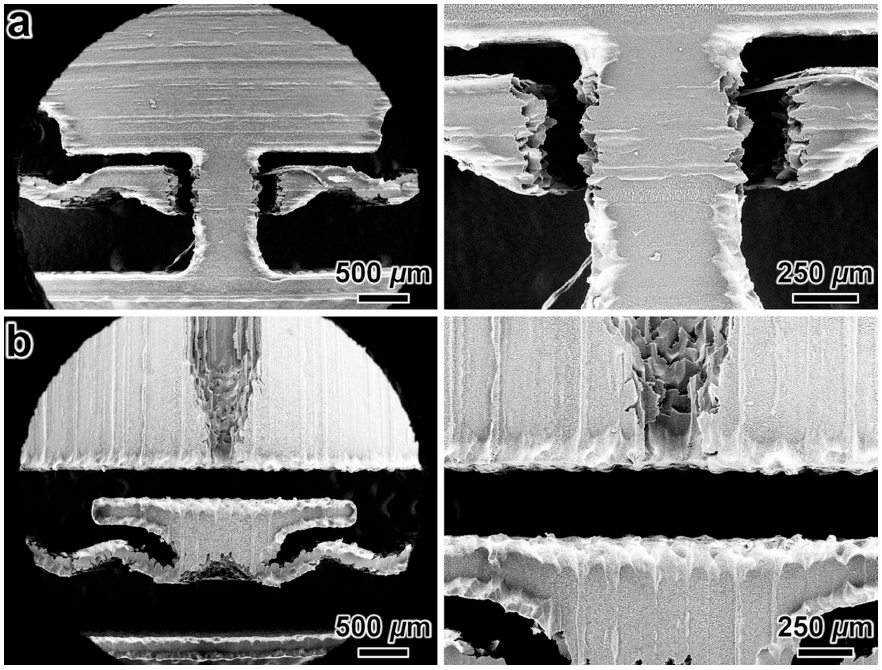


Figure 5.46 Scanning electron micrographs showing the piston interfaces and surface roughness of the 3D-printed **(a)** fluidic diode, and **(b)** fluidic transistor. Reproduced from Ref. 316 with permission of the RSC.

The simulated and experimental performance of the 3D-printed transistors and diodes differ largely in their behavior during valve closing; specifically, while the simulations demonstrated complete valve closure (Figs. 5.11f and 5.32d), the experimental devices were not able to fully inhibit fluid flow while "closed"(Figs. 5.11c,d, 5.29d, and 5.30d). At the roughness scale of the 3D-printed transistors[20], this effect is likely the result of the surface irregularities produced by the

[20] At much finer surface textures, squeeze-film effects would likely become more dominant

MJM-based 3D printing. The computer models used atomically smooth surfaces in their simulations and contained no provision for surface-surface repulsion effects, forcing the pseudo-static simulations to terminate when the plates were too close, to avoid surface clipping. In contrast, experimental transistors exhibited surface resolution of approximately 32 μm, with surface roughness of ±95 μm in-plane and ±35 μm out-of-plane (Fig. 5.46). Additionally, the devices would be expected to exhibit nanoroughness of ≈ 600 nm, as discussed in Section A.1.1 [117]. Analytical models are able to more closely mimic the transistor behavior by including a small repulsion term that prevents complete valve closure (see Section 5.3.1.3 for a general treatment of valve closure, as well as Section 5.6.2.4(IV) and Section 5.7.2.1(I) for the diode and transistor smooth-piston approximations, respectively).

These closure problems would likely be reduced by fabricating microfluidic components using 3D printers with higher resolution or through alternate manufacturing techniques (*e.g.*, through SLA). Additionally, roughness may be mitigated through post-processing procedures and surface treatments. However, any roughness mitigation technique would have the potential for further performance disruption by either over-etching and damaging the device structure or by fusing disparate components, preventing movement of internal components. This latter concern would be particularly acute for roughness mitigation methods that involve depositing polymer on the surface to fill microcavities.

In addition to the fluidic blocking behavior, we also observed a second notable difference between the simulation and experimental results: when using the 3D Systems-reported flexural modulus (1159 MPa) in simulations, the experimentally fabricated 3D-printed fluidic components exhibited far greater mechanical flexibility than that predicted from the theoretical simulations. More comparable results were obtained when the modulus was decreased by a factor of twenty to compensate. This phenomenon was not entirely negative. For example, the 3D-printed capacitors were able to store more fluid (increasing their capacitance) (Fig. 5.9g-h) and the diodes and transistors were able to close under smaller pressures, since less pressure was needed to overcome the elasticity of the membrane. We suspect a combination of three factors caused the difference between simulated and experimental displacement (and therefore suspected elastic modulus): (i) the elastic modulus was permanently reduced during the hot oil bath needed to remove the support material; (ii) the structural material was not deposited completely regularly, leading to internal lacunae or thinner portions of the membrane; and (iii) the elastic modulus reported by 3D Systems is overgenerous. The high temperature-induced color-change lends support to permanent structural changes when the devices were cleaned in the hot oil. Additionally, the lower rupture pressure of

the sinusoidal membranes lends support to hypothesis (ii), suggesting the irregular surfaces were easier to damage.

Multiple aspects of device performance would be improved by using printers with enhanced fabrication precision and resolution. This change would not only lead to improved component performance (*e.g.*, smoother surfaces would enable more efficient blocking and smaller deposition lines would lead to stronger component structure) it would also enable further scaling of 3D-printed circuit components and systems.

Nevertheless, the work presented here has two distinct limitations related to the properties of the Projet™3000 HD 3D printer and the support material (Visijet M3 Crystal). First, printer surface roughness limited the circuit components' usefulness by allowing a relatively high leakage current through the devices [344]. Second, the Visijet M3 material is cytotoxic: in a test comparing the efficacy of MJM techniques to stereolithography methods, Zhu *et al.* determined that the Viisijet M3 Crystal material exhibited the highest biotoxicity [117], as well as other limitations such as optical properties or low surface roughness [88, 93]. For situations in which biocompatibility is prioritized, alternative MJM materials (*e.g.*, clear, biocompatible MED610 [345]) and/or post-processing procedures (*e.g.*, biocompatible surface coatings such as Paralyne C) may be more suitable. One potential "easy" fix may be to simply re-calibrate the 3D-printer — according to Engitype representative John Savage, the extremely rough features seen in Figure 5.46 can be caused by misalignment of the support and structural layer print nozzles [344].

Acknowledgments

I would like to thank my co-authors on the original work in Ref. 316 as well as Andreas J. Raulinaitis, Kjell F. Eckman, Aaron Wienkers, My Chung, and Sikun Peng for the assistance with the experimental results for the microfluidic resistors. In addition, I would like to thank Melanie Veale, Shoji Takeuchi, Todd Blatt, F. Nazly Pirmoradi, Thomas Libby, Alic Chen, Mark Oehlberg, and members of the Liwei Lin, Kristofer S. J. Pister, Luke P. Lee, and Micro Mechanical Methods for Biology (M3B) Laboratories.

Chapter 6

Conclusions

A primary driver of state-of-the-art microfluidic technologies has been the need to fabricate complex structures with numerous interconnected components, offering wide-ranging benefits for chemical and biological research. Historically, microfluidic device construction has predominantly relied on conventional micromachining technologies that are rooted in the semiconductor and microelectromechanical systems (MEMS) industries, these processes (as well as soft lithography) require expensive equipment and facilities and are therefore inherently limited as a method for rapid prototyping. Not only are new innovations in fabrication techniques required to improve the functionality of microfluidic lab-on-a-chipapplications, but also autonomous and integrated microfluidic circuit components are needed to ensure the microfluidic functionality can be performed on the titular chip. This dissertation has developed three methods for resolving the fabrication and control problems of microfluidics using a combination of standard microfluidic and MEMS manufacture techniques with the emerging techniques of additive manufacturing and 3D printing.

First, we presented optofluidic lithography as a means of fabricating moving microfluidic structures within a microchannel. The methodology presents several adaptations over previous methods of microfluidic control and of optofluidic lithography. For example, optofluidic lithography only requires a single poly(dimethyl siloxane) (PDMS) layer and thus avoids costly and complex bonding steps needed in multi-level soft lithography. Additionally, by working primarily within existing techniques, optofluidic lithography is relatively accessible to microfluidics researchers. Using optofluidic lithography, we have demonstrated several variants of microfluidic control mechanisms, including passive diodes (which provide for one-way flow rectification) and current source (which allows fluid flow rates to remain flat within a larger pressure range) as well as actively controllable microfluidic gain valves (with dynamic microfluidic gain). We then presented a theory of the

microfluidic gain valve and current source, showing the effect of integrated springs, device leakage, and device load on performance. The analyses show that while highly versatile and flexible, optofluidic lithography is not without fundamental performance limits. For example, reductions in leak-rate come at the cost of reductions in processing speed, a problem which requires multi-level microfluidic fabrication techniques to overcome, and there vitiates one of the primary advantages of optofluidic lithography.

Next, we developed a technique for combining soft lithography with 3D-printing, a more effective technique for microfluidic fabrication and one that could render optofluidic lithography practical in the future: rather than make the mold for the PDMS using traditional lithographic techniques, multi-jet modeling was used to 3D print the mold instead. By combining the versatility of 3D printing with the ideal mechanical and biological properties of PDMS, this work potentially opens a new class of manufacturing techniques for multilayer microfluidic systems. These new techniques enabled double-sided microfluidic devices to be fabricated in a single molding step and involved alignment marks (which allowed the assembly of fine features without the need for a microscope) and custom 3D-printed stamps (which selectively applied PDMS adhesive to bonding interfaces without channel clogging). In demonstration, microfluidic devices were fabricated to include two channels levels, non-planar membranes/valves, vertical interconnects (vias between channel levels, and built-in inlets/outlets for easy linkage with external systems, all a single-step process. In addition, a single-piece pneumatic membrane valve — Analogous to a "Quake"-valve — was tested to show that the 3D-printed transfer molding process could be effectively applied to standard microfluidic applications. Unfortunately, relatively to soft lithography, current 3D-printing processes have substantially lower feature resolution and higher surface roughness than. Although advancement in 3D-printing technology is expected to resolve some of these problems, the variability meant that the membrane was thicker than intended and the roughness prevented full valve closure.

More significantly, 3D-printed molding still does not resolve one of the primary limitations of soft lithography: the requirement that microfluidic structures be monolithic (or near-monolithic) for the PDMS to be successfully removed from the mold in a repeatable manner. While features such as overhangs and underpasses can be fabricated in the mold and even successfully filled with PDMS, generally either the PDMS or the mold breaks upon removal from the mold. To resolve this limitation, we then demonstrated a fully 3D-printed method for fabricating microfluidic devices. This technique has a far greater[1] mechanical and geometric flexibility, it comes at the cost

[1] If not unlimited, due to the requirements that supporting material be removed from the device

of no-longer being able to use PDMS with its ideal optical, biological, and mechanical properties. Using multi-jet modeling methodologies, we 3D-printed microfluidic circuit elements (resistors, capacitors, diodes, and transistors) and tested them for their potential use in regulating microfluidic systems. The 3D-printed circuit elements were then studied through a combination of experimental, simulation, and analytical methods, as well as integrated into more complex microfluidic circuits (including half- and full-wave microfluidic rectifiers). These features were designed to exhibit similar transfer functions to their electronic counterparts (both independently and when connected to larger integrated microfluidic circuit networks). The performance was not exactly equivalent, however. The 3D-printed transistors exhibited nothing resembling saturation current (a quantum phenomenon) and showed the characteristic r^{-3} dependence of microfluidic systems with two critical dimensions, ultimately showing closer performance to vacuum triodes than to actual transistors. The analytical models demonstrate many of the key features seen in the experimental results, but could not be reliably verified; due to the large number of coefficients that naturally arise in the analytical model, overfitting was a consistent problem.

Ultimately, when combined with fully-realized microfluidic IF-gate and CMOS-analog components, this research may allow for fabrication of analog microfluidic operational-amplifiers, which could allow for fully-analog control of microfluidic systems using high-gain amplification of small pressure signals, and the CAD-based nature of the design process makes it simple for researchers to readily combine multiple microfluidic components into larger integrated microfluidic circuit networks. Taken together, these techniques allow for the synthesis of well-known microfluidic techniques, the favorable properties of PDMS with the rapid prototyping and geometric flexibility of additive manufacturing; by eliminating much of the headache of microfabrication, microfluidic devices self-regulated through intricate hydraulic-analogy circuitry and programmable logic.

Appendix A

ProJet™3000 3D Printer

All of the IFC components and systems in this dissertation were built via the MJM additive manufacturing process using ProJet™3000HD 3D printers (3D systems) in the Center for Interdisciplinary Biological Inspiration in Education and Research (CiBER) and the Center for Information Technology Research in the Interest of Society (CITRIS) Invention Lab at the University of California, Berkeley.

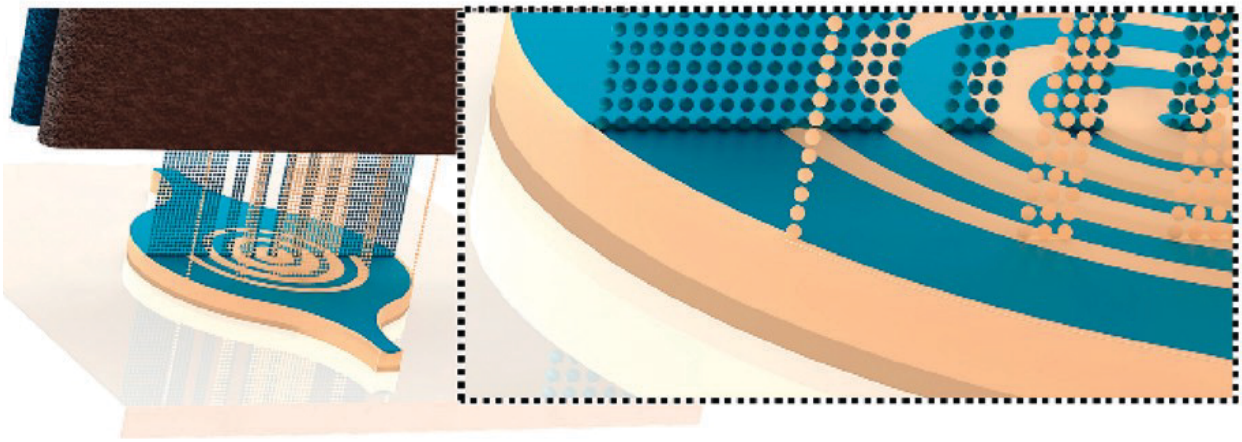


Figure A.1 Conceptual view of ProJet™3000 3D Printer output during the 3D printing process. The multijet nozzles deposit either VisiJet EX200 structural material (beige) or Visijet S100 support wax (blue), which is subsequently removed.

The 3D CAD models (in STL format) were imported into the ProJet Accelerator software (3D systems) in the "Ultra High Definition" mode, which converts the models into single-layer slices (32 μm n height). The system uses piezo printhead technology to deposit layers of either photocurable plastic resin (Visijet EX200, Fig. A.1 — beige); or wax support material (S100, Fig. A.1 — blue) using different printheads for each material. After depositing a full layer of EX200 and/or

S100, the build platform is exposed to UV for photocuring, and the surface is milled to tolerance to ensure layer smoothness. This process is repeated until completion. For the components presented in this dissertation, the average build time averaged approximately four to six hours, with structure height (*i.e.*, number of layers) being the critical factor affecting the overall print time. [1] Following completion of the 3D printing process, the components typically adhered to the aluminum build plate which was removed from the printer and placed in a freezer for 15 minutes. The low temperature allowed for differential contraction of the aluminum build plate relative to the components, as well as increasing the brittleness of the support material. This combination of effects aided the removal of 3D-printed components from the aluminum build plate.

A.1 Printing and Material Information

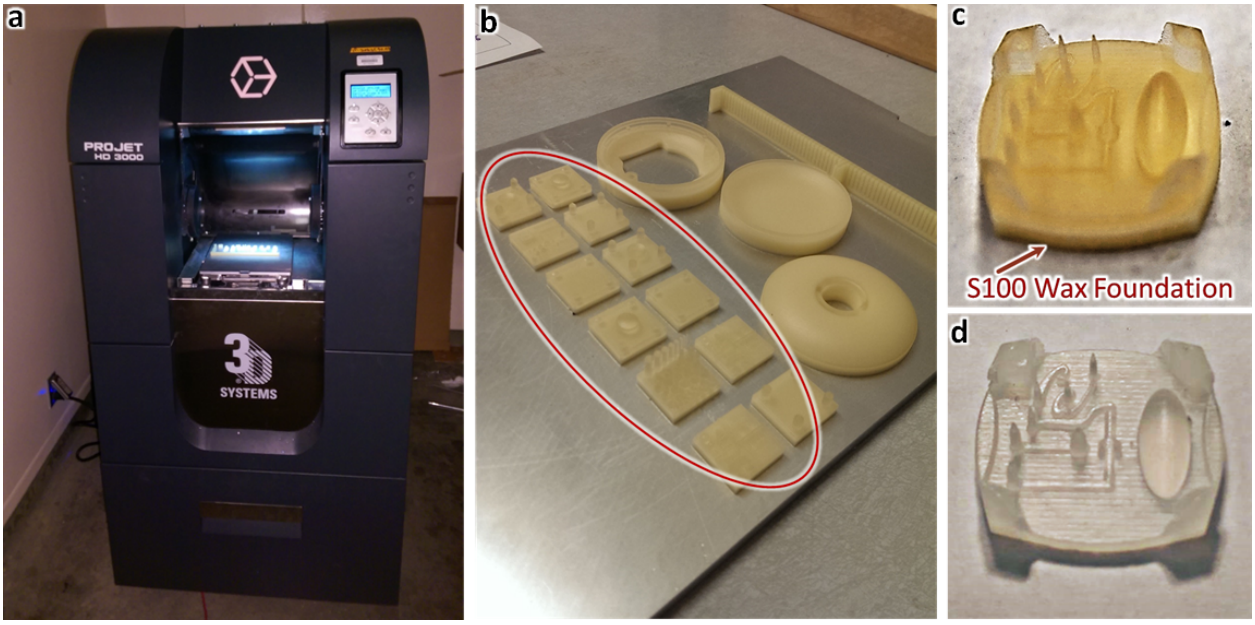


Figure A.2 ProJet™3000 3D Printer output. **(a)** The printer itself with a completed print sitting on the print tray. **(b)** Aluminum print tray with still bonded 3D-printed molds (circled). For cost and time-saving considerations, this print run was shared with other users of the CiBER laboratories. **(c)** A single 3D printed mold before wax has been removed and **(d)** mold after the removal of wax.

Microfluidic components were designed and converted from a positive to a negative mold shape using the computer-aided design program SolidWorks. 3D printing of molds was achieved using a ProJet™3000 3D printer (3D Systems, Rock Hill, SC, USA). The ProJet™3000 printer, printing

[1] Component spacing plays a secondary role in print time, with overall times reduced 10-20% with closely spaced build layouts

in UHD mode, first lays down a 2 mm thick layer of VisiJet®S100 Support Material (sacrificial wax), resulting in smooth bottom surfaces of devices. [2] Next, the printer alternately deposits HD Systems proprietary structural epoxy (VisiJet®EX200 plastic material [339, 346] and sacrificial wax support material (VisiJet®S100 hydroxylated wax [347]) in 0.35 μm layers. The wax was used as a temporary support for cavities and overhangs and was removed during post-processing. The print is deposited on an aluminum tray and can print within a volume of 127x178x203 mm^3 with a resolution of ∼50 μm for extruded features and ∼100 μm for intruded features.[3] For more information, see the documentation on the 3D Systems website. Links for the ProJet™HD3000 3D Printer documentation are listed in the citations for this work, including the ProJet HD 3000 brochure [348], the EX200 Resin table of values [339], the EX200 MSDS [346], and the S100 MSDS [347].

A.1.1 Surface Roughness and Roughness Mitigation

A consistent problem with the ProJet3000 printer is the degree of surface roughness it creates; asperities of 20 μm occur every 0.5 mm. This is largely a feature of the printer's built-in resolution and will increasingly become a non-issue as printers improve. To attempt to mitigate roughness as a limitation, we engaged in numerous experiments to attempt to reduce the overall surface roughness of the mold to allow for smoother Glass-PDMS and PDMS-PDMS bonding in later steps. Ultimately, all attempted techniques resulted in either no effect or a worsening of roughness, and we were forced to use liquid PDMS (ℓPDMS) as a binding agent to overcome the surface asperity.

The effect of surface roughness on optical properties has been well studied [349, 350, 351, 352] and may be partially summarized by the Rayleigh criterion, which is approximately

$$Ra_t = \frac{2\pi}{\lambda}\sigma_h \frac{|n_1 - n_2|}{2} \tag{A.1}$$

for normal transmission from one dielectric to another, where λ is the wavelength, σ_h is the surface RMS (root mean square) height, and n_1 and n_2 are the dielectric constants of the two media, and where $Ra_t > \frac{\pi}{2}$ for an optically rough material [352]. Choosing $n_1 = 1$ for vacuum, $n_2 = 1.4$ for

[2] In standard operation, the sacrificial wax is used as a temporary support for cavities and overhangs, but the 3D molding project avoided such structures as they are harder to clean and were unnecessary here.

[3] 3D Systems cites an elastic modulus of 1.159 GPa [339], although comparison of experimental tests and simulation performed in the Lin Lab suggest the proper modulus, post wax removal, is closer to 1/10 or 1/20 that value [316].

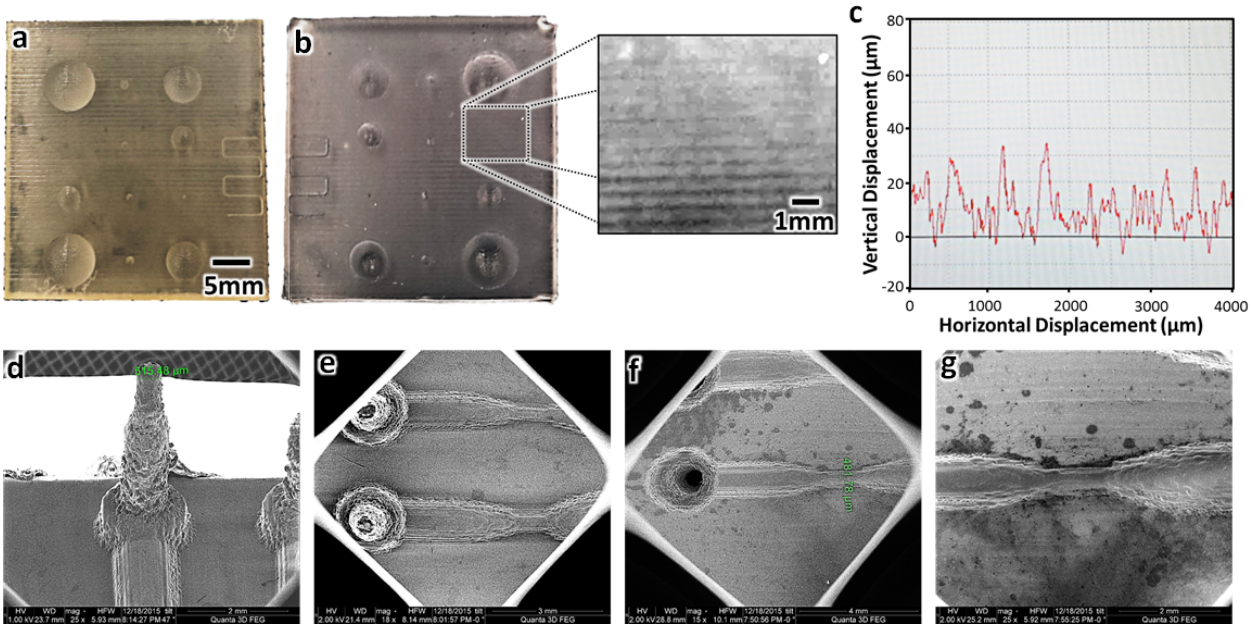


Figure A.3 Surface roughness of 3D printed mold and transferred PDMS. Top: Sample device to test surface roughness. Bottom: SEMs of Single layer device (4.2.1) **(a)** 3D printed mold with visible roughness and **(b)** corresponding molded PDMS with magnified insert highlighting roughness. **(c)** Profilometer measurements of 3D printed mold showing ≈ 20-30 µm surface asperity every 0.5 mm. **(d)** Angled view of single-layered mold showing roughness of built-in inlet generation pillar (diameter 515 µm). **(e)** Top view showing layering pattern of channel mold. **(f)** Corresponding molded PDMS showing high fidelity of transfer of surface roughness, and **(g)** zoomed view. Note that the dark splotches in (f) and (g) are artifacts from improper conductive surface treatment of the PDMS before the SEM scans.

PDMS [353] and $\lambda \approx 500$ nm (*i.e.*, for the average wavelength of visible light), PDMS will appear optically rough for $\sigma_h > 625$ nm. Notably, the Rayleigh criterion is similar to the 600 nm RMS roughness of the 3D printed molds observed by Walczak *et al.*, explaining the observed optical opacity [117].

(I) Solvents (IPA, Ethanol, Acetone, GooGone®)

Swelling (to various degrees) of mold surface and pickup of white powdery layer. Some effect in removing wax, but negligible and counteracted by damage to surface of VisiJet material.

(II) H_2O_2 (1M) and NaOH (1M)

Neither H_2O_2 or NaOH had any noticeable effect on mold or on wax.

(III) H_2SO_4

H_2SO_4 had no noticeable effect on mold in concentrations lower than 50% H_2SO_4. At very high concentrations (98%, Sigma Aldrich), H_2SO_4 began to discolor the surface of the molds, taking

on thick slimy texture. This layer could be rinsed off leaving the mold with slightly reduced surface texture. Ultimately, H_2SO_4 led to slight reduction in aspect ratio and corner definition and *did* remove the large print lines from the 3D printer, but caused an overall increase in surface roughness, possibly due to the remove of long polymer units from the mold. The new surface roughness was more uniform, but the effect was not significant to make up for other difficulties in the method. We postulate that the effects are only present at very high acid concentrations because the molds are only affected by the well-known dehydrating properties of the H_2SO_4 (most evident at very low pH), and not by the corrosive effects due to protonation.

(IV) HNO_3 (0.1M)

Nitric Acid (HNO_3) not cause surface effects, but instead was absorbed fully into the 3D printed mold, causing a systemic and permanent mold color change to orange. Additionally, mold became highly brittle and could be broken without serious effort.

A.1.2 Color and Visual Texture Change

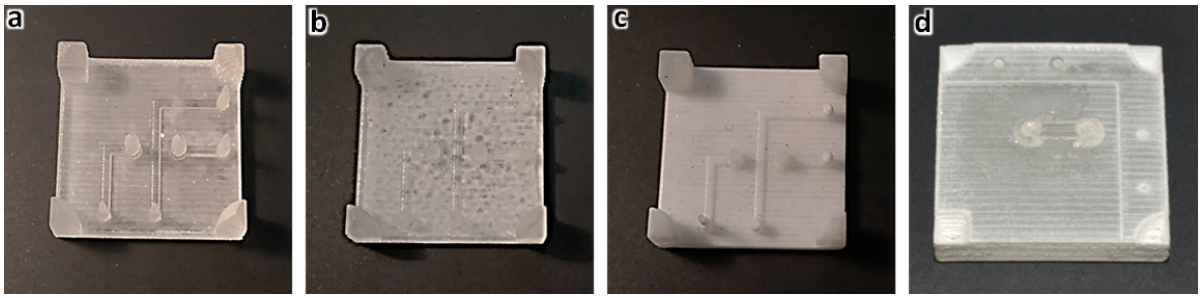


Figure A.4 Differences in color and texture change on 3D printed transfer molds: **(a)** Standard color of VisiJet200 material after cleaning, **(b)** mottled visual texture, **(c)** All-white surface coloration, and **(d)** Powdery texture (and surface curvature) after acetone absorption.

The visual appearance of the 3D printed molds made of VisiJet200 material does not remain constant over the device lifetime. When the devices first emerge from the printer, they are a deep golden yellow color, with higher degrees of orange for devices exposed to more UV light (Fig. A.4a). During the ProJet manufacturing process, each applied layer is followed by an exposure of UV light to cure the layer. Thus, print runs that have tall devices will experience far more flashes of UV than print runs that contain short devices. Additionally, molds left out where they can be exposed to sunlight will eventually deepen in color, provided they are exposed to no other processes.

Once the molds are baked with curing PDMS, they begin to take on a spider-web appearance (Fig. A.4b). While the physical texture is not noticeably changed, the visual texture alters noticeably, sometimes making it difficult to identify the specific mold, as the spider web texture camouflages physical features. We are unsure the specific reason for this color change, as the time scale for the change may be radically different for different devices. However, devices that have been silane treated may undergo the changes more rapidly. Frequently, but unpredictably, the devices may take on a solid off-white color and remain that through repeated moldings. We are unsure what causes this transformation, but generally welcome it because the devices are far easier to identify once the surface takes on a solid visual texture (Fig. A.4c). If the molds are placed in a solvent such as acetone, IPA, or commercially available solvents like GooGone®, the surface of the device will pick up a powdery white texture which is not generally removable, even if the mold is thoroughly washed in oil or soapy water and/or baked in the oven to facilitate the evaporation of solvents (Fig. A.4d). Additionally, the molds pick up a curvature from the swelling resulting from the solvent absorption. This particular color change can therefore be avoided.

Appendix B

Syringe Pump as Current Source

Introduction

This section describes some of the procedures for analyzing microfluidic behavior when driven by a syringe pump (current source) and/or by a pressure source. These analyses make use of the hydraulic analogy and explain certain transient effects in the use of syringe pumps, explaining some of the difficulties that arise from controlling microfluidic systems with syringe pumps and without feedback mechanisms. The analysis makes use of the modeling properties of the Laplace Transform — namely that the Laplace Transform converts between the time domain and the frequency domain, which is necessary for the analysis of time-dependent capacitor-based systems. More specifically, the relation $\Delta P = Q \times Z$, where Z is the complex impedance, is only true in the frequency domain:

$$P(s) = Q(s)Z(s). \tag{B.1}$$

In the time domain, the convolution theorem is needed, and the equation becomes the less-useful form

$$P(t) = Q(t) \star Z(t) \tag{B.2}$$

or

$$\mathcal{L}(P(s)) = \mathcal{L}(Q(s)) \star \mathcal{L}(Z(s)) \tag{B.3}$$

where $\star$ represents the convolution operator. One notable feature of this analysis is that the pressure nearer to the flow generation P_1 experiences a large pressure spike, whereas the farther pressure

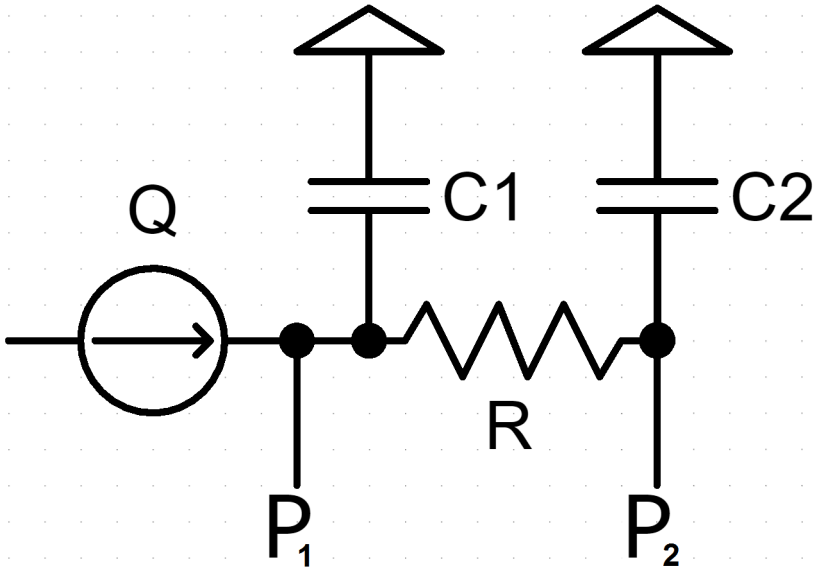


Figure B.1 When a syringe pump forces fluid into a leak-free fluidic circuit at a defined flow rate Q, pressure P_1 builds in the system. The system can be represented by two capacitors C_1 and C_2 separated by a resistance R. Note that C_1 represents the combination of capacitances from the syringe pump and from the circuit itself. Additionally, capacitance C_2 can be measured by comparing pressure P_2 and flow rate Q_2.

P_2 sees the spike buffered by the resistor located between P_1 and P_2. This in part explains the reason experiments were performed with a large resistor located between the pressure source and the experiment rather than with the resistor between the device and the drain; this positioning of the resistor lowered absolute pressure spikes in the system, such as seen in Fig. 4.29.

B.1 Analytical Model of Step-function syringe motion

For a syringe that starts moving at time $t = 0$ with a constant velocity $v = \frac{q_0}{A}$, where A is the syringe area, and suddenly stops at time $t = t_0$, the resulting flow rate can be modeled as

$$q(t) = \begin{cases} 0 & \text{for } t < 0 \\ q_0 & \text{for } 0 \leq t < t_0 \\ 0 & \text{for } 0 \leq t. \end{cases} \tag{B.4}$$

The behavior of the object in the frequency domain is found by taking the Laplace transform

$$Q(s) \equiv \mathcal{L}\{q(t)\} = \frac{q_0(1 - e^{-st_0})}{s}, \tag{B.5}$$

where $s \sim i\omega$.

The complex impedance of this system $Z(s)$ is

$$Z(s) = \left(\frac{1}{C_1 s}\right) \parallel \left(R + \frac{1}{C_2 s}\right) \tag{B.6}$$

$$= \frac{1 + RC_2 s}{(C_1 + C_2)s + RC_1 C_2 s^2} \tag{B.7}$$

$$= \frac{1}{(C_1 + C_2)s} + \frac{RC_2^2}{(C_1 + C_2)^2 (1 + R(C_1 \parallel C_2)s)}, \tag{B.8}$$

where the final term was obtained through partial fraction decomposition and by substitution with $C_1 \parallel C_2 \equiv \frac{C_1 C_2}{C_1 + C_2}$.

The pressure $P(s)$ is therefore 7

$$P(s) = Q(s)Z(s) \tag{B.9}$$

$$= \frac{q_0(1 - e^{-st_0})}{s} \frac{1 + RC_2 s}{(C_1 + C_2)s + RC_1 C_2 s^2} \tag{B.10}$$

$$\implies p(t) = \begin{cases} \frac{q_0 RC_2^2}{(C_1 + C_2)^2}\left(1 - e^{-t/R(C_1 \| C_2)}\right) + \frac{q_0 t}{C_1 + C_2}, & \text{for } 0 \le t < t_0 \\ \frac{q_0 RC_2^2}{(C_1 + C_2)^2}\left(-e^{-t/R(C_1 \| C_2)} + e^{-(t - t_0)/R(C_1 \| C_2)}\right) + \frac{q_0 t_0}{C_1 + C_2}, & \text{for } t \ge t_0 \end{cases} \tag{B.11}$$

The behavior for both time scales exhibit a time constant

$$\tau = R(C_1 \parallel C_2) \tag{B.12}$$

In the $0 \le t < t_0$ case, see that there is a steady-state flow profile

$$\frac{q_0 RC_2^2}{(C_1 + C_2)^2} + \frac{q_0 t}{C_1 + C_2} \tag{B.13}$$

which is a linearly increasing pressure ramp at the rate $\frac{q_0 t}{C_1 + C_2}$ with an offset $\frac{q_0 RC_2^2}{(C_1 + C_2)^2}$. This last term acts as a sort of advance "shock" because fluid takes time RC_2 to travel through the resistor and final capacitor; accordingly, there is a fluid build up at the measuring site immediately out of the syringe pump.

For the $t \ge t_0$ case, we can add and subtract 1 from the term in the parentheses to obtain the

following form:

$$p(t;t \geq t_0) = \frac{q_0 R C_2^2}{(C_1+C_2)^2}\left[\left(1-e^{-t/R(C_1\|C_2)}\right)-\left(1-e^{-(t-t_0)/R(C_1\|C_2)}\right)\right]+\frac{q_0 t_0}{C_1+C_2} \tag{B.14}$$

$$= \frac{q_0 R C_2^2}{(C_1+C_2)^2}\left[\left(1-e^{-t/\tau}\right)-\left(1-e^{-(t-t_0)/\tau}\right)\right]+\frac{q_0 t_0}{C_1+C_2}, \tag{B.15}$$

which shows that the steady-state "shock" forms exponentially beginning at time $t = 0$ and then decays beginning at time $t = t_0$, both occurring with the same time constant $\tau \equiv R(C_1 \parallel C_2)$. The first term $\left(1-e^{-t/\tau}\right)$ represents the transient that results from the transition from $q = 0$ to $q = q_0$ at time $t = 0$ and the second is the counter-transient at time $t = t_0$.

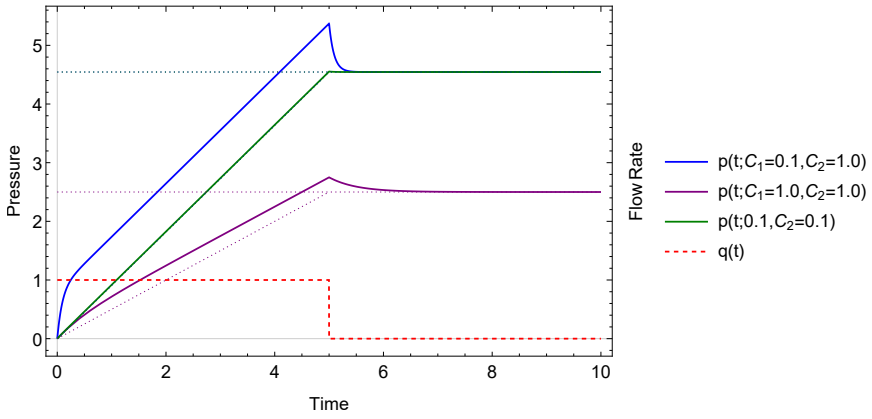
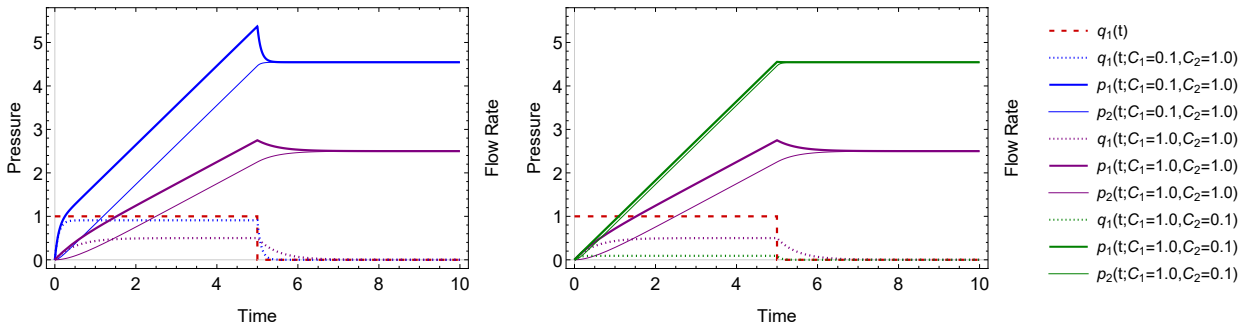
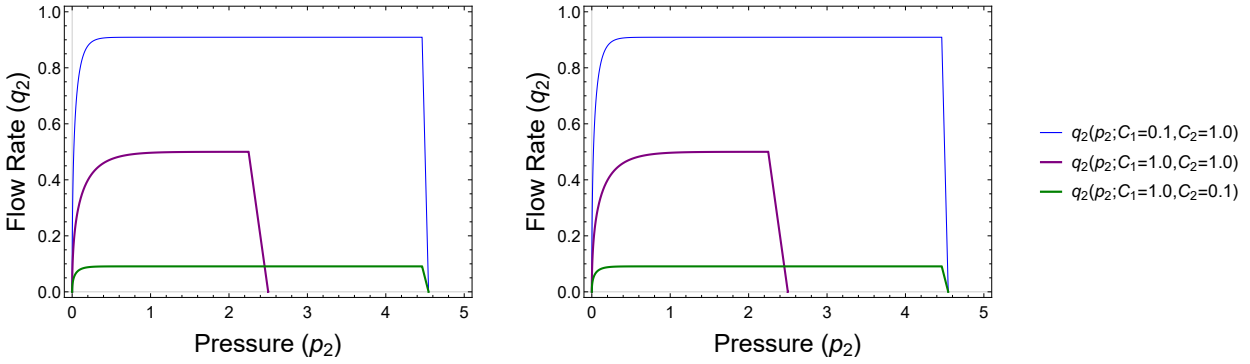


Figure B.2 Behavior of the syringe pump-charged fluidic capacitor. Thick lines represent the pressure profile and thin dotted lines represent the ultimate steady state pressure after the pump ($q(t)$) is disengaged.



(a) Varying C_1 for fixed C_2 **(b)** Varying C_2 for fixed C_1

Figure B.3 Behavior of the syringe pump capacitor P_1 measurements for varying capacitances. Higher C_1 leads to a larger transient response during both filling and un-filling, while higher C_2 allows for more fluid to be stored at the system at lower input pressures.



(a) Varying C_1 for fixed C_2 **(b)** Varying C_2 for fixed C_1

Figure B.4 Response to step function with varying C_1. (a) Q_2P_2 relationship and (b) V_2P_2 relationship, showing expected linear response to constant capacitance C_2. Although changing C_1 allows different amounts of fluid to enter the system, the slope of V_2P_2 does not change with differing C_1, underscoring the importance of putting the flow and pressure sensors as close to the ultimate capacitance as possible. Response to step function with varying C_2. (a) Q_2P_2 relationship and (b) V_2P_2 relationship, showing different response curves due to differing C_2. As expected, the slope of the V_2P_2 curve is directly dependent on the capacitance.

B.1.1 Addition of a parasitic resistance R_{par}

A system with a small leak (*e.g.*, fluid leakage through a small hole or air diffusion through the membrane of capacitor C_2) can be represented by adding a (large) resistor R_2 in parallel with capacitor C_2. While the exact details of the full analysis are relatively unimportant, the leak has a few noteworthy consequences.

First, at full steady-state for $t < t_0$ (*i.e.*, while the syringe pump is still moving), the frequency $s = 0$ and so the capacitors act like an open circuit,[1] leading to a constant flow rate Q through the system, which is governed by Ohm's law. Therefore, pressure $P_1 = Q(R_1 + R_2)$ and $Q_1 = Q$.

The full dynamics of the system become increasingly complicated as more *RC* components are added. This system in particular exhibits two time constants as a result of the two solutions to the quadratic equations needed to separate the denominator. We can view the dynamics of the system by separating out the resistance R_{tot} into the form

$$R_{\text{tot}} = \frac{R + R_{\text{par}} + C_2 R R_{\text{par}} s}{1 + (C_1 R + (C_1 + C_2) R_{\text{par}}) s + C_1 C_2 R R_{\text{par}} s^2} \tag{B.16}$$

$$= \frac{R + R_{\text{par}} + C_2 R R_{\text{par}} s}{(C_1 C_2 R R_{\text{par}})(s - s_{\text{fast}})(s - s_{\text{slow}})} \tag{B.17}$$

[1] *i.e.*, the capacitors become "full"

where

$$\frac{s_{\text{fast}}}{s_{\text{slow}}} = -\frac{C_1R + (C_1+C_2)R_{\text{par}}}{2C_1C_2RR_{\text{par}}} \pm \frac{\sqrt{\frac{1}{4}(C_1(R+R_{\text{par}}) + C_2R_{\text{par}})^2 - C_1C_2RR_{\text{par}}}}{2C_1C_2RR_{\text{par}}}. \tag{B.18}$$

Equation B.17 is now separable, where s_{fast} and s_{slow} correspond to the fundamental frequencies of operation. We therefore can get time constants $\tau = -\frac{1}{s}$ giving

$$\frac{\tau_{\text{fast}}}{\tau_{\text{slow}}} = \frac{C_1(R+R_{\text{par}})}{2} + \frac{C_2R_{\text{Par}}}{2} \mp \sqrt{\frac{1}{4}(C_1(R+R_{\text{par}}) + C_2R_{\text{par}})^2 - C_1C_2RR_{\text{par}}}. \tag{B.19}$$

Equation B.19 makes clear why the terms "fast" and "slow" have been used: due to the behavior of the convolution, any step impulse response will then have fast and slow transient behavior. The full filter function in the time domain is then

$$r_{\text{tot}}(t) = \frac{(R+R_{\text{par}}+C_2RR_{\text{par}}s_{\text{fast}})}{C_1C_2RR_{\text{par}}(s_{\text{fast}}-s_{\text{slow}})}e^{s_{\text{fast}}t} - \frac{(R+R_{\text{par}}+C_2RR_{\text{par}}s_{\text{slow}})}{C_1C_2RR_{\text{par}}(s_{\text{fast}}-s_{\text{slow}})}e^{s_{\text{slow}}t} \tag{B.20}$$

and any time response for P_1 can be found by the convolution theorem:

$$P(t) = Q(t) * r_{\text{tot}}(t), \tag{B.21}$$

showing that $P(t)$ will have the same exponential behavior as the filter $r_{\text{tot}}(t)$.

If we take the limit of $R \gg R$, we get a fast time constant

$$\tau_{\text{fast}} \xrightarrow{R_{\text{par}} \gg R} (C_1 \parallel C_2)R + O(R_{\text{par}})^{-1} \tag{B.22}$$

which behaves like the time constant in equation B.12. There is also a slow transient which forces the system to behave more closely like a pressure-driven *RC* circuit

$$\tau_{\text{slow}} \xrightarrow{R_{\text{par}} \gg R} (C_1+C_2)R_{\text{par}} + O(R_{\text{par}})^{0} \tag{B.23}$$

The fluid equilibrates at a maximum pressure of $q_0(R+R_{\text{par}})$ as expected for fluid forced to flow across resistors R and R_{par} in series. The fast time constant τ_{fast} does not make a substantial impact over the very long-term.

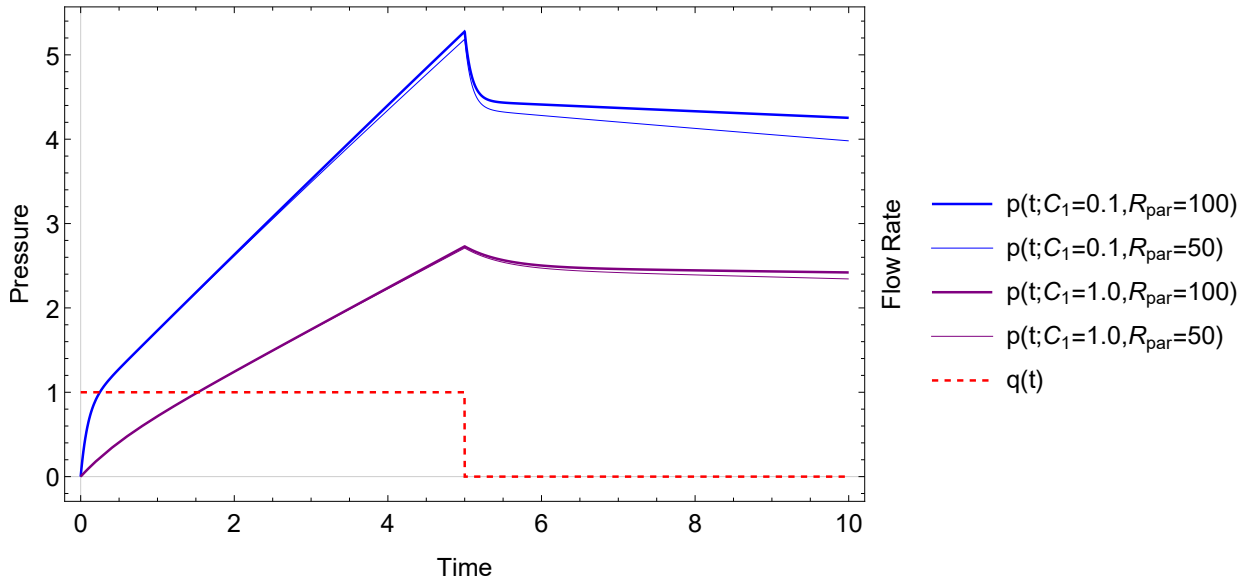


Figure B.5 Behavior of the syringe pump-charged fluidic capacitor with the addition of a large parasitic resistance R_{par} that allows fluid and pressure to slowly drain from the system. The system displays two time constants: an fast constant τ_{fast} which corresponds to immediate transient relaxation, and a slow constant τ_{slow} which shows the long-term *RC* behavior of the leaking system.

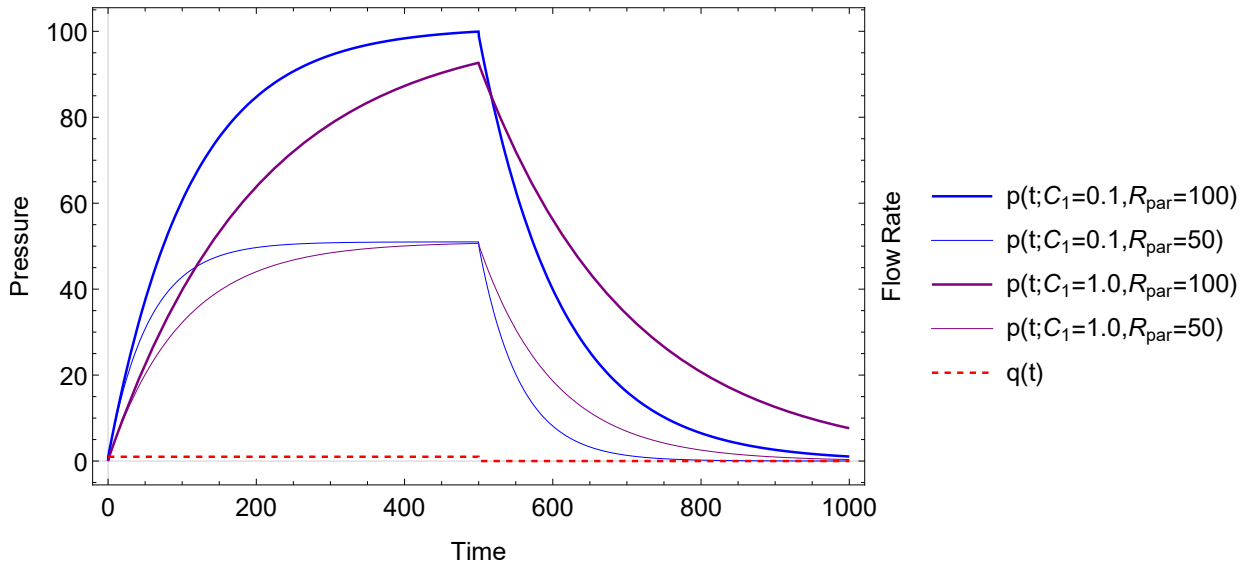


Figure B.6 Long-term behavior of the syringe pump-charged fluidic capacitor with the addition of a large parasitic resistance R_{par}. This figure sets $t_0 = 500$ to show the system stabilizing at pressure $P_{\text{max}} = q_0(R + R_{\text{par}})$ and then decaying. Moreover, the figure shows that the long-term steady-state behavior does not depend on C_1 although C_1 does influence the decay rate τ_{slow}.

Appendix C

The Complete* Works of "Hilbert and Sullivan"

The legendary partnership of Gilbert and Sullivan began in 1875 with the comic (and brief) operetta *Trial by Jury*. This operetta wrapped brutal satire towards the legal profession in catchy music and quickly became a runaway hit, leading to thirteen additional collaborations. Gilbert's librettos never shied away from influential targets: Judges, the police, and even the bumbling Admiral Joseph Porter from HMS Pinafore (based on First Lord of the Admiralty William Henry Smith, widely believed to have received his position as "Ruler of the Queen's Navee" through political cronyism). Regrettably for these poetical punching bags (and fortunately for his audiences), Sullivan's gift for "ear worms"[1] meant that their incompetence was literally sung in the streets by the *hoi polloi* who were unable to get the music out of their heads.

Since their original publication, these songs have taken on a life of their own as they have been rewritten, parodied, and even (in extreme circumstances) performed as originally written. The *Mikado's* "List Song" (which generally needs rewording due to racism and sexism in the original) has been rewritten to mock the latest nuisances as far back as Gilbert's time, and the *Pirates of Penzance's* "I am the very model of a Modern Major General" has seen too many parodies to count (although I cannot recommend Kevin Wald's 1996 *Xena: Warrior Princess* version enough [355]). In writing my own parodies, I find myself in the illustrious company of Tom Lehrer, Allan Sherman, the *Animaniacs*, and *Family Guy*. For the past 140 years, the operettas of Gilbert and Sullivan have been continuously performed, in venues ranging from the Metropolitan Opera House

* As of submission of this thesis

[1] That catchy piece of music that you cannot stop from playing in your head [354]

down to the Point Reyes Dance Palace; "in which case," English soprano Anna Russell once noted, "it seems a pity that there weren't a few more of them" [356].[2]

David Hilbert (1862-1943) was a German mathematician who performed foundational work in the fields of set theory and geometry. It is a testament to his impact that all of quantum mechanics takes place within the eponymous Hilbert spaces. Other than by enabling the wonderful pun-name under which I write all my G&S parodies, or by deeply confusing generations of physics undergraduates, Hilbert has little to do with this concert. (My musical theater parodies belong to "Rodgers and Heisenberg" and pop music (including *Science Man* at the end) is the domain of "Feynman and Garfunkel.") At the very end, I've even slipped in a wholly original composition, "chronicling" the adventures of my quantum professor, a resident of UC Berkeley's Birge Hall.

These "Hilbert and Sullivan" parodies were written over the course of my graduate career. While they were written as a source of stress-relief in good times and in bad, I've found that the tenor of each individual parody bears little resemblance to my mental state when I wrote them. Many of the situations described herein have happened to somebody, but generally not to me personally.[3] In other words, "any resemblance to people or events is purely coincidental and should not be seen as a reflection of graduate life at UC Berkeley." Someday, I hope to oblige Ms Russell by combining these parodies into a full operetta: "UC Pinafore, or, the Slave of Tenure". Sneaking them into my dissertation will have to suffice until then.

Acknowledgments

I would like to thank everyone who contributed a line or two (or more) to help make these parodies work. In no particular order: Jay Daigle, Mollie Kimchi-Schwartz, Kosuke Iwai, Melanie Veale. Lastly, I need to give special thanks to Tom Lehrer for his inspiration, Deborah Benedict for recruiting me to sing (real) Gilbert and Sullivan, and most importantly to my father Steven Glick and grandfather Gene Glick who got me started on Mr. Lehrer and Gilbert and Sullivan at a tender and impressionable age. This is most assuredly your fault.

– Casey Carter Glick

– 1 May 2017

[2] I encourage you to listen to her take on "How to write your own Gilbert and Sullivan opera" [356].

[3] For example, I have never had cause to wear a radiation suit

Table of Contents

Original Operetta	**Year**	**Parody Title**	**Page**
HMS Pinafore	1879	When I was a grad	242
		I'm called little Undergrad	243
		Data fair to see	244
		A physicist has a cunning mind	245
		I am Professor of the Intro Class	246
		He is a Physics Grad	247
The Gondoliers	1880	Rising Early in the Morning	248
		And all shall equal be	249
The Mikado	1885	I've got a little list	250
		See how the Fates their grants allot	251
		Three undergrads from school are we	252
Pirates of Penzance	1879	Hail Alcohol	253
		When a student's not engaged in his assignment	254
The Sorcerer	1878	My name is John Remington Rems	255
The Yeoman of the Guard	1888	Oh! A Hardworking Grad	256
Iolanthe	1882	Homework Set Song	257
Billy Joel	1973	Science Man	258
Casey Glick	2015	The Hero of Birge	259

When I was a grad

-Music by Sir Arthur Sullivan (1878)
-Words by Casey Glick (December 2011)
Inspired by original lyrics from *HMS Pinafore* by William S. Gilbert ("When I was a lad")

When I was a grad, I worked a year
Keeping Social Hour stocked with beer.
My weekly emails set the mood
With promises of alcohol and of free food.
With promises of alcohol and of free food

The drinking went so splendidly,
That now I'm a professor with a PhD
The drinking went so splendidly,
That now he's a professor with a PhD

The beer I did so well supply
That soon I was promoted to a GSI
My teaching post I so abhorred
I mumbled all my lectures right into the board.
He mumbled all his lectures right into the board

The blackboard learned so well, you see,
That now I'm a professor with a PhD.
The blackboard learned so well, you see,
That now he's a professor with a PhD.

My teaching caused such wide dismay
The college elevated me to head TA.
I made sets due the day of the exam
And scheduled all the lectures right at 8 AM.
He scheduled all the lectures right at 8 AM.

The students so despised me
That now I'm a professor with a PhD.
The students so despised he
That now he's a professor with a PhD.

So many students dropped en masse
That I rewrote the textbook for the intro class
I imitated Jackson's style
And obfuscated points I knew were most worthwhile
And obfuscated points he knew were most worthwhile

My book it so lacked clarity
That now I'm a professor with a PhD
His book it so lacked clarity
That now he's a professor with a PhD

In writing texts I proved such a force
That I was made reviewer for a funding source.
I funded those who'd cite my book
Rejecting other grants without a second look.
Rejecting other grants without a second look.

Those grants they so well cited me
That now I'm a professor with a PhD
Those grants they so well cited he
That now he's a professor with a PhD

Now students all, your fears allay,
If your heart is set on heading up a lab some day
Just listen to my simple scheme
And graduate with honors and your self-esteem
And graduate with honors and your self-esteem

Just answer with: "It's trivial to see"
And you all may be professors with a PhD
Just answer with: "It's trivial to see"
And you all may be professors with a PhD

I'm called Little Undergrad

-Music by Sir Arthur Sullivan (1878)
-Words by Casey Glick (8 February 2016)
Inspired by original lyrics from *HMS Pinafore* by William S. Gilbert ("I'm called Little Buttercup")

Hail, researchers – scientists distinguished
I've services (ere joy is whole extinguished)
Assign me a task at which to take a stab
And welcome Little Undergrad to Lab

I'm called Little Undergrad – "Work, Little Undergrad"
(Tears are in ample supply)
But still I'm called Undergrad - hard-working Undergrad
Studious Undergrad, I

I've redox titrations, and membrane filtrations
To concentrate, cleanse, or distill
My earnest endeavor: to process whatever
My profs and TAs would instill

I work through all hours and give up on showers
Acknowledging friendships foregone,
For these circumstances augmented my chances
To earn my diploma anon

Then bye-bye to Undergrad – dear little Undergrad
Grad school departing am I;
For soon your dear Undergrad: Shall have an Undergrad,
Shall make her Undergrad cry!

Data fair to see

-Music by Sir Arthur Sullivan (1878)
-Words by Casey Glick (November 19 2014)
Inspired by original lyrics from *HMS Pinafore* by William S. Gilbert ("A maiden fair to see")

Oh data fair to see, which verifies theory –
The grail of all our questing,
Pursuant to our goal, our heavy heart and soul
Must slog through endless testing.

Must slog through endless testing

For any research field, sweet data is a shield
A ward against privation
For grants and fame accrue to all researchers who
Can garner earned citation

Can garner earned citation

Results are coming now and at first glance allow
A dash of hope be tasted:
PULLS OUT DATA PRINTOUT
Oh pity, pity me, point oh-five-one is P
My efforts all were wasted

Oh pity, pity me, point oh-five-one is P
My efforts all were wasted

*Point oh-**five**-one: **his** ef**forts** wasted*

A physics grad has a cunning mind

-Music by Sir Arthur Sullivan (1878)
-Words by Casey Glick (November 2014)

Inspired by original lyrics from *HMS Pinafore* by William S. Gilbert ("A British Tar is a souring soul")

A physics grad has a cunning mind
As sharp as a diamond blade
Her projects large and small are successful one and all –
Never cancelled or delayed.

Her tests should run and success resound,
Her data should plot and her graphs astound,
Her praises should sing and her grants come through,
And her papers publish painlessly through peer-review.

Her eyes should flash with a curious spark,
And burn with a rocket's flame,
Her soaring mind set free with sufficient Delta V,
Acquiring wide acclaim.

Her prose should flow and her talks beguile,
Her pen should scratch and her code compile,
Her theories shown worthy of being pursued
For they're always proved within an order magnitude

Of magnitude!
Of magnitude!
Of magnitude!

I am Professor of the Intro Class

-Music by Sir Arthur Sullivan (1878)
-Words by Casey Glick (February 2014)
Inspired by original lyrics from *HMS Pinafore* by William S. Gilbert ("I am the Captain of the Pinafore")

My faithful class, good morning
Sir, good morning
I hope you all slept well?
We're sleepy, and you sir?
I was up reasonably late, preparing to teach you all today
You lecture well, sir!

I am Professor of the Intro Class
And a dedicated prof you are
You're very, very kind, and with that frame of mind,
I'm convinced that you'll go far
We're very, very kind, and with that frame of mind
He's convinced that we'll go far
My lectures I prepare with love and toil and care
And speak with cautious grace,
I've never been accused of making you confused,
And I never never lose my place
What never?
No never
What never? **FLIPS DESPERATELY THROUGH NOTES**
Hardly ever?
He'll hardly ever lose his place!
Then give a cheer (and cast your votes): for the staid Professor and his lecture notes
Then give a cheer (and cast your votes): FOR Professor and his lecture notes

I try my best to educate you all
We owe our knowledge all to you
You're remarkably astute in your scholarly pursuit
And I'm proud of your efforts, too
We're remarkably astute in our scholarly pursuit
And he's proud of our efforts too
Every problem that I write teaches valuable insight,
Even those with grunge and grime;
Although their purpose may be a bit unclear today…
They never, never waste your time
What never?
No Never
What never? *STUDENT SHOWS PROFESSOR A VERY LONG PROBLEM SET*
Well, hardly ever
He'll hardly ever waste our time
Then give a cheer with no regrets for the shrewd Professor and his problem sets
Give a cheer with no regrets FOR: Professor and his problem sets

I've taught the Intro Class for thirty years
He knows the crannies and the nooks
I inform and entertain, keeping anecdotes germane
And make sure that I've read the books
He'll inform and entertain, keeping anecdotes germane
And is sure to have read the books
Each concept I present, every point and argument,
I deliberately and faithfully relate
Though my talks might twist and wend right until the very end,
I never never finish late
What never?
No Never
What never? *STUDENT POINTS TO CLOCK/WATCH*
Well, hardly ever
He'll hardly ever finish laaaate
Then give a cheer (and pray we pass) to the prompt Professor of the Intro Class
Give a cheer (and pray we pass) TO: Professor of the Intro Class

He is a Physics Grad

-Music by Sir Arthur Sullivan (1878)
-Words by Casey Glick (December 2011)
Inspired by original lyrics from *HMS Pinafore* by William S. Gilbert ("He is an Englishman")

He is a physics grad.
For he himself has said it
And has posted it on Reddit
That he is a physics grad

(That he is a physics grad)

Oh he might have done biology
Finance or anthropology
Or perhaps done chemistry
(Or perhaps done chemistry)

But in spite of all alliances
He could forge with other sciences
He remains a physics grad

(But in spite of all alliances
He could forge with other sciences
He remains a physics grad)

Rising early in the morning: a physicist's day

-Music by Sir Arthur Sullivan (1889)

-Words by Casey Glick (November 2011)

Inspired by original lyrics from *The Gondoliers* by William S. Gilbert ("Rising early in the morning")

Rising early in the morning
Give my clock a hateful stare
Snooze without its timely warning
Wash my face and comb my hair.
Summon massive burst of will
For my journey up the hill.

First I time evolve a function
While collapsing (with compunction)
Some arbitrary wave or Dirac ket.
Then I normalize a state or
Project by an operator
To diagonalize a basis or a set

Then I'll boost to an inertial Lorentz frame
Where I'll find the laws of physics stay the same
And light's invariant velocity
's a postulate of relativity

After that I'll find essential
Gravitational potential
Be corrected for my GPS to function quite alright.
Finding spacetime is distorted,
Newton's laws by mass contorted,
Singularities whose gravity can overpower light.

Publish papers in a journal
On a schedule half-nocturnal
Responding to reviewers in a manner uncontrite.
Calculating geodesics,
Downing beer and analgesics,
Crunching numbers, simulations, working late into the night.

Oh, the undergrads complain:
"Can you grade this set again?"
And our mentors find impractical our need for food and rest,
But the privilege and pleasure
That we treasure beyond measure
Is disproving most of physics with a single simple test

Directing my attention
To an optical invention
Like the cloak that Harry Potter once possessed:
Fiber optics placed in serial,
A new metamaterial,
A place that's safe to hide and get some rest.

Then I'll try to find magnetic monopoles,
Superluminal neutrinos, or black holes,
Or probe the secrets of cosmology:
What are dark matter and dark energy?

After that I'll measure factors
In my nuclear reactors,
Taking care to keep enclosed within my radiation suit,
Build a TEM wave guide or
Use the Large Hadron Collider
To determine if my operators actually commute

Applying new heuristics,
Using Bose-Einstein statistics,
We'll derive exact solutions (if we have to) now and then:
Hamiltonians quadratic,
Naught but change adiabatic,
Why complicate the model if you're good to factor ten?

Oh, biologists imply
That we oversimplify,
Claiming cows are not as spherical as physicists conclude.
But the culminating pleasure
That we treasure beyond measure
Is deriving all of science to an order magnitude.

And all shall equal be

-Music by Sir Arthur Sullivan (1880)
-Words by Casey Glick (November 20 2015)
Inspired by original lyrics from *The Gondoliers* by William S. Gilbert ("For everyone who feels inclined")

Marco and Giuseppe:
For physicists we seek to find
Some natural units of a kind,
With constants each to One assigned,
And all shall equal be!

Take Newton's gravitation G,
And light speed's universal C,
Fine structure α we decree:
They all shall equal be

π of circle constant fame,
Both h and ħ made the same,
And i and Φ we now proclaim:
They all shall equal be!

Electron's charge, electron's mass,
The weight of Earth and Sun *en masse*,
The R of an Ideal Gas:
They all shall equal be

Bohr's radius and magneton,
Both δ and its ε,
And Euler's Number Pantheon:
They all shall equal be!

For physicists we seek to find
Some natural units of a kind,
With constants each to One assigned,
With constants each to One assigned,
And all shall equal be!

Work here, work there,
Analyses everywhere.
Work here, work there,
Analyses everywhere.
We'll set 'em to One,
We'll set 'em to One,
And all shall equal be!

Chorus:
Work here, work there,
Analyses everywhere.
Work here, work there,
Analyses everywhere.
We'll set 'em to One,
We'll set 'em to One,
And all shall equal be!

Both Newton's G and Einstein's C,
And Euler's γ, Euler's e,
The mass of Earth, the mass of Sun,
The mass of Proton set to one,
Avogadro's N resized,
And h, ħ renormalized,
Bohr's radius and magneton,
And δ, ε.

For physicists we seek to find
Some natural units of a kind,
With constants each to One assigned,
With constants each to One assigned,
And all shall equal be!

Our Praise we sing!
For work now halfway done!
It's all a string
With Value Equal One!
Our Praise, our Praise,
Our Praise we sing!
Praise we sing, Praise we sing!

I've got a Little List

-Music by Sir Arthur Sullivan (1885)
-Words by Casey Glick (November 2012)

Inspired by original lyrics from *The Mikado* by William S. Gilbert ("As some day it may happen")

As some day it may happen that a victim must be found,
I've got a little list — I've got a little list
Of society offenders who might well be underground,
And who never would be missed — who never would be missed!
Those pestilential nuisances who email you with spam
The internet con-artist and his Nigerian Scam.
There's Big Bang Theory viewers who assume they know our life,
The "family values" senator who's cheating on his wife
And bankers who, for Ponzi schemes, got slapped upon the wrist
They'd none of them be missed, they'd none of them be missed.

There's theorists who claim that every particle's a string,
Vaccine denialists, they're all upon the list.
And anyone insisting "Sociology's" a thing.
They never would be missed, they never would be missed.
Colloquium attendees of a "most ingenious" kind
Who've "proven" Albert Einstein wrong, and need to speak their mind,
Premeds who fight for half a point, TAs who barely teach,
Professors incoherent in their mumbled blackboard speech.
And that dread spacetime anomaly, the physics lyricist,
They'd none of them be missed, they'd none of them be missed.

Written for UC Berkeley Physics Phollies, December 2012

See how the Fates their grants allot

-Music by Sir Arthur Sullivan (1885)
-Words by Casey Glick (11 February 2014)

Inspired by original lyrics from *The Mikado* by William S. Gilbert ("See how the Fates their gifts allot")

See how the Fates their Grants allot
For A got Tenure, B did not.
Yet B is worthy, I dare say
Of more seniority than A.

Is B more worthy?

I should say: her works are cited more than A

Yet A is funded, amply funded:
College-funded, VC-funded, DARPA-funded plentif'ly
Elevated sans delay:
Tenured undeserving A…

If I were Chairman (which I'm not)
B should have earned A's Tenure slot
And A should resign in ignomy
(That is assuming I am B)

But should A vanish?

That should he (of course, assuming I am B)

B should be funded, amply funded:
College-funded, VC-funded, DARPA-funded plentif'lly
But remains a postdoc she,
Lowly meritorious B…

Three undergrads from school

-Music by Sir Arthur Sullivan (1885)
-Words by Casey Glick (January 2016)

Inspired by original lyrics from *The Mikado* by William S. Gilbert ("Three little maids from school")

Three undergrads from school are we,
Earning our Ba**che**lor's Degree,
Filled with collegiate *esprit*,

Three undergrads from school!

A: Late to class so I need to run
B: Buying a textbook just for fun
C: Thrilled for the term that's just begun

Three undergrads from school

Three undergrads with apps impending
Panicky emails out are sending
Hoping for letters recommending –

Three undergrads from school,
Three undergrads from school!

A: One undergrad has a rule of thumb
B: Two undergrads to a lecture come
C: Three undergrads is the total sum

Three undergrads from school!

To three undergrads give one an A
Two undergrads complain and say,
"Can't get a PhD that way!"

Three undergrads from school!

Three undergrads with apps impending
Panicky emails out are sending
Hoping for letters recommending –

Three undergrads from school,
Three undergrads from school!

Hail Alcohol

-Music by Sir Arthur Sullivan (1879)
-Words by Casey Glick (July 2013)
Inspired by original lyrics from *Pirates of Penzance* by William S. Gilbert (Hail Poetry)

Student:

Although in our careers, we often sin by overthinking,
Our overcluttered minds find absolution when we're drinking.[1]
Though we read Kittel or Reif, or use Ising Model's spin, it
'Tis a sober, somber life without a drop of alcohol in it.

Chorus of academics:[2]
Hail Alcohol, thou ichor fine
Thy courage flows from laden vine
Hail, spirits, beer, or alicant[3]
All hail, all hail, divine intoxicant!

`

1 *Alternate verse:*
Although in our careers, we often find we're overthinking,
Our cluttered minds can oft be cured by calculated drinking.

2 *Alternate chorus:*
Hail Alcohol, thou ichor grand
Thy courage flows when held in hand
Hail, spirits, beer, or alicant
All hail, all hail, divine intoxicant!

3 Alicant: a type of wine

When a student's not engaged in his assignment

-Music by Sir Arthur Sullivan (1879)
-Words by Casey Glick (November 2014)

Inspired by original lyrics from *Pirates of Penzance* by William S. Gilbert
(When a felon's not engaged in his employment)

When a student's not engaged in his assignment *his assignment*
Or preparing for a project or exam, *or exam,*
In his hobbies or his quest for self-refinement *self-refinement*
He'll cavort rather than stay at home and cram. *home and cram*

Though the pupil'd rather catch up with his mother *with his mother*
Than complete the paper only just begun *just begun*
Oh take one consideration with another: *with another,*
A professor's lot is not a happy one! *OH!*

When our pedagogic duty's to be done, to be done
A Professor's lot is not a happy one!
Happy one!

When the enterprising learner's not a-learning, *not a-learning*
When the theorist's not a-postulating strings *-lating strings*
She'd prefer to sate desires she's been yearning *she's been yearning*
Or to listen to the Campanille's rings *–nille's rings*

Oh our feelings we with difficulty smother *–culty smother*
When our pedagogic duty's to be done *to be done*
Oh take one consideration with another, *with another,*
A Professor's lot is not a happy one! *OH!*

When our pedagogic duty's to be done, to be done
A Professor's lot is not a happy one!
Happy one!

My name is John Remington Rems

-Music by Sir Arthur Sullivan (1878)
-Words by Casey Glick (August 2013)

Inspired by original lyrics from *The Sorcerer* by William S. Gilbert ("My name is John Wellington Wells")
Dedicated to the members of the Berkeley Sensors and Actuators Center (BSAC)

My name is John Remington Rems
I'm a master of everything MEMS
From gyros, spectrometers,
Accelerometers,
Micro- and nano- systems.

If you're making a battery pack
Or piezoelectrical stack,
Or all of above
Check the offices of
All the students and profs in BSAC.

We've a first-class array of devices
That we've built, optimized, or annealed.
And at quite economical prices
We're a match for each group in the field.
We control epitaxy's enviro,
If rotation's of utmost concern,
And etch you a very small gyro, a gyro
That senses each way that you turn.

For it can resonate
(Flexures and solid state)
Anchors vibration nodes
(Transverse or goblet modes).
PSG sacrifice (freeing the bulk device)
Etching and other fab's
Done in the nano labs.

Just check with BSAC admin;
Pister or Wu, Liepmann;
Huggins, or Muller, Lee;
Javey, or White, Horsly;
And also Maharbiz, Nguyen;
Boser, Pisano, Lin;
And also there's Kim, Delane,
Richard, who keep us on schedule
(and marg'nally sane)!!!

If there's something you think that you lack
(Your machine is a bit out of whack?)
Or all of above
Check the offices of
Any student or prof in BSAC.

We can fill your needs for leads
With gold or grapheme sheeting,
Or p-dope moles of holes
For circuits or thermal sheeting.
We can fill your wells with cells
And that without pipetting,
And sort your crops of drops
With light or electrowetting.

Then if you plan it we: research organity,
Set aside vanity for all humanity,
'Voiding profanity as the mundanity
Pushes us closer to verge of insanity.

We work with biology, tissue histology,
Ferro-rheology, 'lectrotechnology,
Modern gizmology,[1] graph systemology,
And since we're at college, we
Study the mental effects of zymology![2]
Oh!!

My name is John Remington Rems
I'm a master of everything MEMS
From gyros, spectrometers,
Accelerometers,
Micro- and nano- systems.

If there's something you think that you lack
From advice to a piezo stack,
Or all of above
Check the offices of
Every student and prof in BSAC!!

Notes:

1. Gizmology: Study of gadgets
2. Zymology: Study of fermentation

Oh! A hardworking grad

-Music by Sir Arthur Sullivan (1888)
-Words by Casey Glick (August 2016)

Inspired by original lyrics from *The Yeoman of the Guard* by William S. Gilbert ("Oh! A private buffoon")

Oh! A hardworking grad is a light-hearted lad if you're asking around the department
His work so consumes that nobody assumes that he'd even require an apartment.
Though from morning to night he just drips with insight driving science's onward progression;
There are rules that a gent with a scholarly bent must observe if he'd keep his profession.
There's a few little rules, really more of a stack
That all researching fools on the tenuring track
Must observe if they love their profession

A disciplined mind runs experiments blind and refrains from all premature peaking
But the PI may say "it looks funny that way; I suggest just a little more tweaking"
So you poke and you prod in a manner slipshod while each change makes you subtly queasier:
Though your code was once strong, your PI thought it wrong, claiming "Excel's so very much easier"
Your integrity thrashes - your fate doesn't bode
Very well when he trashes your elegant code,
Claiming "Excel's so very much easier."

A new project begins with the noblest of sins: with a thirst for creative endeavor.
You lit-search and brainstorm and your faculties swarm with ideas so damnably clever
But with flash of dismay you are stripped of your sway (despite pleading impeccably logicked)
When the postdoc in lab makes an arrogant grab for control of your shiny new project.
Though you're left with a place on the authorship list,
In this publishing race you're completely dismissed
When the postdoc takes over your project.

Though you shake with the flu and a headache or two and you're sleeping in patterns destructive
If your deadlines don't slide they may not even chide if you're properly prim and productive
Though a loved one has died or you're hollow inside from depression unhale and unrighted
Bless your hearts they don't mind, they're exceedingly kind, they don't blame you so long as you're cited!
You'll receive their support for all five or ten years
If you never fall short due to pain or to tears:
They don't blame you so long as you're cited!

The Homework Set Song

-Music by Sir Arthur Sullivan (1882)
-Words by Casey Glick (September 2015)
Inspired by original lyrics from *Iolanthe* by William S. Gilbert ("The Nightmare Song")

Work, uncompleted, robs me of my rest,
Work, stressful work, my headache fierce and blaring
Work, the bulk of which lies mainly unaddressed,
And seethes against my efforts, tears, and swearing.

When you're staring, awake with a dreadful headache, at a homework assignment in front of you
And you've read the notes through, and there's naught you can do that will make this set cease to disgruntle you.
For your thoughts are a mess and your sense of progress has been stalled into irregularity
And your fellow befuddled grad students are huddled together in strained solidarity

But by seven o'clock, you're all dusted with chalk, and you've only six parts left remaining!
And you're on the right track, and think "I'll have a snack and then finish without even straining."
Then your one consolation, the brief numeration, is dashed as the printer engages
For before, it had jammed, and now this time the damned printer spits out another eight pages.

Then for hours you're stuck, so you pray for some luck and you sub in the terms you've remaining
And you cancel a ton, and get one equals one, and accept that you're under constraining…
So you try once *again* to correctly constrain, and then rewrite for comfort and clarity,
And again you're distressed for the term you've expressed in your homework now violates parity.

So you pour through your work as you search for the quirk of the sign error giving you trouble
And its right at the start, and work after that part has been basically reduced to rubble.
With a sob and a sigh you then slog to part (i) and find "Banach" and not "Hilbert" spaces,
For there's nothing from class that helps clear the morass when you lose orthonormalized bases.

And it says in part (g) take the answer from (b) and then prove that it's Lorentz covariant,
So you start to erase, for if (g) were the case, then light-speed is no longer invariant.
You rub the work out and exclaim with a pout and a feeling of great animosity,
You *were* right in part (g) and the term you called "c" was a constant and not light's velocity!

With your terms redefined and with two parts combined, maybe now the result will converge on you
Then you see with a glance that there isn't a chance that more errors won't start to emerge on you:
Though you've Minkowski space, it's quite clear from the trace that the vacuum has peculiarities,
Like photons with masses, and three distinct classes of white holes and nude singularities.

You're a little perplexed, but you check in the Text and perform just a little refinement
And you note with chagrin that the answer therein's not the one listed on the assignment.
But it's near the solution; the right substitution's in one of Abramowitz' tables,
But your work's so behind that you might as well find the solution within Aesop's Fables.

Though you aim for perfection one unfinished section has driven you near to despairing,
You're completely distraught and your eyes are bloodshot and you've practically given up caring…

Then you hear the bells chime and you notice the time, and you'd be so irate if you turned it in late,
And you're saying your prayers as you run to the stairs, and your race was unplanned, but you've homework in hand
And it wasn't for naught as it drops through the slot, then the Grader TA comes to take it away
And you know in your heart how to fix that last part of the problem that couldn't be mended.
But the homework's now due, so no matter: you're through
For this set was too long (ditto, ditto my song)
And thank goodness they're both of them ended!

Science Man

-Music by Billy Joel (1973)
-Words by Casey Glick (December 2013)
Inspired by original lyrics from *Piano Man* by Billy Joel

It's nine o'clock on a Saturday
My labmates look barely alive
There's an old grad working next to me
On a theory he hopes to derive.

He says, "Son can you find me an article
By an author I'm sure I once knew
There's a theorem suggested
and gracefully tested
In 'Letters' or 'Physics Review'"

La di da

Run us a test you're the Science Man
Run us a test tonight
We're all in the mood for some data now
And we've got some funding in sight

Now Larry the postoc's a friend of mine
Who works at the LHC.
And it caused him distress
that the Higgs had a rest
Mass of one-twenty-five GeV

He says, "Casey, this research is killing me,
Where's my strangelets,
my black holes in space?
I could get me some sleep or a family
If I could get out of this place"

La di da

Now Paul studies Stat Mech and Thermo books
And never had time for a life.
And his single ambition's to learn equipartition
From Kittel and Kramer and Reif

And the undergrad's working in Powerpoint
And the chemist titrates an unknown
Yes they're sharing a project called loneliness
But it's better than working alone

Run us a test you're the science man,
Run us a test tonight
We really could use us some data now
For this grant app that we've gotta write

It's a pretty full lab for a Saturday
(My advisor is noting who's here)
He's hoping we find him a miracle
And a visit to Stockholm next year

And the lab bench is smelling like ethanol
And the centrifuge shifts into gear.
As the complex machine runs its standard routine,
I ask "man, what am I doing here?"

La di da

Run us a test you're the Science Man
Run us a test tonight
Our theories are looking for data now
With p less than point zero 5

The Hero of Birge:
The Ballad of Littlejohn

Casey Glick



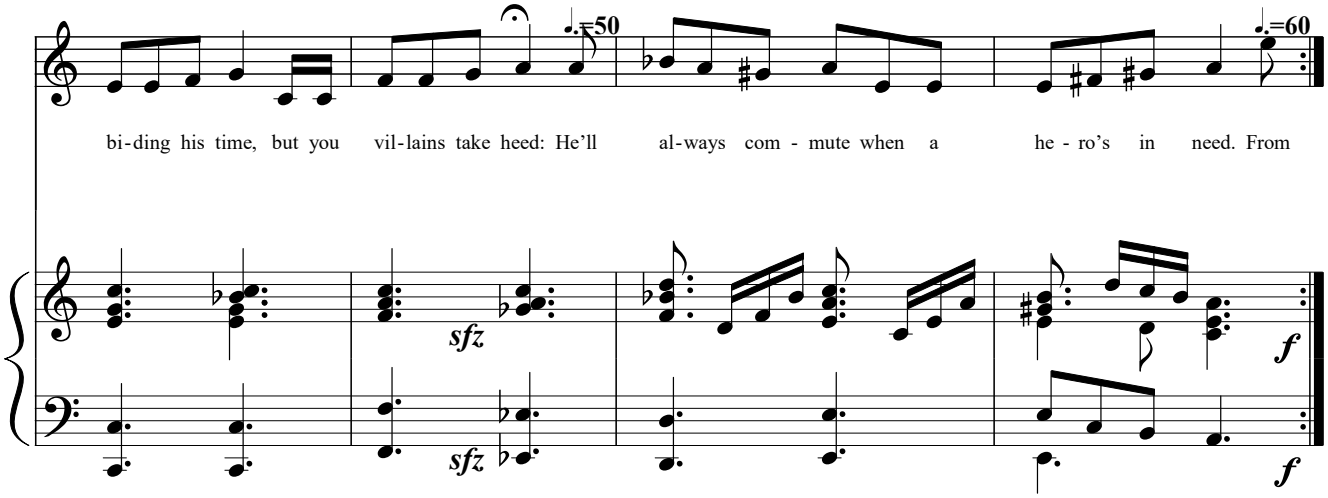
Lyrics written May 2012
Music writen December 2015


When cap-tured on con-ference in the land of Cor - nell Our he - ro was locked in a
They called him to re - scue a vil-lage in dread Of a gi - ant that baked all their
A prin-cess was trapped in a ow-er so high Our he - ro took pity as he
mf
mf
dank dun-geon cell. In a pri - son that e'er would have held me or you, He
bones in - to bread. The gi - ant so quick - ly was cut down to size When re-
hanced to walk by. A reat quan - tum lad - de he um - mone o own And
3.
charged at the wall and he tun-neled right through. From phy-si - cist Lit-tle-john, He - ro of Birge
- norm - al - i - za-tion be - got his de - mise. From
raised up her hopes as he low-ered her down. From
f
f
ff
ff


♩=70
ritard.
Then in flew a dra-gon, its fear-some wings spread And the
mf
mf
chem-ists, bi-o-lo-gists, en-gi-neers fled. And though knights tried to raise the beast's en-tro-py higher, All their
cresc.
cresc.
𝅗𝅥.=60
par-ti-tions failed as they brave-ly caught fire. But our phys-i-cist knew it was time to at-tack And
ff
ff


pulled a sharp ei - gen - state off of his back An - nihi - la - tion vec - tors flew
ritard.
thick through the air And the state of that dra-gon was ground - ed for e'er.
ff
ff
♩.=40
The dra-gon was slain and the prin-cess re-leased His pa-pers were pub-lished, ci - ta-tions in-creased. He's
mf
mf

to chorus



Coda





Bibliography

1 Balagadde, F. K., You, L., Hansen, C. L., Arnold, F. H. & Quake, S. R. Long-term monitoring of bacteria undergoing programmed population control in a microchemostat. *Science* **309**, 137–40 (2005).

2 Lee, C. C. *et al.* Multistep synthesis of a radiolabeled imaging probe using integrated microfluidics. *Science* **310**, 1793–6 (2005).

3 Thorsen, T., Maerkl, S. J. & Quake, S. R. Microfluidic large-scale integration. *Science* **298**, 580–4 (2002).

4 Sochol, R. D., Casavant, B. P., Dueck, M. E., Lee, L. P. & Lin, L. A dynamic bead-based microarray for parallel DNA detection. *Journal of Micromechanics and Microengineering* **21**, 054019 (2011).

5 Tan, W. & Takeuchi, S. A trap-and-release integrated microfluidic system for dynamic microarray applications. *Proc Natl Acad Sci U S A* **104**, 1146–1151 (2007).

6 Sochol, R. D. *et al.* Dual-mode hydrodynamic railing and arraying of microparticles for multi-stage signal detection in continuous flow biochemical microprocessors . *Lab Chip* **14**, 1405–1409 (2014).

7 Sochol, R. D., Li, S., Lee, L. P. & Lin, L. Continuous flow multi-stage microfluidic reactors via hydrodynamic microparticle railing. *Lab Chip* **12**, 4168–77 (2012).

8 Tan, W. & Takeuchi, S. Dynamic microarray system with gentle retrieval mechanism for cell-encapsulating hydrogel beads. *Lab Chip* **8**, 259–266 (2008).

9 Sackmann, E. K., Fulton, A. L. & Beebe, D. J. The present and future role of microfluidics in biomedical research. *Nature* **507**, 181–189 (2014).

10 Xia, Y. N. & Whitesides, G. M. Soft lithography. *Angewandte Chemie-International Edition* **37**, 551–575 (1998).

11 Kuribayashi-Shigetomi, K., Onoe, H. & Takeuchi, S. Cell origami: self-folding of three-dimensional cell-laden microstructures driven by cell traction force. *PLoS One* **7**, e51085 (2012).

12 Teshima, T., Ishihara, H., Iwai, K., Adachi, A. & Takeuchi, S. A dynamic microarray device for paired bead-based analysis. *Lab Chip* **10**, 2443–2448 (2010).

13 Yager, P. *et al.* Microfluidic diagnostic technologies for global public health. *Nature* **442**, 412–418 (2006).

14 Hol, F. J. & Dekker, C. Zooming in to see the bigger picture: microfluidic and nanofabrication tools to study bacteria. *Science* **346**, 1251821 (2014).

15 van Lintel, H. T. G., van De Pol, F. C. M. & Bouwstra, S. A piezoelectric micropump based on micromachining of silicon. *Sensors and Actuators* **15**, 153–167 (1988).

16 Harrison, D. J. *et al.* Micromachining a miniaturized capillary electrophoresis-based chemical analysis system on a chip. *Science* **261**, 895–7 (1993).

17 Harrison, D. J., Manz, A., Fan, Z., Luedi, H. & Widmer, H. M. Capillary electrophoresis and sample injection systems integrated on a planar glass chip. *Analytical Chemistry* **64**, 1926–1932 (1992).

18 Quake, S. R. & Scherer, A. From micro- to nanofabrication with soft materials. *Science* **290**, 1536–1540 (2000).

19 Whitesides, G. M. The origins and the future of microfluidics. *Nature* **442**, 368–373 (2006).

20 Aumiller, G. D., Chandross, E. A., Tomlinson, W. J. & Weber, H. P. Submicrometer resolution replication of relief patterns for integrated optics. *Journal of Applied Physics* **45**, 4557–4562 (1974).

21 Duffy, D. C., McDonald, J. C., Schueller, O. J. & Whitesides, G. M. Rapid prototyping of microfluidic systems in poly(dimethylsiloxane). *Anal Chem* **70**, 4974–84 (1998).

22 Whitesides, G. M., Ostuni, E., Takayama, S., Jiang, X. & Ingber, D. E. Soft lithography in biology and biochemistry. *Annual review of biomedical engineering* **3**, 335–373 (2001).

23 Kim, P. *et al.* Soft lithography for microfluidics: a review. *BioChip Journal* **2**, 1–11 (2008).

24 Unger, M. A., Chou, H. P., Thorsen, T., Scherer, A. & Quake, S. R. Monolithic microfabricated valves and pumps by multilayer soft lithography. *Science* **288**, 113–116 (2000).

25 Mosadegh, B. *et al.* Integrated elastomeric components for autonomous regulation of sequential and oscillatory flow switching in microfluidic devices. *Nature physics* **6**, 433–437 (2010).

26 Jensen, E. C., Bhat, B. P. & Mathies, R. A. A digital microfluidic platform for the automation of quantitative biomolecular assays. *Lab Chip* **10**, 685–691 (2010).

27 Grover, W. H., Skelley, A. M., Liu, C. N., Lagally, E. T. & Mathies, R. A. Monolithic membrane valves and diaphragm pumps for practical large-scale integration into glass microfluidic devices. *Sensors and Actuators B: Chemical* **89**, 315 – 323 (2003).

28 Schudel, B. R., Choi, C. J., Cunningham, B. T. & Kenis, P. J. A. Microfluidic chip for combinatorial mixing and screening of assays. *Lab Chip* **9**, 1676–1680 (2009).

29 Devaraju, N. S. G. K. & Unger, M. A. Pressure driven digital logic in PDMS based microfluidic devices fabricated by multilayer soft lithography. *Lab Chip* **12**, 4809–4815 (2012).

30 Tsao, C.-W. & DeVoe, D. L. Bonding of thermoplastic polymer microfluidics. *Microfluidics and Nanofluidics* **6**, 1–16 (2009).

31 Schlautmann, S., Besselink, G. A. J., Prabhu, G. R. & Schasfoort, R. B. M. Fabrication of a microfluidic chip by UV bonding at room temperature for integration of temperature-sensitive layers. *Journal of Micromechanics and Microengineering* **13**, S81 (2003).

32 Satyanarayana, S., Karnik, R. N. & Majumdar, A. Stamp-and-stick room-temperature bonding technique for microdevices. *Journal of Microelectromechanical Systems* **14**, 392–399 (2005).

33 Koerner, T., Brown, L., Xie, R. & Oleschuk, R. D. Epoxy resins as stamps for hot embossing of microstructures and microfluidic channels. *Sensors and Actuators B: Chemical* **107**, 632–639 (2005).

34 Chueh, B.-h. *et al.* Leakage-free bonding of porous membranes into layered microfluidic array systems. *Analytical chemistry* **79**, 3504–3508 (2007).

35 Samel, B., Chowdhury, M. K. & Stemme, G. The fabrication of microfluidic structures by means of full-wafer adhesive bonding using a poly(dimethylsiloxane) catalyst. *Journal of Micromechanics and Microengineering* **17**, 1710 (2007).

36 Weaver, J. A., Melin, J., Stark, D., Quake, S. R. & Horowitz, M. A. Static control logic for microfluidic devices using pressure-gain valves. *Nature Physics* **6**, 218–223 (2010).

37 Mosadegh, B., Agarwal, M., Torisawa, Y.-s. & Takayama, S. Simultaneous fabrication of PDMS through-holes for three-dimensional microfluidic applications. *Lab Chip* **10**, 1983–1986 (2010).

38 Kartalov, E. P., Walker, C., Taylor, C. R., Anderson, W. F. & Scherer, A. Microfluidic vias enable nested bioarrays and autoregulatory devices in Newtonian fluids. *Proceedings Of The National Academy Of Sciences Of The United States Of America* **103**, 12280–12284 (2006).

39 Au, A. K., Lee, W. & Folch, A. Mail-order microfluidics: evaluation of stereolithography for the production of microfluidic devices. *Lab Chip* **14**, 1294–1301 (2014).

40 Lai, D. *et al.* Simple multi-level microchannel fabrication by pseudo-grayscale backside diffused light lithography. *RSC Adv.* **3**, 19467–19473 (2013).

41 Martinez, A. W., Phillips, S. T., Butte, M. J. & Whitesides, G. M. Patterned paper as a platform for inexpensive, low-volume, portable bioassays. *Angewandte Chemie-International Edition* **46**, 1318–1320 (2007).

42 Martinez, A. W. *et al.* Simple telemedicine for developing regions: Camera phones and paper-based microfluidic devices for real-time, off-site diagnosis. *Analytical Chemistry* **80**, 3699–3707 (2008).

43 Martinez, A. W., Phillips, S. T., Whitesides, G. M. & Carrilho, E. Diagnostics for the Developing World: Microfluidic Paper-Based Analytical Devices. *Analytical Chemistry* **82**, 3–10 (2010).

44 Butt, J., Mebrahtu, H. & Shirvani, H. Peel and tensile test investigation of aluminium 1050 foil parts made with a new additive manufacturing process. *International Journal of Rapid Manufacturing* **5**, 95–115 (2015).

45 Glick, C. C. Generating binary states using a microfluidic channel. US 8844570 B2 (2014).

46 Gaughran, J., Boyle, D., Murphy, J., Kelly, R. & Ducrée, J. Phase-selective graphene oxide membranes for advanced microfluidic flow control. *Microsystems & Nanoengineering* **2** (2016).

47 Mosadegh, B. *Design and fabrication of microfluidic integrated circuits using normally-closed elastomeric valves*. Ph.D. thesis, The University of Michigan (2010).

48 Devaraju, N. G. & Unger, M. A. Method and systems for microfluidic logic devices. US 9371965 B2 (2013).

49 Leal, L. G. *Advanced transport phenomena: fluid mechanics and convective transport processes* (Cambridge University Press, 2007).

50 Tabeling, P. *Introduction to microfluidics* (Oxford University Press on Demand, 2005).

51 Choi, D., Kang, T., Cho, H., Choi, Y. & Lee, L. P. Additional amplifications of SERS via an optofluidic CD-based platform. *Lab Chip* **9**, 239–243 (2009).

52 Kim, N., Dempsey, C. M., Zoval, J. V., Sze, J. & Madou, M. J. Automated microfluidic compact disc (CD) cultivation system of Caenorhabditis elegans. *Sensors And Actuators B-Chemical* **122**, 511–518 (2007).

53 Iwai, K., Sochol, R. & Lin, L. Finger-powered, pressure-driven microfluidic pump. In *Micro Electro Mechanical Systems (MEMS), 2011 IEEE 24th International Conference on*, 1131–1134 (IEEE, 2011).

54 Iwai, K., Higa, A., Sochol, R. & Lin, L. Finger-powered microdroplet generator. In *2011 16th International Solid-State Sensors, Actuators and Microsystems Conference*, 230–233 (IEEE, 2011).

55 Iwai, K., Sochol, R., Lee, L. & Lin, L. Finger-powered bead-in-droplet microfluidic system for point-of-care diagnostics. In *Micro Electro Mechanical Systems (MEMS), 2012 IEEE 25th International Conference on*, 949–952 (IEEE, 2012).

56 Iwai, K. *et al.* Finger-powered microfluidic systems using multilayer soft lithography and injection molding processes. *Lab Chip* **14**, 3790–3799 (2014).

57 Kirby, B. J., Shepodd, T. J. & Jr., E. F. H. Voltage-addressable on/off microvalves for high-pressure microchip separations. *Journal of Chromatography A* **979**, 147–154 (2002). 15th International Symposium on Microscale Separations and Analysis.

58 Sochol, R. D. *et al.* Single-layer microfluidic "disc"diodes via optofluidic lithography for ultra-low reynolds number applications. In *17th Int. Conf. Miniaturized Systems for Chemistry and Life Sciences (MicroTAS 2013), Freiburg, Germany* (2013).

59 Sochol, R. D. *et al.* Single-layer microfluidic "spring" diodes via optofluidic lithography for ultra-low reynolds number applications. In *Solid-State Sensors, Actuators and Microsystems (TRANSDUCERS & EUROSENSORS XXVII), 2013 Transducers & Eurosensors XXVII: The 17th International Conference on*, 2201–2204 (IEEE, 2013).

60 Glick, C. C. *et al.* Pressure gain in single-layer microfluidics devices via optofluidic lithography. In *Solid-State Sensors, Actuators and Microsystems (TRANSDUCERS & EUROSENSORS XXVII), 2013 Transducers & Eurosensors XXVII: The 17th International Conference on*, 404–407 (IEEE, 2013).

61 Glick, C. *et al.* Single-layer microfluidic current source via optofluidic lithography. In *Micro Electro Mechanical Systems (MEMS), 2015 28th IEEE International Conference on*, 551–554 (IEEE, 2015).

62 McDonald, J. *et al.* Fabrication of microfluidic systems in poly(dimethylsiloxane). *Electrophoresis* **21**, 27–40 (2000).

63 Sochol, R. D. *et al.* Microfluidic bead-based diodes with targeted circular microchannels for low Reynolds number applications. *Lab Chip* **14**, 1585–1594 (2014).

64 Zhao, D. S., Roy, B., McCormick, M. T., Kuhr, W. G. & Brazill, S. A. Rapid fabrication of a poly (dimethylsiloxane) microfluidic capillary gel electrophoresis system utilizing high precision machining. *Lab Chip* **3**, 93–99 (2003).

65 Qu, X., Sang, F. & Ren, J. Fabrication of pdms/glass microchips by twofold replication of pdms and its application in genetic analysis. *Journal of Separation Science* **29**, 2390–2394 (2006).

66 Wilson, M. E. *et al.* Fabrication of circular microfluidic channels by combining mechanical micromilling and soft lithography. *Lab Chip* **11**, 1550–1555 (2011).

67 Anderson, J. R. *et al.* Fabrication of topologically complex three-dimensional microfluidic systems in pdms by rapid prototyping. *Anal Chem* **72**, 3158–64 (2000).

68 Zhang, M., Wu, J., Wang, L., Xiao, K. & Wen, W. A simple method for fabricating multi-layer PDMS structures for 3D microfluidic chips. *Lab Chip* **10**, 1199–1203 (2010).

69 Li, X. *et al.* Desktop aligner for fabrication of multilayer microfluidic devices. *Review of Scientific Instruments* **86** (2015).

70 Chen, X., Cui, D. F., Liu, C. C. & Li, H. Microfluidic chip for blood cell separation and collection based on crossflow filtration. *Sensors and Actuators B: Chemical* **130**, 216–221 (2008). Proceedings of the Eleventh International Meeting on Chemical Sensors IMCS-11IMCS 2006IMCS 11.

71 LaVan, D. A., Lynn, D. M. & Langer, R. Moving smaller in drug discovery and delivery. *Nat Rev Drug Discov* **1**, 77–84 (2002).

72 Mata, A., Fleischman, A. J. & Roy, S. Fabrication of multi-layer su-8 microstructures. *Journal of Micromechanics and Microengineering* **16**, 276 (2006).

73 Waits, C. M., Modafe, A. & Ghodssi, R. Investigation of gray-scale technology for large area 3D silicon MEMS structures. *Journal of Micromechanics and Microengineering* **13**, 170 (2003).

74 Chen, Q. *et al.* A rapid and low-cost procedure for fabrication of glass microfluidic devices. *Journal Of Microelectromechanical Systems* **16**, 1193–1200 (2007).

75 Paul, D. *et al.* A "dry and wet hybrid" lithography technique for multilevel replication templates: Applications to microfluidic neuron culture and two-phase global mixing. *Biomicrofluidics* **5**, 024102 (2011).

76 Henke, W., Hoppe, W., Quenzer, H. J., Staudt-Fischbach, P. & Wagner, B. Simulation and experimental study of gray-tone lithography for the fabrication of arbitrarily shaped surfaces. In *Micro Electro Mechanical Systems, 1994, MEMS'94, Proceedings, IEEE Workshop on*, 205–210 (1994).

77 Nam, Y., Kim, M. & Kim, T. Fabricating a multi-level barrier-integrated microfluidic device using grey-scale photolithography. *Journal of Micromechanics and Microengineering* **23**, 105015 (2013).

78 Seo, K. D., Kim, D. S. & Sánchez, S. Fabrication and applications of complex-shaped microparticles via microfluidics. *Lab Chip* **15**, 3622–3626 (2015).

79 Loomis, J., Ratnayake, D., McKenna, C. & Walsh, K. M. Grayscale lithography–automated mask generation for complex three-dimensional topography. *Journal of Micro/Nanolithography, MEMS, and MOEMS* **15**, 013511 (2016).

80 Tseng, P., Murray, C., Kim, D. & Di Carlo, D. Research highlights: printing the future of microfabrication. *Lab Chip* **14**, 1491–5 (2014).

81 O'Neill, P. F. *et al.* Advances in three-dimensional rapid prototyping of microfluidic devices for biological applications. *Biomicrofluidics* **8**, 052112 (2014).

82 Kim, J. Y., Baek, J. Y., Lee, K. A. & Lee, S. H. Automatic aligning and bonding system of pdms layer for the fabrication of 3D microfluidic channels. *Sensors and Actuators A: Physical* **119**, 593–598 (2005).

83 Atencia, J. & Beebe, D. J. Controlled microfluidic interfaces. *Nature* **437**, 648–655 (2005).

84 Sheng, P. & Wen, W. Electrorheological fluids: Mechanisms, dynamics, and microfluidics applications. *Annual Review of Fluid Mechanics* **44**, 143–174 (2012).

85 Crump, S. S. Apparatus and method for creating three-dimensional objects. US5121329 (1992).

86 Miller, B. W. *et al.* 3D printing in X-ray and gamma-ray imaging: A novel method for fabricating high-density imaging apertures. *Nuclear Instruments and Methods in Physics Research Section A: Accelerators, Spectrometers, Detectors and Associated Equipment* **659**, 262–268 (2011).

87 Wu, S.-Y., Yang, C., Hsu, W. & Lin, L. 3D-printed microelectronics for integrated circuitry and passive wireless sensors. *Microsystems & Nanoengineering* **1**, 1–9 (2015).

88 Therriault, D., White, S. R. & Lewis, J. A. Chaotic mixing in three-dimensional microvascular networks fabricated by direct-write assembly. *Nature materials* **2**, 265–271 (2003).

89 Ahn, B. Y. *et al.* Omnidirectional printing of flexible, stretchable, and spanning silver microelectrodes. *Science* **323**, 1590–3 (2009).

90 Wu, W., DeConinck, A. & Lewis, J. A. Omnidirectional printing of 3D microvascular networks. *Adv Mater* **23**, H178–83 (2011).

91 Miller, J. S. *et al.* Rapid casting of patterned vascular networks for perfusable engineered three-dimensional tissues. *Nat Mater* **11**, 768–74 (2012).

92 Gelber, M. K. & Bhargava, R. Monolithic multilayer microfluidics via sacrificial molding of 3D-printed isomalt. *Lab Chip* **15**, 1736–1741 (2015).

93 Kolesky, D. B. *et al.* 3D bioprinting of vascularized, heterogeneous cell-laden tissue constructs. *Advanced Materials* **26**, 3124–3130 (2014).

94 Hwang, Y., Paydar, O. H. & Candler, R. N. 3D printed molds for non-planar PDMS microfluidic channels. *Sensors and Actuators A: Physical* **226**, 137–142 (2015).

95 Hwang, Y. *et al.* Capillary flow in PDMS cylindrical microfluidic channel using 3-d printed mold. *Journal of Microelectromechanical Systems* **25**, 238–240 (2016).

96 Hull, C. W. Apparatus for production of three-dimensional objects by stereolithography. US4575330 (1986).

97 Au, A. K., Bhattacharjee, N., Horowitz, L. F., Chang, T. C. & Folch, A. 3D-printed microfluidic automation. *Lab Chip* **15**, 1934–41 (2015).

98 Bhargava, K. C., Thompson, B. & Malmstadt, N. Discrete elements for 3D microfluidics. *Proc Natl Acad Sci U S A* **111**, 15013–8 (2014).

99 Rogers, C. I., Qaderi, K., Woolley, A. T. & Nordin, G. P. 3D printed microfluidic devices with integrated valves. *Biomicrofluidics* **9**, 016501 (2015).

100 Shallan, A. I., Smejkal, P., Corban, M., Guijt, R. M. & Breadmore, M. C. Cost-effective three-dimensional printing of visibly transparent microchips within minutes. *Analytical Chemistry* **86**, 3124–3130 (2014). PMID: 24512498.

101 Zhu, F. *et al.* Three-dimensional printed millifluidic devices for zebrafish embryo tests. *Biomicrofluidics* **9**, 046502 (2015).

102 A K Au, N. B. & Folch, A. 3D-Printed Microvalves and Micropumps. *MicroTAS 2014* 1–3 (2014).

103 Urrios, A. *et al.* 3D-printing of transparent bio-microfluidic devices in peg-da. *Lab Chip* **16**, 2287–2294 (2016).

104 Maruo, S., Nakamura, O. & Kawata, S. Three-dimensional microfabrication with two-photon-absorbed photopolymerization. *Opt Lett* **22**, 132–4 (1997).

105 Klein, F. *et al.* Elastic fully three-dimensional microstructure scaffolds for cell force measurements. *Adv Mater* **22**, 868–71 (2010).

106 Klein, F. *et al.* Two-component polymer scaffolds for controlled three-dimensional cell culture. *Advanced Materials* **23**, 1341–1345 (2011).

107 He, Y. *et al.* "overpass" at the junction of a crossed microchannel: an enabler for 3D microfluidic chips. *Lab Chip* **12**, 3866–9 (2012).

108 Lim, T. W. *et al.* Three-dimensionally crossing manifold micro-mixer for fast mixing in a short channel length. *Lab Chip* **11**, 100–3 (2011).

109 Tumbleston, J. R. *et al.* Additive manufacturing. continuous liquid interface production of 3D objects. *Science* **347**, 1349–52 (2015).

110 Rosochowski, A. & Matuszak, A. Rapid tooling: the state of the art. *Journal of Materials Processing Technology* **106**, 191–198 (2000).

111 Yamane, M. *et al.* Apparatus and method for forming three-dimensional article. US 5059266 A (1991).

112 Thomas A. Almquist, D. R. S. Thermal stereolithography. US 5672312 A (1997).

113 Sochol, R. D. *et al.* 3D printed microfluidic circuitry via multijet-based additive manufacturing. *Lab Chip* **16**, 668–78 (2016).

114 Au, A. K., Huynh, W., Horowitz, L. F. & Folch, A. 3D-printed microfluidics. *Angew Chem Int Ed Engl* **55**, 3862–81 (2016).

115 Bhattacharjee, N., Urrios, A., Kang, S. & Folch, A. The upcoming 3D-printing revolution in microfluidics. *Lab Chip* **16**, 1720–42 (2016).

116 Lee, K. G. *et al.* 3D printed modules for integrated microfluidic devices. *RSC Advances* **4**, 32876 (2014).

117 Walczak, R. & Adamski, K. Inkjet 3D printing of microfluidic structures-on the selection of the printer towards printing your own microfluidic chips. *Journal of Micromechanics and Microengineering* **25**, 085013 (2015).

118 Feygin, M., Shkolnik, A., Diamond, M. N. & Dvorskiy, E. Laminated object manufacturing system. US 5730817 A (1998).

119 Mueller, B. & Kochan, D. Laminated object manufacturing for rapid tooling and patternmaking in foundry industry. *Computers in Industry* **39**, 47–53 (1999).

120 Hudson, S. E. & Brockmeyer, E. Printing Teddy Bears: A Technique for 3D Printing of Soft Interactive Objects. https://www.disneyresearch.com/project/printed-teddy-bears/.

121 Wang, W., Conley, J. G. & Stoll, H. W. Rapid tooling for sand casting using laminated object manufacturing process. *Rapid Prototyping Journal* **5**, 134–141 (1999).

122 Daufenbach, C. & McMillin, S. Solid freeform fabrication of functional ceramic components using a laminated object manufacturing technique. In *Solid Freeform Fabrication Symposium Proceedings. Austin, TX: The University of Texas at Austin*, 17 (DTIC Document, 1994).

123 Zhong, H. *et al.* Preparation of SiC Ceramics by laminated object manufacturing and pressureless sintering. *Journal of Ceramic Science and Technology* **6**, 133–140 (2015).

124 Windsheimer, H., Travitzky, N., Hofenauer, A. & Greil, P. Laminated Object Manufacturing of Preceramic-Paper-Derived Si?SiC Composites. *Advanced Materials* **19**, 4515–4519 (2007).

125 Abgrall, P. *et al.* A novel fabrication method of flexible and monolithic 3D microfluidic structures using lamination of su-8 films. *Journal of Micromechanics and Microengineering* **16**, 113 (2006).

126 Abgrall, P., Conedera, V., Camon, H., Gue, A.-M. & Nguyen, N.-T. SU-8 as a structural material for labs-on-chips and microelectromechanical systems. *Electrophoresis* **28**, 4539–4551 (2007).

127 Klank, H., Kutter, J. P. & Geschke, O. Co2-laser micromachining and back-end processing for rapid production of PMMA-based microfluidic systems. *Lab Chip* **2**, 242–246 (2002).

128 Focke, M. *et al.* Lab-on-a-Foil: microfluidics on thin and flexible films. *Lab Chip* **10**, 1365–1386 (2010).

129 Malek, C. K., Robert, L. & Salut, R. Femtosecond laser machining and lamination for large-area flexible organic microfluidic chips. *The European Physical Journal Applied Physics* **46**, 12503 (2009).

130 McDonald, J. C. *et al.* Prototyping of microfluidic devices in poly(dimethylsiloxane) using solid-object printing. *Anal Chem* **74**, 1537–45 (2002).

131 Comina, G., Suska, A. & Filippini, D. PDMS lab-on-a-chip fabrication using 3D printed templates. *Lab Chip* **14**, 424–430 (2014).

132 Hwang, Y., Paydar, O. H. & Candler, R. N. Pneumatic microfinger with balloon fins for linear motion using 3D printed molds. *Sensors and Actuators A: Physical* **234**, 65–71 (2015).

133 Kaigala, G. V., Ho, S., Penterman, R. & Backhouse, C. J. Rapid prototyping of microfluidic devices with a wax printer. *Lab Chip* **7**, 384–7 (2007).

134 Thomas, M. S. *et al.* Print-and-peel fabrication for microfluidics: What's in it for biomedical applications? *Annals of Biomedical Engineering* **38**, 21–32 (2009).

135 Lobo Júnior, d. E. O. *et al.* High fidelity prototyping of PDMS electrophoresis microchips using laser-printed masters. *Microsystem Technologies* **21**, 1345–1352 (2015).

136 Comina, G., Suska, A. & Filippini, D. 3D printed unibody lab-on-a-chip: Features survey and check-valves integration. *Micromachines* **6**, 437–451 (2015).

137 Glick, C. C. *et al.* Fabrication of double-sided microfluidic structures via 3D printed transfer molding. In *Hilton Head 2016 Workshop* (Transducer Research Foundation, 2016).

138 Glick, C. C. *et al.* Rapid assembly of multilayer microfluidic structures via 3D-printed transfer molding and bonding. *Microsystems & Nanoengineering* **2** (2016).

139 Bonyár, A. *et al.* Characterization of rapid pdms casting technique utilizing molding forms fabricated by 3D rapid prototyping technology (RPT). *International Journal of Material Forming* **7**, 189–196 (2012).

140 Chan, H. N. *et al.* Direct, one-step molding of 3D-printed structures for convenient fabrication of truly 3D pdms microfluidic chips. *Microfluidics and Nanofluidics* **19**, 9–18 (2015).

141 Temiz, Y., Lovchik, R. D., Kaigala, G. V. & Delamarche, E. Lab-on-a-chip devices: How to close and plug the lab? *Microelectronic Engineering* **132**, 156–175 (2015). Micro and Nanofabrication Breakthroughs for Electronics, MEMS and Life Sciences.

142 McDonald, J. C. *et al.* Prototyping of microfluidic devices in poly(dimethylsiloxane) using solid-object printing. *Analytical Chemistry* **74**, 1537–1545 (2002). PMID: 12033242.

143 Kamei, K. *et al.* 3D printing of soft lithography mold for rapid production of polydimethylsiloxane-based microfluidic devices for cell stimulation with concentration gradients. *Biomedical Microdevices* **17**, 1–8 (2015).

144 Hong, C., Bao, D., Thomas, M. S., Clift, J. M. & Vullev, V. I. Print-and-peel fabrication of microelectrodes. *Langmuir* **24**, 8439–42 (2008). PMID: 18646733.

145 Huh, D. *et al.* Microfabrication of human organs-on-chips. *Nat Protoc* **8**, 2135–57 (2013).

146 Huh, D. *et al.* A human disease model of drug toxicity-induced pulmonary edema in a lung-on-a-chip microdevice. *Sci Transl Med* **4**, 159ra147 (2012).

147 Huh, D. *et al.* Reconstituting organ-level lung functions on a chip. *Science* **328**, 1662–8 (2010).

148 Leslie, D. C. *et al.* Frequency-specific flow control in microfluidic circuits with passive elastomeric features. *Nature Physics* **5**, 231–235 (2009).

149 Mosadegh, B., Bersano-Begey, T., Park, J. Y., Burns, M. A. & Takayama, S. Next-generation integrated microfluidic circuits. *Lab Chip* **11**, 2813–2818 (2011).

150 Chen, Y. & Pepin, A. Nanofabrication: conventional and nonconventional methods. *Electrophoresis* **22**, 187–207 (2001).

151 Gates, B. D. *et al.* New approaches to nanofabrication: molding, printing, and other techniques. *Chem Rev* **105**, 1171–96 (2005).

152 Joo, S. & Brown, R. B. Chemical sensors with integrated electronics. *Chemical reviews* **108**, 638–651 (2008).

153 Alarie, J. P., Jacobson, S. C. & Ramsey, J. M. Electrophoretic injection bias in a microchip valving scheme. *Electrophoresis* **22**, 312–7 (2001).

154 Zhang, M., Wu, J., Niu, X., Wen, W. & Sheng, P. Manipulations of microfluidic droplets using electrorheological carrier fluid. *Phys. Rev. E* **78**, 066305 (2008).

155 Kenis, P. J. A., Ismagilov, R. F. & Whitesides, G. M. Microfabrication inside capillaries using multiphase laminar flow patterning. *Science* **285**, 83–85 (1999).

156 Hediger, S., Fontannaz, J., Sayah, A., Hunziker, W. & Gijs, M. A. M. Biosystem for the culture and characterisation of epithelial cell tissues. *Sensors and Actuators B: Chemical* **63**, 63–73 (2000).

157 Klemic, K. G., Klemic, J. F., Reed, M. A. & Sigworth, F. J. Micromolded pdms planar electrode allows patch clamp electrical recordings from cells. *Biosens Bioelectron* **17**, 597–604 (2002).

158 Abdelgawad, M. & Wheeler, A. R. Low-cost, rapid-prototyping of digital microfluidics devices. *Microfluidics and Nanofluidics* **4**, 349–355 (2007).

159 So, J. H. & Dickey, M. D. Inherently aligned microfluidic electrodes composed of liquid metal. *Lab Chip* **11**, 905–911 (2011).

160 Li, W. *et al.* Squeeze-chip: a finger-controlled microfluidic flow network device and its application to biochemical assays. *Lab Chip* **12**, 1587–1590 (2012).

161 Dubrow, R., Kennedy, C. & Nagle, R. Microfluidic devices and systems incorporating cover layers. US6251343 B1 (2001).

162 Mazouchi, A. & Homsy, G. M. Thermocapillary migration of long bubbles in polygonal tubes. i. theory. *Physics of Fluids* **13** (2001).

163 Nagle, R. & Dubrow, R. Integrated devices and systems for performing temperature controlled reactions and analyses. US 6171850 B1 (2001).

164 Ferguson, G. S., Chaudhury, M. K., Sigal, G. B. & Whitesides, G. M. Contact adhesion of thin gold films on elastomeric supports: cold welding under ambient conditions. *Science* **253**, 776–8 (1991).

165 Kim, J., Surapaneni, R. & Gale, B. K. Rapid prototyping of microfluidic systems using a pdms/polymer tape composite. *Lab Chip* **9**, 1290–3 (2009).

166 Gou, H. L., Xu, J. J., Xia, X. H. & Chen, H. Y. Air plasma assisting microcontact deprinting and printing for gold thin film and pdms patterns. *ACS Appl Mater Interfaces* **2**, 1324–30 (2010).

167 Baraket, A. *et al.* Development of a flexible microfluidic system based on a simple and reproducible sealing process between polymers and poly(dimethylsiloxane). *Microelectronic Engineering* **111**, 332–338 (2013).

168 Morent, R. *et al.* Adhesion enhancement by a dielectric barrier discharge of pdms used for flexible and stretchable electronics. *Journal of Physics D: Applied Physics* **40**, 7392 (2007).

169 Poenar, D. P., Iliescu, C., Carp, M., Pang, A. J. & Leck, K. J. Glass-based microfluidic device fabricated by parylene wafer-to-wafer bonding for impedance spectroscopy. *Sensors and Actuators A: Physical* **139**, 162–171 (2007).

170 Jackson, J. D. *Classical electrodynamics* (Wiley, 1999).

171 Chen, J. Z., Darhuber, A. A., Troian, S. M. & Wagner, S. Capacitive sensing of droplets for microfluidic devices based on thermocapillary actuation. *Lab Chip* **4**, 473–80 (2004).

172 Wang, L., Zhang, M., Li, J., Gong, X. & Wen, W. Logic control of microfluidics with smart colloid. *Lab Chip* **10**, 2869–74 (2010).

173 Li, S. *et al.* A novel method to construct 3D electrodes at the sidewall of microfluidic channel. *Microfluidics and Nanofluidics* **14**, 499–508 (2013).

174 Senturia, S. D. *Microsystem Design* (Kluwer Academic Publishers, Norwell, MA, USA, 2001).

175 Gawad, S. *et al.* Fabrication of a microfluidic cell analyzer in a microchannel using impedance spectroscopy. In *Microtechnologies in Medicine and Biology, 1st Annual International, Conference On. 2000*, vol. 10.1109/MMB.2000.893791, 297–301 (2000).

176 Jasbir, N. P., Bozena, K., Bonnie, L. G. & Byron, D. G. A sacrificial su-8 mask for direct metallization on pdms. *Journal of Micromechanics and Microengineering* **19**, 115014 (2009).

177 Choi, J. W. *et al.* 3-dimensional electrode patterning within a microfluidic channel using metal ion implantation. *Lab Chip* **10**, 783–8 (2010).

178 Rosset, S., Niklaus, M., Dubois, P. & Shea, H. R. Metal ion implantation for the fabrication of stretchable electrodes on elastomers. *Advanced Functional Materials* **19**, 470–478 (2009).

179 Bakhtina, N. A. *et al.* Novel ionic liquid-polymer composite and an approach for its patterning by conventional photolithography. In *Micro Electro Mechanical Systems (MEMS), 2015 28th IEEE International Conference on*, 97–101 (IEEE, 2015).

180 Jiguet, S., Bertsch, A., Hofmann, H. & Renaud, P. Conductive SU8-silver composite photopolymer. In *Micro Electro Mechanical Systems, 2004. 17th IEEE International Conference on. (MEMS)*, vol. 10.1109/MEMS.2004.1290538, 125–128 (2004).

181 Fujigaya, T., Haraguchi, S., Fukumaru, T. & Nakashima, N. Development of novel carbon nanotube/photopolymer nanocomposites with high conductivity and their application to nanoimprint photolithography. *Advanced Materials* **20**, 2151–2155 (2008).

182 Sun, Y., Gates, B., Mayers, B. & Xia, Y. Crystalline silver nanowires by soft solution processing. *Nano Letters* **2**, 165–168 (2002).

183 Jiguet, S., Bertsch, A., Hofmann, H. & Renaud, P. Conductive SU8 Photoresist for Microfabrication. *Advanced Functional Materials* **15**, 1511–1516 (2005).

184 Lu, K.-Y. *et al.* Three dimensional electrode array for cell lysis via electroporation. *Biosensors and Bioelectronics* **22**, 568–574 (2006). Selected Papers from the 2nd International Meeting on Microsensors and Microsystems.

185 Ota, H. *et al.* Application of 3D printing for smart objects with embedded electronic sensors and systems. *Advanced Materials Technologies* (2016).

186 Siegel, A. C., Bruzewicz, D. A., Weibel, D. B. & Whitesides, G. M. Microsolidics: Fabrication of three-dimensional metallic microstructures in poly(dimethylsiloxane). *Advanced Materials* **19**, 727–733 (2007).

187 Siegel, A. C. *et al.* Cofabrication of electromagnets and microfluldic systems in poly(dimethylsiloxane). *Angewandte Chemie-International Edition* **45**, 6877–6882 (2006).

188 Hoogvliet, J. C., Dijksma, M., Kamp, B. & van Bennekom, W. P. Electrochemical pretreatment of polycrystalline gold electrodes to produce a reproducible surface roughness for self-assembly: A study in phosphate buffer ph 7.4. *Analytical Chemistry* **72**, 2016–2021 (2000). PMID: 10815959.

189 Gong, X. & Wen, W. Polydimethylsiloxane-based conducting composites and their applications in microfluidic chip fabrication. *Biomicrofluidics* **3** (2009).

190 Liu, L. *et al.* Design and integration of an all-in-one biomicrofluidic chip. *Biomicrofluidics* **2**, 34103 (2008).

191 Niu, X., Peng, S., Liu, L., Wen, W. & Sheng, P. Characterizing and Patterning of PDMS-Based Conducting Composites. *Advanced Materials* **19**, 2682–2686 (2007).

192 Majid Kazemian, A. & Sulabha, K. K. Giant piezoresistive response in zinc-polydimethylsiloxane composites under uniaxial pressure. *Journal of Physics D: Applied Physics* **41**, 135405 (2008).

193 Hu, C., Liu, C., Chen, L. & Fan, S. Semiconductor behaviors of low loading multiwall carbon nanotube/poly (dimethylsiloxane) composites. *Applied Physics Letters* **95**, 103103 (2009).

194 Grilli, S. *et al.* Hybrid ferroelectric-polymer microfluidic device for dielectrophoretic self-assembling of nanoparticles. *RSC Adv.* **4**, 2851–2857 (2014).

195 Junho, J., Jun, S. & Grodzinski, P. Micropumps based on alternating high-gradient magnetic fields. *IEEE Transactions on Magnetics* **36**, 2012–2014 (2000).

196 Psaltis, D., Quake, S. R. & Yang, C. Developing optofluidic technology through the fusion of microfluidics and optics. *Nature* **442**, 381–386 (2006).

197 Yao, G. & Tan, W. Molecular-beacon-based array for sensitive dna analysis. *Anal Biochem* **331**, 216–23 (2004).

198 Wen, W., Huang, X., Yang, S., Lu, K. & Sheng, P. The giant electrorheological effect in suspensions of nanoparticles. *Nature Materials* **2**, 727–30 (2003).

199 Zhang, M. *et al.* Microdroplet-based universal logic gates by electrorheological fluid. *Soft Matter* **7**, 7493–7497 (2011).

200 Sun, Y., Nelson, B. J., Potasek, D. P. & Enikov, E. A bulk microfabricated multi-axis capacitive cellular force sensor using transverse comb drives. *Journal of Micromechanics and Microengineering* **12**, 832 (2002).

201 Ahn, K., Agresti, J., Chong, H., Marquez, M. & Weitz, D. A. Electrocoalescence of drops synchronized by size-dependent flow in microfluidic channels. *Applied Physics Letters* **88** (2006).

202 Priest, C., Herminghaus, S. & Seemann, R. Controlled electrocoalescence in microfluidics: Targeting a single lamella. *Applied Physics Letters* **89** (2006).

203 Mugele, F. & Baret, J.-C. Electrowetting: from basics to applications. *Journal of Physics: Condensed Matter* **17**, R705 (2005).

204 Chung, S. K., Rhee, K. & Cho, S. K. Bubble actuation by electrowetting-on-dielectric (ewod) and its applications: A review. *International Journal of Precision Engineering and Manufacturing* **11**, 991–1006 (2010).

205 Frieder, M. & Jean-Christophe, B. Electrowetting: from basics to applications. *Journal of Physics: Condensed Matter* **17**, R705 (2005).

206 Paik, P., Pamula, V. K., Pollack, M. G. & Fair, R. B. Electrowetting-based droplet mixers for microfluidic systems. *Lab Chip* **3**, 28–33 (2003).

207 Pollack, M. G., Shenderov, A. D. & Fair, R. B. Electrowetting-based actuation of droplets for integrated microfluidics. *Lab Chip* **2**, 96–101 (2002).

208 Fair, R. B. Digital microfluidics: is a true lab-on-a-chip possible? *Microfluidics and Nanofluidics* **3**, 245–281 (2007).

209 Fair, R. B., Khlystov, A., Srinivasan, V., Pamula, V. K. & Weaver, K. N. Integrated chemical/biochemical sample collection, pre-concentration, and analysis on a digital microfluidic lab-on-a-chip platform. In *Optics East*, 113–124 (2004).

210 Paik, P. Y., Pamula, V. K. & Chakrabarty, K. Adaptive cooling of integrated circuits using digital microfluidics. *IEEE Transactions on Very Large Scale Integration (VLSI) Systems* **16**, 432–443 (2008).

211 Link, D. R. *et al.* Electric Control of Droplets in Microfluidic Devices. *Angewandte Chemie-International Edition* **45**, 2556–2560 (2006).

212 Takhistov, P., Indeikina, A. & Chang, H.-C. Electrokinetic displacement of air bubbles in microchannels. *Physics of Fluids* **14** (2002).

213 Lagally, E. T., Simpson, P. C. & Mathies, R. A. Monolithic integrated microfluidic dna amplification and capillary electrophoresis analysis system. *Sensors and Actuators B: Chemical* **63**, 138–146 (2000).

214 Schwartz, Wang & Bruinsma. Cell locomotion and focal adhesions are regulated by the mechanical properties of the substrate–discussion. *Biological Bulletin* **194**, 349–350 (1998).

215 Schwarz, U. S. *et al.* Calculation of forces at focal adhesions from elastic substrate data: The effect of localized force and the need for regularization. *Biophysical Journal* **83**, 1380–1394 (2002).

216 Sameoto, D. E. Reversible bonding of microfluidic channels using dry adhesives. 20150343442 (2015).

217 Engel, L. *et al.* Actuation of a novel pluronic-based hydrogel: Electromechanical response and the role of applied current. *Sensors and Actuators B: Chemical* **191**, 650–658 (2014).

218 Kim, S. J. *et al.* Behavior in electric fields of smart hydrogels with potential application as bio-inspired actuators. *Smart materials and structures* **14**, 511 (2005).

219 Andersson, H. & van den Berg, A. Microfluidic devices for cellomics: a review. *Sensors and Actuators B: Chemical* **92**, 315–325 (2003).

220 Voldman, J., Gray, M. L., Toner, M. & Schmidt, M. A. A microfabrication-based dynamic array cytometer. *Anal Chem* **74**, 3984–90 (2002).

221 Leigh, S. J., Bradley, R. J., Purssell, C. P., Billson, D. R. & Hutchins, D. A. A simple, low-cost conductive composite material for 3D printing of electronic sensors. *PLoS One* **7**, e49365 (2012).

222 Schmitz, M. *et al.* Capricate: A fabrication pipeline to design and 3D print capacitive touch sensors for interactive objects. In *In UIST'15*, Series Capricate: A Fabrication Pipeline to Design and 3D Print Capacitive Touch Sensors for Interactive Objects, 253–258 (2015).

223 Mireles, J. *et al.* Fused deposition modeling of metals. In *23rd Annual International Solid Freeform Fabrication Symposium*, Series Fused Deposition Modeling of Metals, 836–845 (2012).

224 Ketterl, T. P. *et al.* A 2.45 ghz phased array antenna unit cell fabricated using 3-d multi-layer direct digital manufacturing. *IEEE Transactions on Microwave Theory and Techniques* **63**, 4382–4394 (2015).

225 Swensen, J. P., Odhner, L. U., Araki, B. & Dollar, A. M. Printing three-dimensional electrical traces in additive manufactured parts for injection of low melting temperature metals. *Journal of Mechanisms and Robotics* **7**, 021004 (2015).

226 Espalin, D., Muse, D. W., MacDonald, E. & Wicker, R. B. 3D printing multifunctionality: structures with electronics. *The International Journal of Advanced Manufacturing Technology* **72**, 963–978 (2014).

227 v. Osch, T. H. J., Perelaer, J., de Laat, A. W. M. & Schubert, U. S. Inkjet printing of narrow conductive tracks on untreated polymeric substrates. *Advanced Materials* **20**, 343–345 (2008).

228 Ahn, B. Y. & Lewis, J. A. Amphiphilic silver particles for conductive inks with controlled wetting behavior. *Materials Chemistry and Physics* **148**, 686–691 (2014).

229 Lewis, J. A., Duoss, E. B. & Twardowski, M. Sol gel inks. US 7956102 B2 (2011).

230 Lewis, J. A., Ahn, B. Y. & Duoss, E. B. Metal nanoparticle inks. US 7922939 B2 (2010).

231 Gasser, R. B. *et al.* Single-strand conformation polymorphism (sscp) for the analysis of genetic variation. *Nature Protocols* **1**, 3121–3128 (2007).

232 Voxel8. Multi-material digital manufacturing (2016).

233 Periard, D., Malone, E. & Lipson, H. Printing embedded circuits. In *In 18th Solid Freeform Fabrication Symposium*, Series Printing Embedded Circuits, 6–8 (Austin TX, 2007).

234 Ahmadloo, M. & Mousavi, P. A novel integrated dielectric-and-conductive ink 3D printing technique for fabrication of microwave devices. In *Microwave Symposium Digest (IMS), 2013 IEEE MTT-S International*, 1–3 (IEEE, 2013).

235 Ahmadloo, M. & Mousavi, P. Application of novel integrated dielectric and conductive ink 3D printing technique for fabrication of conical spiral antennas. In *Antennas and Propagation Society International Symposium (APSURSI), 2013 IEEE*, 780–781 (IEEE, 2013).

236 Ahmadloo, M. Design and fabrication of geometrically complicated multiband microwave devices using a novel integrated 3D printing technique. In *Electrical Performance of Electronic Packaging and Systems (EPEPS), 2013 IEEE 22nd Conference on*, 29–32 (IEEE, 2013).

237 Mirzaee, M., Noghanian, S., Wiest, L. & Chang, I. Developing flexible 3D printed antenna using conductive abs materials. In *Antennas and Propagation & USNC/URSI National Radio Science Meeting, 2015 IEEE International Symposium on*, 1308–1309 (IEEE, 2015).

238 Arnal, N. *et al.* 3D multi-layer additive manufacturing of a 2.45 ghz rf front end. In *Microwave Symposium (IMS), 2015 IEEE MTT-S International*, 1–4 (IEEE, 2015).

239 Liang, M., Shemelya, C., MacDonald, E., Wicker, R. & Xin, H. 3-d printed microwave patch antenna via fused deposition method and ultrasonic wire mesh embedding technique. *IEEE Antennas and Wireless Propagation Letters* **14**, 1346–1349 (2015).

240 Shemelya, C. *et al.* Multi-layer off-axis patch antennas fabricated using polymer extrusion 3D printing. In *Antennas and Propagation (EuCAP), 2016 10th European Conference on*, 1–5 (IEEE, 2016).

241 Chieh, J. C. S., Dick, B., Loui, S. & Rockway, J. D. Development of a ku-band corrugated conical horn using 3-d print technology. *IEEE Antennas and Wireless Propagation Letters* **13**, 201–204 (2014).

242 Paulsen, J. A., Renn, M., Christenson, K. & Plourde, R. Printing conformal electronics on 3D structures with aerosol jet technology. In *Future of Instrumentation International Workshop (FIIW), 2012*, Series Printing conformal electronics on 3D structures with Aerosol Jet technology, 1–4 (IEEE, 2012).

243 Shemelya, C. *et al.* Multi-layer archimedean spiral antenna fabricated using polymer extrusion 3D printing. *Microwave and Optical Technology Letters* **58**, 1662–1666 (2016).

244 Moscato, S. *et al.* Infill-dependent 3-d-printed material based on ninjaflex filament for antenna applications. *IEEE Antennas and Wireless Propagation Letters* **15**, 1506–1509 (2016).

245 Moscato, S., Moro, R., Pasian, M., Bozzi, M. & Perregrini, L. Innovative manufacturing approach for paper-based substrate integrated waveguide components and antennas. *IET Microwaves, Antennas & Propagation* **10**, 256–263 (2016).

246 DÁuria, M. *et al.* 3-d printed metal-pipe rectangular waveguides. *IEEE Transactions on Components, Packaging and Manufacturing Technology* **5**, 1339–1349 (2015).

247 DeNava, E. *et al.* Three-dimensional off-axis component placement and routing for electronics integration using solid freeform fabrication. In *Solid Freeform Fabrication Symposium, The University of Texas at Austin, Austin TX*, 4–6 (2008).

248 Jang, S. H., Oh, S. T., Lee, I. H., Kim, H.-C. & Cho, H. Y. 3-dimensional circuit device fabrication process using stereolithography and direct writing. *International Journal of Precision Engineering and Manufacturing* **16**, 1361–1367 (2015).

249 Lopes, A. J. *et al.* Expanding rapid prototyping for electronic systems integration of arbitrary form. In *17th Annual Solid Freeform Fabrication Symposium, University of Texas at Austin, Austin, TX, Aug*, 14–16 (2006).

250 Medina, F. *et al.* Hybrid manufacturing: integrating direct-write and stereolithography. *Proceedings of the 2005 Solid Freeform Fabrication. Journal of Manufacturing Science and Engineering* (2005).

251 Navarrete, M. *et al.* Integrated layered manufacturing of a novel wireless motion sensor system with gps. Tech. Rep., DTIC Document (2007).

252 Joe Lopes, A., MacDonald, E. & Wicker, R. B. Integrating stereolithography and direct print technologies for 3D structural electronics fabrication. *Rapid Prototyping Journal* **18**, 129–143 (2012).

253 Castillo, S., Muse, D., Medina, F., MacDonald, E. & Wicker, R. Electronics integration in conformal substrates fabricated with additive layered manufacturing. In *Proceedings of the 20th Annual Solid Freeform Fabrication Symposium*, 730–737 (2009).

254 Macdonald, E. *et al.* 3D printing for the rapid prototyping of structural electronics. *IEEE Access* **2**, 234–242 (2014).

255 Lu, Y., Vatani, M. & Choi, J.-W. Direct-write/cure conductive polymer nanocomposites for 3D structural electronics. *Journal of Mechanical Science and Technology* **27**, 2929–2934 (2013).

256 Vatani, M., Lu, Y., Engeberg, E. D. & Choi, J.-W. Combined 3D printing technologies and material for fabrication of tactile sensors. *International Journal of Precision Engineering and Manufacturing* **16**, 1375–1383 (2015).

257 Geterud, E. G., Bergmark, P. & Yang, J. Lightweight waveguide and antenna components using plating on plastics. In *Antennas and Propagation (EuCAP), 2013 7th European Conference on*, 1812–1815 (IEEE, 2013).

258 Huang, Y., Gong, X., Hajela, S. & Chappell, W. J. Layer-by-layer stereolithography of three-dimensional antennas. In *2005 IEEE Antennas and Propagation Society International Symposium*, vol. 1, 276–279 (IEEE, 2005).

259 Macor, A., de Rijk, E., Alberti, S., Goodman, T. & Ansermet, J. P. Note: three-dimensional stereolithography for millimeter wave and terahertz applications. *Rev Sci Instrum* **83**, 046103 (2012).

260 von Bieren, A., de Rijk, E., Ansermet, J.-P. & Macor, A. Monolithic metal-coated plastic components for mm-wave applications. In *2014 39th International Conference on Infrared, Millimeter, and Terahertz waves (IRMMW-THz)*, 1–2 (IEEE, 2014).

261 Swissto-12. website: http://www.swissto12.com/.

262 Yang, C. *et al.* 3D printed rf passive components by liquid metal filling. In *Micro Electro Mechanical Systems (MEMS), 2015 28th IEEE International Conference on*, 261–264 (IEEE, 2015).

263 Sideris, C. *et al.* Automated design of a 3D printed waveguide surface coupler. In *2015 IEEE International Symposium on Antennas and Propagation & USNC/URSI National Radio Science Meeting*, 318–319 (IEEE, 2015).

264 Nayeri, P. *et al.* 3D printed dielectric reflectarrays: low-cost high-gain antennas at sub-millimeter waves. *IEEE Transactions on Antennas and Propagation* **62**, 2000–2008 (2014).

265 Zhu, R., Lipworth, G., Zvolensky, T., Smith, D. R. & Marks, D. L. Versatile manufacturing of split-block microwave devices using rapid prototyping and electroplating. *IEEE Antennas and Wireless Propagation Letters* **16**, 157–160 (2016).

266 Pandey, S., Gupta, B. & Nahata, A. Terahertz plasmonic waveguides created via 3D printing. *Opt Express* **21**, 24422–30 (2013).

267 Lewis, J. A. & Ahn, B. Y. Device fabrication: Three-dimensional printed electronics. *Nature* **518**, 42–3 (2015).

268 Balagaddé, F. K., You, L., Hansen, C. L., Arnold, F. H. & Quake, S. R. Long-term monitoring of bacteria undergoing programmed population control in a microchemostat. *Science* **309**, 137–140 (2005).

269 Hua, Z. *et al.* A versatile microreactor platform featuring a chemical-resistant microvalve array for addressable multiplex syntheses and assays. *Journal of Micromechanics and Microengineering* **16**, 1433 (2006).

270 Lee, D. W. & Cho, Y. High-radix microfluidic multiplexer with pressure valves of different thresholds. *Lab Chip* **9**, 1681–1686 (2009).

271 Lee, D. W., Doh, I., Kim, Y. & Cho, Y.-H. Advanced combinational microfluidic multiplexer using multiple levels of control pressures. *Lab Chip* **13**, 3658–3662 (2013).

272 Lee, D. W., Doh, I., Kim, Y. & Cho, Y. H. Advanced combinational microfluidic multiplexer for fuel cell reactors. *Journal of Physics: Conference Series* **476**, 012045 (2013).

273 Wang, C.-H. & Lee, G.-B. Pneumatically driven peristaltic micropumps utilizing serpentine-shape channels. *Journal of Micromechanics and Microengineering* **16**, 341 (2006).

274 Huang, C.-W., Huang, S.-B. & Lee, G.-B. Pneumatic micropumps with serially connected actuation chambers. *Journal of Micromechanics and Microengineering* **16**, 2265 (2006).

275 Huang, S.-B., Wu, M.-H., Cui, Z., Cui, Z. & Lee, G.-B. A membrane-based serpentine-shape pneumatic micropump with pumping performance modulated by fluidic resistance. *Journal of Micromechanics and Microengineering* **18**, 045008 (2008).

276 Duncan, P. N., Nguyen, T. V. & Hui, E. E. Pneumatic oscillator circuits for timing and control of integrated microfluidics. *Proceedings of the National Academy of Sciences* **110**, 18104–18109 (2013).

277 Duncan, P. N., Ahrar, S. & Hui, E. E. Scaling of pneumatic digital logic circuits. *Lab Chip* **15**, 1360–1365 (2015).

278 Kim, J., Stockton, A. M., Jensen, E. C. & Mathies, R. A. Pneumatically actuated microvalve circuits for programmable automation of chemical and biochemical analysis. *Lab Chip* **16**, 812–819 (2016).

279 Lee, K. G. *et al.* 3D printed modules for integrated microfluidic devices. *RSC Advances* **4**, 32876–32880 (2014).

280 Kim, J., Kang, M., Jensen, E. C. & Mathies, R. A. Lifting gate pdms microvalves and pumps for microfluidic control. *Analytical chemistry* **84**, 2067 (2012).

281 Zamir, M. *The physics of pulsatile flow* (Springer, 2000).

282 Duncan, M. W., Aebersold, R. & Caprioli, R. M. The pros and cons of peptide-centric proteomics. *Nature Biotechnology* **28**, 659–664 (2010).

283 Bruus, H. *Theoretical microfluidics*, vol. 2 (MIC-Department of micro and Nanotechnology, Technical University of Denmark, 2005).

284 Fine, R. A. & Millero, F. J. Compressibility of water as a function of temperature and pressure. *The Journal of Chemical Physics* **59**, 5529–5536 (1973).

285 Lopez, J. Lecture notes in fluid mechanics, BIEN 501 (2007).

286 Hong, C.-C., Choi, J.-W. & Ahn, C. H. A novel in-plane passive microfluidic mixer with modified tesla structures. *Lab Chip* **4**, 109–113 (2004).

287 Reichmuth, D. S., Shepodd, T. J. & Kirby, B. J. On-chip high-pressure picoliter injector for pressure-driven flow through porous media. *Analytical Chemistry* **76**, 5063–5068 (2004). PMID: 15373443.

288 Kirby, B. J., Reichmuth, D. S., Renzi, R. F., Shepodd, T. J. & Wiedenman, B. J. Microfluidic routing of aqueous and organic flows at high pressures: fabrication and characterization of integrated polymer microvalve elements. *Lab Chip* **5**, 184–190 (2005).

289 Ernest F. Hasselbrink, J., Shepodd, T. J. & Rehm, J. E. High-pressure microfluidic control in lab-on-a-chip devices using mobile polymer monoliths. *Analytical Chemistry* **74**, 4913–4918 (2002). PMID: 12380812.

290 Chung, S. E. *et al.* Optofluidic maskless lithography system for real-time synthesis of photopolymerized microstructures in microfluidic channels. *Applied Physics Letters* **91**, 041106 (2007).

291 Chung, S. E., Park, W., Shin, S., Lee, S. A. & Kwon, S. Guided and fluidic self-assembly of microstructures using railed microfluidic channels. *Nature Materials* **7**, 581–587 (2008).

292 Chung, S. E., Jung, Y. & Kwon, S. Three-Dimensional Fluidic Self-Assembly by Axis Translation of Two-Dimensionally Fabricated Microcomponents in Railed Microfluidics. *Small* **7**, 796–803 (2011).

293 Beebe, D. J. *et al.* Functional hydrogel structures for autonomous flow control inside microfluidic channels. *Nature* **404**, 588–590 (2000).

294 Vázquez, M. & Paull, B. Review on recent and advanced applications of monoliths and related porous polymer gels in micro-fluidic devices. *Analytica Chimica Acta* **668**, 100–113 (2010).

295 Kim, D. & Beebe, D. A bi-polymer micro one-way valve. *Sensors And Actuators A-Physical* **136**, 426–433 (2007).

296 Doh, I. & Cho, Y. Passive flow-rate regulators using pressure-dependent autonomous deflection of parallel membrane valves. *Lab Chip* **9**, 2070–2075 (2009).

297 Dingle, R. B. & Dingle, R. *Asymptotic expansions: their derivation and interpretation*, vol. 48 (Academic Press London, 1973).

298 Langlois, W. E. & Deville, M. O. *Slow viscous flow* (Springer, 1964).

299 Lin, S., Zhao, L., Guest, J. K., Weihs, T. P. & Liu, Z. Topology optimization of fixed-geometry fluid diodes. *Journal of Mechanical Design* **137**, 081402 (2015).

300 Zhang, S., Winoto, S. & Low, H. Performance simulations of tesla microfluidic valves. In *2007 First International Conference on Integration and Commercialization of Micro and Nanosystems*, 15–19 (American Society of Mechanical Engineers, 2007).

301 Goldstein, S. *Modern developments in fluid dynamics: an account of theory and experiment relating to boundary layers, turbulent motion and wakes*, vol. 1 (Clarendon Press, 1938).

302 Schlichting, H., Gersten, K., Krause, E., Oertel, H. & Mayes, K. *Boundary-layer theory*, vol. 7 (Springer, 1960).

303 Loverich, J., Kanno, I. & Kotera, H. Single-step replicable microfluidic check valve for rectifying and sensing low reynolds number flow. *Microfluidics and Nanofluidics* **3**, 427–435 (2007).

304 Nguyen, N.-T., Truong, T.-Q., Wong, K.-K., Ho, S.-S. & Low, C. L.-N. Micro check valves for integration into polymeric microfluidic devices. *Journal of Micromechanics and Microengineering* **14**, 69 (2003).

305 Sochol, R. D. *et al.* A single-microbead-based microfluidic diode for ultra-low Reynolds Number applications. In *Micro Electro Mechanical Systems (MEMS), 2012 IEEE 25th International Conference on*, 160–163 (2012).

306 Purcell, E. M. Life at low reynolds number. *American journal of physics* **45**, 3–11 (1977).

307 Razavi, B. *Fundamentals of Microelectronics* (John Wiley & Sons, Inc, Hoboken, NJ, USA, 2008).

308 Gray, P. R. & Meyer, R. G. *Analysis and design of analog integrated circuits* (John Wiley & Sons, Inc., 1990).

309 Eric W. Weisstein. Lambert W-Function. http://mathworld.wolfram.com/LambertW-Function.html. Visited on 17/04/16.

310 Sochol, R. D. *et al.* Single-layer "domino" diodes via optofluidic lithography for ultra-low Reynolds number applications. In *Micro Electro Mechanical Systems (MEMS), 2013 IEEE 26th International Conference on*, 153–156 (2013).

311 Chiu, D. *et al.* Patterned deposition of cells and proteins onto surfaces by using three-dimensional microfluidic systems. *Proceedings Of The National Academy Of Sciences Of The United States Of America* **97**, 2408–2413 (2000).

312 Abdelgawad, M. *et al.* A fast and simple method to fabricate circular microchannels in polydimethylsiloxane (PDMS). *Lab Chip* **11**, 545–551 (2011).

313 Toepke, M. W. & Kenis, P. J. A. Multilevel microfluidics via single-exposure photolithography. *Journal of the American Chemical Society* **127**, 7674–7675 (2005). PMID: 15913346.

314 Gray, B. *et al.* Novel interconnection technologies for integrated microfluidic systems1. *Sensors and Actuators A: Physical* **77**, 57–65 (1999).

315 Au, A. K., Huynh, W., Horowitz, L. F. & Folch, A. 3D-printed microfluidics. *Angewandte Chemie International Edition* **55**, 3862–3881 (2016).

316 Sochol, R. D. *et al.* 3D printed microfluidic circuitry via multijet-based additive manufacturing. *Lab Chip* – (2016).

317 Yuen, P. K. & Goral, V. N. Low-cost rapid prototyping of flexible microfluidic devices using a desktop digital craft cutter. *Lab Chip* **10**, 384–387 (2010).

318 Tseng, P., Murray, C., Kim, D. & Di Carlo, D. Research highlights: printing the future of microfabrication. *Lab Chip* **14**, 1491–1495 (2014).

319 Ho, C. M. B., Ng, S. H., Li, K. H. H. & Yoon, Y.-J. 3D printed microfluidics for biological applications. *Lab Chip* **15**, 3627–3637 (2015).

320 Amin, R. *et al.* 3D-printed microfluidic devices. *Biofabrication* **8**, 022001 (2016).

321 Bhattacharjee, N., Urrios, A., Kang, S. & Folch, A. The upcoming 3D-printing revolution in microfluidics. *Lab Chip* **16**, 1720–1742 (2016).

322 Farré-Lladós, J., Casals-Terré, J., Voltas, J. & Westerberg, L. G. The use of rapid prototyping techniques (RPT) to manufacture micro channels suitable for high operation pressures and μpiv. *Rapid Prototyping Journal* **22**, 67–76 (2016).

323 Altan, T. *et al.* Advanced techniques for die and mold manufacturing. *CIRP Annals–Manufacturing Technology* **42**, 707–716 (1993).

324 Maltezos, G., Johnston, M., Maltezos, D. G. & Scherer, A. Replication of three-dimensional valves from printed wax molds. *Sensors and Actuators A: Physical* **135**, 620–624 (2007).

325 Duncombe, T. A., Parsons, J. F. & Böhringer, K. F. Directed drop transport rectified from orthogonal vibrations via a flat wetting barrier ratchet. *Langmuir* **28**, 13765–13770 (2012). PMID: 22934529.

326 Stroock, A. D. & Whitesides, G. M. Components for integrated poly (dimethylsiloxane) microfluidic systems. *Electrophoresis* **23**, 3461–3473 (2002).

327 Dippenaar, D. J. & Schreve, K. 3D printed tooling for vacuum-assisted resin transfer moulding. *The International Journal of Advanced Manufacturing Technology* **64**, 755–767 (2013).

328 Velvé-Casquillas, G., La Berre, M., Terriac, E. & Bertholle, F. PDMS thickness vs spin-coating speed (2009). http://www.elveflow.com/microfluidic/PDMS%20thickness%20VS%20spin%20speed.pdf.

329 David, J. R. *et al.* Method of conforming an adherent film to a substrate by application of vacuum. 6872268 (2005).

330 Torres, M. *et al.* Monitoring of the curing process of composite structures by tunnelling junction sensors. *Sensors and Actuators A: Physical* **235**, 256–264 (2015).

331 Cassano, C. L., Simon, A. J., Liu, W., Fredrickson, C. & Hugh Fan, Z. Use of vacuum bagging for fabricating thermoplastic microfluidic devices. *Lab Chip* **15**, 62–66 (2015).

332 Chen, P.-C., Liu, Y.-M. & Chou, H.-C. An adhesive bonding method with microfabricating micro pillars to prevent clogging in a microchannel. *Journal of Micromechanics and Microengineering* **26**, 045003 (2016).

333 Squires, T. M. & Quake, S. R. Microfluidics: Fluid physics at the nanoliter scale. *Reviews Of Modern Physics* **77**, 977 (2005).

334 Eddings, M. A., Johnson, M. A. & Gale, B. K. Determining the optimal PDMS-PDMS bonding technique for microfluidic devices. *Journal of Micromechanics and Microengineering* **18**, 067001 (2008).

335 Whitesides, G. The 'right' size in nanobiotechnology. *Nature Biotechnology* **21**, 1161–1165 (2003).

336 GmbH, A. P. Viscopedia — A free encyclopedia for viscosity (2016). http://www.viscopedia.com/viscosity-tables/substances/paraffin-wax/.

337 Syvum Technologies. Transport phenomena fluid mechanics problem solution bsl : Radial flow of a newtonian fluid between two parallel disks. http://www.syvum.com/cgi/online/serve.cgi/eng/fluid/fluid306.html.

338 Na, T. Y. & Hansen, A. G. Radial flow of viscous non-newtonian fluids between disks. *International Journal of Non-Linear Mechanics* **2**, 261–273 (1967).

339 3D Systems. VisiJet® EX 200 Plastic Datasheet (2009). http://www.3dsystems.com/products/datafiles/visijet/datasheets/Visijet_EX200_Info_0509.pdf.

340 Sochol, R. *et al.* Bead-Immobilized Molecular Beacons for High Throughput SNP Genotyping Via a Microfluidic System. *Micro Electro Mechanical Systems, 2009. MEMS 2009. IEEE 22nd International Conference on* 304–307 (2009).

341 Nguyen, T., Ahrar, S., Duncan, P. & Hui, E. Microfluidic finite state machine for autonomous control of integrated fluid networks. In *Proceedings of Micro Total Analysis Systems*, 741–743 (2011).

342 Heijboer, J. P. *Transmitting valves: the use of pentodes, tetrodes and triodes in transmitter circuits*, vol. 7 (Philips' Technical Library, 1951).

343 Reich, H. J. *Theory and applications of electron tubes* (McGraw-Hill Book Company, inc., 1944).

344 Savage, J. personal communication. Representative to Engitype, Inc.

345 Monie, D. D. & Bhatia, S. K. *Bioprinting of Dynamic Human Organs-on-Chips: Enabling Technologies for Rapid Drug Development and Personalized Medicine*, 123–137 (Springer, New York, 2015), 1 edn.

346 3D Systems. VisiJet® EX 200 Plastic MSDS (2009). http://www.3dsystems.com/products/datafiles/visijet/msds/EX200/24184-S12-00-A_SDS_Reach_English_EX_200.pdf.

347 3D Systems. VisiJet® S100,S300 Support Material MSDS (2012). http://www.3dsystems.com/products/datafiles/visijet/msds/s100-s300/23126-S02-02-B-MSDS-US-VisiJet-S100-S300.pdf.

348 3D Systems. ProJet™ HD 3000 Technical Specifications (2009). http://www.3dsystems.com/products/datafiles/projet/ProJet_HD_3000_Brochure_USEN.pdf.

349 Mills, D. L. & Maradudin, A. A. Surface roughness and the optical properties of a semi-infinite material; the effect of a dielectric overlayer. *Phys. Rev. B* **12**, 2943–2958 (1975).

350 Krč, J., Zeman, M., Kluth, O., Smole, F. & Topič, M. Effect of surface roughness of ZnO:Al films on light scattering in hydrogenated amorphous silicon solar cells. *Thin Solid Films* **426**, 296–304 (2003).

351 Ragheb, H. & Hancock, E. R. The modified Beckmann-Kirchhoff scattering theory for rough surface analysis. *Pattern Recognition* **40**, 2004–2020 (2007).

352 Pinel, N., Bourlier, C. & Saillard, J. Degree of roughness of rough layers: extensions of the rayleigh roughness criterion and some applications. *Progress In Electromagnetics Research B* **19**, 41–63 (2010).

353 Whitesides, G. M. & Tang, S. K. Fluidic optics. In *SPIE Optics + Photonics*, 63290A–63290A (International Society for Optics and Photonics, 2006).

354 Earworm. https://en.wikipedia.org/wiki/Earworm.

355 Wald, K. The Heroine Barbarian. http://math.uchicago.edu/~wald/lit/heroine_barbarian.html.

356 Russell, A. How To Write Your Own Gilbert And Sullivan Opera (1953).